Jan Długosz University in Częstochowa

Faculty of Science and Technology

Department of Theoretical Physics

PhD THESIS

Myron Rudysh

Theoretical study of I-III-VI₂ group chalcopyrite crystals for photovoltaic application

Supervisor:

dr hab. Michał Piasecki, Prof. UJD

Field of exact and natural sciences

Physical science discipline

Częstochowa, 2022

To my family

AKNOWLEDGEMENT

CONTENT

ABSTRACT

Semiconducting chalcogenide materials are widely used in various electronics devices and have characteristics that make them attractive for practical use in various fields. In particular, an important application of chalcogenide materials is their use in photovoltaics to convert solar energy into electricity. Promising materials for solar energy are chalcogenide semiconductors with chalcopyrite structure having the formula I-III-VI$_2$. These materials reveal a number of advantages over others and have attracted the attention of researchers. The optimal band gap and high absorption coefficient make chalcogenides promising as thin-film absorbing materials in high-performance heterojunction solar cells. One of the representatives of such materials is copper indium gallium selenide $CuIn_{1-x}Ga_xSe_2$ (CIGS). It demonstrates the efficiency of solar energy conversion up to 23.4% and in the perovskite/CIGS tandem solar cells – 24.2%. Therefore, the study of semiconductor materials is an important and relevant task.

Despite the large number of complex and expensive experimental research, theoretical modeling within different approaches takes an important place in the study and search for new functional materials. Therefore, the process of new materials creation and their properties optimization for the different applications can be expensive and not efficient without predictive theoretical guidance. Thus, the preferable initial stage of new materials design is the computer modeling and simulations of their physical properties.

The aim of the present work was to investigate the structural, electronic, optical, elastic and vibrational properties of the I-III-VI$_2$ (I = Cu, Ag, III = Al, Ga, In, VI = S, Se, and Te) crystals using theoretical methods. To date, a comprehensive theoretical study of the properties of crystals of the studied group has not been performed. There are some studies of materials of this group, the analysis of which is complicated by the use of different methods and approximations that give different limitations and, as a consequence, different deviations from the experiment. In the presented work a series of theoretical studies of the physical properties of the I-III-VI$_2$ (I = Cu, Ag, III = Al, Ga, In, VI = S, Se, Te) crystal family were carried out within the unified approach.

The band-energy structures of eighteen crystals of the titled group were studied and the origin of their energy bands was clarified using the density functional theory together with the LDA and GGA exchange-correlation functionals. The effect of changes in the cationic-anionic composition on the structure of these electronic levels in crystals has been

elucidated. Quantitative and qualitative characteristics of the band structures of these crystals are evaluated.

The disadvantages of applying the standard calculation method for energy levels corresponding to *d*-electrons for crystals with In and Ga ions are shown. For such crystals it is proposed to use calculations with Hubbard corrections (DFT + *U*) to take into account the drawbacks of standard calculation methods.

The optical spectra of crystals of I-III-VI$_2$ group, including dielectric functions, absorption spectra, refractive indices, etc., were calculated. The possibility of using these materials as absorbing layers in solar cells is shown.

The linear electro-optics, electrogyration coefficients and second-order nonlinear susceptibility of AgGaS$_2$ crystals are calculated in the frame of the DES model. Using dispersion of the electronic polarizability volumes calculated using the Lorentz–Lorenz formula, the value of nonlinear susceptibility for $\lambda = 1064$ nm is obtained.

Elastic properties, which includes obtaining elastic coefficients C_{ij}, bulk modulus *B*, Young's modulus *E*, shear modulus *G* and Poisson's ratio *v* were calculated for eighteen crystals of the studied group. The tendency of changes of properties and their anisotropy at isomorphic substitutions of cationic-anionic composition is shown. 3D distribution surfaces of elastic modulus and their planar projections were constructed. These allowed to show visually the change of anisotropy when the composition of the material changes.

The correlation analysis of structure-properties and properties-properties relations for selected quantities is carried out. A number of correlations were found that show the functional dependences between the physical parameters for the studied group of crystals.

The peculiarities of the phonon spectrum in AgGaX$_2$ crystals (where X = S, Se, Te) are clarified within the framework of harmonic approximation. A symmetric classification of vibrational modes is performed and the consistency of theoretical results to experimental ones is shown, which verifies the technique used. The structure and transformation of the phonon spectrum at isomorphic substitution of the S $\rightarrow$ Se $\rightarrow$ Te anions are shown.

The possibility of controlling the optical, electronic and elastic properties of crystals by forming substitutional solid solutions on the example of the CuGa(S$_{1-x}$Se$_x$)$_2$ system for *x* = 0, 0.25, 0.5, 0.75, and 1 has been investigated.

In conclusion, a comprehensive theoretical study of electronic structure, optical, elastic and vibrational properties of crystals of the I-III-VI$_2$ group have been performed within the theory of density functional. The possibility of applying and modifying the properties of materials for efficient use as materials for solar energy is shown.

STRESZCZENIE

Półprzewodnikowe materiały chalkogenkowe są szeroko stosowane w różnych urządzeniach elektronicznych i mają właściwości, które czynią je atrakcyjnymi do stosowania w różnych dziedzinach. W szczególności ważnym zastosowaniem materiałów chalkogenkowych jest ich wykorzystanie w fotowoltaice do przekształcania energii słonecznej w energię elektryczną. Obiecującymi materiałemi dla energetyki słonecznej są półprzewodniki chalkogenkowe o strukturze chalkopirytowej o wzorze I-III-VI$_2$. Materiały te mają wiele zalet w porównaniu z innymi i przyciągnęły uwagę naukowców ze względu na optymalną przerwę energetyczną i wysoki współczynnik absorpcji, co czyni je obiecującymi jako cienkowarstwowe materiały pochłaniające w wysokowydajnych heterozłączowych ogniwach słonecznych. Jednym z przedstawicieli takich materiałów jest selenek miedziowo-indowo-galowy $CuIn_{1-x}Ga_xSe_2$ (CIGS). Wykazuje on efektywność konwersji energii słonecznej do 23.4%, a w ogniwach słonecznych tandemowych perowskit/CIGS – 24.2%. Dlatego badanie materiałów półprzewodnikowych jest ważnym i aktualnym zadaniem.

Pomimo dużej liczby skomplikowanych i kosztownych badań eksperymentalnych, modelowanie teoretyczne w ramach różnych podejść zajmuje ważne miejsce w badaniach i poszukiwaniu nowych materiałów funkcjonalnych. W związku z tym proces tworzenia nowych materiałów i optymalizacji ich właściwości dla różnych zastosowań może być kosztowny i nieefektywny bez predykcyjnych wskazówek teoretycznych. Dlatego preferowanym początkowym etapem projektowania nowych materiałów jest modelowanie komputerowe i symulacje ich właściwości fizycznych.

Celem niniejszej pracy było zbadanie właściwości strukturalnych, elektronowych, optycznych, sprężystych i wibracyjnych kryształów I-III-VI$_2$ (I = Cu, Ag, III = Al, Ga, In, VI = S, Se i Te) metodami teoretycznymi. Do tej pory nie przeprowadzono kompleksowego teoretycznego badania właściwości kryształów badanej grupy. Istnieje kilka badań materiałów z tej grupy, których analizę komplikuje stosowanie różnych metod i przybliżeń, które dają różne ograniczenia i w konsekwencji różne odchylenia od eksperymentu. W prezentowanej pracy przeprowadzono szereg badań teoretycznych właściwości fizycznych kryształów rodziny I-III-VI$_2$ (I = Cu, Ag, III = Al, Ga, In, VI = S, Se, Te) w ramach podejścia zunifikowanego.

Zbadano strukturę pasmowo-energetyczną osiemnastu kryształów wskazanej grupy i wyjaśniono pochodzenie ich pasm energetycznych wykorzystując teorię funkcjonału gęstości wraz z funkcjonałami wymienno-korelacyjnymi LDA i GGA. Wyjaśniono wpływ

zmian składu kationowo-anionowego na strukturę tych poziomów elektronowych w kryształach. Oceniane są ilościowe i jakościowe charakterystyki struktur pasmowych tych kryształów.

Pokazano wady stosowania standardowej metody obliczania poziomów energetycznych odpowiadających d-elektronom dla kryształów z jonami In i Ga. Proponuje się wykorzystanie obliczeń z poprawkami Hubbarda (DFT+U), aby uwzględnić wady standardowych metod obliczeniowych.

Obliczono widma optyczne kryształów z grupy I-III-VI$_2$, w tym funkcje dielektryczne, widma absorpcyjne, współczynniki załamania itp. Pokazano możliwość wykorzystania tych materiałów jako warstwy absorbującej w ogniwach słonecznych.

W ramach modelu DES obliczono liniową elektrooptykę, współczynniki elektrowirowania i nieliniową podatność drugiego rzędu kryształów AgGaS$_2$. Wykorzystując dyspersję elektronowych objętości polaryzowalności obliczonych ze wzoru Lorentza–Lorenza otrzymano wartość nieliniowej podatności dla λ = 1064 nm.

Obliczono właściwości sprężyste dla osiemnastu kryształów z badanej grupy, w tym zachowanie współczynników sprężystości C_{ij}, modułu sprężystości B, modułu Younga E, modułu ścinania G oraz współczynnika Poissona v. Pokazano tendencję do zmian właściwości i ich anizotropii przy izomorficznych podstawieniach składu kationowo-anionowego. Skonstruowano trójwymiarowe powierzchnie rozkładu modułu sprężystości i ich rzuty planarne, co pozwoliło na wizualne ukazanie zmiany anizotropii przy zmianie składu materiału.

Przeprowadzono analizę korelacyjną zależności struktura-właściwości i właściwości-właściwości dla wybranych wielkości. Znaleziono szereg korelacji, które wykazują funkcjonalną zależność pomiędzy parametrami fizycznymi dla badanej grupy kryształów.

Wyjaśniono osobliwości widma fononowego w ramach przybliżenia harmonicznego w kryształach AgGaX$_2$ (gdzie X = S, Se, Te). Przeprowadzono symetryczną klasyfikacje modów oscylacyjnych i pokazano zgodność wyników teoretycznych z eksperymentalnymi, co weryfikuje zastosowaną technikę. Pokazano strukturę i transformację widma fononowego przy izomorficznym podstawieniu anionu S → Se → Te.

Zbadano możliwość kontrolowania właściwości optycznych, elektronowych i sprężystych kryształów poprzez tworzenie stałych roztworów podstawieniowych na przykładzie układu $CuGa(S_{1-x}Se_x)_2$ dla $x = 0$, 0.25, 0.5, 0.75 i 1.

Podsumowując, możemy stwierdzić, że przeprowadzone są kompleksowe teoretyczne badania kryształów grupy $I-III-VI_2$, a mianowicie struktury elektronowej, właściwości optycznych, sprężystych i wibracyjnych w ramach teorii funkcjonału gęstości. Pokazano możliwości zastosowania i modyfikacji właściwości materiałów w celu efektywnego wykorzystania jako materiałów do energii słonecznej.

LIST OF ABBREVIATIONS

ARC   antireflective coating

BE   binding energy

BOA   Born-Oppenheimer approximation

BSI   birefringence sign inversion

BZ   Brilluoin zone

B3LYP   Becke, 3-parameter, Lee–Yang–Parr

CASTEP   CAmbridge Serial Total Energy Package

CA-PZ   Caperly-Alder-Perdew-Zunger

CBM   conduction band minimum

CIAS $CuIn_{1-x}Al_xSe_2$

CIGS $CuIn_{1-x}Ga_xSe_2$

CP   chalcopyrite

DES   dipole-dipole interaction electron-cloud shifting model

DFPT   density functional perturbation theory

DFT   density functional theory

DOS   density of states

GGA   generalized gradient approximation

IBZ   irreducible Brilluoin zone

IP   isotropic point

IR   infrared

FF   fill factor

KS   Kohn-Sham

LCAO   linear combination of atomic orbitals

LDA   local density approximation

LIDT   laser-induced damage threshold

MT   muffin-tin

NCPP   norm-conserving pseudopotential

OPO   optical parametric oscillator

OVC   ordered vacancy compound

PBE   Perdew-Burke-Ernzerhof

PDOS   partial density of states

PPs   pseudopotential

PT	phase transition
PV	photovoltaics
PVMB	potential-variation mixed-basis
PW	plane wave
R	Raman
SAC	second anion coordination
SCF	self-consistent field
TE	termoelectric
USPP	ultrasoft pseudopotential
VB	valence band
VBM	valence band maximum
VWN	Vosko-Vilk-Nusair
XC	exchange and correlation
XES	X-ray emission spectroscopy
XPS	X-ray photoelectron spectroscopy
XRD	X-ray diffraction
ZB	zinc blende

LIST OF SYMBOLS

A	acoustic anisotropy
A^U	universal anisotropy index
A_1, A_2, A_3	shear anisotropy indices
A_B	bulk anisotropy of polycrystal
A_G	shear anisotropy of polycrystal
B	bulk modulus
c	speed of light
C_n	rotation by $2\pi/n$ (proper rotation)
C_{ij}	elastic constants
D_r	standard relative deviation
$D(\omega)$	phonon density of states
d_r	relative change of volume
d_{ij}	nonlinear optical coefficient
e	electron charge
E_g	bandgap energy
E	Young's modulus
E	identity
E_F	Fermi level
$E[n]$	total energy as a functional of the electron density
f_h	bond iconicity
G	shear modulus
h	Plank's constant
H	Hamiltonian operator
I_{sc}	short circuit current
k	wave number
$\mathbf{k}$	wave vector
k_B	Boltzmann constant
l_i	directional cosines
m_0	electron rest mass
m^*	effective mass
n	refractive index
$N(E)$	density of states

Q_d	dynamical charge
r_{ij}	electrooptic coefficient
R_{xy}, R	Pearson's correlation coefficient
S_{ij}	elastic constant
u	cation shift
U	Habbard parameter
V_{max}	maximum value of sound speed
V_{min}	minimum value of sound speed
V_H	Hartree potential
V_{XC}	exchange-correlation potential
V_{oc}	open-circuit voltage
Z^*	Born charge
α	absorption coefficient
α_{ij}	polarizability tensor
Δ_{CF}	crystal field energy
Δ_g	scissor operator
Δn	birefringence
$\varepsilon(\omega)$	complex dielectric function
ε_∞	high-frequency dielectric constant
ε_0	dielectric permittivity of vacuum/static dielectric constants
η	tetragonal deformation
Θ_D	Debye temperature
λ	wavelength
μ	carrier mobility
ν	frequency
v_{ij}	Poisson's ratio
ρ	crystal density
ρ_{ij}	optical rotation tensor
σ	conductivity
σ_x, σ_y, σ_z	reflection planes perpendicular to x, y, and z, respectively
τ	electron relaxation time
$\tau_{k\beta}$	displacenet of kth atom in β-direction
ϕ	basis function of single electron wave function
χ_i	character

χ_{ij}	dielectric susceptibility
Ψ	many body wave function
ψ	single-electron wave function
ω	angular frequency
$\hbar$	Plank's constant divided by 4π (Dirak's constant)
$\otimes$	direct product
$\oplus$	direct sum

1. INTRODUCTION

Rapid increasing of energy consumption together with continuous use of the technologies based on combustion of the hydrocarbons can be defined as the key environmental problem nowadays. The permanent necessity of increasing the production of the electrical energy make the search of alternative sources of energy very actual. The use of solar energy is being given more and more attention on the planet. Conversion of the solar energy into electricity by using solar cells offers a unique opportunity for the environment friendly production of electrical energy and can provide the energetical independence of European countries. Various materials, both organic and inorganic, have been successfully tested for such photovoltaic (PV) applications. As a result, remarkable progress in this field has been achieved, [1−4] and the search for new materials with improved performance is never stopped. The use of solar cells is becoming increasingly popular year by year. These facts make research in this area extremely popular and important. The development of these technologies reduces the cost of materials and increases the efficiency of solar cells. Their application in different spheres gives hope that people will finally stop poisoning the Earth's atmosphere, which will positively affect their health and improve ecological situation.

Nowadays considerable progress has been achieved in the development of experimental methods of chalcopyrite (CP) production. At the same time, very rapid advances in reliable computational methods based on the density functional theory (DFT) have paved a broad way towards increasing the importance of so-called "theoretical experiments", when thoroughly performed calculations replace or forego experiments and even predict unknown materials and their properties [5,6]. Such "theoretical experiments" are relatively costless, if compared to the real laboratory equipment; however, the results of such calculations serve as extremely useful guides for setting up a proper direction in the search for new efficient materials.

Chalcopyrite compounds form a very large and versatile group of materials, which are used as active absorbers in solar cells [5, 6], spintronics [7,8] and IR lasers [5,9], LED etc. Typically, they are ternary semiconductors with general chemical formula I-III-VI$_2$ (I = Cu, Ag, III = In, Ga, Al, VI = S, Se, Te etc.) or II-IV-V$_2$ (II = Be, Mg, Zn, Cd, IV = C, Si, Ge, Sn, V = N, P, As, Sb etc). There exist a very few systematic studies of the CP, which

would offer comparison of their main properties and explanation of differences or similarities existing between various compounds. This will fill in this gap by consistent and systematic studies of a wide range of physical properties of CP crystals.

Since I-III-VI$_2$ ternary semiconductors with chalcopyrite structure have been shown to be very suitable materials for solar cell panels, this study will be devoted to the theoretical investigation of titled group of CP materials using an *ab initio* method based on DFT.

The crystals of I-III-VI$_2$ group are attractive objects for study both from fundamental and applied points of view because of their potential applications. They can be used as active elements for nonlinear optics, as optical filters, LED application, high-efficiency quantum dots for photocatalysis (for example CuGaS$_2$ crystal [10]), sensors and, most prospective-in solar cell application. Also, possibility to produce the high quality thin films makes CP very attractive for thin-films sensors and solar cells. In the literature we can find separate researches concerning particular properties of the CP and few theoretical studies of band structure, optical as well as elastic properties [11]. A very few systematic study of the CP, which would offer comparison of their properties and establishing of general tendency of properties behavior during composition change motivate us to carry out such investigation.

The goal of the presented study is the systematic and consistent study using the DFT of electronic, optic, elastic and other physical properties, as well as establishing of the relationship between the structure-property and property-property dependences of I-III-VI$_2$ ternary CP semiconductors for solar cells application.

Object of study: band structure, peculiarities of the formation of electronic states of the valence band and the conduction band, the nature of the chemical bond in the crystals, optical, elastic and vibrational properties of ternary semiconductors of group I-III-VI$_2$, influence of isomorphic substitution on structure and properties.

Subject of study: ternary semiconductor crystals of group I-III-VI$_2$ with chalcopyrite structure.

The aim and tasks of the work

The aim of the dissertation is an investigation of structural, electronic, optical, elastic and vibrational properties of the I-III-VI$_2$ (I = Cu, Ag, III = Al, Ga, In, VI = S, Se, and Te) crystals using theoretical methods.

Thesis of work

Modification of the cationic-anionic composition of I-III-VI$_2$ crystals is an effective way of tuning the properties of the materials useful for photovoltaic applications.

Hypothesis:

1. Theoretical simulations allow to estimate effectively the quantitative and qualitative characteristics of I-III-VI$_2$ crystals.

2. The relationships between structure-property and property-property of I-III-VI$_2$ group crystals can be revealed using theoretical calculations.

3. A gradual change of the composition of the I-III-VI$_2$ group crystals allows fine-tuning of the material parameters.

4. The use of the DFT+U technique can correct some of the special shortcomings of the description of the interaction of d-electrons in I-III-VI$_2$ systems.

5. Variation of chemical composition (which includes partial or complete anion or cation substitution) should strongly affect the optical and electronic properties of solar cell materials.

The tasks of the dissertation are:

1. To investigate the electronic structure, genesis of electronic levels of crystals of I-III-VI$_2$ group with the structure of chalcopyrite using DFT methodology with different corrections.

2. To study theoretically the nature of chemical bonding, optical functions and peculiarities of structure change during the isomorphic substitution of I-III-VI$_2$ crystals.

3. To calculate the elastic coefficients and elastic modules for I-III-VI$_2$ crystals.

4. To investigate the mechanical stability and propagation of acoustic waves in I-III-VI$_2$ crystals. To obtain the speed of acoustic waves propagation in materials and evaluate their anisotropy.

5. To make a description of vibrational properties and lattice dynamics of the AgGaX$_2$ system (X = S, Se, and Te). To perform the symmetric analysis of vibrations.

6. To investigate the effect of isomorphic substitution of S $\rightarrow$ Se in the CuGa(S$_{1-x}$Se$_x$)$_2$ system on the structure, electronic, optical and elastic properties of the compound.

Scientific novelty:

1. A complex theoretical study of electronic and physical properties of crystals with the structure of chalcopyrite belonging to I-III-VI$_2$ group is performed for the first time in the framework of density functional theory, within unified approach and using LDA and GGA functionals.

2. The possibility of correct description of electronic states using the DFT + U technique for correction of the position of electronic d-levels and band gap underestimation was shown for the first time.

3. Nonlinear optical parameters for the AgGaS$_2$ crystal were characterized within the dipole-dipole interaction electron-cloud shifting model.

4. Based on the theoretical-group analysis of the three-dimensional structure of chalcopyrite crystals, the selection rules for optical dipole transitions are established. A symmetric analysis of vibrational spectra of I-III-VI$_2$ crystals is performed.

5. A number of structure-property and property-property dependences for crystals of I-III-VI$_2$ group are obtained.

6. The formation of substitutional solid solution is shown to be an effective method of modification of structural, electronic, optical and elastic parameters of CuGaS$_2$ crystals.

7. It was shown that replacement of S $\rightarrow$ Se in the CuGa(S$_{1-x}$Se$_x$)$_2$ system have a significant sensitivity of the physical parameters to the composition of the compound, which allows controlling of its properties. The compounds with $x = 0.68$ have the lowest value of the deformation parameter η, which is consistent with the experiment.

1.1. List of publications on the subject of the thesis

1. **M.Ya. Rudysh**, P.A. Shchepanskyi, A.O. Fedorchuk, M.G. Brik, V.Yo. Stadnyk, G.L Myronchuk, E.A. Kotomin, M. Piasecki, Impact of anionic system modification on the desired properties for CuGa(S$_{1-x}$Se$_x$)$_2$ solid solutions, *Computational Materials Science*, 196, 110553, 2021.

2. **M.Ya. Rudysh**, A.I. Kashuba, P.A. Shchepanskyi, R.Yu. Petrus, V.Yo. Stadnyk, M. Piasecki, Calculation of the vibrational spectra of AgGaS$_2$ crystal with chalcopyrite structure, *Journal of Physical Study*, 25(3), 3704, 2021.

3. **M.Ya. Rudysh**, P.A. Shchepanskyi, A.O. Fedorchuk, M.G. Brik, C.-G. Ma, G.L. Myronchuk, M. Piasecki, First-principles analysis of physical properties anisotropy for

the Ag_2SiS_3 chalcogenide semiconductor, *Journal of Alloys and Compounds*, 826, 154232, 2020.

4. **M.Ya. Rudysh**, M. Piasecki, G.L. Myronchuk, P.A. Shchepanskyi, V.Yo. Stadnyk, O.R. Onufriv, M.G. Brik, $AgGaTe_2$ – the thermoelectric and solar cell material: structure, electronic, optical, elastic and vibrational features, *Infrared Physics and Technology*, 111, 103476, 2020.

1.2. Conference activities

Oral presentations

1. **M.Ya. Rudysh**, M.G. Brik, O.R. Onufriv, M. Piasecki, V.Yo. Sradnyk, P.A. Shchepanskyi, "*Ab initio study of crystal structure and physical properties of chalcopyrite $CuGa(S_2)_x(Se_2)_{1-x}$ solid solution*", V Ukrainian-Polish-Lithuanian meeting on physics of ferroelectrics, Uzhhorod, Ukraine, September 18-20, 2018.

2. **M.Ya. Rudysh**, M.G. Brik, M. Piasecki, "*Electronic structure, elastic and optical properties simulation of $CuGa(S, Se)_2$ chalcopyrite solid solution: DFT study*", Young scientists conference on semiconductor physics «Lashkaryov's readings 2019», Kyiv Ukraine, April 2-5, 2019.

3. **M.Ya. Rudysh**, M.G. Brik, M. Piasecki, G.L. Myronchuk, "*Optical spectra and band structure of Cu-based chalcopyrite for solar cell application: theoretical study*", International Conference of students and young scientists in theoretical and experimental physics "HEUREKA-2019", Lviv, Ukraine, May 14-16, 2019.

4. **M.Ya. Rudysh**, G.L. Myronchuk, "*Anisotropy and elastic properties of ternary chalcogenide Ag_2XS_3 (where X = Si, Ge and Sn)*", International conference of students and young scientists in theoretical and experimental physics "HEUREKA-2019", Lviv, Ukraine, May 14-16, 2019.

5. **M.Ya. Rudysh**, M. Piasecki, M.G. Brik, "*Theoretical study of electronic structure and physical properties of $AgGaTe_2$ chalcopyrite crystal*", International workshop for young scientists "Functional materials for technical and biomedical applications", Koropovo-Kharkiv, Ukraine, September 9-12, 2019.

6. **M.Ya. Rudysh**, G.L. Myronchuk, A.O. Fedorchuk, M.G. Brik, M. Piasecki, "*Changing the physical properties of $CuGa(S_{1-x}Se_x)_2$ by changing the composition*", 10th international conference Relaxed, nonlinear and acoustic optical processes and materials "RNAOPM 2020", Lutsk-Like Svityaz', Ukraine, June 25-29, 2020.

7. **M.Ya. Rudysh**, M. Piasecki, M.G. Brik, V.Yo. Stadnyk, G.L. Myronchuk, *"Theoretical investigation of electronic structure and physical properties of ABC_2 group crystals: DFT study"*, International workshop for young scientists "Functional materials for technical and biomedical applications", Koropovo-Kharkiv, Ukraine, September 7-10, 2020.

8. **M. Rudysh**, *"Application of DFT+U method for study of the ABC_2 group crystals"*. International Conference of students and young scientists in theoretical and experimental physics "HEUREKA-2020", Lviv, Ukraine, October 6-7, 2020.

9. **M.Ya. Rudysh**, *"Modelling of vibrational properties of $AgGaS_2$ crystals"*, III International internet conference for young researchers and students «Topical Issues of Fundamental and Applied Studies», Lutsk, Ukraine, April 12-13, 2021.

10. **M.Ya. Rudysh**, M. Piasecki, M.G. Brik, *"Investigation of electronic and elastic properties of $AgGaTe_2$ chalcopyrite crystals: DFT study"*, III International internet conference for young researchers and students «Topical Issues of Fundamental and Applied Studies», Lutsk, Ukraine, April 12-13, 2021.

11. **M. Rudysh** *"Elastic properties and anisotropy of I-III-VI_2 chalcopyrite crystals"* International conference of students and young scientists in theoretical and experimental physics «HEUREKA-2021», Lviv, Ukraine, May 18-20, 2021.

12. **Rudysh M.Ya.** *"Computational study of vibrational properties of $AgGaX_2$ (S = S, Se, and Te) crystals"* / M.Ya. Rudysh, G.L. Myronchuk, M.G. Brik, M. Piasecki // International conference of students and young scientists in theoretical and experimental physics «HEUREKA-2021», Lviv, Ukraine, May 18-20, 2021.

13. **M.Ya. Rudysh**, O.Y. Khyzhun, A.O. Fedorchuk, P.A. Shchepanskyi, V.Yo. Stadnyk, M.G. Brik, M. Piasecki *"Position of electronic d-levels of I-III-VI_2 group crystals"*, Fourth international conference "Actual Problems of Fundamental Science" (APFS'2021), Lutsk-Lake "Svityaz'", Ukraine, June 01-05, 2021.

14. **M.Ya. Rudysh**, G.L. Myronchuk, *"Simulation of the vibrational properties of $CuAlS_2$ crystals"*, Fourth international conference "Actual Problems of Fundamental Science" – (APFS'2021), Lutsk-Lake "Svityaz'", Ukraine, June 01-05, 2021.

15. **M. Rudysh**, G. Myronchuk, O. Khyzhun *"Peculiarities of the dynamical properties in $AgAlS_2$ chalcopyrite crystals"* X International seminar "Properties of ferroelectric and superionic system", Uzhhorod, Ukraine, October, 26-27, 2021.

16. **M.Ya. Rudysh,** A. Popov, M. Piasecki, M.G. Brik, G.L. Myronchuk *"Hydrostatic pressure influence on structure and properties of $AgAlS_2$ crystals"* 13th Workshop on Current Problems in Physics, Lviv, Ukraine, October, 25-27, 2021.

17. **M.Ya. Rudysh**, G.L. Myronchuk, M. Piasecki, V.Yo. Stadnyk, R.S. Brezvin, P.A. Shchepanskyi, "*Ab initio study of electronic, optical, elastic, and vibrational properties of AgAlS$_2$ crystal*", XI International conference relaxed, nonlinear and acoustic optical processes and materials "RNAOPM-2022", Lutsk, Ukraine, June 01-05, 2022.

Poster

1. **M. Rudysh**, M. Brik, M. Piasecki, P. Shchepanskyi and V. Stadnyk "*Electronic structure and physical properties study of Ag$_2$XS$_3$ (X = Si, Ge, Sn) ternary semiconductors*", Joint conferences on advanced materials "Functional and Nanonstructured Materials (FNMA'2017) and Physics of Disordered Systems (PDS'2017)", Lviv-Yaremche, Ukraine, September 25-29, 2017.

2. **M.Ya. Rudysh**, A.O. Fedorchuk, M. G. Brik, M. Piasecki, I.V. Kityk, P.A. Shchepanskyi, "*Structure and properties of Ag$_2$XS$_3$ (X = Si, Ge) ternary chalcogenide*", IX International scientific conference "Relaxed, nonlinear and acoustic optical processes and materials" (RNAOPM'2018), Lutsk–Lake "Svityaz", Ukraine, June 1–5, 2018.

3. **M.Ya. Rudysh**, M.G. Brik, M. Piasecki, V.Yo. Stadnyk, A.S. Krymus, P.A. Shchepanskyi, "*Electronic structure, optical and elastic properties of CuInX$_2$ (X = S, Se, and Te) crystals*", Third international conference "Actual Problems of Fundamental Science", Lutsk-Lake Svityaz', Ukraine, June 01-05, 2019.

4. **M.Ya. Rudysh**, M.G. Brik, M. Piasecki, A.O. Fedorchuk, G.L. Myronchuk, "*Ab initio study of crystal structure and physical properties of CuGa(S$_x$Se$_{1-x}$)$_2$ solid solutions*", XXII international seminar on physics and chemistry of solids "ISPCS 2020", Lviv, Ukraine, June 17-19, 2020.

1.3. Grants and scientific projects

- Grant number 2018/29/N/ST3/02901 „*Theoretical investigation of physical properties of chalcopyrite semiconductors for solar cell applications*" financed by the National Science Centre (Poland) realised from 31.01.2019 – 30.01.2022.

2. LITERATURE REVIEW OF STRUCTURE AND PROPERTIES OF I-III-VI$_2$ GROUP MATERIALS

2.1. Structure and synthesis of I-III-VI$_2$ (I = Cu, Ag, III = Al, Ga, In, VI = S, Se, and Te) crystals

2.1.1. Structure and origin of I-III-VI$_2$ group crystals

The I-III-VI$_2$ (or $A^I B^{III} C_2^{VI}$) crystals, where I = Cu, Ag, III = Al, Ga, In, VI = S, Se, and Te, are known to be crystallized in the chalcopyrite (CP) structure. These crystals are ternary semiconducting materials that belong to the group of diamond-like compounds. For this materials as a prototype phase is the CuFeS$_2$ crystal (the group is named after the mineral CuFeS$_2$ – chalcopyrite) [1]. Those materials are strongly related with the binary compounds $A^{II} C^{VI}$ and can be estimated by doubling of binary compound unit cell: $A^I B^{III} C_2^{VI} = 2 A^{II} C^{VI}$ (A^{II} – Zn, Cd, Hg; C^{VI} – S, Se, Te). At the same time, binary structures are derived from crystals such as C, Ge, and Si.

Let us consider in more detail the origin and relationship of chalcopyrites between several classes of semiconductor materials that are actively used in practice in electronics. In Fig. 2.1 depicted a schematic diagram showing the relationship of some semiconductor materials originated from a diamond-type structure. Today, one of the most famous materials used in modern semiconductor electronics is silicon. The silicon has a face-centered cubic diamond-like lattice. One way to form new materials from the structure of this crystal is to use a chemical substitution process. The easiest way is to replace one chemical element with atoms of the same group. Thus, crystals such as C and Ge can be obtained. Other, more complex compounds can be obtained by replacing a combination of elements that together must satisfy the octet rule which states that each atom can combine either by transfer of valence electrons from one atom to another atom must lose or gain electrons in order to achieve an octet. A semiconductors of group-IV element (C, Si, Ge) crystallize in the structure with tetrahedral bonds and four valence electrons. According to the Grimm-Sommerfeld rule [2], different combinations of compounds with the same tetrahedral bonds

are possible if the average number of valence electrons remains four. Since this condition holds for Si, the other materials derived from Si also have a tetrahedral structure.
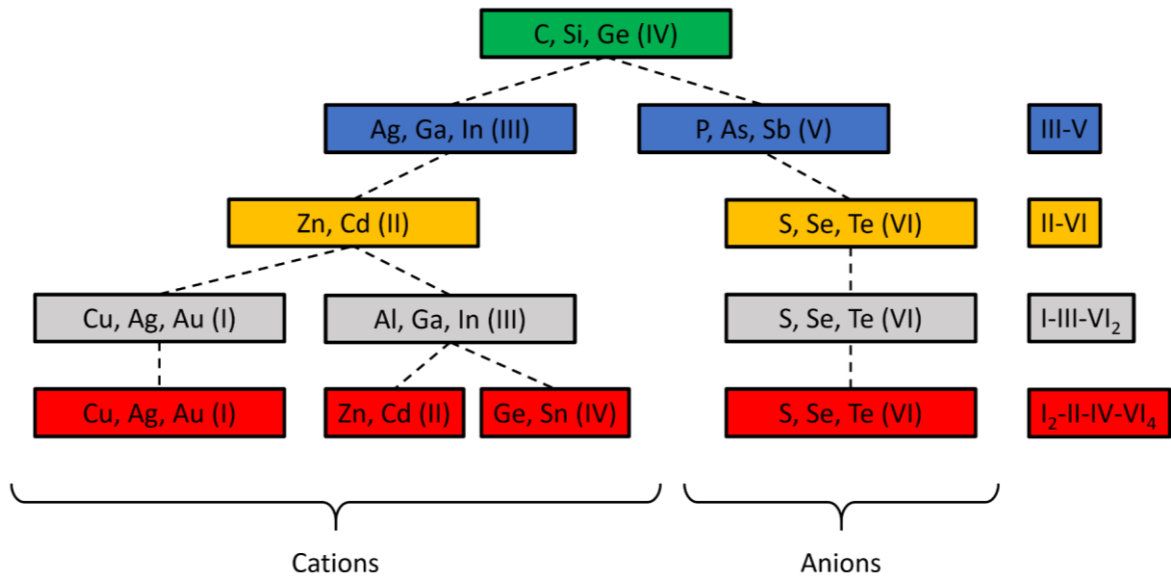
Figure 2.1. The origin of the binary, ternary and quaternary semiconductors derived from the face centered cubic structure of IV-elements.

A binary structure can be derived from the diamond structure by replacing the group-IV element by either one group-III and group-V element or by one group-II and group-VI element. This crystal structure is called zinc blende (ZB) structure [3]. An example of a material with a ZB structure are crystals ZnS, ZnSe (the name stems from the mineral ZnS) shown in the illustration on Fig. 2.2. This structure is very common for semiconductors e.g. GaAs, GaP, InAs, InSb, CdTe, etc. Crystals with the ZB structure has a unit cell with the space group symmetry F-43m (T_d^2). The structure of this crystals is disordered and is characterized by cationic disorder.

From binary compounds, as shown in Fig. 2.1 and 2.2, it is possible to form ternary semiconductor materials of group I-III-VI₂ by performing the ordered substitution of elements of group II. If the group-II element is further replaced by half a group-I and half a group-III element, the chalcopyrite structure is formed. Chalcopyrite materials at the normal conditions has a body centred Bravais lattice. The crystal has a tetragonal symmetry with the $I\overline{4}2d$ (D_{2d}^{12}) symmetry (space group #122). The crystal cell has four formula units ($Z = 4$). As already mentioned, these materials are formed from three types of atoms. Each atom of groups I and III is tetragonally bonded to four VI-atoms. The lowering of the symmetry
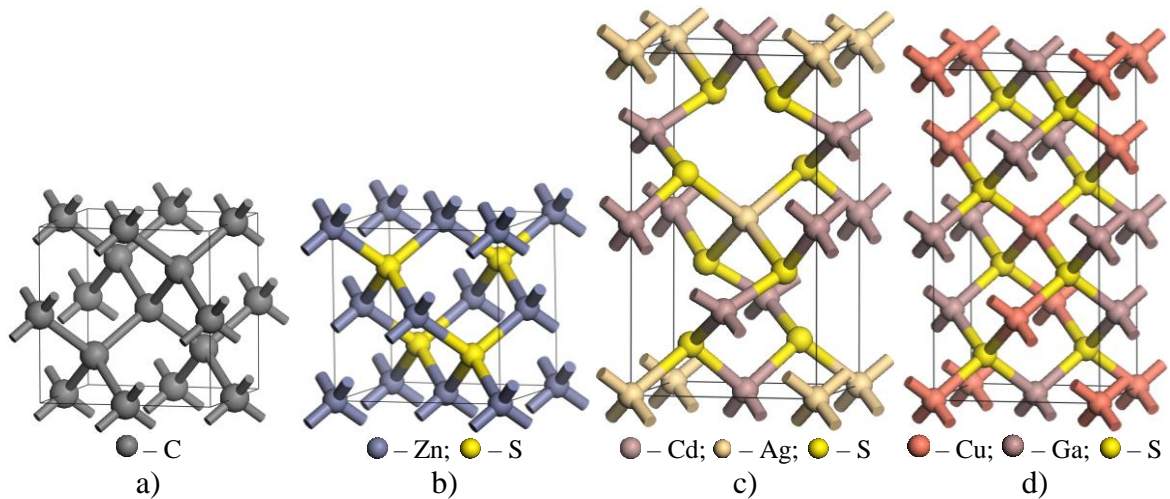
Figure 2.2. The wiev of an elementary cell for representatives of some crystalline groups derived from the diamond structure: a) face-centered cubic lattice of diamond β-prototype, C, b) ZnS – face-centered cubic lattice of sphalerite, (prototype ZnS), c) face-centered tetragonal lattice of thiogalate (prototype CdGa$_2$S$_4$), d) body-centered tetragonal lattice of chalcopyrite (prototype CuFeS$_2$).

leads to significant differences between these two tetrahedral structures. In the chalcopyrite structure, each A and B cation is bonded to four C nearest neighbors and each anion has two A cations and two B cations as nearest neighbors. Consequently, the cations form two separate AC$_4$ and BC$_4$ tetrahedra, while the corners of the anion-centered tetrahedron are occupied by two pairs of A and B atoms. Moreover, while the anion has twelve other anions as second nearest neighbors (as in the ZB structure), each cations has four cations of the same kind and eight cations of the other kind as second nearest neighbors. For instance, the cation A has 4A cations (2 in the *y-z* plane and 2 in the *x-z* plane) and 8B cations (4 in the *x-y* plane, 2 in the *x-z* plane and 2 in the *x-z* plane) as second nearest neighbors [4].

The presence of two cations with different chemical properties introduces in the cell two kinds of structural distortions, one geometrycal (tetragonal distortion) and one crystallographic (internal distortion). The former takes into account the compression or dilatation of the crystal lattice along the *z*-axis and is measured by dimensionless parameters like the axial ratio $\rho = c/a$ between the lattice parameters, the tetragonal deformation $\eta = c/2a$ or the tetragonality parameter $\delta = 2 - c/a$.

In the ABC$_2$ compounds, the η values range from 0.885 for MgSiP$_2$ to 1.00, for CuInS$_2$. The latter is a consequence of the unequality of the cation-anion bond lengths, according to which the equilibrium position of the anion is not exactly at the center of the relative tetrahedron (Fig. 2.3). In other words, the anion, which in the ZB lattice occupies

the position $u_{zb} = 1/4$, is shift along the x or y axes by an amount $\sigma = u - u_{ZB}$. In general, the anion is shifted toward the pair of the high valent cations, but in the $CuB^{III}C_2^{VI}$ (B^{III} = In, Tl; C^{VI}= S, Se, Te) and $ZnSnC_2^V$ (C^V = P, As, Sb) compounds, a displacement in the opposite direction is found. The σ values range from –0.06 for CuT1S₂ to about +0.06 for AgGaS₂.

The effect of the structural distortions spreads all over the crystal lattice, involving variations in the interatomic distances and bond angles. Summarizing the literature information about structure of CP materials, the following items can be singled [4]:

1. The bond lengths A–C and B–C become functions of the parameters η, u, and a;

2. The AC₄ and BC₄ tetrahedra are distorted, each of them leading to a pair of anion-anion distances and a pair of anion-cation-anion angles, these latter with multiplicity 4 and 2;

3. The anion-centered tetrahedron gives rise to two angles for the A–C–B interaction and one angle for each A–C–A and B–C–B interactions;

4. The cation-cation distances are independent of the internal distortion.

The detailed structure of the unit cell of the CP crystal is shown in Fig. 2.3 a. Here green-type I atoms, red – III, and yellow is the atoms of group VI. Tetragonal deformation is characterized by the deviation of the unit cell parameter c from the doubled value of the a-parameter, which describe the unit cell dimentions a in ZB structure. That is, this parameter characterizes the general deviation of the structure of CP from the ZB. The parameter of tetragonal deformation is usually introduced as a geometric parameter $\eta = c / 2a$, where a and c are the unit cell parameters. This parameter for CP can be non equal to unity (less than one). The second parameter of internal curvature is the displacement of the anion from its ideal tetrahedral position by the u value. The anions are shifted from their ideal tetrahedral positions by the value of u, which is a function of the lattice parameters. The u is the function of unit cell parameter:

$$u = \frac{1}{4} + \left(\frac{R_{\text{I-VI}}^2 - R_{\text{III-VI}}^2}{a^2} \right).$$

(2.1)

If we express the u parameter through a and c, the Eq. 2.2 can be written as

$$u = \frac{1}{2} - \left[\frac{c^2}{32a^2} - \frac{1}{16} \right]^{\frac{1}{2}}.$$

(2.2)

Presence of two cationic sublattices, rather than one, leading to the existence of two near-neighbor chemical bonds A – C and B – C. Generally, the bond length of A – C and B – C are different (none equal) $R_{AC} \neq R_{BC}$. Two bond lengths can be described byexpressions [1]:

$$R_{AC} = a\left[u^2 + \frac{(1+\eta^2)}{16} \right]^{\frac{1}{2}}, \qquad (2.3)$$

$$R_{BC} = a\left[\left(u^2 - \frac{1}{2}\right)^2 + \frac{(1+\eta^2)}{16} \right]^{\frac{1}{2}}. \qquad (2.4)$$

Tetrahedral coordination assumes that the type of chemical bond is substantially covalent with sp^3 hybridization. Because atoms are different, there is an ionic bond component. Comparing the crystal lattice of CP with ZB, we can see that for the structure of ZB binary compounds, such as GaAs, each atom has four identical cations as the nearest neighbors. All four bond lengths are identical. Accordingly, the charge distribution around these bonds is also the same. In this case, it corresponds to the values of the lattice deformation parameters for zinc blende $u = 0.25$ and $\eta = 1$. At the same time, for crystals of the CP group, the equilibrium positions of the cation are closer to one pair of cations than to another. For CP we refer this case as non-ideal case ($u \neq 0.25$ and $\eta \neq 1$). Thus, the two near-neighbor distances A – C and B – C can be calculated by Eq. 2.3 and Eq. 2.4. As a result of changes in bond lengths compared to ZB, which has a significant impact on the properties of the material and the band gap. Chalcopyrites have a low packing factor (are loosely packed crystals). The positions of atoms of different types in the cell of chalcopyrite group I-III-VI$_2$ crystal (in Wyckoff notation) are as follows:

I – 4a: (0, 0, 0)

III – 4c: (0.0, 0.0, 0.5)

VI – 8d: (u, 0.25, 0.125)

where u is the parameter of anion displacenemt. The u parameter corresponds to only for the x coordinate of anion for those pure systems, then whole the y and z component remain the same.

As presented in Fig. 2.3 b each A and B atom is tetrahedrally coordinated to four C atoms, while each C atom is again tetrahedrally coordinated to two A and two B atoms by sp^3 bonds. In fact, all the features of chalcopyrite compounds arise due to the relative

ordering (and non-equivalence) of these two different bonds. This inequality is the reason for considering functional applications in nonlinear optics.

a)   b)

Figure 2.3. Structure of the chalcopyrite type crystal's unit cell (a) and the elementary morphologically the most important component of diamond-like structures, an irregular tetrahedron with shifted by u anion (a common case consisting of an anion C surrounded by two cations A and two cations B).

The scheme of formation of valence bonds in compounds $A^{I}B^{III}C_2^{VI}$ is as follows (Fig. 2.4). Two atoms of chalcogen give the atoms of the elements of group I and group III four electrons. The fifth, missing electron, to fill all empty *p*-orbitals, is formed by mating s^2 - electrons of the element of the III group. As a result of this, and also the subsequent hybridization, all conditions for emergence of tetrahedral hybrid covalent bonds are created.

ground state   compound

Figure 2.4. Scheme of chemical bonds formation in $A^{I}B^{III}C^{VI}_2$ compound.

All compounds of this group are characterized by an exponential dependence of the specific electrical conductivity on temperature and have large values of thermo-

electromotive force and photoconductivity. In this group of tetrahedral phases, as well as in binary semiconductors $A^{II}B^{VI}$, the properties naturally change with increasing atomic masses of the components. Thus, argentum-containing compounds melt at a lower temperature than the same type of copper-containing compounds. During the transition from gallium-containing to thallium-containing compounds, there is also a decrease in the melting temperature and the band gap of these compounds. The practical application of these compounds lies in the same field as the compounds $A^{II}B^{VI}$ [5].

As can be seen from Fig. 2.1. similarly, to the approach discussed above, it is possible to move to more complex quaternary materials. Thus, instead of atoms of groups III incorporation of the atoms of II and IV group allows to I$_2$-II-IV-VI$_4$ crystals can be obtained.

2.1.2. Growing of I-III-VI$_2$ group crystals

Both structural and physicochemical properties of the material depend on the composition and stoichiometry. Therefore, the development of technologies for obtaining materials is a continuous process aimed at obtaining a method of synthesis of the material of predetermined quality with minimal cost. Depending on the type of synthesized material (single crystal, polycrystal, thin films, nanoparticles) use certain methods of synthesis.

The choice of method for crystals growing depends on a number of factors inherent in this material. In particular, they include the following [1]:

- the compound chemical reactivity and that of its elements,
- the elemental vapor pressures
- growth-temperature dissociation pressure of the compound
- mealting point of the compound, whether the compound melts or freezes congruently or incongruently
- the degree to which a single phase is maintained given deviation from stoichiometry
- presence/absence and nature of phase transitions.

As a result of these many considerations, the difficulty of growth tends to increase significantly for greater numbers of constituent atomic elements; thus, growth quality of ternary semiconductors has lagged behind that of their binary counterparts.

Chalcopyrites are generally grown in closed system due to the affinity to oxygen of the constituent elements. Growth methods for I-III-VI$_2$ and II-IV-V$_2$ include chemical vapor

deposition and direct melt techniques including directional solidification. $ZnGeP_2$ specifically has been grown through the latter class of methods: the vertical Bridgman method [6–8], vertical gradient freeze [9], and horizontal gradient freeze [10] techniques.

One of the popular methods of crystal synthesis is the method of crystal growing from melt. For crystals of the chalcopyrite group, the following compounds are obtained in two ways: 1) by slow heating of the calculated amounts of starting elements in pumped quartz ampoules by the reaction, for example,

$$Cu + In + 2Se = CuInSe_2, \tag{2.5}$$

according to the selected mode of synthesis; 2) fusion of chalcogenides of metals of groups I and III in equimolar ratios, by reaction, for example,

$$Cu_2Se + In_2Se_3 = 2CuInSe_2. \tag{2.6}$$
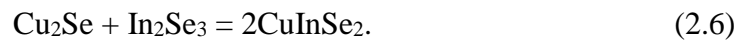
In both cases, vibration mixing improves the results of the synthesis, due to better mixing of the molten components, which eliminates the phenomenon of liquation in the alloy, and prolonged annealing at elevated temperatures improves its homogenization [5].

Figure 2.5. Photograph of synthesized $AgGaS_2$ polycrystal by two temperature vapor transport method [11].

An example of crystal growth is the synthesis carried out in [11]. Here Yang et.al. [11] performed the synthesis of $AgGaS_2$ crystals in the form of polycrystals were synthesized by two temperature vapor transport method and $AgGaS_2$ single crystal were grown by vertical gradient freezing method. $AgGaS_2$ polycrystalline materials were synthesized directly from high purity (99.9999%) Ag, Ga and S element by means of two temperature vapor transport method [12]. The general view of the polycrystalline $AgGaS_2$ crystals is shown in Fig. 2.5.

$AgGaS_2$ single crystals were grown using vertical gradient freezing method from polycrystalline materials. $AgGaS_2$ polycrystalline materials were put into a quartz ampoule

which was evacuated under 1×10^{-3} Pa before it was sealed. Then the sealed quartz ampoule was hung on a descent device which was driven by servo motor. The whole quartz ampoule was located in the upper zone of the growth furnace, the seed part was located at the temperature gradient area. The temperature of the upper zone of the furnace was 1050 °C, the temperature gradient was 10 °C/cm, and the temperature of the lower part of furnace was 880 °C. After the quartz ampoule was heated to the setting temperature and hold for about 48 h, then the temperature was cooled gradually from seed part to melt zone until the ingot temperature reach 990 °C. After growth, the whole furnace was cooled by 50 °C/h to room temperature and 45 mm diameter, 140 mm length as-grown ingot was obtained as shown in Fig. 2.6 a).

a)   b)   c)
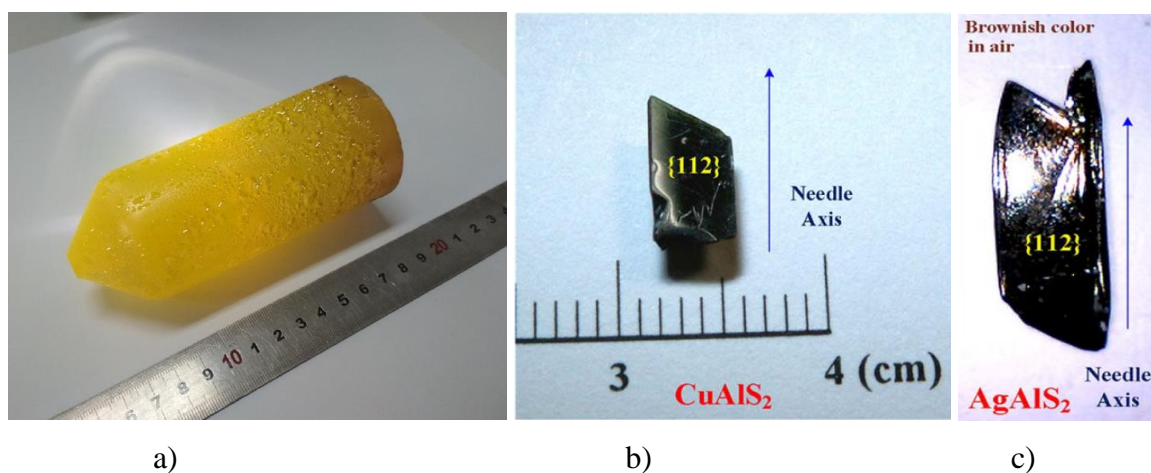
Figure 2.6. Photos of the grown single crystals of a) $AgGaS_2$, b) $CuAlS_2$, c) $AgAlS_2$ chalcopyrite semiconductors reported in [11,13].

In [13], $CuAlS_2$ and $AgAlS_2$ chalcopyrite crystals have been grown by the chemical vapor transport method using ICl_3 as the transport agent. About 10 g of the elements together with an appropriate amount of transport agent ICl_3, was cooled with liquid nitrogen, evacuated to $\sim 10^{-6}$ Torr, and sealed in a quartz ampoule (22 mm OD, 17 mm ID, and 20 cm in length). The growth system is a horizontal three-zone tube furnace. The mixture compounds were heated to 875°C very slowly, which is necessary to avoid any explosions. The growth temperature was set as 800°C ← 875°C → 800°C with a gradient of −3.75°C⁄cm. The process was maintained for 240 h to form large single crystals. After the growth process, the as-grown crystals show lightgreen color ($CuAlS_2$) with apparent needle-like outline shape. The synthetic $AgAlS_2$ crystals essentially form white and transparent color with apparent crystalline faces inside the quartz ampoule. The photos of the $CuAlS_2$ and $AgAlS_2$ crystals taken from [13] is shown in Fig. 2.6. b) and c).

2.2. Physical properties of I-III-VI$_2$ crystals

2.2.1. Electronic structure

Theoretical study of electronic structure

Knowledge about the electronic structure of crystalline materials provides important information about the position of energy levels, which is useful for explaining the properties of physical processes that occur in the compound. Research on the electronic structure of materials is based on finding out the location, degeneracy, energy and dispersion of electronic levels for a particular compound that has a certain crystal structure and symmetry. Such studies can be divided into two major groups – experimental and theoretical.

Theoretical methods of studying the electronic structure of the materials are to consider the structure of the material (crystallographic data), which is obtained from the experiment, and use of a models that provide information about electronic states. In particular, such methods include the Hartree-Fock method [14], the model potential model [15], tight-binding model [16], pseudopotential method [17], density functional theory (DFT) [18,19], Green function method [20,21], etc. Earlier, the use of these theories made it possible to study the electronic structure of semiconductor compounds, such as ZnS [22], GaAs [23], CdS, CdSe [24], Tl_4SnS_3 [25] and many other important materials for semiconductor electronics. Additionally, information about the symmetric properties of electronic states can be obtained using group theory, which was done, for example, for $AgInP_2S_6$ crystals [26], $CsGeI_3$ [27], etc.

A number of works [28–36] and many others are devoted to the theoretical study of the electronic structure of crystals of group I-III-VI$_2$. In [28,37,38] Poplavnoi et.al. performed theoretical modeling of the band-energy structure of chalcopyrite crystals of group I-III-VI$_2$. In these works, the calculation of the band structure was performed using the non-self-consistent empirical pseudopotential method [39]. This method neglects the noble-atom *d*-orbitals. In particular, in [28] the study of the band structure of $AgGaS_2$, $AgGaSe_2$, $AgGaTe_2$ crystals was reported.
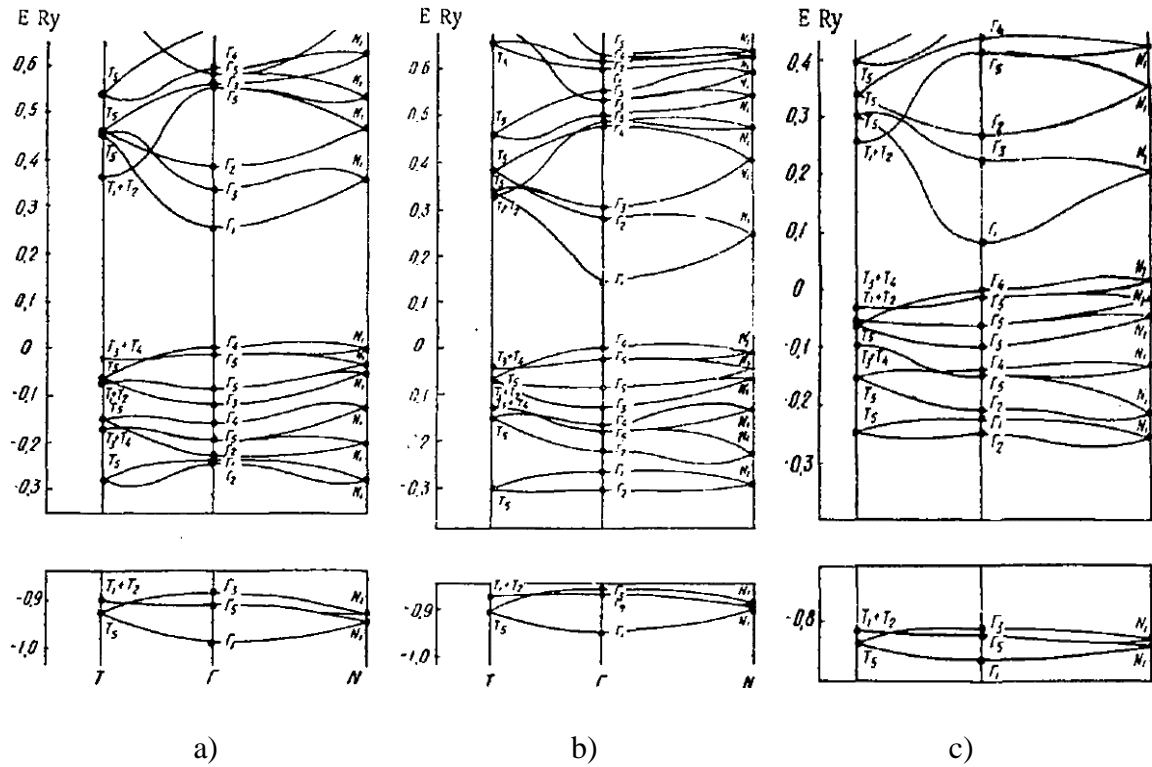
Figure 2.7. Band structure of the AgGaS₂ a), AgGaSe₂ b), and AgGaTe₂ c) crystals.

Calculations are performed with and without consideration of the displacement of anion atoms not changing the crystalline-lattice symmetry. The calculated band-energy structures for these crystals are shown in Fig. 2.7. It is shown that the conduction band of the compounds is simple. The bottom of conduction band was located at the point $\Gamma(\Gamma_1)$. Closest supplementary minima are located at distances ~1 eV. On the other hand, the valence band has a complex structure. Concurrent maxima are located at the Brillouin zone (BZ) points Γ and N. At the point T there is also a supplementary valence band maximum (VBM) at distance of several tenths of an eV. In AgGaS₂ and AgGaSe₂ the top of the valence band is located at the point $\Gamma(\Gamma_4)$. At the same point at a distance Δ_{cr} there exists a double level Γ_5 which branches with consideration of spin-orbital interaction. The level at point N practically coincides with the top of the valence band in AgGaS₂ and is below it by ~0.1 eV in AgGaSe₂. In AgGaTe₂ the top of the valence band is located at point N and the level Γ_4 lies 0.31 eV lower [28]. The authors showed that anion displacement affects the conduction band only slightly and has a more significant effect on the valence band. From the analysis of these results it follows that the optical transitions that form the fundamental absorption edge must correspond to the band gap of the indirect type. However, from optical studies it follows that the band gap of the considered crystals is of the direct type. Therefore, we can say that the

methods used in [28] allows only in the first approximation to obtain information about the structure of electronic levels, but does not describe electronic states well enough.

The first self-consistent calculations of the band-energy structure for CP crystals were performed by Bent et. al. [40] for CuInSe$_2$ crystal. The potential-variation mixed-basis (PVMB) approach was used for this purpose. This method avoids pseudopotential approximations and solves the all-electron problem self-consistently within the DFT approach [19].

In [29], similar calculations were performed using the PVMB method for CuAlS$_2$, CuGaS$_2$, CuInS$_2$, CuAlSe$_2$, CuGaSe$_2$ and CuInSe$_2$ crystals. From the calculations it follows that the upper valence band has its maximum at the $\Gamma_{4v}^{(2)}$ point in the zone center. Conduction band minimum, is at the Γ_{1c} point, hence all six materials have a direct band gap in contrast to results of [40]. There are two secondary maxima in the upper valence band within 1 eV of the valence band maximum (VBM), located at $N_{1v}^{(5)}$ and T$_{3v}$ + T$_{4v}$, with the former being always closer to the VBM than the latter. The minimum of the upper valence band always occur at or near the $N_{1v}^{(4)}$ point, with secondary minima at $\Gamma_{4v}^{(1)}$ and T$_{4v}$ + T$_{5v}$. At the center of the Brillouin zone near the VBM authors has found the crystal-field splitting pair $\Gamma_{4v}^{(1)}$ (single degenerated) and $\Gamma_{5v}^{(2)}$ (doubly degenerate). With the use of the sign convention of the crystal field (CF) splitting between the them is given by $\Delta_{CF} = E(\Gamma_{5v}^{(2)}) - E(\Gamma_{4v}^{(2)})$ [1]. It represents the effects of the existence of two distinct cations, tetragonal distortion, and anion displacement. It was shown by Bent et. al. [40] that six chalcopurite crystals can be divided into two groups according to the magnitude of Δ_{CF}. Whereas CuInX$_2$, (X = S, Se) have a small tetragonal distortion η = 1.004 – 1.0065 and show a very small Δ_{CF}. The remaining four materials have a noticeable tetragonal compression and as a consequence they show $\Delta_{CF} < 0$.

Work [41] is devoted to the study of the electronic structure of AgAlM$_2$ (M = S, Se, Te) chalcopyrite semiconductors using the DFT-based self-consistent tight-binding linear muffin tin orbital (TB-LMTO) method. The calculated equilibrium values of the lattice constants, anion displacement parameter u, tetragonal distortion η and bond lengths are in good agreement with experimental values. It was shown that these semiconductors are the direct band gap semiconductors with band gaps 1.98 eV, 1.59 eV and 1.36 eV, respectively. These results obtained within LDA limitations are in agreement with the respective experimental values of 3.13 eV, 2.55 eV and 2.27 eV [42,43]. Further stady showed that the

electronic properties of these semiconductors significantly depend on structural distortion and the type of hybridization. A detailed study of the total density of states (DOS) and partial density of states (PDOS) shows that p–d hybridization between Ag d-and anion p-orbitals drastically reduces the band gap. The reduction is 51 %, 47 %, and 42 %, for M = S, Se and Te, respectively. But the band gap increases due to anion displacement, in contrast to the result obtained by Jaffe et.al. [44] in the case of CuInSe$_2$. This is due to the relative value of the anion displacement parameter u. In the case of AgAlM$_2$, u increases, whereas for CuInSe$_2$ it decreases with respect to the ideal value $u = 0.25$ corresponding to the binary ZB structure. The bandgap enhancement due to anion distortion is 9.8%, 8.2% and 5.1%, respectively, for AgAlM$_2$ (M = S, Se and Te). The total DOSs and PDOSs further showed that there is a significant effect on the electronic properties due to structural distortion and the presence of p–d hybridization.

Figure 2.8 shows the band-energy structure of CuAlTe$_2$ and AgAlTe$_2$ crystals calculated from first-principles calculations by Huang et. al. [45]. The calculations were performed with the DFT as implemented in the Vienna Ab-initio Simulation Package (VASP) [46] together with the generalized gradient approximation (GGA) in the form of Perdewe-Burkee-Ernzerhof (PBE) [47] as exchange and correlation (XC) functional [45]. The study considers the tellurides with a proper band gap (i.e. CuAlTe$_2$ (2.06 eV) and AgAlTe$_2$ (2.27 eV)) as the photocathode candidates investigated by first-principles calculations.

It is known that narrowing the band gap of photoelectrode decreases the driving force for the redox reactions of water. A compromised width around 2.0 eV is considered as the appropriate band gap of photoelectrode forwater splitting [48–50]. The other requirements for the photoelectrode are also needed, such as band edge positions that straddle the water redox potentials, high carrier mobility to facilitate the electron-hole separation, large surface area and sufficient stability under reaction conditions etc. [45].

Fig. 2.8 presents the band structure of CuAlTe$_2$ and AgAlTe$_2$ calculated with the GGA-PBE method. Both of them have direct band gaps at the Γ point. The calculated band gaps are 1.00 eV for CuAlTe$_2$ and 1.06 eV for AgAlTe$_2$, which are smaller than the experimental values 2.06 eV for CuAlTe$_2$ and 2.27 eV for AgAlTe$_2$ [29].

Fig. 2.9. presents the DOS of CuAlTe$_2$ and AgAlTe$_2$ crystals. It was shown that CuAlTe$_2$ and AgAlTe$_2$ crystals have the same bonding characters [45]. From –6 to –5 eV, the electron density consists of a bonding state of Al-s, Te-s, and Te-p. From –4 to –2 eV, the electron density involves a bonding state of Cu-d (or Ag-d) and Te-p. The topmost

valence band (–2 to 0 eV) is mainly an anti-bonding state of Cu-*d* (or Ag-*d*) and Te-*p*. Moreover, the bottommost conduction band has the character that is mainly an anti-bonding component of Al-*s*, Te-*s*, and Te-*p*. The VBM is determined by primarily the Cu – Te (or Ag – Te) interaction, whereas the CBM is determined by primarily the Al – Te interaction.
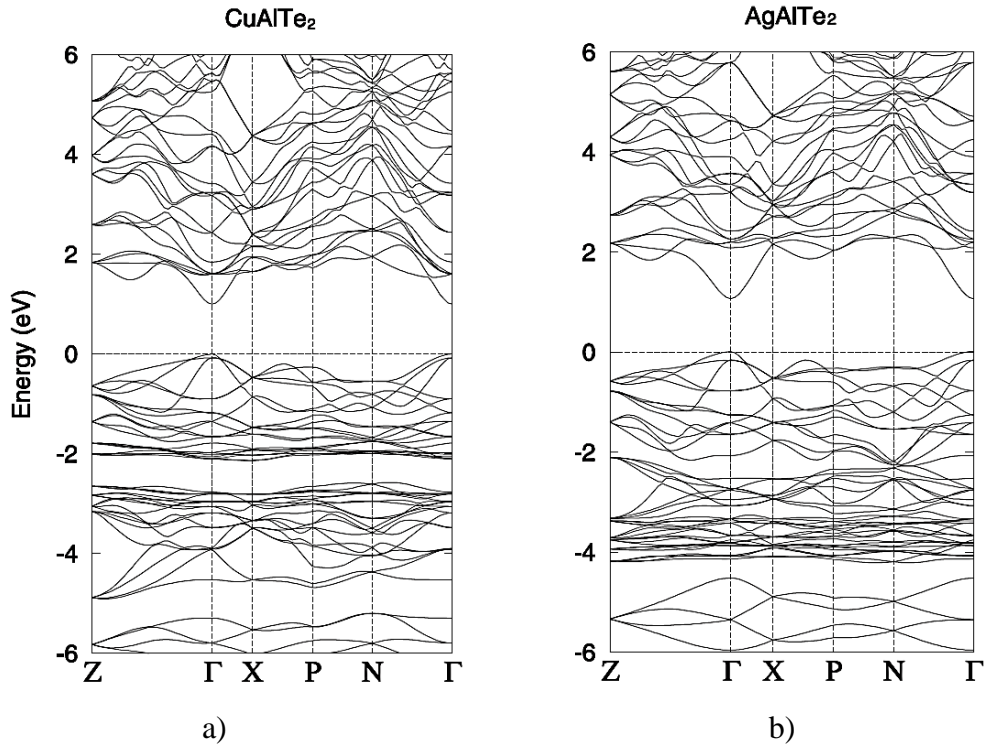

Figure 2.8. The band structures of CuAlTe$_2$ and AgAlTe$_2$ demonstrate that both of them have a direct fundamental band gap at the Γ-point.
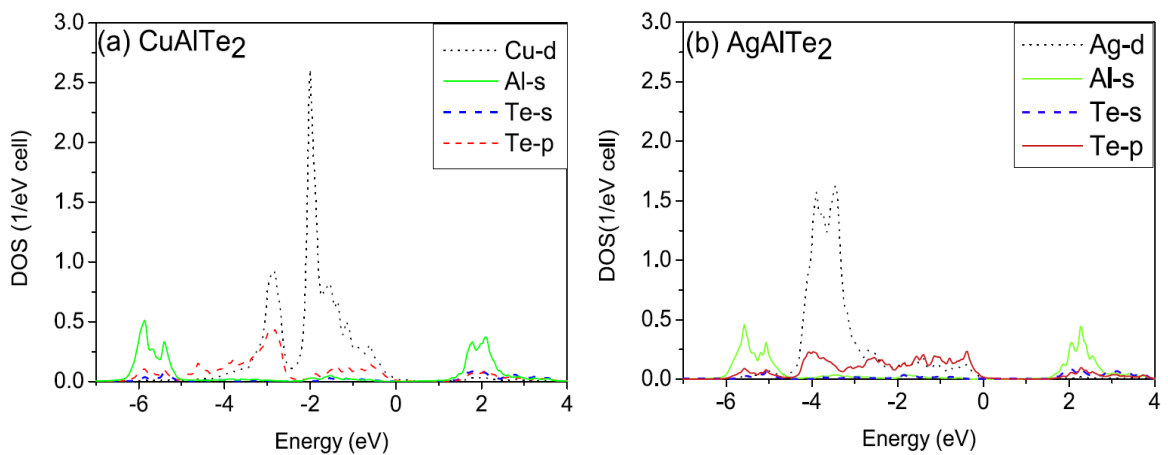

Figure 2.9. The angular-momentum resolved density of states of CuAlTe$_2$ (a) and AgAlTe$_2$ (b), which are scaled by $1/(2l + 1)$ in order to better visualize the contributions from the different orbitals.

As can be seen, the differences on the DOS between CuAlTe$_2$ and AgAlTe$_2$ are that Cu-*d* mainly locates at the topmost valence band whereas Ag-*d* mainly locates at lower band from –4 to –2 eV, which can be explained by the atomic orbital energies and the bonding character. The theoretical atomic orbital energies relative to vacuum of Cu-3*d*, Ag-4*d*, and Te-5*p* are – 5.39 eV, –7.73 eV, and –6.20 eV [51], respectively. Owing to the atomic orbital energy of Te-5*p* higher than that of Ag-4*d* but lower than that of Cu-3*d*, Ag-4*d* dominates at the bonding state (lower energy part) after the formation of Ag – Te bond while Cu-3*d* at the anti-bonding state (higher energy part) after the formation of Cu – Te bond. Since the difference (0.81 eV) on the atomic orbital energy between Cu-3*d* and Te-5*p* is much smaller than that (1.53 eV) between Ag-4*d* and Te-5*p*, Cu – Te bond can have stronger bonding interaction than Ag – Te bond, which is verified by that there is a clear bonding/antibonding splitting around –2.5 eV in the DOS of CuAlTe$_2$ but not in the DOS of AgAlTe$_2$ [45].

From the analysis of the band structure, the authors obtained the values of the effective masses of charge carriers for the studied crystals. The electron and hole effective masses of AgAlTe$_2$ are very light in [001]-direction. This is beneficial for an efficient carrier separation.

Table 2.1. Effective masses of the electrons and holes in CuAlTe$_2$ and AgAlTe$_2$ in units of the free electron mass m_0.

	Effective masses	CuAlTe$_2$	AgAlTe$_2$
Electrons	m^*_{100}, m^*_{010}	0.10	0.11
	m^*_{001}	0.10	0.10
Holes	m^*_{100}, m^*_{010}	0.53	0.65
	m^*_{001}	0.11	0.11

It was also shown by authors that the band edge positions of AgAlTe$_2$ straddle the water redox potentials. In combination with the suitable band gap energy and light carrier effective masses along [001]-direction, AgAlTe$_2$ has the capacity of being a good candidate for water splitting [45]. Additionally it was shown that to increase the absorbing ability on visible light, Ga-doping can adjust the band gap of AgAlTe$_2$ to an appropriate value and remain the reasonable band edge positions of AgAlTe$_2$, which is suggested as an effective approach to optimize its electronic structure for water splitting [45]. Self-consistent calculations using a scalar relativistic full-potential linearized augmented plane wave

method were carried out using the WIEN2k package [52] for $CuAlX_2$ (X = S, Se, Te) were conducted in [53]. The XC is treated within the local density approximation (LDA) and scalar relativistic equations are used to obtain self-consistency. The Kohn–Sham equations are solved using a basis of linear augmented plane-waves. The potential and charge density in the muffin-tin (MT) spheres are expanded in spherical harmonics with $l_{max} = 8$ and non-spherical components up to $l_{max} = 6$.

a)

b)

c)
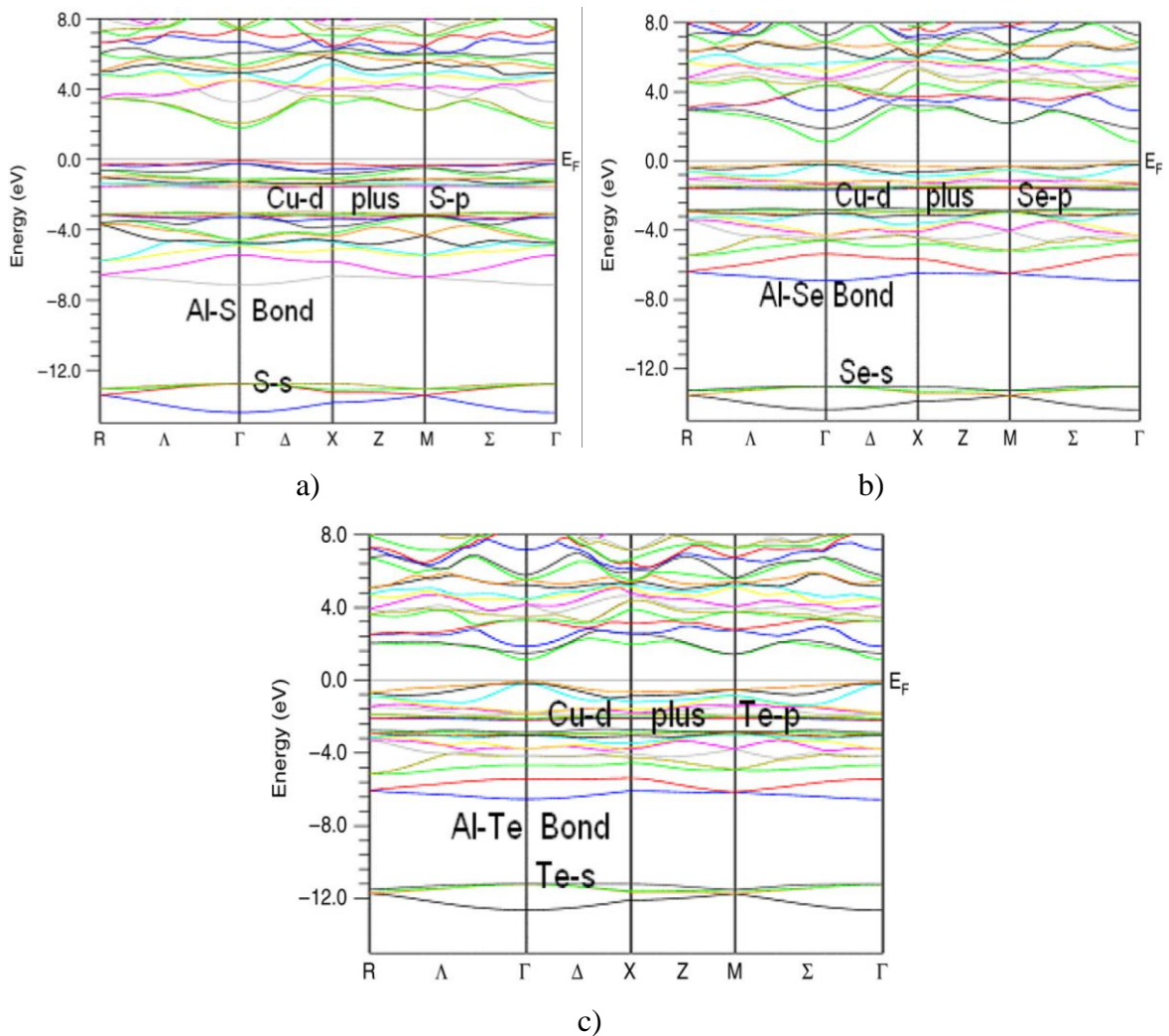
Figure 2.10. Band structure for the $CuAlX_2$ (X = S, Se, Te) compounds calculated using the WIEN2k package with LDA functional.

In all cases, the VBM and the conduction band minimum (CBM) are located at Γ resulting in a direct energy gap of 2.7, 2.1, and 1.6 eV for $CuAlS_2$, $CuAlSe_2$ and $CuAlTe_2$, respectively. In $CuAlSe_2$ and $CuAlTe_2$ crystals a reduction of the bandgap in comparison to $CuAlS_2$ is observed. The reduction in the bandgap was attributed to the fact that the CBM has strong cation s-states whereas the other states in the conduction band are more strongly mixed with other atomic orbitals such as anion p-states. In the conduction bands shifting the

Cu *s*-states has a small effect while shifting Al *s*-states have a strong effect in increasing the bandgap, remaining the valence bands unchanged [53]. Hence, the conduction band shift towards Fermi energy (E_F) when we move from S to Se to Te. The overall reduction in gap is consistent with an overall weakening of the bonds, and, therefore, with a smaller bonding anti-bonding splitting [53].

A comparison of the experimental and theoretical band gaps is given in Table 2.2. The calculated energy gaps are smaller than the experimental gaps as expected from an LDA calculation [54].

Table 2.2. Lattice parameters and bandgaps for the $CuAlX_2$ (X = S, Se, Te) compounds

Parameter	$CuAlS_2$	$CuAlSe_2$	$CuAlTe_2$
E_g^{Exp} (eV)	3.49[a,b], 3.50[c]	2.71[a], 2.67[d], 2.70[c]	2.45[e], 2.06[f]
E_g^{Theory} (eV)	2.05[a], 2.44[g], 2.7[h]	1.65[a], 1.57[h], 2.1[h]	1.6[h]

[a] Ref. [29]., [b] Ref. [55]., [c] Ref. [56]., [d] Ref. [42]., [e] Ref. [57]., [f] Ref. [58]., [g] Ref. [59].,
[h] Ref. [53].

In the Fig. 2.11 the DOS and PDOS for $CuAlS_2$, $CuAlSe_2$, and $CuAlTe_2$ crystals are shown [53]. For this grorp of materials the conduction band minimum and above has contributions from X *s/p*-, Cu *s/p*-, and Al *s/p*-states. The trends in the band structures (as we move from S to Se to Te) can be summarized as follows: (1). The second group in $CuAlSe_2$ and $CuAlTe_2$ is shifted towards higher energies by around 0.5 eV in comparison with $CuAlS_2$, which reduces the bandwidth of both $CuAlSe_2$ and $CuAlTe_2$ with respect to $CuAlS_2$. (2). The band gap between the two groups of Cu *d*- and X *p*-electrons in the top of the valence bands is decreased when moving from S to Se to Te. (3). The bandwidth of the conduction band increases slightly by around 0.7 eV on going from S to Se to Te causing reduction of the gap between the valence and conduction bands. From the PDOS, we note a strong hybridization between Cu *d*- and X*p*-states around −4 eV. Following Yamasaki et. al. [59] authors defined degree of hybridization by the ratio of Cu *d*-states and X *p*-states within the muffin-tin sphere. Based on this one can say that the hybridization between Cu *d*- and X *p*-states becomes weak when moving from S to Se to Te. Also it can be noted that Cu *s*-states are strongly hybridized with Cu *p*-states at around −13.0 eV, and Al *s*-states with Al *p*-states around −1.0 and 4.0 eV. The Al *p*-states are strongly hybridized with Cu *s*- and Cu *p*-states

at around -13.0 eV and with Cu s-states at around -5.0 eV. Also Al p-states hybridize with Al s- and Cu s-states at around -1.0 and 2.5 eV.

a)

b)

c)

d)

e)

f)

g)

h)

i)
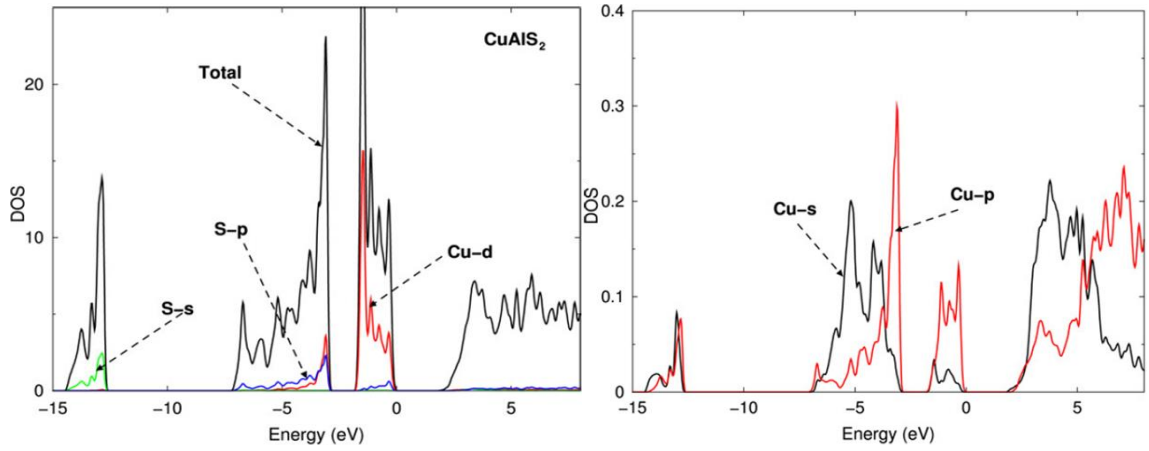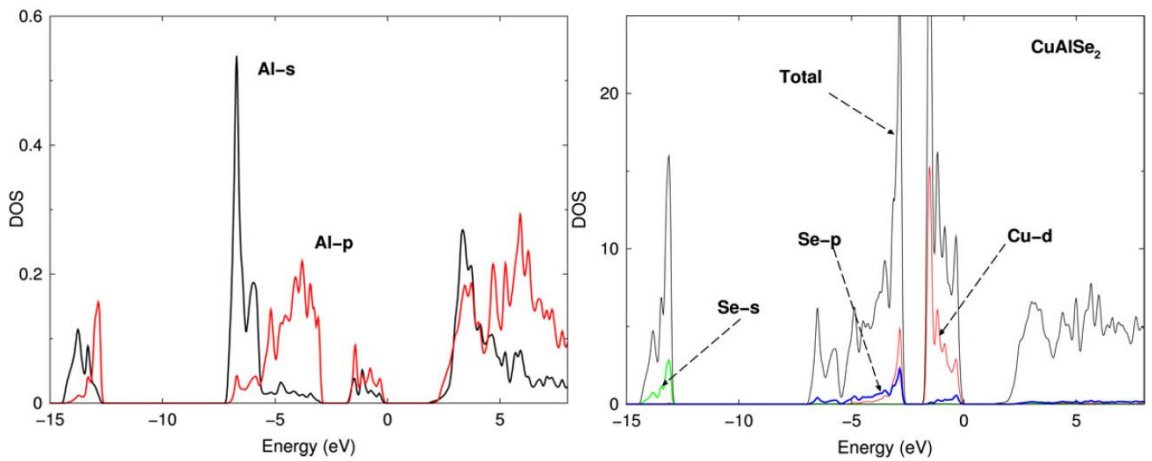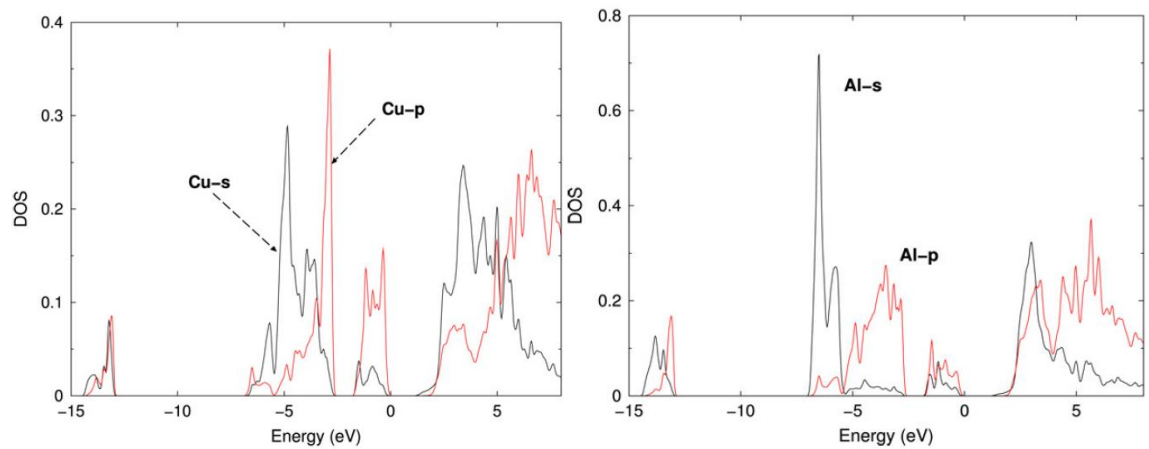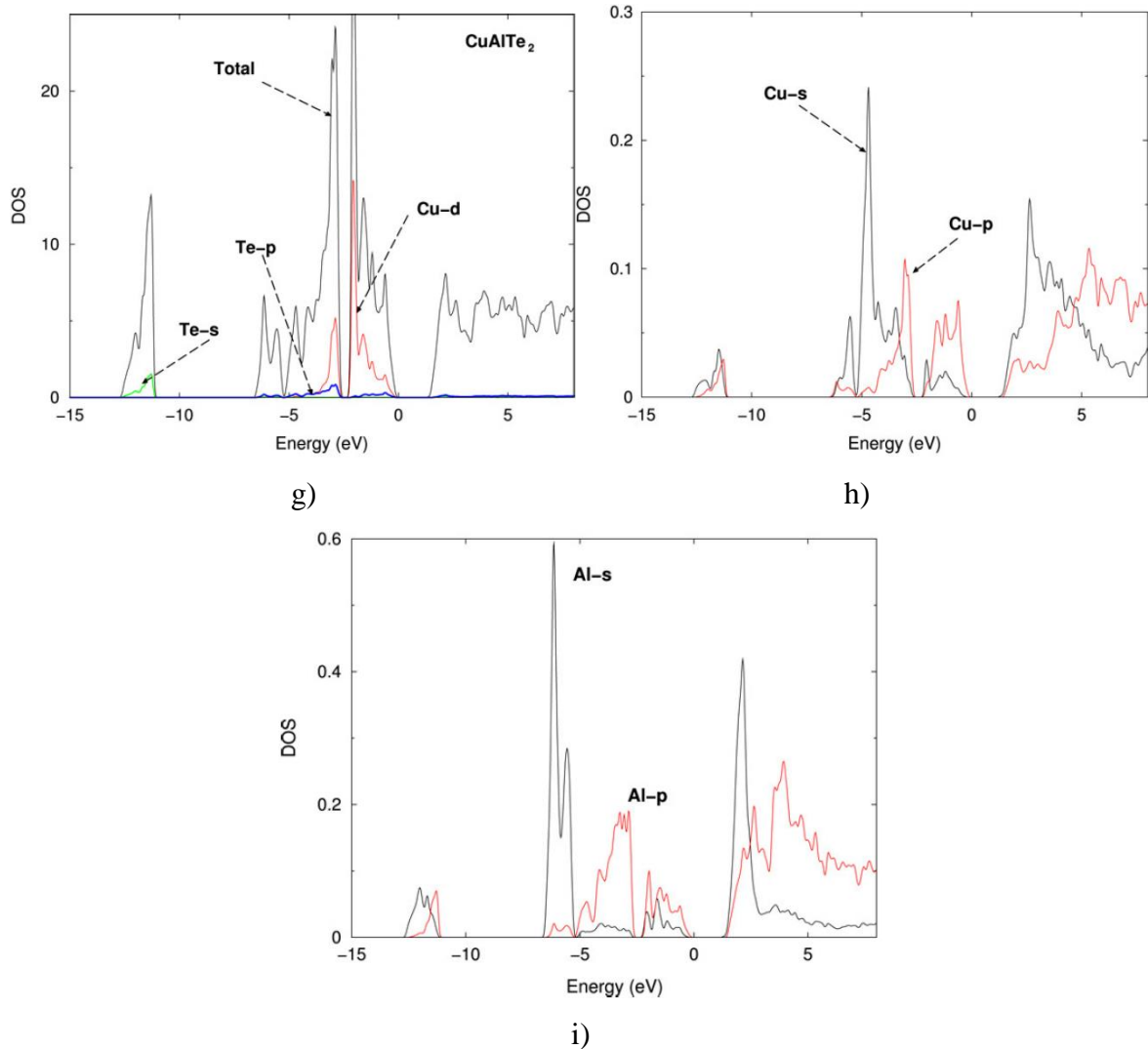
Figure 2.11. Total density of states (states /eV unit cell), along with Cu *s/p/d*, X-*s/p*, and Al *s/p* partial densities of states for: CuAlS₂ (form a to c); CuAlSe₂ (from d to f); CuAlTe₂ (from g to i).

Experimental investigation of electronic levels in I-III-VI₂ chalcopyrite crystals

From the literature we know about several works devoted to the experimental study of the band-energy structure using X-ray photoelectron spectroscopy (XPS) for crystals I-III-VI₂, which proved to be a powerful method for studying the structure of deep (core) and valence states in the material [29,60–63]. Earlier in [64–67] it was shown that experimental methods of XPS and X-ray emission spectroscopy (XES) are an extremely informative method for studying the structure of electronic levels of the valence band top, and showed excellent agreement with theoretical calculations, which confirmed their reliability.

Kuznetsova et.al. in [61] are performed the investigation of the evolution of the valence-band structure at gradually increasing copper content has been analysed by XPS in

In$_2$Se$_3$, CuIn$_5$Se$_8$, CuIn$_3$Se$_5$, and CuInSe$_2$ single crystals. The XPS measurements were carried out using monochromated Al Kα line: hv = 1486.6 eV. The analysed samples were cleaved under high vacuum conditions in preparation chamber and then moved for XPS measurements without breaking vacuum. All the XPS spectra were measured under ultrahigh vacuum ~2 × 10^{-10} Torr using PHI 5600ci spectrometer with the total-energy resolution set to 0.2 eV. No noticeable charges of the sample surfaces by high-intensity Al Kα beam has been observed during the measurements. In order to improve the quality, all the analysed XPS spectra have been deconvoluted using a Gaussian line shape with the standard full width at half maximum (FWHM) of 0.34 eV.
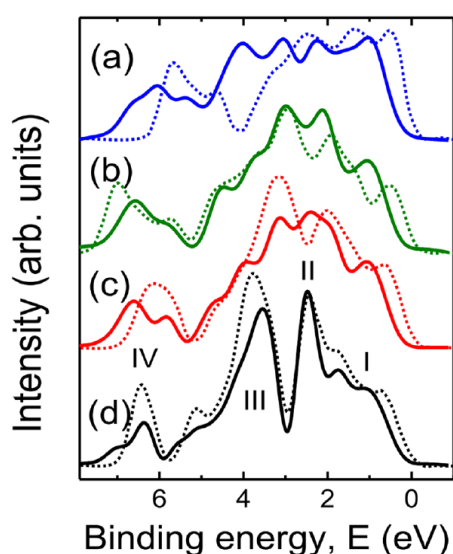
Figure 2.12. Solid lines are experimental XPS spectra of the valence band in In$_2$Se$_3$ (a), CuIn$_5$Se$_8$ (b), CuIn$_3$Se$_5$ (c), and CuInSe$_2$ (d): dependence of the photoelectron intensity $I(E)$ on the binding energy E. Dotted lines are the calculated total DOS, presented with a 0.3 eV Lorentzian broadening and where the energy scale refers to the valence band maximum.

The experimental XPS spectra of the top of the valence band in In$_2$Se$_3$, CuIn$_5$Se$_8$, CuIn$_3$Se$_5$, and CuInSe$_2$ are shown in Fig. 2.12 on a binding energy scale. Calculated total DOS, for these compounds, presented with a 0.3 eV Lorentzian broadening, are also shown in Fig. 2.12 on the energy scale referring to the valence band maximum.

The authors found that the gap between the (II) non-bonding band and the (III) bonding band well seen in the theoretical DOS of CuInSe$_2$ not always can be found resolved in the XPS spectra. This peculiarity was related to the quality of the material and the surface.

The observed changes in the valence band structure of the four compounds suggest that the degree of *p-d* hybridization is directly determined by the copper content and by decreasing the concentration of copper the repulsion of the bonding and non-bonding states can be tuned. A comparison of these spectra with calculated total and angular-momentum resolved DOS revealed the main trends of this evolution. The formation of the theoretically

predicted gap between the bonding and non-bonding states has been observed in both experimental XPS spectra and theoretical DOS [61].

Another work devoted to the study of XPS spectra of a number of chalcopyrite crystals of groups I-III-VI$_2$ and II-IV-V$_2$ is performed by Rife et. al. [60]. Crystals such as ZnGeP$_2$, ZnGeAs$_2$, CuGaS$_2$, CuA1S$_2$, CuInSe$_2$, and AgInSe$_2$ are considered here. A Hewlett-Packard 5950A spectrometer employing monochromatized aluminum Kα radiation was used to measure XPS spectra. The resolution was equal to –0.55 eV. Data were taken on samples that were cleaved (crushed) immediately prior to insertion into the spectrometer. Because only very weak 1s-lines of oxygen and carbon were observed, effects of surface contamination are believed to be minimal.

Rife et. al. [60] performed the investigation of XPS spectra for CuGaS$_2$ crystal in the energy range from 6 to –19 eV. The obtained experimental spectrum for this crystal is shown in Fig. 2.13. It was found that the overlaying peaks of the XPS spectrum are denoted as V_0, which are 2 eV below the VBM originate mainly from Cu 3d-atoms. These levels contain some admixture of S 3p-states. The lower energy peak, labled by the authors as V_4, is compared to the s-electrons of the cations, while V_5 peak is attributed to the S 3s-states. The Ga 3d-electron spin-orbit douplet appears near the –19 eV. The identified XPS features of studied in [60] chalcopyrite crystals are collected in Table 2.3.
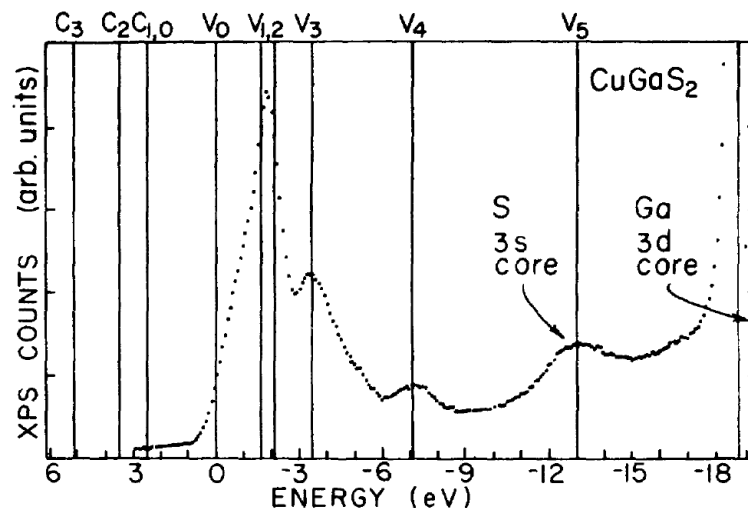
Figure 2.13. XPS data for CuGaS$_2$ with identified critical levels in conduction and valence bands. The Ga 3d core levels are roughly –19 eV below the top of the valence band V_0 The state V_5 is attributed to sulfur 3s core states. V_4 probably identies s-states centered on the cations and V_1 and V_2 are predominately Cu 3d in character.

Fig. 2.14 shows the XPS spectra meshuared for $CuInSe_2$ crystals. From the analysis of X-ray data and UV photoemission results [68] the authors of [60] conclude that sholder at –0.5 eV and overlaying peak at –2.1 eV and XPS spectra of the $CuInSe_2$ crystal originate mostly from the Cu $3d$-states. Like the $CuGaS_2$ crystal, d-states probably contain substantial p-state admixture. At the energy –13 eV and –17.6 eV it is observed the Se $4s$- and In $4d$-core levels. For the In $4d$-levels for $CuInSe_2$ the spin-orbital splitting is ~0.80 eV [68]. This value is consistent with barely divisible in the spectrum doublet seen in XPS spectra [60].

Table 2.3. Energy location (in eV) of identified XPS and density of states regions relative to the indicated top of the valence band. Correlation of labels not necessarily implied between specimens for levels C_1, C_2, C_3, C_4, V_1, V_2, and V_3.

Level	$CuGaS_2$	$CuInSe_2$	$AgInSe_2$
C_4	6.8	—	—
C_3	5.1	3.4	4.5
C_2	3.5	2.9	3.0
C_1	2.5	1.4	1.3
C_0	2.5	1.1	1.3
V_0	0.0	0.0	0.0
V_1	–1.6	–2.1	–1.0
V_2	–2.1	–2.1	–4.3
V_3	–3.4	–3.3	–4.3
V_4	–7.1	–6.3	—
V_5	–13.0	–13.0	–12.4
Core			
$d_{5/2}$	–18.8	–17.2	–16.7
$d_{3/2}$	–19.3	–18.0	–17.6
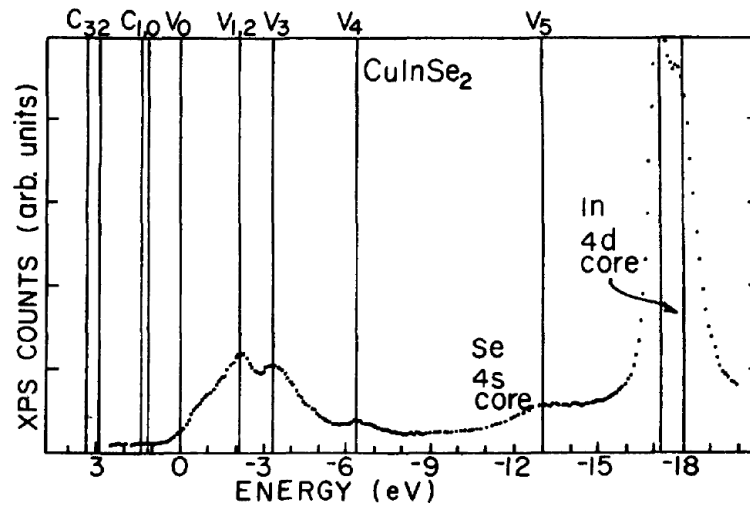
Figure 2.14. XPS data for CuInSe$_2$ with identified or inferred critical levels in conduction and valence bands. The In 4d-core levels are roughly –17.6 eV below the top of the valence band V_0. The state V_5 is attributed to Se 4s-core states. V_4 probably identifies s-states centered on the cations and states $V_{1, 2}$ are predominately hybridized Cu 3d-states.
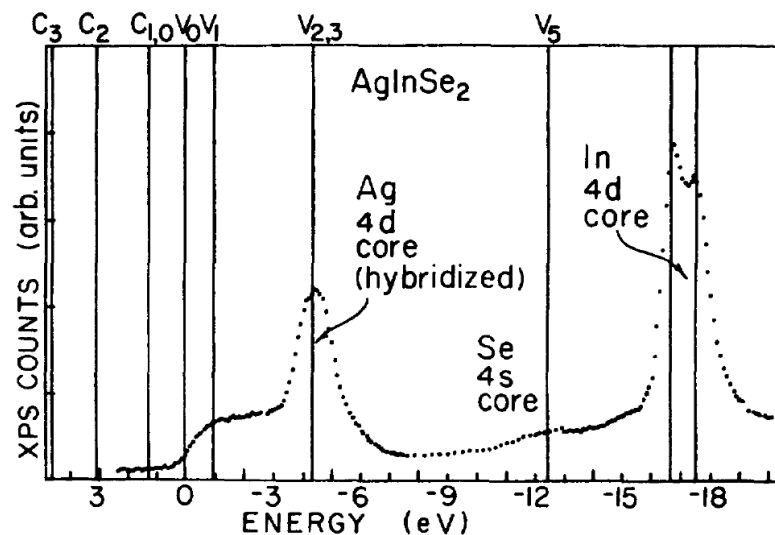
Figure 2.15. Experimantal XPS data for AgInSe$_2$ chalcopyrite. The Ag 4d spin-orbit splitting is not resolved but the splitting is seen for the In 4d-core states.

Figure 2.15 shows the XPS spectra for the AgInSe$_2$ crystal. The obtained spectra is close to the CuInSe$_2$ crystal. The exception is that the d-level of Ag atoms lies deeper in the valence band compared to the copper atom. Ag-d levels hybridize less with the p-states of Se at the top of the valence band than to the copper d-states in CuInSe$_2$ (17 % vs 34 % from electroreflectance measurements [1]). Therefore, AgInSe$_2$ d-states are fletter and the band gap shift from the II-VI analog is less than for the case of CuInSe$_2$. XPS spectra showed In-4s spin-orbit splitting of 0.65 eV is expected in [69] are not resolved [60].

In [60] the authors was not able to obtain XPS spectra of $CuAlS_2$ crystal. The authors limited themselves to examining the reflection spectra and analyzing the experimental results from [62,63] , which are presented up to 10 eV below the top of the valence band.

2.2.2. Optical properties of chalcopyrite crystals of I-III-VI₂ group

Isotropic point in the semiconducting crystals

The phenomenon of birefringence sign inversion (BSI) is realized quite often. Isotropic point (IT) is found in a number of binary semiconducting compounds: CdS [70–74], CdSe [74,75], ZnO [76,77], MgF_2 [78], ZnS [79]. In [80–82], a study of the spectral position of IT in mixed crystals was performed. The BSI point was also found in a number of chalcopyrite semiconductor compounds of the $A^I B^{III} C_2^{VI}$ and $A^{II} B^{IV} C_2^V$ type [1,83–86]. In the Table. 2.4 listed some of these crystals that have a BSI point. The value of λ_0 is given at room temperature, except for the CdSe crystal.

The spectral position of IP in the crystal depends on the production technology, the stoichiometry of the composition, the presence of impurities, external fields, temperature, pressure, etc., and therefore may differ from sample to sample. This fact explains the differences of the order of 1–5 nm in the definition of λ_0 of a particular crystal, which are found in the literature. For example, in cadmium thiogalate $CdGa_2S_4$, which is obtained from the gas phase, IP was observed at $\lambda_0 = 488.2$ nm [87–89], while the Bridget-Stockbarger method shifts it to a maximum of $\lambda_0 = 491.6$ nm.

The study of the physics of the phenomena that lead to BSI allows us to predict the ways of inducing IP in various crystals. The starting point in the case of analysis of the causes that lead to the phenomenon of BSI is the nature of the structural ordering of atoms in the lattice of a compound.

Thus, for example, for a sequence of crystals with the structure of chalcopyrite ($AgGaS_2$, $CdGa_2S_4$, $CdGa_2Se_4$, $InPS_4$), the transition from one crystal to another is accompanied by the appearance of an ordered sequence of cationic vacancies, the concentration of which increases from two in the cell S_4. This allows us to determine the role of structural defects in the overall picture of physical interactions that determine the spectral behaviour of dispersion curves of crystals.

Table 2.4. Semiconducting materials that have the birefringence sign inversion.

Crystal	Wavelength IP, λ_0, nm	Structural type
MgF$_2$	119.4	Rutile
Al$_2$O$_3$	142.6	Corundum
BaLaGa$_3$O$_7$	300	Chalcopyrite
ZnS	340	Wurtzite
ZnO	396	Wurtzite
CdGa$_2$S$_4$	487.2	Thiogallate
CdGa$_2$S$_4$	488.2	Thiogallate
CdSiP$_2$	514.5	Chalcopyrite
AgGaS$_2$	497.4	Chalcopyrite
CdS	523	Wurtzite
CuAlSe$_2$	530	Chalcopyrite
CuGaS$_2$	640	Chalcopyrite
CdSe	710 (77 K)	Wurtzite
CdSiP$_2$	730	Chalcopyrite
AgGaSe$_2$	810	Chalcopyrite
LiNbO$_3$	7500	Perovskite

The study of the spectral dependence of the birefringence $\Delta n(\lambda)$ of AgGaS$_2$ and CdGa$_2$S$_4$ crystals was performed by the interferential method of polarized rays [86,87] on oriented plane-parallel plates of different thickness. The obtained dispersion $\Delta n(\lambda)$ is characteristic of wide-band anisotropic semiconductors [85]: almost constant value in the long-wavelength region and strong dispersion near the fundamental-absorption edge. This suggests that the dispersion of ternary compounds with chalcopyrite structure, as in the case of binary semiconductors, can be qualitatively described on the basis of the model, which is collecting the contribution of near-edge optical transitions and high-energy transitions in the depth of its absorption band, where the first contribution determines the dispersion, the second - the values of n_o, n_e and Δn. The sign Δn in the region of transparency depends on the ratio of these contributions, since the first one is almost always negative due to its strong dispersion, and the second is always positive in tetragonally compressed crystals [90]. A negative sign of Δn indicates the predominance of the contributions of the near-edge optical transitions. In addition, the authors of [90] showed that in the case of approaching the fundamental absorption edge Δn decreases, in IP it becomes zero and then, changing the sign, increases. This fact, as well as the existence of IP, indicates that in AgGaS$_2$ and CdGa$_2$S$_4$ crystals, as in all $A^{I}B^{III}C_2^{VI}$ and $A^{II}B^{IV}C_2^{V}$ compounds, the positive dispersion

$\dfrac{d\Delta n}{dv}$ is due to tetragonal compression of the crystal lattice [91,92], which causes the characteristic splitting of the valence band.

Calculation of the energy spectrum of cadmium thiogallate crystals shows that the top of the valence band and the bottom of the conduction band are localized at the point Γ, and the bottom of the conduction band corresponds to the representation Γ_1, and the top valence band – Γ_3 [93]. Without taking into account the spin-orbit interaction, the top of valence band consists of two levels Γ_3 and $\Gamma_2 + \Gamma_4$ splited by the intrinsic crystalline field. Analysis of the results of the calculation of the band structure [93–95] and the reflection spectra in the region of fundamental absorption [96–98] shows that the minimum band gap E_g in CdGa$_2$S$_4$ is determined by direct transitions $\Gamma_3 \rightarrow \Gamma_1$ with an energy of 3.43 eV, which are allowed for polarization $\mathbf{E} \parallel c$. Transitions $(\Gamma_2 + \Gamma_4) \rightarrow \Gamma_1$ are allowed for polarization $\mathbf{E} \perp c$, with energy – 3.67 eV. The value of crystal spiting in AgGaS$_2$ and CdGa$_2$S$_4$ is of the same order ($\Delta \approx 0.24$ eV) and correlates with the degree of tetragonal compression of these crystals. This circumstance causes a sharper increase of the refractive index n_e compared to n_o in the case of approaching the edge of self-absorption, which leads to the intersection of the dispersion curves n_e and n_o and explains the detected dependence $\Delta n(\lambda)$.

The close values of n_e and n_o in the CdGa$_2$S$_4$ crystal indicate that in this crystal high-energy interband transitions are allowed for polarizations $\mathbf{E} \parallel c$ and $\mathbf{E} \perp c$ and occur at almost the same energies, which is consistent with the energy position of the features in the reflection spectra of CdGa$_2$S$_4$ for both polarizations [95,97,99]. In AgGaS$_2$ crystals, on the contrary, the oscillator strength of near-edge transition for polarization $\mathbf{E} \parallel c$ are significantly dominated by the oscillators strength of the near-edge transitions for $\mathbf{E} \perp c$, which leads to an increase in Δn in the area of transparency of AgGaS$_2$ compared with CdGa$_2$S$_4$.

The CdSiP$_2$ crystal is the only representative of the $A^{II}B^{IV}C_2^{V}$ group of compounds that is optically negative in the region of transparency and for which the relation $E_g(\mathbf{E} \parallel c) < E_g(\mathbf{E} \perp c)$ (E_g is the band gap width) is fulfilled, and it is also characterized by IP at $\lambda_0 = 515.6$ nm [83]. A similar situation was found for some compounds of the $A^{II}B^{IV}C_2^{V}$ type, for example, CuGaS$_2$. Conversely, a CdS crystal, which is optically positive in the long-wavelength region of the spectrum, changes its sign to the opposite during the transition through the point $\lambda_0 = 523$ nm, because the relation $E_g(\mathbf{E} \parallel c) > E_g(\mathbf{E} \perp c)$ is valid for it.

Based on this, we conclude [89]: if the birefringence of an arbitrary crystal in the region of transparency has a negative (positive) sign, and the structure of energy zones is such that $E_g(\mathbf{E} \parallel c) < E_g(\mathbf{E} \perp c)$ or $E_g(\mathbf{E} \parallel c) > E_g(\mathbf{E} \perp c)$, it can necessarily be characterized by the wavelength λ_0 near the absorption edge, for which $\Delta n = n_e - n_o$.

The authors of [89] also concluded that the origin of IP in semiconductor crystals is due to the structure of the energy zones of the crystal and the anisotropy of interband transitions, which determine the rapid growth of one of the refractive indices when approaching the edge of fundamental absorption and change the birefringence sign. Therefore, IP in such crystals is located near the edge of its own absorption from the long-wavelength part of the spectrum.

Analysis of the Table. 2.4 shows that IP is observed mainly in crystals with symmetry of wurtzite and chalcopyrite. Of particular interest are crystals whose birefringence changes its sign in the IR region of the spectrum. Based on them, it is possible to create selective IR filters. Among the crystals that have BSI in the IR region of the spectrum can be distinguished lithium niobate ($\lambda_0 = 7500$ nm) [98].

Nonlinear optical effects in I-III-VI₂ crystals

Nonlinear optical phenomena (NLO) were discovered almost immediately after the invention of the laser. In the early 1960s, Peter Franken first observed second-harmonic (SHG) optical signals in a SiO_2 crystal [100]. Since then, materials with high nonlinear optical responses have attracted considerable attention due to their widespread use in laser technologies, such as the generation of coherent radiation in the IR range, the design of optical parametric oscillators and analytical devices. Such devices are used to detect various chemicals, both elements and compounds that have certain vibrational spectra.

Nonlinear optical application of materials is of great importance today for various areas of our lives. The use of nonlinear optical parametric devices carry out ecological monitoring of air pollutants in the environment. Another possible use is also the analysis of human respiration in medicine [101,102]. Figure 2.16 shows some other possible ways to apply the nonlinear optical effects presented in [103].

Nonlinear optics includes a range of phenomena that occur during the interaction of intense electromagnetic radiation of the optical range of the spectrum with the environment. Such high-intensity radiation is generated by lasers. During the interaction of intense optical radiation with the medium, the linear dependence of the polarization of the

medium with the electric field strength of the electromagnetic wave is lost, which leads to the appearance of nonlinear optical effects.
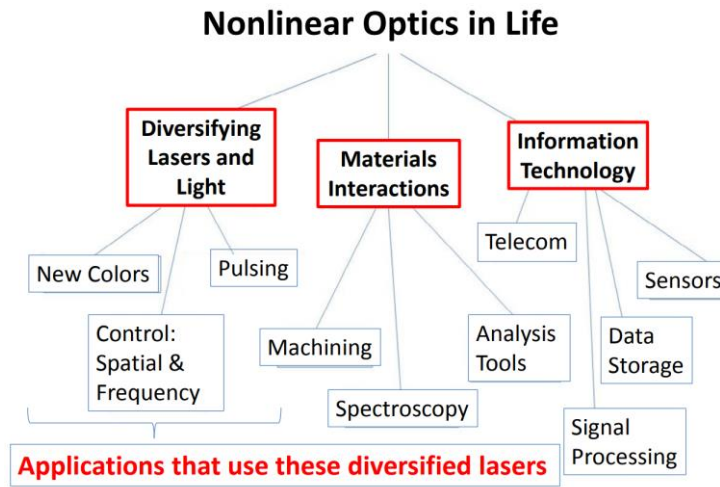
Nonlinear Optics in Life

Figure 2.16. Scheme for organizing nonlinear optical applications [103].

When light propagates through linear materials, it excites electrons in the medium, which, oscillating with the same frequency as the excitation, again emit light with the same optical frequency. But some crystals show a different behavior. They consist of asymmetric molecules whose atoms have very different electron densities. When an electron in such a medium is excited by an electromagnetic wave, it tends to move mainly in the direction of atoms with a higher electron density. His movement is distorted. The electron therefore re-emits optical frequencies different from its excitation frequency. Thus, these crystals can lead to the division of the incident wave into two others with different frequencies. They do not simply respond to optical excitation. Therefore, their name is "nonlinear." Thus, when they are illuminated, nonlinear materials generate two different waves, which are called "daughter waves". Energy conservation is the only limitation for possible frequency combinations: all pairs of wavelengths can a priori be generated as long as the energy is conserved. In this optical system, the emitted frequencies depend on the choice of a non-absorbing part of the energy less than the band gap.

Under the action of an electromagnetic wave with an electric field strength vector E_i in the medium, an electric polarization $\mathbf{P}_i$ occurs. Since $\mathbf{P} = \varepsilon_0 \chi \sim E$, its dependence on the component of electrical voltage can be expanded in a series:

$$\mathbf{P} = \varepsilon_0 \left[\underbrace{\chi^{(1)} \cdot \mathbf{E}}_{\text{linear}} + \underbrace{\chi^{(2)} \cdot \mathbf{E} \cdot \mathbf{E} + \chi^{(1)} \cdot \mathbf{E} \cdot \mathbf{E} \cdot \mathbf{E} + ...}_{\text{non-linear}} \right], \qquad (2.7)$$

or can be written as

$$\mathbf{P} = \mathbf{P}^L + \mathbf{P}^{NL}, \tag{2.8}$$

where $\mathbf{P}^L$ is linear polarization and $\mathbf{P}^{NL}$ is nonlinear part of polarization. This equation can be rewritten using indeces

$$P_i = \varepsilon_0 \left[\chi_{ij} \cdot E_j + \chi_{ijk} \cdot E_j \cdot E_k + \chi_{ijkl} \cdot E_j \cdot E_k \cdot E_l + ... \right], \tag{2.9}$$

where χ_{ij}, χ_{ijk}, χ_{ijkl} are linear, quadratic, and cubic etc. terms of susceptibility (the repeated index means the summation). Nonlinear optics studies the susceptibilities of the second and higher orders. The phenomena described by the first term (linear term) correspond to the propagation of optical waves in a medium with a linear response.

The efficiency of NLO crystals is mainly determined by its ability to double the frequency of laser radiation. Therefore, we consider in more detail SHG in particular in the crystals of group I-III-VI$_2$.

The SHG signal is described by the second order dielectric susceptibility $\mathbf{P}^{(2)} = \varepsilon_0 \chi^{(2)} \cdot \mathbf{E} \cdot \mathbf{E}$, also called the second harmonic generation. Let's rewrite this number in vector writing:

$$P_i^{(2)} = \varepsilon_0 \sum_{j,k=1}^{3} \chi_{ijk}^{(2)} E_j E_k . \tag{2.10}$$

If we calculate, for example, $P_1^{(2)}$, we will have:

$$\begin{aligned}
P_1^{(2)} = \varepsilon_0 (&\chi_{111}^{(2)} E_1 E_1 + \chi_{112}^{(2)} E_1 E_2 + \chi_{113}^{(2)} E_1 E_3 + \chi_{121}^{(2)} E_2 E_1 + \\
&\chi_{122}^{(2)} E_2 E_2 + \chi_{123}^{(2)} E_2 E_3 + \chi_{131}^{(2)} E_3 E_1 + \chi_{132}^{(2)} E_3 E_2 + \chi_{133}^{(2)} E_3 E_3)
\end{aligned}, \tag{2.11}$$

In the pulsation field located outside the absorption resonance, Kleinman [104] demonstrated that the tensor $\chi^{(2)}$ is symmetric with respect to the permutations of the three indices i, j, and k. Then we get the following relations:

$$\chi_{ijk} = \chi_{ikj} = \chi_{jik} = \chi_{jki} = \chi_{kij} = \chi_{kji}, \tag{2.12}$$

and only 10 components of the tensor remain independent. To simplify the record, it is customary to write $d_{il} = \chi_{ijk}/2$, the elements of which are related by the following correspondence $jk \rightarrow l$ ($xx = 1$, $yy = 2$, $zz = 3$, $yz = zy = 4$, $xz = zx = 5$ та $yx = yx = 6$), which gives:

$$
\begin{bmatrix} P_x \\ P_y \\ P_z \end{bmatrix} = \frac{\varepsilon_0}{2} \begin{bmatrix} \chi_{xxx} & \chi_{xyy} & \chi_{xzz} & \chi_{xyz} & \chi_{xxz} & \chi_{xxy} \\ \chi_{yxx} & \chi_{yyy} & \chi_{yzz} & \chi_{yyz} & \chi_{yxz} & \chi_{yxy} \\ \chi_{zxx} & \chi_{zyy} & \chi_{zzz} & \chi_{zyz} & \chi_{zxz} & \chi_{zxy} \end{bmatrix} \cdot \begin{bmatrix} E_x E_x \\ E_y E_y \\ E_z E_z \\ 2E_y E_z \\ 2E_x E_z \\ 2E_x E_y \end{bmatrix}, \tag{2.13}
$$

which means that the tensor d is written as:

$$
\begin{bmatrix} P_x(2\omega) \\ P_y(2\omega) \\ P_z(2\omega) \end{bmatrix} = \varepsilon_0 \begin{bmatrix} d_{11} & d_{12} & d_{13} & d_{14} & d_{15} & d_{16} \\ d_{21} & d_{22} & d_{23} & d_{24} & d_{25} & d_{26} \\ d_{31} & d_{32} & d_{33} & d_{34} & d_{35} & d_{36} \end{bmatrix} \cdot \begin{bmatrix} E_x^2(\omega) \\ E_y^2(\omega) \\ E_z^2(\omega) \\ 2E_y(\omega)E_z(\omega) \\ 2E_x(\omega)E_z(\omega) \\ 2E_x(\omega)E_y(\omega) \end{bmatrix}, \tag{2.14}
$$

Non-zero values of the second-order dielectric susceptibility are observed only for crystals without a center of symmetry.

For the system of symmetry to which the crystals $I\bar{4}2d$ (D_{2d}^{12}) belong, we have equality of such nonlinear optical coefficients

$$ d_{14} = d_{xyz} = d_{25} = d_{yxz}; $$

$$ d_{36} = d_{zxy}, \tag{2.15} $$

Then the matrix of nonlinear optical coefficients for crystals with $I\bar{4}2d$ symmetry will have the following form

$$
\begin{pmatrix} 0 & 0 & 0 & d_{14} & 0 & 0 \\ 0 & 0 & 0 & 0 & -d_{14} & 0 \\ 0 & 0 & 0 & 0 & 0 & d_{36} \end{pmatrix}. \tag{2.16}
$$

The effective value of the nonlinear coefficient for I-III-VI₂ crystals $d_{eff} = d_{36} \cdot \sin\theta \cdot \sin2\varphi$ and for $\theta = 90°$ and $\varphi = 45°$, $d_{eff} = d_{34}$. For NLO practical application in different experimental equipment, the requirements for the value of the effective NLO coefficient differ. In the general case, for practical application in UV and deep UV regions, it is sufficient that the d_{eff} is equal to d_{36} for KH₂PO₄ (KDP, $d_{36} = 0.39$ pm/V). For the IR region, the effective NLO coefficient must be proportional to or an order of magnitude greater than in KTiOPO₄ (KTP, $d_{eff} \sim 3$ pm/V).

The growth of E_g leads to a decrease in the NLO coefficient, so when searching for and developing new NLO materials, the balance between d_{eff} and E_g should be assessed

[105]. The independent second-order NLO coefficients for the $I\overline{4}2d$ group are the only ones $d_{14} = d_{36}$.

In Table 2.5 nonlinear optical parameters of several crystals of group I-III-VI$_2$ were collected and, for comparison, similar information about other NLO crystals was shown.

Table 2.5. Some parameters of ternary NLO crystals for IR spectral range [101,106].

Crystal	Transparency window, μm	E_g, eV	Nonlinear coefficient, pm/V @ μm	Damage threshold, MW cm^{-2}
AgGaSe$_2$	0.76–18	1.80	$d_{36} = 39.5$@10.6	13 30 ns@2000 nm
ZnGeP$_2$	0.74–12	2.00	$d_{36} = 75$@9.6	100 10 ns@2090 nm
CdGeAs$_2$	2.3–18	0.54	$d_{36} = 186$@10.6	160 30 ns@9.55 μm
HgGa$_2$S$_4$	0.55–13	2.84	$d_{36} = 27.2$@10.6	40 30 ns@1064 nm
CdSiP$_2$	0.52–9	2.20-2.45	$d_{36} = 84.5$@4.56	25 14 ns@1064 nm
AgGaS$_2$	0.47–13	2.70	$d_{36} = 12.6$@10.6	34 14 ns@1064 nm
LiGaS$_2$	0.32–11.6	4.15	$d_{31} = 5.8$ $d_{24} = 5.1$@2.3	>240 14 ns@1064 nm
LiGaSe$_2$	0.37–13.2	3.34	$d_{31} = 9.9$ $d_{24} = 7.7$@2.3	80 5.6 ns@1064 nm
LiInS$_2$	0.34–13.2	3.57	$d_{31} = 7.25$ $d_{24} = 5.66$@2.3	40 14 ns@1064 nm
LiInSe$_2$	0.46–14	2.86	$d_{31} = 11.78$ $d_{24} = 8.17$@2.3	40 10 ns@1064 nm
BaGa$_4$S$_7$	0.35–13.7	3.54	$d_{32} = 5.7$@2.3	>240 14 ns@1064 nm
AgInSe$_2$	1.2-18[*]	1.24	$d_{36} = 55.9$@10.6	—
CuGaS$_2$	—	2.43	$d_{36} = 14.5$@10.6	—
CuGaSe$_2$	1-17[*]	1.68	$d_{36} = 44.2$@10.6	—
CuInS$_2$	—	1.51	$d_{36} = 10.6$@10.6	—
CuAlSe$_2$	0.5-5[*]	2.50	—	—
Li$_{0.60}$Ag$_{0.40}$GaS$_2$[**]	—	3.40	$d_{36} = 20.61$@10.6	292.4 14 ns@1064 nm[**]

* Ref. [107], **Ref.[108].

AgGaS$_2$, AgGaSe$_2$, and ZnGeP$_2$ are the only three NLO crystals commercially available NLO materials to date for IR region for second-order harmonic generation (SHG), among which AgGaS$_2$ has the highest figure of merit for NLO interactions in the IR region. AgGaS$_2$ crystallizes in the tetragonal $I\overline{4}2d$ structure, is transparent from 0.53 to 12 μm,

[109] with a transparency edge at 550 nm that is made use of in OPOs, difference frequency mixing, and in direct infrared (IR) countermeasure systems [109]. AgGaS$_2$ also has a high NLO coefficient (d_{36} = 15.9 pmV@10,64 at 2.53 μm) [110]. However, AgGaS$_2$ possesses a seriously low laser-induced damage threshold (LIDT) that originates from its narrow band gap (E_g = 2.58 eV) and the photodarkening effect of silver, [111–113] which dramatically shortens the device longevity. Previous studies have tried to increase LIDT to replace Ag by Li carrying the same positive charge but with no d-electrons, which can effectively eliminate the d–d and d–p electronic transitions [101]. Although exhibiting wider E_g = 4.15 eV and consequently higher LIDT because of the proportional relationship of LIDT $\propto E_g$, [114–116] LGS exhibits a much lower SHG because the crystal structure has collapsed into a lower $Pna2_1$ orthorhombic symmetry, generating a dramatic reduction of the NLO coefficient (d_{36} =5.8 pmV@1 μm) [116].

Chen et. al. [117] showed the possibility of Ag to Li substitution in a surprisingly wide concentration range from 0–0.60 in an AgGaS$_2$ crystal. This replacement led to pushing up the bottom of the conduction band and flattening the top of the valence band. The Li substitution tunes the E_g from 2.58 (x = 0, AgGaS$_2$) to 3.40 eV (x = 0.60, Li$_{0.60}$Ag$_{0.40}$GaS$_2$), a record wide value enables Li$_{0.60}$Ag$_{0.40}$GaS$_2$ to exhibit 8.6 times stronger LIDT @ 1064 nm when AgGaS$_2$ is compared. More significantly, despite the inversely proportional relation, $d_{ij} \propto 1/E_g$, Li$_{0.60}$Ag$_{0.40}$GaS$_2$ exhibits a d_{36} = 20.61 pmV @ 10.64 μm that is 1.1 times higher than that of AgGaS$_2$, which is consistent with the SHG intensity observations at both 1064 and 2100 nm.

2.4. Photovoltaic application of chalcopyrite crystals of I-III-VI₂ group

2.4.1. Solar cells based on I-III-VI₂ materials as absorbing layer

Solar cells made from a wafer of crystalline or polycrystalline silicon are the dominant technology in the commercial market today [118]. These solar panels are used in everyday life in all parts of our world and provide autonomy of various devices, or are used as a source of alternative energy. However, the cost of such batteries is quite high. Thin film solar cells [119] are another type of light coversion devices. Thin-film technology has a number of advantages, such as low material consumption (in the first generation solar cells, the absorber layer thickness is 100-150 microns, while in thin-film batteries it is 1.5-2.5 microns [120]) ,

which leads to a reduction in production costs, the application of thin-film elements is possible on surfaces of any configuration (car surface, glass facades of buildings), the ability to effectively perceive scattered solar radiation, a relatively high efficiency (up to 20%), relatively long service life (efficiency decreases by 10-15% of the initial efficiency [121]).

The practical use of materials of group I-III-VI$_2$ has also found its place in photovoltaics, where materials of this group is used as an absorbent element, due to its high absorption coefficient, which for this group of materials is ~ 10^5 cm^{-1} [1]. Such a large value of the absorption coefficient allowed the use of materials of this group in a new class of solar cells, called thin-film solar cells. These cells use a thin film made of CP material as an absorbent layer. This approach proved to be quite advantageous due to the high efficiency and significant material savings, which in turn gives economic benefits to the use of batteries such as industrial photovoltaic cells.

The history of CIGS began in the early 1950s when the ternary compound CuInSe$_2$ was first synthesized and semiconducting properties were identified. Since then, this material has been the basis of many studies of thin-film solar cells based on CP materials. Merdes et.al. [122] we report externally confirmed total area efficiencies exceeding 12.8% for CdS/Cu(In,Ga)S$_2$ based solar cells. These are the highest reported confirmed efficiencies of CdS/Cu(In,Ga)S$_2$ based thin film solar cells. The Cu(In,Ga)S$_2$ absorber was prepared from sputtered metals subsequently sulfurized using rapid thermal processing in sulfur vapor. An In/(Cu,Ga) precursor layer stack was deposited by DC magnetron sputtering on Mocoated float glass substrates [122]. Basic structural and electrical properties of the devices are presented in Fig. 2.17.
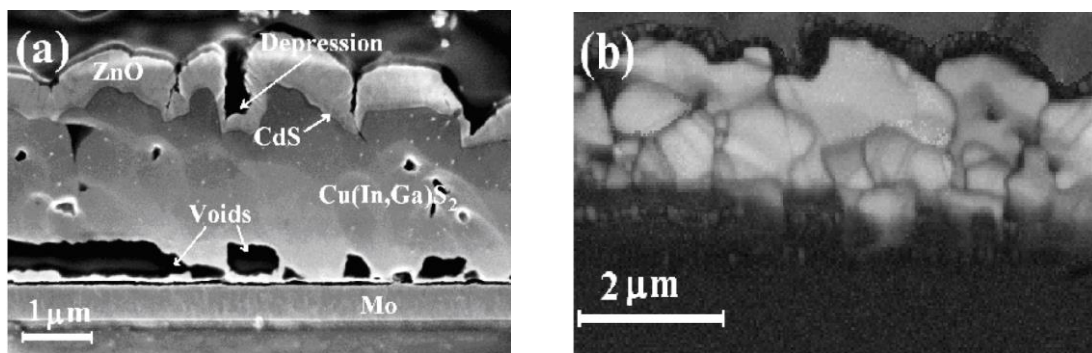

Figure 2.17. (a). SEM image acquired on a cross-section of the solar cell. (b). EBSD pattern quality map taken from the same area [122].

In Fig. 2.18 (a) the EDX elemental distribution maps were acquired using an acceleration voltage of 7 kV. The signals of the Si-K, Mo-L, Ga-L, In-L, Cd-L and Zn-L lines are given

superposing a SEM image. The layered structure of the CIGS absorber is apparent, where the Ga-rich phase remains at the back of the CIGS layer while the In-rich one is located close to the CdS/ZnO layers.
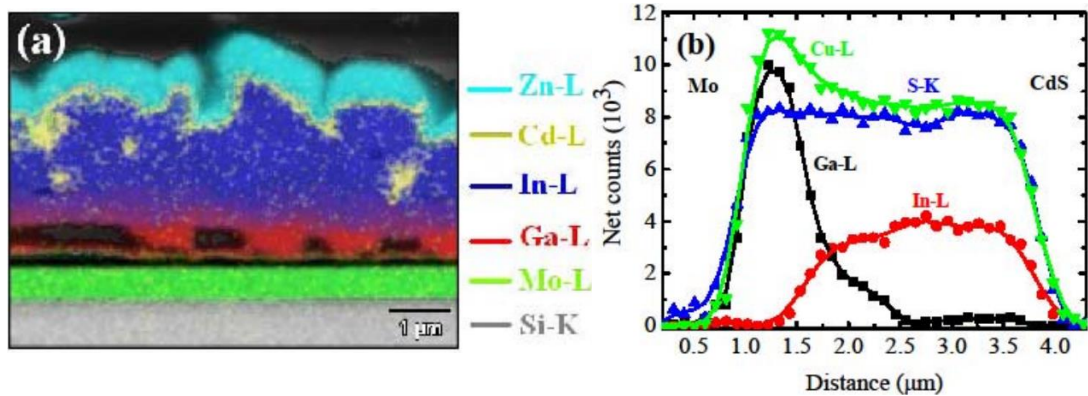
Figure 2.18. EDX elemental distribution maps acquired on the cross-section of the sample. (a) Elemental distribution profiles of Cu, In, Ga and S extracted from the elemental distribution maps. (b) the absorber layer depth, measured at the same area [122].

However, here interdiffusion has clearly taken place between CuGaS$_2$ and CIS as evidenced by the colored patterns [122]. In Fig. 2.18 (b), the EDX elemental distribution profiles extracted from the maps in Fig. 2.18 (a) are plotted against the CIGS layer depth. The position of the Mo and CdS buffer layer are indicated in the figure. The gallium concentration is highest close to the back contact and decreases gradually towards the surface. However, gallium is still detected unambiguously in the CIGS adjacent to the CdS layer. A gallium content of about 3-4 at.% is detected in the part of the absorber adjacent to the CdS layer [122].

Figure 2.19. (a) Comparison of the experimental external quantum efficiency of the 12.8 % and the 12.6 % efficient best solar cells. (b) Simulated external quantum efficiencies of the 12.8 % and 12.6 % efficient solar cells [122].

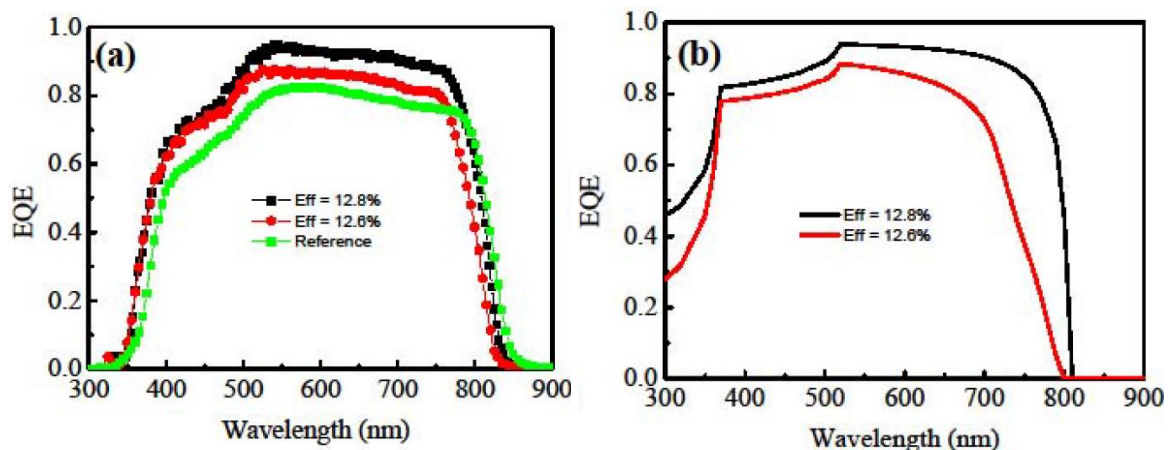In Fig. 2.19 (a) are plotted the external quantum efficiencies (EQE) of the 12.6 % and 12.8 % efficient cells in addition to the quantum efficiency of a reference solar cell with an efficiency of 7.8 %, an open circuit voltage of 657 mV, a short circuit current of 20.2 mA/cm^2 and a fill factor of 59 %. The reference solar cell absorber was prepared using the experimental conditions described in this work however the additional high temperature step was omitted for comparison. Authors have shived that the reference solar cell has a much lower quantum efficiency (not exceeding 80 %) compared to the champion cells. A shift is also observed in the blue region of the spectrum for the reference sample [122]. The 12.8 % efficient solar cell shows a better current collection between 500 and 800 nm compared to the 12.6 % efficient solar cell. In Fig. 2.19 (b) are plotted the resulting simulated external quantum efficiencies of the 12.8 % and 12.6 % efficient solar cells [122].

2.4.2. Simulation of the PV characteristics of I-III-VI₂-based solar cells

A number of scientific works are devoted to the theoretical modeling of solar cells based on CP materials [123–127]. In particular, they highlighted the results of the study of such chalcopyrite materials as $CuIn_{1-x}Ga_xSe_2$ (CIGS), $AgInTe_2$, $CuIn_{1-x}Al_xSe_2$, (CIAS). The purpose of these studies is the theoretical modeling of solar cells and the study of their characteristics using different physical models. Such studies are important because they allow to theoretically model the profile of the solar cell and calculate their various characteristics, including efficiency. Changing the parameters of the studied cells, such as the number of layers, the type of material from which they are made and their characteristics, the thickness of these layers, etc. make it possible to predict the behavior of the efficiency of such devices. This, in turn, allows scientists and technologists to predict the parameters of solar cells and identify possible ways to achieve better performance in the experiment. Often, modeling is an effective way to predict information about the properties of the solar cell and provides economic benefits by reducing the need to make many experimental samples and conducting a large number of measurements.

In [123], a theoretical study of the compound CIGS as a material for solar cells was reported. The purpose of this investigation was to enhance the efficiency of the solar cell by varying the thickness of each layer and optimizing the anti-reflective coating layer, as well. The optimization takes into account the defects in different layers and at interfaces. This

work is based on numerical simulation of the solar cell using the program T-CAD, which is a module of the program SILVACO [128]. Examined and numerically optimized an anti-reflective layer carried out using Atlas module together with the effect of the defects on the CIGS based solar cell performance also was studied in [123]. A CIGS based solar cell structure with new proposed thicknesses of different layers has been proposed.

The CIGS based solar cell studied in [123] is based on data reported in [129]. The following layers in this structure are *n*-ZnO, i-ZnO, *n*-CdS, and *p*-CIGS are the window, intrinsic, buffer, and absorbent layers, respectively. Here the $CuIn_{1-x}Ga_xSe_2$ (*x* = 0.4) is the active layer since it is responsible of light absorption.

Light reflection at the surface of the solar cell is considered as a loss because it weakens its performance. An antireflective coating layer (ARC) is used to reduce the loss of solar energy associated with the reflection of light from the surface of the solar panel. The reflectance at a quarter wavelength at the device's surface is given by

$$R = \left(\frac{n_0 n_{ZnO:Al} - n_{ARC}^2}{n_0 n_{ZnO:Al} + n_{ARC}^2} \right),$$ (2.17)

where n_0, $n_{ZnO:Al}$, and n_{ARC} are the refractive indices of the air, ZnO doped with aluminum atoms, and ARC layer, respectively [123]. In order to get a zero reflectance, the following condition should be satisfyed

$$n_{ARC}^2 = n_0 n_{ZnO:Al}.$$ (2.18)

In case, if for the system, $n_0 = 1$ and $n_{ZnO:Al} = 1.92$ at 550 nm, considering the Eq. 2.18 the reflectance equals zero when $n_{ARC} = 1.386$. This refractive index value is close to the real value of the MgF$_2$ refractive index (1.38) [123,130]. Therefore, the thin layer of MgF$_2$ is used for ARC.

For the computer simulation, the AM 1.5 spectrum was used at incident power density of 100 mW/cm^2. Fig. 2.20 shows the short-current density (a), open-circuit voltage (b), conversion efficiency (c), and fill factor (d) as a function of MgF$_2$ ARC layer thickness with and without defects. J_{SC} increases from 31.56 to 33.98 mA/cm^2 (ΔJ_{SC} = 2.42 mA/cm^2 equivalent to 7.67 %) for device with defects when using 0.11 µm MgF$_2$ layer thickness. In the case of device without defects, the shortcurrent density increases from 34.15 to 36.7 mA/cm^2 (ΔJ_{SC} = 2.55 mA/cm^2 which means 7.47 %). For device with defects, the efficiency increases from 19.09 without ARC to 20.61 % with the use of 0.11 µm MgF$_2$ layer (augmentation of 7.96 %) as depicted in Fig. 2.20 c. For device without defects, the

efficiency increases from 21.64 (without ARC) to 23.33 % with the use of 0.11 μm MgF$_2$ layer (augmentation of 7.81 %). The effect of ARC layer on both V_{OC} and FF is negligible as illustrated in Fig. 2.20 b and d, respectively. The increment in J_{SC} and η is caused by the suppression of reflected light at the cell surface via MgF$_2$ layer which allowed allowed more carriers to be photogenerated. Figure 2.20 indicates that the results are too optimistic when the defects are not taken into account. J_{SC} decreases by about 7.5 % and η decreases by about 11.7 % when defects are introduced.
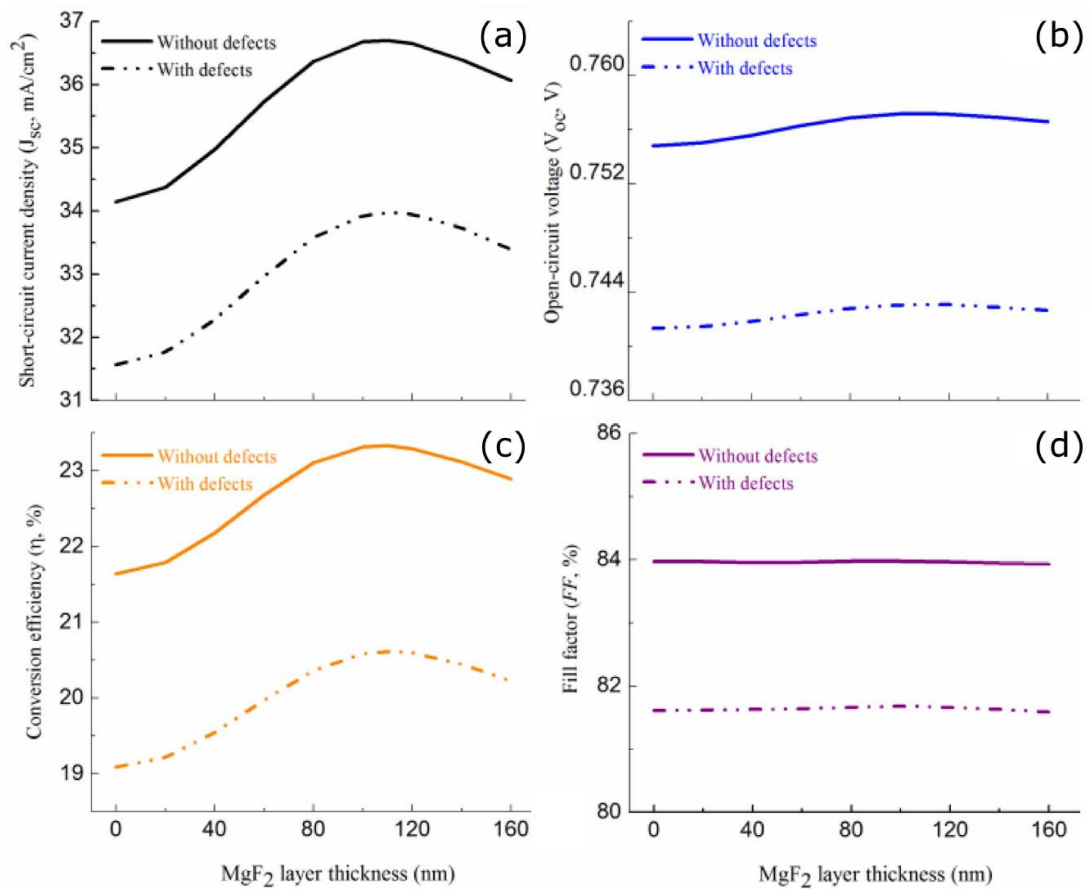
Figure 2.20. Short-current density (a), open-circuit voltage (b), conversion efficiency (c), and fill factor (d) as a function of MgF$_2$ ARC layer thickness with and without defects.

The curves of current density as a function of anode voltage for devices with and without defects for devices (containing MgF$_2$ layer as ARC) with defects and experimental, taken from [123,129] are nearly identical (see Fig. 2.21). Also, it was shown that the quantum efficiency of device with defect and that of experimental are close to each other [123]. Study of the impact of defect of donor density change from 10^{14} to 10^{15} cm^{-3} showed that both J_{SC} and V_{OC} decrease with the increasing of defect density. J_{SC} drops from 33.98 to 32.75

mA/cm^2 (a decrease of 03.62 %) for a defect density from 10^{14} to 10^{15} cm^{-3}, respectively. From its side, V_{OC} tumbles from 0.743 to 0.704 V (a diminution of about 5.25 %). The fill factor undergoes a diminution of 13.25 % (from 20.61 to 17.88 %) and 5.1 % (from 81.68 to 77.53 %), respectively.

Figure 2.21. Current density J vs anode voltage for CIGS based solar cell.

It was found that by increasing the thickness of each of the window or buffer layers, the conversion efficiency underwent a remarkabl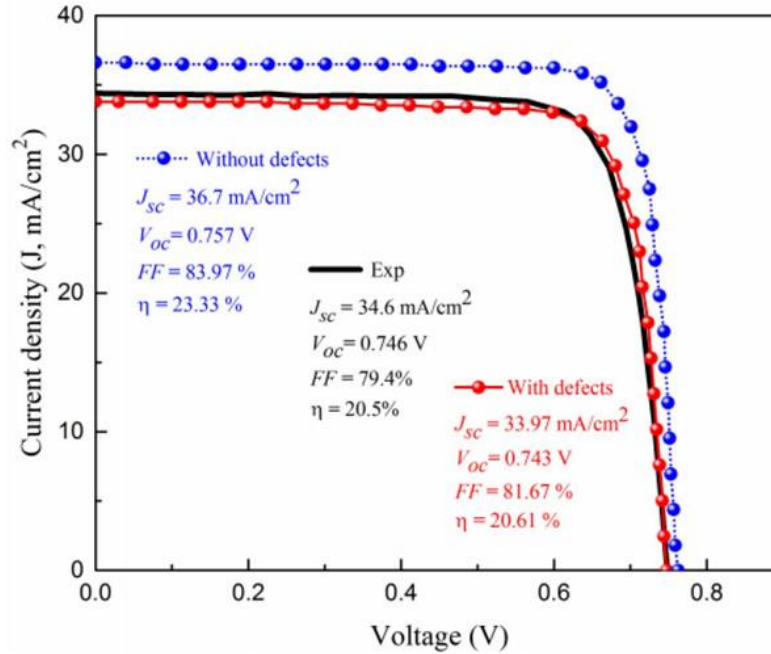e decrease. Increasing the absorbent layer thickness enhances the conversion efficiency considerably. Structure with the best performance has a 0.11 μm ARC MgF$_2$ thickness, 10^{14} cm^{-3} donor defects density in CIGS, and ZnO:Al, i-ZnO, CdS, and CIGS thicknesses of 0.25, 0.06, 0.03, and 1.6 μm, respectively, which gives a 20.64 % conversion efficiency.

The authors of [126] also performed a simulation of a solar cell based on the absorbing layer formed by CIGS material using AFORS-HET software. In this work, the buffer layer formed by the thin film of CdS is replaced by ZnS because this material is not toxic compared to CdS. The structure of such a cell consists of the following layers: *n*-ZnO: Al / *i*-ZnO / *n*-ZnS / *p*-CIGS / Mo. Thus, a polycrystalline thin-film solar cell was modeled where the key parts are *p*-CIGS absorber layer and *n*-ZnS buffer layer. The characteristics of these key parts: thickness and Ga-content of the absorber layer, thickness of the buffer layer and doping concentrations of absorber and buffer layers have been investigated to optimize the conversion efficiency. It is shown, a maximum conversion efficiency of 26 % with a short-circuit current of 36.9 mA/cm^2, an open circuit voltage of 824 mV, and a fill factor of 85.5 %.

In [124], the material Cu(In, Al)S$_2$ (CIAS) was theoretically investigated using the program SCAPS-1D (a Solar Cell Capacitance Simulator) [131], the solar cell was modeled and its characteristics were studied. The thin-film solar cell model based on the CIAS compound used in this work consisted of the following layers: CIAS – 3000 nm; CdS – 60 nm; ZnO 80 nm; ZnO: Al – 500 nm. In this work, the parameters given in [124] were used for calculations.
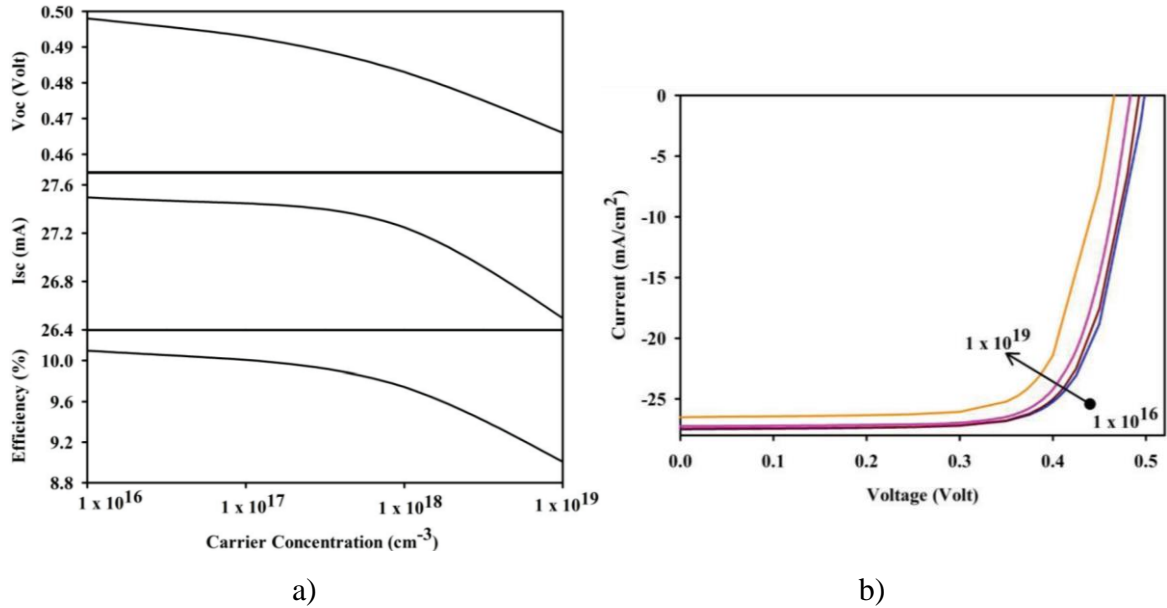

a)   b)

Figure 2.22. Variation in solar cell parameters influenced by carrier concentration of absorber layer (a), and I-V curve of the CIAS solar cell as a function of carrier concentration (b).

The authors show a significant effect of changes in the concentration of charge carriers from 1×10^{16} to 1×10^{19} cm^{-3} on all parameters of the solar cell. Fig. 2.22 shows the change in open circuit voltage, short circuit current and in efficiency of the CIAS solar cell. Plot of open circuit voltage varies nearly linearly with the change in the carrier concentration. As concentration increases the V_{oc} improves and reaches maximum at about 0.5 V. Variation of short circuit current and efficiency varies non-linearly with carrier concentration. Above 10^{18} cm^{-3} concentration both I_{sc} and efficiency doesn't changes much. Both these values improve with increasing in the concentration values. Maximum I_{sc} and the efficiency were observed at 10^{16} cm^{-3} carrier concentration, i.e. 27.5 mA and 10.1 % respectively. The *I-V* curves of the CIAS solar cell by varying the carrier concentration is shown in Fig. 2.22 b.

The obtained results show the conversion efficiency is significant depends on the variation of carriers concentration. By utilizing the absorbing photon as much as possible i.e. without the considering internal defect of the material the highest efficiency was

achieved is 10.1 %, which can be further improved by setting up perfect band edge and certain operating condition of the device.

N. Benseddik et al. [125] reported the numerical study of $AgInTe_2$ solar cells using SCAPS-1D program. $AgInTe_2$ is a new promising material for the manufacture of solar cells. The general view of the schematic structure of the solar battery based on $AgInTe_2$/CdTe is shown in Fig. 2.23. It consists of ohmic contacts and two layers: *n*-type CdTe, and *p*-type $AgInTe_2$. The authors [125] investigated the change in thickness and doping of buffer and absorber layers, while keeping the other parameters unchanged to check the effect of thickness on the performance of the $AgInTe_2$ solar cells.
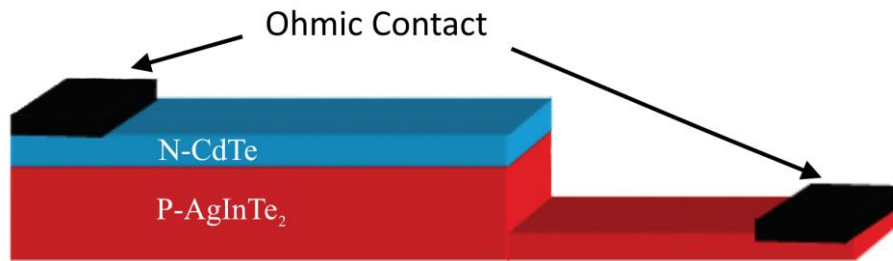

Figure 2.23. Schematic structure of an $AgInTe_2$/CdTe solar cell.

The thickness of the absorbing layer varied from 0.5 μm to 5 μm. The changings of PV parameters with the thickness of absorber layer is shown in Figure 2.24 a. The efficiency increases as during the increasing of the absorption layer thickness, due to the increased exciton generation has been shown [125]. When the absorber layer thickness increases, the longer wavelength of illumination will produce a good amount of electron–hole pair generation. By reducing the absorber layer thickness, the depletion layer becomes very close to the back contact and more electrons will be captured by the back contact for recombination. The optimized thickness of the absorber layer is obtained to be equal to 5 μm. At this thickness the maximum power conversion efficiency is 18.67 % and Jsc = 69.43 mA/cm², V_{oc} = 0.428 V, FF = 61.33 % [125].

Like the absorbing layer, for the buffer layer formed by the CdTe compound, a change in the layer thickness also leads to significant changes in the PV parameters. Figure 2.24 b shows the effect of the buffer layer thickness from 0.1 to 0.5 μm on the main photovoltaic parameters V_{oc}, Jsc, FF and η of $AgInTe_2$/CdTe solar cell [125]. The increase of the thickness of the CdTe buffer layer leads to decrease PV parameters. The decreasing of buffer layer thicknesses produces more photogenerated minority carriers easily reach the depletion

region and can therefore contribute to the total photocurrent. As a consequence, the optimal thickness of the buffer layer is equal to 0.1 μm.
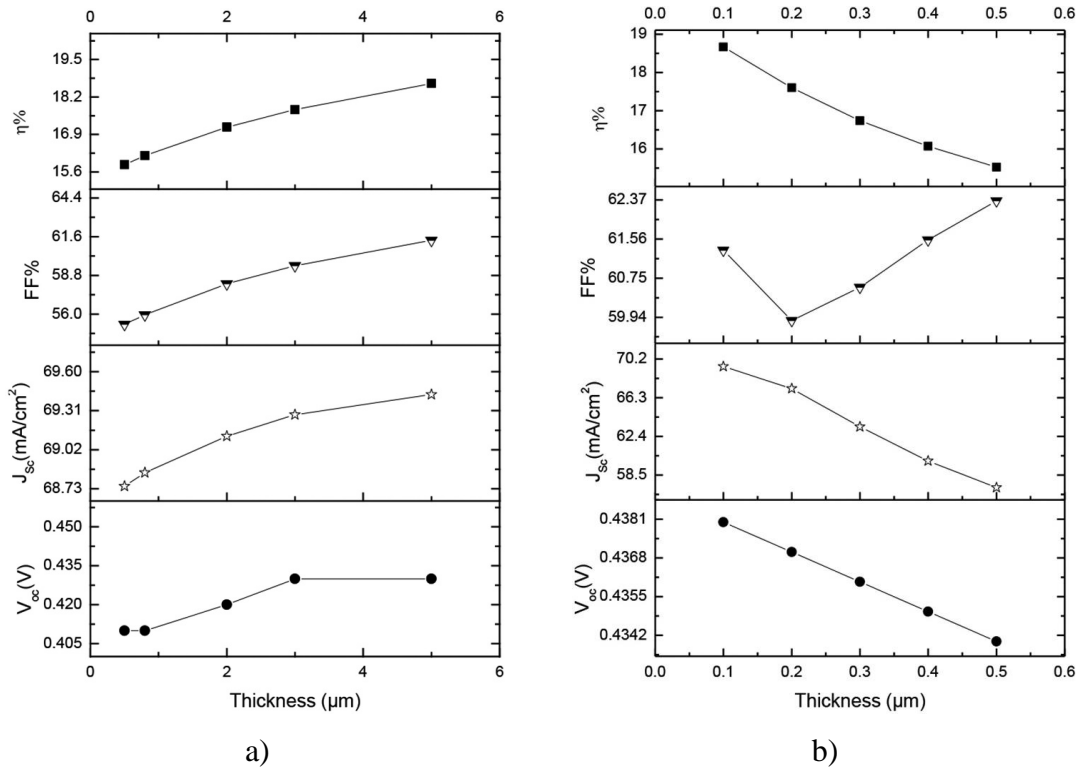

a)   b)

Figure 2.24. Effect of various thickness of AgInTe$_2$ absorber layer (a) and of CdTe buffer layer (b).

Figure 2.25 exhibits the effect of different doping concentration of AgInTe$_2$ absorber layer on the main PV parameters V_{oc}, J_{SC}, FF and η of AgInTe$_2$ /CdTe solar cell. The doping concentration of the AgInTe$_2$ layer varies from 5×10^{16} to 10^{18} cm^{-3}. Other parameters are kept constant such as AgInTe$_2$ thickness to 5 μm, CdTe thickness to 0.1 μm and doping concentration of CdTe layer to $N_D = 10^{17}$ cm^{-3}. The Efficiency η, the V_{OC} and the FF are increased significantly with the increase of the acceptor concentration N_A from 5×10^{16} cm^{-3} to a tolerable limit of 1×10^{18} cm^{-3}. But the short-circuit current density J_{SC} first increases and then decreases with the increase of doping concentration. This degradation is due to the increase of the free carrier charge recombination which takes place within the bulk. The efficiency reaches its maximum value of 25.01 %. Thus, an optimum performance of AgInTe$_2$ thin-film solar cells can be obtained for an acceptor concentration of about 1×10^{18} cm^{-3}.

The doping concentration of the CdTe layer varies from 5×10^{15} to 10^{17} cm^{-3}. With an increase in the donor concentration of the buffer layer, there is increase in open-circuit voltage (V_{oc}), efficiency (η) and fill factor (FF). After reaching the 2×10^{16} cm^{-3} value of donor carrier concentration, J_{SC} decreases. If we further increase the concentration, V_{oc} is set

to be same. The reason behind that is by an increase of donor concentration the mobility of the carriers decreases. To give an efficient output from a solar cell the optimum value of CdTe buffer layer carrier concentration taken was $1 \times 10^{17} \text{cm}^{-3}$.
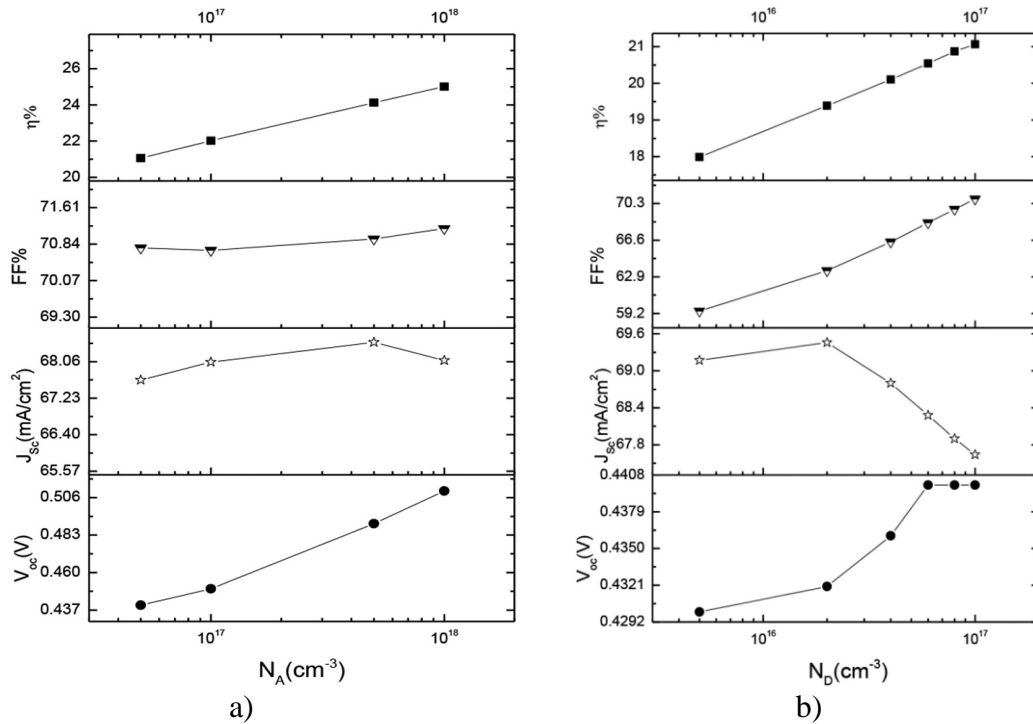
Figure 2.25. Effect of various doping of AgInTe₂ absorber layer (a), and of CdTe buffer layer (b).

In [127] the intermediate layer from MoSe₂ between the back contact and the CIGS absorber was added. It was predicted that an overall efficiency of 24 % can be achieved by reducing the back surface recombination and Schottky barrier with sub-micrometer a thick CIGS absorber.

Using of the ordered vacancy compound (OVC) at buffer/absorber interface in CIGS solar cell structure have been investigated using ADEPT 2.1 simulator. [132] Besides, CuIn₃Se₅ has been used as an OVC layer that assists to improve the conversion efficiency to an optimized level of over 25 % by reducing the recombination rate. Moreover, the optimized short circuit current (J_{sc}) and corresponding open-circuit voltage (V_{oc}) yield a higher fill factor (FF) of 86.22 %, which, therefore, results in an optimum efficiency of the CIGS cell estimated as 25.68 % under AM 1.5 irradiance.

2.5. Conclusions

1. A literature review of the structure and some physical properties of crystals of I-III-VI$_2$ group with the chalcopyrite structure was carried out. It is shown that the crystals of group I-III-VI$_2$ belong to the tetragonal symmetry $I\bar{4}2d$ (D_{2d}^{12}) (space group # 122) and have four formula units ($Z = 4$). The crystal lattice is derived from a binary compound with a zinc blende structure. It is shown that there are two types of crystal lattice deformation in these crystals. The first type of deformation is tetragonal deformation $\eta = c/2a$ and the second is the displacement of the anion atom described by the parameter u.

2. The scheme of formation of valence bonds for crystals of I-III-VI$_2$ group is considered. It is shown that the deformations of the crystal lattice are due to the fact that the anion atom has a different environment formed by atoms of two species. These are atoms of group I and atoms of group III respectively. The result is inequality of bond lengths I – VI and III – VI.

3. The electronic structure of crystals with chalcopyrite structure was studied both experimentally and modeled by theoretical methods. The electronic structure of crystals of I-III-VI$_2$ group is similar to that of binary analogue with zinc blende structure. It is shown that the electronic structure is significantly affected by the inequality of the length of cation-anionic bonds.

4. A review of the literature showed that crystals with the structure of chalcopyrite have interesting optical properties that have important applications. Nonlinear optical coefficients, which are of great importance, determine the commercial use of these materials and the IR region. The presence of an isotropic point and a large value of the absorption coefficient together with appropriate band gap value showed the prospect of using these crystals as optical filters, absorbing layers in photovoltaics and other devices elements on practice.

3. METHOD OF THE ELECTRONIC STRUCTURE CALCULATION

Computer modelling plays an important role in the development of modern science. Today, theoretical studies of processes and phenomena allow to supplement and explain the phenomena and processes occurring in systems of varying complexity. Often the obtained simulation results describe the properties of the real objects quite accurately, which allows to replace the conduct of experimental research with computer simulation. Particularly attractive is the proposal to move from experiment to modelling in cases where the performing of experimental research requires expensive and complex equipment, or when the experiment cannot be created in the laboratory.

3.1. General concept of quantum mechanics. Wave function

In classical physics, based on Newton's equations, we are dealing with large particles, and object. However, moving to much smaller particles, such as an electron, results in quantum effects that are not described by classical physics. There are special quantum laws. To consider quantum effects, it is necessary to use its own mathematical apparatus, which puts operators in line with physical quantities. In quantum mechanics, any object (atoms, elementary particles or state, etc.) is described by a wave function. The wave function is a mathematical tool for describing the quantum state [133]. The wave function is a function of coordinate, momentum, or spin and time and is denoted as Ψ. The wave function has no physical meaning, but the square of the modulus of the wave function contains the amplitude of the probability of finding an electron in the certain state.

For using of the function as a wave function there are certain conditions that must be satisfied by the function to be applied as a wave function. These include:

- The wave function Ψ must be single valued.

- The wave function Ψ must be "smooth" – continuous everywhere (all its partial derivatives must also be continuous).

- The probability of finding the particle at moment of time t in an interval Δx must be in the interval [0, 1].

■ The wave function Ψ must be quadratically integrable. This means that the integral $\int \Psi^* \Psi d\tau$ must exist.

■ The wave functions must form an orthonormal set (the wave functions must be normalized and orthogonal).

■ The wave function must satisfy the boundary conditions of the quantum mechanical system it represents.

The physical meaning of the wave function has its squared modulus $|\Psi(x,t)|^2$ that is the probability density. The expression $\int \Psi^* \Psi dx$ means the probability of finding the *i*-th particle at time *t* in the coordinate range $[x_i, x_i + dx]$.

3.2. Description of electronic levels in solids

In solid state physics, various theoretical models are used to study the electronic properties of materials, which provide information on the structure of electronic levels and related physical properties. All these methods are reduced to different ways of solving of a main equation of quantum mechanics – the Schrödinger equation (or wave equation). For a system consisting of *N* interacting particles with potential energy *U* and mass m_k in the Cartesian coordinate system, the Schrödinger wave equation will look like this:

$$\left(-\frac{\hbar^2}{2m} \nabla^2 + U \right) \Psi = i\hbar \frac{\partial \Psi}{\partial t} , \qquad (3.1)$$

where $\Psi(\{x\},t)$ is a wave function which describes the particle, and it is a function of the coordinates of the particles *x* and time *t*. If there is no dependence on time (the evolution of a system does not under the consideration (the energy has some defined values)), then this equation is called stationary

$$\left(-\frac{\hbar^2}{2m} \nabla^2 + U \right) \Psi = E\Psi . \qquad (3.2)$$

Solving the stationary Schrödinger equation, can be found the eigenvalues *E* and the corresponding solutions are eigenfunctions. Discrete values of energy *E* corresponds to the energy position of the corresponding energy levels.

Equation (3.2) can be represented in a compact operator form:

$$\hat{H}\Psi = E\Psi , \qquad (3.3)$$

where $\hat{H}$ is the operator of Hamiltonian for system of the particles:

$$H = T + U .\tag{3.4}$$

where T is the operator of kinetic energy of a particle, and U is the potential energy operator of a particle. Thus, the solution of the Schrödinger equation is reduced to the problem of eigenvalues and eigenfunctions of the total energy operator of the system H. This problem can be solved analytically for a hydrogen atom, while for more complex systems (e.g. H_2^+ ion molecule) an exact analytical solution of the Schrödinger equation is impossible. Therefore, the solution of this equation is sought with the help of numerical methods and with the use of various approximations that simplify this problem.

In general, these methods are divided into *ab initio* and semi-empirical. Semi-empirical methods greatly simplify the problem described above by using in the model a parameters, necessary for the calculations, obtained from the experiment. *Ab initio* methods are based solely on physical laws and allow to calculate the properties of the material without the use of any experimental data. These methods use a minimum number of assumptions and simplifications. Despite some differences in these two classes of methods, they are not fundamentally different. The most popular today are the basic methods based on the theory of density functional, the main provisions of which are given in the next section.

3.3. Fundamentals of density functional theory (DFT)

After the development of Hartree-Fock theory [134] the most effective and popular method for calculation the quantum systems are the method based on the theory of density functional [19,134]. It was an important step towards solving the problem of finding the solutions of the wave equation. This approach reduced the problem of solving a $3N$-dimensional equation (for example, the description of 10 electrons requires 30 parameters) to N separate three-dimensional equations for a system consist of the large number of particles. This assumption allowed using of the electron density $n(\mathbf{r})$ instead of the complex N-particle wave functions $\Psi(\mathbf{r}_1, \mathbf{r}_2, \mathbf{r}_3 ..., \mathbf{r}_N, t)$, where $n(\mathbf{r}) = |\Psi(\mathbf{r})|^2$. This significantly reduces the computational costs for the practical application of the method to molecules, solids and materials with a large number of atoms [134].

Density functional theory was proposed by Kohn and Hohenberg in 1964. The birthday of the DFT coincide with the publication of the manuscript by Pierre Hohenberg and Walter Kohn in 1964 entitled "Inhomogeneous electron gas" [18] in the Physical Review Journal. For this theory in 1998, the Nobel Prize was awarded to the Walter Kohn

and Lu Jen Sham. DFT is the basis for a variety of numerical methods for *ab initio* modelling of the electronic structure and properties of molecular systems and condensed phases. DFT-based calculations have attracted a lot of attention in the field of condensed matter physics in recent decades and have become one of the most commonly used theoretical tools in this field.

Despite the fact that DFT is based on the classical Thomas-Fermi model [134], its theoretical substantiation was developed with the formulation of two Hohenberg-Kon theorems [18].

Theorem I (uniqueness): The ground state density $n(\mathbf{r})$ of bonded system of interacting electrons in some external potential $V_{ext}(\mathbf{r})$ determines this potential uniquely to within a trivial additive constant.

From the first theorem we have that the external potential V_{ext}, which by definition is a measure of the interaction between electrons and nuclei, can be represented not by a wave function describing the orbitals in the approximation of independent electrons, but by the electron density $n(\mathbf{r})$. This confirms that the external potential and, as a consequence, the Hamiltonian operator of the ground state of electrons can be unambiguously determined only by the electron density.

The number of electrons N interaction with nucleus is determined by integration of electron density $n(\mathbf{r})$

$$\int n(\mathbf{r})dr^3 = N \,. \tag{3.5}$$

Since, the $n(\mathbf{r})$ determines the number of electrons in the system it also determines the ground state wave functions and all other electronic properties. This means that, in the ground state, if the electron density is known it is defines external potential, Hamiltonian, wave function, and all ground-state properties of the system in turn. In particular it is possible to calculate the ground state energy $E_0[n_0]$.

$$E = \left\langle \Psi \left| \hat{H} \right| \Psi \right\rangle = E[n] \,. \tag{3.6}$$

Corollary 1. All properties of the system are completely determined by the ground state electron density $n_0(\mathbf{r})$.

Since the internal energy is a system independent and does not depend on the external potential, a density-dependent internal energy should be there as a universal functional

$F[n(\mathbf{r})]$ although its explicit formula is unknown. Note, that the mathematical form of $F[n(\mathbf{r})]$ should be the same for all systems while the external potential varies from one system to another depending on the kind of nuclei.

$$E[n] = F[n] + \int n(\mathbf{r})V_{ext}dr . \tag{3.7}$$

Then, different Hamiltonians differ only by their external potential, and, if there were two different external potentials that yield the same ground-state electron density, it leads to an apparent contradiction [134].

From the first Hohenberg-Kohn theorem follows

$$E[n] = \langle \Psi \mid H \mid \Psi \rangle = \langle \Psi \mid T + U \mid \Psi \rangle + \langle \Psi \mid V \mid \Psi \rangle = F[n] + \int n(\mathbf{r})V_{ext}dr , \tag{3.8}$$

where T is the kinetic energy of electron, U is the potential energy due to interaction between them, V is the potential energy from the external potential, and $F[n]$ is a universal functional for any electron system. The $E[n]$ reached the minimal value (corresponding the total energy of ground state) at the ground state density $n_0(\mathbf{r})$ that corresponds to V_{ext}.

Theorem II (variational principle): the density $n(\mathbf{r})$ that minimizes the total energy functional $E[n(\mathbf{r})]$ is the exact ground state density $n_0(\mathbf{r})$ ($E[n(\mathbf{r})] > E_0[(\mathbf{r})]$).

This theorem does not give us the exact form of the energy functional $E[n(\mathbf{r})]$. It identified a way to find the minimum energy of a system and proved that the ground state of a system could be searched by using the variational principle. At a given V_{ext}, the minimization of the system energy to the lowest value by the variation of the electron density lead to finding the minimal energy of the system. The electron density $n(\mathbf{r})$ that minimizes the system energy is the truly ground-state electron density $n_0(\mathbf{r})$. It states, that ground-state wave function $\Psi_0(\mathbf{r}_1, ..., \mathbf{r}_n)$ is the wave function, that minimizes the energy functional

$$E[\Psi] = \frac{\langle \Psi \mid H \mid \Psi \rangle}{\langle \Psi \mid \Psi \rangle} , \tag{3.9}$$

where

$$\langle \Psi \mid H \mid \Psi \rangle = \int \Psi^* H \Psi d\mathbf{r} , \tag{3.10}$$

if the ground state is nondegenerate, this means, that for each wave function $\Psi \neq \Psi_0$ the following equation holds:

$$E[\Psi] > E_0 = E[\Psi_0] . \tag{3.11}$$

Starting from the variational principle, it is possible to gaint insights about this energy functional

$$E = \min_{\phi} \left\{ \langle \phi | H | \phi \rangle \right\} = \min_{n} \left\{ \min_{\phi \to n} \left\{ \langle \phi | H | \phi \rangle \right\} \right\} =$$

$$= \min_{n} \left\{ \min_{\phi \to n} \left\{ \langle \phi | T_e + V_{ee} + \sum_{i=1}^{N_e} V_{ext}(\mathbf{r}_i) | \phi \rangle \right\} \right\} = \quad (3.12)$$

$$= \min_{n} \left\{ \min_{\phi \to n} \left\{ \langle \phi | T_e + V_{ee} | \phi \rangle \right\} + \int n(\mathbf{r}) V_{ext}(\mathbf{r}_i) d\mathbf{r} \right\},$$

where $F[n] = \min_{\phi \to n} \left\{ \langle \phi | T_e + V_{ee} | \phi \rangle \right\}$ is a universal functional of the density, but it is not known explicitly.

3.4. Kohn-Sham equation

Kohn and Sham in 1965 reformulated the problem of solving of the Schrödinger wave equation and allowed the density functional theory to be used in practice. The main idea of this approach was to reintroduce a special type of wave functions (a single particle orbitals) into the formalism, to treat the kinetic and interaction energy terms. In contrast to the Hartree-Fock approach [134], where all electrons interact with each other through a Coulomb interaction, the Kohn and Sham approach considers a system consisting of quasiparticles that do not interact with each other. However, these particles interact with an external effective potential V_{eff} that causes them to behave as if they are charged and have the same electron density $n(\mathbf{r})$. That is, the system of interacting electrons where each is considered as a system of non-interacting electrons having the same ground state charge density $n(\mathbf{r})$. For a system of noninteracting electrons, the charge density of the ground state can be represented as the sum of one-electron orbitals $\Psi_i(\mathbf{r})$ which are called Kohn-Sham orbitals (KS):

$$n(\mathbf{r}) = 2 \sum_i | \phi_i(\mathbf{r}) |^2 , \quad (3.13)$$

where i runs from 1 to $N/2$.

Effective local potential includes external potential and electronic interaction taking into account exchange and correlation energies. Then, the energy of system can be written as:

$$E_{KS}[n(\mathbf{r})] = T_s[n(\mathbf{r})] + V_H[n(\mathbf{r})] + V_{ext}[n(\mathbf{r})] + V_{XC}[n(\mathbf{r})], \quad (3.14)$$

where T_s is the kinetic energy of the electron interaction, where subscript "*s*" denotes "single particle", V_H is the contribution described by the classical electrostatic interaction or Hartree energy, V_{ext} the external potential which is formed by ions and other fields (e.g. electric, magnetic), and V_{XC} is a term that describes a special type of interaction of quantum particles and includes the effects of electron exchange and correlation. The first two terms are the same for any system. V_{ext} depends on the specific system under consideration and for different configurations the arrangement of atoms will have its own form. The most difficult task is to describe the exchange-correlation interaction of electrons. Usually this type of interaction is divided into two components $E_{XC} = E_X + E_C$, where E_X is the exchange energy due to the Pauli principle (antisymmetry) and E_C is due to correlations. A many different approaches for description of the *XC* interaction will be discussed in section 3.6.

In order to minimize the energy of the system Eq. 3.14 (i.e. find the energy of the ground state of the particle system) relative to the density and applying the variational principle $\delta E[n(\mathbf{r})] = 0$, we can write a one-particle Schrödinger equation as

$$
\begin{aligned}
0 = \frac{\delta E[n]}{\delta n(\mathbf{r})} &= \frac{\delta T_s[n]}{\delta n(\mathbf{r})} + \frac{\delta V[n]}{\delta n(\mathbf{r})} + \frac{\delta U_H[n]}{\delta n(\mathbf{r})} + \frac{\delta E_{XC}[n]}{\delta n(\mathbf{r})} = \\
&= \frac{\delta T_s[n]}{\delta n(\mathbf{r})} + v(\mathbf{r}) + v_H(\mathbf{r}) + v_{XC}(\mathbf{r})
\end{aligned}
\tag{3.15}
$$

if consider the system of non-interacting particles moving in the arbitrary potential v_s for this system minimization condition is

$$
0 = \frac{\delta E_s[n]}{\delta n(\mathbf{r})} = \frac{\delta T_s[n]}{\delta n(\mathbf{r})} + \frac{\delta V_s[n]}{\delta n(\mathbf{r})} = \frac{\delta T_s[n]}{\delta n(\mathbf{r})} + v_s(\mathbf{r}).
\tag{3.16}
$$

The density that solves the Euler equation is $n_s(\mathbf{r})$. Compared to Eq. 3.15 it is seen that if we take that

$$
v_s(\mathbf{r}) = v(\mathbf{r}) + v_H(\mathbf{r}) + v_{XC}(\mathbf{r}),
\tag{3.17}
$$

the density of the interacting multielectron system in the potential $v(\mathbf{r})$ described by the multiparticle Schrödinger wave equation can be calculated by solving simply the equation of noninteracting single-particle systems in the potential $v_s(\mathbf{r})$. In case of double population of all states, the Kohn-Sham orbital is the solution of the Schrodinger wave equation

$$
\left[-\frac{\hbar^2}{2m} \nabla^2 + v_s(\mathbf{r}) \right] \phi_i(\mathbf{r}) = \varepsilon_i \phi_i(\mathbf{r}),
\tag{3.18}
$$

here, the ϕ_i is the orbitals, called Kohn-Sham orbitals, reproduce the density $n(\mathbf{r})$ of the original system. The electron density in this case is estimated using the following equation:

$$n(\mathbf{r}) = n_s(\mathbf{r}) = \sum_i^N f_i |\phi_i(\mathbf{r})|^2 , \qquad (3.19)$$

where f_i is the occupation of ith orbital, ϕ_i is the i-th orbital. This Eq. 3.18 is named after Kohn and Sham and is called a Kohn-Sham equation. Here the wave functions obeying the orthonormality constraints

$$\int \Psi_i^*(\mathbf{r})\Psi_i(\mathbf{r})dr = \delta_{ij} , \qquad (3.20)$$

where δ_{ij} is Kronecker's delta. Thus, we can write the Kohn-Shaam equation as follows. The wave function minimizes the Kohn-Sham functional energy in Eq. 3.18 satisfy the following eigen value equations,

$$\hat{H}_{KS}\phi_i = \varepsilon_i \phi_i . \qquad (3.21)$$

Here H_{KS} is the Kohn-Sham's Hamiltonian

$$\hat{H}_{KS} = -\frac{\hbar^2}{2m}\nabla^2 + V_{ion}(\mathbf{r}) + V_H(\mathbf{r}) + V_{XC}(\mathbf{r}), \qquad (3.22)$$

where $V_H(\mathbf{r})$ is the Hartree potential

$$V_H(\mathbf{r}) = \int \frac{n(\mathbf{r}')}{|r-r'|} d^3r' , \qquad (3.23)$$

and V_{XC} is the exchange-correlation potential

$$V_{XC}(\mathbf{r}) = \frac{\delta E_{XC}[n]}{\delta n(\mathbf{r})} . \qquad (3.24)$$

3.5. Self-consistent procedure of the Kohn-Sham equation solution

Equation (3.18) can be solved self-consistently according to the algorithm proposed by Kohn and Sham [19,134]. The general view of the procedure for solving the Kohn-Schem equation is illustrated in Fig. 3.1. The self-consistent algorithm can be described as follows. At the first step, the starting (initial) electron density $n(\mathbf{r})$ is set and v_{KS} is built with it. At the second step, substitution the density into the Hamiltonian and solve in the Eq. (3.18), and then solving the differential equation for ϕ_i is performed. Solving the equation gives new one-electron functions ϕ_i, from which in the third step a new electron density is revelled.
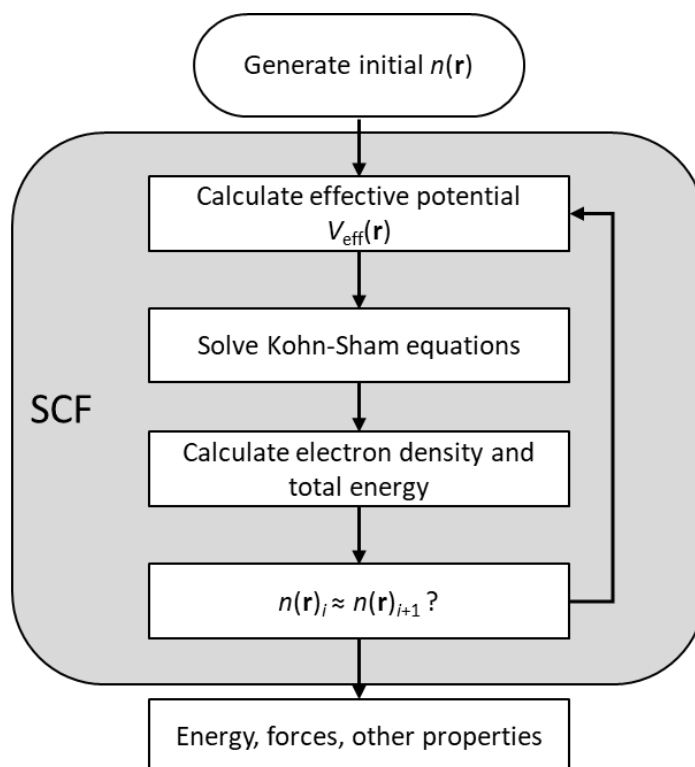
Figure 3.1. Schematic representation of the self-consistent loop used in DFT calculations for Kohn-Sham equations solution.

At the fourth step, it is checked whether the electron density does not differ from the initial one ($|n_{i+1}(\mathbf{r}) - n_i(\mathbf{r})| < \varepsilon$, where ε is the criterion of convergence of the self-consistancy process), whether the electron density corresponds to the ground state. In case where the cycle criterion is not met, the obtained electron density is substituted in the second step of the algorythm and the process is repeated until the desired convergence is achieved. If there is a ground state of the electronic system, it is easy to calculate the forces acting on ions, electronic structure, optical, thermodynamic and other properties of the system.

3.6. Exchange-correlation functionals

As was mentioned in paragraph 3.4, the main problem to perform a precise calculation of electronic structure and physical properties is related with the description of the quantum interaction of electrons named as exchange and correlation interaction. This type of interaction has a quantum nature and exact analytical expression is unknown. The *XC* interaction consist of two exchange and correlation parts. The exchange part corresponds the exchange interaction of electrons. This is the special, appropriate only for quantum

systems contribution to the total energy of many particles system, related with the identity (indistinguishability) of the electrons that occurs between the identical particles. For fermions this interaction is called Pauli's repulsion and is related with the Pauli principles [135]. The correlation part of *XC* term describes the interaction in the electronic systems and is the measure of how much the movement of one electron influence on the all other present electrons. In this case there is the correlated movement between the electrons with antiparallel spin occurring through their mutual Coulomb repulsion. The exact *XC* functional is still unknown and for its description an approximations are used.

For the estimation of the unknown *XC* interaction there is a lot of different approximations and parametrizations developed by scientists. The general goal of those authors was to propose the functional that describes the system as close to the real system as possible giving the results of calculation in excellent agreement with the experiment. Those approximations of *XC* term is classified on different groups. The general scheme of *XC* classification and evolution is depicted in Fig. 3.2. Few often used functionals are considered in this paragraph.
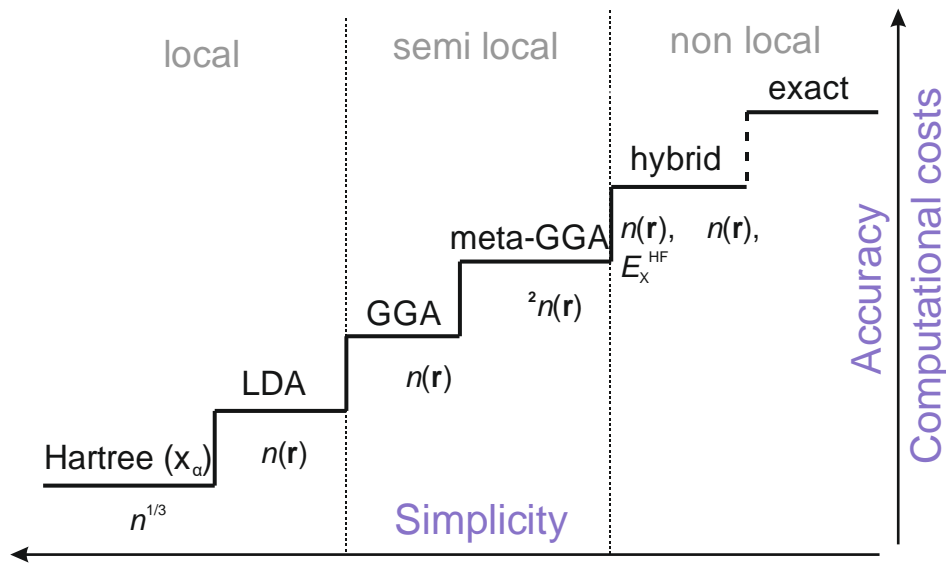
Figure 3.2. The general classification of the *XC* functional used in DFT.

The one of the simplest, important, and commonly used approach of $E_{XC}[n(\mathbf{r})]$ is the local density approximation (LDA) [136]. The *XC* energy value is taken of the electron in the position **r** in the many interacting electrons system with constant density, which is the same as *XC* energy per electron in the uniform electron gas with the same density as in the system at position **r**. In the framework of this approximation the heterogeneous electron

density is treated as locally homogenous (is an analogue of the electron gas) with *XC* energy density $\varepsilon_{XC}[n(\mathbf{r})]$ which is given by the expression

$$E_{XC}^{LDA}[n(\mathbf{r})] = \int \varepsilon_{XC}^{\mathrm{hom}}(n(\mathbf{r}))n(\mathbf{r})dr, \qquad (3.25)$$

where ε_{XC} is the exchange-correlation energy of homogeneous electron gas with the charge density $n(\mathbf{r})$. The charge density is determined by the parametrization of modelling of electron gas by quantum Monte Carlo method. In this approximation the *XC* energy is considered to be dependent only on electron density in a point **r**. Despite the fact that this approximation is quite simple, and the electron gas in a solid is very far from homogeneous, however, the lengths of the bonds in the crystal and molecules are calculated with an accuracy of ~ 1%. To the disadvantages of this method the underestimation of the bond length, cohesion energy, and band gap width can be attributed.

The logical continuation of equation (3.25) and other simplest approach was the appearance of a generalized gradient approximation (GGA). A correction related to the inhomogeneity of the electron density is introduced to the functional (3.26). The gradient of electron density $|\nabla n(\mathbf{r})|$ was taken into account and is taken as the characteristics of inhomogeneity. In the GGA functional the information about charge density gradient $n(\mathbf{r})$ is used for the construction of the more precise functionals [137].

$$E_{xc}^{GGA}[n(\mathbf{r})] = \int \varepsilon_{XC}^{\mathrm{hom}}(n(\mathbf{r}),|\nabla n(\mathbf{r})|)n(\mathbf{r})dr. \qquad (3.26)$$

In such a way the GGA functional include not only the electron density at point **r** (is local as LDA) but take into account the behaviour of this density in a point. This transition from LDA to GGA has led to a significant increase in the accuracy of calculations and often fix the majority of LDA's disadvantages.

Often for the calculations the different class of functionals, called as a hybrid functionals, are used [138]. One of the popular hybrid functional is the Becke, 3-parameter, Lee–Yang–Parr (B3LYP) that can be presented as follows [139], [140]:

$$E_{XC}^{B3LYP}[n(\mathbf{r})] = E_X^{LDA} + a_0(E_X^{HF} - E_X^{LDA}) + a_X(E_X^{GGA} - E_X^{LDA}) + \qquad (3.27)$$
$$+ E_C^{LDA} + a_C(E_C^{GGA} - E_C^{LDA}),$$

where $a_0 = 0.2$, $a_X = 0.72$ and $a_C = 0.81$, E_X^{GGA} and E_C^{GGA} is a generalized gradient approximation: Becke 88 exchange functional [141] and correlation functional of Lee, Yang and Parr [138] for B3LYP, E_X^{LDA}, E_C^{LDA} is a local density approximation Vosko-Wilk-Nusair (VWN) for correlation description [142]. The hybrid functionals often fix the problem of band gap underestimation but requires the much more computational costs (see Fig. 3.2) leading to the limitation of using this functional for systems with large number of electrons.

In order to improve the calculation and fix the band gap problem the different corrections are used to obtained agreement between the experiment and calculations. The detailed description of other functionals like mBJ, sX, HSE and others do not discussed in this chapter and can be found in the literature.

3.7. Pseudopotentials

The pseudopotential or effective potential is used in quantum mechanics and solid state physics as an approximation for the simplified description of complex systems with many particles. The pseudopotential approximation was first introduced by Hans Hellmann in 1930s [143]. The main idea of using pseudopotentials instead of true potentials for atoms is based on the fact that the orbitals of the core electrons are located closer to the nucleus and experience strong oscillations, which would require the expansion of the number of wave functions in terms of too large a set of basis functions (plane waves) when solving the Kohn-Sham equations. Only a valence electrons mainly determine the chemical and physical properties of materials. Therefore, the underlying basic electrons are most often chemically inert and can be considered in the frozen core approximation. In the pseudopotential approximation, core electrons are excluded from the solution of the many-electron problem by replacing the nuclear potential with a pseudopotential that models the core-valence and valence-nuclear interactions.

$$\phi(r) = \begin{cases} \phi(r), & r \leq r_c \\ \Psi(r), & r > r_c \end{cases}, \tag{3.28}$$

where the r_c is a suitable cut-off radius, $\Psi(\mathbf{r})$ is the all-electron wave function, and $\phi(\mathbf{r})$ is the pseudo wave function.

Due to the screening of the nucleus by core electrons, the pseudovalent orbitals have a smoother potential near the nucleus. The concept of pseudization is illustrated in the

Fig. 3.3. Such procedure is equivalent to the substitution of the strong electron-ion potential by weaker pseudopotential, which clearly expressed properties of the valence electrons including the relativistic effects and true valence wave functions (with radial nodes) are replaced by a pseudo wave functions (without nodes). Thuse, the studding system is replaced by a system consist of the pseudovatent electrons and pseudoions Fig. 3.4. The properties of the pseudoion are such that its potential outside a certain cut-off radius r_c coincides with the potential of the true ion, but inside this sphere it is much weaker. It is precisely the weakness of the internal potential that is the main thing in the theory of pseudopotential. In this case, the Schrödinger equation can be solved inside a sphere of radius r_c much easier, since the desired wave function is expanded in a much smaller number of basis functions.
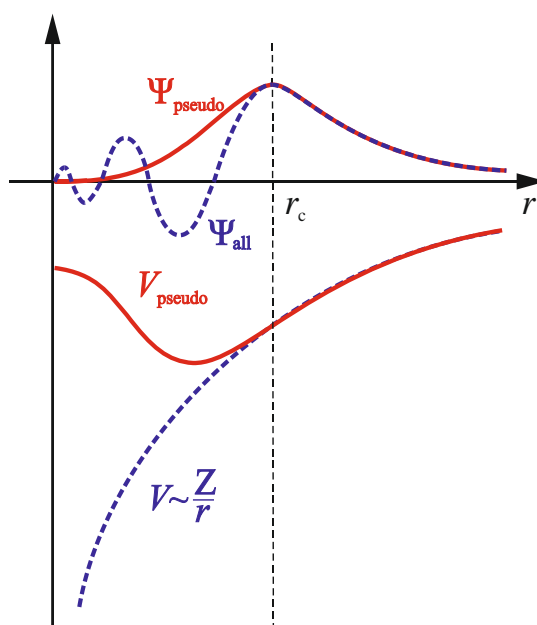

Figure 3.3. Schematic illustration of exact all electron (blue lines) and pseudopotential (red lines) and their corresponding wave functions inside and outside the core region of an atom at position r. The cut-off radius at which the all electron potential and pseudopotential values match is denoted as r_c.

On the Fig. 3.3 the two upper curves show the radial density distribution of the valence orbital $\phi(\mathbf{r})$ and the pseudovalent orbital $\phi^{PS}(\mathbf{r})$, which is smoother near the nucleus (at $r \leq r_c$). The pseudopotential $V^{PS}(\mathbf{r})$ reproduces the central potential $V(\mathbf{r})$ outside the core region ($r > r_c$), but the singularity at zero is smoothed out. The use of the pseudopotential significantly reduces the computational costs (allows reduction of basis set size), not only due to a decrease in the number of orbitals, but mainly due to a decrease in the required basis sets.

For example, let us consider the carbon atom. Assume we want to simulate a carbon system from first-principles. We know that the valence electrons are responsible for bonding. Therefore, we can substitute the full electronic configuration of for the carbon atom with the pseudopotential and $2s^2 2p^2$ valence states (for illustration see the Fig. 3.4).
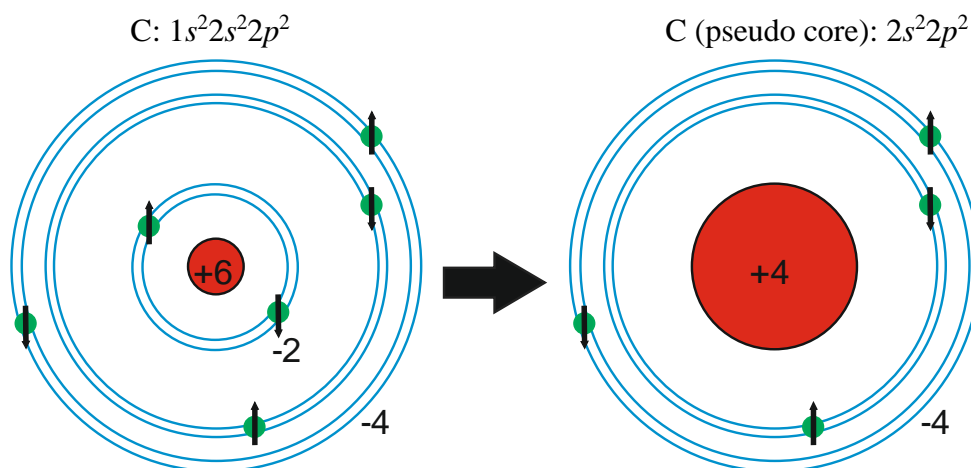
C: $1s^2 2s^2 2p^2$ C (pseudo core): $2s^2 2p^2$

Figure 3.4. Schematic representation of the frozen core and valence electrons for the construction of a pseudopotential of carbon atom.

It should be noted that the pseudopotential method has played a decisive role in the development of the plane wave method in the Kon-Shem approximation, which is the dominant approach in DFT. Value of the r_c is determined from the fitting of the calculated values e.g. coefficient of elasticity with experimental data.

In general, the use of a pseudopotential should result in smooth pseudovalent orbitals that reproduce the chemical properties due to the valence orbitals most reliably, even when switching to a different electronic configuration and chemical environment. These key properties of the pseudopotential are called softness, and transferability. The softer the pseudopotential, the smoother the pseudovalent orbital will be. Therefore, the representation of the orbitals will require a smaller base set, which will lead to fast and efficient calculations. The transferability of a pseudopotential is the main advantage of the pseudopotential method instead of the all-electron based DFT methods implementation. A pseudopotentials are constructed from some certain (fixed) electronic configuration of the atom or ion which is isolated. That is why this pseudopotential reproduce the scuttering properties of a nucleus in this configuration. The transferability can be assessed by ability of the pseudopotential to reproduce values obtained by multielectronic calculations in a wide range of different chemical compounds or other test systems in order to correctly reproduce

the scattering for other atomic configurations and atomic environment. Strategies that can improve the mentioned properties of softness and transferability have been developed to build pseudopotential that meets these requirements.

The most general form of the pseudopotential is as follows:

$$V_{NL} = \sum_{lm} |lm\rangle V_l \langle lm|, \tag{3.29}$$

where $|lm\rangle$ is a spherical harmonics, V_l is a pseudopotential of the angular momentum *l*. The action of this operator leads to the expansion of the electron wave function into spherical harmonics, each of which is then multiplied by the corresponding pseudopotential. If the pseudopotential uses the same potential in each angular momentum is called a local pseudopotential. This type of the pseudopotentials is computationally much more efficient than nonlocal.

The pseudopotentials are divided into two types called as norm-conserving pseudopotential (NCPP) and ultra-soft pseudopotential (USPP).

3.7.1. Norm-conserving pseudopotential

The pseudopotential approximation became especially popular after the appearance of the norm-conserving pseudopotentials. The first norm-conserving pseudopotential was proposed and developed by the by Kleinman and Bylander in 1982 [144]. This method has paved the new way to performing the accurate calculations of solid-state properties. Lets consider two of wave functions – pseudo-wave function Ψ^{PS} and all-electrons wave function Ψ^{AE}. If the charge densities within the core are constructed in the way to be equal for Ψ^{PS} and Ψ^{AE}, the corresponding pseudopotential is called a norm-conserving [145,146]. A lot of the different pseudopotentials are generated to satisfy this condition:

$$\int_0^{r_c} \left| \Psi^{PP}(\mathbf{r}) \right|^2 d\mathbf{r} = \int_0^{r_c} \left| \Psi^{AE}(\mathbf{r}) \right|^2 d\mathbf{r}, \tag{3.30}$$

For generation of a good ab initio pseudopotential there are few generally accepted criteria requirements should be matched for choosing the most optimal pseudopotential [145]:

1. The pseudo-wave function should not have nodes. This is necessary to obtain a smooth pseudo-wave function;

2. The all-electron and pseudo valence eigen values agree for chosen atomic reference configuration (The eigenvalues of both wave functions must be equal/ should be the reproducible by the pseudovalent)

$$\varepsilon^{PS} = \varepsilon^{AE} . \tag{3.31}$$

3. All-electron pseudo valence wave functions agree beyond the chosen core radius r_c. (Real and pseudo wave function agree outside the chosen core radius r_c. (outside the core region)

$$\phi^{PS}(\mathbf{r}) = \Psi(\mathbf{r}), \text{ for } \forall \mathbf{r} \geq r_c . \tag{3.32}$$

4. The logarithmic derivatives of all-electron and pseudo wave functions should agree at the core radius r_c.

5. The integrated charge inside core radius r_c for each wave function agrees (the norm conservation criterion). (Charges concentrated inside a sphere with radius r_c must coincide for both wave functions)

$$\left\langle \Psi_i \middle| \Psi_j \right\rangle - \left\langle \phi_i \middle| \phi_j \right\rangle = \int_0^{r_c} r^2 \phi^*(\mathbf{r})\phi(\mathbf{r})dr - \int_0^{r_c} r^2 \Psi^*(\mathbf{r})\Psi(\mathbf{r})dr = 0 . \tag{3.33}$$

6. The pseudo-wave function must be continuous and twice differentiable.

7. The first energy derivative of the logarithmic derivative of the all-electron and pseudo wave functions agree at r_c.

The generalized norm-conserving condition can be written as follows [145]

$$Q_{ij} = \left\langle \Psi_i \middle| \Psi_j \right\rangle_{r_c} - \left\langle \phi_i \middle| \phi_j \right\rangle_{r_c} = 0 . \tag{3.34}$$

Points (1) and (2) guarantee that the NCPP and the true potential are the same outside the core region.

Point (3) follows since the wave function and its radial derivative are continuous at R_c for any smooth potential.

Point (4) imposes the conservation of the charge in the core region:

$$Q_l = \int_0^{r_c} dr r^2 |\Psi_l(r)|^2 = \int_0^{r_c} dr \phi_l(r)^2 . \tag{3.35}$$

Note that all-electron (AE) and pseudo wave functions are different inside the core region.

Point (4) also means that the normalized pseudo-orbital and true orbital are equal outside the core region (different from OPW functions which are equal to the true functions only if it is not normalized).

Point (5) is crucial for the generation of a good transferable potential.

3.7.2. Ultrasoft pseudopotential

Ultrasoft pseudopotentials were introduced in 1990 by Vanderbilt in order to allow calculations to be performed with the lowest possible cutoff energy for the plane wave basis set [147]. The rationale behind USPP is that, in most cases, a high cutoff energy is only required for the plane wave basis set when there are tightly bound orbitals that have a substantial fraction of their weight inside the core region of the atom. In these situations, the only way to reduce the basis set is to violate the norm-conservation condition by removing the charge associated with these orbitals from the core region. Ultrasoft pseudopotentials relax the norm-conserving constraint to reduce the necessary basis-set size further at the expense of introducing a generalized eigenvalue problem [147].

3.8. Treatment of periodic systems

To solve the one-electron problem, electrons are considered, which are described by a wave function $\Psi(\mathbf{r})$ in the potential field of ions, the charge of which is on average compensated by the charges of valence electrons. From the characteristics of the crystalline state it follows that this potential is periodic, ie $U(\mathbf{r})$ has a three-dimensional lattice periodicity. As is known, in an ideal crystal, atoms are placed periodically in space. This means that there is a vector $\mathbf{R}_n$ at the displacement of the crystal by which the crystal is aligned with itself. Therefore, the points of the crystal with radius vectors $(\mathbf{r})$ and $(\mathbf{r} + \mathbf{R}_n)$ are physically equivalent, so

$$U(\mathbf{r}) = U(\mathbf{r} + \mathbf{R}_n). \tag{3.36}$$

The potential of the periodic system is also periodic in direct space $V(\mathbf{r}) = V(\mathbf{r} + \mathbf{R})$, where

$$\mathbf{R} = m_1\mathbf{a}_1 + m_2\mathbf{a}_2 + m_3\mathbf{a}_3, \tag{3.37}$$

and m_1, m_2, m_3 are integers, $\mathbf{a}_1$, $\mathbf{a}_2$, and $\mathbf{a}_3$ are the basis vectors in three-dimensional space. The last relation expresses the condition of periodicity of the potential field of the crystal.

If the wave function $\Psi(\mathbf{r})$ of the electron is nondegenerate, then in the periodic field of the crystal it differs from the wave function only by a constant factor C,

$$\Psi(\mathbf{r} + \mathbf{R}_n) = C\Psi(\mathbf{r}). \tag{3.38}$$

From the condition of normalization of the wave function it follows that

$$|C|^2 = 1, \tag{3.39}$$

and therefore, the factor C can be represented as

$$C = e^{i(\mathbf{k} \cdot \mathbf{R}_n)}. \tag{3.40}$$

Since the square of the modulus of this quantity is equal to one, in the last expression $\mathbf{k}$ is a constant vector that characterizes the quantum state of the electron in the crystal. It is called the wave vector $\mathbf{k} = 2\pi/\lambda$. It has the dimension of inverse length, so the product $(\mathbf{k} \cdot \mathbf{R}_n)$ is dimensionless. From the Eq. 3.36 and Eq. 3.40 follows that

$$\Psi(\mathbf{r} + \mathbf{R_n}) = e^{i(\mathbf{k} \cdot \mathbf{R_n})} \Psi(\mathbf{r}). \tag{3.41}$$

Therefore, the stationary wave function of the electron in the periodic field of the crystal depends on the wave vector and has the form

$$\Psi_{\mathbf{k}}(\mathbf{r}) = e^{i(\mathbf{k} \cdot \mathbf{R})} U_{\mathbf{k}}(\mathbf{r}), \tag{3.42}$$

where $e^{i(\mathbf{k} \cdot \mathbf{R})}$ is the plane wave, which propagates in the $\mathbf{k}$ direction and is periodic with the lattice period. The functions of $\Psi_{\mathbf{k}}(\mathbf{r}) = e^{i(\mathbf{k} \cdot \mathbf{R})} U_{\mathbf{k}}(\mathbf{r})$ type is called the Bloch functions, while the periodicity of its amplitude is the Bloch theorem. By the substitution of the Eq. (3.42) to Eq. (3.3) we will get

$$H\Psi_{\mathbf{k}}(\mathbf{r}) = E\Psi_{\mathbf{k}}(\mathbf{r}), \tag{3.43}$$

and therefore the energy of the electron in the crystal must depend on the wave vector $\mathbf{k}$, ie $E = E(\mathbf{k})$. Thus, the solution of the Schrödinger equation for an electron in the periodic field of a crystal is a propagating plane wave modulated with the lattice period, and the energy of the electron depends on the wave vector $\mathbf{k}$. This means that in order to obtain fundamental results from the theory, there is no need to know the numerical values of the force field (which cannot be determined), it is enough to know that it is periodic and its period coincides with the lattice period.

Compared with the wave vector of free electrons, the vector $\mathbf{k}$, which characterizes the state of the wave function in the crystal, has certain features. One of them is expressed by relation (3.42) and is that the displacement on the crystal lattice vector $\mathbf{R}$ is reduced to the multiplication of the wave function by $e^{i(\mathbf{k} \cdot \mathbf{R})}$. Another important feature of the wave vector is that to any vector $\mathbf{k}$, which characterizes the state of the electron a crystal, you can add an arbitrary vector of the reciprocal lattice $\mathbf{G}$, and such a change in $\mathbf{k}$ does not change the state of the electron. It follows that the vector $\mathbf{k}$ is determined up to the vector of the inverse lattice $\mathbf{G}$, and the states of the electron with $\mathbf{k}$ and $\mathbf{k} + \mathbf{G}$ are eqvivalent. Since the vector $\mathbf{k}$ is not uniquely defined, it acquires properties that distinguish it from the wave vector of free electrons. For this reason, $\mathbf{k}$ is not called a wave vector but a quasi-wave vector.

Accordingly, the associated momentum $\mathbf{p} = \hbar\,\mathbf{k}$ is called a quasi-momentum, and particles moving in crystals and described by vectors $\mathbf{k}$ are called quasiparticles.

Since the vector $\mathbf{k}$ is defined up to the vector $\mathbf{G}$, therefore, an arbitrary function describing the crystal can be translated into an arbitrary (usually the first) Brillouin zone. This procedure is called reduction to the first zone of Brillouin. The advantage of the scheme of consolidated zones is that the analysis of the behavior of a certain function is sufficient to conduct only in one zone.

3.9. The Kohn-Sham equation in reciprocal space

There are different ways to explain the concept and usefulness of the reciprocal lattice. One popular way is to explain the nature of the interaction of matter with X-rays (detailed description here [148]). This concept is used in physics to solve some problems that are easier to solve in reciprocal space than in direct. A crystal is a set of atoms that can be thought of as a set of points that are evenly and periodically arranged in three-dimensional space. These atoms are located in special positions of the crystal lattice and are characterized by long-range order (this is an ideal crystal). Knowing the structure of the unit cell (atomic coordinates and lattice symmetry), a whole crystal can be constructed using the translational symmetry of this lattice. Any point of this crystal can be described by the vector $\mathbf{r}_l$ which is a linear combination of primitive lattice parameters $\mathbf{a}_1$, $\mathbf{a}_2$, and $\mathbf{a}_3$ in linear space. Then the vector $\mathbf{r}_l$ can be written as follows

$$\mathbf{r}_l = l_1\mathbf{a}_1 + l_2\mathbf{a}_2 + l_3\mathbf{a}_3, \tag{3.44}$$

where l_i is an arbitrary integer numbers in range $0 < l_i < N$. The N is limited by a number of unit cells in the corresponding direction. We will not explain the concept and the details of the diffraction here as this is outside the scope of this thesis. However, these concepts are explained in detail in [148]. A diffraction pattern of a crystal is a map of the reciprocal lattice vectors $\mathbf{b}_1$, $\mathbf{b}_2$, $\mathbf{b}_3$ and are the basis vectors in the reciprocal space. The reciprocal lattice $\mathbf{b}_1$, $\mathbf{b}_2$, $\mathbf{b}_3$ basis vectors can be mathematically constructed from the direct unit cell basis by the following relations

$$\mathbf{b}_1 = 2\pi\frac{\mathbf{a}_2 \times \mathbf{a}_3}{|\mathbf{a}_1 \cdot \mathbf{a}_2 \times \mathbf{a}_3|}\,,\ \mathbf{b}_2 = 2\pi\frac{\mathbf{a}_3 \times \mathbf{a}_1}{|\mathbf{a}_1 \cdot \mathbf{a}_2 \times \mathbf{a}_3|}\,,\ \mathbf{b}_3 = 2\pi\frac{\mathbf{a}_1 \times \mathbf{a}_2}{|\mathbf{a}_1 \cdot \mathbf{a}_2 \times \mathbf{a}_3|}\,. \tag{3.45}$$

Each of this vector is orthogonal to two other lattice vectors. From the orthogonality of those three vectors follows the following relations

$$\mathbf{b}_1 \cdot \mathbf{a}_1 = 2\pi, \qquad \mathbf{b}_2 \cdot \mathbf{a}_1 = 0, \qquad \mathbf{b}_1 \cdot \mathbf{a}_1 = 0,$$
$$\mathbf{b}_1 \cdot \mathbf{a}_2 = 0, \qquad \mathbf{b}_2 \cdot \mathbf{a}_2 = 2\pi, \qquad \mathbf{b}_3 \cdot \mathbf{a}_2 = 0, \qquad (3.46)$$
$$\mathbf{b}_1 \cdot \mathbf{a}_3 = 0, \qquad \mathbf{b}_2 \cdot \mathbf{a}_3 = 0, \qquad \mathbf{b}_3 \cdot \mathbf{a}_3 = 2\pi.$$

Then the linear space can be written by vectors

$$\mathbf{G}_h = h_1\mathbf{b}_1 + h_2\mathbf{b}_2 + h_3\mathbf{b}_3, \qquad (3.47)$$

where h_i is an arbitrary integers numbers. Than the set of vectors $\mathbf{G}_h$ is usually called the reciprocal space, since it is the dual. If we define the reciprocal lattice with the vector $\mathbf{G}$ in way, that

$$e^{i\mathbf{G}\cdot\mathbf{R}} = 1, \qquad (3.48)$$

than the periodic part of Bloch function can be written as

$$u_{n\mathbf{k}}(\mathbf{r}) = \sum_{\mathbf{G}} u_{n\mathbf{k}}(\mathbf{G})e^{i\mathbf{G}\cdot\mathbf{r}}, \qquad (3.49)$$

where coefficients $u_{n\mathbf{k}}(\mathbf{G})$ obtained by the Fourier transform

$$u_{n\mathbf{k}}(\mathbf{G}) = \frac{1}{\Omega}\int_{\Omega} u_{n\mathbf{k}}(\mathbf{r})e^{-i\mathbf{G}\cdot\mathbf{r}}d\mathbf{r}. \qquad (3.50)$$

By the Fourier transform

$$V(\mathbf{r}) = \sum_{\mathbf{G}} \tilde{V}_{\mathbf{G}} e^{i\mathbf{G}\mathbf{r}} = V(\mathbf{r}+\mathbf{R}) = \sum_{\mathbf{G}} \tilde{V}_{\mathbf{G}} e^{i\mathbf{G}(\mathbf{r}+\mathbf{R})} = \sum_{\mathbf{G}} \tilde{V}_{\mathbf{G}} e^{i\mathbf{G}\mathbf{r}} e^{i\mathbf{G}\mathbf{R}}, \qquad (3.51)$$

here $\tilde{V}_{\mathbf{G}}$ is a coefficient of transform. According to the Bloch theorem, the wave function can be written as

$$\Psi_{n,\mathbf{k}}^{KS}(r) = e^{i\mathbf{k}r}u_{n,\mathbf{k}}(\mathbf{r}), \qquad (3.52)$$

where $u_{n,\mathbf{k}}(\mathbf{r})$ is a function which has the same periodicity as the potential, that is $u_{n,\mathbf{k}}(\mathbf{r}) = u_{n,\mathbf{k}}(\mathbf{r}+\mathbf{R})$. Therefore, the wave function can be derived as

$$\Psi_{n,\mathbf{k}}^{KS}(r) = e^{i\mathbf{k}r}u_{n,\mathbf{k}}(\mathbf{r}) = e^{i\mathbf{k}r}\sum_{\mathbf{G}'} \tilde{u}_{n,\mathbf{k}+\mathbf{G}'} e^{i\mathbf{G}'\mathbf{r}} = e^{i\mathbf{k}r}\sum_{\mathbf{G}'} \tilde{u}_{n,\mathbf{k}+\mathbf{G}'} e^{i(\mathbf{k}+\mathbf{G}')\mathbf{r}}, \qquad (3.53)$$

where $\tilde{u}_{n,\mathbf{k}+\mathbf{G}'}$ is the coefficient of the Fourier transform and $\mathbf{G}'$ is the reciprocal vector as $\mathbf{G}$ in Eq. 3.51. Substituting Eq. 3.51 and 3.52 into Kohn-Sham equation are derived as

$$\left(-\frac{\nabla^2}{2}+V^{KS}(\mathbf{r})\right)\Psi_{n,\mathbf{k}}^{KS}(\mathbf{r}) = \sum_{\mathbf{G}'}\frac{(\mathbf{k}+\mathbf{G}')^2}{2}\tilde{u}_{n,\mathbf{k}+\mathbf{G}'} e^{i(\mathbf{k}+\mathbf{G}')\mathbf{r}} + \sum_{\mathbf{G}}\sum_{\mathbf{G}'}\tilde{V}_{\mathbf{G}}\tilde{u}_{n,\mathbf{k}+\mathbf{G}'} e^{i(\mathbf{k}+\mathbf{G}+\mathbf{G}')\mathbf{r}} =$$
$$= \left(\sum_{\mathbf{G}'} e^{i(\mathbf{k}+\mathbf{G}')\mathbf{r}}\right)\left(\frac{(\mathbf{k}+\mathbf{G}')^2}{2}\tilde{u}_{n,\mathbf{k}+\mathbf{G}'} + \sum_{\mathbf{G}}\tilde{V}_{\mathbf{G}}\tilde{u}_{n,\mathbf{k}+\mathbf{G}'-\mathbf{G}}\right), \qquad (3.54)$$

The right side of the Kohn-Sam equation are derived as

$$\varepsilon_{n,\mathbf{k}}^{KS} \Psi_{n,\mathbf{k}}^{KS}(\mathbf{r}) = \left(\sum_{\mathbf{G'}} e^{i(\mathbf{k}+\mathbf{G'})\mathbf{r}} \right) \left(\varepsilon_{n,\mathbf{k}}^{KS} \tilde{u}_{n,\mathbf{k}+\mathbf{G'}} \right), \tag{3.55}$$

From the equation 3.54 and 3.55 the KS equation in reciprocal space for each **G'** is obtained as

$$\sum_{\mathbf{G'}} \left(\frac{(\mathbf{k}+\mathbf{G'})^2}{2} \delta_{\mathbf{G},\mathbf{G'}} + \tilde{V}_{\mathbf{G'}-\mathbf{G}} \right) \tilde{u}_{n,\mathbf{k}+\mathbf{G}} = \varepsilon_{n,\mathbf{k}}^{KS} \tilde{u}_{n,\mathbf{k}+\mathbf{G}}, \tag{3.56}$$

For each **k** the eigen value problem in Eq. 3.56 for the Hamiltonian matrix with the elements $H_{\mathbf{G},\mathbf{G'}}$ and overlaps matrix with elements $S_{\mathbf{G},\mathbf{G'}}$ is solved by the standard method of diagonalization. Thus $\varepsilon_{n,\mathbf{k}}^{KS}$ and $\tilde{u}_{n,\mathbf{k}+\mathbf{G'}}$ are calculated. Further wave functions with $\tilde{u}_{n,\mathbf{k}+\mathbf{G'}}$ are obtained (Eq. 3.53).

Taking into account plane waves, the electronic energy spectrum of crystal $\varepsilon_{n\mathbf{k}} = \varepsilon_n(\mathbf{k})$ in the zone with number n at the k-point of the first Brillouin zone is sought as a solution of the Kohn-Sham equation [134,148] which in the basis of plane waves has the form:

$$\sum_{\mathbf{G'}} (\frac{1}{2}(\mathbf{k}+\mathbf{G})^2 \delta_{\mathbf{G},\mathbf{G'}} + V_H(\mathbf{G}-\mathbf{G'}) + V_{xc}(\mathbf{G}-\mathbf{G'}) +$$
$$+V_{loc}^{ps}(\mathbf{G}-\mathbf{G'}) + V_{nloc}^{ps}(\mathbf{k}+\mathbf{G},\mathbf{k}+\mathbf{G'}))c_{n\mathbf{k}}(\mathbf{G}) = \varepsilon_{n\mathbf{k}} c_{n\mathbf{k}}(\mathbf{G}) \tag{3.57}$$

where V_H is the electrons potential (Hartrie potential); V_{XC} is the exchange-correlation potential that depends on electron density; V_{loc}^{ps} is the local and V_{nloc}^{ps} nonlocal parts of norm conserving pseudopotential; $c_{n,\mathbf{k}}$ is the variational coefficient of wave function expending of electron in the crystal by the plane waves, **G** is the reciprocal cell vectors. In order to solve the system of the Eq. 3.10 the Fourier coefficients for the potentials V_H, V_{XC}, and pseudopotentials V_{loc}^{ps}, and V_{nloc}^{ps} should be known. Here the accuracy of the description of the wave function and therefore the accuracy of the calculation of their energies also depends on how many basis functions there are in Eq. 3.53. The number of plane waves used in the calculations are defined by the cut-off energy for the plane wave basis set (E_{cut}). The calculation time significantly depends on the size of the Hamiltonian matrix (E_{cut}) over time to diagonalize the Hamiltonian matrix. The coefficients $u_{n\mathbf{k}}(\mathbf{G})$ for the eigenfunctions of the lowest energy decrease exponentially with the kinetic energy $(\mathbf{k}+\mathbf{G})^2/2$. Considered in the sum of plane waves are selected using the kinetic energy of the cutoff E_{cut} (which determines the sphere of plane waves). The E_{cut} is used to cut-off the kinetic energy that controls the number of plane waves at a given point **k**. All plane waves inside this "basis sphere" with center in **k** are included in the basis (Fig. 3.1).
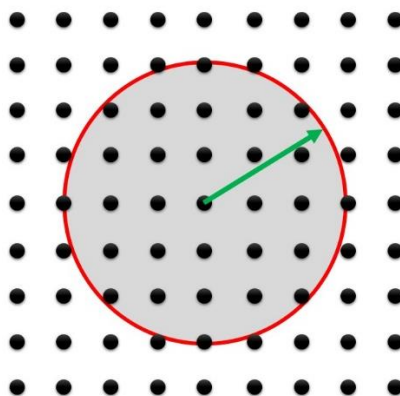
Figure 3.5. Schematic representation of the cutoff energy concept.

3.10. Short description of the CASTEP code

The CASTEP application [149] (CAmbridge Serial Total Energy Package) used in this work is designed for use on Linux, MacOS, and Windows operating systems. It is written in the programming language Fortran 2003, and its architecture allows for parallel calculations on multiple processors. The program is designed to calculate the electronic, optical, elastic, vibrational, and other properties for structure with different symmetry and composition form the first principles. The objects of study can be from simple molecules to complex polyatomic compounds. The basis of plane waves required for calculations is formed on the basis of norm-conserving or ultrasoft pseudopotentials. The program provides for the use of exchange-correlation functionalities in the approximation of LDA, GGA, HF, sX, PBE0, B3LYP, SHE03, SHE06. The program is a set of tools and methods for interaction between the user and the computer system, gives opportunities to work with it: or through the use of text input files (scripts) that contain all the necessary parameters for the program; or through a graphical interface.

To achieve the goals and solve our problems, from the many possibilities inherent in the software code CASTEP [149], we used the following: solving Kohn-Sham equations and determining the energy spectra of crystals, calculating the electron density distribution, calculating total and partial density of states, calculation of optical spectra, calculation of atomic charges and Milliken population, optimization of geometric structure, calculation of effective Born charges, dielectric constant and phonon frequencies, calculation of Raman spectra and infrared spectra, calculation of elastic properties.

The calculation of the energy band structure of the studied crystals was performed within the framework of the density functional theory, for which the electron density was calculated as a result of the procedure of structure optimization and self-consistency.

3.11. Conclusions

1. This section presents the basics of the quantum mechanical approach for describing quantum systems. A review of the methods of calculations of the band-energy structure and physical properties of crystalline materials is carried out.

2. The basic principles of the density functional theory as one of the modern methods of computer materials science are considered. The basic algorithms and approximations used for application in solid state physics are discussed. The use of pseudopotential for simplification of the description of electron-ion interaction in the form of ultrasoft and norm-conserving pseudopotential is considered.

3. The method of studying the electronic structure, optical spectra, density of states, and electron density distribution of crystals in the framework of the electron density functional theory by solving the Kohn-Shem equation has been shown.

4. The main approximations used to describe the exchange-correlation interaction of electrons in solids are presented and considered. Their peculiarities and limitations are discussed. The main types of exchange-correlation functionals such as LDA, GGA, B3LYP are considered.

4. STRUCTURE, ELECTRONIC AND PHYSICAL PROPERTIES OF I-III-VI₂ GROUP CRYSTALS

4.1. Parameters of calculation and crystal structure optimization

The first principles of calculations of total energy, band structure and properties of the family of ternary semiconductor crystals of I-III-VI₂ (I = Ag Cu, III = Al, Ga, In, VI = S, Se, Te) group are carried out in the framework of density functional theory (DFT) [18,19]. The calculations are performed using the Cambridge Serial Total Energy Package (CASTEP) code, which is implementation of DFT and is a modulus of the Materials Studio program [150]. The program uses a pseudopotential method to describe the ionic core, which significantly simplifies computer calculations compared to methods using all-electron wave functions.

When calculating the electronic structure and properties of materials the ion-electron interaction within calculations is described by the Vanderbilt ultrasoft pseudopotential [147]. This pseudopotential require much lower plane wave cutoff energy and has a better transferability in comparison with the norm-conserving one. As basis functions for describing electronic states the wave functions in form of plane waves are used.

The cutoff energy (maximum kinetics energy) $E_{cut} = |\mathbf{k} + \mathbf{G}|^2/2$ for the plane wave basis was fixed to be equal to 350 eV. The cut-off energy value was selected by performing a test of the total energy convergence of the system in relation to the value of the cut-off energy. The valence electrons for atoms that form the I-III-VI₂ group have the following configuration: Cu $3d^{10}\ 4s^1$; Ag $4d^{10}\ 5s^1$; Al $3s^2\ 3p^1$; Ga $3d^{10}\ 4s^2\ 4p^1$; In $4d^{10}\ 5s^2\ 5p^1$; S $3s^2\ 3p^4$; Se $4s^2\ 4p^4$; Te $5s^2\ 5p^4$.

The local density approximation (LDA) with the Ceperley – Alder – Perdew –Zunger (CA – PZ) parameterization [136,151] and the generalized gradient approximation (GGA) with the Perdew – Burke – Ernzerhof parameterization (PBE) [47] were used to take into account the exchange and correlation effects. These methods have shown themselves well in other theoretical studies performed by various authors [64–66,152,153]. All the properties of the investigated crystals were obtained from the self-consistent solution of the

Kon-Shem equations. For self-consistent electronic minimization, the eigen energy convergence tolerance was chosen at $5×10^{-7}$ eV and the tolerance of the electronic total energy convergence was 10^{-5} eV/atom.

The BZ sampling for calculation of the electronic structure and optical spectra was implemented using Monkhorst-Pack **k**-mesh [154]. For calculation of total energy, the $3×3×1$ **k**-mesh was used. For the band structure calculations, density of states $N(E)$ and optical properties of the crystals the $4×4×2$ greed was used. The choice of **k**-mesh was made similarly to the choice of cut-off energy during the test. The study of the convergence of the total energy of the system with respect to the size of the **k**-mesh was carried out. From the convergence test the proper **k**-mesh wsa chosen. In order to prevent the influence of the basis and **k**-mesh on the results of calculations, the optimal value was chosen uniformly. Appropriate test calculations were performed for different cation-anionic compositions of compounds of group I-III-VI₂.

In order to calculate the parameters of the crystals for the electron density $n(\mathbf{r})$ in the ground state, the geometric optimization of the crystal unit cell was performed. The Broyden-Fletcher-Goldfarb-Shanno (BFGS) algorithm [155] was used for geometry optimization of the crystal before calculation of the electronic characteristics (total electronic energy, band energy dispersion $E(\mathbf{k})$, total and partial density of states (PDOS)), dielectric functions and vibrational properties. For the geometric optimization of the crystal structure, the crystal lattice was relaxed. This process implies optimization of the crystal's unit cell parameters and relaxation of the atomic positions. The crystal's space group symmetry was constrained during the optimization process in order to prevent any structure transformations/distortions. The convergence parameters used during optimization were as follows: the maximum force $3×10^{-2}$ eV/Å; maximum pressure $5×10^{-3}$ GPa and maximum displacement $1×10^{-4}$ Å.

Since chalcopyrite crystals belong to $I\bar{4}2d$ symmetry, the crystal lattice in its structure contains 4 primitive cells. Each unit cell contains of 8 atoms. It is known from solid state physics that a primitive cell unambiguously describes the structure and physical properties of a material. Therefore, we used a primitive cell instead of a crystal lattice to calculate the band-energy structure of the studied group of crystals. The structure of a primitive cell for crystals of group I-III-VI₂ is shown in Fig. 4.1. Here the yellow balls are atoms of group I (I = Ag, Cu), the red balls are atoms of group III (III = Al, Ga, In) and the green balls are atoms of group VI (VI = S, Se, and Te).
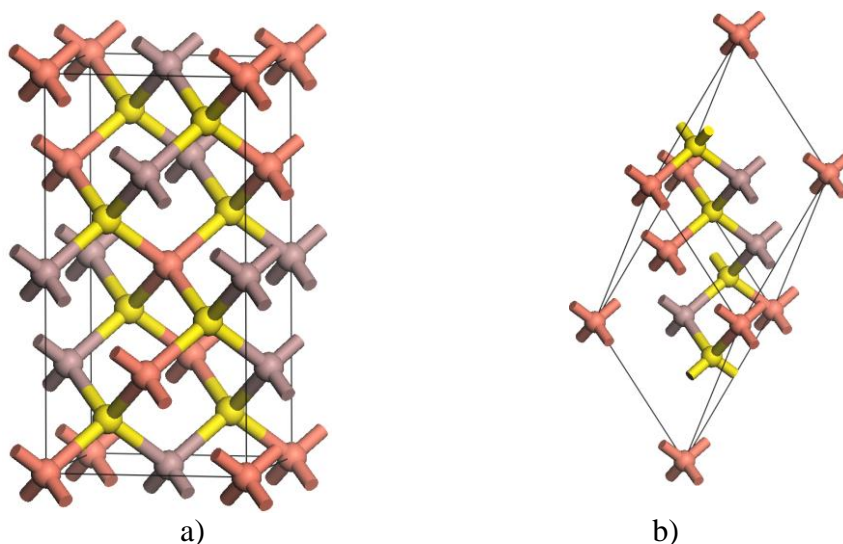
a)   b)

Figure 4.1. Structure of I-III-VI$_2$ group crystals, where ⬤ – atom I; ⬤ – atom III; ⬤ – atom VI: a) crystal unit cell; b) primitive cell.

The structural parameters of the studied materials of the group I-III-VI$_2$ were taken from the literature where their experimental study was carried out [91,156–163]. The unit cell parameters a, c, and the unit cell volume V for 18 crystals are given in Table 4.1. Additionally, in Table 4.2, we listed the fractional experimental coordinates of the atoms in the crystal lattice are expressed in units of the constant lattice a and c.

Geometriy optimization of crystal lattice was performed for all investigated chalcopyrite-type crystals within the framework of the standard procedure available in the CASTEP program. The optimization procedure was carried out until the convergence criteria (specified accuracy) were reached. The input data for this process was experimental information on the crystal structure published in [91,156–163]. The equilibrium parameters of the crystal lattice obtained as a result of optimization are given in Table 4.1 and the corresponding coordinates of the ions are collected in Table 4.2. This procedure is mandatory when performing any calculations based on the density functionality theory, regardless of the program on which the calculations are performed. This minimum value of the energy of the system actually determines the charge density distribution of $n(\mathbf{r})$, which is as close as possible to the real state of the studied crystals.

From the analysis of Table. 4.1 it can be noted that the optimized crystal lattices are quite similar to each other and showed good agreement with the experimental results of other authors. However, it is easy to see that the values of the unit cell volume and the lattice parameters are slightly different from the experimental values. Considering the volume of the unit cell of crystals, it is seen that for all crystals of group I-III-VI$_2$ there is an

overestimation of the volume of the unit cell obtained during optimization using the GGA functional. At the same time, the volume of the unit cell obtained with the LDA functional shows a slight underestimation. This deviation of the ΔV volume for chalcopyrite crystals ranges from 4.47 $Å^3$ for $CuAlTe_2$ crystals (for GGA) to 45.39 $Å^3$ for $AgInTe_2$ crystal (for LDA). Thus, the maximum deviation of the unit cell volume is calculated to be 9 % for the $AgGaTe_2$ crystal (GGA) and the minimum 0.4 % for $CuAlSe_2$ (GGA). A more detailed consideration of the deviation of the chalcopyrite lattice parameters showed the following feature. When using the GGA functional, the lattice parameter a is overestimated for all crystals of group I-III-VI₂, except for $CuAlSe_2$, for which this parameter is slightly less than the experimental value. At the same time, the LDA functional used in the optimization of the crystal structure showed underestimation of the value of the parameter a. However, the situation with the parameter c is somewhat different. As can be seen from the table, the use of the GGA functional gives a slightly higher value of the parameter c for the crystals of the group. However, when calculating with the LDA functional for Ag-containing crystals, the parameter c is higher than the experimental one by 0.2 – 1.9 % and lower than when using the GGA functional.

To compare the optimized crystal structure with the experimental one (Tables 4.1 and 4.2), the parameter of relative deviation of the unit cell volume d_r and relative mean root squared deviation D_r of the distance matrix d_{ij} was used as was done e.g. in [64,65].

$$d_r = \frac{V_c^{(opt)1/3} - V_c^{(exp)1/3}}{V_c^{(exp)1/3}}, \tag{4.1}$$

where $V_c^{(opt)}$ and $V_c^{(exp)}$ are the optimized and experimental unit cell volume, respectively. The relative root mean squared deviation can be calculated using the Eq. 4.2,

$$D_r = \sqrt{\frac{2}{n(n-1)} \sum_{i=1}^{n-1} \sum_{j=i+1}^{n} \frac{(d_{ij}^{opt} - d_{ij}^{\exp})^2}{(d_{ij}^{\exp})^2}}, \tag{4.2}$$

where n is a number of atoms, d_{ij}^{opt} and $d_{ij}^{\exp}$ are the optimized and experimental distances between i and j atom, respectively. Previously, this method of estimating the deviation of the optimized structure of the crystal lattice was used in Refs. [65,152,153] for Ag_2SiS_3, K_2SO_4, $LiNH_4SO_4$ etc. crystals. The calculated values of the deviation of the lattice volume d_r and the deviation of the structure D_r are shown in Figure 4.2. These parameters are calculated by Eqs. (4.1) and (4.2) for crystal lattices optimized using LDA and GGA finctionals. The figure shows that the parameters d_r for volume change calculated with LDA

and GGA methods are quite similar. The relative deviation of the unit cell volume for the GGA functional is positive because the calculated volumes are larger than the experimental ones. For LDA functional, these parameters become negative. This parameter oscillates near the mark 0.02 for GGA functional and around 0.01 for LDA. For the parameter D_r, the calculated values are close to both methods of structure optimization. The parameter $D_r =$ 0.06 is observed for the $CuInSe_2$ crystal. In general, the value of this parameter is also small as for d_r. Generally, the D_r value is close to 0.02. This indicates that the optimized crystal structure is very similar to that obtained experimentally in [91,156–163], i.e. the method gives good agreement.

The evaluation and analysis of the crystal lattice deformation parameters is important when considering the crystal structure of diamond-like crystals. Using formulas given in Section 2.1.1, we obtained the values of the tetragonal deformation parameter η and the anion displacement parameter u. The corresponding calculations were performed for both the experimental structure and optimized with the BFGS method. The values of the parameters η and u are obtained from experimental data and optimized using LDA and GGA functionals are collected in Table 4.1. As can be seen from the table, for most crystals the parameter η is less than one. This suggests that the crystals are compressed in the *c*-direction. For crystals $CuGaSe_2$, $CuGaTe_2$, and $CuInX_2$ (where X = S, Se, and Te) there is almost equality of the parameter η to unity. In order to find the structure – structure relationship, we considered the relation between the tetragonal deformation parameter η and the anion displacement parameter u. In Fig. 4.3. shows the relationship between the parameter of the displacement of the chalcogen atom from the parameter of tetrahedral deformation of the cell of chalcopyrite crystals η. The figure contains both points obtained from the structure optimized using LDA and GGA functionalities, and experimental parameters. From Fig. 4.3. it is seen that the points corresponding to the 18 crystals of group I-III-VI₂ tend to almost linear change of $u(η)$ function. According to this, we conducted a linear regression analysis of this dependence. In order to assess in more detail the degree of correlation of these two material parameters, we analyzed their correlation by calculating the Pearson's correlation coefficient R_{xy} (or R) which is the correlation index (linear dependence) between two variables $x = \{x_1, x_2, …, x_n\}$ and $y = \{y_1, y_2, …, y_n\}$. This parameter is determined from the ratio

$$R_{xy} = \frac{\sum\limits_{i=1}^{n}((x_i - \overline{x})(y_i - \overline{y}))}{\sqrt{\sum\limits_{i=1}^{n}(x_i - \overline{x})^2 \sum\limits_{i=1}^{n}(y_i - \overline{y})^2}} , \qquad (4.3)$$

where $\overline{x} = \dfrac{2}{n}\sum\limits_{i=1}^{n} x_i$ and $\overline{y} = \dfrac{2}{n}\sum\limits_{i=1}^{n} y_i$ is the sample mean x and y, respectively. The Pearson's

correlation coefficient takes the values from $[-1, +1]$. The closer R is to -1 or $+1$, the stronger linear correlation is. If the $R = 0$, there is no correlation between the two sets of parameters. It can be seen from the figures that the points fit well by the linear fit, and these lines are described by the equations: 1) $u(\eta) = 0.64683 - 0.3815\eta$ — for experimental data; 2) $u(\eta) = 0.66436 - 0.40593\eta$ — for LDA calculated; 3) $u(\eta) = 0.64683 - 0.3815\eta$ — for GGA calculated parameters. Hence we can say that in crystals I-III-VI$_2$ there is a negative correlation u with η. The corresponding values of Pearson's coefficients are -0.84, -0.97, -0.97 for experiment, and calculated with GGA and LDA functionals data, respectively.
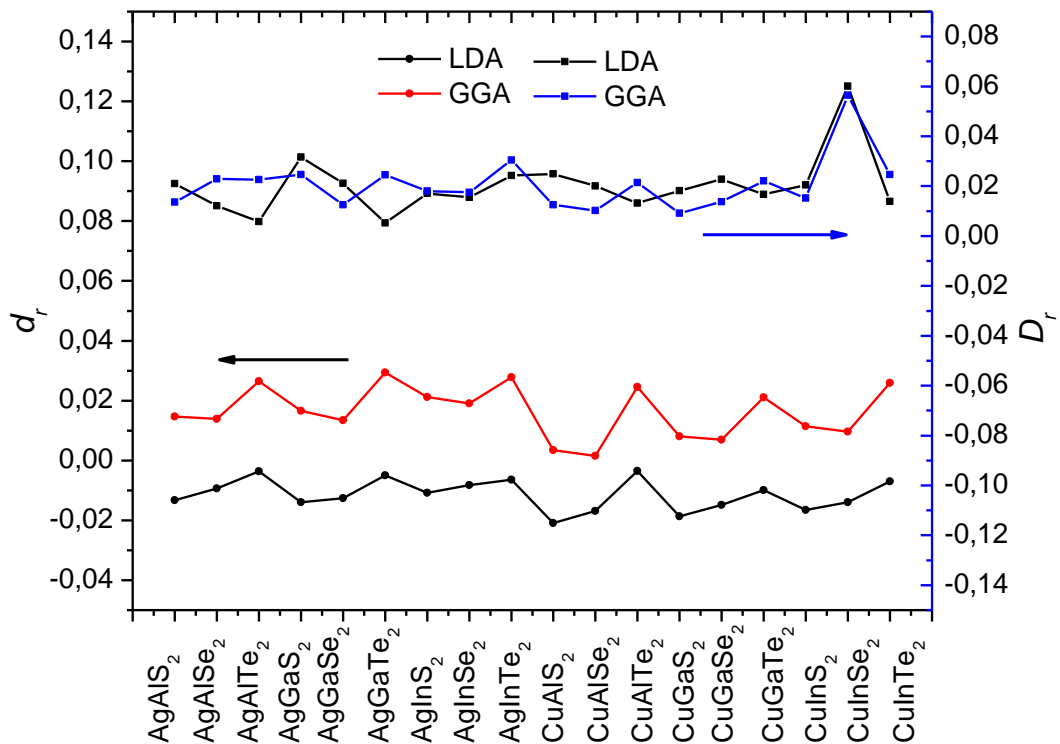

Figure 4.2. Calculated parameter of relative deviation of the unit cell volume d_r, and relative root mean squared deviation D_r calculated for I-III-VI$_2$ crystals.
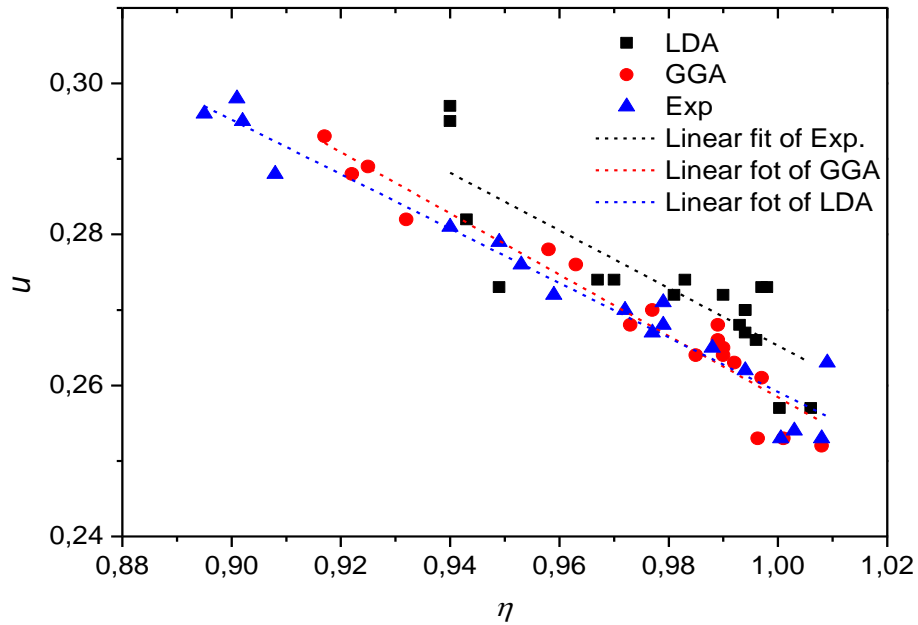
Figure 4.3. Correlation of *u* with η distortion parameters obtained from experimental, LDA and GGA calculated crystal structure.

In general, the system of investigated chalcopyrite crystals of I-III-VI$_2$ group can be presented as in Fig. 4.4. This systematization is based on the Welker's diagram proposed for the search for hypothetical binary compounds A^3B^5 with semiconductor properties [164].
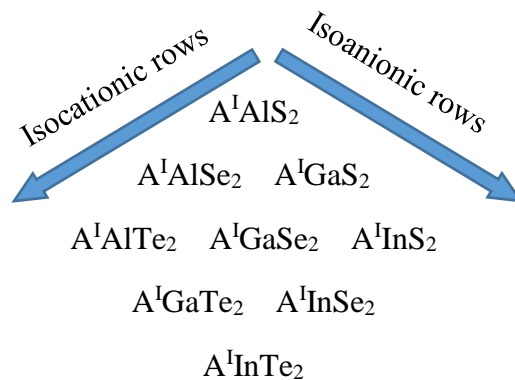

Figure 4.4. Welkers's diagram for $A^IB^{III}C_2^{VI}$ (A = Ag, Cu, B = Al, Ga, In, C = S, Se, and Te).

This representation provides a regularity in the study or prediction of physicochemical properties of large groups of crystals depending on the chemical composition and position in isoanionic and isocationic series. In our case the Welkers's diagram for the system of chalcopyrite crystals I-III-VI$_2$ is shown in Fig. 4.4.

Table 4.1. Reported experimental and calculated lattice parameters for I-III-VI$_2$ group chalcopyrite.

Compound	Source	$a = b$, Å	c, Å	V, Å^3	$c/2a$	u
AgAlS$_2$	LDA	5.5409	10.4139	319.73	0.940	0.295
	GGA	5.7453	10.5322	347.66	0.917	0.293
	Exp.[156]	5.6950	10.2600	332.80	0.901	0.298
AgAlSe$_2$	LDA	5.8135	10.9683	370.70	0.943	0.282
	GGA	5.9960	11.0548	397.45	0.922	0.288
	Exp. [156]	5.9560	10.7500	381.35	0.902	0.295
AgAlTe$_2$	LDA	6.2122	12.0185	463.83	0.967	0.274
	GGA	6.4212	12.3004	507.18	0.958	0.278
	Exp. [156]	6.2960	11.8300	468.93	0.940	0.281
AgGaS$_2$	LDA	5.5798	10.4946	326.75	0.940	0.297
	GGA	5.7850	10.6997	358.08	0.925	0.289
	Exp. [156]	5.7540	10.2950	340.85	0.895	0.296
AgGaSe$_2$	LDA	5.8310	11.0636	376.17	0.949	0.273
	GGA	6.0194	11.2238	406.69	0.932	0.282
	Exp.[157]	5.9921	10.8830	390.76	0.908	0.288
AgGaTe$_2$	LDA	6.2113	12.0551	465.10	0.970	0.274
	GGA	6.4423	12.4072	514.94	0.963	0.276
	Exp. [156]	6.2880	11.9400	472.10	0.949	0.279
AgInS$_2$	LDA	5.7529	11.3067	374.22	0.983	0.274
	GGA	5.9518	11.6241	411.78	0.977	0.270
	Exp.[158]	5.8760	11.1980	386.64	0.953	0.276
AgInSe$_2$	LDA	6.0088	11.7901	425.69	0.981	0.272
	GGA	6.1921	12.0443	461.82	0.973	0.268
	Exp.[159]	6.1038	11.7118	436.34	0.959	0.272
AgInTe$_2$	LDA	6.3960	12.6687	518.28	0.990	0.272
	GGA	6.6289	13.0571	573.77	0.985	0.264
	Exp.[160]	6.4672	12.6331	528.38	0.977	0.267
CuAlS$_2$	LDA	5.1910	10.3461	278.80	0.997	0.273
	GGA	5.3343	10.5492	300.18	0.989	0.268
	Exp.[161]	5.3336	10.4440	297.10	0.979	0.271
CuAlSe$_2$	LDA	5.4815	10.8974	327.44	0.994	0.270
	GGA	5.5934	11.0656	346.21	0.989	0.266
	Exp. [156]	5.6170	10.9220	344.60	0.972	0.270
CuAlTe$_2$	LDA	5.9421	11.8123	417.08	0.994	0.267
	GGA	6.1145	12.1258	453.36	0.992	0.263
	Exp.[156]	5.9760	11.8040	421.55	0.988	0.265
CuGaS$_2$	LDA	5.2231	10.3757	283.07	0.993	0.268
	GGA	5.3719	10.6319	306.81	0.990	0.265
	Exp.[91]	5.3474	10.4743	299.51	0.979	0.268
CuGaSe$_2$	LDA	5.4995	10.9354	330.74	0.994	0.270
	GGA	5.6301	11.1422	353.19	0.990	0.264
	Exp.[162]	5.5550	11.2100	345.92	1.009	0.263
CuGaTe$_2$	LDA	5.9304	11.8099	415.36	0.996	0.266
	GGA	6.1123	12.1919	455.50	0.997	0.261
	Exp.[156]	5.9940	11.9100	427.90	0.994	0.262
CuInS$_2$	LDA	5.4341	10.9370	322.98	1.006	0.257
	GGA	5.5868	11.2576	351.38	1.008	0.252
	Exp. [91]	5.5228	11.1323	339.57	1.008	0.253
CuInSe$_2$	LDA	5.7147	11.4112	372.67	0.998	0.273
	GGA	5.8454	11.7076	400.05	1.001	0.253
	Exp.[163]	5.7876	11.6045	388.71	1.003	0.254
CuInTe$_2$	LDA	6.1243	12.2520	459.55	1.000	0.257
	GGA	6.3354	12.6236	506.68	0.996	0.253
	Exp.[156]	6.1670	12.3400	469.31	1.001	0.253

Table 4.2. The experimental and calculated fractional atomic coordinates for I-III-VI$_2$ group crystals.

Crystal	Atom	Ref.	Exp.			LDA			GGA		
			x/a	*y/b*	*z/c*	*x/a*	*y/b*	*z/c*	*x/a*	*y/b*	*z/c*
1	2	3	4	5	6	7	8	9	10	11	12
AgAlS$_2$	Ag	[156]	0	0	0	0	0	0	0	0	0
	Al		0	0	0.5	0	0	0.5	0	0	0.5
	S		0.300	0.25	0.125	0.286	0.25	0.125	0.294	0.25	0.125
AgAlSe$_2$	Ag	[156]	0	0	0	0	0	0	0	0	0
	Al		0	0	0.5	0	0	0.5	0	0	0.5
	Se		0.270	0.25	0.125	0.278	0.25	0.125	0.287	0.25	0.125
AgAlTe$_2$	Ag	[156]	0	0	0	0	0	0	0	0	0
	Ga		0	0	0.5	0	0	0.5	0	0	0.5
	Te		0.260	0.25	0.125	0.264	0.25	0.125	0.267	0.25	0.125
AgGaS$_2$	Ag	[156]	0	0	0	0	0	0	0	0	0
	Ga		0	0	0.5	0	0	0.5	0	0	0.5
	S		0.304	0.25	0.125	0.280	0.25	0.125	0.286	0.25	0.125
AgGaSe$_2$	Ag	[157]	0	0	0	0	0	0	0	0	0
	Ga		0	0	0.5	0	0	0.5	0	0	0.5
	Se		0.288	0.25	0.125	0.273	0.25	0.125	0.282	0.25	0.125
AgGaTe$_2$	Ag	[156]	0	0	0	0	0	0	0	0	0
	Ga		0	0	0.5	0	0	0.5	0	0	0.5
	Te		0.260	0.25	0.125	0.263	0.25	0.125	0.265	0.25	0.125
AgInS$_2$	Ag	[158]	0	0	0	0	0	0	0	0	0
	In		0	0	0.5	0	0	0.5	0	0	0.5
	S		0.264	0.25	0.125	0.251	0.25	0.125	0.259	0.25	0.125
AgInSe$_2$	Ag	[159]	0	0	0	0	0	0	0	0	0
	In		0	0	0.5	0	0	0.5	0	0	0.5
	Se		0.258	0.25	0.125	0.246	0.25	0.125	0.251	0.25	0.125
AgInTe$_2$	Ag	[160]	0	0	0	0	0	0	0	0	0
	In		0	0	0.5	0	0	0.5	0	0	0.5
	Te		0.262	0.25	0.125	0.240	0.25	0.125	0.244	0.25	0.125
CuAlS$_2$	Cu	[161]	0	0	0	0	0	0	0	0	0
	Al		0	0	0.5	0	0	0.5	0	0	0.5
	S		0.268	0.25	0.125	0.251	0.25	0.125	0.257	0.25	0.125
CuAlSe$_2$	Cu	[156]	0	0	0	0	0	0	0	0	0
	Al		0	0	0.5	0	0	0.5	0	0	0.5
	Se		0.260	0.25	0.125	0.247	0.25	0.125	0.251	0.25	0.125
CuAlTe$_2$	Cu	[156]	0	0	0	0	0	0	0	0	0
	Al		0	0	0.5	0	0	0.5	0	0	0.5
	Te		0.250	0.25	0.125	0.238	0.25	0.125	0.243	0.25	0.125
CuGaS$_2$	Cu	[91]	0	0	0	0	0	0	0	0	0
	Ga		0	0	0.5	0	0	0.5	0	0	0.5
	S		0.254	0.25	0.125	0.245	0.25	0.125	0.248	0.25	0.125
CuGaSe$_2$	Cu	[162]	0	0	0	0	0	0	0	0	0
	Ga		0	0	0.5	0	0	0.5	0	0	0.5
	Se		0.259	0.25	0.125	0.241	0.25	0.125	0.248	0.25	0.125
CuGaTe$_2$	Cu	[156]	0	0	0	0	0	0	0	0	0
	Ga		0	0	0.5	0	0	0.5	0	0	0.5
	Te		0.250	0.25	0.125	0.236	0.25	0.125	0.238	0.25	0.125

1	2	3	4	5	6	7	8	9	10	11	12
CuInS$_2$	Cu	[91]	0	0	0	0	0	0	0	0	0
	In		0	0	0.5	0	0	0.5	0	0	0.5
	S		0.229	0.25	0.125	0.214	0.25	0.125	0.219	0.25	0.125
CuInSe$_2$	Cu	[163]	0	0	0	0	0	0	0	0	0
	In		0	0	0.5	0	0	0.5	0	0	0.5
	Se		0.269	0.25	0.125	0.214	0.25	0.125	0.218	0.25	0.125
CuInTe$_2$	Cu	[156]	0	0	0	0	0	0	0	0	0
	In		0	0	0.5	0	0	0.5	0	0	0.5
	Te		0.225	0.25	0.125	0.213	0.25	0.125	0.215	0.25	0.125

4.2. Electronic structure of I-III-VI₂ group crystals

4.2.1. Band structure calculation

The wide application areas of the ternary semiconductors are determined by their band gaps. The sutable for practical use in different devices band gap value, its character (direct or indirect gap) and dispersion of the electronic states generally determine the physical properties of a studied material, making the investigation of electronic properties to be a very important problem. Its study is necessary to understand the physical phenomena observed in the experiment and is important for explaining many physical processes and interpreting the experimental results. The electronic structure also provide an important information about the material, which can be used for development of devices based on these materials. Therefore, the study of the band structure is an important and actual task. The structure of the edges of the valence band and the conduction band plays an important role for diamond-like materials. Depending on the relative position of the absolute maxima and minima, as well as the symmetry of the respective energy levels, there are direct and indirect forbidden gap materials.

The band structure of the I-III-VI₂ crystals was calculated using the pseudopotential method in the framework of the DFT with plane waves as the basis functions using LDA and GGA methods which are known to be widely used for similar calculations of the material properties of different nature [33,64,66,152]. These methods have proven to be in good agreement with the experimental results and at the same time do not require significant computational time as when using hybrid methods or functional of a much more complex

form. Before calculating the electronic structure and properties of the crystal, a test of the convergence of the total energy with respect to the size of the **k**-grid and the cut-off energy of plane waves was performed. The calculation of the band energy structure was performed at points of high symmetry and along the lines connecting them in the first Brillouin zone. As mentioned earlier, calculations in this work were performed for a primitive cell of crystals I-III-VI$_2$. The general view of the first Brillouin zone for the tetragonal symmetry of the chalcopyrite crystal cell (a) and for its primitive cell (b) is shown in Fig. 4.5. In current study, the calculated for I-III-VI$_2$ crystals band structure is obtained using the LDA and GGA functionals. The results obtained by these two methods are quite similar and qualitatively do not differ. Thus, for the sake of brevity in the further analysis we will mainly use the results obtained from the GGA functional. The calculated band-energy diagrams $E(k)$ of crystals

a)   b)
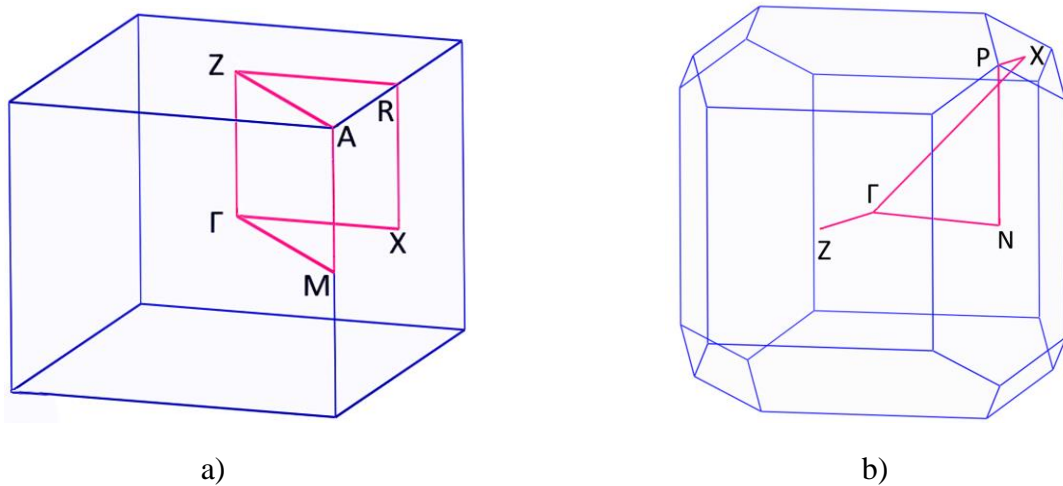
Figure 4.5. The first Brilluoin zone structure for unit cell (a) and primitive cell (b) of the chalcopyrite I-III-VI$_2$ group crystals.

I-III-VI$_2$ were constructed at points and along the directions of high symmetry in the 1-st BZ as shown in Fig. 4.6 and Fig. 4.7 in the following directions: Z → Γ → X → P → N → Γ. The coordinates of these points are as follows (in units of $2\pi/a_i$): Z(0, 0, 1/2), A(1/2, 1/2, 1/2), M(1/2, 1/2, 0), Γ(0, 0, 0), R(0, 1/2, 1/2), X(0, 1/2, 0), Γ(0, 0, 0).

The calculation of the band energy structure was performed in the energy range from –20 eV to 15 eV. For a more detailed analysis of the structure of energy levels of the crystals of studied group, the band diagram is constructed in the vicinity of the band gap. Figs. 4.6 and 4.7 shows the band energy diagram of the studied compounds in the energy range from –8 to 8 eV obtained by GGA *XC* functional [152,165,166]. This allows us to better analyze

the structure of the electronic levels of the crystal, which correspond to the transitions of the electron near the absorption edge.

The energy levels for crystals of I-III-VI$_2$ group can be divided into two zones. The conduction band for the studied crystals is formed by energy levels with energies greater than the energy E_g, and the valence band is located at energies less than 0 eV. In current study, this value corresponds to the Fermi level and is comparable to the valence band maximum. As one can see, the band gap of all investigated crystals is of direct type. The conduction band minima and valence band maxima are located at the center of BZ and labeled as Γ. Such features obtained by us coincide with the results of calculations obtained by other authors in [31,33,45,53]. At the same time, the direct type of forbidden zone was confirmed by studies of the edge of fundamental absorption [167–169] and others.

For all eighteen crystals of the study group, the theoretically calculated values of the band gap E_g for LDA and GGA functionals are shown in Fig. 4.8. It can be noted that all crystals can be divided into two groups of materials with a similar tendency to change E_g. The first group of materials is crystals where the cation I is formed by silver ions of Ag, which occupy position 4a in the crystal lattice. The second group of crystals is formed by copper atoms as cations of group I. The largest band gap in both rows of crystals obtained for compounds AAlS$_2$, where A = Cu, Ag. The largest band gap value is 2.01 eV (1.99 eV) for the AgAlS$_2$ crystal obtained for LDA (GGA) functionals, respectively. This value is less than the experimental one (3.15 – 3.2 eV) for the AgAlS$_2$ crystal presented in Refs. [13,42]. This underestimation is about 30% of the experimental value of E_g. The CuAlS$_2$ crystal showed a slightly lower value of E_g equal to 1.93 (1.79) for LDA (GGA) functionals. The experimental value of the band gap for it is $E_g = 3.5$ eV [170].

For clarity of comparison of experimental and theoretical band gap values the dependence of its experimental value on theoretically received in this work is constructed. Fig. 4.9 summarize DFT calculated band gaps and their comparison with experimental data from literature [1,42,43]. The figure shows that the values of the band gap for both exchange-correlation functionals are smaller than the experimental values for the whole group I-III-VI$_2$. This underestimation is a typical characteristic of these DFT-based methods, which is well known in the literature [66,134]. Also, it is reported that such an underestimation can be up to 50 % or more of the actual value of E_g, and depends on the specific material. Previously, we obtained such an underestimation for a number of others, both semiconductor (such as Ag$_2$SiS$_3$ [152], MnVO$_4$ [171], LiNa$_5$MoO$_{30}$ [66], Bi$_3$TeBO$_9$ [172], etc.) and

Figure 4.6. Band structure of AgBC$_2$ (B = Al, Ga, and In; C = S, Se, and Te) crystals calculated using GGA functional a) AgAlS$_2$; b) AgAlSe$_2$; c) AgAlTe$_2$; d) AgGaS$_2$; e) AgGaSe$_2$; f) AgGaTe$_2$; g) AgInS$_2$; h) AgInSe$_2$; i) AgInTe$_2$.
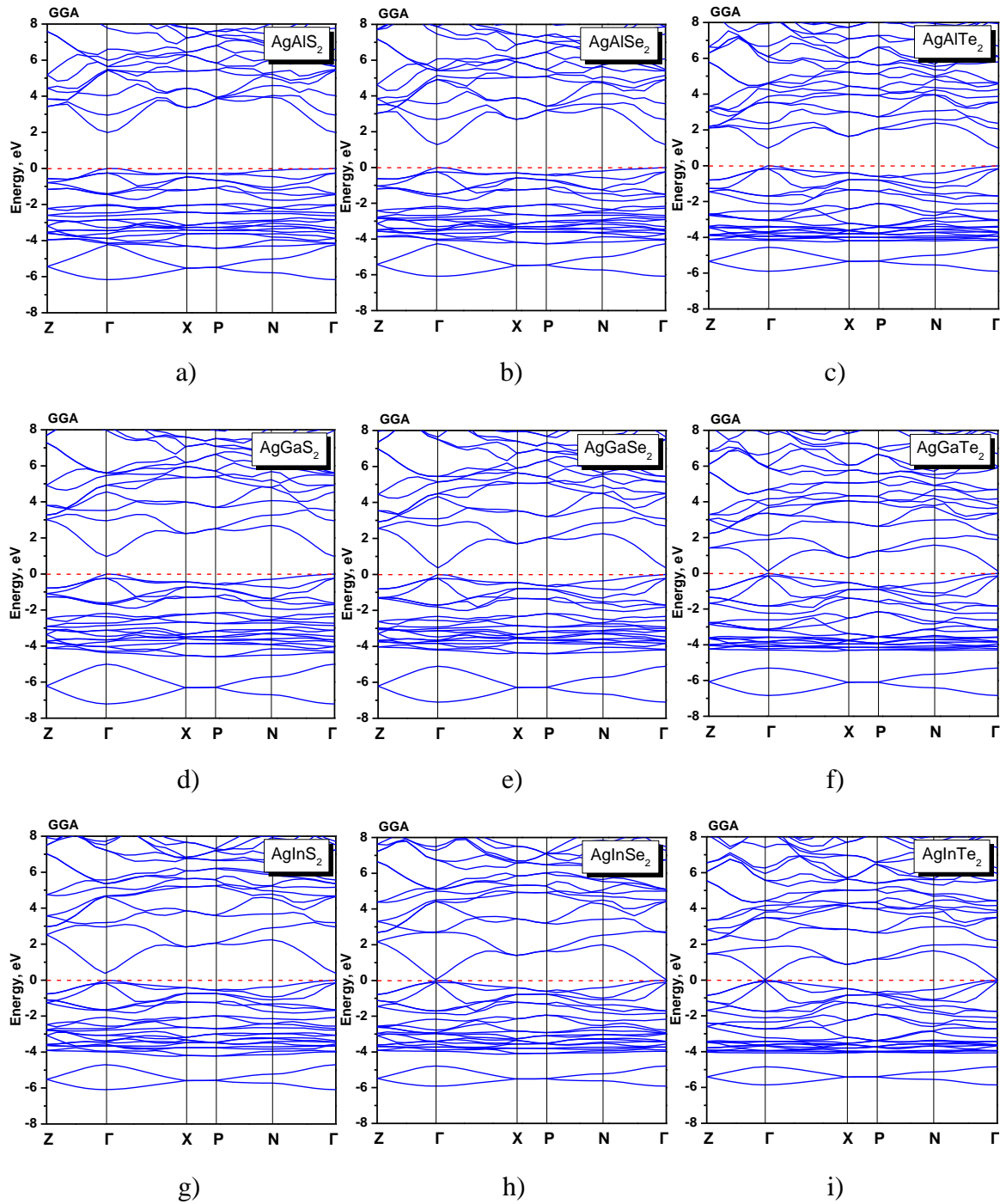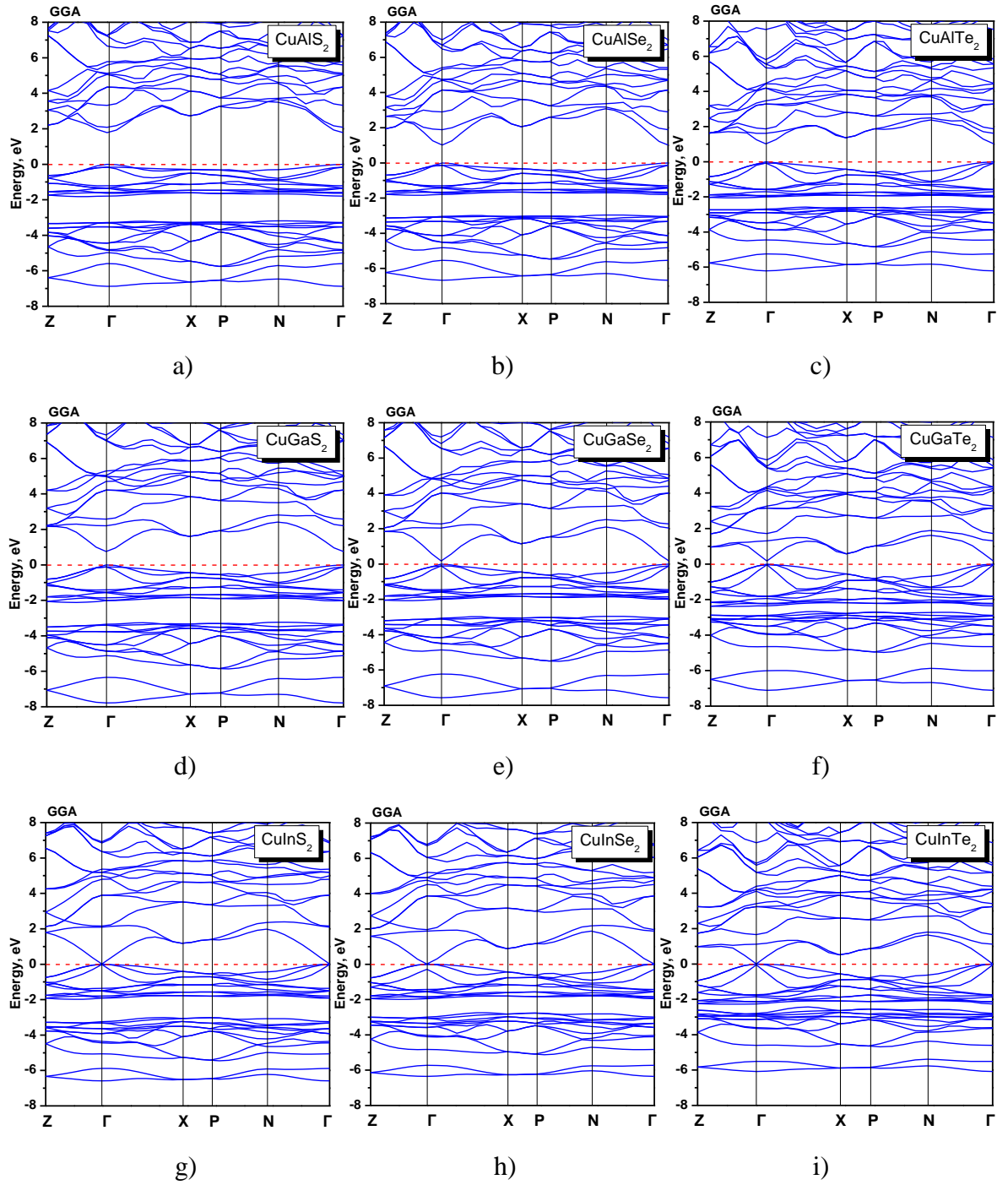
Figure 4.7. Band structure of CuBC₂ (B = Al, Ga, and In; C = S, Se, and Te) crystals calculated using GGA functional a) AgAlS₂; b) AgAlSe₂; c) CuAlTe₂; d) CuGaS₂; e) CuGaSe₂; f) CuGaTe₂; g) CuInS₂; h) CuInSe₂; i) CuInTe₂.
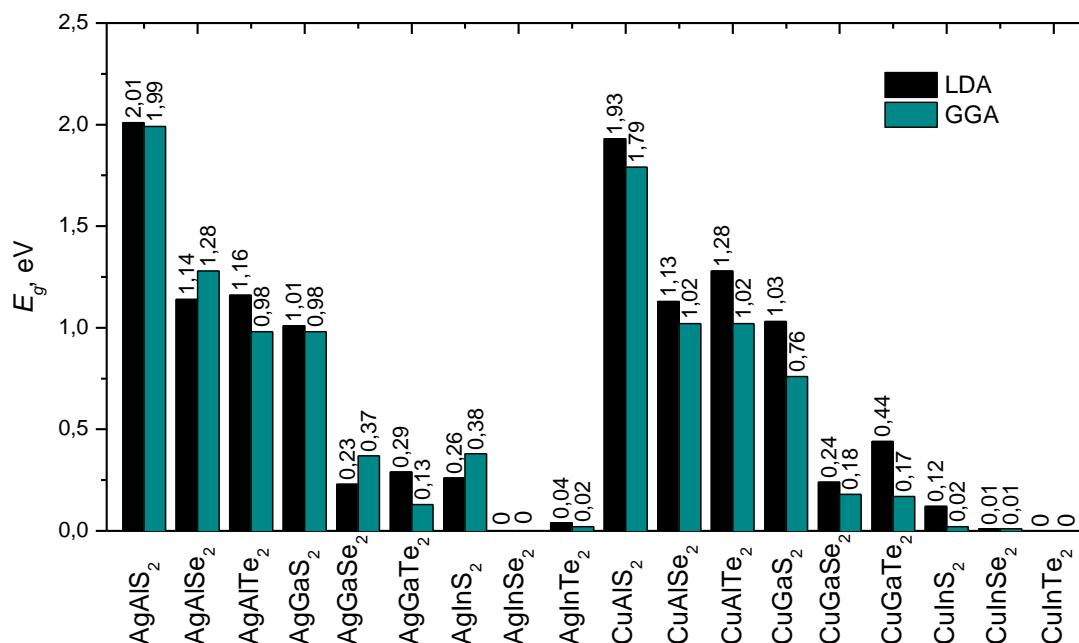
Figure 4.8. The band gap values of the I-III-VI$_2$ group crystals calculated using the LDA and GGA functionals.

dielectric crystals with a large band gap (LiNH$_4$SO$_4$ [64,65], K$_{1.75}$(NH$_4$)$_{0.25}$SO$_4$ [173], LiNaSO$_4$ [174] etc.). We established that this underestimation in the number of crystals A$_2$BX$_4$ group is about 2 eV [64,65,173,174]. A few general trends are observed from Figs. 4.9. The points in the figure can be divided into three regions. The region of the largest values of E_g corresponds to AgAlS$_2$ CuAlS$_2$ crystals. Another region is formed by AgAlSe$_2$, AgAlTe$_2$, AgGaS$_2$, CuAlSe$_2$, CuAlTe$_2$, and CuGaS$_2$ crystals. The third region, which is characterized by the smallest band gap, includes AgGaSe$_2$, AgGaTe$_2$, AgInS$_2$, AgInSe$_2$, AgInTe$_2$, CuGaSe$_2$, CuGaTe$_2$, CuInS$_2$, CuInSe$_2$, and CuInTe$_2$ crystals. In general, the band gap increases with an increase of electronegativity of the III and VI ions: from In to Ga to Al and from Te to Se to S. There is no general trend when considering the effect of the I cations.

It is well known that the two functionals used here (LDA and GGA) which are not hybrid tend to underestimate the band gap. Nevertheless, it is worth noting that the calculations performed in this study does not include any exitonic or quasiparticle effects. Also, it is should be mentioned that the calculations with DFT performed using CASTEP code can not be performed using the spin-orbit coupling. For some materials is observed significant spin-orbit coupling effects. They can lead to the splitting of band gap by up to 1 eV.
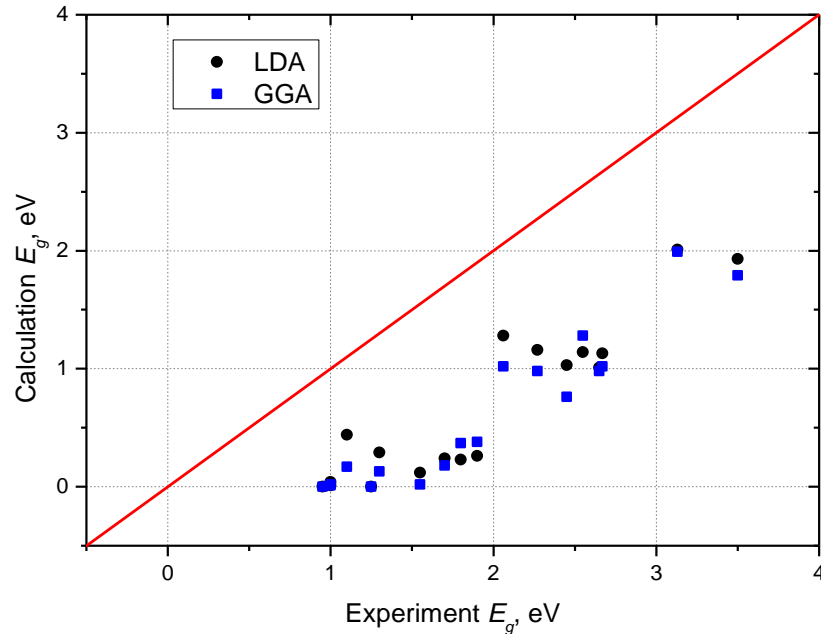
Figure 4.9. Comparison between experimental and DFT calculated band gaps of I-III-VI$_2$ chalcopyrites.

Considering the parameters of the band-energy structure of the crystals of group I-III-VI$_2$, we constructed the dependence of the band gap of the molar mass of the crystal for eighteen crystals of the studied group. Corresponding dependences $E_g(\mu)$ for calculation with the LDA and GGA functionals data together with the experimental values of bandgap are shown on Fig. 4.10. As one can see, the obtained theoretical values of bandgap are smaller than the experimental because drawback of those two methods. Hence, it should be mentioned, that for both mathods, there is a functional dependence of $E_g(\mu)$, similar to the experimental one. There is a negative correlation between the band gap and the molar mass of the crystal. The results of linear regression are shown by the dushed line in Figs. 4.10. The figure shows the equation for the lines describing this dependence. The calculated values of the Pearson's coefficient are: 0.64 for LDA; 0.66 for GGA; 0.81 for experimental values. From the obtained Pearson's coefficients it follows that the calculated values of the band gap are less correlated with the molar mass than the experimental ones.

For chalcopyrite crystals, there is a significant reduction in the band gap compared to zinc dlende for which the band gap is in the range of 2.4 eV for CdS and 3.5 eV for ZnS. The calculated smallest band gap energy is equal to $E_g = 0$ eV for CuInTe$_2$ and AgInSe$_2$ crystals for both LDA and GGA methods, and corresponds metallic behavior of the material.
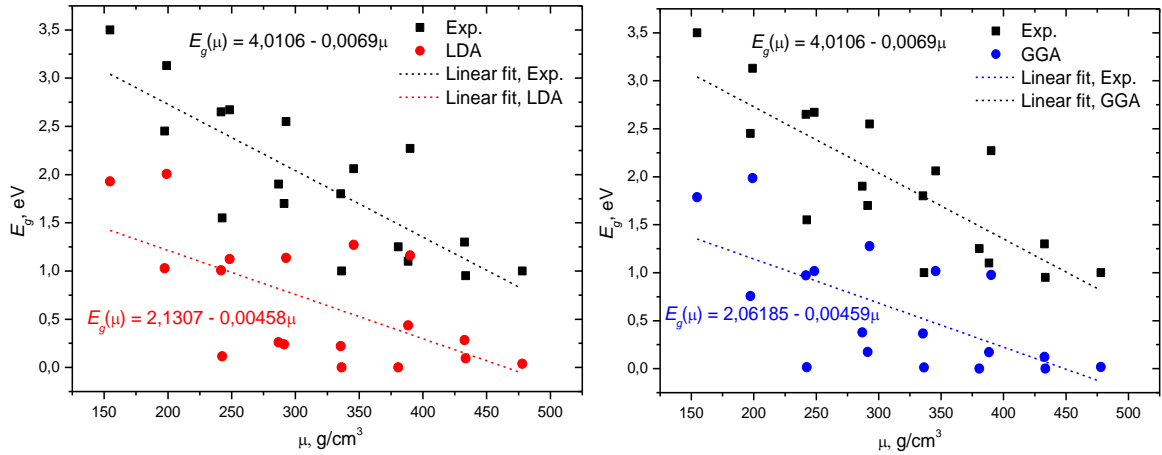
Figure 4.10. The molar mass dependence of the band gap value for I-III-VI$_2$ crystals.

Table 4.3. The scissor operator value Δ_g applied for correction of band gap value underestimation of I-III-VI$_2$ crystals for LDA and GGA functionals.

Crystal	Δ_g, eV (LDA)	Δ_g, eV (GGA)	Crystal	Δ_g, eV (LDA)	Δ_g, eV (GGA)
AgAlS$_2$	1.124	1.145	CuAlS$_2$	1.571	1.713
AgAlSe$_2$	1.414	1.275	CuAlSe$_2$	1.546	1.654
AgAlTe$_2$	1.109	1.294	CuAlTe$_2$	0.788	1.044
AgGaS$_2$	1.643	1.679	CuGaS$_2$	1.423	1.693
AgGaSe$_2$	1.579	1.435	CuGaSe$_2$	1.461	1.526
AgGaTe$_2$	1.017	1.177	CuGaTe$_2$	0.664	0.928
AgInS$_2$	1.639	1.523	CuInS$_2$	1.434	1.535
AgInSe$_2$	1.250	1.250	CuInSe$_2$	1.000	0.988
AgInTe$_2$	0.961	0.984	CuInTe$_2$	0.857	0.950

The experimentally established values of band gap for those crystals in [175] are equal to 0.95 eV and 1.25 eV, being greater than the calculated ones. Such an underestimation of the band gap value is typical for calculations with the LDA and GGA functionals [65,174,176,177]. In order to overcome it, we used the scissor operator Δ_g, which shifts the conduction band to the higher energies without any modification of the calculated eigenfunctions. The corrected value of the band gap can be written then as follows:

$$E_g^{\text{corr}} = E_g^{\text{calc}} + \Delta_g. \tag{4.4}$$

The scissor operator values needed for matching with the experimental E_g are equal $\Delta_g = E_g^{\text{corr}} - E_g^{\text{calc}}$, and is tabulated for the titled materials in Table 4.3 for the LDA and GGA calculations, respectively. These values can be usual for the CP crystals [152].

As shown in the Fig. 4.6 and 4.7 the band structure of the I-III-VI₂ crystals reveals a significant dispersion of energy levels. The highest dispersion of band structure is observed for the levels calculated around the center of the Brillouin zone (to the Γ point). The top of the valence band of I-III-VI₂ crystal, located at Γ point is formed by three energy levels, while the valence band maximum for ZB crystals is formed by three times degenerate level Γ_{15}. This level consists of *p*-states of the anion and *d*-orbitals of the cation. In CP crystals at Γ-point these levels are splited so that the highest level is non-degenerate, while the two lower levels intersect at Γ-point. This ordering of levels corresponds to the splitting of energy levels into two states due to the presence of the crystal field and corresponds to the deformation of the crystal structure $c/2a \neq 1$, whereas for a structure with parameter $c/2a = 1$ the threefold degeneration of the highest energy level is observed. For a few crystals (CuInS₂, CuInSe₂, CuInTe₂, CuGaSe₂, CuGaTe₂, etc.) the top of valence band is formed by the almost triply degenerated level. For those materials the parameter η is equal or close to 1, as shown when considering the structural parameters in paragraph 4.1.

Figure 4.11 schematically shows the location of energy levels that form the edge of fundamental absorption for the case $\eta \neq 1$ and $\eta = 1$. The bottom of the conduction band is formed by anti-binding states Γ_1 formed mainly with *s*-states of cations and *s*-states of anions. For chalcopyrite crystals, as the symmetry of the D_{2d}^{12} group crystal decreases, the degenerate Γ_{15} level, which corresponds to the states at the top of the valence band, splits into the nondegenerate Γ_4 level and the twice degenerate Γ_5 state (Fig. 4.11). This splitting occurs due to the action of a crystal field. The magnitude of the crystal field is determined by the following expression:

$$\Delta_{CF} = E(\Gamma_5) - E(\Gamma_4), \tag{4.5}$$

where $E(\Gamma_5)$ and $E(\Gamma_4)$ are energy levels Γ_5 and Γ_1, respectively. It is assumed that the magnitude of the crystal field Δ_{CF} is positive if the level of Γ_5 is higher than Γ_4 in energy, and vice versa. The values of the crystal field Δ_{CF} obtained in this work and published by other authors are given in Table 4. 4.
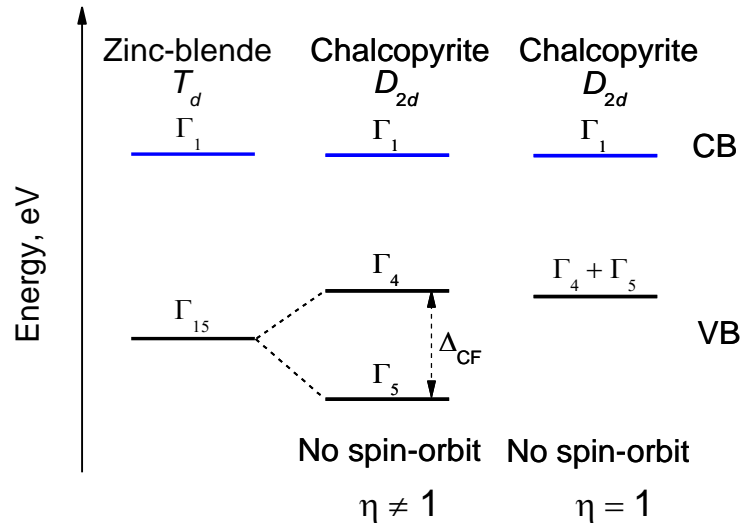
Figure 4.11. Schematic visualization of band edges at Γ point of Brilluoin zone for the zinc-blende and chalcopyrite compounds without spin-orbit splitting of levels.

According to the selection rules, which will be considered in more detail in paragraph 6.1, allowed in the Brillouin zone center are transitions $\Gamma_4 \rightarrow \Gamma_1$ and $\Gamma_5 \rightarrow \Gamma_1$, which correspond to electron transitions for polarization of a wave absorbed parallel and perpendicular to the crystallographic axis c, respectively. As can be seen from Table 4.4, the values of the crystal field obtained in this work agrees well with the previously published data, which indicates the reliability (high accuracy) of our results [1,31,33,51,53,62,168,178]

Table 4.4. Crystal field energy obtained for crystals of I-III-VI$_2$ group with GGA functional and literature data from [175].

Crystal	Δ_{CF}, eV	Δ_{CF}, eV (lit.)	Crystal	Δ_{CF}, eV	Δ_{CF}, eV (lit.)
AgAlS$_2$	−0.262	—	CuAlS$_2$	−0.173	−0.130
AgAlSe$_2$	−0.248	—	CuAlSe$_2$	−0.145	−0.170
AgAlTe$_2$	−0.173	—	CuAlTe$_2$	−0.098	−0.130
AgGaS$_2$	−0.248	−0.280	CuGaS$_2$	−0.126	−0.129
AgGaSe$_2$	−0.229	−0.250	CuGaSe$_2$	−0.103	−0.139
AgGaTe$_2$	−0.140	—	CuGaTe$_2$	−0.042	−0.080
AgInS$_2$	−0.159	−0.165	CuInS$_2$	−0.001	−0.005
AgInSe$_2$	−0.117	−0.120	CuInSe$_2$	−0.285	−0.006
AgInTe$_2$	−0.080	—	CuInTe$_2$	−0.056	—
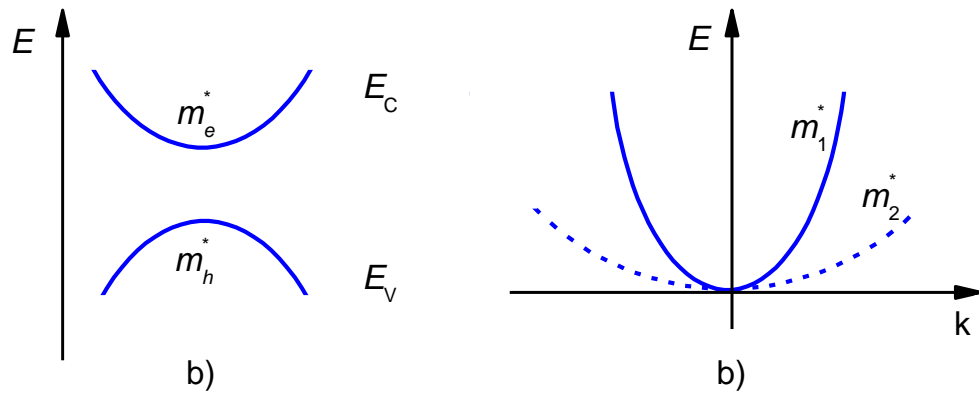
Figure 4.12. Schematic representation of the conduction bands minima for two different effective masses m^*a) and origin of effective mass for electron and hole b).

and other. As can be seen from Table 4.4 crystals AgInTe$_2$, CuInS$_2$, CuInSe$_2$, CuInTe$_2$ have a small value of the crystal field energy. This value is consistent with the fact that the parameter of tetragonal deformation goes to one. There is also agreement with the results presented in [29,44] obtained from self-consistent DFT calculations.

One of the important parameters of the material that can be obtained from the band diagram $E(\mathbf{k})$, and makes it possible to estimate the potential of the semiconductor material is the effective mass of charge carriers m^* at the band extrema of the electronic band structures. The effective mass is one of the main characteristics of an electron in a solid as a quasiparticle. If there is a minimum or maximum of the energy $E(k)$ at point k_0, it can be expanded in a series in the vicinity of the point:

$$E(k) = E(k_0) + \frac{1}{2}\sum_{\alpha,\beta} \frac{\partial^2 E}{\partial k_\alpha \partial k_\beta}\bigg|_{k=k_0} \cdot (k_\alpha - k_{0\alpha}) \cdot (k_\beta - k_{0\beta}) + ... \quad (4.6)$$

If cut the expansion at quadratic terms and take into account that at point of an extremum the first derivatives are equal to zero. And if assume that all components of wave vector are orthogonal we will get the energy of electrons in periodic structure:

$$E(k) = \frac{1}{2}\sum_{\alpha} \frac{\partial^2 E}{\partial k_\alpha^2}\bigg|_{k=0} \cdot k_\alpha^2 \quad (4.7)$$

Obtained equation is very similar to the equation for free electrons

$$E(k) = \frac{\hbar k^2}{2m}. \quad (4.8)$$

To bring the description of electron motion in periodic field of the crystal lattice the inverse effective mass tensor is introduced.

The effective mass of the charge carriers is related to the band structure by the following equation

$$\left(\frac{1}{m*}\right)_{ij} = \frac{1}{\hbar^2}\frac{d^2E}{dk_i k_j}, \tag{4.9}$$

where m^* effective mass, $\hbar$ - reduced Plank's constant, i and j is the x, y, and z, and are a direction in the reciprocal space, $E_n(k)$ is the dispersion relation for the n electronic band. Conducting band minimum $\frac{d^2E}{dk^2} > 0$, that corresponds $m^* > 0$ characterizes the effective mass of the electron. For a branch of the band structure corresponding to the valence band maximum $\frac{d^2E}{dk^2} < 0$ for which $m^* < 0$, describes the effective mass of the hole (Fig. 4.12 a). In Fig. 4.12 b schematically shows the dependence of the curvature of the electronic level in the vicinity of the extremum. The effective mass is related to the curvature of the electronic level. The greater the curvature of the level, the smaller the effective mass and vice versa. In Fig. 4.12 showed two electronic levels which correspond to the effective masses of charge carriers in the crystal. Levels with greater curvature correspond m_1^* (shown by a solid line). The branch with less curvature corresponds to m_2^* and $m_2^* > m_1^*$. The charge effective mass is determined in units of electron rest mass m_e (is the free electron rest mass).

In the general case, the effective mass is a symmetric tensor quantity. The right-hand side of Eq. 4.9 can be written as a symmetric tensor of rank 2 as follows

$$\frac{d^2E(k)}{dk^2} = \begin{pmatrix} \dfrac{d^2E(k)}{dk_x^2} & \dfrac{d^2E(k)}{dk_x dk_y} & \dfrac{d^2E(k)}{dk_x dk_z} \\ & \dfrac{d^2E(k)}{dk_y^2} & \dfrac{d^2E(k)}{dk_y dk_z} \\ & & \dfrac{d^2E(k)}{dk_z^2} \end{pmatrix}. \tag{4.10}$$

To obtain the effective mass of charge carriers of crystals I-III-VI₂, the extremums of the conduction bands and the valence band were determined from Figs. 4.6 and 4.7, and calculated the band structure in the selected interval near the extremum of the zone in two directions $\Gamma - X$ and $\Gamma - Z$. At definite **k**-points along two specific symmetry axes X and Z,

the $E(k)$ diagram is fitted around the CBM and VBM with the parabolic finction. The effective mass was determined from the approximation of Eq. 4.11 of the corresponding zone near these extremes

$$E(k) = E_0 + \frac{\hbar^2}{2m*}(k - k_0)^2, \qquad (4.11)$$

where E_0 is the energy of extremum, $\hbar$ is reduced Planck's constant, k is a wave vector, k_0 is a location of the band extremum in k-space. The calculated with LDA and GGA methods effective masses of charge carriers for I-III-VI₂ crystal in units of m_e for $Z - \Gamma - X$ directions are collected in Table 4.5. Comparing the obtained effective masses, we can say that the effective mass of the holes m_h* is greater than the effective mass of the electron m_e*. This suggests that the top of the valence band has a weaker dispersion than the bottom of the conduction band. It is also worth noting that the effective mass in the $\Gamma - X$ direction is greater than in the $\Gamma - Z$. A number of other crystals of semiconductor and dielectric nature have a similar dispersion [152,171,172]. However, it should be noted that there may be another situation. In particular, earlier in [66] we obtained results suggesting that the effective mass of an electron is much larger than the effective mass of a hole. This is accompanied by interesting effects.

From the analysis of Table 4.5 it can be seen that the effective mass in the $\Gamma - X$ direction is greater than in the $\Gamma - Z$. This indicates that in the $\Gamma - Z$ direction there should be greater mobility of charge carriers than in the $\Gamma - X$ direction. Considering the replacement of the cationic-anionic composition in crystals of group I-III-VI₂ with the structure of chalcopyrite, we can see the following trends. The anionic substitution $S \rightarrow Se \rightarrow Te$ reduces the effective mass in the $Z - \Gamma$ direction. For all crystals of the studied group there is a decrease in the effective mass at $S \rightarrow Se \rightarrow Te$. This statement is true for both the effective mass of electrons and the effective mass of holes. For the effective mass of holes m_h* in both $\Gamma - X$ and $\Gamma - Z$ directions, the absolute value of the effective mass obtained for the calculation with the GGA functional is greater than the obtained LDA. It should be noted here that the above trend is observed for all crystals except for some Te – containing for $\Gamma - Z$ direction of the Brillouin zone. For most crystals, the absolute mass of the hole is greater for $\Gamma - X$ than for $\Gamma - Z$. The cationic substitution of $Ag \rightarrow Cu$ also leads to a decrease in the effective mass of the charge carriers. A corresponding change is observed for both the effective mass of the holes and the effective mass of the electrons. Despite the large number of theoretical works in the literature, there are only effective masses obtained for a few crystals. For comparison, Table 4.6 shows the effective masses of charge carriers of crystals

I-III-VI$_2$ reported in the literature [106,175,179–188]. Also, it should be noted that the cited literature does not indicate for which direction the Brillouin zone, and often by what method the effective masses are obtained, which does not allow a direct comparison of our values with those available in the literature.

Table 4.5. The calculated effective mass of charge carriers in I-III-VI$_2$ crystals calculated with LDA/GGA method (in m_e unit) for Z – Γ – X directions.

Crystal	m_h^*		m_e^*	
	Γ – X	Z – Γ	Γ – X	Z – Γ
AgAlS$_2$	–2.057/–3.093	–0.361/–0.362	0.263/0.250	0.231/0.219
AgAlSe$_2$	–0.984/–1.529	–0.159/–0.190	0.155/0.174	0.133/0.156
AgAlTe$_2$	–0.546/–0.692	–0.114/–0.113	0.128/0.157	0.113/0.128
AgGaS$_2$	–1.042/–1.621	–0.170/–0.199	0.170/0.201	0.149/0.179
AgGaSe$_2$	–0.775/–1.055	–0.044/–0.070	0.086/0.120	0.068/0.113
AgGaTe$_2$	–0.453/–0.590	–0.041/–0.030	0.066/0.093	0.054/0.066
AgInS$_2$	–0.838/–1.195	–0.082/–0.095	0.148/0.175	0.094/0.239
AgInSe$_2$	–0.721/–0.970	–1.010/–0.211	0.403/0.037	0.090/0.032
AgInTe$_2$	–0.435/–0.567	–0.022/–0.728	0.070/0.077	0.092/0.041
CuAlS$_2$	–1.145/–1.544	–0.383/–0.447	0.334/0.261	0.979/0.216
CuAlSe$_2$	–0.764/–1.025	–0.156/–0.182	0.146/0.164	0.132/0.139
CuAlTe$_2$	–0.456/–0.580	–0.126/–0.119	0.115/0.119	0.113/0.107
CuGaS$_2$	–0.706/–0.945	–0.174/–0.179	0.156/0.181	0.146/0.150
CuGaSe$_2$	–0.554/–0.754	–0.048/–0.053	0.061/0.085	0.052/0.067
CuGaTe$_2$	–0.365/–0.485	–0.096/–0.041	0.052/0.058	0.052/0.040
CuInS$_2$	–0.812/–1.025	–0.674/–1.860	0.064/0.339	0.055/0.676
CuInSe$_2$	–0.603/–0.886	–0.845/–1.840	0.058/0.096	0.072/0.120
CuInTe$_2$	–0.416/–0.540	–0.405/–0.507	0.029/0.111	0.031/0.074

The effective mass of charge carriers also characterizes various electronic processes and is related to the carrier mobility μ, which is determined from the equation $\mu = \dfrac{e\tau}{m^*}$, where e is the electronic charge, τ is a scattering time introduced to account for the scattering of the electron by impurities and phonons. τ depends on the collisions of conduction holes

with phonons (τ_{ph}), impurity atoms (τ_i), impurity atoms and grain boundaries, or any crystal imperfections (τ_{GB}) [189]

$$\frac{1}{\tau} = \frac{1}{\tau_{ph}} + \frac{1}{\tau_i} + \frac{1}{\tau_{GB}} .$$

(4.12)

Mobility is important for the practical application of the material in photocatalysis, photovoltaics, etc. Since carrier mobility is inversely proportional to the effective mass of charge carrier, the reduction of m^* leads to an improvement in the mobility of charge carriers μ and as a consequence is expressed in an increase in the conductivity of the material following the equation

$$\sigma = eN\mu .$$

(4.13)

Thus, we can conclude that the substitutions of Ag → Cu, Al → Ga → In, and S → Se → Te lead to an increase in conductivity in I-III-VI$_2$ materials.

Table 4.6. The charge carriers effective mass for electron and hole of I-III-VI$_2$ crystals (in m_e unit) reported in the literature.

Crystal	m_e^*	m_h^*
AgAlS$_2$	0.0911[a]; 0.07[b]; 0.07[b]	5.55[b]; 5.62[b]
AgAlSe$_2$	—	—
AgAlTe$_2$	—	—
AgGaS$_2$	0.04[b]; 0.23[c]	0.94[b]; 0.72[c]
AgGaSe$_2$	0.43[d]; 0.17[c]	0.23[d]; 0.73[c]
AgGaTe$_2$	0.08[e]; 0.05[e]	0.57[e]; 0.05[e]
AgInS$_2$	0.04[b]	0.89[b]
AgInSe$_2$	0.12[c]	0.39[c]
AgInTe$_2$	0.05[e]; 0.04[e]	0.59[e]; 0.04[e]
CuAlS$_2$	0.06[b]; 0.42[f]; 0.83[f]	1.19[b]; 2.24[f]; 3.84[f]; 1.03[f]; 0.09[a]
CuAlSe$_2$	0.21[f]; 0.20[f]; 0.16[j]	1.11[f]; 1.69[f]; 0.53[f]; 0.75[j]
CuAlTe$_2$	0.13[g]; 0.36[f]; 1.98[f]	0.69[g]; 0.44[f]; 0.63[f]; 0.26[f]
CuGaS$_2$	0.13[h]; 0.04[b]; 0.26[f]; 0.25[f]; 0.13[c]	0.69[h]; 0.78[b]; 0.89[f]; 1.29[f]; 0.37[f]; 0.69[c]
CuGaSe$_2$	0.15[f]; 0.53[d]; 0.14[c]; 0.14[i]	0.56[f]; 0.46[f]; 0.25[f]; 0.40[d]; 1.20[c]
CuGaTe$_2$	0.16[f]; 0.15[f]	0.40[f]; 0.46[f]; 0.16[f]
CuInS$_2$	0.12[j]; 0.03[h]; 0.03[b]; 0.16[c]	0.93[j]; 1.3[g]; 1.87[b]; 1.30[c]
CuInSe$_2$	0.12[j]; 0.087[g]; 0.09[c]; 0.09[i]	0.98[j]; 0.087[g]; 0.73[c]
CuInTe$_2$	0.16[k]; 0.062[i]; 0.1[j]	0.78[k]; 1.28[j]

Ref. [a] [180]; Ref. [b] [181]; Ref. [c] [182]; Ref. [d] [183]; Ref. [e] [184]; Ref. [f] [185]; Ref. [g] [175]; Ref. [h] [106]; Ref. [i] [186]; Ref. [j] [187]; Ref. [k] [188].

4.2.2. Density of states

An effective way to analyze in detail the band structure of a crystal and the origin of electronic levels is to further calculate the total and partial density of electronic states for individual atoms and the orbital moments of electrons. In order to establish the genesis of crystal orbitals from the atomic states of the elements that are part of the crystals of group I-III-VI$_2$, calculations of the total $N(E)$ and local/partial density of states were performed. The DOS of a system describes the number of states per interval of energy at each energy level that are available to be occupied. By partial density of states is meant the density of states with a given symmetry of the wave function, for example Ag $3s$, S $3p$, In $4d$, etc., while the local density of states is the density of states calculated for a particular type of atom that makes up the crystal structure.

In this work, the density of states was calculated by a modified tetrahedra method [190]. The total densities of electronic states were calculated using eigenfunctions $\psi_{i,k}(\mathbf{r})$ and eigenvalues $E(\mathbf{k})$ obtained from band calculations [190]

$$N(E) = \frac{2}{\Omega_{BZ}} \sum_i \int_{\Omega_{BZ}} \delta(E - E_i(\mathbf{k})) d\mathbf{k} . \qquad (4.14)$$

And the number of electron in the unit cell is given by

$$N = \int_{-\infty}^{E_F} N(E) dE . \qquad (4.15)$$

The partial density of electronic states was calculated using the equation:

$$n(E) = \frac{2}{\Omega_{BZ}} \sum_i \int_{\Omega_{BZ}} Q_{\mathbf{k}}^{sl} \delta(E - E_i(\mathbf{k})) d\mathbf{k} , \qquad (4.16)$$

where i is the number of energy zone, Ω_{BZ} is the volume of first Brillouin zone, $Q_{\mathbf{k}}^{sl}$ defines the charge of l-type of symmetry, that contained inside the atomic sphere, which surrounds an atom of type s-type in the unit cell.

Fig. 4.13 shows the total and partial density of states of the ABC$_2$ crystals calculated using the GGA functional. For CuBC$_2$ crystals where B = Al, Ga, In and C = S, Se, Te, the total density of state the corresponding crystals is located on the top panel of the figures. The figures show that the total density of states can be divided into three parts. The first part of the state density graph corresponds to the energy range from 0 to 15 eV. This region is

formed by the states of the conduction band and includes the region where the DOS intensity is zero (the region from 0 eV to the energy value corresponding to E_g), and the region of $E > E_g$ formed by the density of states at the levels of the conduction band. The part of the energy range that corresponds to the density of states with $E > E_g$ is characterized by a wide zone formed by a large number of overlapping peaks. This zone occupies an energy range from E_g to 15 eV. There are no isolated peaks in this range, in particular those with high intensity. This statement is valid for all crystals of the investigated group ABC₂. It should be noted that the intensity of the DOS function of the conduction band is significantly lower than the peaks of the valence band, which may be due to the greater dispersion of the energy levels of the conduction band compared to the valence band. This statement is also in good agreement with the effective mass values for these compounds calculated in paragraph 4.2. Thus, for strongly bound valence electrons, the effective mass of charge carriers is much larger than the effective mass of free electrons in the conduction band.

The valence band of crystals in the ABC₂ group is formed by a group of levels ranging from 0 eV to –20 eV. They can be divided into two subgroups of levels. The first subgroup of levels forms the top of the valence band. It is formed by two intense bands with maxima ranging from 0 to –7 eV. There is a tendency that the anionic substitution of S → Se → Te leads to the convergence of two bands in crystals of the CuBC₂ type. For crystals with Te, a fusion of these two bands is observed. For crystals containing Ag, this region is continuous in the range from 0 to –7 eV. The second group of levels of the valence band is formed by peaks near –14 eV. For crystals AAlS₂, AAlSe₂, AAlTe₂, where A = Cu, Ag, this region is formed by one peak at –13 eV, while for crystals ABC₂ with ions B = Ga, In there is an additional peak with less energy than the peak in AAlC₂ crystals at –14 eV.

For a more detailed understanding of the origin of these bands, consider the partial density of states for the eighteen investigated crystals of the ABC₂ group depicted in Fig. 4.13. From the consideration of the partial density of electronic states for crystals with copper atoms as an element of the first group, the following can be said. For crystals of the CuBC₂ type, as can be seen from the figure, the maximum of the valence band is formed by 3*d*-states of copper atoms. These states are represented by an intense peak of 3*d*-electrons with a small contribution of 3*p*-, 4*p*- and 5*p*-states of the chalcogen atoms S, Se, and Te, respectivly. The 4*s*-electrons of copper atoms form a small peak at energies from –6 to –4 eV with an intensity close to zero. The main contribution of these states is in the conduction band. Two peaks lying close to each other and originated from Cu 3*d*-states are formed by split *d*-states under the action of a tetrahedral crystal field of surrounding atoms. As a result,

there are two sublevels with symmetry t_2 lying at higher energies and e lying below. For aluminum atoms, the 3s states form a low-intensity peak at about –6 eV, while the wider band formed by two Al peaks at energies form –5 to –2.5 eV and from –2.5 to 0 eV is formed by electrons weaker than 3s at 3p intensity. For Al atoms the 3s-states form the peack of low intensity at approximetly –6 eV, whole the whider band is frmed of two states of Al at energy form –5 to –2.5 eV and from –2.5 to 0 eV is originated from 3p-electrons with weaker intensity than 3s. For crystals with B = Ga, In, 4s- and 4p- as well as 5s- and 5p-states, respectively, form similar to crystals with aluminum peaks shifted by 1.5 – 2 eV in the direction of lower energies. It is also worth noting that in crystals with Ga and In the electronic configuration contains 3d- and 4d-electrons. This levels are located at the energy –15 eV. For the crystals containing the B = Ga, In, the 4s- and 4p- as well as 5s- and 5p-tates, respectively, form similar to the Al atoms peaks shifted on 1.5 – 2 eV to the lower energy. Also, it should be noted, that in crystals with Ga and In, the electronic configuration contains 3d- and 4d-electrons. This levels are located at the energy –15 eV.

The following can be said about the states of chalcogen atoms. For CuBC$_2$ crystals where B = Al, Ga, In and C = S, Se, and Te, the structure of energy levels of chalcogen atoms formed by electrons is quite similar. The bands formed by S 3s and Se 4s are located at energies of –13 eV.

In crystals with C = Te, the peak of Te 5s-states is shifted toward higher energies and is approximately located at –11 eV. The states of 3p-, 4p-, and 5p-electrons for S, Se, and Te, respectively, form wide bands at the top of the valence band from –7.5 to 0 eV. This band is formed of three main peaks. The first is associated with hybridized 3s-, 4s-, and 5s-states of Al, Ga, In atoms, respectively. The second is the main peak of the p-states of the chalcogen atom. Such a peak as well as the first low-intensity is associated with overlap of Cu 3d-, and Cu p-electron clouds.

The two peaks of the Ag 4d-states have similar intensities. These peaks, as in the case of copper atoms, are formed by the states of t_2 symmetry, which lies at higher energies, and by the states e, which is below. In the AgBC$_2$ series, the S $\rightarrow$ Se $\rightarrow$ Te transition transforms the peak corresponding to the Ag 4d-states, the band of which passes from two peak to single-peak at E from 0 to –5 eV. It also becomes more intense and is accompanied by a shift to –5 eV. This may mean an increase in the covalence of the Ag – C bond.

Replacement of component B in the AgBC$_2$ series, namely Al $\rightarrow$ Ga $\rightarrow$ In, leads to the convergence of two closely spaced bands of Ag d-states. With this substitution, in the case of B = Al there is a slight change in the energy levels s and p - states in AgAlX$_2$ crystals.
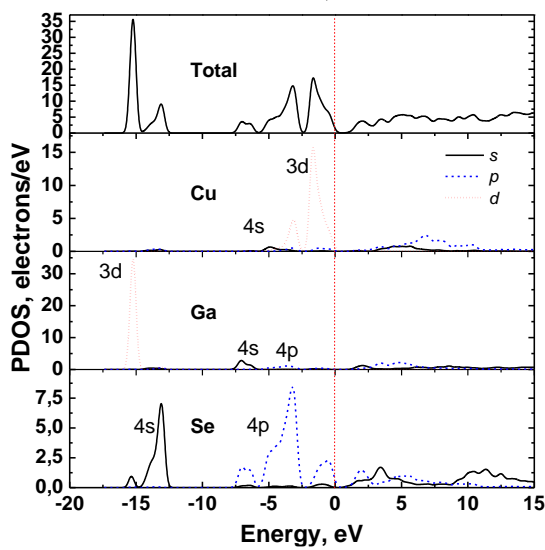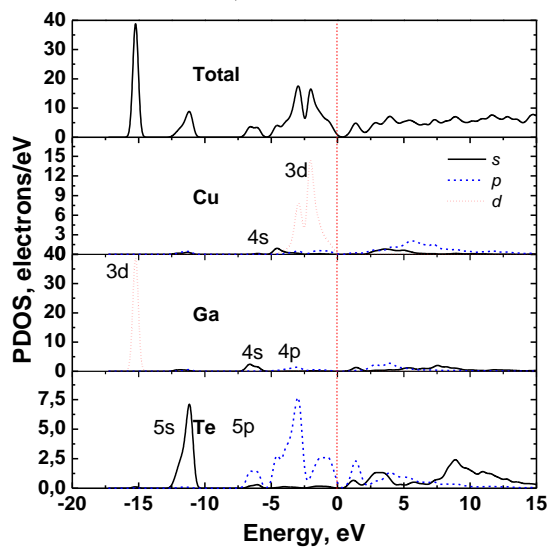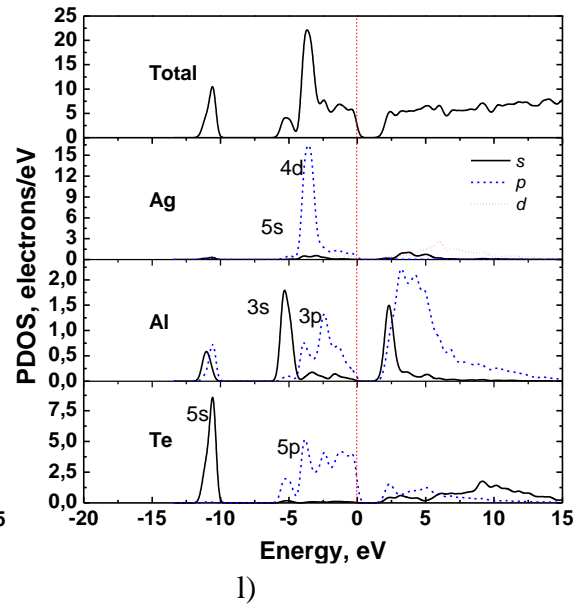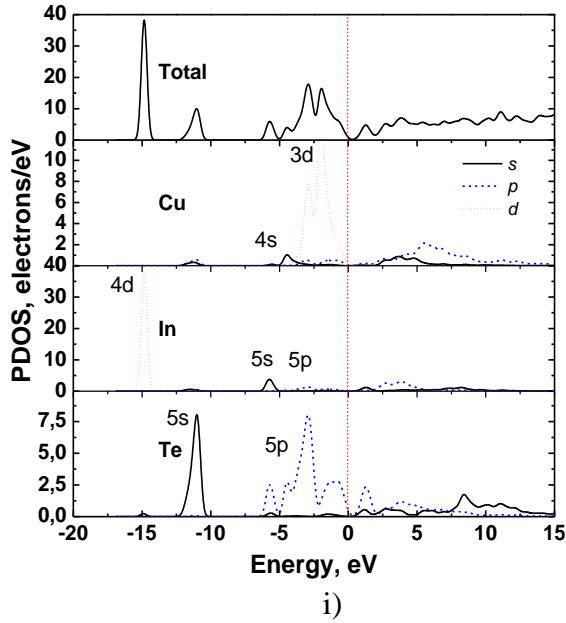
a)

b)

c)

d)

e)
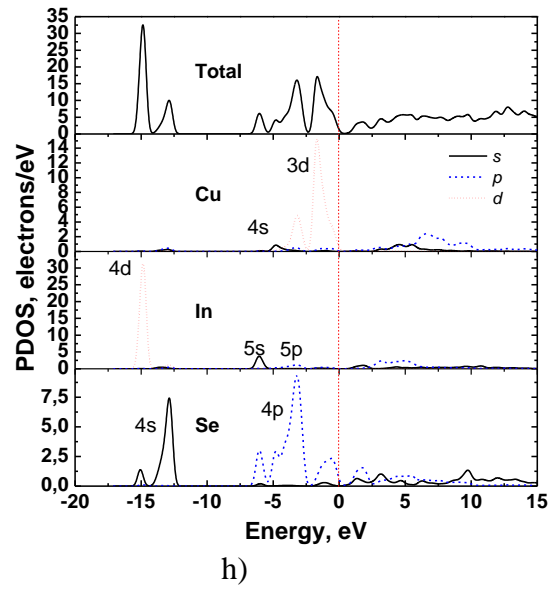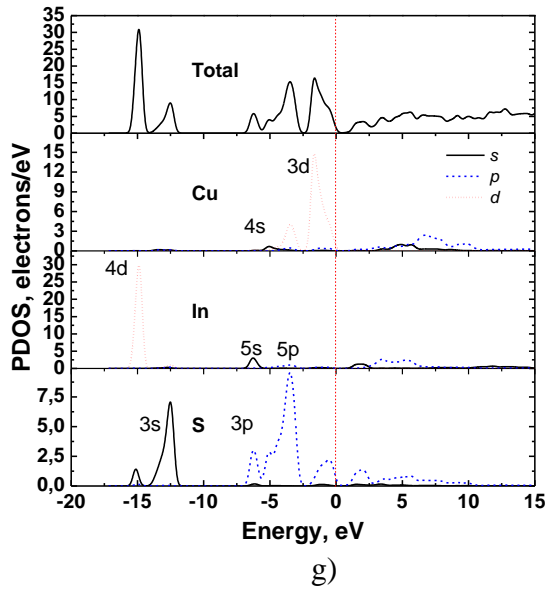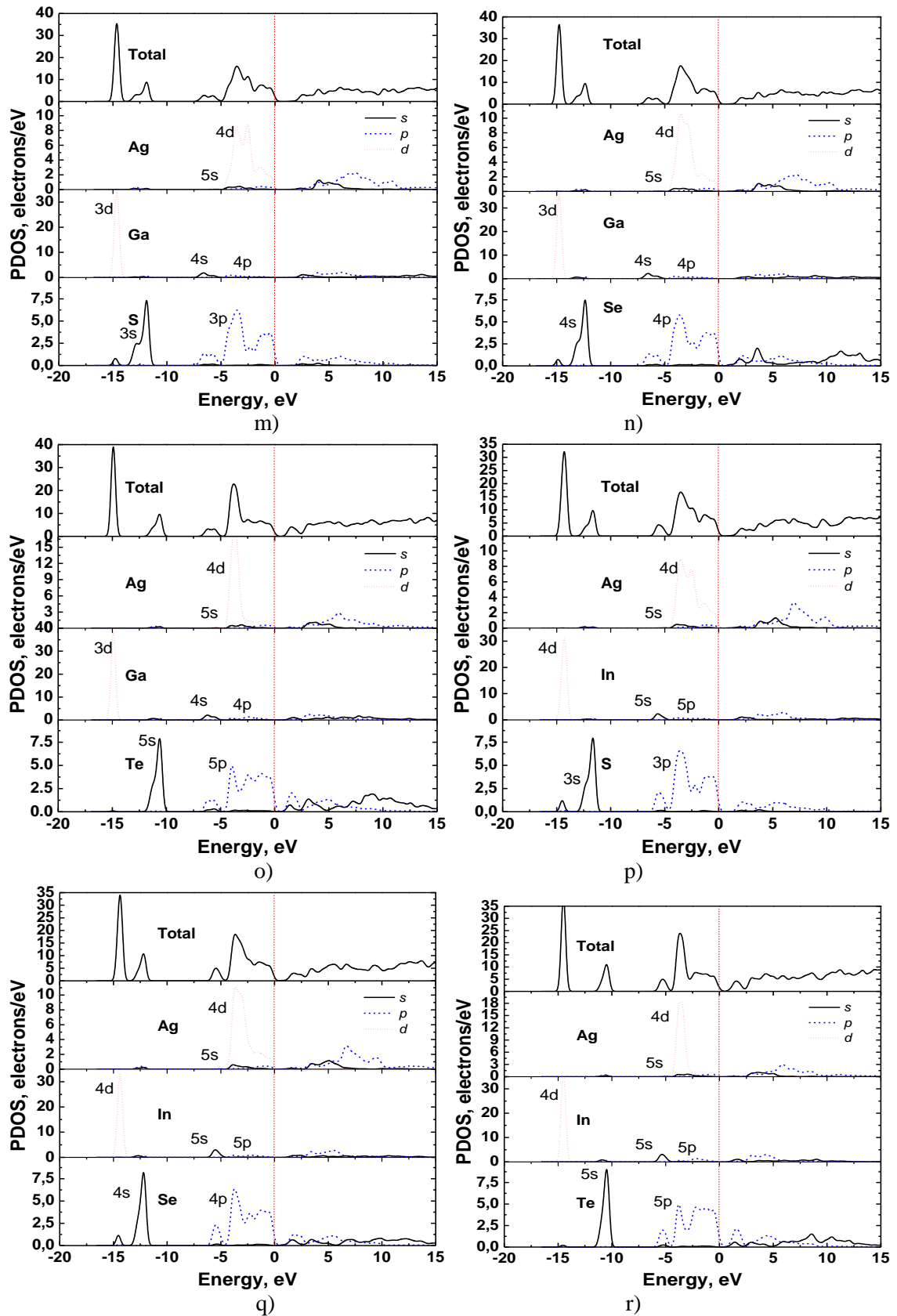
f)

g)

h)

i)

j)

k)

l)
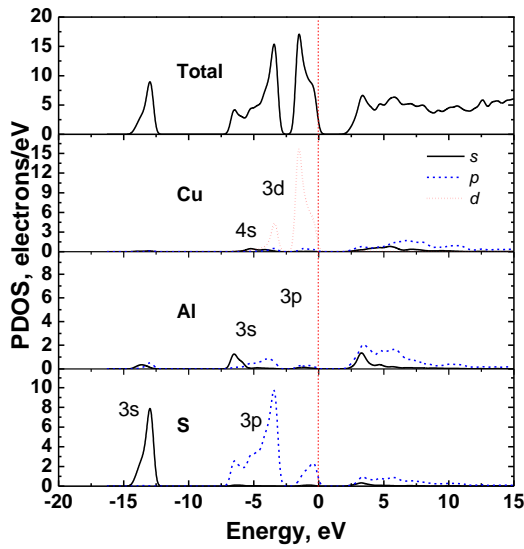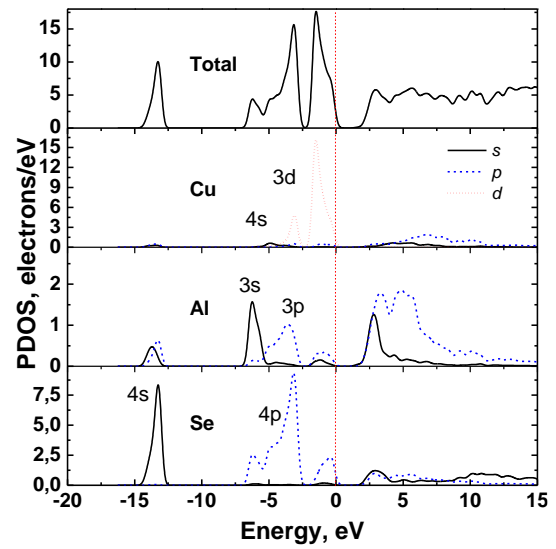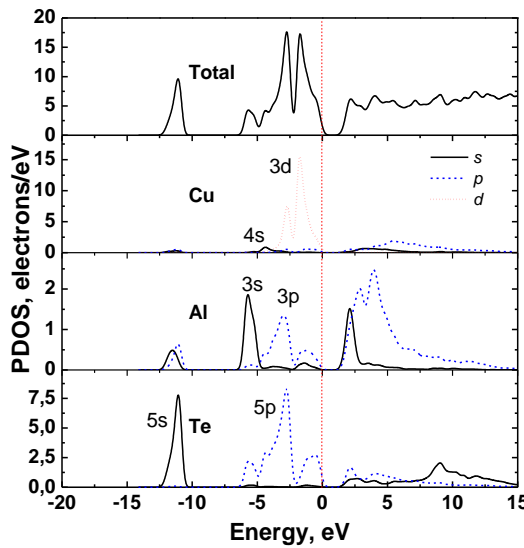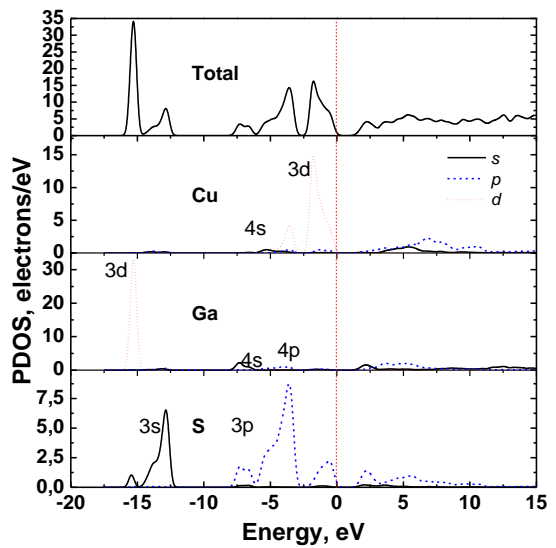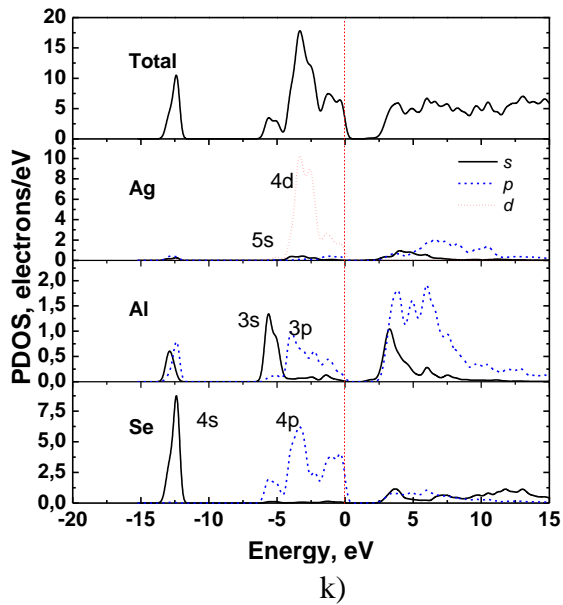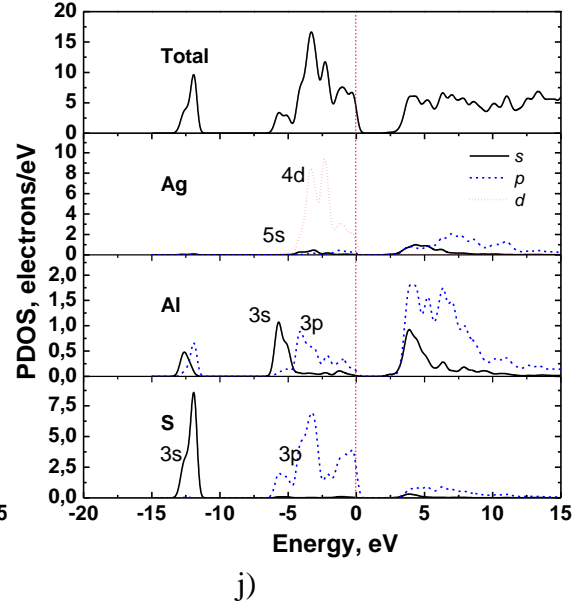
Figure 4.13. Total and partial density of stated of ABC₂ (A = Cu, Ag, B = Al, Ga, and In; C = S, Se, and Te) crystals calculated using GGA functional a) CuAlS₂; b) CuAlSe₂; c) CuAlTe₂; d) CuGaS₂; e) CuGaSe₂; f) CuGaTe₂; g) CuInS₂; h) CuInSe₂; i) CuInTe₂, j) AgAlS₂; k) AgAlSe₂; l) AgAlTe₂; m) AgGaS₂; n) AgGaSe₂; o) AgGaTe₂; p) AgInS₂; q) AgInSe₂; r) AgInTe₂.

There is an increase in the Al-*s* peak at –5 eV at S → Se → Te with its slight shift toward lower energies. The conduction band also shows a narrowing of the band of *s*-states of Al atoms that form the bottom of the conduction band.

AgGaX₂ crystals have a slightly different structure of $N(E)$ spectra. Here, the states of Ga atoms make a significant contribution to the density of states. These atoms have a high-intensity band at an energy of –15 eV. An additional gallium peak appears on the density of state spectrum, which is very narrow and has the highest intensity. In AgGaX₂ crystals, the anionic substitution of S → Se → Te leads to a slight shift of the Ga 3*d*-peak toward lower energies of ~ 1 eV.

In general, the density of states for X chalcogen undergoes significant changes during the transition from AgAlX₂ → AgGaX₂ → AgInX₂. For the crystals AgInX₂ it is observed the similar behgavior of $N(E)$ for the In ions. Here, In 4*d*-states create a narrow peack of the localized electrons at –15 eV, similarely as in Ga. Substitution S → Se → Te leads to the shifting of the peack In-4*d* by 1 eV to the lover energy.

4.2.3. Mulliken charges and chemical bonding

The interaction between atoms in a solid is determined by a chemical bond. There are known to be covalent, ionic, metallic, hydrogen, and van der Waals chemical bonds. Each of them is characterized by strength and method of its formation. Depending on the type of chemical bond, different physical properties are observed in the material. Therefore, the study of the characteristics of chemical bonding and related parameters are important for finding a relationship between the structure and properties of materials. The useful information on chemical bonding can be extracted from the atomic charges and bond population analysis. Such studies can be conducted from the first principles and provide important information about the interaction of atoms in the material being studied on the basis of information about the crystal structure using appropriate developed algorithms. An example of such an analysis is the analysis using the Mulliken formalism [191,192]. Analysis of Milliken's charges (both bond population and atomic charges) is especially useful for evaluating the nature of the chemical bond in the materials.

In order to study the peculiarities of the chemical bond in compounds I-III-VI$_2$ and to elucidate the effect of isomorphic substitution on the change in the nature of these bonds, we calculated and analyzed Mulliken charges for atoms and the bond (overlap) population. Mulliken overlapping population analysis was proposed by Mulliken [191]. This approach is representing the distribution of charge in atoms, as well as the inter-atom bonding. Mulliken population analysis [192], could help investigators to get information about the distribution of charge among the atoms in the simulated system and study the nature of bonding. A high value of the bond population indicates a covalent type of bonding, and a low value indicates an ionic nature. Positive and negative values indicate bonding and antibonding states, respectively. The calculation of charges is based on the method of linear combination of atomic orbitals (LCAO).

Population analysis in CASTEP was performed using the Mulliken formalism [191]. The implementation of this method was carried out by Segall et al. [150,193]. As mentioned in Chapter 3, the CASTEP program uses the PW basis to calculate the band energy structure and other system parameters. A disadvantage of the use of a PW basis set is that, due to the delocalized nature of the PW states, it provides no information about the localization of the electrons. In contrast, the LCAO basis set can provide a natural way of specifying quantities such as atomic charge, bond population, charge transfer and so forth. Population analysis in CASTEP is performed by projecting the PW states onto a localized basis using a technique described by Sanchez-Portal et al. [193]. The eigenstates $\left|\psi_\alpha(k)\right\rangle$, obtained from the PW calculation when sampling at a given wavevector k, are projected onto Bloch functions formed from a LCAO basis set $\left|\phi_\mu(k)\right\rangle$. Therefore, in Mulliken analysis, [191] the Mulliken charge associated with a given atom A, is determined by

$$Q(A) = \sum_k W_k \sum_\mu^{\text{on } A} \sum_v P_{\mu v}(k) S_{v\mu}(k) \,, \tag{4.17}$$

where W_k are the weights associated with the calculated k-points in the Brillouin zone. The $P_{\mu v}(k) = \left\langle \phi_\mu(k) \,|\, \hat{\rho}(k) \,|\, \phi_v(k) \right\rangle$ ($\hat{\rho}(k)$ is the density operator) and $S_{v\mu}(k) = \left\langle \phi_v(k) \,|\, \phi_\mu(k) \right\rangle$ denote the density matrix and the overlap matrix, respectively. The Mulliken charge provides a means of estimating partial atomic charges, and it represents the difference between the gross atom population and the number of electrons on the isolated free atom, which is the atomic number Z. It is widely accepted that the absolute magnitude of the atomic charges yielded by population analysis have little physical meaning, as they display a high degree of

sensitivity to the atomic basis set with which they were calculated [194]. However, for a consistent basis set, the relative values can provide us with some useful information [150,192]. In addition to providing an objective criterion for bonding between atoms, the overlap population may be used to assess the covalent or ionic nature of a bond.

We firstly performed a Mulliken population analysis of atoms for the crystals of the study group. The atomic populations for the I-III-VI₂ compounds in units of the proton charge calculated using LDA and GGA functionals are collected in Table 4.7. The table shows that the calculated charges of atoms differ significantly from the nominal charges of free ions. Deviation of the effective charges from the formal ones anticipated from the chemical formula is another confirmation of strong hybridization effects charge transfer between atoms and dominating covalent character of the chemical bonding in the studied crystal. The table shows that the atoms of aluminum, gallium and indium for almost all crystals show a positive value of the charge in the structure of the crystals of the chalcopyrite group. The exceptions are Ga atoms in the AgGaTe₂ (–0.09 for LDA), CuGaTe₂ (–0.03 for LDA) and AgInTe₂ (–0.08 for LDA) CuInTe₂ (–0.12 for LDA) crystals. For AgAlC₂ crystals, the charges of the atoms are greater than the charges of the CuAlX₂ crystals. The analysis of the obtained results showed that in the system ABC₂ for which B = Ga, In and C = S the charges of atoms for compounds with Ag are greater than the charges of crystals with Cu. At the same time, for crystals with AgBC₂ where B = Ga, In, and C = Se, and Te, the charges for crystals with A = Ag are smaller than charges of crystals with the A = Cu.

In both subgroups of crystals (with the A = Ag and Cu) there is a general tendency that for all compounds with cations B = Al, Ga, and In the Milliken atomic charges decrease their value for ions in the crystal structure with isomorphic anion substitution S → Se → Te. Also from consideration of the table it is possible to notice the following. The charge of the sulfur anion is negative. For Se, there is also a small negative sign close to zero. However, for crystals with Te, their charge is positive.

The shortest bond lengths between the constituent atoms of I-III-VI₂ compounds calculated using LDA and GGA functionals together with bond overlap populations are collected in Table 4.8. Considering the chemical bonds for eighteen crystals of group I-III-VI₂ whose parameters are collected in the table, we can note the following. As can be seen from the table, the calculated bond lengths and population values for GGA and LDA methods are in good agreement with each other. The bond lengths calculated using the LDA functional are slightly shorter than obtained using the GGA. This behavior is due to the peculiarities of the LDA and GGA functionals, which is expressed in the overbonding of

atoms for LDA functional and overestimation of the bond length values for GGA functional. In general, for crystals of the ABC$_2$ group, the calculated bond lengths for crystals with A = Ag show that the distance between the A – C atoms is greater than the distance between the B – C atoms. The exception to this observation is AgInSe$_2$ crystals for which the Ag – Se distance is greater than the In – Se bond. And AgInTe$_2$ for which the Ag – Te bond is larger than In – Te. For crystals with cation atoms A = Cu, the bond lengths between the B – C atoms are longer than the bonds between the A – C atoms.

The population of chemical bonds between atoms in the structure of chalcopyrite-type ABC$_2$ crystals shows that for crystals with A = Ag cations the population of B – C type bonds is greater than A – C bonds, for all subgroup crystals except AgInSe$_2$ and AgInTe$_2$ compounds for which the chemical bond population is B – C is smaler than for A – C. In CuBC$_2$ crystals, the population of B – C bonds is higher than for A – C for CuAlS$_2$, CuAlSe$_2$, and CuAlTe$_2$. For other crystals, the population of A – C is higher than for B – C. For compounds such as AgGaSe$_2$, AgGaTe$_2$, and CuGaSe$_2$ and CuGaTe$_2$, the population populations of the B – C bonds are negative, which is associated with antibonding states.

For a more detailed analysis of the type of chemical bond, we calculated the ionicity parameter of bond using the following equation [195]:

$$f_h = 1 - e^{-\frac{|P_c - P|}{P}}, \tag{4.18}$$

where P is the overlap population of a bond, a P_c – is the overlap population of the bond in a pure covalent crystal of that specific structure or cluster. f_h is equal to zero for a purely covalent bond and to unity for a purely ionic bond. Usually the bonds in different types of structures would have different values of P_c. The calculated value of the ionic bond for eighteen crystals of group I-III-VI$_2$ is given in Table 4.8. As can be seen from the table, crystals of group I-III-VI$_2$ have a covalent type of chemical bond with a high contribution of the ionic component. As can be seen, for most crystals of this group there is a difference from the ionicity of the bond for A – B and B – C by the value from 0.1 to 0.5. This difference may be the reason for the presence of deformation in crystals of the CP type. For crystals containing silver atoms in the structure, it is observed that the effect of the isomorphic substitution S → Se leads to an increase in the ionicity of the B – C bond and the replacement of Se → Te to its decrease, so that f_h (AgBSe$_2$)> f_h (AgBTe$_2$)> f_h (AgBS$_2$). At the same time, for the A – C bond there is a dependence that the replacement of S → Se → Te leads to a decrease in the value of the ionicity of the bond. For a crystal with Cu for compounds with B = Al, In, f_h (CuBSe$_2$)> f_h (CuBTe$_2$)> f_h (CuBS$_2$). However, for crystals with gallium, we

Table 4.7. Atomic populations (by Mulliken) (in units of the proton charge) of the constituent atoms of I-III-VI$_2$ group crystal (GGA/LDA data).

	Species	s	p	d	Total	Charge (e)
AgAlS$_2$	Ag	0.48/0.45	0.40/0.30	9.89/9.92	10.77/10.67	0.23/0.33
	Al	0.85/0.86	1.27/1.25	0.00/0.00	2.13/2.11	0.87/0.89
	S	1.81/1.83	4.74/4.78	0.00/0.00	6.55/6.61	−0.55/−0.61
AgAlSe$_2$	Ag	0.60/0.56	0.73/0.63	9.89/9.92	11.22/11.11	−0.22/−0.11
	Al	1.05/1.04	1.49/1.42	0.00/0.00	2.55/2.47	0.45/0.53
	Se	1.51/1.55	4.60/4.66	0.00/0.00	6.11/6.21	−0.11/−0.21
AgAlTe$_2$	Ag	0.70/0.67	0.85/0.75	9.89/9.91	11.44/11.34	−0.44/−0.34
	Al	1.19/1.22	1.68/1.62	0.00/0.00	2.87/2.84	0.13/0.16
	Te	1.48/1.52	4.37/4.39	0.00/0.00	5.84/5.91	0.16/0.09
AgGaS$_2$	Ag	0.57/0.55	0.61/0.50	9.87/9.90	11.05/10.95	−0.05/0.05
	Ga	0.73/0.76	1.49/1.41	10.00/10.00	12.21/12.17	0.79/0.83
	S	1.82/1.84	4.55/4.60	0.00/0.00	6.37/6.44	−0.37/−0.44
AgGaSe$_2$	Ag	0.64/0.60	0.75/0.64	9.87/9.90	11.25/11.14	−0.25/−0.14
	Ga	1.13/1.17	1.62/1.53	10.00/10.00	12.76/12.70	0.24/0.30
	Se	1.58/1.59	4.42/4.49	0.00/0.00	6.00/6.08	0.00/−0.08
AgGaTe$_2$	Ag	0.72/0.70	0.88/0.77	9.87/9.90	11.47/11.37	−0.47/−0.37
	Ga	1.30/1.31	1.79/1.69	10.00/10.00	13.09/13.00	−0.09/0.00
	Te	1.53/1.57	4.19/4.25	0.00/0.00	5.72/5.81	0.28/0.19
AgInS$_2$	Ag	0.55/0.53	0.52/0.42	9.87/9.90	10.95/10.85	0.05/0.15
	In	0.91/0.91	1.29/1.22	9.99/9.99	12.18/12.13	0.82/0.87
	S	1.85/1.87	4.59/4.64	0.00/0.00	6.43/6.51	−0.43/−0.51
AgInSe$_2$	Ag	0.65/0.62	0.74/0.64	9.86/9.89	11.26/11.15	−0.26/−0.15
	In	1.35/1.31	1.45/1.36	9.99/9.99	12.79/12.66	0.21/0.34
	Se	1.52/1.57	4.45/4.53	0.00/0.00	5.98/6.10	0.02/−0.10
AgInTe$_2$	Ag	0.73/0.70	0.84/0.72	9.88/9.90	11.44/11.33	−0.44/−0.33
	In	1.49/1.48	1.60/1.51	9.99/10.00	13.08/12.98	−0.08/0.02
	Te	1.47/1.52	4.27/4.32	0.00/0.00	5.74/5.84	0.26/0.16
CuAlS$_2$	Cu	0.51/0.50	0.55/0.44	9.84/9.86	10.89/10.80	0.11/0.20
	Al	0.88/0.89	1.28/1.25	0.00/0.00	2.16/2.14	0.84/0.86
	S	1.79/1.81	4.68/4.72	0.00/0.00	6.47/6.53	−0.47/−0.53
CuAlSe$_2$	Cu	0.65/0.62	0.87/0.77	9.85/9.86	11.37/11.25	−0.37/−0.25
	Al	1.05/1.05	1.50/1.43	0.00/0.00	2.55/2.47	0.45/0.53
	Se	1.50/1.55	4.54/4.59	0.00/0.00	6.04/6.14	−0.04/−0.14
CuAlTe$_2$	Cu	0.74/0.72	1.02/0.91	9.86/9.87	11.62/11.50	−0.62/−0.50
	Al	1.19/1.21	1.70/1.65	0.00/0.00	2.88/2.86	0.12/0.14
	Te	1.46/1.49	4.29/4.33	0.00/0.00	5.75/5.82	0.25/0.18
CuGaS$_2$	Cu	0.61/0.60	0.75/0.66	9.82/9.83	11.18/11.09	−0.18/−0.09
	Ga	0.73/0.75	1.51/1.44	10.00/10.00	12.24/12.18	0.76/0.82
	S	1.79/1.82	4.49/4.54	0.00/0.00	6.29/6.36	−0.29/−0.36
CuGaSe$_2$	Cu	0.68/0.66	0.90/0.79	9.82/9.83	11.40/11.28	−0.40/−0.28
	Ga	1.03/1.03	1.63/1.54	10.00/10.00	12.65/12.57	0.35/0.43
	Se	1.62/1.64	4.36/4.44	0.00/0.00	5.98/6.08	0.02/−0.08
CuGaTe$_2$	Cu	0.76/0.76	1.07/0.96	9.83/9.84	11.66/11.56	−0.66/−0.56
	Ga	1.23/1.26	1.81/1.71	10.00/10.00	13.03/12.97	−0.03/0.03
	Te	1.53/1.55	4.13/4.18	0.00/0.00	5.66/5.74	0.34/0.26
CuInS$_2$	Cu	0.59/0.59	0.66/0.57	9.81/9.83	11.06/10.98	−0.06/0.02
	In	0.94/0.94	1.31/1.24	9.99/9.99	12.24/12.17	0.76/0.83
	S	1.82/1.84	4.53/4.58	0.00/0.00	6.35/6.43	−0.35/−0.43
CuInSe$_2$	Cu	0.69/0.67	0.89/0.78	9.81/9.82	11.39/11.27	−0.39/−0.27
	In	1.33/1.28	1.46/1.37	9.99/9.99	12.78/12.65	0.22/0.35
	Se	1.52/1.57	4.40/4.48	0.00/0.00	5.92/6.04	0.08/−0.04
CuInTe$_2$	Cu	0.76/0.76	1.03/0.92	9.84/9.84	11.63/11.53	−0.63/−0.53
	In	1.48/1.46	1.64/1.54	9.99/9.99	13.12/12.99	−0.12/0.01
	Te	1.42/1.49	4.20/4.25	0.00/0.00	5.62/5.74	0.38/0.26

Table 4.8. Lengths and overlap populations of the shortest atomic bonds, and bond ionicity of I-III-VI$_2$ crystal (GGA/LDA functional).

	Bond	Population	Length (Å)	f_i
AgAlS$_2$	Al — S	0.60 / 0.59	2.24055 / 2.28092	0.487
	Ag — S	0.24 / 0.21	2.47463 / 2.57713	0.958
AgAlSe$_2$	Al — Se	0.52 / 0.51	2.37811 / 2.40464	0.603
	Ag — Se	0.28 / 0.25	2.57042 / 2.66933	0.924
AgAlTe$_2$	Al — Te	0.57 / 0.55	2.60997 / 2.68112	0.530
	Ag — Te	0.39 / 0.36	2.71423 / 2.80543	0.791
AgGaS$_2$	Ga — S	0.46 / 0.45	2.27561 / 2.32674	0.691
	Ag — S	0.38 / 0.35	2.47019 / 2.57237	0.804
AgGaSe$_2$	Ga — Se	–0.37 / –0.44	2.40502 / 2.43963	0.818
	Ag — Se	0.43 / 0.41	2.56482 / 2.66808	0.734
AgGaTe$_2$	Ga — Te	–0.73 / –0.42	2.61736 / 2.70081	0.309
	Ag — Te	0.52 / 0.47	2.71089 / 2.81254	0.603
AgInS$_2$	In — S	0.42 / 0.42	2.47354 / 2.52797	0.749
	Ag — S	0.35 / 0.32	2.48012 / 2.58714	0.844
AgInSe$_2$	In — Se	0.20 / 0.19	2.60028 / 2.65252	0.982
	Ag — Se	0.38 / 0.36	2.57104 / 2.66146	0.804
AgInTe$_2$	In — Te	0.32 / 0.30	2.79783 / 2.87910	0.881
	Ag — Te	0.44 / 0.41	2.72456 / 2.83327	0.720
CuAlS$_2$	Al — S	0.58 / 0.57	2.24095 / 2.27988	0.515
	Cu — S	0.34 / 0.31	2.24945 / 2.32300	0.856
CuAlSe$_2$	Al — Se	0.55 / 0.54	2.37979 / 2.41045	0.559
	Cu — Se	0.32 / 0.30	2.35801 / 2.41619	0.881
CuAlTe$_2$	Al — Te	0.60 / 0.58	2.60917 / 2.66374	0.487
	Cu — Te	0.46 / 0.42	2.52777 / 2.61716	0.691
CuGaS$_2$	Ga — S	0.42 / 0.40	2.27323 / 2.32399	0.749
	Cu — S	0.52 / 0.49	2.24025 / 2.31215	0.603
CuGaSe$_2$	Ga — Se	–0.63 / –0.47	2.40591 / 2.43716	0.444
	Cu — Se	0.44 / 0.45	2.34835 / 2.42173	0.720
CuGaTe$_2$	Ga — Te	–0.45 / –0.50	2.61192 / 2.68792	0.705
	Cu — Te	0.59 / 0.58	2.51838 / 2.60220	0.501
CuInS$_2$	In — S	0.38 / 0.36	2.47463 / 2.52939	0.804
	Cu — S	0.48 / 0.45	2.25207 / 2.32944	0.662
CuInSe$_2$	In — Se	0.12 / 0.11	2.59910 / 2.64321	0.999
	Cu — Se	0.46 / 0.44	2.35906 / 2.43052	0.691
CuInTe$_2$	In — Te	0.28 / 0.21	2.78904 / 2.87552	0.924
	Cu — Te	0.53 / 0.51	2.52821 / 2.61658	0.588

obtained that f_h (CuGaS$_2$)> f_h (CuBTe$_2$)> f_h (CuBSe$_2$). Also, as expected, the ionicity of the bond is inversely proportional to its population. Table 4.8 showed that the compounds of the CP group have a mixed ion-covalent type of chemical bond with a large proportion of ionicity. The largest fraction of ionicity was obtained for the CuInSe$_2$ crystal ($f_h = 0.999$), which indicates an almost ionic type of bond between In and Se atoms.

4.3. Optical properties of chalcopyrite crystals

4.3.1. Calculation of dielectric function and related optical spectra

The practical use of materials for building on their basis a variety of optical devices operating in the range of different wavelengths and, in particular, optoelectronic devices require a detailed study of the optical properties of materials in a wide range of spectrum. Such studies are extremely important for characterizing the material and determining the suitability or effectiveness of their use in a devices. At the same time, the study of the optical properties of a material is an important task for understanding the electronic structure and explaining other physical properties. The optical properties of materials depend on the interaction of electromagnetic radiation with matter. This interaction is related to the wavelength λ, the frequency ω of the radiation, and the properties of the material, such as dielectric constant ε, refractive index n, and so on. When light falls on a material, their interaction in the general case can be characterized into several types. It can be absorbed by matter, reflected, or passed through. The relative extent of absorption, transmission or reflection depends on the properties of the material. Such interactions of electromagnetic radiation with matter occur simultaneously, and the nature of these interactions indicates the structure of energy levels and the crystal in general. Research in the low-energy (long-wavelength) region of the spectrum is important for the construction of various optical devices, such as filters, modulators, etc. The high-energy (short-wavelength) region, with energies larger than the band gap, which corresponds to interband electron transitions, is important for various processes related to light absorption. In particular, light absorption is important when using chalcopyrite materials in photoelectrochemistry as an absorbing layer in photovoltaics, which is important in the design of photocells and is currently an urgent task for scientists.

In practice, absorption spectra are often used in the study of materials to analyze the location of electronic levels, to study of the fundamental absorption edge [196]. For materials with a high light absorption coefficient, such studies cannot be performed in a wide range of energies, so their reflection spectra are studied. From reflection spectra after some processing it is possible to receive dielectric function which is connected with other optical functions.

Dielectric function is the one of the main optical characteristics of a solid, which can express other optical properties and describe the optical response of the medium. In this work, we investigated the dielectric function for I-III-VI₂ group crystals and other optical properties of the material such as refractive index n, reflection coefficient R, absorption coefficient α. The dielectric constant $\varepsilon(\omega)$, which by its nature is a complex function and contains information about the optical properties of the material. Complex frequency-dependent dielectric function can be written as:

$$\varepsilon(\omega) = \varepsilon_1(\omega) + i\varepsilon_2(\omega), \tag{4.19}$$

where $\varepsilon_1(\omega)$ and $\varepsilon_2(\omega)$ are its real and the imaginary parts, respectively. The imaginary part of dielectric function $\varepsilon_2(\omega)$ reflects the processes involved in light absorption. The imaginary part, of the complex dielectric constant $\varepsilon_2(\omega)$, consists of two parts: one due to intraband transition caused by the incident electromagnetic wave and the other due to interband transition. For metals, intraband transition was considered whereas interband transition is for semiconducting materials. Besides, the interband transition is of two types, direct band and indirect band transitions. The intraband excitations are manifested at low photon energies. Their frequencies are described in the simplest cases by the Drude – Lorentz theory. Due to little contribution towards dielectric function, indirect interband transitions can be neglected, although it provides information regarding electron-phonon scattering. The direct interband transitions contributes mainly to the dielectric function (imaginary part) which can be found out from the momentum matrix between occupied and unoccupied wave functions. Given the simplification of the problem by introducing a number of approximations $\varepsilon_2(\omega)$ can be determined based on the results of the band calculation. Such a simplification is a one-electron approximation for calculating the excitation energy, a dipole approximation in calculating the intensity of transitions, and also taking into account only direct transitions, ie, conserving the **k**-vector, transitions from occupied to virtual states. Thus, from electronic transitions in solids $\varepsilon_2(\omega)$ can be estimated by integration of elements of dipole matrix operator between the filled states of valence band and empty levels of conduction band

$$\varepsilon_2(\hbar\omega) = \frac{2\pi e^2}{\Omega\varepsilon_0} \sum_{k,v,c} \left|\left\langle \psi_k^c \left| u\mathbf{r} \right| \psi_k^v \right\rangle\right|^2 \delta\left(E_k^c - E_k^v - E\right), \tag{4.20}$$

where e is the electron charge, ε_0 is the dielectric permittivity of vacuum; Ω is the unit cell volume; ψ_k^c and ψ_k^v are the wave functions of the conduction band and valence band in k-space, respectively; u is the incident photon polarization vector; $\mathbf{r}$ is the operator of electron position, and $E = \hbar\omega$ is the photon energy. This expression is similar to Fermi's golden rule for time-dependent perturbations. The $\varepsilon_2(\omega)$ can be thought of as detailing the real transitions between the unoccupied and occupied electronic states. The matrix elements of position and momentum operators are related as [197]

$$\left\langle \psi_k^c \mid r \mid \psi_k^v \right\rangle = \frac{1}{i\omega m} \left\langle \psi_k^c \mid p \mid \psi_k^v \right\rangle + \frac{1}{\hbar\omega} \left\langle \psi_k^c \mid V_{nl} \mid \psi_k^v \right\rangle, \tag{4.21}$$

where p is the momentum operator, $\hbar\omega$ is the energy difference between occupied and unoccupied energy levels, m is the electron mass and V_{nl} is the non-local pseudopotential (angular momentum dependent potentials).

The peak of the imaginary part of the dielectric function corresponds to electronic transitions from the valence to conduction bands, depending on the electronic transition energy of the conduction and valence band, i.e., the band-gap energies. The instrumental smearing of 0.3 eV is used to simulate the broadening effects.

The real part of the dielectric function $\varepsilon_1(\hbar\omega)$ is related to its imaginary part $\varepsilon_2(\hbar\omega)$ by the Kramers – Kronig transform relations. Thus the real part ε_1 can be obtained from the imaginary, calculated from Eq. 4.20.

$$\varepsilon_1(\hbar\omega) = 1 + \frac{2}{\pi} \int_0^\infty \frac{\omega' \varepsilon_2(t) d\omega'}{\omega'^2 - (\hbar\omega)^2}. \tag{4.22}$$

The quantity $\varepsilon_1(\omega)$ represents how much a material becomes polarized when an electric field is applied due to creation of electric dipoles in the material while $\varepsilon_2(\omega)$ represents absorption in the material. When a material is transparent $\varepsilon_2(\omega)$ is zero, but becomes nonzero when absorption begins.

Amorphous materials are characterized by one dielectric function in all directions of light wave propagation in the material. However, in crystalline materials to describe the properties in different directions using the dielectric constant tensor, which is a material tensor of 2nd rank ε_{ii}.

The materials of I-III-VI₂ group belongs to the crystals of the middle category for which the dielectric function tensor is simplified to the following components $\varepsilon_{11} = \varepsilon_{22} \neq \varepsilon_{33}$.

Therefore, the dielectric constant has two independent components $x = y$ and z. According to the symmetry, the CP crystals are uniaxial with the optical axis directed along the z direction. For the directions x and y the electric field $\mathbf{E}$ is perpendicular to the optical axis of the crystal while for z the direction is parallel and is denoted as $\mathbf{E} \perp z$ and $\mathbf{E} \parallel z$ respectively.

In Fig. 4.14 the spectra of dielectric functions in the polarization light of I-III-VI$_2$ crystals calculated for photon energies from 0 up to 20 eV for polarization vector [100] and [001] are shown. We have used a 0.5 eV Gaussian smearing for all calculations. As can be seen from the figure, all crystals of groups I-III-VI$_2$ have similar spectra of the real and imaginary parts of the dielectric function. In Fig. 4.14. the left panel corresponds to the real part of the dielectric function of the crystal of the investigated group of chalcopyrites. Accordingly, the right panel shows the imaginary parts of the complex dielectric function. Each figure in the upper left corner has a designation that indicates that the graph belongs to one of the eighteen crystals of group I-III-VI$_2$.

From analysis of the dielectric function spectra obtained from Eqs. 4.20 and 4.22, the following regularities in the spectra are observed for the investigated group of crystals. For the real part of the dielectric function, a smooth monotonic increase in the value of $\varepsilon_1(\omega)$ was found in the range from 0 eV to almost 2-3 eV. In this interval it is clear that the dielectric function has a slight anisotropy. When the anion is replaced in the structure of S $\rightarrow$ Se $\rightarrow$ Te crystals, a decrease in anisotropy is observed for almost all compounds. The exceptions are CuInX$_2$ crystals where X = S, Se, Te for which the replacement of sulfur atoms by heavier atoms leads to a slight increase in anisotropy. In the specified energy range, the dielectric function in the x direction is greater than in the z direction (except for the AgGaTe$_2$ crystal for which $\varepsilon_{1,x} < \varepsilon_{1,z}$). As the energy of the incident photon increases, a change in the behavior of the dielectric function is observed. It ceases to increase monotonously and forms a series of peaks. The first peak, for all crystals except AgAlSe$_2$, is the most intense and ranges from 8 (for AgGaS$_2$) to 18 (for CuGaTe$_2$ [165]). After reaching its maximum, the real part of the dielectric function begins to decline smoothly. As $\varepsilon_1(\omega)$ decreases as the photon energy increases. The value of $\varepsilon_1(\omega) = 0$ is observed for all crystals of I-III-VI$_2$ group, after which the function becomes negative. This region has a significant anisotropy in comparison with the low-energy region from 0 to 3 eV. It is seen that in this energy region the dielectric function in the x direction has a lower intensity value than in the z direction. Near the minimum of the dielectric function ε_1, its anisotropy also increases. After reaching the minimum value of the real part of the dielectric constant and the beginning of its growth,

there is a significant convergence of the curves of the dielectric functions for the two directions, which indicates a decrease in anisotropy with increasing photon energy. The value of the energy at which the dielectric function goes to zero is different for different crystals and is in the range from 5.5 to 9 eV. As can be easily seen from the figures, for CuBC$_2$ crystals the energy at which $\varepsilon_1(\omega)$ becomes equal to zero is almost the same as for AgBC$_2$ crystals. It should be noted that there is a tendency which shows that the replacement of the anion S $\rightarrow$ Se $\rightarrow$ Te leads to a decrease in the energy at which the real part of the dielectric function will become zero. Also, the figures show that the replacement of Al $\rightarrow$ Ga $\rightarrow$ In cations also has a slight decrease in the transition energy to zero $\varepsilon_1(\omega)$. This behavior of the dielectric function indicating the transparency of these compounds above the energy at which $\varepsilon_1(\omega) = 0$. Near 20 eV, the real part again passes the mark 0 and begins to grow monotonically to unity. For crystals containing tellurium atoms in their structure, the transition from negative to positive dielectric constant occurs at an energy of approximately 18 eV for all ABTe$_2$ crystals.

The Fig. 4.14 (right panel) shows the imaginary part of the dielectric function, which is directly related to the absorption processes. On the spectra of the imaginary part of the dielectric function of crystals I-III-VI$_2$ constructed in different crystallographic directions (Fig. 4.14) we see that for the first critical point of the dielectric function the fundamental absorption edge occurs at energies corresponding to the band gap energy in the crystal. (see Table 4.9.). With increasing of the energy, a typical rapid increase in $\varepsilon_2(\omega)$ is observed. We observe a significant anisotropy of the dielectric function depending on the optical polarization. Previously, similar behavior of the dielectric function was obtained for CdS films [177] and CdSe [198] and the Ag$_2$SiS$_3$ crystal [152], etc. The first peak in the spectrum of the dielectric function corresponds to the optical transitions that form the edge of the fundamental absorption. These are transitions from the levels of the top of the valence band at the level of the bottom of the conduction band. For x polarization of incident light ($\mathbf{E} \perp z$) the absorption corresponds to transitions between states $\Gamma_5 \rightarrow \Gamma_1$ and for z polarization of light ($\mathbf{E} \parallel z$) transitions occur between states with symmetry $\Gamma_4 \rightarrow \Gamma_1$. The peak corresponding to the lowest energy in the range from 0 to 5 eV can be attributed to the optical transitions of the electron from the band forming the top of the valence band, namely the p-state of the chalcogen atom (S, Se, or Te) hybridized with the d-states of Cu atoms and Ag, at the level of the bottom of the conduction band. They in turn are formed hybridized s- and p-states of cation atoms Cu / Ag and Al / Ga / In. The lowest peak can also be associated with $d \rightarrow p$ transitions of electrons of Cu / Ag atoms from the highest level of t_2 states.
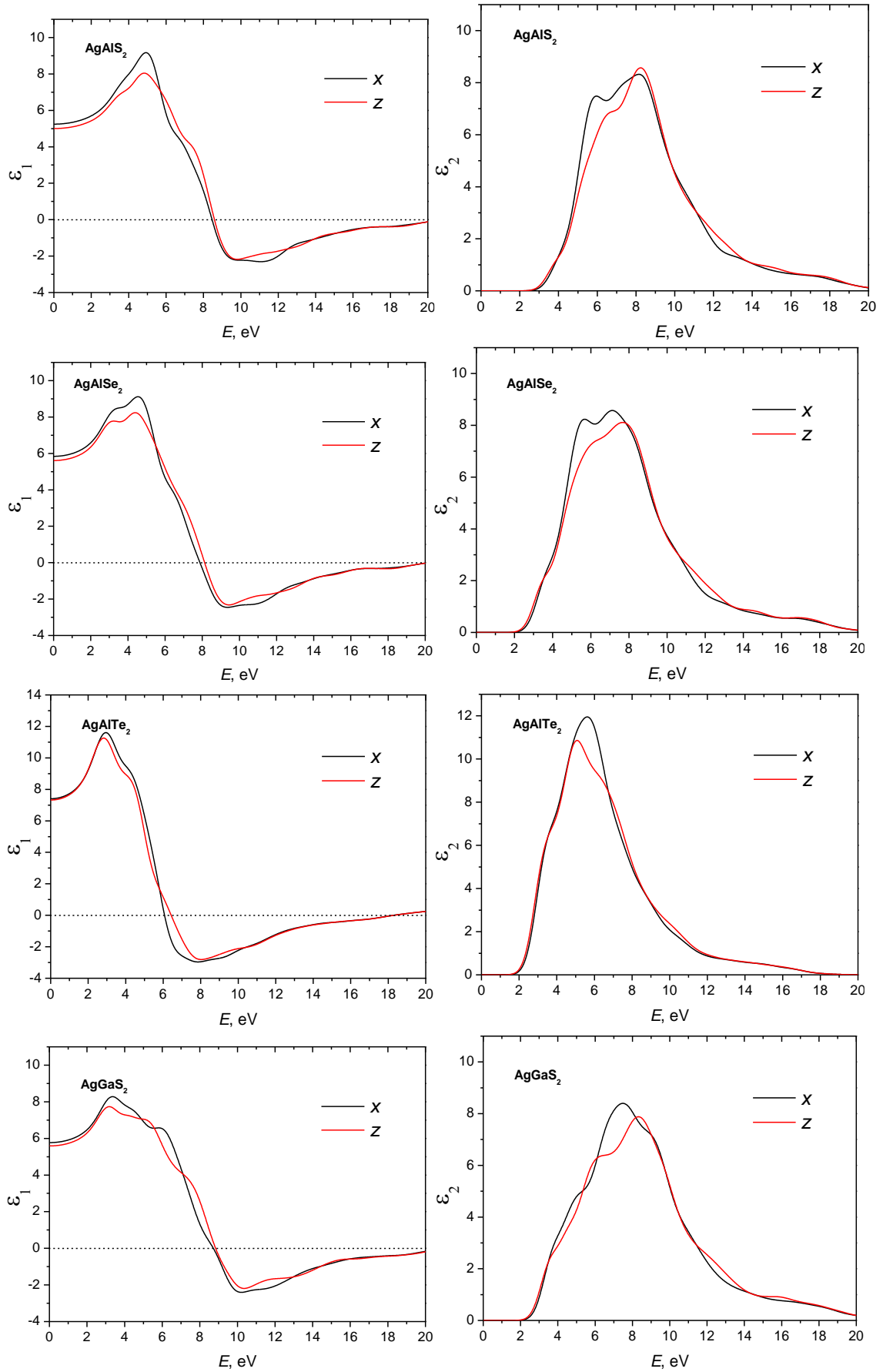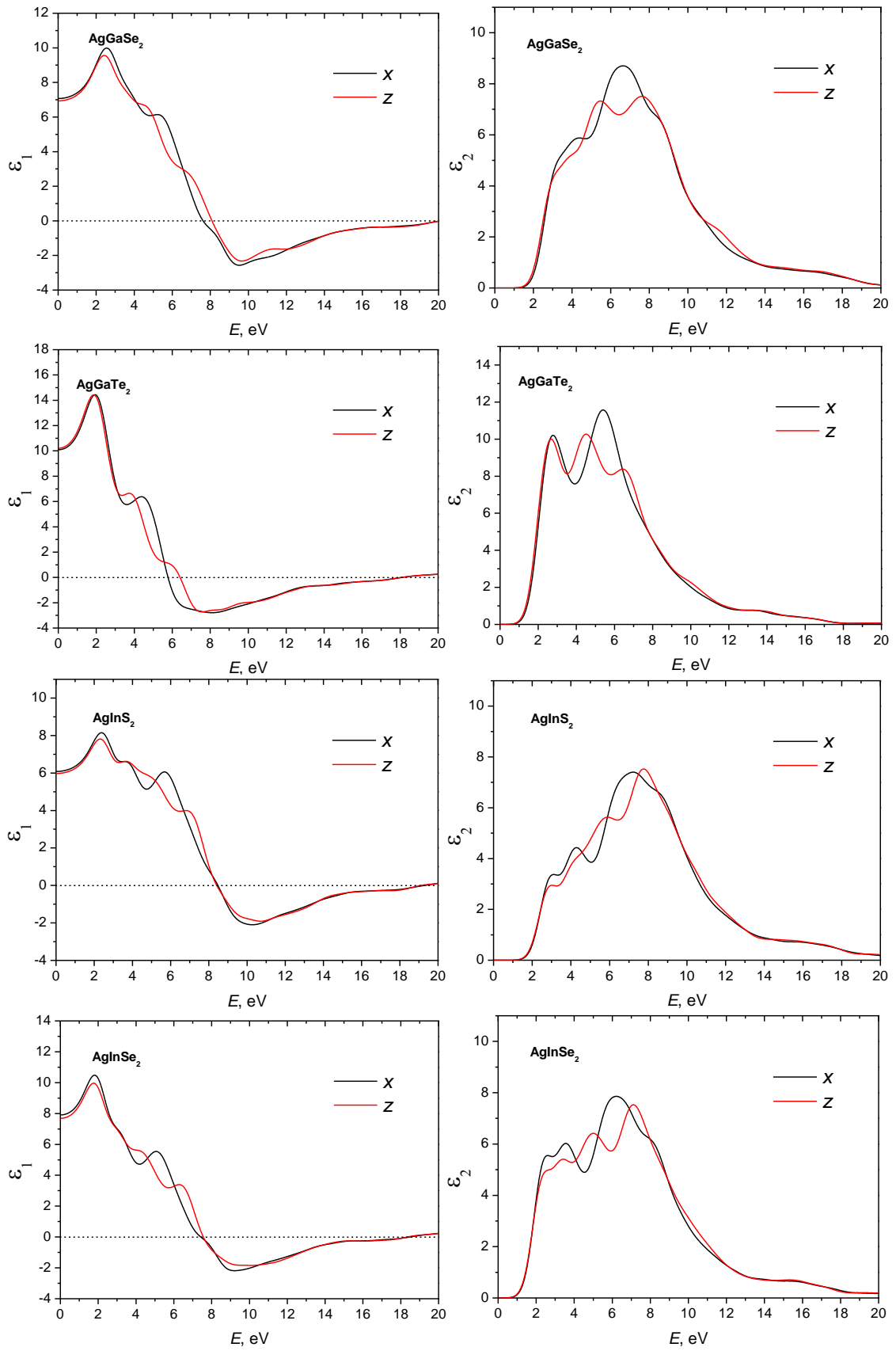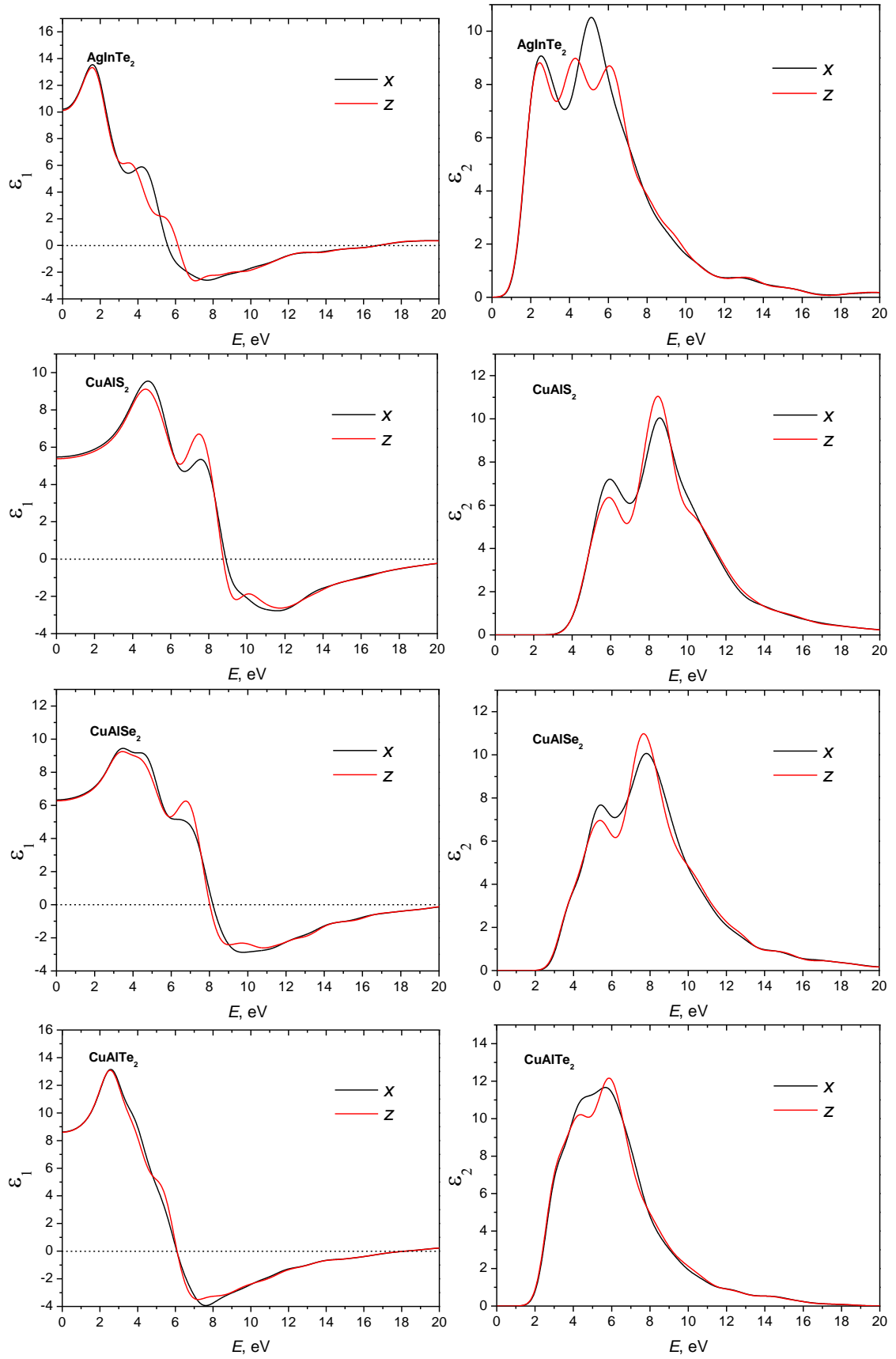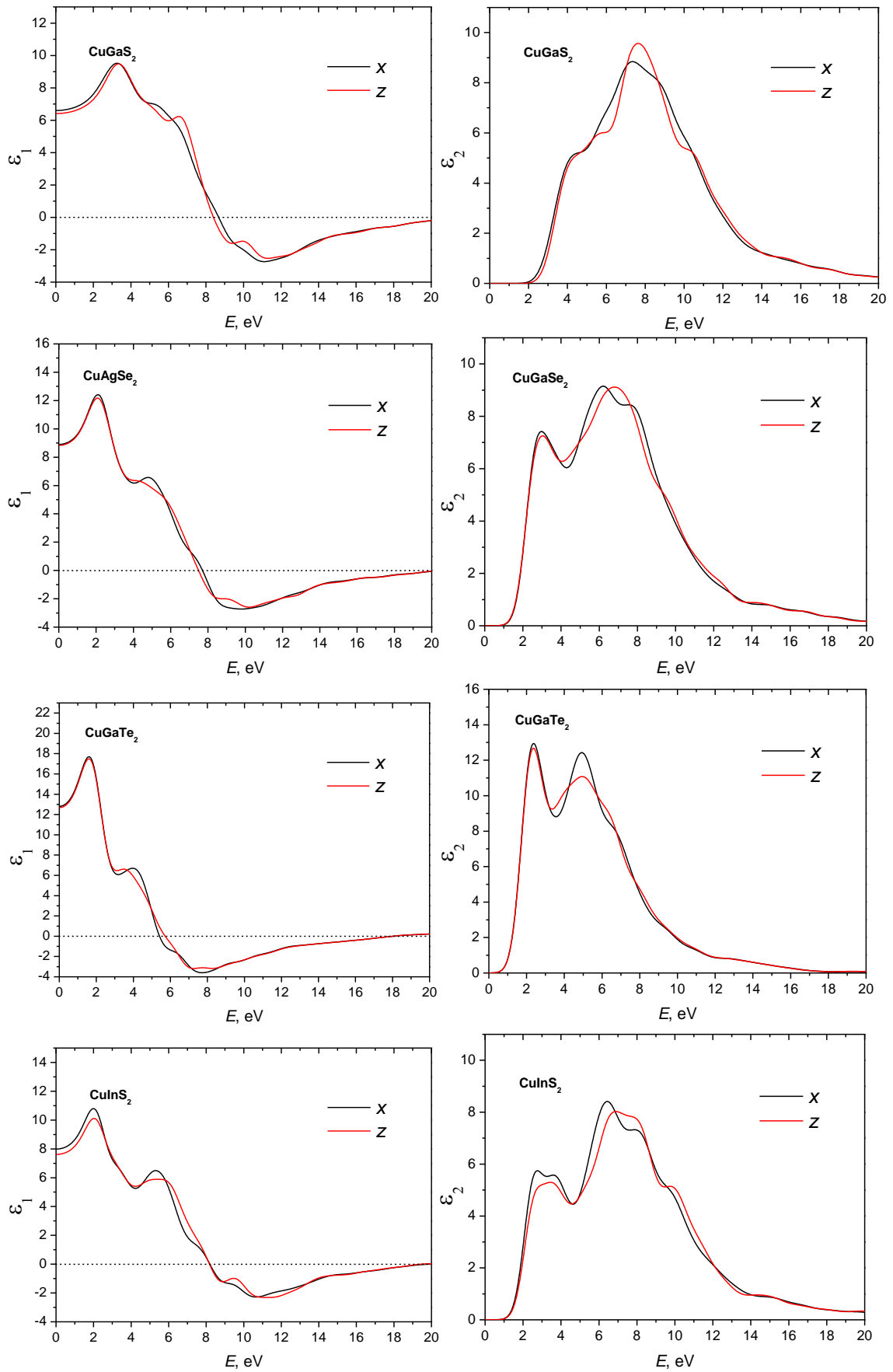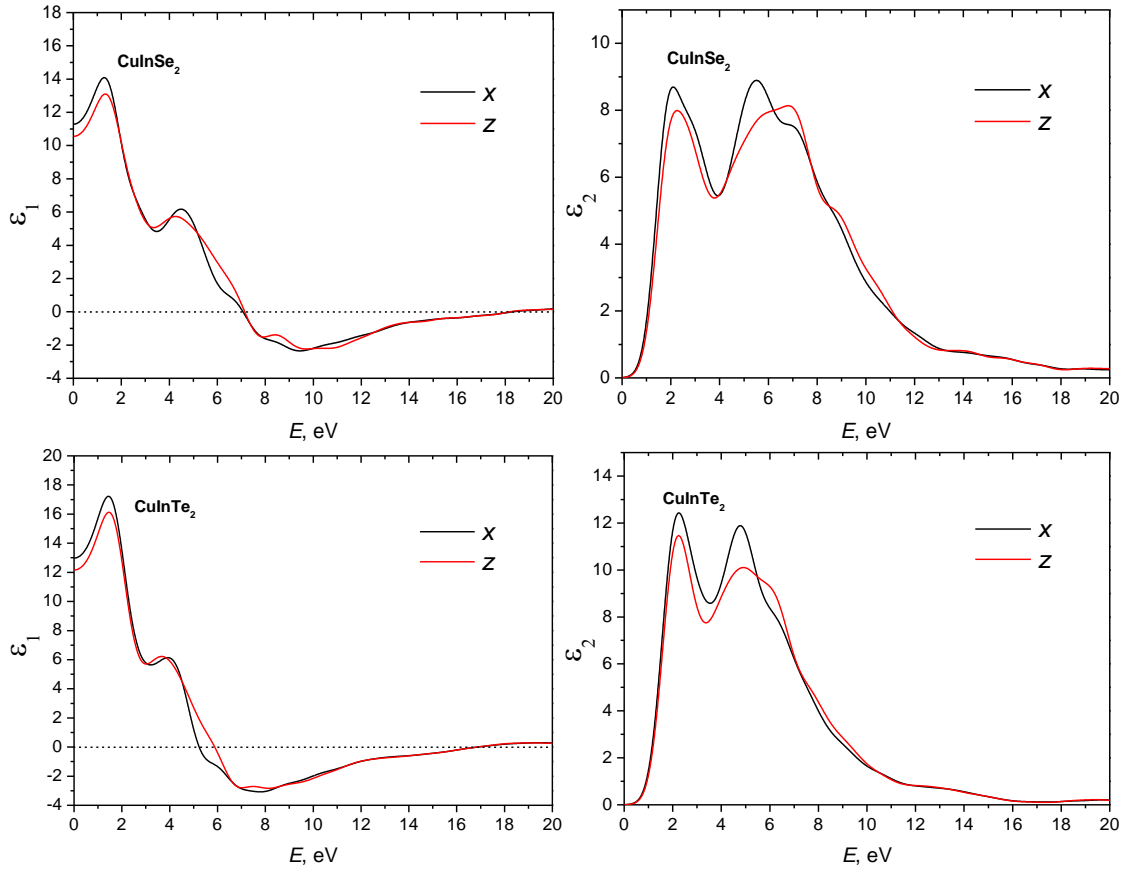
Figure 4.14. Dispersion of the real $\varepsilon_1(\omega)$ and imaginary $\varepsilon_2(\omega)$ part of dielectric function of I-III-VI$_2$ crystals calculated using GGA functionals.

Then the peak at ε_2 at higher energies corresponds to $d \rightarrow p$ transitions from Cu / Ag states with lower energy which corresponds to the symmetry *e*. At energies greater than 8-9 eV, the dielectric function begins to gradually decrease and at energies about 20 eV becomes close to zero, which corresponds to the absence of absorption.

The values of the static dielectric function for crystals of group I-III-VI$_2$ calculated using LDA and GGA methods are listed in Table 4.10. In this table some optical characteristics of the studied group of crystals are collected, namely the static value of the dielectric function $\varepsilon_1(0)$, the refractive index $n(0)$ and the birefringence $\Delta n(0)$. From the calculated table it is seen that for static values of the real part of the dielectric function ε_1 it is observed that for calculation with LDA functional it is greater than those obtained with GGA functional, except for CuGaSe$_2$ crystal for *x* and *z* directions and for CuInS$_2$ for *z*-direction. There is a tendency to increase the value of the static dielectric function for crystals I-III-VI$_2$ when replacing the anion S $\rightarrow$ Se $\rightarrow$ Te and Al $\rightarrow$ Ga $\rightarrow$ In. Moreover, anionic substitution leads to a faster change of $\varepsilon_1(0)$ than the replacement of cation III. The highest values of the static dielectric function were obtained for CuGaTe$_2$ and CuInTe$_2$ crystals.

The degree of anisotropy of optical functions was also calculated for the crystals of the studied group. Uniaxial anisotropy of the dielectric function of crystals I-III-VI$_2$ can be calculated using the following expression

$$\delta\varepsilon = \frac{\varepsilon_0^z - \varepsilon_0^x}{\varepsilon_0^{tot}}, \qquad (4.23)$$

where ε_0^z and ε_0^x are the static dielectric constants, and ε_0^{tot} is the total dielectric constant. Uniaxial anisotropy of dielectric function for crystals of the study group are collected in Table 4.9.

Table 4.9. Uniaxial anisotropy of the dielectric function of I-III-VI$_2$ group crystals calculated for LDA/GGA functional.

Crystal	$\delta\varepsilon$	Crystal	$\delta\varepsilon$
AgAlS$_2$	–0.01454/–0.01557	CuAlS$_2$	–0.00438/–0.00567
AgAlSe$_2$	–0.01044/–0.01332	CuAlSe$_2$	–0.00621/–0.00314
AgAlTe$_2$	–0.00258/–0.00361	CuAlTe$_2$	–0.00165/–0.00082
AgGaS$_2$	–0.00847/–0.01053	CuGaS$_2$	–0.0079/–0.0096
AgGaSe$_2$	–0.0359/–0.00688	CuGaSe$_2$	–0.0143/–0.00247
AgGaTe$_2$	0.0556/0.003885	CuGaTe$_2$	–0.00346/–0.00336
AgInS$_2$	0.00027/–0.00594	CuInS$_2$	–0.03099/–0.01585
AgInSe$_2$	–0.00663/–0.00938	CuInSe$_2$	–0.02411/–0.02208
AgInTe$_2$	–0.00399/–0.00309	CuInTe$_2$	–0.02309/–0.02147

Previously, the results of study of the dielectric functions for AgGaTe$_2$, CuAlSe$_2$, CuGaSe$_2$, etc., crystals were reported in Refs. [34,199,200]. For the comparison of the obtained in this work theoretical dielectric functions with the experimental, we shown on Fig. 4.15 a) and b) the both set of data for AgGaTe$_2$ crystal (experimental and calculated). As one can see, the obtained peack position is in good agreement with the experimental data taken from [199]. The obtained results show the ability of the theoretical simulations give the significant and credibile results that are in consistency with the experiment.
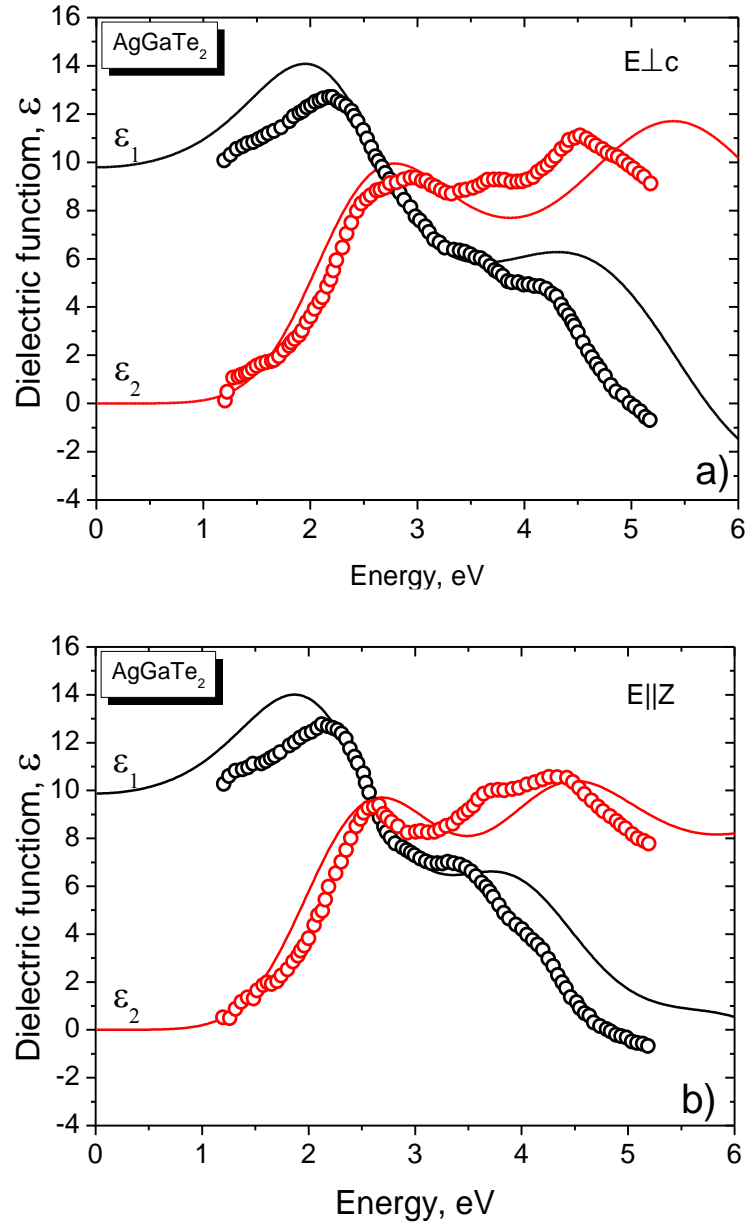
Figure 4.15. The real (a) and imaginary (b) parts of the dielectric functions of the AgGaTe₂ semiconductor obtained using GGA (PBE) calculations (narrow line). The bold line present results of ellipsometry measurements [199].
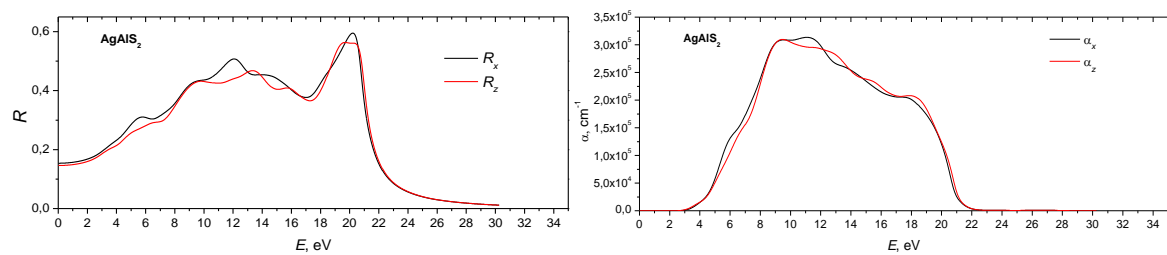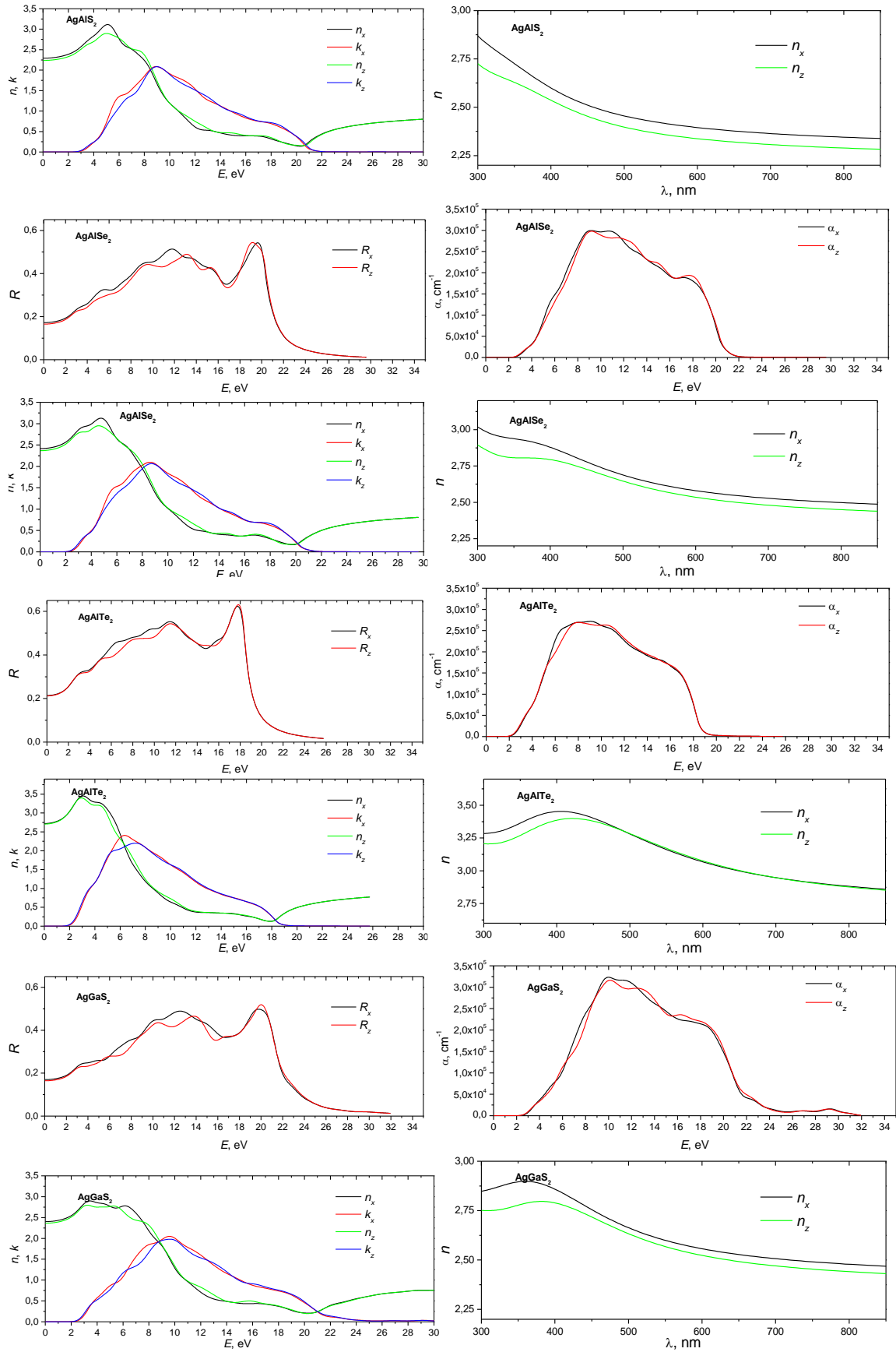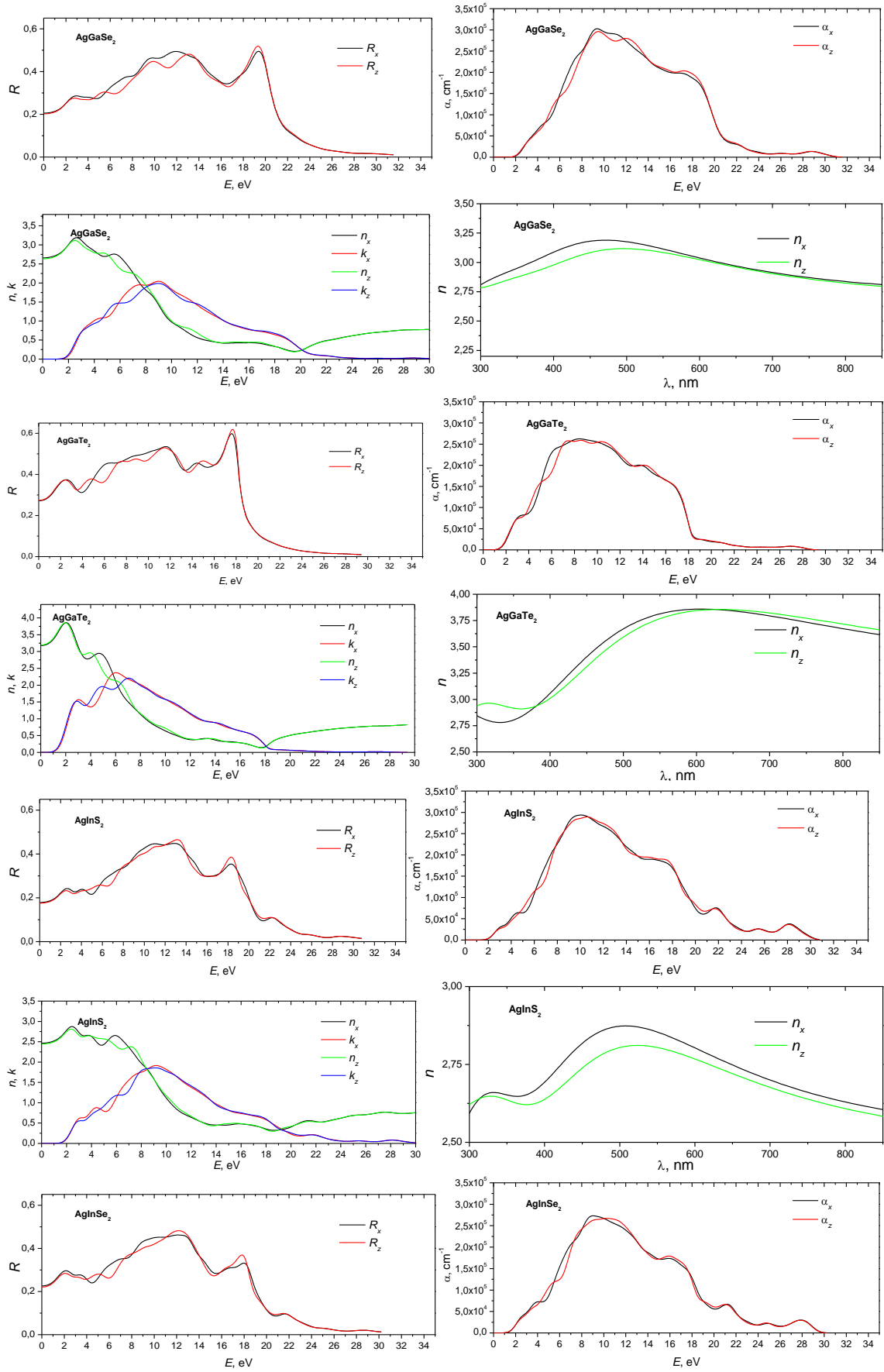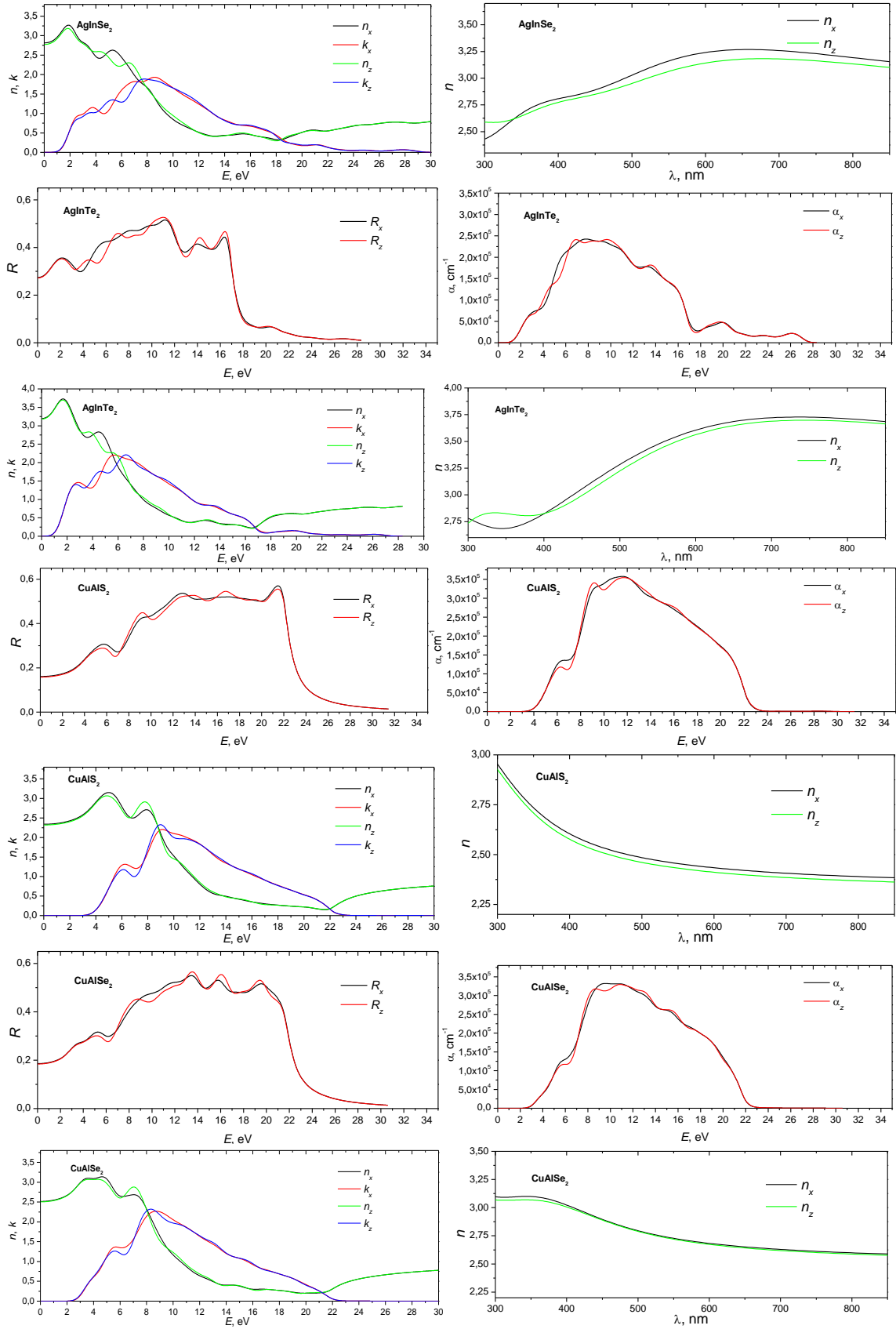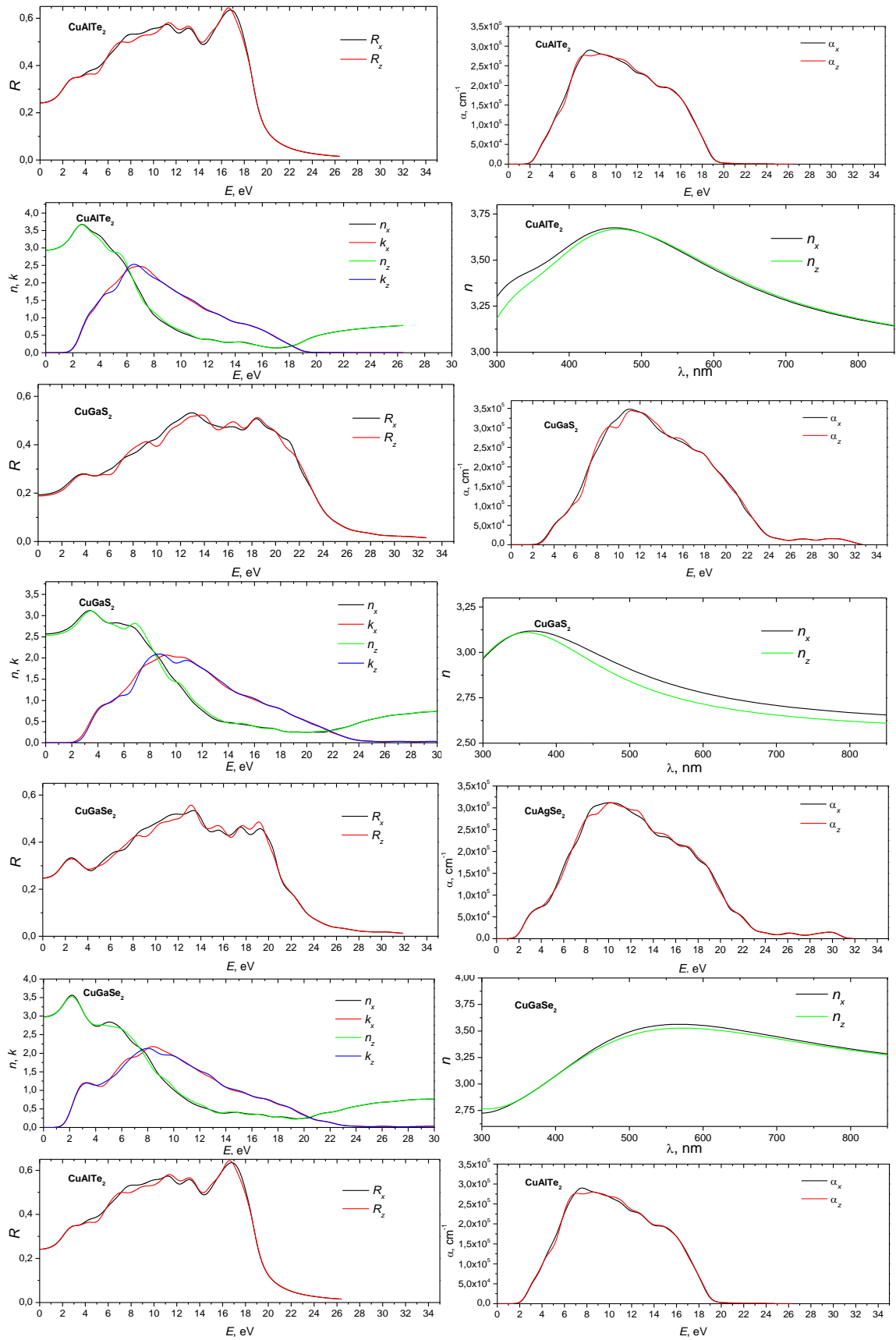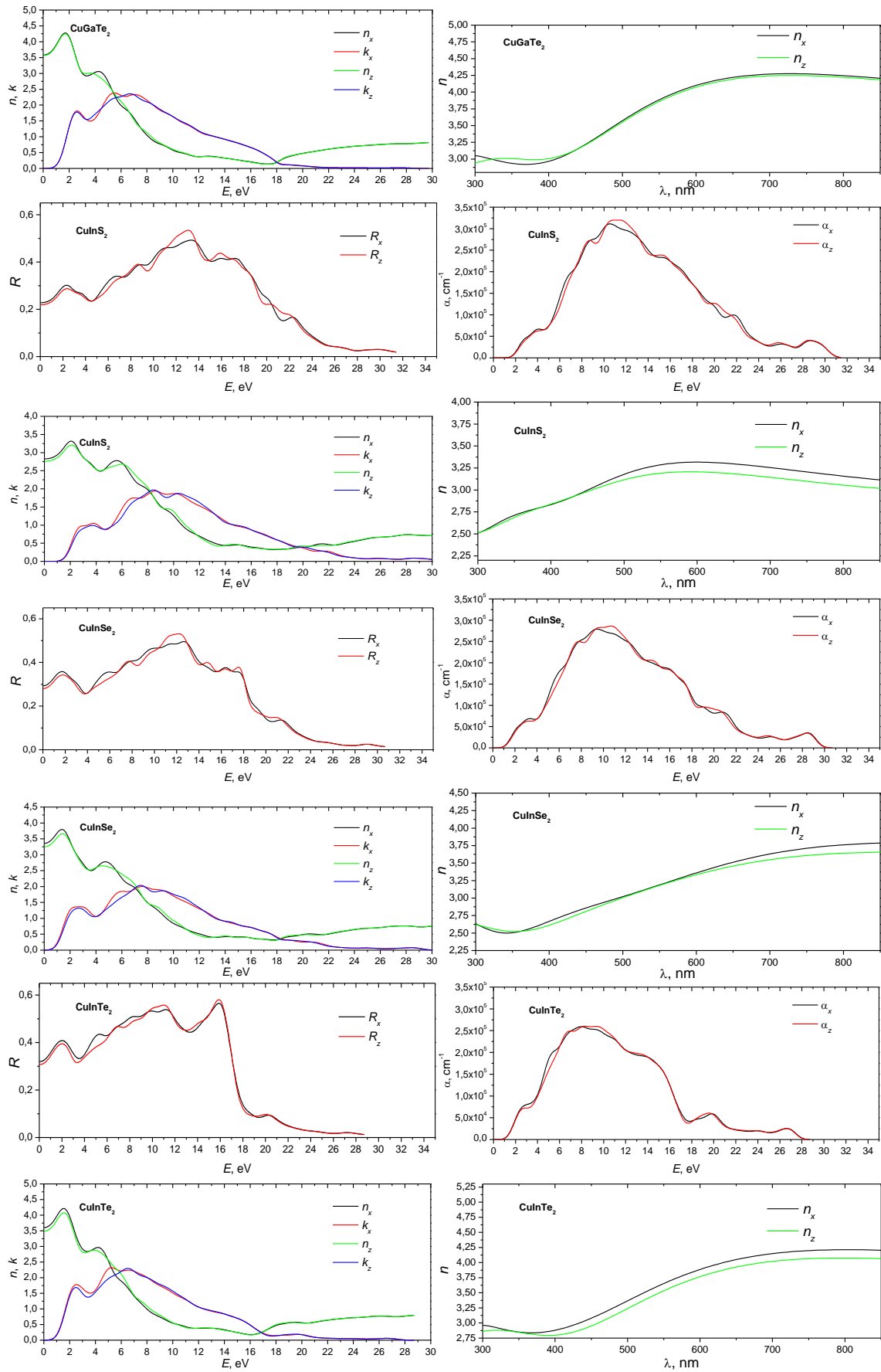
Figure 4.16. The reflectance *R*, absorption coefficient α, refractive index *n* and extinction coefficient *k* of I-III-VI₂ crystals calculated using the GGA functional.

Table 4.10. Optical parameters of I-III-VI$_2$ crystals calculated with LDA/GGA functionals.

Crystal	$\varepsilon_{1,x}(0)$	$\varepsilon_{1,z}(0)$	$n_x(0)$	$n_z(0)$	$\Delta n(0)$
AgAlS$_2$	5.6998/5.2447	5.4548/5.0034	2.3875/2.2901	2.3356/2.2368	0.0519/0.0533
AgAlSe$_2$	6.4192/5.8414	6.2202/5.6110	2.5337/2.4169	2.4941/2.3687	0.0396/0.0482
AgAlTe$_2$	8.0123/7.4052	7.9504/7.3252	2.8306/2.7213	2.8197/2.7065	0.0109/0.0148
AgGaS$_2$	6.2852/5.7704	6.1268/5.5900	2.5071/2.4021	2.4752/2.3644	0.0319/0.0377
AgGaSe$_2$	7.9011/7.0796	7.8233/6.9345	2.8109/2.6588	2.7970/2.6333	0.0139/0.0255
AgGaTe$_2$	10.8715/10.0928	11.0539/10.2109	3.2971/3.1769	3.3249/3.1954	-0.0278/-0.0185
AgInS$_2$	6.6473/6.0809	6.6527/5.9731	2.5783/2.4660	2.5548/2.4440	0.0235/0.0220
AgInSe$_2$	9.1784/7.9076	8.9970/7.6871	3.0297/2.8121	2.9995/2.7727	0.0302/0.0394
AgInTe$_2$	11.0544/10.2169	10.9455/10.1224	3.3250/3.1964	3.3088/3.1819	0.0162/0.0145
CuAlS$_2$	5.8915/5.4740	5.8144/5.3814	2.4273/2.3396	2.4113/2.3198	0.0160/0.0198
CuAlSe$_2$	6.7894/6.3297	6.6636/6.2703	2.6057/2.5159	2.5815/2.5041	0.0242/0.0118
CuAlTe$_2$	9.3894/8.6261	9.3430/8.6048	3.0642/2.9371	3.0565/2.9334	0.0077/0.0037
CuGaS$_2$	7.07925/6.5998	6.9127/6.4116	2.6607/2.5690	2.6292/2.5322	0.0315/0.0368
CuGaSe$_2$	8.6376/8.8990	8.2722/8.3333	2.9392/2.9833	2.8761/2.9722	0.0631/0.0111
CuGaTe$_2$	13.5406/12.8142	13.4007/12.6856	3.6799/3.5799	3.6609/3.5617	0.0190/0.0182
CuInS$_2$	8.0094/7.9876	7.2872/7.6138	2.8299/2.8262	2.6995/2.7594	0.1304/0.0668
CuInSe$_2$	12.1127/11.2907	11.2573/10.5589	3.4803/3.3605	3.3553/3.2495	0.1250/0.1110
CuInTe$_2$	13.2500/12.9859	12.3528/12.1671	3.6404/3.6039	3.5148/3.4885	0.1256/0.1154

As mentioned earlier, the dielectric function is related to other optical parameters of the crystals that can be derived from it. Thus, using Eqs. 4.24 and 4.25, we can obtain from the spectra of the dielectric function the values of the refractive indices $n(\omega)$ and the extinction coefficient $k(\omega)$ [152,172].

$$n(\omega) = \sqrt{\frac{\left(\varepsilon(\omega)_1^2 + \varepsilon(\omega)_2^2\right)^{1/2} + \varepsilon(\omega)_1}{2}} \quad , \tag{4.24}$$

$$k(\omega) = \sqrt{\frac{\left(\varepsilon(\omega)_1^2 + \varepsilon(\omega)_2^2\right)^{1/2} - \varepsilon(\omega)_1}{2}} \quad . \tag{4.25}$$

Another parameter of the material that characterizes its optical properties is its reflection spectrum. The reflection coefficient R can be obtained for the normal incidence onto plate surface by the following equation:

$$R(\omega) = \frac{\left(n(\omega) - 1\right)^2 + k(\omega)}{\left(n(\omega) + 1\right)^2 + k(\omega)} . \tag{4.26}$$

It is known, that the absorption coefficient can be evaluated by the following relation:

$$\alpha(\omega) = \frac{2k(\omega)\omega}{c}. \tag{4.27}$$

Also other spectral quantities, such as the loss function $L(\omega)$, descries the energy lost by an electron passing through a homogeneous dielectric material, and optical conductivity $\sigma(\omega)$, not discussed in this study, can be calculated.

In Fig. 4.16 shows the spectral dependence of the reflection spectrum $R(\omega)$ and the absorption coefficient $\alpha(\omega)$ of the refractive indices $n(\omega)$ and the extinction coefficient $k(\omega)$ as a function of the photon energy in the spectral range from 0 to 30 eV. As can be seen from Fig. 4.16. the reflection spectra for crystals of the chalcopyrite group with the chemical formula I-III-VI$_2$ can be described as follows. For all crystals with the cation I = Ag, the reflection coefficient at the energy of the incident photon 0 eV is in the range of approximately 0.18 – 0.23, and for crystals with I = Cu, the reflection coefficient is in the range from 0.19 to 0.26. Anion replacement has been found to have the greatest effect on the static reflection coefficient, which is accompanied by its increase when sulfur atoms are replaced by heavier chalcogen ions.

The increase in photon energy is accompanied by an increase in the reflection coefficient R. This gradual increase for crystals with silver atoms continues the value of $R = 0.5$, followed by a slight decrease in the reflection coefficient to 0.45. With a slight increase in energy, there is a clearly defined peak at 18 – 20 eV, which reaches a value of the reflection coefficient of about $R = 0.6$. This is followed by a sharp decrease in the reflection coefficient, which leads to zero. The situation is similar for crystals with copper atoms. However, for the compounds CuInS$_2$ and CuInSe$_2$ after reaching the peak value of the reflection coefficient $R = 0.5$ at an energy of 12 eV, a gradual decrease in the reflection is observed without the presence of a well-isolated peak at energies of 18 – 20 eV. Also, it should be noted that for all crystals there is a clear shift towards lower energies of the threshold value R with the replacement of S → Se → Te. It is also found that the reflectivity of I-III-VI$_2$ crystals is high in visible and ultraviolet region up to 20 eV.

The absorption spectra $\alpha(\omega)$ are obtained from the dielectric function using Eq. 4.27. shown in Fig. 4.16. The spectral dependence $\alpha(\omega)$ shows a weak anisotropy for the x and z directions, at low energies ($E < 5$eV) and at high energies ($E > 18$ eV). At an intermediate value of energy, the anisotropy of the absorption index is somewhat more significant. In general, all crystals of group I-III-VI$_2$ showed significant absorption. The maximum absorption for such materials is in the range of 2.6×10^5 to 3.5×10^5 cm^{-1}. Analysis of the

calculated spectral dependences of the absorption index showed that the crystals of the study group with copper atoms have stronger absorption than compounds with silver atoms. For AgBC₂ crystals, where B = Al, Ga, In, the absorption index is in the range of $2.6 - 3 \times 10^5$. Cu-containing materials have a higher value of α than Ag-bearing ($2.6 - 3.5 \times 10^5$). Also, it should be noted that the isomorphic replacement of the cation Al → Ga → In and the anion S → Se → Te reduces the absorption of chalcopyrite materials. From the above it follows that Cu-containing crystals as their strong absorption can be effective materials for use as an absorbing layer in thin-film end cells. Also, because Cu-containing materials have a higher absorption coefficient than Ag-containing materials, they may be better absorbent materials for PV. Also, in Fig. 4.16 shows the spectral dependence of the refractive indices of $n(\lambda)$ crystals of group I-III-VI₂ in the range of 300-800 nm.

4.3.2. Calculation of LNO properties of AgGaS₂ crystal

DES -calculation

DES model of calculations based on classical polarizability theory of optical activity [201] can be successfully applied to determine the parameters of electrogyration, electro-optic and second-harmonic generation effects [202]. There are many results of validation of the DES approach (see e.g., [202–205]).

According to DES [202] the virtual shift x_i of electron cloud is calculated using its electronic polarizability α ($x_i = \left(4\pi\varepsilon_0/e\right)\sum_j \alpha'_{ij} E_j^{Loc}$, $\mathbf{E}^{Loc} = \left(\dfrac{2+\varepsilon'}{3}\right)\mathbf{E}^{Ext}$ where e is the electron charge, ε_0 the permittivity of free space, $\alpha' = \alpha/4\pi\varepsilon_0$ the electronic polarizability volume, ε' the effective relative dielectric constant, $\mathbf{E}^{Ext}$ the external electric field). As a result, the main equations of DES approach are [202]:

$$\varepsilon_{ij}\left(E_k^{Ext}\right) - \varepsilon_{ij}\left(0\right) = 2\sum_k d_{ijk} E_k^{Ext} \; ;$$

$$a_{ij}\left(E_k^{Ext}\right) - a_{ij}\left(0\right) = \sum_k r_{ijk} E_k^{Ext} \; ; \qquad (4.28)$$

$$\rho_{ij}\left(E_k^{Ext}\right) - \rho_{ij}\left(0\right) = \frac{180}{n\lambda}\sum_k g_{ijk} E_k^{Ext} \; .$$

Here, ε_{ij} denotes relative dielectric constants, n the refractive index, λ the wavelength of light, a_{ij} the polarization tensor, r_{ijk} the linear electro-optic tensor of the third rank, g_{ijk} the electrogyration tensor, d_{ijk} the second-order nonlinear susceptibility tensor.

The electronic polarizability volumes refinement silver thiogallate of crystals

Let us consider the results of calculations performed for AgGaS$_2$ crystals at $\lambda = 632.8$ nm (the information about the absolute structural data of crystals are expressed in [206]). The values of the polarizability volumes are varied within a large limited range and chosen when best agreement between calculated and experimental mean refractive index is observed. It is necessary to note that silver thiogallate crystals are optically negative ($\Delta n < 0$) and this peculiarity is, in addition, taken in to account in our calculations (see Fig. 4.17). In contrast, the experimental measured optical parameters for these materials (in direction [010]) are [207]: $\rho = 94$ deg/mm (the optical rotation was measured using the high-accuracy universal polarimeter), $n_o = 2.5532$, $n_e = 2.5066$, respectively.

The following refinement values of electronic polarizability volumes are obtained: $\alpha'_{Ag} = 0,313$ Å^3, $\alpha'_{Ga} = 0.010$ Å^3, $\alpha'_{S} = 6.333$ Å^3 (Fig. 4.17). The calculated values of refractive indices and optical rotations are: $\rho_{11} = -131$ deg/mm, $\rho_{22} = 131$ deg/mm, $\rho_{33} = 0$ deg/mm and $n_o = 2,5346$, $n_e = 2,5246$.
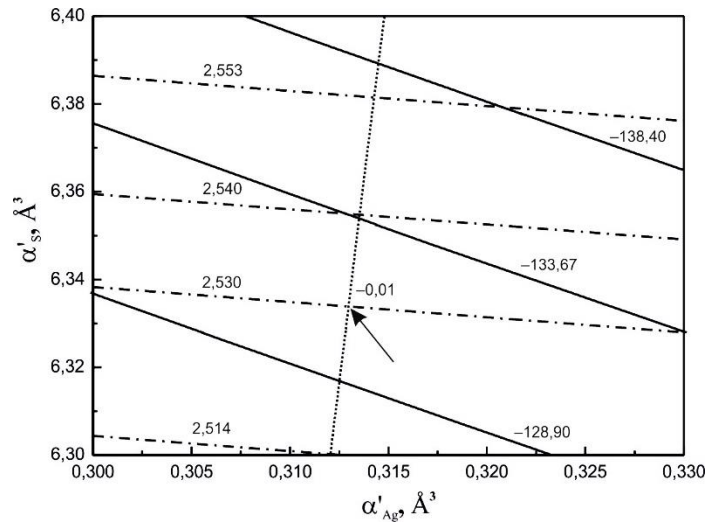
Figure 4.17. Contour plot of the calculated optical rotation (solid lines), mean refractive index (dashdotted lines) and linear birefringence (dotted lines) for AgGaS$_2$ crystals ($\alpha'_{Ga} = 0.010$ Å^3).

It is known, that information about effective relative dielectric constant (low frequency dielectric constant [202,203]) is still needed for DES calculations. In our case there is $\varepsilon' = 6$ (see, e.g., [208]), respectively. Using this parameter, as well as calculated

polarizabilities (at $\lambda = 632.8$ nm) we obtained the next values of linear electro-optic coefficients (at constant strain): $r_{41} = 2.5$ pm/V, $r_{52} = 2.5$ pm/V and $r_{63} = 3.2$ pm/V (the contracted indices are used: $1 = 11$, $2 = 22$, $3 = 3$, $4 = 23$, etc). In contrast, components of the r_{ij} tensor known from the literature are $r_{41} = 4.0$ pm/V, $r_{63} = 3.0$ pm/V [209]. Good agreement of theoretically calculated and experimentally obtained r components is clearly seen. On the other hand, the calculated value of the electrogyration tensor component (at $\lambda = 632.8$ nm) is $g_{41} = -0.043$ pm/V (experimental value obtained at $\lambda = 498$ nm is 2.03 pm/V [210]).

Using the Clausius–Mossotti equation, one can estimate the wavelength dependence of the α' to calculate the electronic polarizability volumes for 1064 nm (as has earlier been done, e.g., for the SiO$_2$ crystals in [201]). As a result, the calculated nonlinear susceptibility are: $d_{36} = -38.6$ pm/V (literature data 28.9 pm/V [209]).

It is necessary to note that the calculation method based on polarizability theory of optical activity [201] have been applied for these materials in [207]. In contrast, the optical rotation and refractive indices were calculated more precisely for AgGaS$_2$ using only the electronic polarizability volumes for S ions (the values of α'_{Ga} and α'_{Ag} were neglected) [207]. Nevertheless, the α'_{Ga} and α'_{Ag} should necessary be taken into account (see e.g., the list of polarizabilities in [211]) in DES model because of values of the non-linear optical parameters strongly depend not only from α'_S but from the all α'_{Ag}, α'_{Ga} and α'_S polarizabilities, respectively.

4.4. Application of DFT + U approach for correction of d-levels position for Ga and In atoms

In Fig. 4.18. the total density of electronic states for AgGaS$_2$, AgInSe$_2$, CuGaS$_2$, and CuInSe$_2$ crystals calculated using the GGA functional together with the superimposed curves of XPS spectra obtained experimentally by J. C. Rife et. al. and J.E. Jaffe et. al. [29,60] in the energy range from 0 to -20 eV is shown. This spectral region is of considerable interest because it plays a key role in the formation of chemical bonds and is responsible for most of the physicochemical properties of the material. The DOS curve shown in Fig. 4.18 corresponds to the results shown in Fig. 4.13 derived from GGA functional. The figure shows a good coordination of the location of the electronic bands of the valence band top for

the four investigated crystals. The intensity distribution of the peaks of the VB region for all bands in the DOS spectrum is well reproduced by experimental XPS spectra obtained by other authors (elsewere) [29,60]. The location of the electronic levels of the experimentally and theoretically calculated results in the range from 0 to –14 eV shows good agreement. However, the bands with the lowest energy corresponding to the Ga-3d and In-4d states show a significant difference in location compared to the band positions obtained on the experiment. The position of the experimental band of d-states is at lower energies than obtained from theoretical calculations. Thus, the experimental band for the CuGaS$_2$ crystal is at energy $E = -18.54$ eV, while the calculated suga has a maximum at $E = -15.27$ eV.
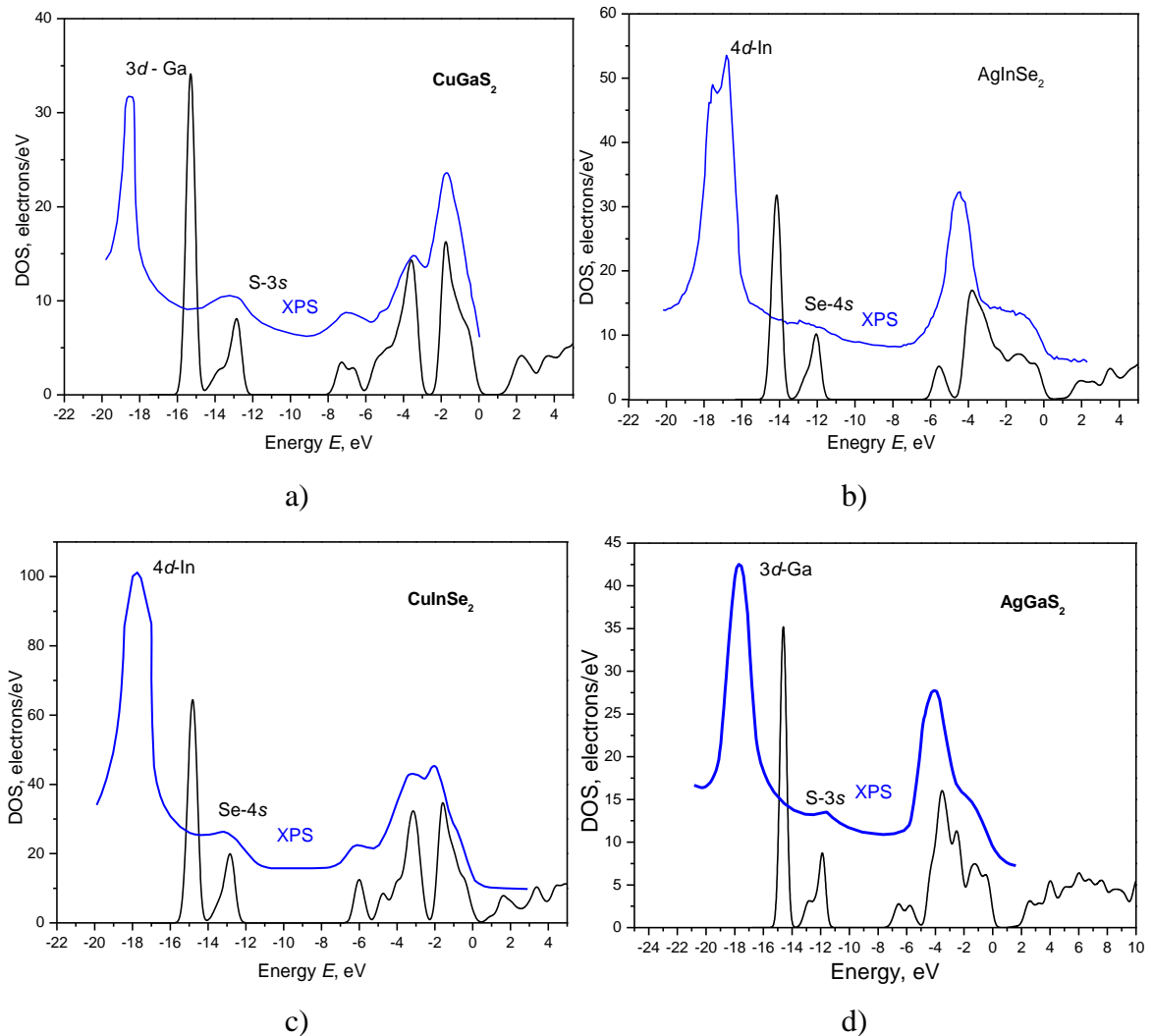
a)

b)

c)

d)

Figure 4.18. Calculated densities of state for AgGaS$_2$, AgInSe$_2$, CuGaS$_2$, та CuInSe$_2$ crystals together with the experimental XPS spectra taken from literature [29,60].

For the AgInSe$_2$ crystal, the peak of the 4d-states of indium in the experimental XPS spectra is located at the energy $E = -17.26$ eV and the calculated energy value for this peak is $E = -$

14.54 eV [60]. For the CuInSe$_2$ crystal, the theoretical position 4d-states of In is located at $E = -14.8$ eV while the experimental spectra showed the -17.76 eV. Similarely, for AgGaS$_2$ crystal a theoretically obtained band for Ga-3d states at $E = -14.62$ eV is also shifted toward the higher energy compared with XPS spectra ($E = -17.71$ eV).

Table 4.11 summarizes the values of the position shift of the d-levels of Ga atoms, and In in the AgGaS$_2$, AgInSe$_2$, CuGaS$_2$, and CuInSe$_2$ crystals. From the table it can be seen that for crystals with the gallium cation the level shift is greater than for crystals with indium. The corresponding level shift for the studied materials is in the range from 2.72 eV to 3.27 eV. Also, for the crystals considered in this section, there is a tendency, that for crystals that contain copper atoms in their structure have a greater shift of these levels compared to Ag-containing crystals by $\sim 0.18 - 0.24$ eV.

Considering this shift in levels positions, we can say that DFT does not describe well the d-levels for Ga and In atoms in the CP-type materials. Therefore, it is necessary to use the corrections that will allow to obtain the proper results of calculations that will be in better consistent with the experiment.

Table 4.11. The energy shifting of the d-levels position for AgGaS$_2$, AgInSe$_2$, CuGaS$_2$, and CuInSe$_2$ crystals relative to the energy of experimental position of d-level obtained from XPS spectra.

Crystal	ΔE, eV
AgGaS$_2$	3.09
AgInSe$_2$	2.72
CuGaS$_2$	3.27
CuInSe$_2$	2.96

It is a well-known fact that the use of DFT leads to errors that occur when using LDA and GGA functionals. Such methods include the use of scissor operator Δ_g which is used to increase the band gap material [150], self-interaction correction (SIC) [212,213], and Hubbard-U correction [214]. In particular, one of the methods that is a popular extension of DFT, namely DFT $+ U$ and can be used for this kind of problems related to the shift of electronic levels is the use of the Hubbard correction method. Hubbard's correction is a well-

known tool used in calculations. Its advantage is that the calculated results are reliable, as its calculation procedure is simple, and it is less expencive. Typically, this method is used to study strongly correlated systems and systems with localized d- and f-electrons. Strongly correlated materials include, in particular, oxides of transition metals, materials in which d- or f-electron shells with narrow energy ranges are not completely filled.

Anisimov et al. [215–217] introduced an orbital-dependent term known as on-site Coulomb repulsion energy, U into the XC term of LDA and GGA. They are now referred to as LDA + U or GGA + U. This approach is described by the expressed as follows

$$E_{\mathrm{LDA}+U}[n(\mathbf{r})] = E_{\mathrm{LDA}}[n(\mathbf{r})] + E_U[n(\mathbf{r})] - E_{dc}. \qquad (4.29)$$

Here, $n(\mathbf{r})$ is the electronic density, E_{LDA} is the energy obtained from conventional LDA (or GGA for $E_{\mathrm{GGA}+U}$) functional, E_U is the Hubbard type energy, and E_{dc} is the double-counting correction energy. In different programs, the Hubbard parameter can be described in different way. It can be consist of two parameters Coulomb energy U and the exchange energy J or they can be combined into a single parameter known as on-site Coulomb repulsion U. In this study the single on-site Coulomb repulsion U which been implemented in CASTEP computer code was used [150,218]. The on-site Coulomb interactions are very strong for localized d- and f-electrons but, in some cases, can also be important for localized orbitals of p-electrons [219,220]. Typically, the parameter U takes the values from 2 to 10 eV, depending on system.

The previously described approach was used in the study of compounds of different types [26,171,221]. Для кристалів ZnO incorporation of both $U_{d,\mathrm{Zn}}$ and $U_{p,\mathrm{O}}$ has successfully reproduced correct band gap [221]. The application of $U_d + U_p$ led to the downward shift of the hybridized Zn $3d$- and O $2p$-states, to the upward shift of Zn-$4s$ states, and then to the broadening of the band gap (in the range of 3.1 eV to 3.4 eV). Therefore, the less expansive of DFT + U ($U_d + U_p$) method is shown to produce high accuracy results of electronic properties of ZnO [221].

In order to test this approach on other semiconductor materials, we have previously studied MnV_2O_6 crystals. In this work in order to obtain the correct band gap value of MnV_2O_6, we take into account the GGA + U technique (Fig. 4.19). For Mn and V atoms, which has the unfilled d-shell electrons we set up the Habbard parameter equal to $U_{d,\mathrm{Mn}} = 4$ eV and $U_{d,\mathrm{V}} = 3.5$ eV. As result, we obtained the band gap value 1.46 eV calculated using the GGA + U approach, which is in well agreement with literature [222].
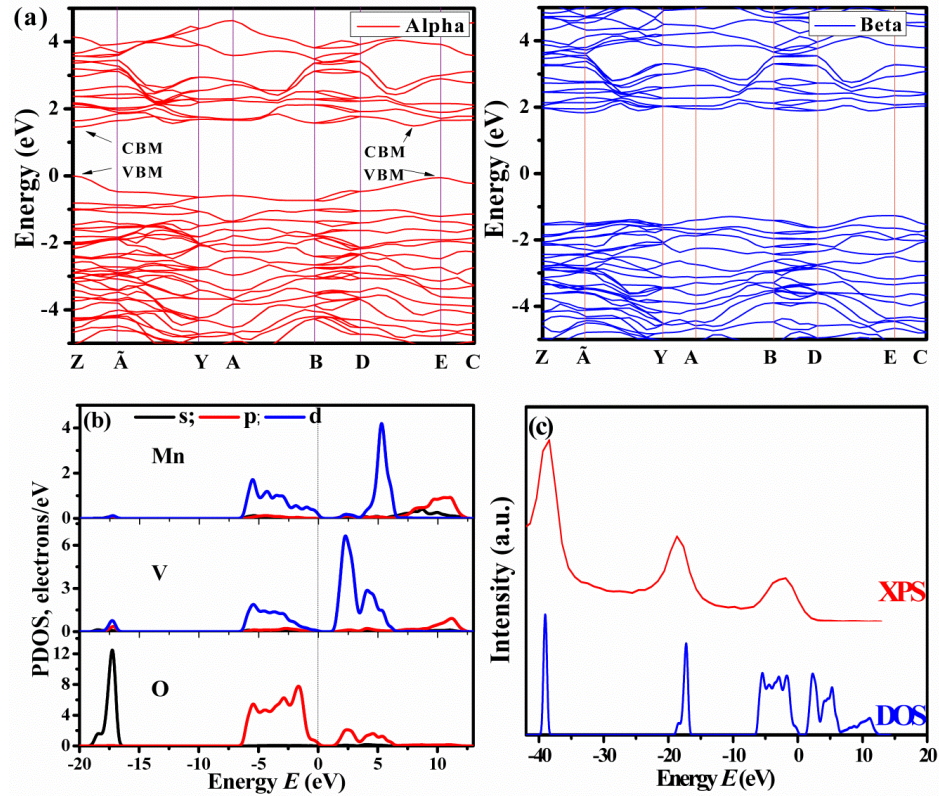
Figure 4.19. (a) Calculated electronic band structure using GGA+*U* method, (b) Partial density of states and (c) Total density of states (DOS) calculated using GGA+*U* approach and comparison of experimental XPS spectrum of MnV_2O_6 crystal.

The theoretical calculation of the band structure and density of states for MnV_2O_6 crystal and experimental results of XPS spectra are in excellent agreement. It confirms, that the performed calculations with GGA + *U* approach are described in correct direction of the system. Obtained in [171] results showed that the use of the above method is effective for adjusting the results of calculations to take into account the Coulomb interaction of strongly correlated materials and localized *d*-states. In view of this, we used the Hubbard correction to correct the alignment of the bands corresponding to the *d*-electrons for the crystals of the chalcopyrite group.

To determine the effect of the Hubbard parameter on the positions of the electronic *d*-levels, we performed a series of calculations with different values of the parameter *U*. In Fig. 4.20. (a) the results of calculations of the total density of electronic states for the $CuGaS_2$ crystal are given. This figure shows a set of DOS curves corresponding to different values of the parameter *U* from 0 to 8 eV. As the figure shows, the application of the Hubbard parameter to a $CuGaS_2$ crystal leads to a slight change in the density of states in the region of the valence band top. There is a slight effect of the parameter *U* on the intensity of the

band that forms the top of the valence band and its shift to the region of lower energies. This behavior is manifested when using the parameter $U = 2$ eV. Further increase of this parameter does not lead to changes in the density of electronic states up to $U = 8$ eV. The figure shows that with increasing value of the Hubbard parameter, the low-energy peak corresponding to the Ga $3d$-states of the CuGaS$_2$ crystal shifts monotonically toward lower energies. Such a shift leads to improved theoretical results. Figure 4.20 (b) shows the dependence of the position of the Ga $3d$-band depending on the value of the Hubbard parameter used for these calculations. As can be seen from Figures 4.20 (a) and (b), the position of the band shifts monotonically toward lower energies with increasing parameter U. Using $U_{d,\,Ga} = 8.10$ eV leads to the combination of the calculated peak with the experimental peak of the XPS spectra [60].

In Fig. 4.20 (c) shows calculated DOS for AgInSe$_2$ crystal. The black line corresponds to the calculation without the corrections ($U = 0$). The application of the correction to the $4d$-states of indium atoms leads to a slight shift of the most intense peak of the valence band peak. A further increase in the value of $U_{d,In}$ does not affect on any of the bands in the DOS spectrum except the $4d$-levels of indium atoms. There is also a tendency to shift the position of d-levels of indium with increasing value of the correction towards lower energies. This dependence also has a linear form, as for the CuGaS$_2$ crystal (see Fig. 4.4 (d). For the AgInSe$_2$ crystal, the application of the correction $U_{d,In} = 5.72$ eV leads to a shift of the level to the value of energy –17.26 eV, which corresponds to the experiment [29,60]. Figure 4.20 (e) and (f) illustrate the effect of the Hubbard parameter on the electronic structure of CuInSe$_2$ crystal. The nature of the change in the electronic structure for this crystal corresponds to the behavior of the AgInSe$_2$ crystal. From the figures it can be seen that for CuInSe$_2$ crystal $4d$ indium level is shifted to the value –17.76 eV (experimental position taken from [60]) at energies $U_{d,In} = 6.92$eV. Finally, on the Fig. 4.20 (g) and (h) are depicted the results of using the Hubbard parameter for AgGaS$_2$ crystal. For this crystal, as it was mentioned before, the experimental levels of Ga $3d$-electrons are located at –17.71 eV. This position is reached using the correction parameter $U_{d,Ga} = 7.12$ eV. For AgGaS$_2$, similarely to other crystals, the structure of higher energy levels remains almst unchanged. The small redestrbution of the peak intensity is found for the valence band maximum.
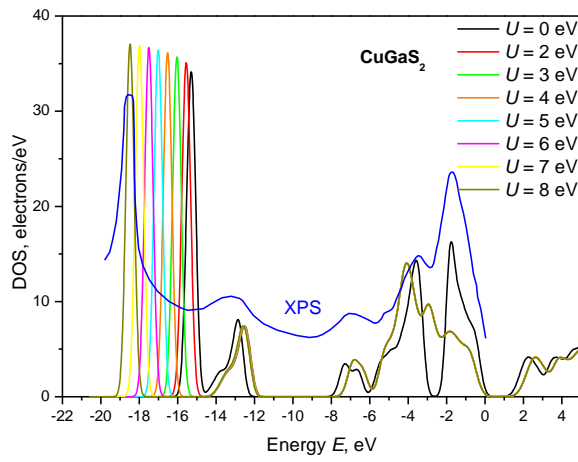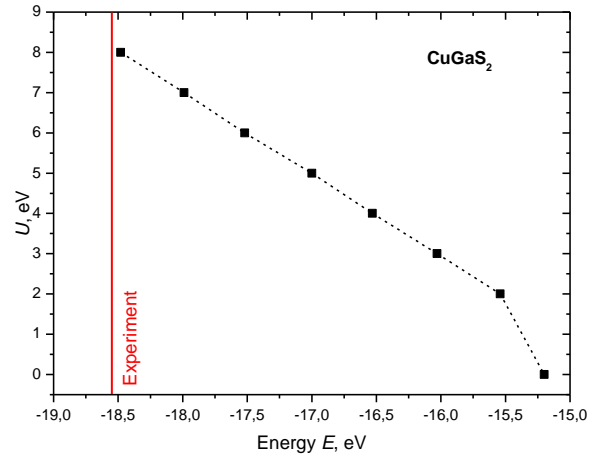
a)

b)
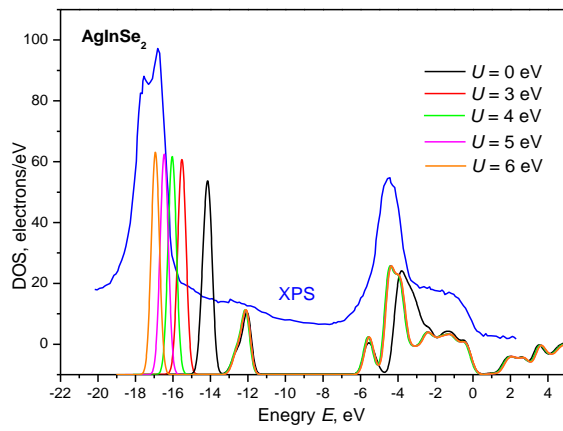
c)
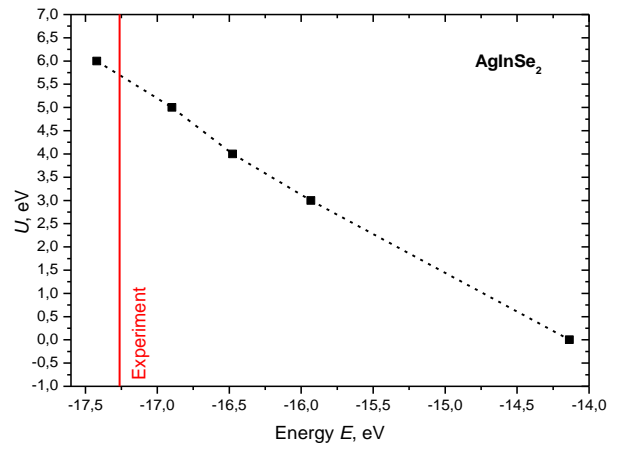
d)
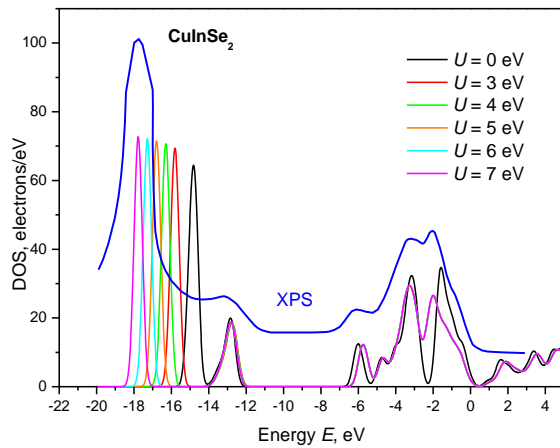
e)
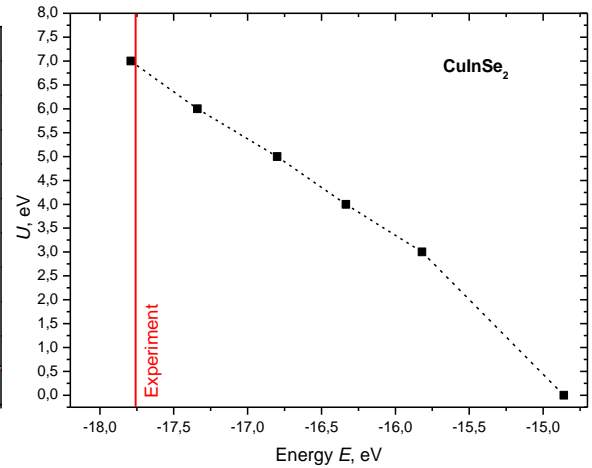
f)
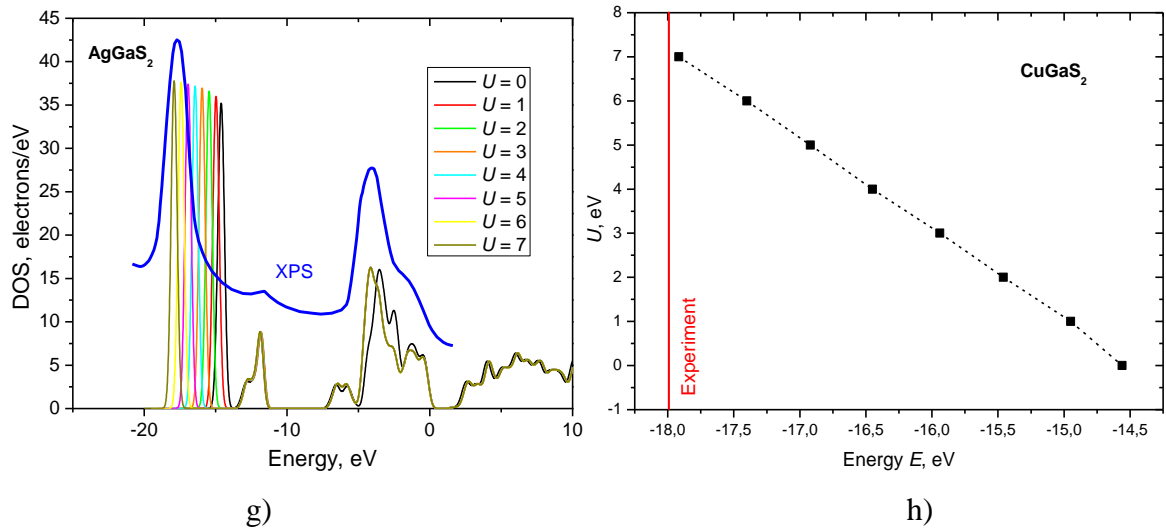
g)   h)

Figure 4.20. Calculated density of state for $AgGaS_2$, $AgInSe_2$, $CuGaS_2$, та $CuInSe_2$ crystals with using different values of Hubbard parameter U, together with the experimental XPS spectra taken from literature [29,60].

The band positions of the In $4d$- and Ga $3d$-states together with the obtained U values for the $AgGaS_2$, $AgInSe_2$, $CuGaS_2$, and $CuInSe_2$ crystals are collected in the Table 4.12. As can be seen from the table, the value of the Hubbard parameter required to correct the interaction of strongly localized d-electrons for crystals with Ga is higher than the corresponding value for In. Also, it is seen that this parameter for crystals with Cu is greater than for crystals with Ag. Thus, the example of $AgGaS_2$, $AgInSe_2$, $CuGaS_2$, $CuInSe_2$ crystals shows the efficiency of using the Hubbard parameter for CP crystals in order to take into account the interaction of d-electrons.

Table 4.12. Position of d-levels of cations Ga and In in some crystals of I-III-VI₂ ($AgGaS_2$, $AgInSe_2$, $CuGaS_2$, $CuInSe_2$) and corresponding U parameter values.

Crystal	E, eV	U, eV
$AgGaS_2$	−17.71	7.12
$AgInSe_2$	−17.26	5.72
$CuGaS_2$	−18.54	8.10
$CuInSe_2$	−17.76	6.92

4.5. Conclusions

1. The structure of the crystal's unit cells of I-III-VI$_2$ group is considered. It is found that the structure of the crystals of the studied group optimized by the BFGS method is close to the experimental. The lattice parameters and, as a consequence, the volume of the unit cell differ slightly from the experimental values. It was found that the difference of the optimized cell volume is in the range of $\Delta V = 4.47$ (for CuAlTe$_2$) for GGA to 45.39 Å^3 (for AgInTe$_2$) for LDA. It is shown that using GGA functional lead to overestimated volume of the unit cell while for LDA functional underestimation is observed.

2. Geometric optimization of the lattice structure for crystals with Ag showed a feature consisting in atypical overestimation of the optimized lattice parameter c when using the LDA functional for optimization. c-parameter is greater than the experimental value by 0.2 – 1.9%, but remains smaller than the value obtained using the GGA functional.

3. A correlation was found between the tetragonal strain parameter η and the anion displacement parameter u. It is shown that the anion displacement parameter in the structure of I-III-VI$_2$ crystals has a linear dependence on the tetragonal deformation parameter η. It was found that increasing η lead to decreasing of the parameter u. This dependence is characterized by a strong negative correlation.

4. It was found that for crystals of I-III-VI$_2$ group the top of the valence band and the bottom of the conduction band are in the center of the Brillouin zone. Observed is the underestimation of the band gap width for both LDA and GGA functional in comparison with the experimental values. The functional dependence of the band gap E_g on the molar mass μ of the studied crystals was revealed. It is shown that with increasing molar mass, the value of the band gap decreases. Pearson's coefficient indicates a weak negative dependence ($R = 0.64$ for LDA; $R = 0.66$ for GGA) on the band gap, while for experimental values of the band gap, this dependence is stronger ($R = 0.81$).

5. It is shown that the top of the valence band for crystals of I-III-VI$_2$ group is formed by the levels of Γ_4 and Γ_5 symmetry split by the crystal field. The values of the crystal field energies obtained from the band-energy structure agree well with the literature data. The effective masses of charge carriers for the directions of the Brillouin zone $\Gamma - X$ and $\Gamma - Z$ are calculated from the curvature of the energy branches of the bottom of the conduction band and the top of the valence band. It is shown that $m_h{}^*$ is greater than $m_e{}^*$. The anionic substitution S → Se → Te reduces the effective mass in the $\Gamma - Z$ direction. Cationic substitution Ag → Cu leads to decrease in the effective mass of both holes and electrons.

6. From the calculations of total and partial density of states the detailed structure of energy bands in crystals is received. Analysis of the calculated state density diagrams showed that the top of the valence band is formed by *d*-states of elements of group I (Cu, Ag), which are split under the action of a crystal field, with a small contribution of *s*- and *p*-states of other elements. Energy levels at energies smaller than 10 eV are formed by *d*-states of elements of group III (Al, Ga, and In) and do not reveal splits. The chemical bonds of the crystals group under study were analyzed using Mulliken charges and the population of bonds overlap. The high degree of ionicity of the chemical bonds was additionally evaluated.

7. A number of optical spectra for crystals of I-III-VI₂ group such as dielectric function ε, reflection *R*, absorption α, refractive indices *n* and extinction *k* are calculated. It is shown that the dielectric function in the region of small energy values has low anisotropy and the replacement of S $\to$ Se $\to$ Te leads to its reduction except for $CuInX_2$ compounds. At higher energies the anisotropy of optical functions increases. It is shown that crystals of this group have strong absorption (α lies in the range from 2.6 to 3.5×10^5 cm^{-1}). It has been also shown that the crystals with copper have stronger absorption than that with silver atoms, so such materials are more promising for the application as absorbing layer in solar cells.

8. The linear electro-optic, electrogyration coefficients and second-order nonlinear susceptibility of $AgGaS_2$ crystals have been calculated in the frame of the DES model. While selecting in a relevant way the electronic polarizability volumes of the ions, we have achieved satisfied agreement of the calculated and experimental optical anisotropy parameters for the light wavelengths $\lambda = 632.8$ nm. In addition, using the dispersion of the electronic polarizability volumes calculated with the Lorentz – Lorenz formula, we have calculated the value of nonlinear susceptibility for $\lambda = 1064$ nm.

9. It is shown that the calculations based on the pseudopotential method with using LDA and GGA functionals lead to a shift in the position of the localized *d*-orbitals to higher energy for I-III-VI₂ crystals. On the example of $AgGaS_2$, $AgInSe_2$, $CuGaS_2$, and $CuInSe_2$ crystals, it is shown that the application of the Hubbard correction DFT + *U* can correct the shortcomings of this method.

5. ELASTIC PROPERTIES AND ACOUSTIC WAVES IN I-III-VI$_2$ CRYSTALS

5.1. Elastic and acoustic properties of I-III-VI$_2$ group crystals

5.1.1. Prediction of the elastic properties of solids

Study of elastic properties of materials is important from both fundamental and applied point of view, in particular for designing devices based on them. Elastic properties reflect the interatomic interactions and are related with some fundamental physical properties.

The ability of a crystalline solid to change its shape under the influence of external load and return to its original equilibrium state (to restore its size and initial shape) after the cessation of this influence is called elasticity. It determines the mechanical properties of a solid body and is characterized by elastic modulus of that can be calculated or measured experimentally. The mechanical properties of materials are very important for their practical applications and provide crucial information about the nature of force in a solid. Also, it provides deep insight into the dynamical and mechanical behavior of different materials. The elastic constants indicate the response of the materials to an external stress and provide an important information regarding the bonding characteristics, anisotropy and hardness, the cohesion of a material, specific heat, the Debye temperature, Grüneisen parameter and thermal expansion, respectively. They are closely related to the long-wavelength phonon spectra etc. [223,224]. In particular, having data on elastic constants, we can characterize the ductility, stability, brittleness and stiffness of materials. In terms of crystal anisotropy studies, elastic properties are of special interest.

Elastic properties as well as many other fundamental parameters of materials can be predicted from the ab initio calculations of total energy in the ground state. The CASTEP program used in this work allows for high-precision calculations of elastic constants of a stable crystals C_{ij}. Also, based on these results from the elastic constants calculation the basic modulus of elasticity, such as the Young's modulus (E), the shear modulus (G), the

volumetric modulus of elasticity (*B*) and the Poisson's ratio (*v*) can be revealed. Such studies are important and can be used as an alternative to experimental measurements, and allow high-precision characterization of materials.
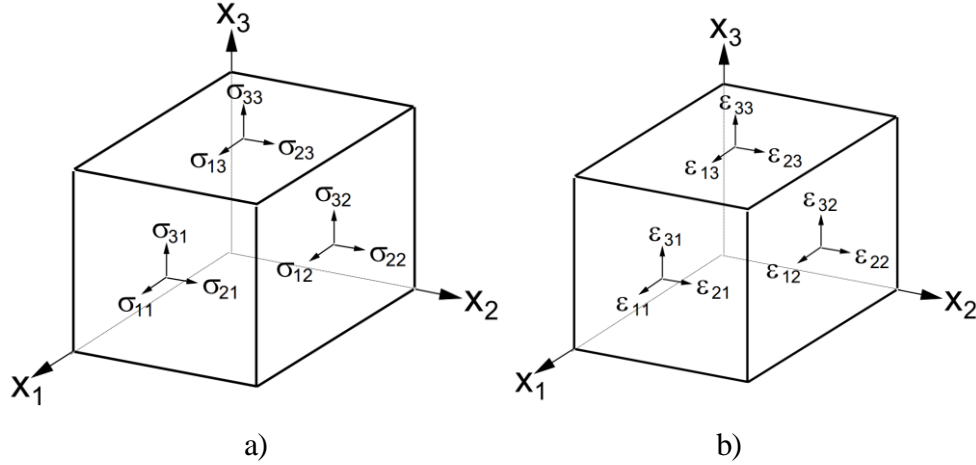
a)   b)

Figure 5.1. Determination of stress components σ_{ij} and strains ε_{ij} on the faces of a unit cube: (a) Stress notation; (b) Strain notation.

The main concepts that characterize the elasticity of the crystal are stress (force acting per unit area) and deformation (reaction to the applied effect). The stress state at each point of the elastic body is described by the mechanical stress tensor σ (Fig. 5.1). In the general case, the stress state of the body is determined by a system of 9 components. Three of these, are normal and 6 are shear [148]. The tensor of mechanical stress and elastic deformations is a symmetric tensor of the second rank, i.e. they can be reduced to the main axes (6 components σ_{ij} and ε_{ij} are enough to describe such tensors). A general view of the stress and strain matrices i following

$$\sigma_{ij} = \begin{pmatrix} \sigma_{xx} & \sigma_{xy} & \sigma_{xz} \\ \sigma_{yx} & \sigma_{yy} & \sigma_{yz} \\ \sigma_{zx} & \sigma_{zy} & \sigma_{zz} \end{pmatrix}, \qquad \varepsilon_{ij} = \begin{pmatrix} \varepsilon_{xx} & \varepsilon_{xy} & \varepsilon_{xz} \\ \varepsilon_{yx} & \varepsilon_{yy} & \varepsilon_{yz} \\ \varepsilon_{zx} & \varepsilon_{zy} & \varepsilon_{zz} \end{pmatrix}. \qquad (5.1)$$

If the direction of the main axes is chosen for the coordinate axis, then the shear stress components will be equal to zero and 3 components will suffice. Stress and strain tensors are field and do not describe the properties of crystals, and therefore do not depend on their symmetry. They depend on the applied force and their characteristic surface is set by the

direction of external force. Only in the case of thermal expansion is the strain tensor associated with the symmetry of the crystal. According to Hooke's law, at rather low stresses the deformation is proportional to the magnitude of the applied stress. For anisotropic materials (crystals) the Hooke's law has the following form

$$\sigma_{ij} = C_{ijkl}\varepsilon_{kl}, \qquad (5.2)$$

and vice versa

$$\varepsilon_{ij} = S_{ijkl}\sigma_{kl}, \qquad (5.3)$$

where σ_{ij} is mechanical stress tensor, C_{ijkl} the elastic constants tensor, which is characterize the resistance of the material to elastic deformation, S_{ijkl} is the elastic compliance that define how easily the material can be strained, ε_{kl} the deformation tensor. Tensor C_{ijkl} (where $i, j, k, l = 1, 2, 3$) is the four-rank tensor which connects mechanical stress and strain contains 81 components. As follows from the symmetry of the tensors ε_{ik} and σ_{ij}, the C_{ij} tensor are symmetric by the first (or last) two indices. Let us introduce a two-index representation of the elastic stiffness tensor to be used below ($C_{ijkl} \rightarrow C_{vu}$), by exploiting Voigt's notation. Using the convolution of indices 11→1, 22→2, 33→3, 23→4, 13→5, 12→6 one can obtain the Eq. 5.2 in the form $\sigma_j = C_{ij}\varepsilon_i$ ($i, j = 1...6$) [225]. As a result of using two indices, the tensor of the 4th rank can be written in the form of a matrix containing 36 components.

The resulting matrix is symmetrical about the diagonal and, accordingly, a 21 of 36 coefficients are independent. Depending on symmetry of the crystal, the number of independent constants decreases. Due to the symmetry of the crystal, some matrix elements are equal to each other, and some are fixed and equal to zero. Thus, for each symmetry of the crystal, matrices of elastic constants are derived which fully describe the elastic properties of the material belonging to this symmetry. With increasing of the symmetry to cubic there are only three independent elastic constants due to equality: $C_{11} = C_{22} = C_{33}$; $C_{12} = C_{23} = C_{13}$; and $C_{44} = C_{55} = C_{66}$ [148] (see Table 5.1). The independent coefficients of the elastic constants matrix for all types of symmetry are given in Table 5.1.

Since the I-III-VI$_2$ crystals belongs to the tetragonal class of symmetry, the equalities of the coefficients $C_{22} = C_{11}$, $C_{23} = C_{13}$, $C_{44} = C_{55}$ are valid as a consequence of the symmetry of the crystal. Therefore, there are 6 independent components of the tensor (C_{11}, C_{12}, C_{13}, C_{33}, C_{44}, and C_{66}) for the crystal (see Table 5.1). Therefore, the generalized Hooke's law (Eq. 5.2) for I-III-VI$_2$ crystals in the crystal structure of chalcopyrite can be written as:

$$
\begin{pmatrix} \sigma_x \\ \sigma_y \\ \sigma_z \\ \tau_{yz} \\ \tau_{xz} \\ \tau_{xy} \end{pmatrix} = \begin{pmatrix} C_{11} & C_{12} & C_{13} & 0 & 0 & 0 \\ C_{12} & C_{11} & C_{13} & 0 & 0 & 0 \\ C_{13} & C_{13} & C_{33} & 0 & 0 & 0 \\ 0 & 0 & 0 & C_{44} & 0 & 0 \\ 0 & 0 & 0 & 0 & C_{44} & 0 \\ 0 & 0 & 0 & 0 & 0 & C_{66} \end{pmatrix} \begin{pmatrix} \varepsilon_{xx} \\ \varepsilon_{xx} \\ \varepsilon_{xx} \\ \gamma_{yz} \\ \gamma_{xz} \\ \gamma_{xy} \end{pmatrix}. \tag{5.4}
$$

where σ and τ are characterize the tensile and shear stresses, as well as γ and ε are tensile and shear deformation, respectively. Thus, the behavior of the material under the action of stress will be completely described by Eq. 5.4.

Table 5.1. Independent elastic constants for seven types of crystal symmetry.

Unit cell parameters	Angles	Crystal type	Number of component	Independent elastic coefficient
—	—	Isotropic	2	C_{11}, C_{12}
$a = b = c$	$\alpha = \beta = \gamma = 90°$	Cubic	3	C_{11}, C_{12}, C_{44}
$a = b \neq c$	$\alpha = \beta = 90°$ $\gamma = 120°$	Hexagonal	5	C_{11}, C_{12}, C_{13}, C_{33}, C_{44}
$a = b \neq c$	$\alpha = \beta = \gamma = 90°$	Tetragonal	6	C_{11}, C_{12}, C_{13}, C_{33}, C_{44}, C_{66}
$a \neq b \neq c$	$\alpha = \beta = 90°$ $\gamma = 120°$	Trigonal	6	C_{11}, C_{12}, C_{13}, C_{33}, C_{14}, C_{44}
$a \neq b \neq c$	$\alpha = \beta = \gamma = 90°$	Orthorhombic	9	C_{11}, C_{22}, C_{33}, C_{12}, C_{13}, C_{23}, C_{44}, C_{55}, C_{66}
$a \neq b \neq c$	$\alpha = \gamma = 90°$ $\beta \neq 90°$	Monoclinic	13	C_{11}, C_{22}, C_{33}, C_{12}, C_{13}, C_{23}, C_{44}, C_{55}, C_{66}, C_{16}, C_{26}, C_{36}, C_{45}
$a \neq b \neq c$	$\alpha \neq \beta \neq \gamma \neq 90°$	Triclinic	21	C_{11}, C_{12}, C_{13}, C_{14}, C_{15}, C_{16}, C_{22}, C_{23}, C_{24}, C_{25}, C_{26}, C_{33}, C_{34}, C_{35}, C_{36}, C_{44}, C_{45}, C_{46}, C_{55}, C_{56}, C_{66}

DFT together with the pseudopotential method allows calculations of total energy for any crystal structures. Thus, we can deform the obtained equilibrium structure, determine the total energy of the crystal, and from the obtained results to establish elastic constants. The elastic constants are proportional to the second-order coefficient in the polynomial expansion of total energy as a function of the deformation parameter δ.

The elastic constants can be obtained by selecting the deformation applied to the crystal and then the calculation of the resulting pressures. The tensor of the elastic constants

can be defined by means of the Taylor expansion of the total energy $E(V, \delta)$ of the studied system with respect to a small strain δ of the unit cell volume V [172]:

$$E(V,\delta) = E(V_0,0) + V_0 \left(\sum_i \tau_i \xi_i \delta_i + \frac{1}{2} \sum_{ij} C_{ij} \delta_i \xi_i \delta_j \xi_j \right) + O(\delta^3), \qquad (5.5)$$

where $E(V_0, 0)$ is the energy of the unstrained system, V_0 is the equilibrium volume, τ_0 is an element of the stress tensor, and ξ_i is a Voigt index factor. Considering of no initial stress ($\tau_i = 0$), the energy change was derived from the second derivatives of the total energy with respect to different combination of strains. The relationship between the strain energy (E_s) and the elastic stiffness tensors, is

$$E_s(V,\delta) = \frac{1}{2} V_0 \sum_{ij} C_{ij} \delta_i \xi_i \delta_j \xi_j, \qquad (5.6)$$

and the elastic constant C_{ij} can be obtained by fitting Eq. (5.6). This method of determining elastic constants is called the strain-stress method. As mentioned above, the strain-stress method is also a general approach for investigating the elastic constants of materials.

Table 5.2. The lattice parameters for deformed unit cell of the tetragonal symmetry, the expression relating the δ and ε variables, the finite Lagrangian strain tensor (Voigt notation) and the value of the second derivative, $(1/2V)(d^2E/d\varepsilon^2)$, in terms of the elastic constants (ε being deformation coordinate and E the energy) [30].

Strained cell	ε	Strain (η)	$\dfrac{d^2E}{d\varepsilon^2}$
$\left(a+\delta,\ a+\delta, \dfrac{c+c\delta}{a}, 90, 90, 90 \right)$	$\dfrac{(a+\delta)^2}{a^2} - 1$	$\left(\dfrac{\varepsilon}{2}, \dfrac{\varepsilon}{2},\ \dfrac{c\varepsilon}{2a},\ 0,0,0 \right)$	$\dfrac{1}{4}(C_{11}+C_{12}) + \dfrac{1}{8}C_{33} + \dfrac{1}{2}C_{13}$
$\left(a+\delta,\ a+\delta, c, 90, 90, 90 \right)$	$\dfrac{(a+\delta)^2}{a^2} - 1$	$\left(\dfrac{\varepsilon}{2}, \dfrac{\varepsilon}{2},\ 0,\ 0,0,0 \right)$	$\dfrac{1}{4}(C_{11}+C_{12})$
$\left(a,\ a, \dfrac{c+c\delta}{a}, 90, 90, 90 \right)$	$\dfrac{(a+\delta)^2}{c^2} - 1$	$\left(0,\ 0,\ 0, \dfrac{\varepsilon}{2}, 0, 0 \right)$	$\dfrac{1}{8}C_{33}$
$\left(a,\ a+\delta, c, 90, 90, 90 \right)$	$\dfrac{(a+\delta)^2}{a^2} - 1$	$\left(0,\ 0,\ \dfrac{\varepsilon}{2}, 0, 0, 0 \right)$	$\dfrac{1}{8}C_{11}$
$\left(a,\ a, c, 90, 90+\delta, 90 \right)$	$\sin \delta$	$(0,0,0,0,\ \varepsilon,\ 0)$	C_{44}
$\left(a,\ a, c, 90, 90, 90+\delta \right)$	$\sin \delta$	$(0,0,0,0,0,\ \varepsilon)$	C_{66}

5.1.2. Elastic properties of I-III-VI₂ group crystals

For each deformation, the crystal is relaxed at the internal degrees of freedom of the cell atoms. Elastic constants are defined as proportional to the coefficient of the quadratic term in δ (in a polynomial fit of total energy as a function of strain parameter). The elastic constants are calculated at the optimized structures, which can be used to obtain reliable elastic properties of compounds. The relationship between deformations and elastic constants is shown in Table 5.2. For each deformation scheme, six small $\delta = 1 \times 10^{-3}$ values of the deformation amplitude are considered and the elastic constants can be obtained through partial differentials of stress to strain. After calculating all the elastic constants, the mechanical properties of the material can be characterized.

Table 5.3. Elastic stiffness constants C_{ij} (in GPa) of I-III-VI₂ group crystals calculated using LDA/GGA functionals.

Crystal	C_{11}	C_{33}	C_{44}	C_{66}	C_{12}	C_{13}
AgAlS₂	104.2/84.6	97.1/77.6	38.18/37.5	44.4/39.1	70.2/51.5	70.1/52.2
AgAlSe₂	89.0/72.6	79.8/64.1	34.4/30.3	36.0/29.9	57.2/43.3	56.9/43.0
AgAlTe₂	77.1/59.1	75.4/54.1	17.6/12.7	25.7/28.2	56.1/34.3	56.2/33.6
AgGaS₂	98.6/82.0	92.7/71.9	41.2/37.0	41.4/40.7	64.7/47.5	64.7/46.5
AgGaSe₂	88.1/63.4	79.7/65.8	31.4/30.7	32.2/29.7	56.9/34.9	55.2/40.5
AgGaTe₂	70.4/49.3	66.0/48.3	31.5/23.6	29.6/26.4	41.4/30.1	42.1/28.0
AgInS₂	85.4/63.6	80.8/66.3	32.6/30.2	34.9/27.8	59.4/39.9	60.7/41.6
AgInSe₂	72.7/49.4	70.3/42.6	22.4/17.8	24.7/15.6	51.6/25.8	50.9/22.7
AgInTe₂	55.2/42.2	55.6/40.4	21.6/20.1	17.5/16.1	33.9/25.5	35.8/26.2
CuAlS₂	130.0/109.9	131.5/109.4	58.8/50.8	57.9/51.5	79.1/63.2	82.2/66.6
CuAlSe₂	107.3/98.1	109.4/95.0	47.4/51.8	46.1/48.8	65.1/55.7	66.8/57.5
CuAlTe₂	87.3/72.8	86.1/69.9	38.6/33.3	37.7/33.1	50.9/40.9	51.1/41.5
CuGaS₂	132.3/107.4	134.0/106.7	60.0/51.5	59.9/50.5	79.5/60.7	80.4/61.9
CuGaSe₂	108.9/92.4	104.4/89.2	49.5/49.0	49.2/48.3	65.8/50.3	65.6/50.4
CuGaTe₂	89.2/69.3	81.3/70.3	40.4/32.3	40.5/32.6	51.6/37.7	50.4/35.6
CuInS₂	106.3/86.1	108.0/85.0	44.8/40.0	42.1/38.3	71.3/54.6	71.9/55.2
CuInSe₂	89.2/68.3	89.1/72.3	38.2/30.46	37.0/33.8	59.0/45.3	58.7/50.3
CuInTe₂	77.3/51.7	75.5/49.5	31.4/21.1	32.1/20.0	49.1/39.2	47.4/39.4

When studying the selected group of crystals, calculations were performed by two methods that include LDA and GGA *XC* functionals. The calculated components of C_{ij}

tensor using LDA and GGA functionals for the I-III-VI$_2$ crystals are collected in Table 5.3. Knowing of the elastic constants and modulus is important for technological aims, in manufacturing process and crystal preparation. It is known, that for practical application is important to obtain stable crystal structure. Verification of the mechanical stability of the I-III-VI$_2$ crystal was conducted using the well-known Born criteria (Eq. 5.7). For the chalcopyrite crystal structure stability of tetragonal symmetry, the obtained elastic constants meet the requirements of mechanical stability criteria [226]:

$$C_{ii} > 0 \ (i = 1, 2, 3, 4, 5 \text{ and } 6),$$
$$(C_{11} - C_{12}) > 0; (C_{11} + C_{33} - 2C_{13}) > 0, \quad (5.7)$$
$$2[(C_{11} + C_{12}) + C_{33} + 4C_{13}] > 0.$$

As one can see from the Table 5.3, calculated elastic constants C_{ij} for the group of crystals I-III-VI$_2$ completely satisfies the all criteria (5.7), indicating the mechanical stability of their structure. By inspection of the elastic coefficients C_{11}, $C_{12,}$ $C_{13,}$ $C_{33,}$ C_{44}, C_{66} one can conclude, that the coefficients are positive for all crystals of I-III-VI$_2$ group. The elastic constants in the materials under consideration are quite small (lower than 100 GPa). In general, from Table 5.3 it is seen that the coefficients C_{ij} differ from each other. As can be seen, the elastic constants for the calculation using the LDA method has a higher values of C_{ij} than for the GGA functional. The overestimation is due to the overbinding problem of the LDA method, which leads to underestimation of the bond lengths in materials of different nature. As seen from Table 5.3, the C_{11} and C_{33} constants are the largest for the I-III-VI$_2$ materials, indicating the strongest resistance of the crystal to axial compression along the x and z directions and satisfy the relation $C_{11} > C_{33}$. Here for the crystals AgInTe$_2$, CuAlS$_2$, CuAlSe$_2$, CuGaS$_2$ and CuInS$_2$ the calculated elastic constants C_{11} and C_{33} is almost equal in the range of calculation error. Therefore we can assume that those coefficients, probably also obeys the inequality. The largest coefficient is C_{11} means that in the x and y directions, at the same pressures, the crystal is less compressed than in the z direction. The values of C_{11} and C_{33} differ one to another, that indicate on anisotropy of elastic properties. The data in table shows that the shear coefficients C_{12} and C_{13} are close to each other, showing the same interaction in the respective shear directions. It can be seen that the coefficients of elasticity satisfy the following inequality $C_{11} > C_{33} > C_{12} > C_{13} > C_{44} > C_{66}$.

Using the C_{ij} values, the linear compressibility along the principal axes of the lattice can be evaluated. For the trigonal structure, the following relations give the linear compressibilities k_a and k_c along the a- and c-axis respectively in term of elastic constants

$$k_a = -\frac{1}{a}\frac{\partial a}{\partial p} = \frac{C_{33} - C_{13}}{C_{33}(C_{11} + C_{12}) - 2C_{13}^2} \, , \tag{5.8}$$

$$k_c = -\frac{1}{c}\frac{\partial c}{\partial p} = \frac{C_{11} + C_{12} - 2C_{13}}{C_{33}(C_{11} + C_{12}) - 2C_{13}^2} \, . \tag{5.9}$$

Also, the bulk compressibility χ can be calculated as

$$\chi = \frac{1}{V}\frac{\partial V}{\partial p} = 2\chi_a + \chi_c \, . \tag{5.10}$$

The results of the calculation obtained in this work are presented in Fig. 5.2. The presented figure show that the calculated linear compressibility coefficients obtained with the GGA functional show the higher value of k than for revealed with the LDA functional. One can see from the figure, that the compressibility k has the clear tendency on its change. The sawtooth form of the compressibility change is typical for the I-III-VI₂ crystals. The transition from CuAlS₂ to AgInTe₂ crystal is supported in general by the increasing of the k values. During the change of composition the compressibility can be divided into structural element substitution. The change of all Cu → Ag, Al → Ga → In, and S → Se → Te lead to the increasing of the compressibility. The higher influence on the compressibility has the anion substitution S → Se → Te leading to rapid increase in k value. The cation substitution can be described by the smoother change in compressibility.
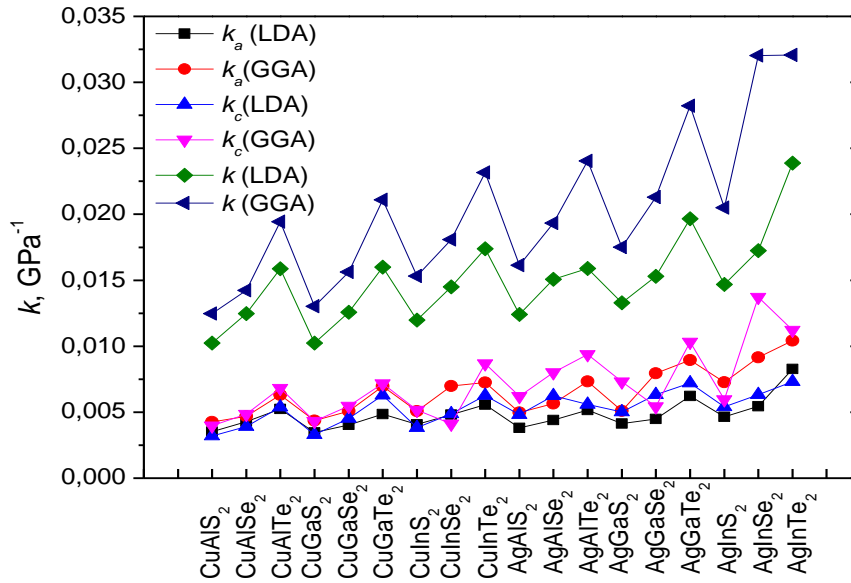
Figure 5.2. The linear compressibility k_a, k_c, and k of I-III-VI₂ group crystals calculated with using the LDA and GGA functionals.

The elastic coefficients are related to the elastic compliance by expression $C_{ij} = S_{ij}^{-1}$. Therefore, the elastic compliance coefficients easily can be obtained from the matrix of elastic constants. The elastic compliance coefficients calculated of crystals under

investigation for both *XC* functionals (LDA and GGA) are collected in Table 5.4. A number of the parameters describing the elastic properties, such as ground state Young's modulus *E*, Poisson's ratio *v*, bulk *B* and shear *G* modulus also can be obtained from the elastic coefficients calculated for the single crystal.

The important information that describes the elastic properties of I-III-VI$_2$ crystals can also be obtained by the anisotropic Young's modulus E_i and Poisson's ratio v_{ij} [227]

$$E_i = \frac{1}{S_{ii}}, \qquad (5.11)$$

$$v_{ij} = \frac{S_{ij}}{S_{ii}}, \qquad (5.12)$$

where S_{ij} is elastic compliance coefficients, *i* and *j* = 1, 2, 3.

The Young's modulus *E* is the ratio of stress against strain and it is a measure of the stiffness of the material. The Young's modulus E_x, E_y and E_z can be estimated from elastic compliance S_{ij}. Becouse of the symmetry of the materials the E_x and E_y modulus are equal for tetragonal crystals. The calculated using Eq. 5.11 Young's modulus for studied crystals are collected in Table 5.5. The values of the Young's modulus obtained from the calculations showed that the obtained values with the LDA functional are slightly greater than or equal to the GGA for both *x* and *z* components. As seen from the table, the Young's modulus in *x*-direction ($E_x = E_y$) is higher than in *z*-direction (E_z). This means that in the *x*- and *y*-directions the material is less tensile. Since *E* is a measure of stiffness, a material with the large *E* is supposed to be stiff. The results show, that the CuGaS$_2$ crystal is stiffer than the other crystals. At the same time, the crystals with the Te as cation are less stiff.

When the beam of a certain material is stretched at both ends then there will be an increase in length along the longitudinal dimension. At the same time, there will be a decrease along the lateral dimension. The ratio of the decrease in the lateral dimension to the increase in longitudinal described what is known as Poisson's ratio. The calculated Poisson's ratio *v* in different direction are calculated using the Eq. 5.12 and collected in Table 5.5. Similarly, to the Young's modulus, the Poisson's ratio obtained with the LDA functional show the grater values then for GGA. As a result of the crystal symmetry the following components of Poisson's ratio are equal: $v_{xy} = v_{yx}$, $v_{zx} = v_{zy}$, $v_{xz} = v_{yz}$. Generally, for the studied crystals the Poisson's ratio obeys the following inequality $v_{xz} > v_{zx} > v_{xy}$.

5.1.3. Calculation of polycrystalline elastic modulus

The calculated parameters that characterize the elastic properties of the investigated group of crystals, presented in Table. 5.6 allow the analysis of not only the mechanical properties of crystalline materials, but also polycrystals of these compounds. Often, in practice it is not possible to obtain elastic modules for a single crystal material. Therefore, elastic modules for polycrystalline material are investigated. Considering polycrystalline materials as a set of single crystals with a random orientation, it is possible to calculate isotropic polycrystalline elastic modules. They are obtained by calculating the average of anisotropic elastic constants for single crystal. Compared with single crystals, the elastic properties of polycrystals have greater application significance. Such polycrystalline elastic modules include the bulk modulus B, the shear modulus G, the Young's modulus E, and the Poisson's ratio v.

There are several models for determining the bulk modulus of solids: Voigt model in which assuming the uniform strain (index V), Reuss model assuming the uniform stress throught polycrystal (index R) and Hill model (index H). This approach is called Voigt – Reuss – Hill (VRH) approximation [228–230]. The bulk modulus B and the shear modulus G differ in magnitude for the Reuss and Voigt schemes. Also, the bulk modulus can be determined from the Birch [231] or Birch-Murnagan [232] equation of state by examining the dependences $E(V)$ or $V(P)$, respectively. The results obtained by different methods should give the same results for the values of the bulk modulus.

For tetragonal crystal symmetry, the bulk modulus B_{VHR} and the shear modulus G_{VHR} can be received using the Voigt-Reuss-Hill average schemes [228–230]

$$B_V = \frac{2}{9}\left(C_{11} + C_{12} + 2C_{13} + \frac{C_{33}}{2} \right), \tag{5.13}$$

$$B_R = \frac{C^2}{M}, \tag{5.14}$$

where $C^2 = (C_{11} + C_{12})C_{33} - 2C_{13}^2$, and $M = C_{11} + C_{12} + 2C_{33} - 4C_{13}$,

Table 5.4. The elastic compliance coefficients S (in GPa^{-1}) for I-III-VI$_2$ group crystals calculated using LDA/GGA functionals.

Crystal	S_{11}	S_{33}	S_{44}	S_{66}	S_{12}	S_{13}
AgAlS$_2$	0.02155/0.02269	0.02455/0.02662	0.02618/0.02663	0.02253/0.02559	−0.00787/−0.00752	−0.00987/−0.01021
AgAlSe$_2$	0.02341/0.02567	0.02818/0.03110	0.02908/0.03297	0.02778/0.03342	−0.00803/−0.00846	−0.01097/−0.01154
AgAlTe$_2$	0.03388/0.02982	0.03571/0.03353	0.05681/0.07844	0.03889/0.03541	−0.01365/−0.01042	−0.01506/−0.01207
AgGaS$_2$	0.02160/0.02165	0.02417/0.02593	0.02428/0.02703	0.02416/0.02457	−0.00788/−0.00726	−0.00957/−0.00930
AgGaSe$_2$	0.02332/0.02787	0.02657/0.03078	0.03182/0.03254	0.03102/0.03370	−0.00870/−0.00726	−0.01012/−0.01267
AgGaTe$_2$	0.02581/0.03663	0.02910/0.03502	0.03172/0.04246	0.03373/0.03787	−0.00862/−0.01533	−0.01095/−0.01234
AgInS$_2$	0.02858/0.03081	0.03342/0.03043	0.03071/0.03315	0.02868/0.03593	−0.00994/−0.01129	−0.01400/−0.01224
AgInSe$_2$	0.03360/0.03093	0.03500/0.03461	0.04467/0.05612	0.04048/0.06409	−0.01382/−0.01135	−0.01433/−0.01043
AgInTe$_2$	0.03508/0.04479	0.03732/0.04964	0.04632/0.04983	0.05717/0.06196	−0.01181/−0.01516	−0.01499/−0.01920
CuAlS$_2$	0.01453/0.01613	0.01497/0.01719	0.01699/0.01966	0.01726/0.01942	−0.00512/−0.00526	−0.00588/−0.00661
CuAlSe$_2$	0.01734/0.01772	0.01736/0.01922	0.02110/0.01931	0.02169/0.02050	−0.00632/−0.00584	−0.00673/−0.00719
CuAlTe$_2$	0.02019/0.02347	0.02072/0.02527	0.02588/0.03003	0.02655/0.03018	−0.00727/−0.00795	−0.00766/−0.00922
CuGaS$_2$	0.01380/0.01591	0.01371/0.01638	0.01666/0.01941	0.01669/0.01981	−0.00512/−0.00550	−0.00521/−0.00603
CuGaSe$_2$	0.01701/0.01770	0.01813/0.01865	0.02020/0.02039	0.02031/0.02068	−0.00618/−0.00604	−0.00680/−0.00658
CuGaTe$_2$	0.01968/0.02290	0.02213/0.02146	0.02477/0.03093	0.02468/0.03063	−0.00691/−0.00878	−0.00792/−0.00715
CuInS$_2$	0.02039/0.02311	0.02009/0.02402	0.02232/0.02502	0.02374/0.02612	−0.00818/−0.00860	−0.00813/−0.00942
CuInSe$_2$	0.02364/0.03318	0.02351/0.03602	0.02616/0.03293	0.02702/0.02961	−0.00950/−0.01024	−0.00931/−0.01595
CuInTe$_2$	0.02521/0.05761	0.02504/0.06491	0.03186/0.04732	0.03117/0.05006	−0.01026/−0.02226	−0.00938/−0.02811

Table 5.5. The Young's modulus E (in GPa), and Poisson's ratio v for I-III-VI$_2$ group crystals calculated using LDA/GGA functionals.

Crystal	E_x, GPa	E_z	v_{ij}		
			$xy = yx$	$zx = zy$	$xz = yz$
AgAlS$_2$	46.40370/44.05944	40.73319/37.55688	0.3656/0.3313	0.4020/0.3835	0.4581/0.4499
AgAlSe$_2$	42.70061/38.95346	35.48293/32.14863	0.3429/0.3299	0.3894/0.3712	0.4687/0.4497
AgAlTe$_2$	29.51589/33.52501	28.00051/29.81763	0.4031/0.3495	0.4219/0.3601	0.4448/0.4049
AgGaS$_2$	46.29038/46.16980	41.37258/38.56263	0.3652/0.3352	0.3963/0.3588	0.4434/0.4296
AgGaSe$_2$	42.87624/35.87660	37.63130/32.48859	0.3731/0.2608	0.3812/0.4116	0.4343/0.4546
AgGaTe$_2$	38.74079/27.29687	34.35902/28.55438	0.3340/0.4187	0.3764/0.3526	0.4244/0.3371
AgInS$_2$	34.98081/32.45354	29.91548/32.86015	0.3478/0.3667	0.4190/0.4022	0.4900/0.3973
AgInSe$_2$	29.75768/32.32383	28.56918/28.88537	0.4113/0.3669	0.4096/0.3015	0.4266/0.3374
AgInTe$_2$	28.50233/22.32208	26.79019/20.14426	0.3367/0.3385	0.4018/0.3869	0.4274/0.4287
CuAlS$_2$	68.80402/61.99567	66.79552/58.17257	0.3524/0.3263	0.3933/0.3848	0.4051/0.4101
CuAlSe$_2$	57.65459/56.41496	57.57902/52.00938	0.3644/0.3299	0.3878/0.3739	0.3883/0.4056
CuAlTe$_2$	49.52082/42.59141	48.25218/39.56507	0.3605/0.3386	0.3700/0.3650	0.3798/0.3929
CuGaS$_2$	72.42566/62.85316	72.91294/61.03773	0.3712/0.3461	0.3799/0.3686	0.3773/0.3796
CuGaSe$_2$	58.75630/56.47515	55.15537/53.59674	0.3634/0.3415	0.3754/0.3530	0.3999/0.3720
CuGaTe$_2$	50.80152/43.66639	45.17987/46.58310	0.3513/0.3836	0.3579/0.3332	0.4025/0.3123
CuInS$_2$	49.02373/43.26115	49.76596/41.63187	0.4011/0.3723	0.4048/0.3926	0.3988/0.4079
CuInSe$_2$	42.29988/30.13859	42.53034/27.76218	0.4023/0.3089	0.3963/0.4428	0.3941/0.4807
CuInTe$_2$	39.65616/17.35716	39.93569/15.40493	0.4072/0.3865	0.3750/0.4330	0.3724/0.4879

Table 5.6. Calculated bulk modulus B (in GPa), shear modulus G (in GPa), Young's modulus E (in GPa), the B_H/G_H ratio and Poisson's ratio ν for the I-III-VI$_2$ group crystals calculated using LDA/GGA functionals.

Crystal	B_V, GPa	B_R, GPa	B_H, GPa	G_V, GPa	G_R, GPa	G_H, GPa	B_H/G_H	E	ν
AgAlS$_2$	80.66/62.10	80.53/61.99	80.60/62.04	30.48/28.89	24.75/23.51	27.62/26.22	2.92/2.37	74.37/68.95	0.3462/0.3148
AgAlSe$_2$	66.67/51.96	66.42/51.73	66.54/51.84	26.73/23.44	22.12/19.88	24.43/21.66	2.72/2.39	65.30/57.04	0.3364/0.3166
AgAlTe$_2$	62.96/41.71	62.95/41.61	62.95/41.66	16.26/15.46	14.33/13.78	15.29/14.62	4.12/2.85	42.43/39.27	0.3877/0.3429
AgGaS$_2$	75.35/57.42	75.27/57.10	75.31/57.26	31.13/29.30	25.17/24.33	28.15/26.82	2.68/2.13	75.09/69.59	0.3338/0.2974
AgGaSe$_2$	65.61/47.13	65.35/46.92	65.48/47.03	24.91/23.33	21.65/19.40	23.28/21.37	2.81/2.20	62.44/55.68	0.3411/0.3027
AgGaTe$_2$	50.88/35.47	50.84/35.43	50.86/35.45	23.95/18.75	20.36/15.59	22.16/17.17	2.30/2.06	58.05/44.35	0.3098/0.2915
AgInS$_2$	68.11/48.85	68.07/48.78	68.09/48.82	24.71/22.32	19.11/18.33	21.91/20.33	3.11/2.40	59.36/53.56	0.3547/0.3172
AgInSe$_2$	58.07/31.53	58.04/31.21	58.06/31.37	18.04/14.93	15.49/14.36	16.76/14.65	3.46/2.14	45.87/38.03	0.3683/0.2979
AgInTe$_2$	41.88/31.16	41.86/31.16	41.87/31.16	16.16/14.37	14.33/11.94	15.24/13.16	2.75/2.37	40.77/34.61	0.3377/0.3149
CuAlS$_2$	97.63/80.23	97.60/80.22	97.61/80.22	44.97/39.49	37.73/33.47	41.35/36.48	2.36/2.20	108.70/95.03	0.3144/0.3026
CuAlSe$_2$	80.17/70.31	80.15/70.30	80.16/70.31	36.52/38.49	31.30/31.44	33.91/34.96	2.36/2.01	89.16/89.97	0.3146/0.2867
CuAlTe$_2$	62.97/51.47	62.97/51.46	62.97/51.46	30.15/26.04	26.32/22.54	28.23/24.29	2.23/2.12	73.68/62.96	0.3050/0.2961
CuGaS$_2$	97.68/76.72	97.67/76.72	97.68/76.72	46.53/39.82	39.73/34.16	43.13/36.99	2.26/2.07	112.79/95.60	0.3076/0.2923
CuGaSe$_2$	79.55/63.99	79.51/63.97	79.53/63.98	37.98/37.47	31.91/31.40	34.94/34.44	2.28/1.86	91.43/87.60	0.3084/0.2718
CuGaTe$_2$	62.74/47.42	62.56/47.41	62.65/47.41	31.39/26.11	26.79/23.47	29.09/24.79	2.15/1.91	75.57/63.33	0.2990/0.2774
CuInS$_2$	83.43/65.26	83.42/65.26	83.43/65.26	33.36/29.78	27.44/24.21	30.40/27.00	2.74/2.42	81.32/71.18	0.3375/0.3182
CuInSe$_2$	68.94/55.61	68.94/55.29	68.94/55.45	28.75/23.10	23.66/17.34	26.20/20.22	2.63/2.74	69.76/54.09	0.3313/0.3374
CuInTe$_2$	57.57/43.19	57.54/43.16	57.56/43.17	24.71/14.78	21.34/10.21	23.02/12.49	2.50/3.46	60.94/34.17	0.3236/0.3681

$$G_V = \frac{M + 3C_{11} - 3C_{12} + 12C_{44} + 6C_{66}}{30} \quad , \tag{5.15}$$

$$G_R = \frac{15}{\left(\dfrac{18B_V}{C^2} + \dfrac{6}{(C_{11} - C_{12})} + \dfrac{6}{C_{44}} + \dfrac{3}{C_{66}} \right)} . \tag{5.16}$$

Since the *V* and *R* equations represent the upper and lower limits for polycrystalline modules, in practice the average value of these two expressions is obtained. Such an approach is called Hill's formulas. The parameters obtained by Hill are defined as the arithmetic mean of the parameters *B* and *G* obtained by the Voigt and Reuss scheme.

$$B_H = \frac{B_V + B_R}{2} , \tag{5.17}$$

$$G_H = \frac{G_V + G_R}{2} . \tag{5.18}$$

The Young's *E* modulus and Poisson's ratio *v* values for polycrystalline materials can be expressed in form *B* and *G* modulus. The theoretical values of the Young's *E* modulus and Poisson's ratio *v* values has been calculates from following equations

$$E = \frac{9B_H G_H}{(3B_H + G_H)} , \tag{5.19}$$

$$v = \frac{3B - 2G}{2(3B + G)} . \tag{5.20}$$

Here, the subscripts *V*, *R* and *H* denote the Voigt's, Reuss's and Hill's notation, respectively. The estimated values of the bulk modulus, shear modulus, Young's modulus and Poisson's ratio of titled compound are collected in Table 5.6. The highest calculated Young's modulus value is observed for CuGaS$_2$ crystal. For this crystal the *E* = 112.79 GPa (95.60 GPa) for LDA (GGA) functional, respectively. For the AgInTe$_2$ crystal the lowest value of young's modulus was received: 40.77 GPa for LDA functional and 34.61 GPa for GGA functional. The substitution of cation atom to the heavier atom S → Se → Te leads to the decreasing of the *E* value.

Poisson's ratio (*v*) defined as the ratio of transverse strain to the longitudinal strain is used to reflect the stability of the material against shear and provides information about the

nature of the bonding forces. It takes the value: $0 < v < 1/2$. By using the v parameter, the ductility and brittleness of materials may be tested. The low value of Poisson's ratio indicates a large compression of volume and when $v = 0.5$ no volume change occurs [233]. The bigger the Poisson's ratios the better the plasticity of material. The present calculated result of the Poisson's ratio shows that the I-III-VI$_2$ group of materials is of good plasticity. The $v = 0.25$ and $v = 0.5$ are the lower limit and upper limit for central forces in solids, respectively. The obtained value of Poisson's ratio (v) for I-III-VI$_2$ is larger than the lower limit value ($v = 0.25$), which indicates that the interatomic forces of I-III-VI$_2$ are central forces.

The bulk modulus B is defined as a measure of how solids resistant to compression under the action of hydrostatic pressure. A solid with the higher B are more incompressible. As seen from the table, the VHR calculated bulk moduli are lower than 100 GPa. That indicates the relative softness of I-III-VI$_2$ crystal. The highest bulk modulus for the calculated group of crystals is equal to 83.43 GPa (65.26 GPa) for LDA and GGA functional. This value corresponds to the CuInS$_2$ compound. The smallest value of bulk modulus B is for AgInTe$_2$ crystal, that is equal to 41.87 GPa for LDA and 31.16 GPa for GGA respectively.

Comparing the materials of the studied group with other important reference values such as for glass (35-50 GPa) and diamond (443 GPa), we can also say that these crystals are relatively soft.

Based on the bulk and shear moduli, the characteristics of the crystal such as plasticity and ductility can be estimated. For this purpose, the Pugh's criterion [234], which operate the B_H/G_H ratio in order to determine whether a material is brittle or ductile, is used. This relation give reference for the judgment of the ductility of material. The critical value for Pugh's ratio is equal to 1.75. If the ratio is lower than the 1.75, the material is brittle otherwise material is ductile. For the titled group of crystals, the Pugh's ratio B_H/G_H is calculated using two functionals (LDA and GGA) are listed in Table 5.6. The results received during the calculations with the LDA functional showed the larger values than with the GGA functional. For the studied crystals B_H/G_H ratio is between 4.12 (3.46) to 2.15 (1.86) for LDA (GGA) functional, respectively. All coefficients showed the value of B/G greater than the critical value 1.75. Therefore, all crystals of I-III-VI$_2$ group are of high ductility. The largest value of B/G ratio was estimated for AgGaTe$_2$ crystal (for LDA) and CuInTe$_2$ (for GGA).
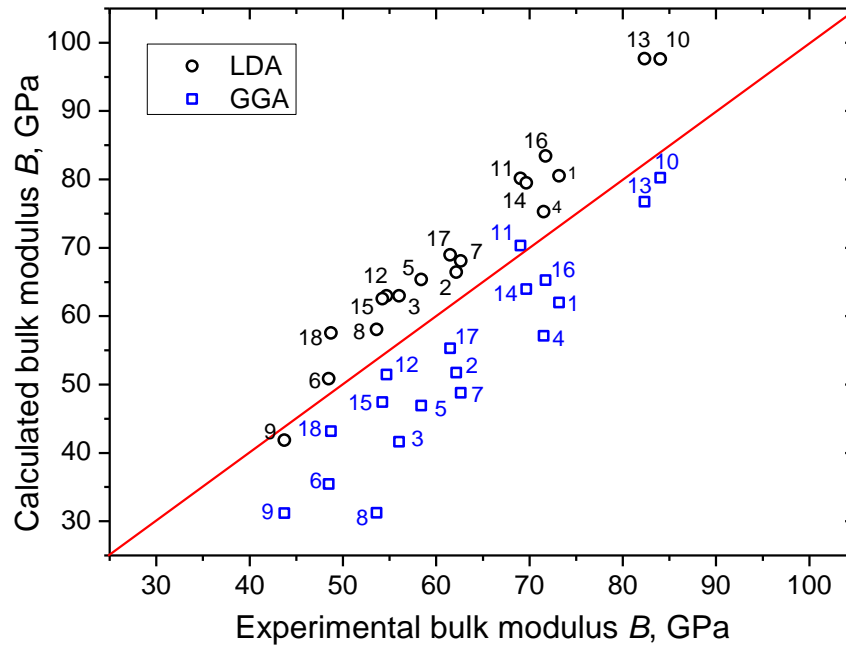
Figure 5.3. Comparison between experimental and DFT calculated bulk modulus of I-III-VI$_2$ chalcopyrites for LDA and GGA functionals.

In order to show the deviation of theoretically calculated bulk modulus values from experimental for I-III-VI$_2$ group of crystals, we plotted the dependence of calculated bulk modulus from the experimental on Fig. 5.3. As can be seen, the bulk modulus calculated with the LDA functional is slightly overestimated. At the same time, the GGA calculated values of *B* is underestimated. For two methods the calculated values show the near linear trend.

An important task in studying the properties of a material is to try to relate them to the structure or other characteristics of the material. The study of correlations can provide information about the structure-property and property-property relationship. For a more detailed analysis of the obtained values of the modulus of elasticity, we attempted to relate them to the crystal structure and other physical properties. Therefore, we constructed several dependences of the bulk modulus of the investigated crystals on other parameters of these crystals. Figure 5.4 shows the dependence of the modulus of elasticity for crystals of group I-III-VI$_2$ on the molar mass of crystals. In Fig. 5.4 a) is shown the results obtained when calculating using the LDA functional and in Fig. 5.5 b) with GGA functional. As can be seen from the figures, the bulk modulus tends to decrease with increasing molar mass of atoms in the crystal. This trend is present for both calculation methods. As can be seen, the change in the bulk modulus with the change in molar mass is almost linear.
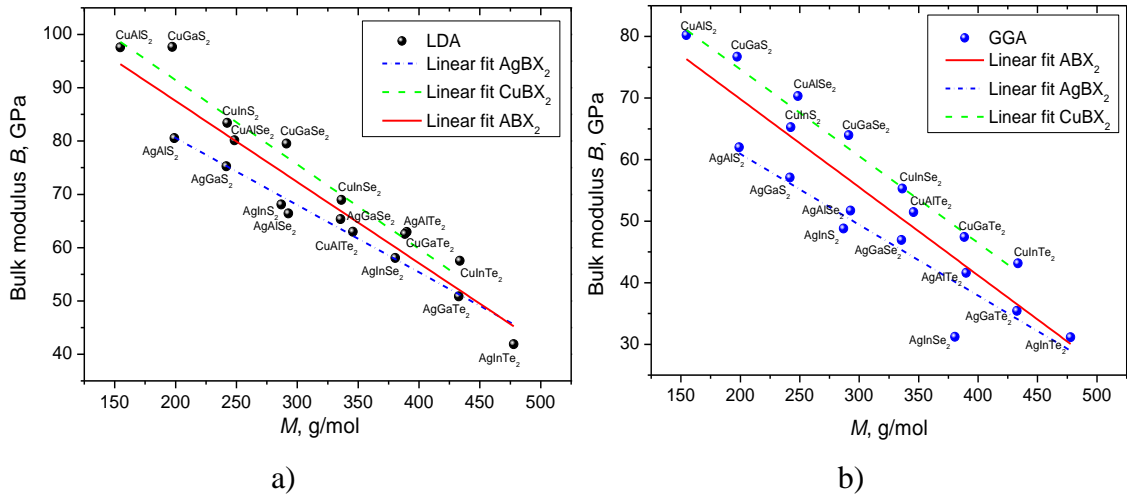
Figure 5.4. Regression plot of (a) Bulk modulus *B* (GPa) versus molar mass *M* for I-III-VI$_2$ compounds for a) LDA and b) GGA calculation.

All sets of crystals show the close to linear dependence. The linear regression analysis has been performer for *B* as function of molar mass *M*. The corresponding trend can be expressed by the formula $B = 117.971 - 0.152\,M$. The calculated Pearson's parameter is equal to $R = -0.943$. The calculated value indicates the strong negative correlation between the bulk modulus and molar mass. Additionally, we applied the linear regression method to two sets of atoms. The first one is the group of Ag bearing crystals, and second one is the Cu bearing compounds. For the Ag bearing crystals, the dependence is described by the following equations: $B = 105.792 - 0.126\,M$, $(R = -0.970)$ – for LDA, and $B = 83.946 - 0.115\,M$, $(R = -0.946)$ – for GGA. For the Cu bearing crystals following equations were estimated: $B = 123.088 - 0.158\,M$, $(R = -0.972)$ – for LDA, and $B = 102.855 - 0.140\,M$, $(R = -0.987)$ – for GGA. By the comparison of the Pearson's correlation parameters one can conclude, that *B*(*M*) dependence is stronger for two separate group of crystals (one with the Ag and other with the Cu ions) than when we consider a total group.

The next considered correlation is the bulk modulus dependence from the unit cell volume. On the Fig. 5.5. the *B*(*V*) plot was done for a) theoretical bulk modulus values versus the theoretical unit cell volume calculated with the LDA and GGA functional; b) experimental values of bulk modulus and unit cell volume. As one can see, the LDA calculated values has the higher values than the GGA, resulting in the higher position of calculated points. Two sets of data have the linear trend with the tendency to decreasing of the *B* value with the increasing of the unit cell volume. Applying the linear regression, the good description by the linear function of calculated data is shown. The Pearson' correlation

coefficients estimated for the theoretically calculated bulk modulus and volume of the unit cell are following: $R = –0.952$ for LDA and $R = –0.919$ for GGA functional. These values show the strong negative correlation of bulk modulus with the *V*. For the experimentally obtained data the calculated correlation parameter $R = –0.965$. From the obtained parameters, one can conclude, that theoretically obtained results correlates in good agreement with the experimental data.
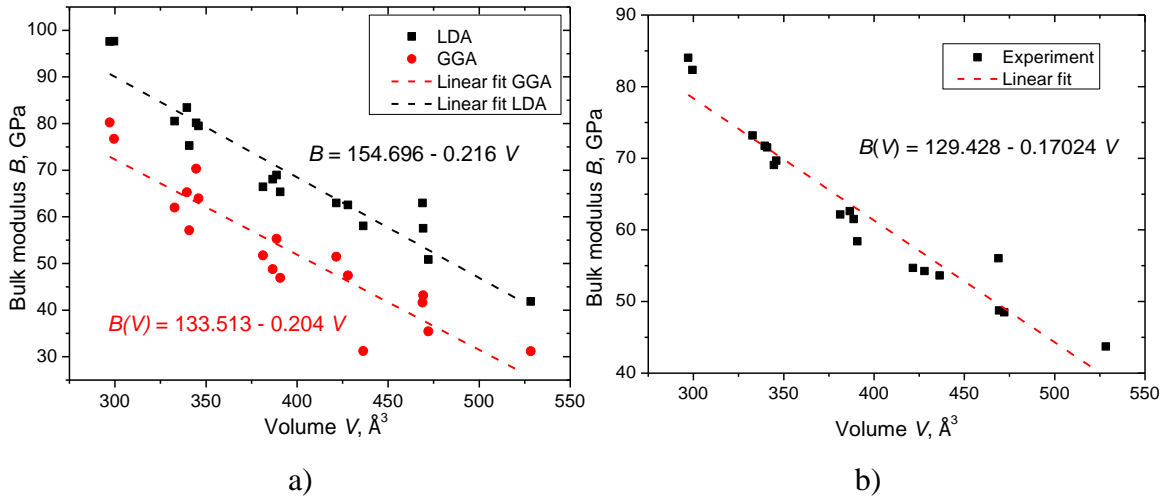
Figure 5.5. The volume dependence of bulk modulus *B* for LDA and GGA calculated (a) and experimental (b) results.
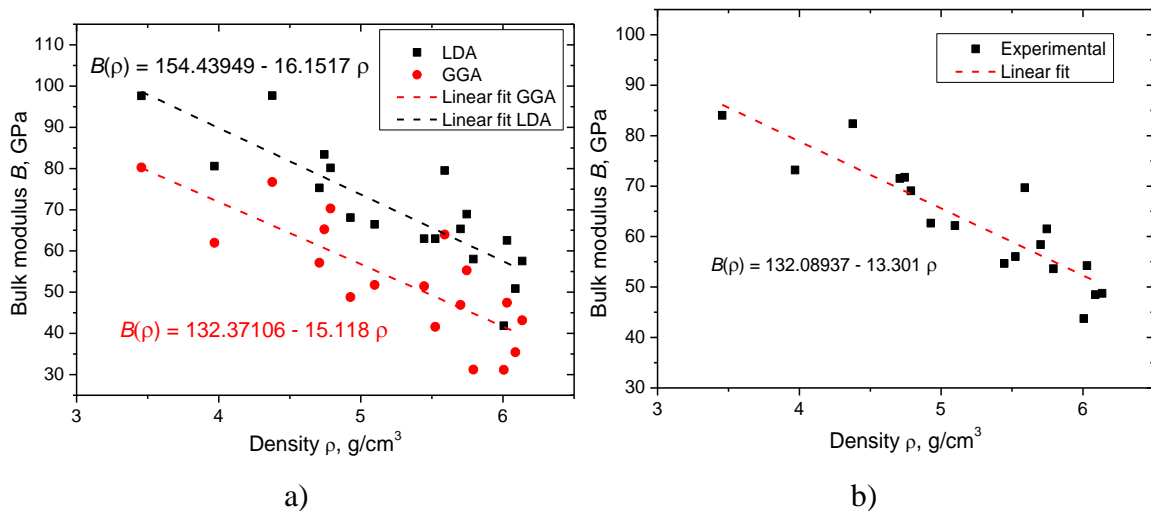
Figure 5.6. The density dependence of bulk modulus *B* for LDA and GGA calculated (a) and experimental (b) results.

In the Fig. 5.6 the crystal density dependence of bulk modulus is plotted for the I-III-VI$_2$ group crystals. The left panel (Fig. 5.6 a)) corresponds to the calculated with GGA and LDA

functional results while right panel (Fig. 5.6 b)) represents dependence of experimental results taken from literature. As can be seen from the figure, for both experimental and calculated data the similar behavior in observed. The increasing of the crystal density lead to the decreasing of B. The $B(\rho)$ dependence, similarly to $B(M)$ and $B(V)$, show the linear trend and can be described by the following equations: $B(\rho) = 154.43949 - 16.1517\,\rho$ for LDA functional, $B(\rho) = 132.37106 - 15.118\,\rho$ for GGA functional, and $B(\rho) = 132.08937 - 13.301\,\rho$ for the experimental data. As can bee sin from the figures, the $B(\rho)$ points has the higher deviation from the trend line compering to $B(V)$ dependence. These results also confirmed through the calculation of the Pearson's correlation parameters. For theoretical bulk modulus the correlation is described as $R = -0.808$ for GGA functional and $R = -0.845$ for LDA. Obtained from the experimental data $R = -0.895$ show the slight stronger negative correlation than the for theoretical.
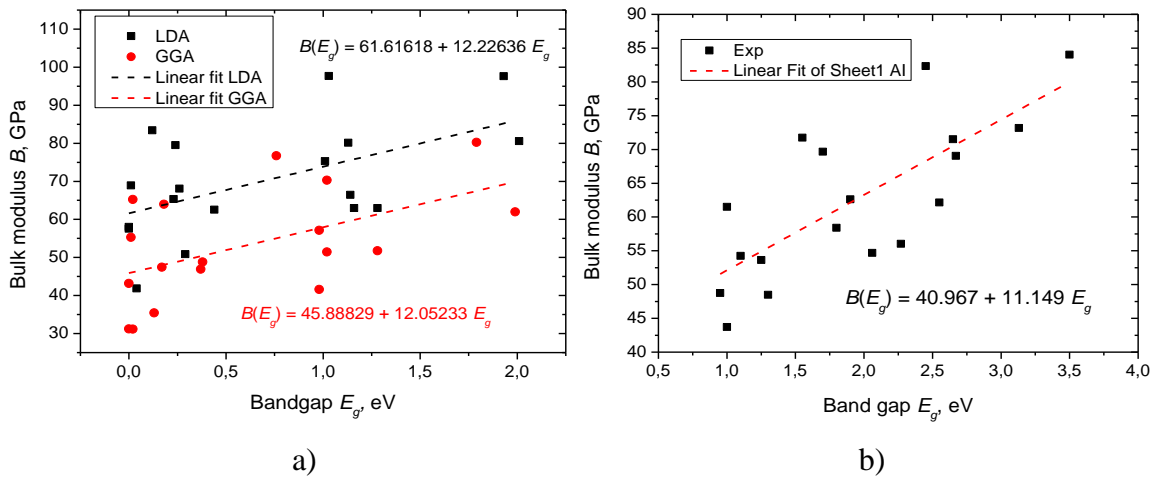
Figure 5.7. Bulk modulus as function of band gap value for LDA and GGA functionals.

The last one considered in this chapter dependence of bulk modulus is the band gap dependence of bulk modulus – $B(E_g)$. The experimental and theoretical dependences of $B(E_g)$ is shown on the Fig. 5.7. Using the linear regression method, the calculated and experimental data was fitted by the linear function. As a result, the following equations was obtained: $B(E_g) = 61.61618 + 12.22636\,E_g$ for calculation with LDA functional; $B(E_g) = 45.88829 + 12.05233\,E_g$ for calculation with GGA functional; $B(E_g) = 40.967 + 11.149\,E_g$ for experimental results. It is easy to see, that both theoretical and experimental data has much higher deviation from the linear dependence. As a confirmation of such deviation the correlation parameters was calculated. For the LDA functional $R = 0.549$, for GGA – $R = 0.531$, as well as $R = 0.753$ for the experimental data.

Calculated Pearson's correlation coefficients is lower than for relations discussed above. Those results indicate significantly lower correlation for $B(E_g)$ than for $B(M)$, $B(V)$ and $B(\rho)$. The general characteristics similar to all considered cases is that the experimental data has a slightly higher correlation than the theoretical data. Also, it should be mentioned that $B(E_g)$ has positive correlation while for other considered dependences correlation is negative.

5.2. Description of anisotropy of elastic properties of I-III-VI₂ crystals

5.2.1. Anisotropy of elastic properties of I-III-VI₂ crystals

As one can see from the Tables 5.3 to 5.6, the I-III-VI₂ crystal possesses the anisotropy of mechanical properties. As mentioned in the previous paragraph, the elastic constants for the studied group of compounds differ from each other, which is a consequence of the anisotropy of this material. The anisotropy of elastic properties is one important physical characteristic. It provides information about the features of chemical bonding in different directions of the crystal. Anisotropy is also associated with the formation and spread of microcracks in materials [152,235]. Particularly strong anisotropy of the material is significant under extreme conditions, such as high pressure. The study of the anisotropy of crystals of compounds as a method of continuing durability and mechanical stabilization and plays an important role in the design of devices and is mainly responsible for the appearance of microcracks in materials. It can be investigated from independent elastic constants by calculating anisotropic factors and constants. It is associated with anisotropy by plastic deformation and the behavior of microcracks in material. For the description of elastic anisotropy, several criteria have been developed to describe it. Anisotropy can be described by the universal anisotropy index A^U and indices that show shear and compression A_G, A_B.

To study the anisotropy of elastic properties, we calculated a set of coefficients that describe the degree of anisotropy of the crystal. In particular, the following three parameters were calculated and used as a measure of the shear anisotropy of the I-III-VI₂ crystals [236] (shear anisotropic factors):

$$A_1 = \frac{4C_{66}}{C_{11} + C_{22} - 2C_{12}} , \quad A_2 = \frac{4C_{55}}{C_{22} + C_{33} - 2C_{23}} , \quad A_3 = \frac{4C_{44}}{C_{11} + C_{33} - 2C_{13}} . \qquad (5.21)$$

Here A_1, A_2, and A_3 are the shear anisotropy factors for three directions (100) (010) and (001) of the shear planes, respectively. For structurally isotropic materials, factors A_1, A_2, and A_3 are equal to one. The deviation from the unit characterizes the degree of shear anisotropy of the material. For tetragonal symmetry of the crystal structure, by taking into account the symmetric peculearities and, as a consequence, the equality of elastic constants, these parameters take the following form

$$A_1 = \frac{2C_{66}}{C_{11} - C_{12}}, \quad A_2 = A_3 = \frac{4C_{44}}{C_{11} + C_{33} - 2C_{13}}. \tag{5.22}$$

The calculated values of parameters A_1 and A_2 are shown in Fig. 5.8.
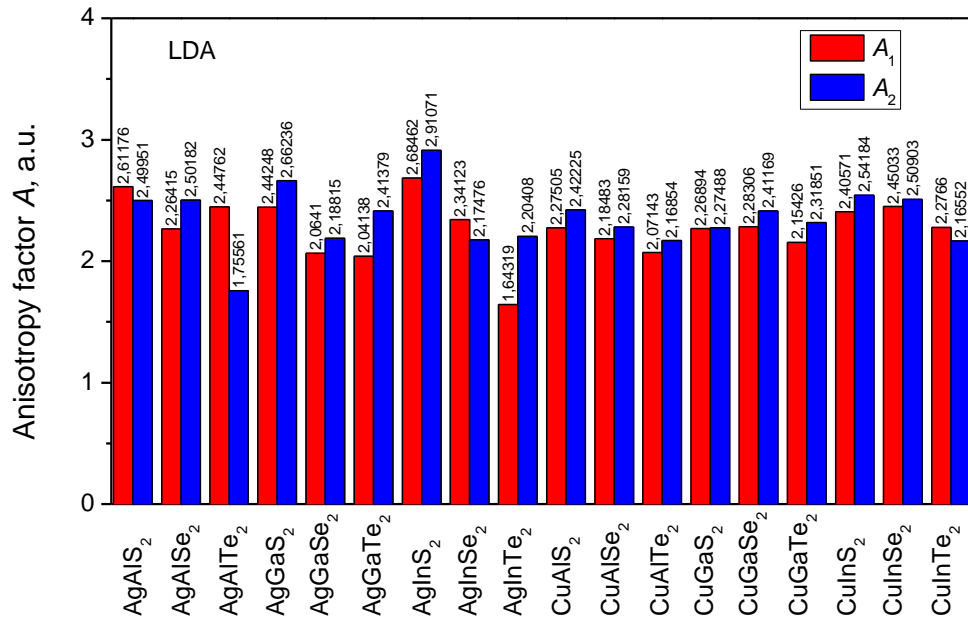
Figure 5.8. Calculated shear anisotropy factors A_1 and A_2 for I-III-VI$_2$ crystals with LDA functional.

The figure shows that the results of the calculation of shear anisotropy factors A_1 and A_2 for LDA and GGA methods are similar, although there are some differences for individual crystals.

The value of the coefficient A_1 is within $1.64 - 2.68$ for LDA and $1.32 - 3.2$ for GGA functionals. The A_2 shear anisotropy factors $1.75 - 2.91$ for LDA and $1.10 - 3.77$ for GGA. In general, as can be seen from the figure for most crystals, the coefficient A_2 is greater than A_1. However, for few crystals AgAlS$_2$, AgAlTe$_2$, and AgInSe$_2$ for LDA calculation as well as for AgAlS$_2$, AgAlTe$_2$, and AgGaTe$_2$ crystals for GGA calculation, the A_1 anisotropy factor is greater than the A_2.

From the analysis of the Fig. 5.8 one can conclude, that for some crystals the A_1 and A_2 indices decreasing during the Al → Ga → In and S → Se → Te isomorphic substitution. There are no strict behavior for all considered crystals.
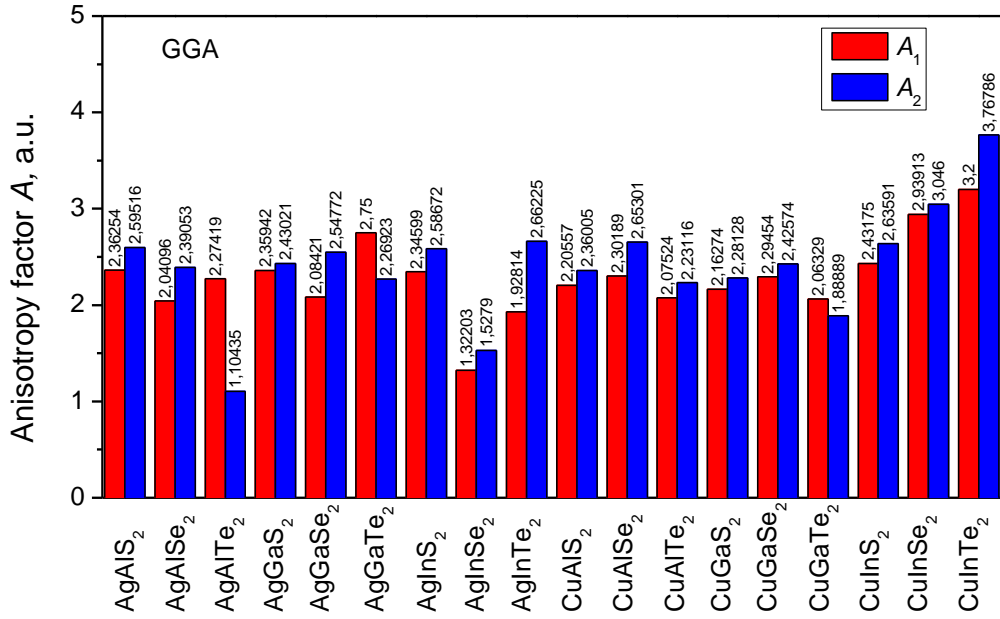
Figure 5.9. Calculated shear anisotropy factors A_1 and A_2 for I-III-VI$_2$ crystals with GGA functional.

The universal anisotropic index A^U, as well as the percentage of anisotropy in compression and shear (A_B and A_G) were also calculated for the I-III-VI$_2$ crystals. Another commonly used parameter for quantifying the anisotropy of elastic properties of materials is the universal anisotropy index A^U, was proposed by Ranganathan and Ostoja-Starzewski [237]. This index shows the general (universal) measure of anisotropy and includes the contribution of both the shear anisotropy G and the bulk anisotropy B. The more it deviates from zero the more pronounced is the elastic anisotropy of the crystal. The isotropy of the elastic properties described by the parameter A^U is represented by the 0 value, whereas the level of deviation from 0 means the degree of elastic anisotropy of the crystal. The A^U parameter can be calculated as follows

$$A^U = 5\frac{G_V}{G_R} + \frac{B_V}{B_R} - 6 , \qquad (5.23)$$

where B_V, B_R, and G_V, G_R are bulk and shear modulus in Voigt and Reuss approximation.

Other parameters for estimating the anisotropy of elastic properties are the factors of anisotropy of the bulk modulus A_B and the factor of anisotropy of the shear modulus A_G. Those factors can be evaluated using following equations:

$$A_B = \frac{B_V - B_R}{B_V + B_R},$$ (5.24)

$$A_G = \frac{G_V - G_R}{G_V + G_R},$$ (5.25)

where G_V and G_R is a shear modulus as well as B_V and B_R are a bulk modulus obtained using Voigt and Reuss scheme, respectively. In an isotropic case the Voigt and Reuss approximation should give the same values for B and G, respectively. Therefore, these indices are equal to zero. If the A_B or A_G anisotropy factors are equal to zero the material is isotropic for bulk and shear properties. If the A_B and A_G values equal to 1 the material is characterized by the maximum elastic anisotropy. Most often is used the A_B and A_G factors in percent (by multiplication of Eq. 5.24 and 5.25 by 100 %). Similar to the universal anisotropy index, the maximum value of A_B and A_G is 100 % and the minimum is 0 %, where zero means isotropy and 100 % represents the maximum of anisotropy.

On Figs. 5.10 – 5.12 is depicted calculated values of mechanical anisotropy factors and modulus of crystals belonging to the I-III-VI$_2$ group. Those results are shown for both LDA and GGA functional. As one can see, the bulk anisotropy factors A_B for all crystals is considerably small, indicating very low anisotropy of bulk modulus. Maximal value is 0.5 % AgInSe$_2$ crystal for GGA functional. For other crystals this anisotropy factor does not exceed 0.2 %. Such small anisotropy factor can indicate that for those crystals the spatial distribution of bulk modulus will have almost spherical shape.

As one can see from Fig. 5.11, the A_G factor of anisotropy, that corresponds to anisotropy of shear modulus G possess a significantly higher values than bulk anisotropy factor. The maximal value of this factor is 18.29 % for CuInTe$_2$ crystal. The smallest anisotropy is observed for AgAlTe$_2$ and AgInSe$_2$ crystals.

On the Fig. 5.12 the values of universal anisotropy index for studied compounds are shown. As one can see from diagrams, the intensity distribution of A^U values show very good similarity with the shear anisotropy factors. This fact is generally caused by very low values of A_B. Therefore, bulk modulus anisotropy contribution almost does not have strong effect on the A^U.
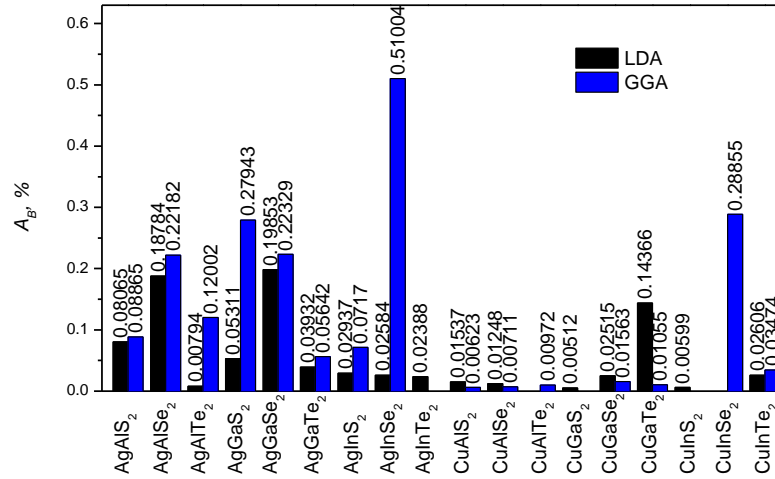
Figure 5.10. Calculated bulk anisotropy index A_B (in %) calculated for I-III-VI$_2$ group crystals with LDA and GGA functionals.
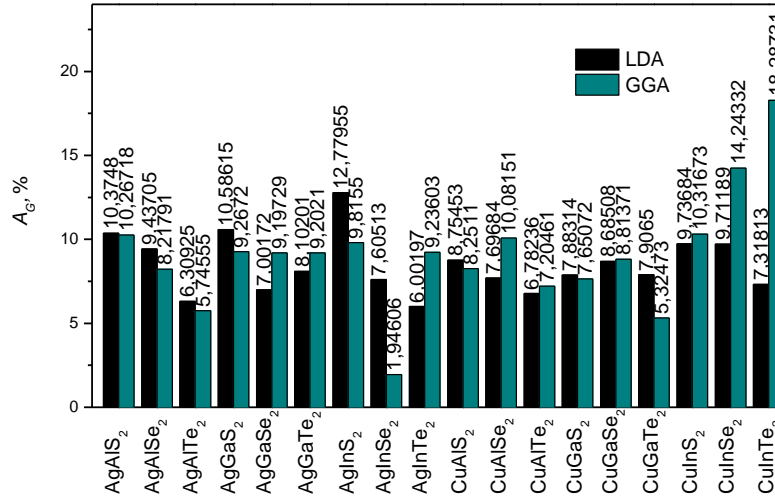
Figure 5.11. Calculated shear anisotropy index A_G (in %) calculated for I-III-VI$_2$ group crystals with LDA and GGA functionals.
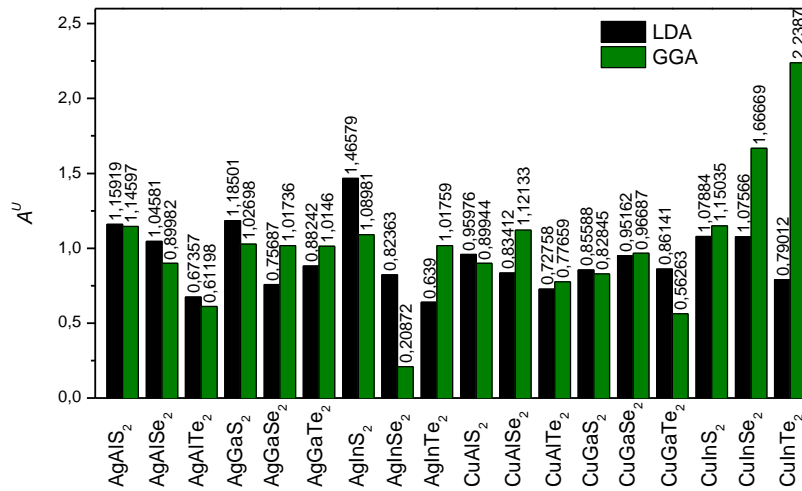
Figure 5.12. Calculated universal anisotropy index A^U calculated for I-III-VI$_2$ group crystals with LDA and GGA functionals.

5.2.2. Spatial distribution of the Young's modulus *E*, bulk modulus *B*, and shear modulus *G*

In addition to the calculation of various anisotropy modules and factors, one of the most popular and widely used methods to show the anisotropy of a material is the construction of three-dimensional (3D) surfaces for the value of the studied parameter. This method is often used to depict piezooptical, piezoelectric, gyration surfaces, etc. It is typically used to show the anisotropy of mechanical properties, such as the anisotropy of the Young's modulus *E*, the bulk modulus *B*, the shear modulus *G*, the Poisson's ratio. The construction of such 3D surfaces allows us to visualize the spatial distribution of the studied parameter, and clearly show how the elastic modules change in different directions in the crystal. In this section, we focus on mechanical parameters such as the Young's modulus *E*, bulk modulus *B*, and shear modulus *G*. The anisotropy for those parameters will be studied by the plotting of the 3D contours of mechanical moduli and planar projections for the studied group of chalcopyrite crystals.

For any crystal the Young's modulus value in the special direction can be obtained from the Eq. 5.26 [152]

$$S_{1111}^{'} = \sum_{n=1}^{3}\sum_{m=1}^{3}\sum_{p=1}^{3}\sum_{q=1}^{3} S_{nmpq} l_{1n} l_{1m} l_{1p} l_{1q} \, , \tag{5.26}$$

where S_{nmpq} is elastic compliance matrix elements, the l_{1n}, l_{1m}, l_{1p} and l_{1q} directional cosines of the new *x'* axis (or [100] direction) in the rotate coordinate system with respect to the original coordinates. The $S_{1111}^{'}$ value is equal to E^{-1}. The general form of the Eq. 5.26 depends on crystal symmetry.

The Eq. 5.26 allows to estimate the *E* value for any direction in the crystal. Taking into account the symmetry of crystal, the final equation for particular crystal's symmetry class can be derivate. Clearly, the exact equation for evaluating *S'*$_{1111}$ should be calculated for each crystal class, because the non-zero elements in the obtained elastic compliance matrix are dependent on crystal symmetry. Generally, simplified *S'*$_{1111}$ equation for the tetragonal symmetry, the directional dependence of Young's is given as:

$$\frac{1}{E} = S_{11}(l_1^4 + l_2^4) + (2S_{13} + S_{44})(l_1^2 l_3^2 + l_2^2 l_3^2) + S_{33} l_3^4 + (2S_{12} + S_{66}) l_1^2 l_2^2 \, , \tag{5.27}$$

where S_{ij} are the elastic compliance constants with using short Voigt notation, l_1, l_2 and l_3 are directional cosines cosα, cosβ and cosγ, respectively. The angles α, β and γ are set in

relation to [100] [010] [001] directions. In this work, we used a spherical coordinate system. Therefore, under spherical coordinates, the directional cosines can be represented by $l_1 = \sin\theta\cos\varphi$, $l_2 = \sin\theta\sin\varphi$, and $l_3 = \cos\theta$, where θ and φ is the polar and azimuthal angle in spherical coordinate system (see Fig. 5.13). Particularely, the uniaxial Young's modulus along the [100] (or [010], [001] and [110] directions are calculated by

$$E_{[100]} = E_{[010]} = \frac{1}{S_{11}}, \tag{5.28}$$

$$E_{[001]} = \frac{1}{S_{33}}, \tag{5.29}$$

$$E_{[110]} = \frac{4}{2S_{11} + 2S_{12} + S_{66}}. \tag{5.30}$$

a)   b)
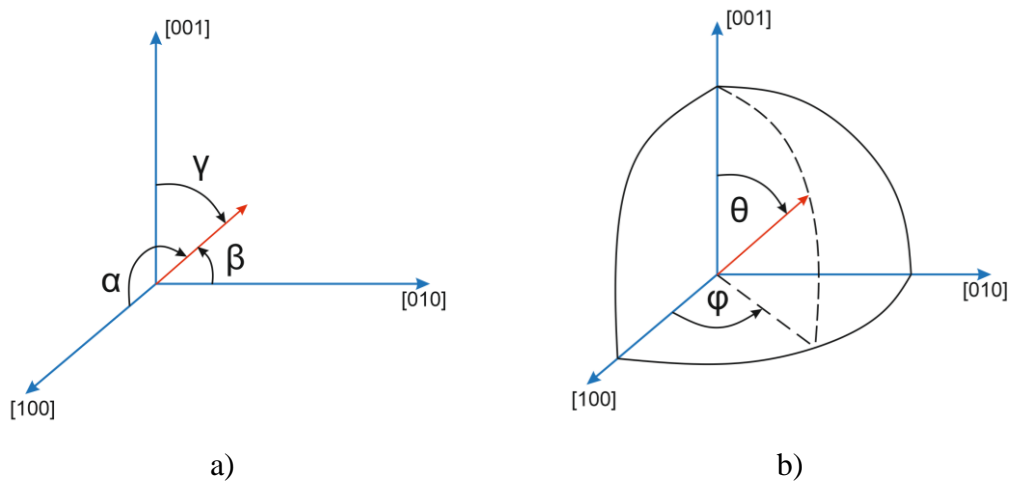
Figure 5.13. Coordinates system and Eulerian angles.

The 3D surface obtained using the Eq. 5.27 takes a spherical shape in a case of isotropic elastic properties. Deviation from the spherical shape indicates the elastic properties anisotropy. The more the surface differs from the spherical shape, the higher material anisotropy is. The degree of deformation of the extent of the sphere is closely related to the level of anisotropy.

The 3D surface plot of Young's modulus for group I-III-VI₂ of crystals shown in the Fig. 5.14. The spatial distribution of the Young's modulus was built using the elastic compliance S_{ij} constants collected in Table 5.4. As seen from the figure, Young's modulus for all crystals of titled group are far from the spherical shape. This fact indicates that the crystals is characterized by a significant spatial anisotropy of Young's modulus. It is shown that the all crystals belonging to the I-III-VI₂ group have anisotropic Young's modulus

owing to the deviation of elastic constants in different directions. Such has a strong dependence on the direction. Especially, the S-bearing crystals have more pronounced anisotropic Young's modulus which are in agreement with the A^U. Young's modulus E along the diagonal directions is the largest so indicates that highest stiffness. The largest anisotropy is observed for the crystals with light anions and with the substitution S → Se → Te decreasing of the anisotropy of Young's modulus is observed. Due to the symmetry of tetragonal crystals, the E values in [100] and [010] directions on (001) plane are exactly identical. Young's modulus only [110] direction is significantly higher than [100] or [010].

A detailed information on the anisotropy of Young's modulus can be obtained from the projections on crystal plains. The Young's modulus along a particular direction can also be used to display the strength of bonds in the corresponding orientations. Such projections give more detailed information about the spatial dependence of the Young's modules than the construction of the 3D surfaces.

The planar projections of Young's modules can be obtained from the Eq. (5.26). Therefore, representation in the crystallographic planes (100), (010), and (001) was shown. The equations for building of the planar projections of Young's modulus are constructed with following constraints:

1) (100) set $\theta = \pi/2$ and change φ.

2) (001) set $\varphi = \pi/2$, and change θ.

For the vizualization of Young's modulus along the different orienatation the (100) and (001) planes projection of Young's modulus are plotted (Fig. 5.14 b). As can be seen from the figure, the projections of Young's modulus show significant anisotropy. The projections of E in two crystallographic planes show the butterfly-shape contours. A similar behavior of the elastic moduli for other CP crystals (MZN₂ (M = Be, Mg; Z = C, Si)) was found in Ref. [238]. It indicates that the Young's modulus has distinct dependence on crystallographic orientation. The degree of this dependence on (001) plane is significantly stronger than in (100) plane.

Planar projection in the (001) crystal plane may be less polarized in different directions. Mohapatra and Eckhardt [239] found that the anisotropy of elastic modules is mainly influenced by off-diagonal elements from the complience matrix such as C_{15}, C_{25}, C_{35} i C_{46}.

As can be seen from Fig. 5.14, the anisotropy of the crystal in the (100) plane is greater than in the (001) plane. This behavior is observed for both the Young's modulus and the bulk modulus. The obtained results for the AgGaS₂ crystal using the LDA functional are

a) b)

AgAlS₂

a) b)

AgAlSe₂

a) b)

AgAlTe₂

a) b)

AgGaS₂

a) b)

AgGaSe₂

a) b)

AgGaTe₂

a) b)

AgInS₂

a) b)

AgInSe₂

a)   b)

AgInTe$_2$

a)   b)

CuAlS$_2$

a)   b)

CuAlSe$_2$

a)   b)

CuAlTe$_2$

a)   b)

CuGaS$_2$

a)   b)

CuGaSe$_2$

a)   b)

a)   b)

CuGaTe₂ CuInS₂

a) b) a) b)
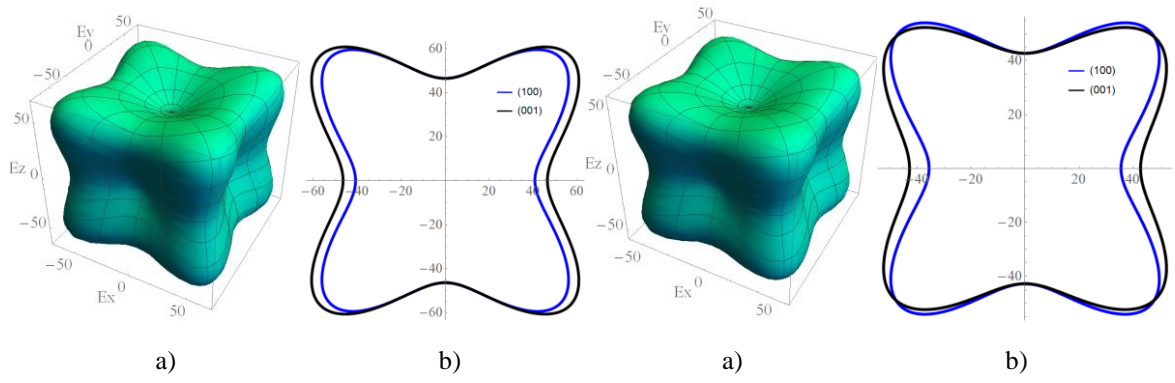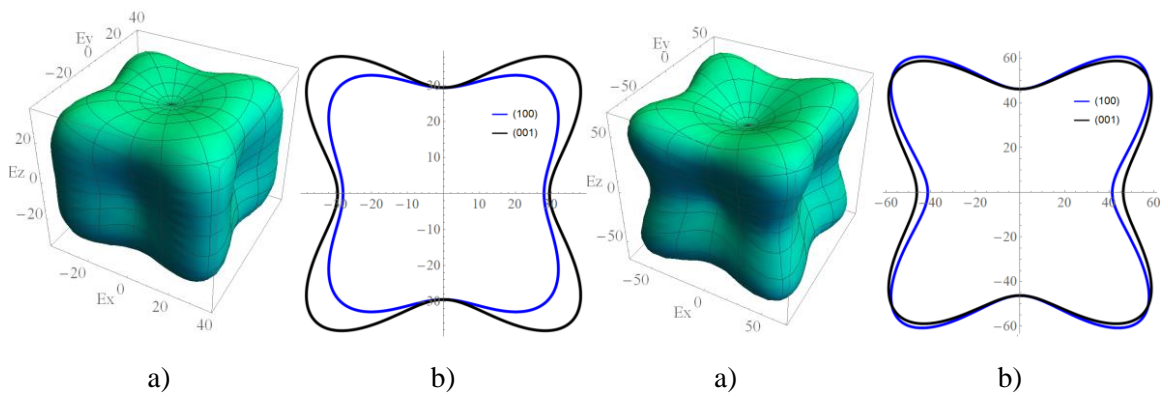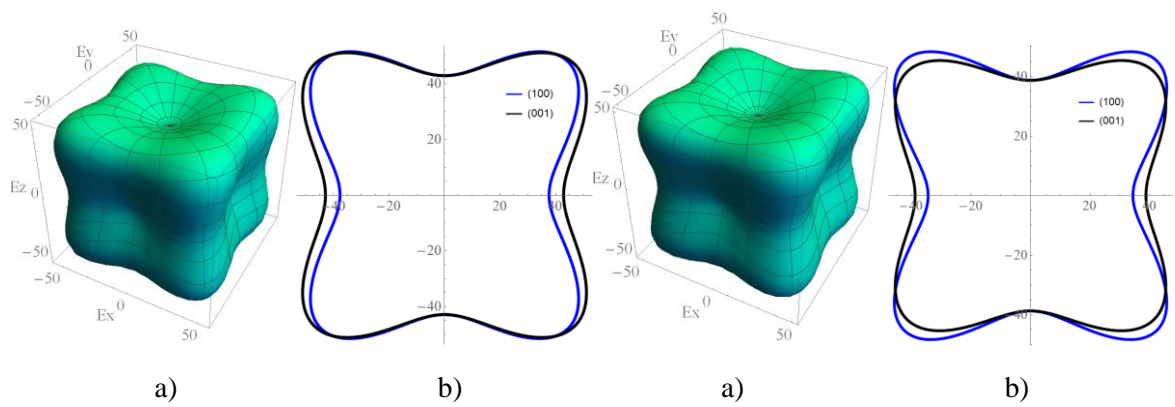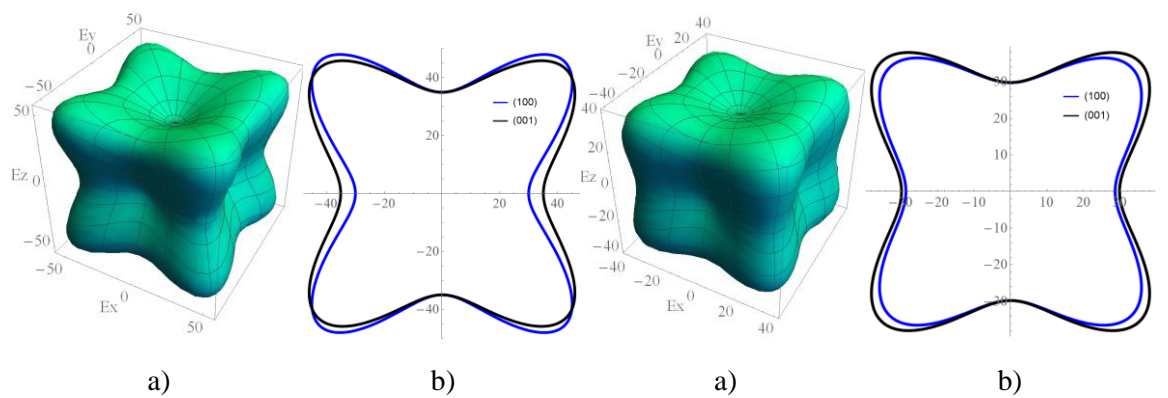
CuInSe₂ CuInTe₂
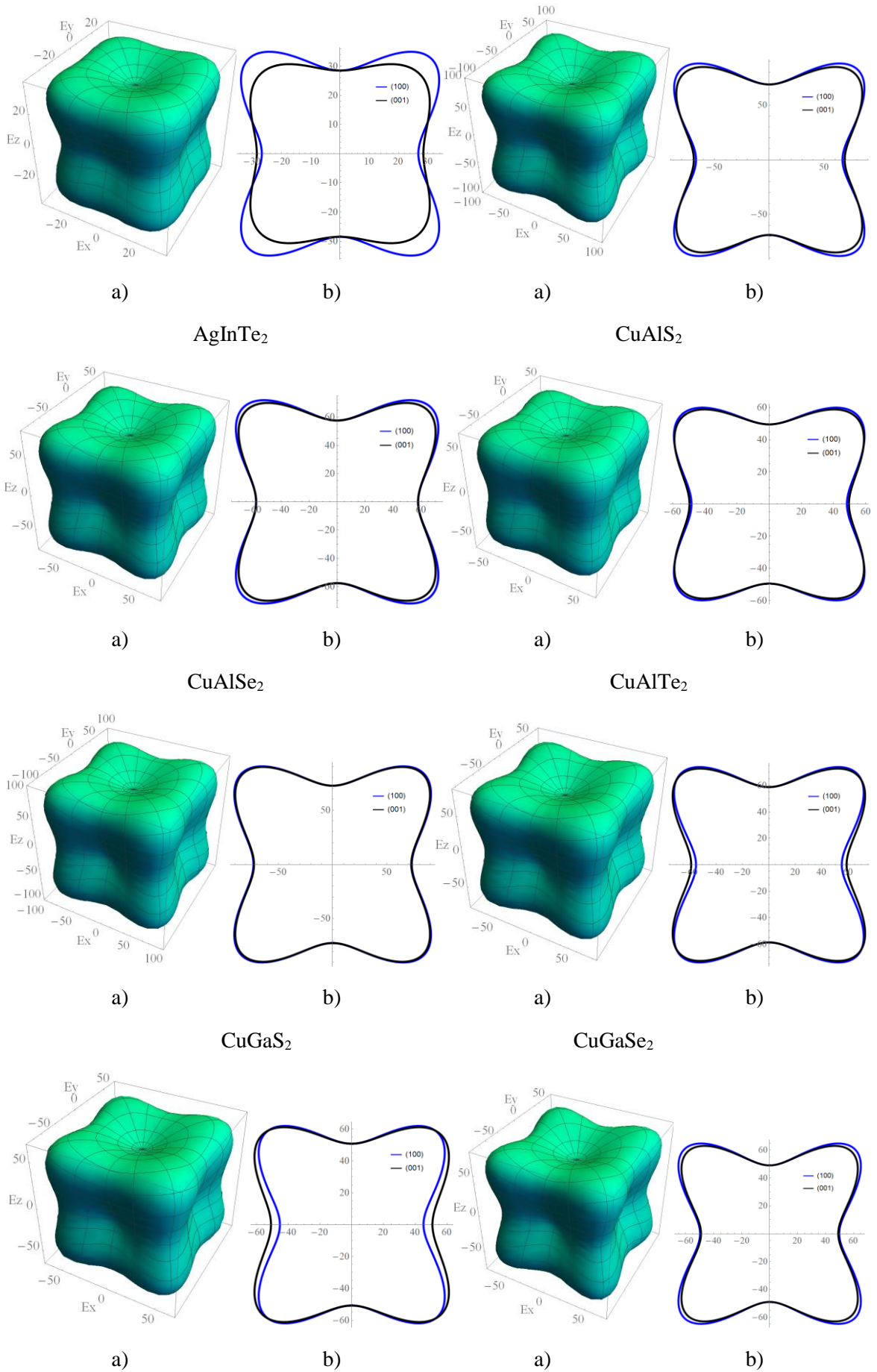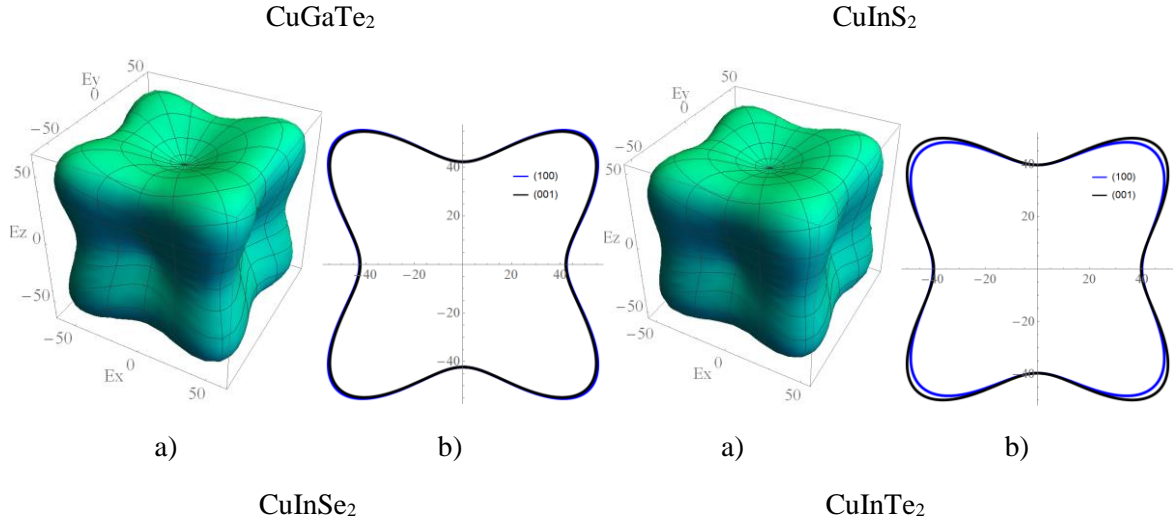
Figure 5.14. 3D surface representation of Young's modulus (*a*), (100) and (001) planar projections of the Young's modulus (*b*), of I-III-VI₂ group crystals plotted for the GGA-calculated elastic compliance coefficients.

qualitatively similar to the results obtained by the GGA method, so for brevity they are presented only for GGA results.

Similarly, to Young's modulus, we constructed the spatial distribution of the bulk modulus for the studied group of crystals. For tetragonal crystal class, the directional dependence of bulk modulus (*B*) are given by following relation:

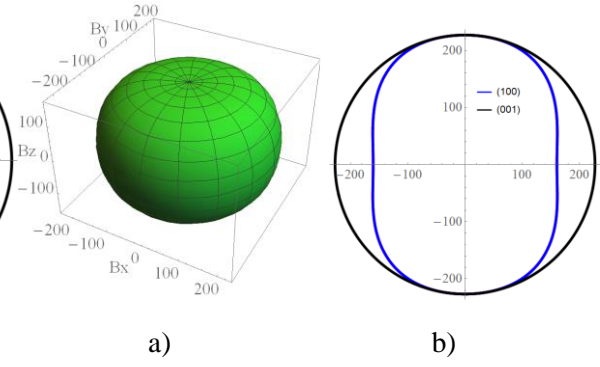$$\frac{1}{B} = (S_{11} + S_{12} + S_{13})(l_1^2 + l_2^2) + (2S_{13} + S_{33})l_3^2, \tag{5.31}$$

where S_{ij} are the elastic compliance constants, l_1, l_2 and l_3 are directional cosines in spherical coordinate system. The 3D surface obtained using the Eq. 5.31 takes a spherical shape in a case of isotropic elastic properties. Deviation from the spherical shape indicates the bulk modulus anisotropy. The three-dimensional distribution of the bulk modulus B are also constructed for the elastic constants S_{ij} calculated for I-III-VI₂ crystals in this work (see Table 5.8).

The spatial distribution of the bulk modulus is shown in Fig. 5.15. As seen from the figure, the crystals of studied group are characterized by an insignificant spatial anisotropy of bulk modulus B. For all studied crystals the shape of the 3D surface of B is very close to the sphere. This fact indicates that the bulk modulus for studied group of crystals exhibits almost isotropic behavior. As can be seen from the figure for all the studied crystals there is a slight tendency to change the shape of the surface. It consists in the fact that when replacing S → Se → Te in crystals containing silver, the figure is stretched along the *z*-direction. In

the crystals with the copper ions, on the contrary, the sphere is compressed along the *z*-direction.

For a more detailed analysis of the change in the bulk modulus, similarly to what was done for Young's modulus, a projection of the *B* on the planes (100) and (001) are constructed. Figure 5.15 b shows the corresponding projections of the modulus of elasticity for the studied crystals of the I-III-VI$_2$ group.

As can be seen from Fig. 5.15, for the crystals with the cation I = Cu, the projection of the bulk modulus *B*, in general, has anisotropy. Among these materials, the CuGaTe$_2$ crystals have a most pronounced anisotropy. In general, crystals I-III-Te$_2$ have a greater anisotropy than the crystals with the anion VI = S or Se. For all the crystals with copper, the following peculiarities can be distinguished. For the bulk modulus of the projection in the (001) plane show a circular shape, which indicates that in this plane, the module *B* is characterized by isotropic behavior for all crystals. Projection *B* in the (100) plane showed the anisotropy of the studied parameter. We can highlight the following characteristic feature. For crystals of CuAlS$_2$, CuAlSe$_2$, and CuGaS$_2$, and CuInS$_2$, a deviation from the circular shape of the projection of *B* modulus on the (100) plane is observed. This deviation has a form of stretching of the obtained contour in the direction [001]. The greatest stretching is observed for the CuAlS$_2$ crystal. For CuGaSe$_2$, CuGaTe$_2$, and CuInTe$_2$ crystals the deformation has the character of a circle compression along the polar [001] axe. For CuAlTe$_2$ and CuInSe$_2$ crystals, the projections in (100) and (001) planes are almost identical. This indicates a high degree of isotropy of the *B* modulus for these two crystals.

In comparison with crystals based on copper, the crystals with silver atoms as I-cation are characterized by a larger anisotropy of the bulk modulus *B*. As can be easily seen from Fig. 5.15 in the (001) plane the distribution of the value of the bulk modulus *B* is uniform, forming a projection in form of a circle. All crystals with silver atoms has this kind of projection in the (001) plane, which also indicates the isotropy of the properties in the [100] and [010] directions. Considering the projection on the (100) plane, it is easy to see that in the *x*-direction the projections for (100) and (001) planes coincide. For the projection on the (100) plane in the [001] direction there is a decreasing of the *B* value in comparison with the values in [100] and [010] directions. The smallest value of the anisotropy of the modulus *B* characteristic of the AgInTe$_2$ crystal is observed in the transition from compression in the [001] direction of the projection in the plane (100) to its stretching, similarly to the crystals with copper.

Similar to the Young's modulus and the bulk modulus, it is useful to study the anisotropy of the shear modulus G. 3D construction of the spatial distribution of the shear modulus G can be done using the following equation:

$$\frac{1}{G} = 2S_{11}(1-l_1^2)l_1^2 + 2S_{11}(1-l_2^2)l_2^2 + 2S_{33}(1-l_3^2)l_3^2 - 4S_{12}l_1^2l_2^2 - 4S_{13}l_1^2l_3^2 - 4S_{13}l_2^2l_3^2 + \\ +1/2S_{44}(l_2^2 + l_3^2 - 4l_2^2l_3^2) + 1/2S_{44}(l_1^2 + l_3^2 - 4l_1^2l_3^2) + 1/2S_{66}(l_1^2 + l_2^2 - 4l_1^2l_2^2)$$ (5.32)

where S_{ij} are the elastic compliance constants, l_1, l_2 and l_3 are directional cosines in spherical coordinate system. As in the previous cases, the spherical shape of the obtained surface corresponds to the isotropic material with respect to the shear action, while the deviation serves as a measure of its anisotropy. In Figure 5.16. the constructed three-dimensional surfaces of the spatial distribution of the shear modulus G for all crystals of the studied group are shown. The corresponding construction was performed for the calculated elastic compliance constants S_{ij} listed in Table 5.4 calculated using the GGA functional. The figure shows that the shape of the constructed surfaces of the shear modulus distribution is far from spherical. The obtained 3D surfaces are characterized by a flower-like shape. Considering the figures, we can see that the replacement of S → Se → Te, and Al → Ga → In leads to a more spherical shape of the spatial distribution of G. Also, the replacement of S → Se → Te reduces the value of the shear modulus.

In Figure 5.16 additional projections of the shear modules on the (100), (010), and (001) planes are given. It is easy to see that crystals with silver are characterized by a significant anisotropy of the shear modulus distribution for all three projection planes. The similarity of the projections on the (100) and (010) planes is observed, while for Young's modulus E and the bulk modulus B, the projections in these planes coincide for all crystals. The CuInTe$_2$ crystal has the smallest anisotropy.

The crystals with copper is characterized by a significant anisotropy of the shear modulus, similar to the crystals with silver atoms. There is also a slight decrease in the anisotropy at the substitution S → Se → Te. It should be noted that for crystals with copper there is a coincidence of projections in the (100) and (010) planes. A slight deviation in coincidence is observed for the CuGaTe$_2$ crystal. Also, the general feature of the spatial distribution of the shear modulus is that the maximum of the values corresponds to the directions of the axes in the crystals [100], [010], and [001]. Accordingly, the minimum value on the projections is characteristic of the angles multiples of θ and $\varphi = 45^\circ$ between the axes. This behavior indicates an inverse relationship between the Young's modulus and the shear modulus for crystals I-III-VI$_2$.
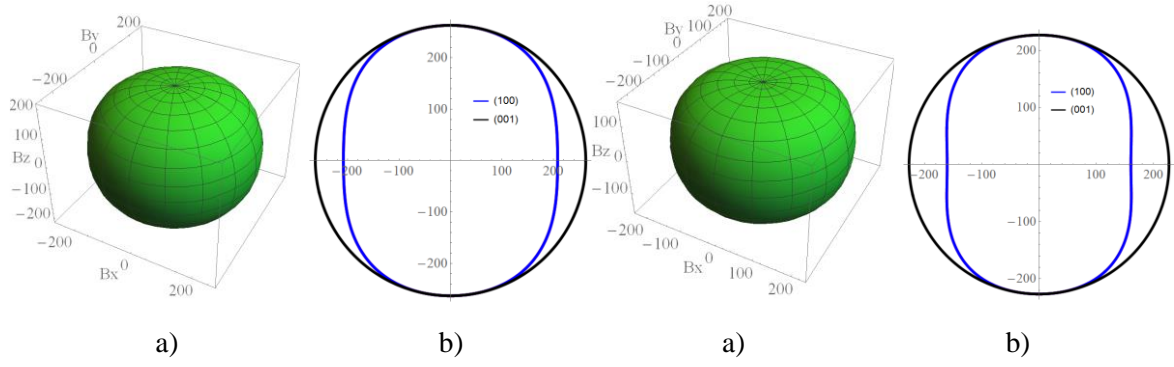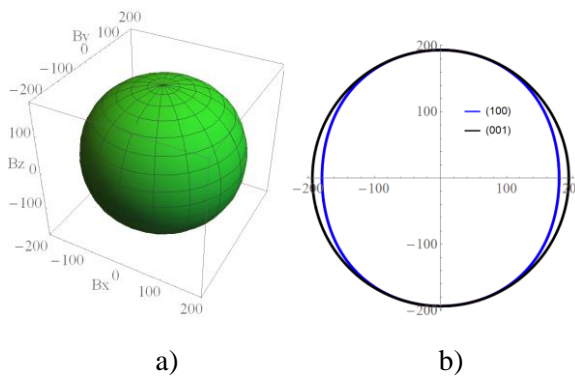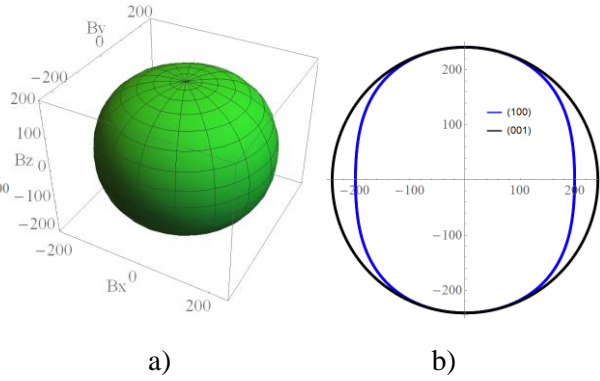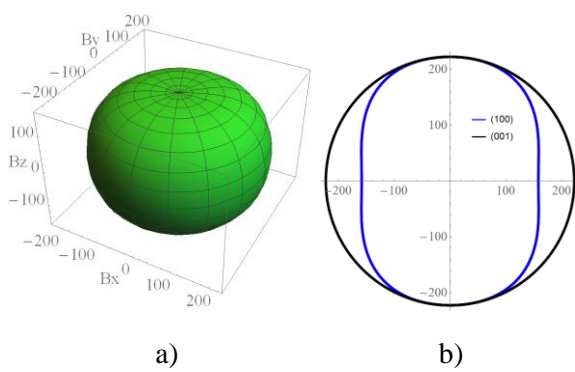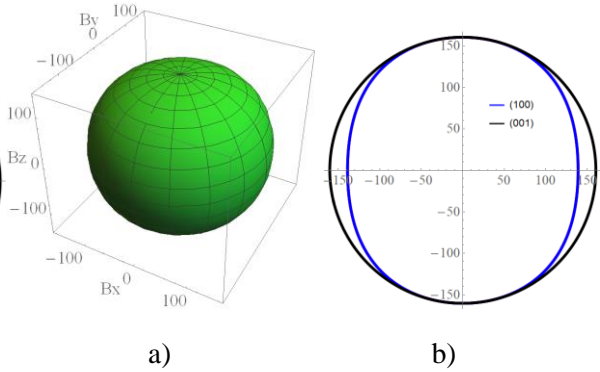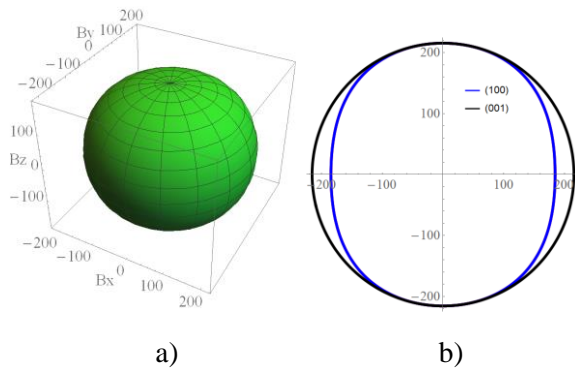
a)   b)   a)   b)

AgAlS$_2$ AgAlSe$_2$

a)   b)   a)   b)

AgAlTe$_2$ AgGaS$_2$

a)   b)   a)   b)

AgGaSe$_2$ AgGaTe$_2$

a)   b)   a)   b)

AgInS$_2$ AgInSe$_2$

a)   b)   a)   b)

AgInTe$_2$ CuAlS$_2$

a)   b)   a)   b)

CuAlSe$_2$ CuAlTe$_2$

a)   b)   a)   b)

CuGaS$_2$ CuGaSe$_2$

a)   b)   a)   b)

CuGaTe$_2$ CuInS$_2$

a) b) a) b)
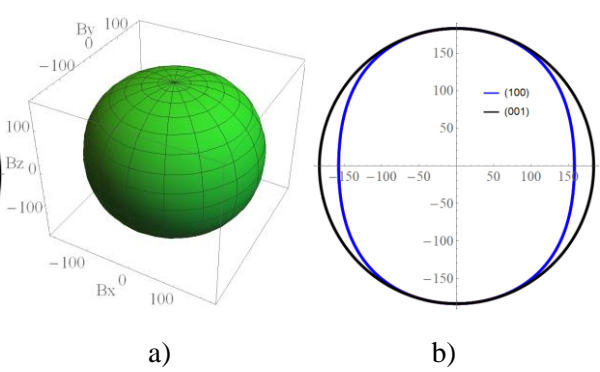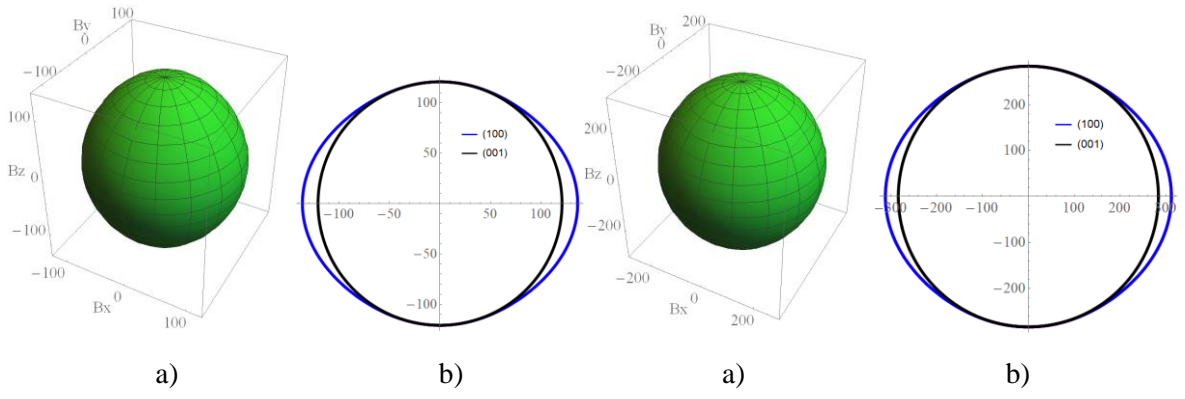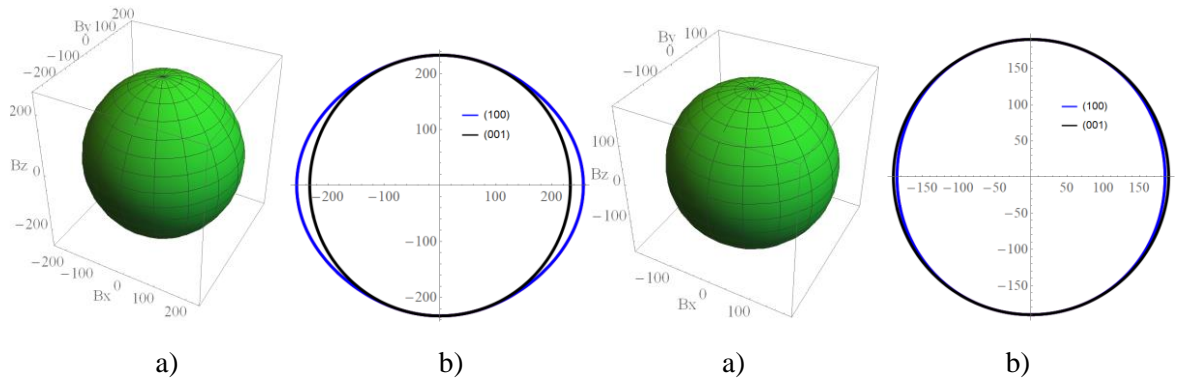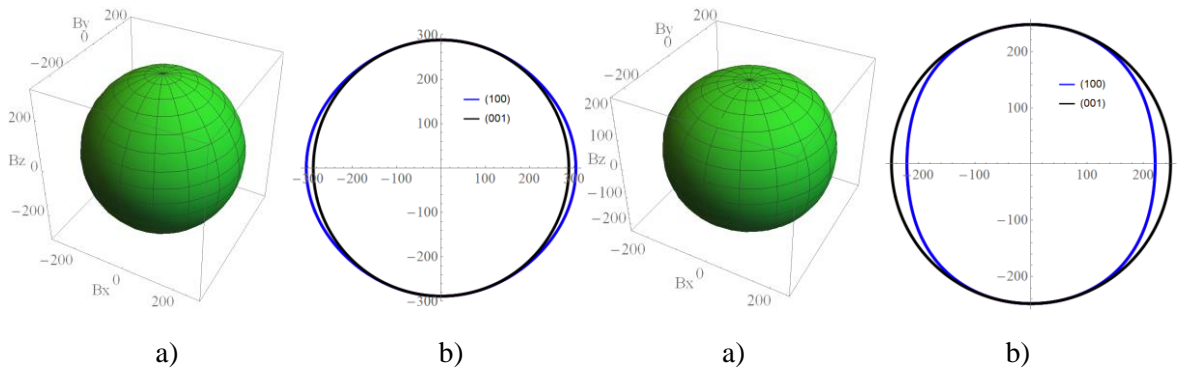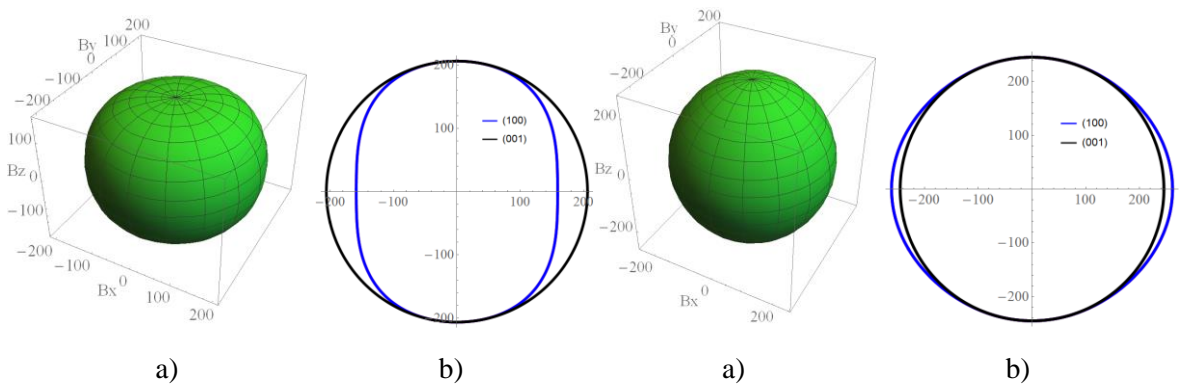
CuInSe$_2$ CuInTe$_2$
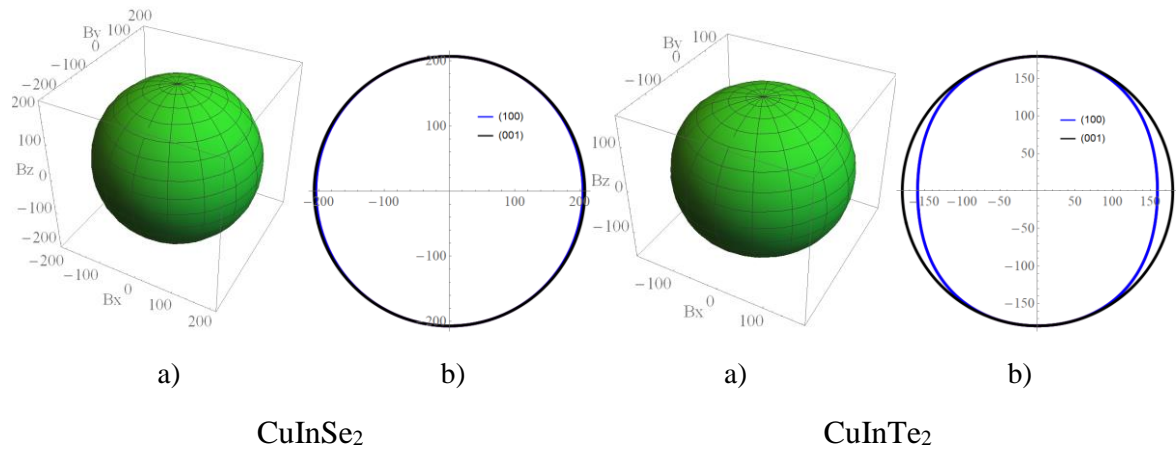
Figure 5.15. 3D surface representation of the bulk modulus B (a), (100) and (001) planar projections of the bulk modulus B (b) of I-III-VI$_2$ crystal plotted for the GGA-calculated elastic compliance.

a) b) a) b)

AgAlS$_2$ AgAlSe$_2$

a) b) a) b)

AgAlTe$_2$ AgGaS$_2$

AgGaSe₂

AgGaTe₂

AgInS₂

AgInSe₂

AgInTe₂

CuAlS₂

CuAlSe₂

CuAlTe₂

a)   b)   a)   b)

CuGaS$_2$ CuGaSe$_2$

a)   b)   a)   b)

CuGaTe$_2$ CuInS$_2$

a)   b)   a)   b)

CuInSe$_2$ CuInTe$_2$
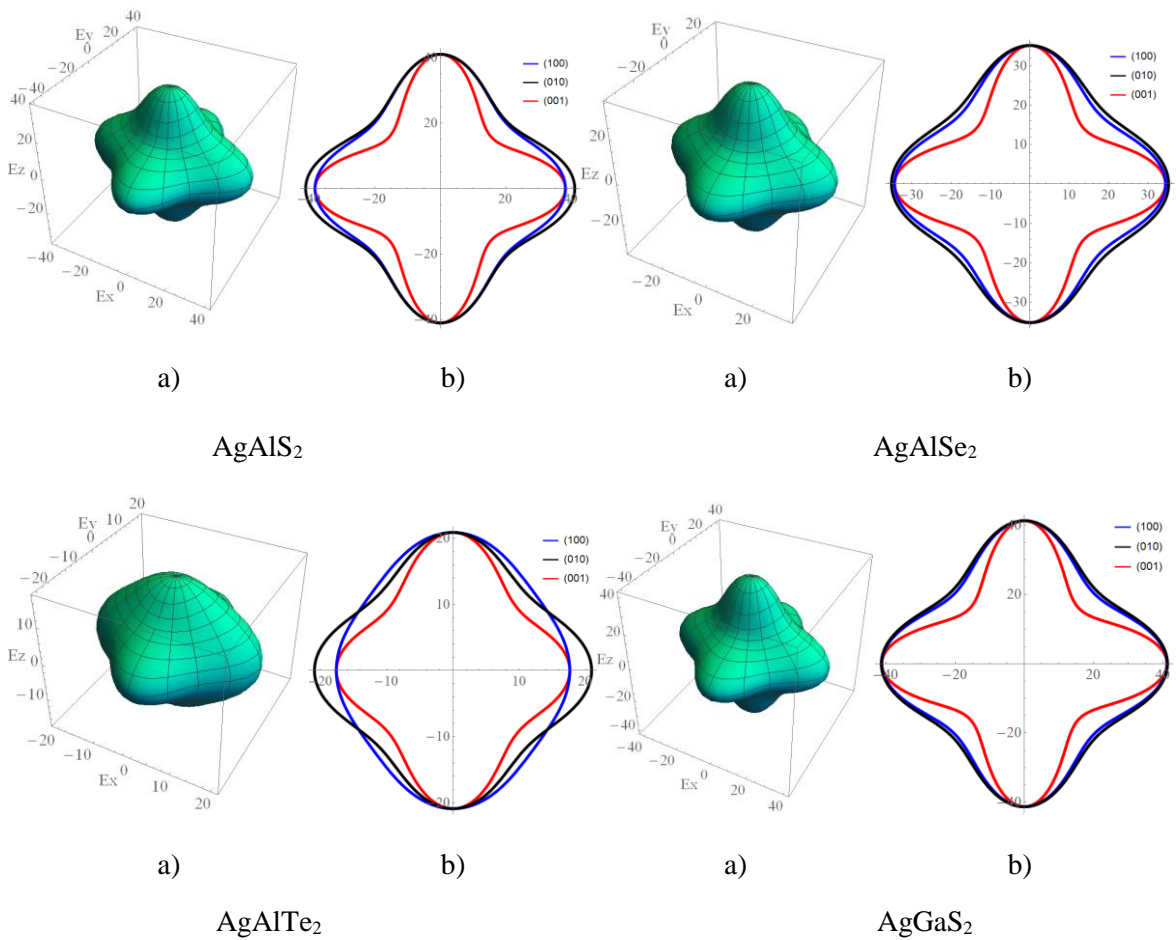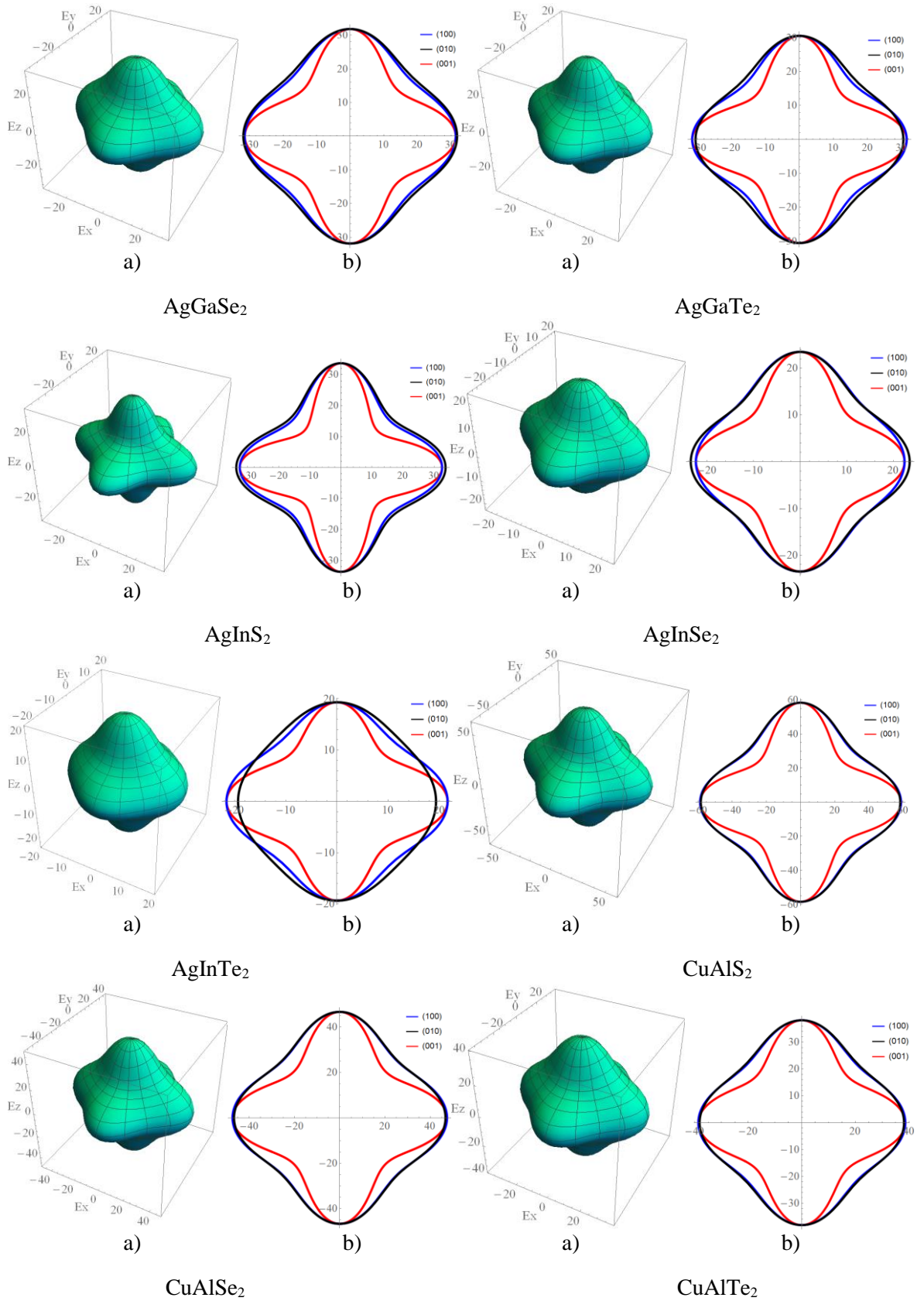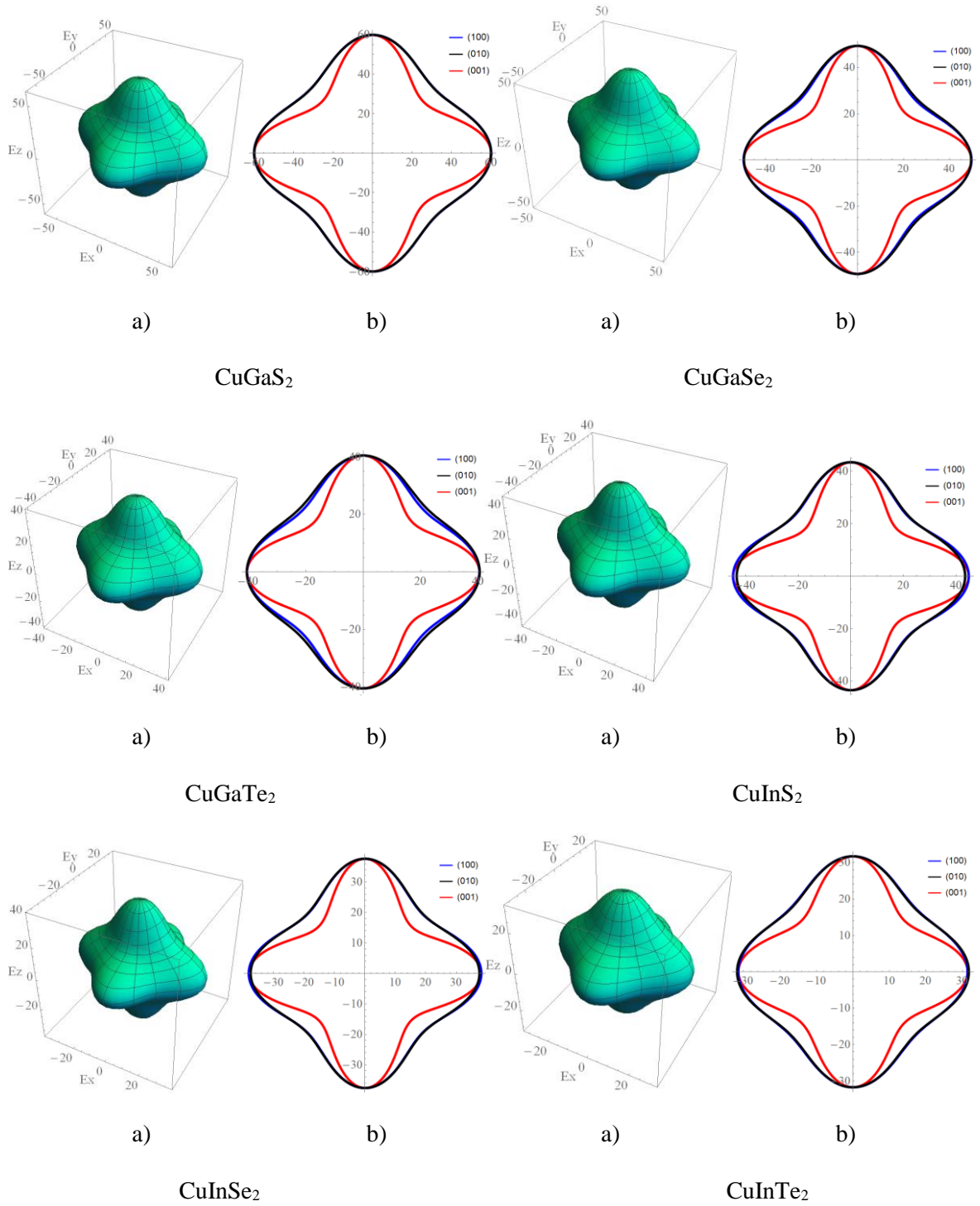
Figure 5.16. 3D surface representation of the shear modulus G (*a*), the (100) and (001) planar projections of the shear modulus (*b*), of I-III-VI$_2$ crystal plotted for the GGA-calculated elastic compliance.

5.2.3 Sound velocities propagation and Debye temperature in I-III-VI₂ group crystals

Study of the sound velocities in a crystal is an important part for asolid-state physics. Phonons are known to play an important role in many physical processes. Thay include electrical conductivity and thermal conductivity. It is known that the low thermal conductivities is known to be largely come from the interference between acoustic branches and the low-lying optical branches in rare-earth pyrochlores with a face-centered-cubic (fcc) crystal [240]. In a crystalline body, acoustic waves in any chosen direction have three vibrational modes. A one mode is longitudinal (LA) and the other two are transversal (TA). In an anisotropic medium there are only certain directions along which elastic waves can propagate in pure longitudinal and transversal modes. Experimentally acoustic methods are used for investigation of propagation of the acoustic waves [148].

It is also possible to estimate the acoustic waves propagation speed using the elastic constants C_{ij} obtained from the basic DFT calculations. In case of an anisotropic medium, the elastic properties change depending on the direction under consideration. Thus, connection of elastic constants with the acoustic wave velocities is markedly complicated. To correlate the parameters of a plane monochromatic wave running in the direction given by a single vector of the wave normal $n(n_1, n_2, n_3)$ with the density of the crystal and its elasticity tensor, the following expression is used:

$$\rho v^2 u_i = C_{ijkl} n_j n_l u_k ,\tag{5.33}$$

where ρ is a density of medium, V is a phase velocity ot the wave, C_{ijkl} is the elastic tensor, u_i is the displacements of points of the medium. The convolution of the elastic tensor on the components of the wave normal is called the Green-Christoffel tensor and is denoted as

$$\Gamma_{ik} = C_{ijkl} n_j n_l .\tag{5.34}$$

Thus, the system of equations (5.33) taking into account (5.34) can be written as

$$\begin{pmatrix} (\Gamma_{11} - \rho v^2) & \Gamma_{12} & \Gamma_{13} \\ \Gamma_{21} & (\Gamma_{22} - \rho v^2) & \Gamma_{23} \\ \Gamma_{31} & \Gamma_{32} & (\Gamma_{33} - \rho v^2) \end{pmatrix} \begin{pmatrix} u_1 \\ u_2 \\ u_3 \end{pmatrix} = 0 .\tag{5.35}$$

Here in Eq. (5.35) ρv^2 is the eigenvalue of the Green-Christoffel tensor, and u is its eigenvector. The system (5.35) will have a solution if its determinant is equal to zero:

$$\det\left[\Gamma_{ij} - \rho v^2 \delta_{ij}\right] u_j = 0 ,\tag{5.36}$$

where δ_{ij} is the Kronecker delta (when $i = j$, $\delta_{ij} = 1$ and when $i \neq j$, $\delta_{ij} = 0$).

The chalcopyrite crystals of group I-III-VI$_2$ are of tetragonal symmetry ($a = b \neq c$, and $\alpha = \beta = \gamma = 90°$). Therefore, using the form of matrix C_{ij} for them the Γ_{ij} components will take simple form:

$$\Gamma_{11} = C_{11}n_1^2 + C_{66}n_2^2 + C_{44}n_3^2 \,;$$

$$\Gamma_{22} = C_{66}n_1^2 + C_{11}n_2^2 + C_{44}n_3^2 \,;$$

$$\Gamma_{33} = C_{44}n_1^2 + C_{44}n_2^2 + C_{33}n_3^2 \,;$$

$$\Gamma_{12} = \Gamma_{21} = (C_{12} + C_{66})n_1 n_2 \,; \qquad (5.37)$$

$$\Gamma_{13} = \Gamma_{31} = (C_{13} + C_{44})n_1 n_3 \,;$$

$$\Gamma_{23} = \Gamma_{32} = (C_{13} + C_{44})n_2 n_3 \,,$$

where C_{ij} is the elastic constants, n_i are directional cosines. In the general case, the roots of Eq. (5.35) give 3 different values of acoustic wave velocities, which will correspond to three mutually perpendicular vectors u_1, u_2, u_3. (i.e. they have mutually orthogonal polarization vectors).

Unlike an isotropic medium, it is not possible to separate acoustic waves in a crystal, in the general case, into longitudinal and transverse ones, because the directions of oscilation, as a rule, do not coincide with the direction of wave propagation and are not orthogonal to it. A wave whose oscillating displacement vector is the smallest angle with the direction of propagation $n(n_1, n_2, n_3)$ is called a quasi-longitudinal QL. The other two waves of the direction of oscillation in which are almost perpendicular to the direction of propagation $n(n_1, n_2, n_3)$ are quasi-longitudinal QTs, which are often further classified by the magnitude of the phase velocity, distinguishing fast FT and slow ST quasi-transverse waves.

However, in crystals there are so-called special directions associated with the elements of symmetry. The axes of symmetry and the directions perpendicular to the planes of symmetry are longitudinal normals (the direction along which a purely longitudinal wave propagates). For axes of higher orders (3, 4, 6) the velocities of both transverse waves coincide and these axes are longitudinal acoustic axes. All directions lying in the plane of symmetry and in the planes perpendicular to the axes of symmetry of paired order (2, 4, 6) are transverse normals (one purely transverse wave along the direction of propagation), and the polarization QL and QT is geometrically indented. Also, the orientation of the longitudinal and transversal normals and acoustic axes may not be related to the direction of

high symmetry. For example, in triclinic crystals there are necessarily longitudinal normals and acoustic axes.

The anisotropy of the elastic properties of crystals of tetragonal symmetry, as mentioned in Section 5.1, characterizes 6 independent components of the elasticity tensor. The solution of Eq. (5.34) and (5.35) for the vectors of the wave normal [100] [110] [001] of such crystals has the following form:

direction [100]:

$$v_1 = \sqrt{C_{11}/\rho}$$ – longitudinal wave;

$$v_{t1} = \sqrt{C_{44}/\rho}$$ – transversal wave, polarization [001];

$$v_{t2} = \sqrt{C_{66}/\rho}$$ – transversal wave, polarization [010];

direction [110]:

$$v_l = \sqrt{C_{11} + C_{12} + C_{66}/2\rho}$$ – longitudinal wave;

$$v_{t1} = \sqrt{C_{44}/\rho}$$ – transversal wave, polarization [001];   (5.38)

$$v_{t2} = \sqrt{(C_{11} - C_{12})/2\rho}$$ – transversal wave, polarization $[1\bar{1}0]$;

direction [001]:

$$v_1 = \sqrt{C_{33}/\rho}$$ – longitudinal wave;

$$v_{t1}\sqrt{C_{66}/\rho}$$ – transversal wave, polarization [100];

$$v_{t1}\sqrt{C_{66}/\rho}$$ – transversal wave, polarization [010],

here ρ is a density of the material. The density of the I-III-VI₂ crystals was calculated from the structureal data.

As a result of theoretical modeling, the elastic constants of crystals of group I-III-VI₂ were used to calculate the velocities of longitudinal and transversal acoustic waves in different crystallographic directions in an anisotropic crystalline medium. The calculation of the phase velocities v of acoustic vibrations was performed using a set of equations (5.38) obtained by solving the system of equations (5.36) for the corresponding vectors of wave normal.

The results of calculation of the acoustic waves propagation speed are collected in Table 5.7. The calculations were performed for two types of functionals describing the exchange-correlation interactions (LDA and GGA). The results obtained with the LDA functional give values of the acoustic wave velocity greater than those obtained with the

GGA functional $v_{LDA} > v_{GGA}$. This trend is observed for all directions of wave propagation and their polarizations. This feature is due to the difference in the coefficients of elasticity for these methods. As can be seen from the table, both transverse and longitudinal sound waves in the I-III-VI$_2$ crystal propagate with considerably different speeds. From the table we also can see that for different directions of propagation of the acoustic waves, the speed of sound of the longitudinal wave satisfies the following inequality $v_{[110]} > v_{[100]} > v_{[001]}$. For transverse waves, the equality of velocities with polarization [001] is observed when propagating along [110] with the speed of sound for the [001] polarization during the propagation along [100] direction, and the speed of sound [010] polarized wave for the [100] direction with the [100] = [010] polarization for the [001] propagation direction. The highest speed of sound propagation for crystals is observed for the direction of propagation [110] for longitudinal polarization [110]. The highest velocity is inherent in the CuAlS$_2$ crystal which is 6855.3 m/s (6319.5 m/s) for the calculations with LDA (GGA) functional, respectively. In the crystals with silver, the highest speed of sound propagation is for AgAlS$_2$ crystals. The corresponding value is equal to 5757.3 m/s (5195.0 m/s) for the calculations with LDA (GGA) functional, respectively. The lowest speed of propagation of acoustic waves in AgInTe$_2$ crystals, which is equal to 1331.9 m/s (1179.1 m/s) and in the CuInTe$_2$ crystal 1516.0 m/s (1009.4 m/s) for LDA (GGA) functional, respectively.

In addition, for chalcopyrite crystals from the calculated data, it is possible to identify general patterns of changes in phase velocities when moving along the series. In particular, it was found that crystals in the structure of which are copper atoms have higher phase velocities of plane waves than crystals in which the cation is silver ions. For crystals with copper atoms, the phase velocity of acoustic waves for both longitudinal and transverse waves decreases during the replacement of the group III Al → Ga → In cation. This dependence is observed for all anions of group VI. When replacing the anion S → Se → Te, a decrease in the speed of sound is also observed. For crystals containing silver atoms, the speed of sound propagation decreases with increasing anion mass (S → Se → Te). The transition from Al → Ga → In similarly leads to a decrease in the velocity for L and T polarizations, similarly to crystals with Cu atoms.

The connection between the calculated longitudinal, transverse and average sound velocities (V_m) for I-III-VI$_2$ compounds shown in Fig. 5.17. In the figure 5.17. is shown the calculated average velocities obtained from LDA and GGA functionals. Both graphics are very similar. As can be seen form figures, the average value V_m in [110] direction is larger than in [100] and [001] directions for most of the crystals.
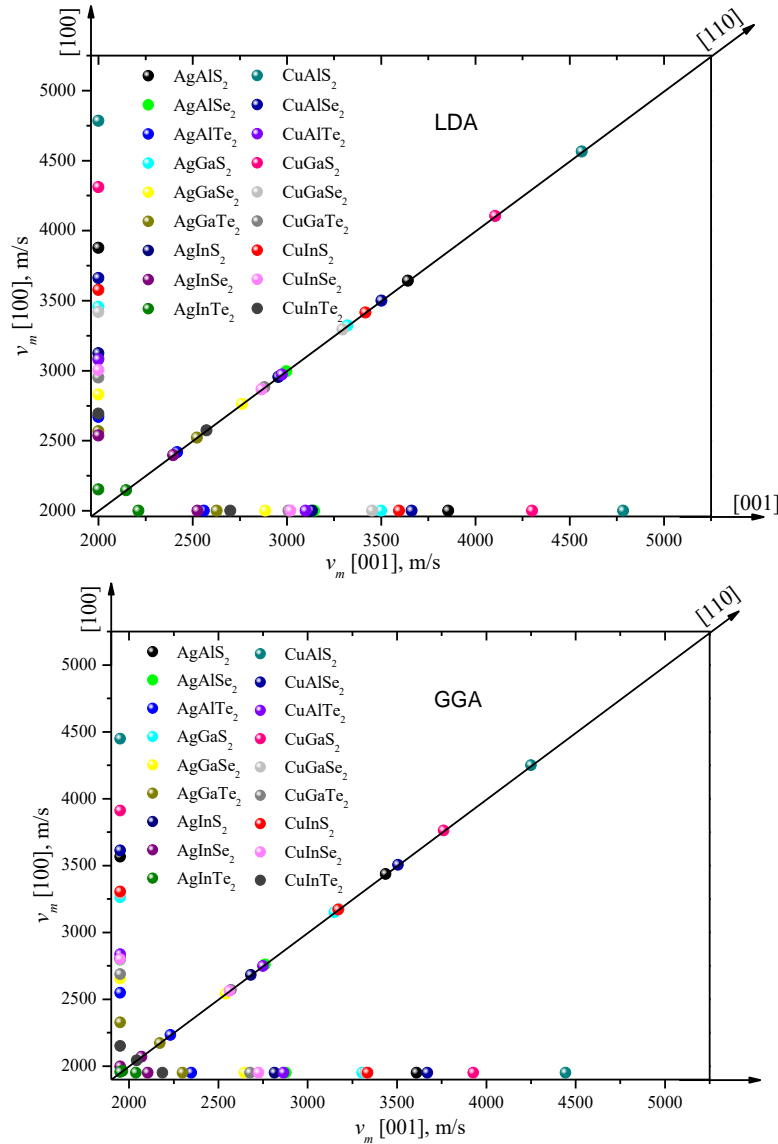
Figure 5.17. The average sound velocities v_m in the [100], [110], and [001] directions of I-III-VI$_2$ group crystals.

To estimate the anisotropy of the speed of acoustic waves in single crystals often use the so-called percentage anisotropy index *A*:

$$A = \frac{V_{max} - V_{min}}{\frac{1}{2}(V_{max} + V_{min})} \times 100\% , \qquad (5.23)$$

where V_{max} and V_{min} are the maximal and minimal values of sound speed in the single crystal, respectively. For any crystal from studied group of compounds the percentage anisotropy index was calculated using the Eq. 5.23. The values of calculated indices *A* for the sound velocity of I-III-VI$_2$ crtystals ate collected in the Table 5.7. As can be noted, the sopund propagation velocity for all crystals show the significant anisotropy. For those crystals the percentage anisotropy index *A* is in the range from 71 to 105 %.

Table 5.7. The sound velocities v (m/s) and anisotropy of sound velocity A (in %) of I-III-VI$_2$ crystals obtained using LDA / GGA calculations results.

Propagation direction	Polarization	AgAlS$_2$	AgAlSe$_2$	AgAlTe$_2$	AgGaS$_2$	AgGaSe$_2$	AgGaTe$_2$	AgInS$_2$	AgInSe$_2$	AgInTe$_2$	CuAlS$_2$	CuAlSe$_2$	CuAlTe$_2$	CuGaS$_2$	CuGaSe$_2$	CuGaTe$_2$	CuInS$_2$	CuInSe$_2$	CuInTe$_2$
[100]	[100](L)	5123.0/4616.1	4178.4/3773.8	3736.3/3271.2	4575.9/4172.9	3931.0/3334.7	3400.8/2845.9	4163.5/3593.0	3542.7/2920.3	3031.7/2650.7	6132.5/5638.5	4734.3/4526.8	4003.9/3656.3	5498.2/4953.8	4414.0/4065.9	3846.7/3390.6	4734.3/4260.8	3940.4/3448.0	3549.7/2903.0
	[010](T)	3344.1/3138.2	2657.4/2421.9	2157.1/2259.6	2965.1/2939.9	2376.5/2282.4	2205.1/2082.5	2661.6/2375.5	2065.0/1641.1	1707.0/1637.3	4092.7/3859.8	3103.1/3192.7	2631.1/2465.4	3699.6/3396.9	2966.9/2939.6	2592.0/2325.5	2979.4/2841.8	2537.8/2425.6	2287.5/1805.6
	[001](T)	3101.1/3073.3	2597.7/2438.0	1785.1/1516.4	2957.9/2803.1	2346.8/2320.5	2274.8/1969.0	2572.4/2475.9	1966.5/1753.0	1896.4/1829.4	4124.3/3833.5	3146.6/3289.4	2662.4/2472.8	3702.7/3430.4	2975.9/2960.8	2588.8/2314.8	3073.5/2904.1	2578.6/2302.6	2262.4/1854.6
[110]	[110](L)	5757.3/5195.0	4626.2/4151.3	4088.0/3682.6	5111.8/4732.1	4285.4/3718.9	3747.8/3295.3	4666.9/4018.4	3872.2/3030.6	3214.3/2883.9	6855.3/6319.5	5256.9/5124.1	1828.1/1711.4	6155.0/5544.7	4942.7/4626.7	4289.2/3779.3	5253.6/4786.3	4397.5/3971.2	3941.4/3266.3
	[1-10](T)	2069.3/2041.7	1766.1/1695.2	1378.8/1498.4	1897.2/1913.9	1654.2/1581.0	1543.4/1255.8	1624.4/1550.9	1349.6/1427.3	1331.6/1179.1	2713.4/2599.0	2099.4/2104.4	1828.1/1711.4	2456.1/2309.8	1963.5/1940.6	1766.0/1619.0	1920.9/1822.3	1621.2/1414.8	1516.0/1009.4
	[001](T)	3101.1/3073.3	2597.7/2438.0	1785.1/1516.4	2957.9/2803.1	2346.8/2320.5	2274.8/1969.0	2572.4/2475.9	1966.5/1753.0	1896.4/1829.4	6167.8/5625.6	3146.6/3289.4	2662.4/2472.8	3702.7/3430.4	2975.9/2960.8	2588.8/2314.8	3073.5/2904.1	2578.6/2302.6	2262.4/1854.6
[001]	[001](L)	4945.4/4421.0	3956.5/3546.0	3694.9/3129.8	4436.8/3907.5	3738.9/3397.3	3292.8/2816.9	4049.9/3668.5	3483.8/2711.9	3042.6/2593.6	6167.8/5625.6	4780.4/4454.7	3976.3/3582.7	5533.4/4937.6	4321.8/3994.8	3672.4/3415.0	4772.0/4233.5	3938.1/3547.5	3508.1/2840.6
	(001) plane (T)	3344.1/3138.2	2657.4/2421.9	2157.1/2259.6	2965.0/2939.9	2376.5/2282.4	2205.1/2082.5	2661.6/2375.5	2065.0/1641.1	1707.0/1637.3	4092.7/3859.8	3103.1/3192.7	2631.1/2465.4	3699.6/3396.9	2966.9/2939.6	2592.0/2325.5	2979.4/2841.8	2537.8/2425.6	22875/1805.6
A		94.2/87.1	89.5/84.0	99.1/84.3	91.7/84.8	88.6/80.7	83.3/89.62	96.7/88.6	96.6/71.9	82.8/83.9	86.6/83.4	85.8/83.6	83.1/81.5	85.9/82.4	86.3/81.8	83.3/80.30	82.9/89.7	92.3/94.9	88.9/105.5

5.3. Calculation of Debye temperature and polycrystalline speeds of sound

Calculations of elastic constants and elastic modulus allow to obtain such an important parameter in solid state physics as a Debye temperature. In solid state physics the Debye model provide a method for estimating the phonon contribution to the specific heat in a solid. Debye temperature Θ_D is the temperature of highest normal mode of vibrations in the crystal. It can be introduced as $\Theta_D k_B = \hbar \omega_D$ where $\hbar$ is the reduced Planck's constant, k_B is Boltsmann's constant, and ω_D is the maximal frequency of lattice vibration. It provides the understanding of the thermodynamics and elastic constants of solids and lot of the physical properties of solids such as melting temperature T_m, heat capacity, thermal expansion, elastic constants, electrical conductivity, etc., which are dependent on the Debye temperature. At a temperature higher than the Debye temperature ($T > \Theta_D$), the vibrational mode in each case is assumed to be equal to $k_B T$ energy. At ($T < \Theta_D$) vibrational modes are rest. Low-temperature vibrations mainly arise from acoustic vibrations. Debye temperature is also closely related to bond strength and thermal conductivity. Therefore, information about can be used to characterize the strength of covalent bonding in solids, as well as to estimate its thermodynamic properties. The higher is Θ_D, the stronger covalent bonding in the material.

From the calculated propagation velocities of longitudinal and transverse acoustic waves which are obtained from the calculated elastic constants and elastic modulus, we can calculate the Debye temperature for chalcopyrite crystals of the studied group. Θ_D can be obtained from Navier's equation

$$\Theta_D = \frac{h}{k_B}\left[\frac{3n}{4\pi}\frac{N_A\rho}{M}\right]^{\frac{1}{3}} v_m, \tag{5.40}$$

where h is the Planck's constant, k_B is Boltsmann's constant, N_A is Avogadro's number, n is the number of atoms in a unit cell, ρ is the density of the material, M is the mass of a unit cell, and v_m is the averaged elastic wave velocity. The averaged elastic wave velocity defined as:

$$v_m = \left[\frac{1}{3}\left(\frac{2}{v_t^3} + \frac{1}{v_l^3}\right)^{-\frac{1}{3}}\right]. \tag{5.41}$$

The used for calculation of the averaged velocity v_m transversal v_t and longitudinal v_l velocities of polycrystalline material are calculated as follows

$$v_l = \left[\frac{(3B+4G)}{3\rho} \right]^{\frac{1}{2}}, \qquad (5.42)$$

$$v_t = \left(\frac{G}{\rho} \right)^{\frac{1}{2}}. \qquad (5.43)$$

where B and G are polycrystalline bulk modulus and shear modulus, respectively, ρ is the density of the material, v_l is the longitudinal sound velocity, and v_t is the transverse sound velocity. The calculated sound velocities v_l, v_t, and v_m, and Debye temperature Θ_D are listed in Table 5.8.

As can be seen from Table 5.7, the calculated acoustic wave velocities for polycrystals in the investigated materials are in good agreement with the calculated and presented in Table 5.8 results obtained for single crystals of group I-III-VI$_2$ given in the previous paragraph.

The table shows that the Debye temperature calculated in this work using the LDA functional is higher than for calculations with the GGA functional. As it is easy to see, it is possible to allocate a trend of dependences of behavior on structure of crystals. In particular, the replacement of the cation of group I showed that the substitution of Cu $\rightarrow$ Ag atoms leads to a decrease in the Debye temperature by an average of 40-100 K. The highest value of the temperature is 435 K, which corresponds to the CuAlS$_2$ crystal. The lowest value of Θ_D among the crystals of the studied group is characteristic of the AgAlTe$_2$ crystal which is equal to 181.5 K.

The table shows that the Debye temperature calculated in this work using the LDA functional is higher than for calculations with the GGA functional. As it is easy to see, it is possible to allocate a trend of dependences of behavior Θ_D on structure of crystals. In particular, the replacement of the cation of group I showed that the substitution of Cu $\rightarrow$ Ag atoms leads to a decrease in the Debye temperature by an average of 40-100 K. The highest value of temperature is 435 K, which corresponds to the CuAlS$_2$ crystal. The lowest value of Θ_D among the crystals of the studied group is characteristic of the AgAlTe$_2$ crystal which is equal to 181.5 K.

Table 5.8. Calculated longitudinal v_l, transverse v_t and average sound velocities v_m, (in m/s), crystal density ρ (in kg/m^3) and Debye temperature Θ_D, (in K) for I-III-VI$_2$ group crystals.

Crystal	v_l	v_t	v_m	ρ	Θ_D	Θ_D (lit.)
AgAlS$_2$	5438.5/ 4942.9	2637.6/ 2569.9	2963.9/ 2875.9	3970.23	320.83/ 311.29	311[a], 286[a], 313[a]
AgAlSe$_2$	4409.4/ 3979.3	2189.1/ 2061.3	2456.8/ 2307.3	5097.73	254.07/ 238.61	241[a], 210[a], 237[a]
AgAlTe$_2$	3884.5/ 3327.5	1663.9/ 1627.0	1880.3/ 1827.5	5522.99	181.50/ 176.41	191[a], 158[a], 181[a]
AgGaS$_2$	4895.2/ 4444.5	2445.0/ 2386.5	2742.9/ 2664.8	4709.04	294.54/ 286.14	255[b], 282[a], 261[a], 215[a], 270[a], 259[a], 276[a]
AgGaSe$_2$	4114.6/ 3639.6	2020.7/ 1936.1	2269.2/ 2163.2	5701.21	232.77/ 221.90	150[c], 210[a], 225[a], 161[a], 156[a], 228[a]
AgGaTe$_2$	3634.4/ 3095.9	1908.0/ 1679.5	2133.8/ 1873.9	6087.18	205.51/ 180.48	182.4[c], 172[a], 129[a], 125[a], 122[a], 172[a]
AgInS$_2$	4444.2/ 3925.8	2108.9/ 2031.4	2372.5/ 2274.1	4926.44	244.28/ 234.14	242[a], 201[a], 238[a]
AgInSe$_2$	3725.8/ 2964.4	1701.0/ 1590.3	1917.2/ 1775.9	5792.39	189.57/ 175.59	186[a], 138[a]
AgInTe$_2$	3217.9/ 2847.8	1592.9/ 1480.3	1788.0/ 1656.5	6005.94	165.87/ 153.67	155.9[b], 159[a], 113[a]
CuAlS$_2$	6647.3/ 6105.6	3458.6/ 3248.6	3870.3/ 3629.7	3456.74	435.11/ 408.07	308, 372, 375, 386a
CuAlSe$_2$	5117.5/ 4942.0	2661.4/ 2702.3	2978.3/ 3013.4	4787.35	318.59/ 322.34	224[a], 272[a], 277[a], 294[a]
CuAlTe$_2$	4298.3 / 3923.9	2276.8/ 2112.0	2544.7/ 2357.8	5445.71	254.52/ 235.82	207[a], 213[a], 303[a]
CuGaS$_2$	5954.8/ 5366.5	3139.3/ 2907.2	3509.8/ 3244.1	4376.49	393.50/ 363.71	356[b], 272[a], 320[a], 340[a], 347[a], 330[a], 338[a]
CuGaSe$_2$	4750.1/ 4434.2	2500.2/ 2482.3	2795.7/ 2762.9	5589.45	298.66/ 295.17	262[b], 195[a], 246[a], 239[a], 258[a], 259[a], 288[a]
CuGaTe$_2$	4102.1/ 3653.5	2196.8/ 2027.9	2453.4/ 2258.7	6028.10	244.16/ 224.79	226.2[b], 146[a], 177[a], 200[a], 202[a], 190[a]
CuInS$_2$	5112.5/ 4620.7	2531.8/ 2386.0	2841.8/ 2671.3	4742.69	305.54/ 287.22	273[b], 284[a], 231[a], 221[a], 272[a], 264[a]
CuInSe$_2$	4252.1/ 3787.4	2135.5/ 1876.0	2395.0/ 2105.7	5745.07	246.12/ 216.39	243.7[b], 221.9[d], 255[a], 170[a], 172[a], 207[a], 219[a]
CuInTe$_2$	3792.9/ 3122.8	1937.1/ 1426.9	2170.3/ 1608.2	6134.71	209.44/ 155.20	191.4[b], 185[a], 194[a], 129[a], 156[a], 174[a]

[a]Ref. [241], [b]Ref. [175], [c]Ref. [106], [d]Ref. [242]

Considering the substitution of amoms of group III, we can see the tendency that in the series Al → Ga → In there is a decrease in Θ_D during the transition to a heavier cation atom. Substitution of Al to Ga reduces the Debye temperature by 10-40 K a for crystals with Cu and for crystals with the Ag cation by 21-26 K. Substitution of Ga → In for crystals in

which the cation I = Cu reduces Θ_D by 34 -87 K whereas for I = Ag this change is slightly smaller and is 39-50 K. Therefore, the transition of the cation of group I from Cu to Ag reduces the effect of replacing the components of the cationic sublattice of the sublattice formed by Al, Ga and In ions on the Debye temperature.

Replacement of S → Se → Te also leads to a decrease in the Debye temperature for all crystals of group I-III-VI$_2$. As for the replacement of cation III and for inons VI, there is less influence on the change of cation of crystals with Ag than for crystals containing the Cu cation.

In [175,241–243], a study of the Debye temperature for the studied group of crystals is reported. In particular, in [175] the experimental results of determining the Debye temperature are given. Comparing the values of Θ_D obtained in this work, we can say that they are in good agreement with the literature data. The differences between the data given by other authors and our results can be explained by the peculiarities of the methods used. In particular, underestimation of bond lengths (in the case of LDA) and their overestimation (in calculations with GGA) affect the elastic constants with which Θ_D is associated. It should also be noted that in these publications [106,175,241,242] there is a large scattering of Θ_D data. In particular, the data obtained on the experimental ones in [175] differ significantly from the others [106,241,242]. Also, in [30] shows the results of the calculation of the Debye temperature for crystals AgGaS$_2$, AgGaSe$_2$, AgGaTe$_2$ (not given in the table) which are 355 K, 288 K, 241 K, respectively. These values obtained by the FP-LAPW method, as can be seen from the table, are significantly overestimated by experimental data. Also, the results obtained are in consistancy with the theoretical data reported by A.K. Kushwaha et.al [244] obtained with the use of the rigid ion model.

It should be noted that usually high Θ_D indicates high thermal conductivity and strong interaction forces strength of atoms. Thus, we can say that the crystals of the group Cu-III-VI$_2$ has higher thermal conductivity than the Ag-III-VI$_2$ crystals. Also, crystals based on the Cu cation have a stronger covalent bond than the Ag-containing chalcopyrites of the study group. Replacement of Al → Ga → In cations and an anion substitution S → Se → Te reduces the bond strength and covalent component.

5.4. Conclusions

1. Calculated are the coefficients of the matrix of elastic constants C_{ij} for 18 crystals of I-III-VI$_2$ group. It is shown that the elastic coefficients obtained with the LDA functional are greater than that with GGA functional because of overbidding characteristic of the LDA functional. The elastic coefficients for all crystals of the studied group satisfy the Born criterion of mechanical stability for the tetragonal crystal structure. It is shown that I-III-VI$_2$ crystals have relatively small elastic coefficients (<100 GPa) and reveal anisotropy. The C_{11} and C_{33} coefficients are the largest by magnitude. The crystals are less compressed along the x- and y-directions than in the z-direction. Here, the calculated elastic constants C_{11} and C_{33} for the AgInTe$_2$, CuAlS$_2$, CuAlSe$_2$, CuGaS$_2$ and CuInS$_2$ crystals are almost equal within the calculation error. The shear coefficients C_{12} and C_{13} are close to each other, showing the same interaction in the respective shear directions. It can be seen that the elastic coefficients satisfy the following inequality $C_{11} > C_{33} > C_{12} > C_{13} > C_{44} > C_{66}$.

2. The calculated linear compressibility coefficients obtained with the GGA functional shows higher value of k than obtained with the LDA functional. The compressibility k has clear tendency on its composition change. The sawtooth form of compressibility change is typical for the I-III-VI$_2$ crystals. The transition from CuAlS$_2$ to AgInTe$_2$ crystal is accompanied in general by increasing the k values. The change of all Cu $\rightarrow$ Ag, Al $\rightarrow$ Ga $\rightarrow$ In, and S $\rightarrow$ Se $\rightarrow$ Te leads to the increasing of the compressibility. The highest influence on the compressibility has the S $\rightarrow$ Se $\rightarrow$ Te anion substitution, leading to rapid increase in k value. The cation substitution can be described by the smoother change in compressibility.

3. It was found that the Young's modulus for crystals of I-III-VI$_2$ group in the x-direction is greater than in the z-direction indicating that the material is less tensile in the x-direction. Calculations show that the CuGaS$_2$ crystal is stiffer than other materials in the studied group. The materials containing Te atoms are less stiff.

4. The bulk modules B and shear modules G for polycrystalline materials are obtained from the calculated elastic constants. It was found that the B/G ratio is in the range of 4.12 (3.46) to 2.15 (1.86) for LDA (GGA) functional. It is greater than the critical value of 1.75. Therefore, the crystals of I-III-VI$_2$ group are characterized by high ductility.

5. The bulk modulus for all crystals of the studied group is calculated and good agreement with the experimental values given in the literature is shown. The functional dependences between the bulk modulus B and a number of parameters of the crystal, such as the molar

mass of the compound, the volume of the unit cell, the density of the crystal, and the value of the band gap are revealed.

4. A number of parameters characterizing the anisotropy of elastic properties of the materials, such as shear anisotropy factors A_1, A_3, and anisotropy indices A_B, A_G, A^U, are calculated. It is shown that the anisotropy of the compression modulus B is small in the studied crystals, while the shear anisotropy is significant.

5. A 3D spatial distributions of the bulk modulus, Young's modulus and shear modulus of I-III-VI$_2$ crystals and their planar projections are constructed. It was found that a significant anisotropy is observed for the Young's modulus, which is the largest for crystals with light anions. Substitution S → Se → Te leads to decreasing of Young's modulus anisotropy. It is shown that the anisotropy in the (100) plane is greater than in (001). It is found that the bulk modulus has a small anisotropy, and the spatial distribution of this modulus has almost a spherical shape. When replacing S → Se → Te in crystals containing silver, the figure is stretched along the z-direction. In the crystals with the copper ions, on the contrary, the sphere is compressed along the z-direction. It is shown that the shear modulus has the largest spatial anisotropy and its projections have a flower-like shape.

6. The propagation velocities of acoustic waves in the crystals of the studied group for different directions of propagation are calculated and their anisotropy is estimated. Based on these results, Debye temperatures are obtained. A good agreement of the calculated Debye temperatures with the experimental data given in the literature is shown.

6. STRUCTURE AND DYNAMICS OF PHONON SUBSYSTEM OF AgGaX$_2$ (X = S, Se, AND Te) CRYSTALS

6.1. Symmetry of phonon modes and selection rules for chalcopyrite crystals with the D_{2d}^{12} space group

6.1.1. Symmetric consideration of crystal structure of I-III-VI$_2$ group crystals

The study of vibrational modes in crystals is of fundamental and practical interest. Since vibrational modes are very sensitive to the chemical composition and structural perfection of the material, their knowledge allows to ensure quality control of the tested samples.

Group theoretical methods of study are seful and informative tools for analyzing the physical properties of crystals. It can be applied to the analysis of fundamental vibrations in crystals and allows to define unambiguously number of vibrations and their type of symmetry. It provides to analyze the activity of modes and specify the conditions for their observation in a particular physical process. These methods are essential for the interpretation of experimental results [245].

The availability of sensitive equipment and its constant improvement allows you to reliably record both single-phonon and multiphon process. Phonons with a very small wave vector $\mathbf{k}$ ($k \sim 10^{-5}$ cm^{-1}) in comparison with the vector $\mathbf{k}$ at the edge of the Brillouin zone ($k \sim 10^{-8}$) take part in single-phonon processes in the infrared (IR) and Raman spectra. Therefore, harmonic processes can be classified assuming that $\mathbf{k} = 0$. In this case, we can assume that the equivalent crystal atoms that differ by the primitive translation vector vibrate in phase in all primitive cells. This approximation significantly simplifies the analysis of phonon spectra in crystals.

During the vibrational spectra study, the initial stage is the classification of fundamental vibrations by types of symmetry in accordance with the symmetry of the crystal structure. Two types of structures are considered for which it is expedient to use a certain method for classification of vibrational modes. For crystals containing isolated structural groups (such as molecules or polyatomic ions) it is convenient to classify the vibrations using the method of positional symmetry. For crystals of complex structure that do not contain

isolated structural groups, the classification is usually carried out using the general method. Isolated structural elements (fragments) cannot be distinguished in the crystal structure I-III-VI₂. Therefore, a variant of the general method [245] is used to classify the vibrational modes.

As a rule, the first-order phonon spectra are of the greatest experimental interest. First-order phonon spectra in solids are limited by excitations of vibrational modes close to the center of the Brillouin zone. Therefore, the analysis of phonon spectra takes into account mainly the Γ-point ($\mathbf{k} = 0$), ie knowledge of only the point group of the studied crystals is required. It should be noted that for some crystals the phenomenon of autointercalation is possible [246] (the formation of superlattices is possible, as a result of which "non-central" modes (ie modes for which $\mathbf{k} \neq 0$) of the original lattice can turn into Γ-type modes, which can make complicate the structure of new peaks, violation of selection rules). Such processes have already been observed in some layered crystals (graphite, PbI₂, dichalcogenides of transition metals) [247].

The Γ-point modes of the first Brillouin zone are a type of fundamental normal vibrations in which all congruent lattice atoms are shifted in phase and each primitive cell participates in the same way. Therefore, to determine and symmetrically classify these vibrations, it is sufficient to take as a basis the primitive cell of the crystal.

Structural studies have shown that tetragonal lattice of chalcopyrite crystals I-III-VI₂ is described by an asymmetric space group of symmetry $D_{2d}^{12} = I\bar{4}2d$ (also known as V_d). The parameters of the crystals cell of the studied group vary depending on the elemental composition as given (Table 4.1). Lest consider the results of symmetry analysis at normal conditions of I-III-VI₂ crystals. Symmetry elements of space group D_{2d}^{12} are following:

$\{h_1(x, y, z)|(0, 0, 0)\};$ $\qquad$ $\{h_{37}(y, x, z) |(0, 0.5, 0.25)\};$

$\{h_2(x, -y, -z) |(0, 0.5, 0.25)\};$ $\qquad$ $\{h_{38}(y, -x, -z) |(0, 0, 0)\};$

$\{h_3(-x, y, -z) |(0, 0.5, 0.25)\};$ $\qquad$ $\{h_{39}(-y, x, -z) |(0, 0, 0)\};$

$\{h_4(-x, -y, z) |(0, 0, 0)\};$ $\qquad$ $\{h_{40}(-y, -x, z) |(0, 0.5, 0.25)\},$

where h_i the notation of symmetry operations according to [248] and after the vertical line are given non-primitive translations. Under the symmetry operation with the designation of the form $h_2(x, -y, -z)$ means that the transformation under the action of h_2 operator the vector $\mathbf{r} = (x, y, z)$ passes into the vector $h_2\mathbf{r} = (x, -y, -z)$. The lattice factor group of I-III-VI₂

crystals is isomorphic to a point group D_{2d} whose order is $h = 8$. The elements of this group, in addition to the identical E, are as follows:

- C_2 – 180 degrees rotation along the principal C_2 axis;

- $C_2^{'}$ – 180 degrees rotation along the axis perpendicular to C_2 axis;

- σ_d – reflection in the dihedral plane (a plane which bisects the angle between two adjacent $C_2^{'}$ rotation axes;

- S_4 – 90 degrees rotation followed by a reflection thought a plane perpendicular to rotation axis.

There are two $C_2^{'}$ axis which are 90 degrees apart, and two σ_d dihedral planes and two S_4 improper axes as rotation either clockwise or anti-clockwise. In the Table 6.1 are given the characters of irreducible representations, which shows that the group D_{2d} is not an Abelian group (commutative), i.e. contains not only one-dimensional irreducible representations. This point group includes 5 irreducible representations, of which 4 are one-dimensional ($A_1 = \Gamma_1$, $A_2 = \Gamma_2$, $B_1 = \Gamma_3$, $B_2 = \Gamma_4$) and one two-dimensional ($E = \Gamma_5$). The absence of the center of inversion significantly affects the rules of selection and properties of the material and allows the emergence of nonlinear optical phenomena.

Table 6.1. Character table for the $D_{2d} = \bar{4}2m$ point group (tetragonal).

$D_{2d}(\bar{4}2m)$	E	$2S_4$	C_2	$2C_2^{'}$	$2\sigma_d$	Linear, rotations	Quadratic	Cubic
A_1	1	1	1	1	1		$x^2 + y^2, z^2$	xyz
A_2	1	1	1	–1	–1	R_z	—	$z(x^2 - y^2)$
B_1	1	–1	1	1	–1		$x^2 - y^2$	—
B_2	1	–1	1	–1	1	T_z	xy	$z^3, z(x^2 + y^2)$
E	2	0	–2	0	0	(T_x, T_y), (R_x, R_y)	(xz, yz)	(xz^2, yz^2) (xy^2, x^2y) (x^3, y^3)

The number of fundamental vibrations is determined by the number of atoms in the primitive cell. The primitive cell of crystal I-III-VI₂ contains $N = 8$ atoms, so the phonon spectrum has $3N = 24$ branches. Three of them are acoustic when at $k \to 0$ the frequency is $\omega \to 0$. The remaining branches are optical.

To carry out the theoretical-group symmetric classification of phonon modes, we calculated the characteristics of the vibrational representation Γ_v, as well as the characters of the representation Γ_a corresponding to the vibrations of the cell as a whole, using the standard method [249]. Since when considering acoustic modes the number of invariant (fixed) particles $N = 1$ (the object is a primitive cell as a whole), the character for the symmetric operation R

$$\chi_a(R) = \pm 1 + 2\cos\theta_R.$$ (6.1)

When calculating the characters of the representation Γ_v, it is necessary to determine a specific number of invariant N_R atoms of a primitive (cell) for each operation R and multiply it by the corresponding partial contribution coefficient. The results obtained for the lattice of crystals I-III-VI₂ are given in Table. 6.2.

As can be seen, the representations of Γ_v and Γ_a are reducible. The decomposition according to the characters of irreducible representations of the Γ_i factor group is made according to the relations:

$$a_{a,i} = \frac{1}{h}\sum_R \chi_a(R)\chi_i(R),$$ (6.2)

$$a_{v,i} = \frac{1}{h}\sum_R \chi_v(R)\chi_i(R),$$ (6.3)

where $h(g)$ is an order of the group, χ_i is the character of irreducible representation of the factor group for the symmetry operator R.

Table 6.2. Characters of Γ_v and Γ_a representation.

I-III-VI₂	E	$2S_4$	C_2	$2C_2^{'}$	$2\sigma_d$
N_R	8	4	4	2	0
θ_R	0	90º	180º	180º	180º
$\cos\theta_R$	1	0	−1	−1	−1
Γ_v	1	2	3	4	7
Γ_a	0	0	1	0	1

Thus, the theoretical group analysis gives the following classification of vibrational modes for lattices of tetragonal chalcopyrites of group I-III-VI₂:

$$\Gamma_v = 1A_1 + 2A_2 + 3B_1 + 4B_2 + 7E, \tag{6.4}$$

$$\Gamma_a = 1B_2 + 1E, \tag{6.5}$$

$$\Gamma_{opt} = 1A_1 + 2A_2 + 3B_1 + 3B_2 + 6E. \tag{6.6}$$

The three phonon modes B_2 and E (mode E is twice degenerate) that correspond to the translations T_Z, T_Y, T_X are acoustic branches. In other words, representations B_2 and E correspond to translational (external) modes associated with the displacement of vectors in the X, Y, and Z directions. Twenty-one optical modes correspond to representations describing sets of normal vibrations from which fully symmetric ($1A_1$), external translation ($3B_2$, $6E$) and close to libration ($2A_2$, $3B_1$).

6.1.2. Infrared absorption spectra

The types of symmetry of vibrations active in IR spectra and in Raman spectra are determined by selection rules established from the constraints imposed by the symmetry of the crystal on the matrix elements of the transition from the initial vibrational state to the final one under the action of a certain perturbation operator. In IR absorption, this operator is a derivative of the dipole moment and is transformed by the vector representation of the Γ_μ factor group, which is isomorphic to the point group of the crystal. In Raman scattering we are dealing with a tensor of polarizability (tensor of the second rank), which in the case of nonresonant scattering is symmetric and transforms according to the representation of Γ_α.

In the language of group theory, the standard selection rules for phonon spectra are determined by the symmetric properties of the transformations of the wave functions of the initial and final states when applying the symmetry operations of the point group of the crystal. Thus, edge transitions will be allowed, and will be written down in the form of formulas

$$\Gamma_i \times \Gamma_\mu \supset \Gamma_1, \tag{6.7}$$

for IR transitions, and

$$\Gamma_i \times \Gamma_\alpha \supset \Gamma_1, \tag{6.8}$$

for Raman transitions, were Γ_i – irreducible representation of factor-group, which corresponds to symmetry of phonon wave function of phonon branch $\omega_i(k)$, Γ_1 – totally symmetric unit representation.

The optical mode of Γ_i symmetry will be active in IR absorption when:

$$a_{\mu,i} = \frac{1}{h}\sum_R \chi_\mu(R)\chi_i(R) \neq 0, \qquad (6.9)$$

where $\chi_\mu(R)$ is character of polar vector representation, which are calculated by the expression

$$\chi_\mu(R) = \pm 1 + 2\cos\theta_R. \qquad (6.10)$$

As one can see, $\Gamma_\mu = \Gamma_a$, therefore, in the IR spectra of crystals of group I-III-VI₂, odd modes are active. Their dipole moments are parallel to three orthogonal crystallographic axes.

If you set the orientation of the fixed ("laboratory") rectangular Cartesian coordinate system *XYZ* relative to the elements of crystal symmetry, eg, $X \parallel C_2(x) \parallel a$, $Y \parallel C_2(y) \parallel b$, $Z \parallel C_2(z) \parallel c$ then it is possible to determine the general rules of selection taking into account the polarizations of both phonon and elementary absorption bands. These general selection rules are summarized in Table. 6.3.

$$\Gamma_\mu = 4B_2 + 7E. \qquad (6.11)$$

Table 6.3. General selection rules for quantum transitions in the tetragonal crystals, estimated for the Γ-point of BZ.

Symmetry of states in different notations of the irreducible representations for D_{2d} group		Allowed optical quantum transitions at Γ-point		
Bethe	Mulliken	$\mathbf{E}\|X$, $(\mathbf{E}\|a)$	$\mathbf{E}\|Y$, $(\mathbf{E}\|b)$	$\mathbf{E}\|Z$, $(\mathbf{E}\|c)$
Γ_1	A_1			
Γ_2	A_2	$\Gamma_1 \leftrightarrow \Gamma_5$	$\Gamma_1 \leftrightarrow \Gamma_5$	$\Gamma_1 \leftrightarrow \Gamma_4$
Γ_3	B_1	$\Gamma_2 \leftrightarrow \Gamma_5$	$\Gamma_2 \leftrightarrow \Gamma_5$	$\Gamma_2 \leftrightarrow \Gamma_3$
Γ_4	B_2	$\Gamma_3 \leftrightarrow \Gamma_5$	$\Gamma_3 \leftrightarrow \Gamma_5$	$\Gamma_3 \leftrightarrow \Gamma_2$
Γ_5	E	$\Gamma_4 \leftrightarrow \Gamma_5$	$\Gamma_4 \leftrightarrow \Gamma_5$	$\Gamma_4 \leftrightarrow \Gamma_1$

6.1.3. Raman spectra

When light is scattered, there is a functional relationship between the excitation field (e.g., a laser radiation field) and the scattered light field through the response function of the medium. In the case of Raman specta is described by a symmetric tensor of the 2nd rank

(Raman polarizability tensor). The symmetry of the components of the scattering (Raman) tensor depends on the symmetry of the crystal. This determines the selection rules for transitions in the Raman spectra. The general form of the Raman tensor is as follows [250]:

$$\alpha_{i,j}_{i,j \to x,y,z} = \begin{bmatrix} \alpha_{xx} & \alpha_{xy} & \alpha_{xz} \\ \alpha_{yx} & \alpha_{yy} & \alpha_{yz} \\ \alpha_{zx} & \alpha_{zy} & \alpha_{zz} \end{bmatrix}. \tag{6.12}$$

For tetragonal crystal syngony, the tensor has 6 independent components: three diagonal and three non-diagonal. As previously mentioned, single crystals of I-III-VI$_2$ group belong to the space group D_{2d}. A set of Raman tensors for 32 crystallographic point groups is collected in [245]. The Raman tensors for CP crystals unit cell is shown in Table 6.4.

Table 6.4. Raman tensors and their symmetries for the D_{2d} point group.

A_1	B_1	B_2	E_x	E_y
$\begin{pmatrix} a & 0 & 0 \\ 0 & a & 0 \\ 0 & 0 & b \end{pmatrix}$	$\begin{pmatrix} c & 0 & 0 \\ 0 & -c & 0 \\ 0 & 0 & 0 \end{pmatrix}$	$\begin{pmatrix} 0 & d & 0 \\ d & 0 & 0 \\ 0 & 0 & 0 \end{pmatrix}$	$\begin{pmatrix} 0 & 0 & e \\ 0 & 0 & 0 \\ e & 0 & 0 \end{pmatrix}$	$\begin{pmatrix} 0 & 0 & 0 \\ 0 & 0 & f \\ 0 & f & 0 \end{pmatrix}$

The Raman tensor for modes A_1 and B_1 has only diagonal terms, so it is difficult to distinguish the components of the scattering tensor by choosing the scattering configuration for this type of vibrations. For other modes active in Raman spectra (they will be defined below), the scattering spectrum will have polarized bands for them.

The absolute values of the components of the Raman tensor are found by comparing the measured intensities with the known cross sections of the Raman for reference materials, such as diamond. However, such studies as the definition of signs have not yet been included in our task.

The actually measured value in the experiment is the scattering intensity [251,252]. The intensities of the Raman bands are expressed by the formula:

$$I_R = I_0 \frac{\omega^4}{4\pi c^3} \alpha_{ij}^2, \tag{6.13}$$

where I_0 is the intesity of the excitation line. For inactive modes, obviously, $I_R = 0$. As mentioned above, the selection rules for the Raman spectra are found by decomposing the summary representation of Γ_α by the nature of the irreducible representations of the Γ_i factor group. A Raman spectra line corresponding to the Γ_i symmetry mode will be allowed if the decomposition coefficient

$$a_{\alpha,i} = \frac{1}{h} \sum_R \chi_\alpha(R) \chi_i(R) \neq 0 \,. \tag{6.14}$$

Characters of Γ_α representation are found by the formula

$$\chi_\alpha(R) = 2\cos\theta_R (\pm 1 + 2\cos\theta_R) \,. \tag{6.15}$$

Table 6.5. Characters of Γ_α representation, $\chi_\alpha(R)$.

$D_{2d} = \bar{4}2m$	E	$2S_4$	C_2	$2C_2^{'}$	$2\sigma_d$
θ_R	0	90º	180º	180º	180º
$2\cos\theta_R$	2	0	–2	–2	–2
Γ_α	1	0	3	4	7

As a result of the decomposition of Γ_α by the characters of irreducible representations of the D_{2d} group we obtain:

$$\Gamma_\alpha = 1A_1 + 3B_1 + 4B_2 + 7E. \tag{6.16}$$

Thus, the six modes in crystals I-III-VI$_2$ are active: A_1 modes correspond to nonzero diagonal elements of the polarizability tensor, and for modes B_1, B_2, and E the components α_{xy}, α_{zx}, α_{zx} α_{xz}, α_{zy}, α_{yz} are nonzero. In the Raman spectra, the most intense are the bands corresponding to fully symmetric A_1-type vibrations that are polarized. Other modes allowed in the Raman spectra have a lower intensity than the A$_1$ mode.

The scattering geometry is usually specified in terms of the Porto [253] notation $k_i(e_i e_s)k_s$ giving the incoming wave vector k_i, incoming polarization e_i, scattered wavevector k_s and polarization e_s. According to the scheme of Porto notation, for Raman spectra of I-III-VI$_2$ crystals transitions to states are allowed:

- A_1 in scuttering geometry (XX), (YY), (ZZ);
- B_1 in scuttering geometry (XX), $(\overline{Y}\overline{Y})$;
- B_2 in scuttering geometry (XY), (YX);
- E_1 in scuttering geometry (XZ), (ZX);
- E_2 in scuttering geometry (YZ), (ZY).

The use of selection rules together with information about the intensities and polarizations of bands in first-order phonon spectra makes it possible to identify the structure of these spectra.

6.2. Vibrational properties of the AgGaS$_2$ crystal

6.2.1. Dynamics of the unit cell from the first principles. Dynamical matrix and phonon frequencies

When considering a dynamics of a lattice, the initial element considered in the crystal are interparticle interactions, which include ion-ion, ion-electron, electron-electron and other interactions that determine the potential energy of interaction between atoms. The minimum of the potential energy curve corresponds to the equilibrium value of the distance between the atoms. At $R > R_0$ the forces of attraction prevail and at $R < R_0$ the repulsion process is observed. The forces acting on an atom are related to the potential energy ratio

$$F = -\text{grad}\, U(\mathbf{r}) = -\frac{dU}{dR}\frac{\mathbf{R}}{R}, \qquad (6.17)$$

At small deviations from the equilibrium positions, the energy $U(R)$ can be decomposed into a series

$$U(R) = U_0(R) + \left(\frac{\partial U}{\partial R}\right)_{R_0}(R - R_0) + \frac{1}{2!}\left(\frac{\partial^2 U}{\partial R^2}\right)_{R_0}(R - R_0)^2 +$$
$$+ \frac{1}{3!}\left(\frac{\partial^3 U}{\partial R^3}\right)_{R_0}(R - R_0)^3 + ... \qquad (6.18)$$

The second term in the expansion $\dfrac{\partial U}{\partial R} = 0$, while $\dfrac{\partial^2 U}{\partial R^2} > 0$. Since at the point of equilibrium the repulsive forces change faster than the attraction, the term $\dfrac{\partial^3 U}{\partial R^3} < 0$. In the harmonic approximation, the third term, as well as terms of higher orders, is equal to 0, so the force $F = -\dfrac{\partial^2 U}{\partial R^2}$ corresponds to Hooke's law. In the harmonic approximation, it is also assumed that the average distances between adjacent atoms correspond to the minimum of the energy curve and are commensurate with the distances of the static crystal model. The atoms oscillate relative to the average equilibrium positions, and the amplitude of oscillations is small enough to be limited by the quadratic term in the $U(R)$ decomposition.

Denote the displacement of the nth atom from the equilibrium state by $\mathbf{u_n} = \mathbf{R} - \mathbf{R_0}$, and the total energy of the system by E. Therefore, based on the decomposition of total energy near the coordinate of structural equilibrium, Eq. 6.18 takes the following form.

$$E = E_0 + \frac{\partial E}{\partial u}u + \frac{1}{2!}\frac{\partial^2 E}{\partial u^2}u^2 + \frac{1}{3!}\frac{\partial^3 E}{\partial u^3}.u^3 + \dots . \tag{6.19}$$

Given the harmonic approximation, we write Eq. 6.19 as follows

$$E = E_0 + \frac{1}{2}\sum \mathbf{u}_{\alpha,k,a} \cdot \Phi_{\alpha,\alpha'}^{k,k'} \cdot \mathbf{u}_{k',\alpha',a} + \dots , \tag{6.20}$$

where $\mathbf{u}_{\alpha,k,a}$ is the atomic displacement k of cell a in the Cartesian direction α, and $\Phi_{\alpha,\alpha'}^{k,k'}$ (a) is force constant matrix

$$\Phi_{\alpha,\alpha'}^{k,k'}(a) = \frac{\partial^2 E}{\partial \mathbf{u}_{\alpha,k}\partial \mathbf{u}_{k',\alpha'}} . \tag{6.21}$$

This matrix represents all effective three-dimensional spring constants between atoms

$$\Phi_{\alpha,\alpha'}^{k,k'}(a) = \frac{\partial^2 E}{\partial \mathbf{u}_{\alpha,k}\partial \mathbf{u}_{k',\alpha'}} = -\frac{\partial F_{\mathbf{u}_{\alpha,k,a}}}{\partial \mathbf{u}_{k',\alpha',a}} . \tag{6.22}$$

For the three-dimensional case, the solution will have the following form

$$\mathbf{u}_{\alpha,k} = \varepsilon_{m,\alpha k,\mathbf{q}}e^{i\mathbf{qR}_{\alpha,k}-\omega t} . \tag{6.23}$$

Taking the derivative of the equation of total energy to get the force, F and substituting this test solution we will get the equation

$$D_{\alpha,\alpha'}^{k,k'}(\mathbf{q})\varepsilon_{m\alpha,k\mathbf{q}} = \omega_{m,\mathbf{q}}^2\varepsilon_{m\alpha,k\mathbf{q}} , \tag{6.24}$$

where ω is a frequency; $\varepsilon_{m\alpha,k\mathbf{q}}$ is phonon eigen vector. $D_{\alpha,\alpha'}^{k,k'}(\mathbf{q})$ is called a dynamic matrix for a system of atoms. It is a Fourier transform matrix of force constants

$$D_{\alpha,\alpha'}^{k,k'}(\mathbf{q}) = \frac{1}{\sqrt{M_k M_{k'}}}C_{\alpha,\alpha'}^{k,k'}(\mathbf{q}) = \frac{1}{\sqrt{M_k M_{k'}}}\sum_a \Phi_{\alpha,\alpha'}^{k,k'}(a)e^{-i\mathbf{qR}_a} , \tag{6.25}$$

where k and k' are atom labels, α and α' are directions. Vibrational frequencies are determined from the eigenvalues of the energy hessian $E(\mathbf{R})$, scaled by masses:

$$\det\left|\frac{1}{\sqrt{M_k M_{k'}}}\Phi_{\alpha,\alpha'}^{k,k'}(\mathbf{q}) - \omega^2\right| = 0 . \tag{6.26}$$

The solutions of the Eq. 6.26 are the eigenvalues and eigen functions. Each set of solutions corresponds to the vibrational modes. Mode frequency $\omega_{m,\mathbf{q}}$ is the square root of the corresponding eigenvalue.

Today, one of the most popular methods for calculating lattice dynamics is the Linear response method [254] of density functional perturbation theory (DFPT). The Hellmann-Feynman theorem is used to calculate the first and second derivatives of $E(\mathbf{R})$ [255,256].

The force constants matrix can be obtained by differentiating the Hellmann-Feynman forces on atoms, with respect to ionic coordinates. As a result, the force acting on the nucleus in the electronic ground state will be:

$$F = -\frac{dE_\lambda}{d\lambda} = -\left\langle \psi_\lambda \left| \frac{dH}{d\lambda} \right| \psi_\lambda \right\rangle. \tag{6.27}$$

This procedure reveals that the force constants matrix depends on the ground state electron charge density and on its linear response to a distortion of atomic positions. Due to the variational principle of the density functional formalism, the second order change in energy depends on the first order change in the electron density.

The DFPT formalism is, in many cases, very similar to the density functional theory (DFT) itself. DFT states that the total energy is the functional of the electron density; thus one can solve the DFT equations by minimizing the total energy. Similarly, the DFPT problem can be solved by minimizing the second order perturbation in the total energy, which gives the first order changes in density, wave functions and potential [257,258].

The electronic second order energy, which is minimized in this approach, as implemented in CASTEP, is:

$$E^{(2)} = \sum_{\mathbf{k},n} \left[\left\langle \psi^{(1)}_{\mathbf{k},n} \mid H^{(0)}_{KS} - \varepsilon^{(0)}_{\mathbf{k},n} \mid \psi^{(1)}_{\mathbf{k},n} \right\rangle + \left\langle \psi^{(1)}_{\mathbf{k},n} \mid v^{(1)} \mid \psi^{(0)}_{\mathbf{k},n} \right\rangle + \left\langle \psi^{(0)}_{\mathbf{k},n} \mid v^{(1)} \mid \psi^{(1)}_{\mathbf{k},n} \right\rangle \right] +$$

$$+ \frac{1}{2} \int \frac{\delta^2 E_{Hxc}}{\delta n(\mathbf{r}) \delta n(\mathbf{r}')} n^{(1)}(\mathbf{r}) n^{(1)}(\mathbf{r}') + \sum_{\mathbf{k},n} \left\langle \psi^{(0)}_{\mathbf{k},n} \mid v^{(2)} \mid \psi^{(0)}_{\mathbf{k},n} \right\rangle, \tag{6.28}$$

where the superscripts refer to the ground state (0) and first (1) and second (2) order changes, respectively. Similar terms have to be evaluated for the ionic terms in the total energy. The preconditioned conjugate gradients minimization scheme can be used to find the minimum of this functional with respect to the first order wave functions. The dynamical matrix for a given $\mathbf{q}$ is then evaluated from the converged first order wave functions and densities [258].

The way to find $\Phi_{is\alpha,jt\beta}$ as a second derivative from total energy is the linear response approximation in the density functional perturbation theory. This method is convenient in case of mall primitive cells. Now that the matrix of force constants is known, and hence $D_{s\alpha,t\beta}$, then the frequencies $\omega(\mathbf{q})_s$ can be obtained for any $\mathbf{q}$, and the phonon density can be calculated.

It should be noted that this method is used not only to study the vibrational properties of materials. The linear response makes it possible to calculate the second derivative of total energy for a given perturbation and, depending on the type of perturbation (its nature), you can calculate the following physical properties, and others:

- perturbation in ionic positions gives the dynamical matrix and phonons;
- perturbation in magnetic field – NMR response;
- perturbation in unit cell vectors – elastic constants;
- perturbation in an electric field – dielectric response.

6.2.2. Phonon structure of AgGaS$_2$ crystals

Today, the density functional theory-based methods, designed to describe the ground state of a large number of interacting atomic nuclei and electrons that form a crystalline solid, is adapted to calculate phonon spectra. This possibility is embedded in the CASTEP program code, which we use in this study. The complex problem is solved relatively simply by applying the method of linear response, based on the Hellman-Feynman theorem, which is implemented to calculate the energy-derived system in the CASTEP code. The essence of the approach is that in the framework of the adiabatic approximation (see Chapter 3) when calculating phonons, the energy of the ground state of the electronic subsystem is calculated as a function of ionic coordinates. Therefore, within the density functional theory is developed a method of linear response, based on the theory of static linear response, which is adapted in the CASTEP code to find the force constants not as the second derivative of the total energy of the electrons of the crystal by nuclear displacements, displacement of atoms in the framework of perturbation theory for DFPT [254].

The first principles calculations of vibrtational properties of AgGaX$_2$ crystals (X = S, Se, and Te) presented in this work were carried out using the plane-waves pseudopotential method based on the DFT [18,19]. The calculations are performed using the CASTEP code. The LDA functional with the CA-PZ parameterization were used to take into account the exchange and correlation effects. This functional has proven to be good at describing both organic and inorganic systems that contain various chemical elements in their structure. Also, its advantages include its simplicity, which is manifested in significantly less calculation time than for other functionals. The cutoff energy for the plane wave basis was fixed at 800 eV. The ion-electron interaction within calculations is modelled by the norm-conserving pseudopotential.

Before the calculation, the geometric optimization of the crystal structure was performed in order to obtain the structure of the ground state. The BFGS algorithm [155]

was used for geometry optimization of the crystal before calculation of the vibrational properties. This process implies optimization of the crystal's unit cell parameters and relaxation of the atomic positions. The crystal's space-group symmetry was constrained during the optimization process in order to prevent any structure transformations/distortions. For self-consistent electronic minimization, the eigen energy convergence tolerance was chosen at 24×10^7 eV and the tolerance of the electronic total energy convergence was 10^{-5} eV/atom. The convergence parameters used during optimization were as follows: the maximum force 3×10^{-2} eV/Å; maximum pressure 5×10^{-3} GPa and maximum displacement 1×10^{-4} Å. The Brillouin zone sampling for calculation was implemented using Monkhorst-Pack **k**-mesh [154] with a greed of $5 \times 5 \times 3$. The density functional perturbation theory and the linear-response approach were used for calculation of the vibrational characteristics [254], namely the phonon frequencies, infrared and Raman spectra, phonon band structure and phonon density of states.

Vibrational modes in solids are in the form of waves with frequencies that depend on the wave vector (similar to electronic energy levels). The dependences $\omega(q)$ are known as dispersion curves. Figure 6.1 (a) shows the phonon band structure $\omega(q)$ calculated along the lines connecting the points of high symmetry of the Brillouin zone. The phonon band structure was studied at the following points of the Brillouin zone: Z – Γ – X – P – N – Γ. As you can see, the band diagram consists of 24 branches, which agrees with the number of modes obtained from symmetric analysis. Of these, 3 are acoustic branches corresponding to the propagation of sound as $\omega \rightarrow 0$ for **q** $\rightarrow 0$. As can be seen from Figure 6.1 in the direction Γ – Z degeneration of the two lower TA branches is observed. The remaining 21 calculated vibrational branches correspond to the optical modes of vibrations. There is an insignificant dispersion of phonons, which increases when approaching the center of the Brillouin zone. At the Γ point it is observed the largest dispersion. Low-frequency optical branches interact with acoustic ones. The highest phonon frequency for the AgGaS$_2$ crystal is 389 cm^{-1} on the segment between the Z – Γ points. As can be seen from the calculated density of states $N(\omega)$, Fig. 6.1 (b) They are at point Γ from 189.4 cm^{-1} to 219.5 cm^{-1} and from 255.9 cm^{-1} to 300.27 cm^{-1}. The frequencies of normal vibrations are given in Table 6.6. of vibrational properties were done using the primitive cell of the crystals.

In Fig. 6.2 shows the density of phonon states $N(\omega)$ projected on individual atoms (partial density of phonon states). As can be seen from Fig. 6.2, the density of states can be divided into three sections – low-frequency, medium-frequency, and high-frequency. The low-frequency part of the spectrum, which lies in the range of 0-75 cm^{-1}, is formed by silver

atoms vibrations. The spectral region from 75 to 190 cm^{-1}, which is the middle region of the phonon spectrum, is formed by the vibrational modes of gallium atoms. The high-frequency region of spectrum corresponds mainly to the vibrations of sulfur atoms. These results are in good agreement with the theoretical calculations performed in [259], which confirms the reliability of the results obtained in this work.
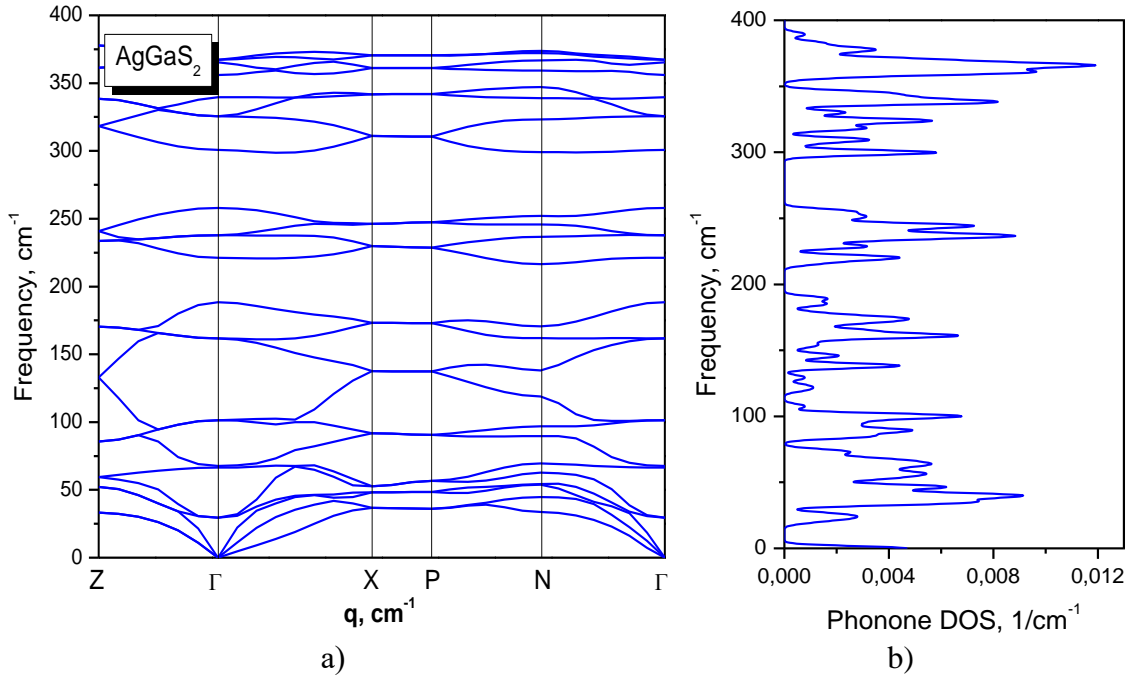
Figure 6.1. The Phonon dispersion curves $\omega(q)$ (a) and the phonon density of states $N(\omega)$ (b) of silver thiogalate AgGaS$_2$ crystal calculated by the method of linear response using the LDA functional. The path is determined in the direction of the Brillouin zone.
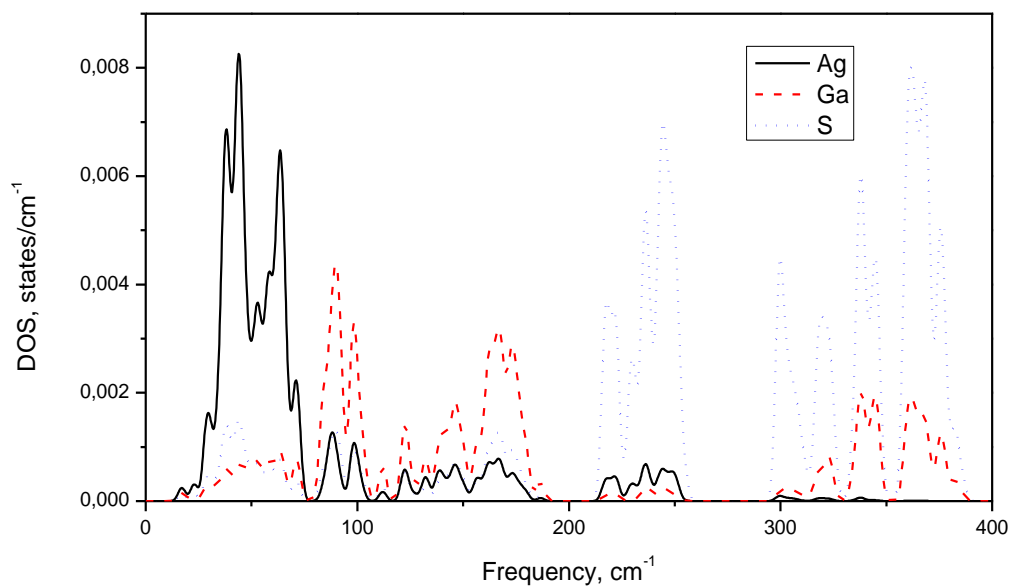
Figure 6.2. The partial phonon density of states $N(\omega)$ of AgGaS$_2$ crystals for Ag, Ga and S atoms calculated by the linear response method using the LDA functional.

In Fig. 6.3 shows the main atomic displacements for the optical modes of the AgGaS$_2$ crystal. The Ag, Ga, and S atoms are denoted by blue, brown and yellow balls, respectively. Their displacement is shown by green arrows. The lower left corner shows the directions of the coordinate system x, y and z, which correspond to the crystallographic axes a, b and c. Each block of atoms that makes up a primitive cell, together with arrows indicating the direction of displacement of atoms, characterizes the vibrations of one mode. The figure shows the types of atomic displacements for the five vibrational modes A_1, A_2, B_1, B_2 and E of the investigated crystal. The frequency of the corresponding vibration is given in parentheses.

A_1 ($\omega = 300.27$ cm^{-1})　　　A_2 ($\omega = 255.98$ cm^{-1})　　　E ($\omega = 100.84$ cm^{-1})

a)　　　　　　　　　　　b)　　　　　　　　　　　c)

B_1 ($\omega = 189.44$ cm^{-1})　　　B_2 ($\omega = 219.41$ cm^{-1})

d)　　　　　　　　　　　e)
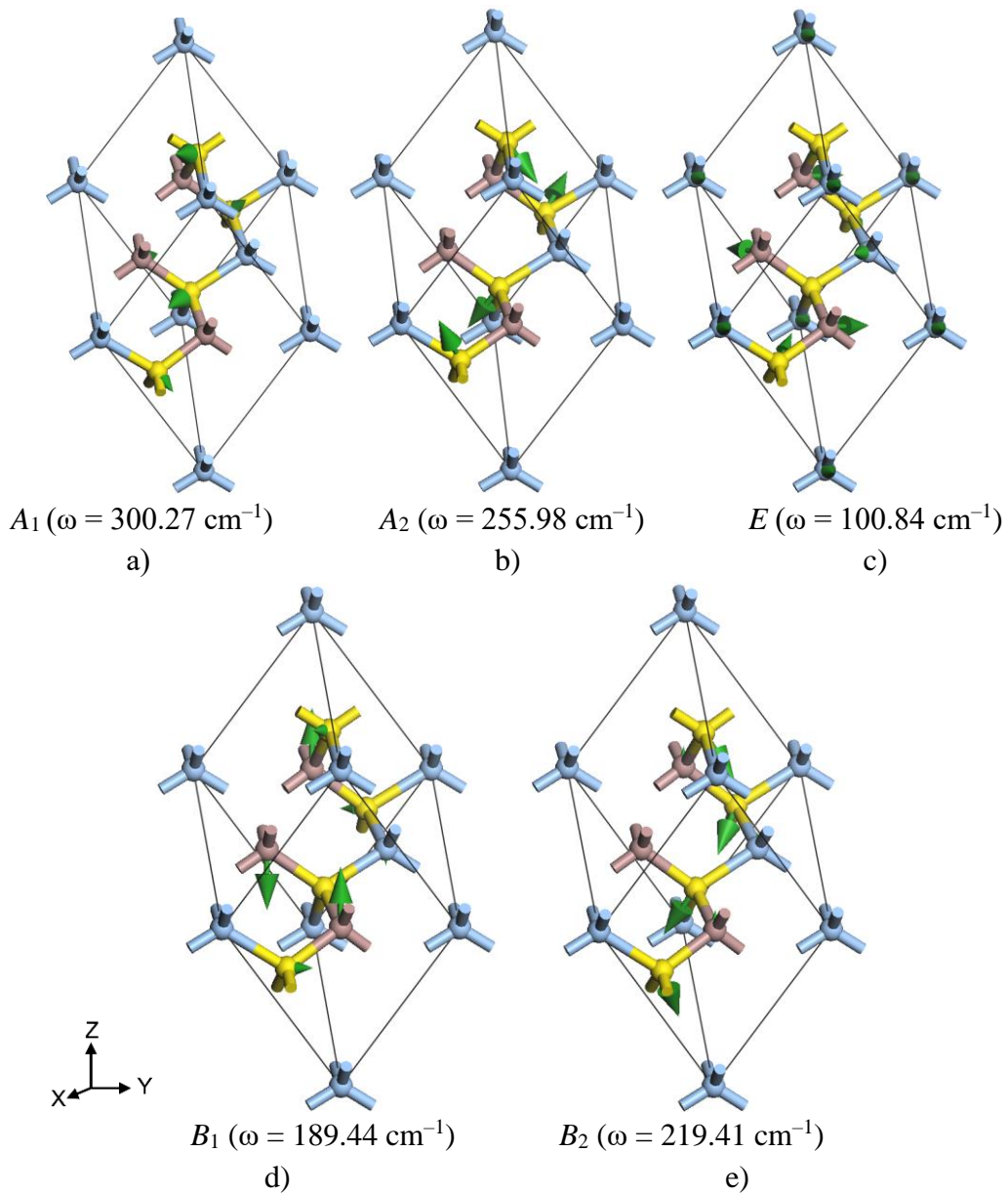
Figure 6.3. Vibrations in the AgGaS$_2$ crystal a) symmetry A_1; b) symmetry A_2; c) symmetry E; d) symmetry B_1; e) symmetry B_2. Ag atoms are blue, Ga atoms are shown in brown and S atoms are yellow balls.

Table 6.6. Comparison of the calculated phonon frequencies (in cm^{-1}) at the point Γ with the experimental spectra of Raman and IR vibrations for the AgGaS$_2$ crystal at room temperature. Two frequencies are presented for studies of Raman spectra and IR spectra corresponding to LO and TO modes.

Assignment	Activity	LDA	R exp.[a]	R exp.[b]	R calc.[c]	IR exp.[d]
A_1	R	300.27	295	297.61	297.20	—
A_2	Silent	255.98	—	—	251.51	—
	Silent	356.97	—	—	357.91	—
E	R, IR	33.65	84.45	64.8	32.02/31.35	65.06
	R, IR	100.84	94.5	91.93	102.07/102.07	96.06
	R, IR	160.90	159.5/160	159.07	166.11/164.11	170.12/157.11
	R, IR	236.99	224/229.5	225.93	244.83/234.83	227.16/221.15
	R, IR	324.25	321.5/346	336.07	357.91/325.89	349.24/321.22
	R, IR	366.43	—	394	380.59/368.92	395.27/367.25
B_1	R	62.46	54	—	65.04	—
	R	189.44	190.5	126.7	192.80	—
	R	337.81	333.5	177.9	339.56	—
B_2	R, IR	67.77	64	—	74.72/74.38	—
	R, IR	219.41	212/237.5	225.93/208.09	265.85/223.48	244.17/214.15
	R, IR	365.24	364/398.5	391.48/362.51	386.26/365.92	383.26/365.25

[a]Ref. [260], [b]Ref. [261], [c]Ref. [259], [d]Ref. [262].
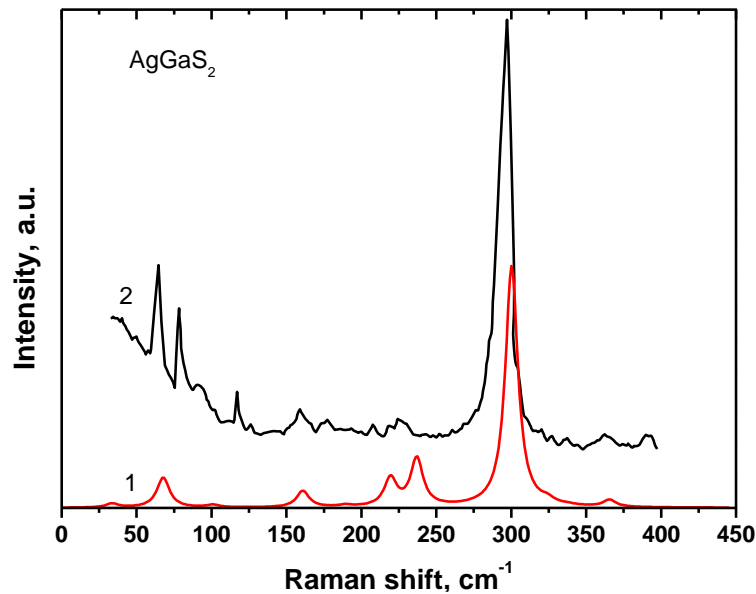
Figure 6.4. Calculated using the LDA functional and experimental [261] Raman spectra for the AgGaS$_2$ crystal.
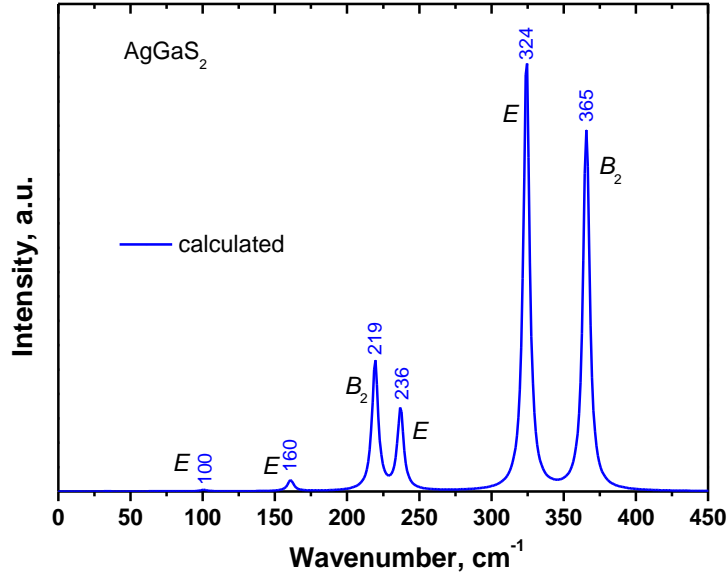
Figure 6.5. The calculated IR spectra of the AgGaS$_2$ crystal obtained using the LDA functional.

6.2.3. Infrared and Raman spectra of AgGaS$_2$ crystal

An important information about the vibrational properties of a crystal lattice can be obtained from the Raman spectra and infrared spectra. In this work, the IR and Raman spectra are calculated under the harmonic approximation, which considers phonon modes as independent ones. The Raman intensities are the changes in the polarizability α of the material under the action of perturbation of phonon mode R:

$$\frac{\partial \tilde{\mu}_{ij}}{\partial R_k} = \frac{\partial^3 E}{\partial G_i \partial G_j \partial R_k} = \frac{\partial^2 F_k}{\partial G_i \partial G_j}, \qquad (6.29)$$

where G is the external electric field of perturbation (photon). Details of calculation of the IR spectra are presented in [263].

Theoretical calculations of Raman spectra for the AgGaS$_2$ crystal are shown in Fig. 6.4. The calculated spectra are given for the wavelength of light of the fundamental beam incident on the investigated crystal λ = 514.5 nm and for the sample temperature T = 300 K. The spectrum was calculated in the frequency range from 0 to 400 cm^{-1}. As can be seen, there is a series of peaks in the spectrum, which corresponds to the vibrations of the structural elements of the AgGaS$_2$ crystal (Fig. 6.4 curve 1). The most intense peack, as predicted from the group analysis theorem, is the band at the frequency of 300.27 cm^{-1},

which corresponds to a totally symmetric vibration of A_1 symmetry. All other vibrational bands active in the Raman spectra have a much lower peak intensity. To compare the calculated Raman spectra with the experiment, in Fig. 6.4 is shown the experimental spectra taken from the literature [261] (Curve 2). Comparing the experimental and theoretical curves of the Raman spectra, their good agreement can be seen. It should be noted that the most intense peak A_1 is slightly shifted towards higher frequencies by magnitude $\Delta\omega \approx 2.7$ cm⁻¹. Such a shift was observed by us earlier for the β-LiNH₄SO₄ crystal [264].

The intensity of peaks, which occurs in the IR spectra can also be calculated numerically. It can be estimated from the change in the electric dipole moment μ of the system with respect to atomic displacement under the phonon mode perturbation R:

$$\frac{\partial \mu_i}{\partial R_k} = \frac{\partial^2 E}{\partial G_i \partial R_k} = \frac{\partial F_k}{\partial G_i},$$

(6.30)

where G is the external electric field of perturbation (photon). Details of calculation of the Raman spectra are collected in [263].

Figure 6.5 shows the theoretically calculated infrared spectra of the AgGaS₂ crystal calculated in the frequency range $\omega = 0 - 400$ cm⁻¹. For the IR spectra of the studied compound, the highest frequency of the vibrational mode is 365.24 cm⁻¹. The spectrum consists of five main peaks. Two peaks at 324.6 cm⁻¹ and 365.6 cm⁻¹ have a high intensity, and two peaks at $\omega = 219.6$ cm⁻¹ and 236.6 cm⁻¹ have an intensity of about 1/4 of the intensity of the highest peak, as well as one peak at 160.9 cm⁻¹ with low intensity. The most intense peak in this spectrum is at $\omega = 324.25$ cm⁻¹, while the peak of slightly lower intensity is at the frequency $\omega = 365.24$ cm⁻¹.

6.2.4. Born effective charge tensor and dielectric constants for AgGaS₂ crystal

The effective Born charge tensor shows the macroscopic electrical response of the crystal to the internal movement of atoms in the crystal. A uniform shift of the cation or anion sublattice generates macroscopic polarization, but does not create a macroscopic electric field, because the periodicity of the sublattice does not change. These charges make it possible to estimate the degree of ionicity of the material, and may be of interest in the analysis of LO-TO splitting, and are defined as induced polarization of a solid P_α along the α-direction for a unit atom displacement $\beta(\tau_{k\beta})$ along the direction belonging to the sublattice

k. According to the theory [258,265], the effective Born charges for the center of the Brillouin zone are calculated as

$$Z^*_{k,\alpha\beta} = \Omega \frac{\delta P_\alpha}{\delta \tau^{q=0}_{k,\beta}}\Bigg|_{E=0},$$ (6.31)

where Ω is the unit cell volume, δP_α is the polarization, and $\delta \tau_{\kappa,\beta}$ is displacement of *k*-th atom in the β-direction. Small values of Z^* indicate uncorrelated atomic displacement, which indicates phase stability.

To calculate the effective Born charges for the AgGaS₂ crystal, we considered independent displacements for all Ag, Ga, and S atoms. It was obtained an electronic contribution to the change in polarization along each *x*, *y*, and *z* direction. The calculation of the dynamic and effective charges of the investigated crystal was performed within the standard procedure for calculating its vibrational spectrum using the CASTEP program and using DFPT, implemented in it by the linear response method. The calculated Born effective charge tensors (Z^*) describing the homogeneous shifts of the Ag, Ga, and S sublattices in an AgGaS₂ crystal, the eigenvalues of the symmetric part $Z^*(\lambda)$, and the dynamic charges Q_d, which are the mean values of the diagonal elements of this tensor, are presented in Table 6.7. The tensors of effective charges are given for one Ag atom with position 4*a* (S_4), one Ga atom with position 4*d* (S_4) – because the others are equivalent, and for two S atoms with position 8*d*. As can be seen from the table, the tensors are diagonal and almost isotropic. For tetragonal crystals, according to its symmetry $Z^*_{xx} = Z^*_{yy} \neq Z^*_{zz}$. The value $Z^*_{xx}/Z^*_{zz} = 1.17$ for silver atoms; $Z^*_{xx}/Z^*_{zz} = 0.94$ – for gallium atoms. The tensor is almost spherical with a small tetragonal curvature, like the crystal structure, due to non-fulfillment of the ratio *c*/2*a* = 1.

Sulfur atoms are located in position 8*d* with lower symmetry (C_2) compared to Ag and Ga atoms. Therefore, the symmetry of the tensor Z^* is lower for S atom. Anions have the following components of the tensor: $Z^*_{S,zz} = -1.88$, whereas $Z^*_{S,xx}$, and also $Z^*_{S,yy} = -1.64$ or -2.12, depending on which curvature parameter *u*. A similar form of the tensor Z^* is reported for the ZnSnP₂ crystal [265]. Also, due to the curvature *u* along the *x* or *y* direction, the following non-diagonal components become non-zero: $Z^*_{S,yz} = \pm 0.73$, $Z^*_{S,zy} = \pm 0.82$, $Z^*_{S,xz} = \pm 0.73$, $Z^*_{S,zx} = \pm 0.82$.

Table 6.7. The Born effective charges Z^*, the eigenvalues of the symmetric part $Z^*(\lambda)$, and the dynamic charges Q_d (in units of charge e) calculated for the AgGaS$_2$ crystal.

Atom	Z^*			$Z^*(\lambda)$	Q_d
Ag	$Z^*_{Ag} = \begin{pmatrix} 1.10 & 0.10 & 0.00 \\ -0.10 & 1.10 & 0.00 \\ 0.00 & 0.00 & 0.94 \end{pmatrix}$			$\begin{pmatrix} 1.10 \\ 1.10 \\ 0.94 \end{pmatrix}$	1.05
Ga	$Z^*_{Ga} = \begin{pmatrix} 2.66 & 0.23 & 0.00 \\ -0.23 & 2.66 & 0.00 \\ 0.00 & 0.00 & 2.82 \end{pmatrix}$			$\begin{pmatrix} 2.66 \\ 2.66 \\ 2.82 \end{pmatrix}$	2.71
S1	$Z^*_{S1} = \begin{pmatrix} -1.64 & 0.00 & 0.00 \\ 0.00 & -2.12 & -0.73 \\ 0.00 & -0.82 & -1.88 \end{pmatrix}$			$\begin{pmatrix} -1.22 \\ -2.78 \\ -1.64 \end{pmatrix}$	−1.88
S3	$Z^*_{S3} = \begin{pmatrix} -2.12 & 0.00 & 0.73 \\ 0.00 & -1.64 & 0.00 \\ 0.82 & 0.00 & -1.88 \end{pmatrix}$			$\begin{pmatrix} -1.22 \\ -2.78 \\ -1.64 \end{pmatrix}$	−1.88

The formal charges of the constituent atoms of AgGaS$_2$ crystals are as follows: Ag +1; Ga +3; S –2 (in charges e). As can be seen from the table, there is a deviation of the dynamic charges relative to the nominal values of free ions 1.047, 2.713, –1.88 for Ag, Ga and S atoms, respectively. Deviation from normal charges indicates a dynamic transfer of charge between ions. Additionally, such a deviation of charges indicates a relatively strong covalent bond between the atoms in this compound. We do not know the literature data on the effective charges for the AgGaS$_2$ crystal.

From the second derivative of the total energy of the system in the electric field, we can obtain the dielectric constant of the system ε [266]. If we consider the contribution to the energy of the system only from the electronic subsystem E_{el}, the dielectric response is a purely optical tensor of the dielectric susceptibility ε_∞ which can be obtained as follows

$$\varepsilon^\infty_{\alpha\beta} = \delta_{\alpha\beta} - \frac{4\pi}{\Omega} \frac{\partial^2 E_{el}}{\partial\varepsilon_\alpha \partial\varepsilon_\beta}, \qquad (6.32)$$

where α and β are the indices of the directions in the Cartesian coordinate system, and Ω is the volume of the primitive cell. Static dielectric constant can be decomposed into different modes and calculated by the generalized Lyddane-Sachs-Teller (LST) ratio.

$$\varepsilon_0 = \varepsilon_\infty \prod_m \frac{\omega^2_{\text{LO},m}}{\omega^2_{\text{TO},m}}, \qquad (6.33)$$

where $\omega_{TO,m}$ is the frequency of the transverse optical mode and $\omega_{LO,m}$ is the frequency of the longitudinal optical mode. This ratio is calculated separately for each polarization. Using the DFPT formalism, we calculated the electron ε_∞ and static dielectric permittivity tensors ε_0 for the crystal under study. According to the symmetry of the crystal, the tensor is diagonal with the following components $\varepsilon_{xx} = \varepsilon_{yy} \neq \varepsilon_{zz}$. The calculated coefficients of the tensors ε_0 and ε_∞ are given in Table 6.8. Both static and electronic dielectric constants, similarly to Born effective charges, have a slight anisotropy (1.03 for ε_∞ and 0.98 for ε_0). The experimental value of the dielectric constant for the AgGaS$_2$ crystal is equal to 10 [267], which agrees well with the average value of the static dielectric function calculated in this work, which is equal to 10.095.

Table 6.8. Static ε_0 and electronic ε_∞ dielectric constants were calculated for the AgGaS$_2$ crystal using the LDA functional.

$\varepsilon_{\alpha\beta}^\infty$		$\varepsilon_{\alpha\beta}$	
$\varepsilon_{xx}^\infty = \varepsilon_{yy}^\infty$	7.50	$\varepsilon_{xx} = \varepsilon_{yy}$	9.79
ε_{zz}^∞	7.31	ε_{zz}	10.04
$\varepsilon_{xx}^\infty / \varepsilon_{zz}^\infty$	1.03	$\varepsilon_{xx} / \varepsilon_{zz}$	0.98

6.3. Vibrational properties of the AgGaSe$_2$ crystal

6.3.1. Phonon spectra of AgGaSe$_2$ crystals

For the AgGaSe$_2$ crystal, the calculated dispersion of phonons is shown in Fig. 6.6. There are 24 vibrational modes in the vibtrational spectrum. As can be seen from the figure, for this crystal there are no negative (imaginary) vibrational frequencies in the calculated spectrum, which indicates the stability of the crystal structure. In the $\Gamma - Z$ direction, as for the AgGaS$_2$ crystal, degeneration of the two lower TA branches is observed. The three acoustic vibrational branches corresponding to the increase of the vibratinal frequency at the distance from the center of the Brillouin zone at the frequency $\omega = 34$ cm^{-1} overlap with the

optical modes of oscillation. For the AgGaSe₂ crystal, as in AgGaS₂, the largest dispersion is observed towards the center of the Brillouin zone. In the X – P direction, the dispersion of phonons is practically absent (vibration frequencies remain constant). The highest vibrational frequency in the crystal is 262 cm^{-1} near the N point of the Brillouin zone.
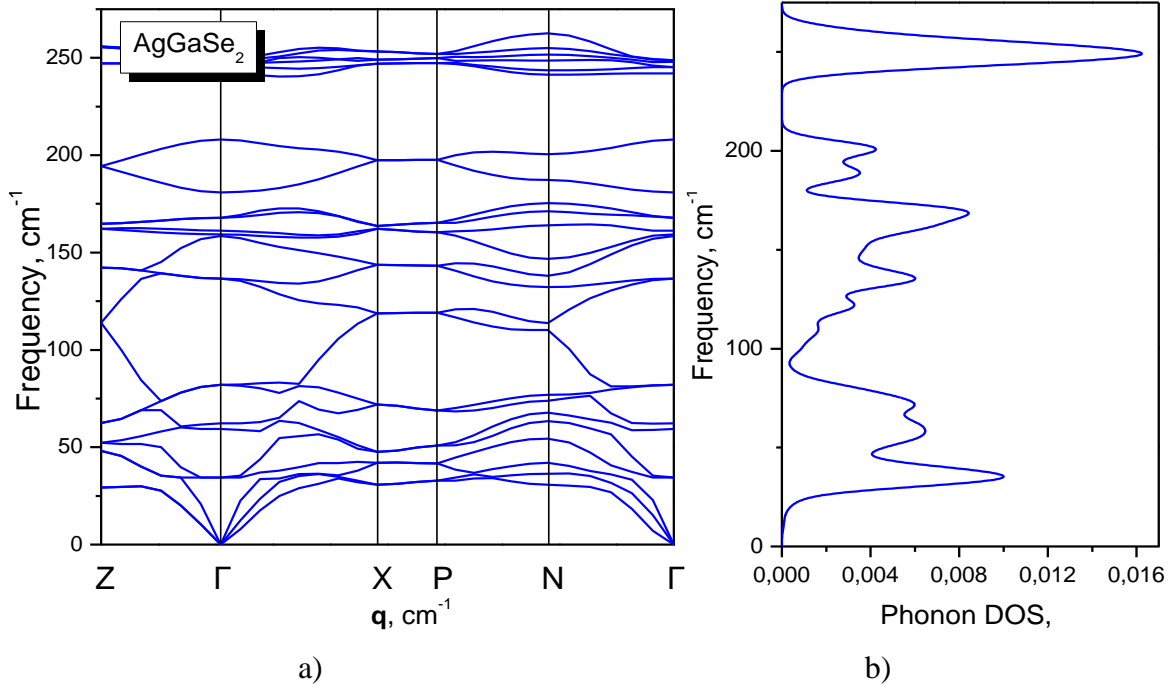
Figure 6.6. The calculated phonon dispersion curves $\omega(q)$ (a) and the phonon density of states $N(\omega)$ (b) of the AgGaSe₂ crystal were calculated by the linear response method using the LDA functional. The path is determined in the direction of the first Brillouin zone. The symbols are adapted to the symmetry of the active structure. Z (1/2, ½, –1/2), Γ (0, 0, 0), X(0, 0, 1/2), P(1/4, 1/4, 1/4), N(0, 0.5, 0).
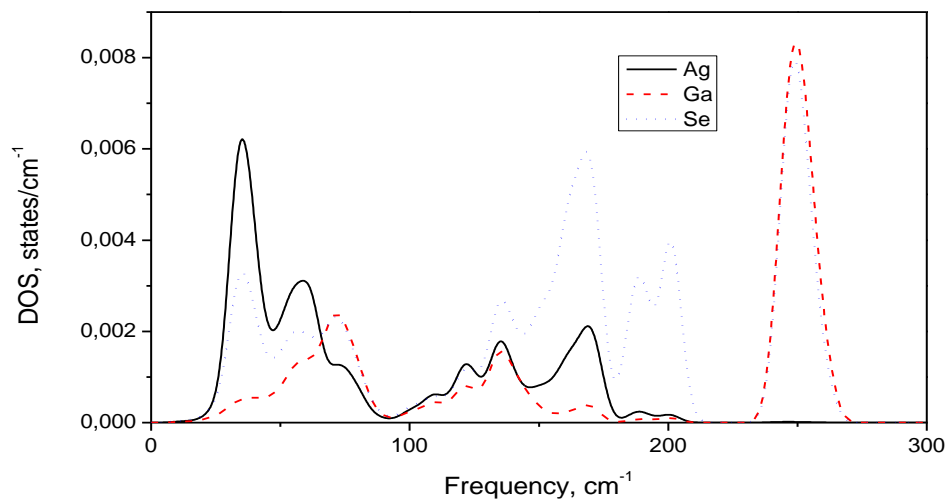
Figure 6.7. The partial phonon density of states $N(\omega)$ in AgGaSe₂ crystals, calculated by the linear response method using the LDA functional for Ag, Ga, and Se atoms.

Calculated for the AgGaSe$_2$ crystal phonon density of states $N(\omega)$ is shown on Fig. 6.6 b). The highest bandle of vibrational levels is separated by a range of forbidden frequencies, which is in the frequency range from 208 to 242 cm^{-1}. The highest density of states corresponds to the bandle of levels with the highest frequencies around 250 cm^{-1}. The calculated frequencies of the normal vibrational modes for the AgGaSe$_2$ crystal at Γ-point are collected in Table 6.9.

In Fig. 6.7. shows the partial density of vibrational states $N(\omega)$ for the AgGaSe$_2$ crystal for three types of constituent atoms (Ag, Ga, and Se$_2$). A clear intensity distribution for individual types of atoms is visible. Similar to AgGaS$_2$ in the AgGaSe$_2$ crystal, the density of phonon states can be divided into three sections. The low-frequency region is formed by vibrational levels of the silver atom. It lies in the frequency range from 0 to 75 cm^{-1}. Weak contribution to the vibrational spectrum of silver atoms is in the range from 0 up to 210 cm^{-1}. You can also observe a slight compression of the vibrational spectrum in the direction of lower frequencies compared to the silver thiogalate crystal. The middle frequency range is formed by vibrations of gallium atoms with a smaller contribution of vibrations of silver atoms. The main contribution of Ga atoms in the middle region of the spectrum corresponds to the interval in the spectral region of 127-211 cm^{-1}. The high-frequency peak with a maximum at 249 cm^{-1} is formed by a mixture of selenium and gallium atom contributions. Thus, the replacement of S $\rightarrow$ Se leads to compression of a wide band of vibrational levels in the high frequency region and the formation of a wide band formed by chalcogen atoms with a small contribution of gallium atoms.

The main atomic displacements for the optical modes of the AgGaSe$_2$ crystal are shown in Figs. 6.8. Ag, Ga and Se atoms are marked with blue, brown and yellow balls, respectively. Their displacement is shown by green arrows. The lower left corner shows the directions of the coordinate system x, y and z which correspond to the crystallographic axes a, b and c. Each block of atoms that makes up a primitive cell, together with arrows indicating the direction of displacement of atoms, characterizes the vibrations of one mode. The figure shows the types of atomic displacements for the five vibrational modes A_1, A_2, B_1, B_2 and E of the investigated crystal. The frequency of the corresponding vibrations is given in parentheses.

A_1 ($\omega = 180.53$ cm^{-1}) A_2 ($\omega = 160.82$ cm^{-1}) E ($\omega = 85.38$ cm^{-1})

a) b) c)

B_1 ($\omega = 157.13$ cm^{-1}) B_2 ($\omega = 159.20$ cm^{-1})
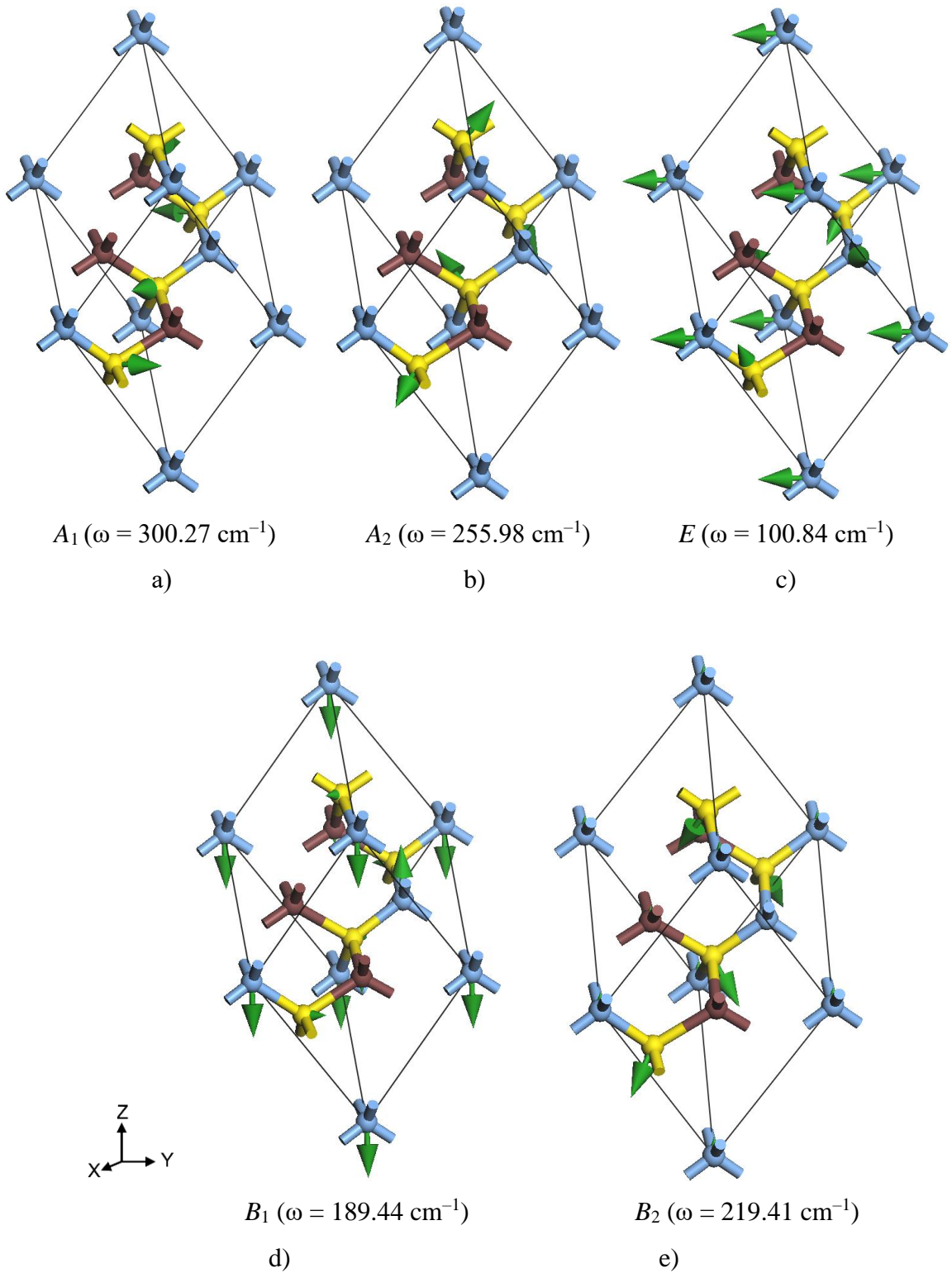
d) e)

Figure 6.8. Vibrations in the AgGaSe₂ crystal a) symmetry A_1; b) symmetry A_2; c) Symmetry E; d) symmetry B_1; e) symmetry B_2. Ag atoms are blue, Ga atoms are brown and Se atoms are yellow balls.

Table 6.9. Comparison of the calculated phonon frequencies (in cm^{-1}) at the point Γ with the experimental Raman spectra and IR vibrations for the $AgGaSe_2$ crystal at room temperature. Two frequencies are presented in some data of studies of Raman spectra and IR spectra corresponding to LO and TO modes.

Mode	Activity	LDA	R exp.[a]	R exp.[b]	IR exp.[b]
A_1	R	180.53	180	181	—
A_2	Silent	160.81	159	—	—
	Silent	204.89	—	—	—
E	R, IR	32.50	—	–/27	—
	R, IR	85.38	—	84 (T+L)	80/79
	R, IR	139.03	136	138/137	137/135
	R, IR	168.92	276	165/162	165/162.5
	R, IR	246.15	—	–/255	250/251
	R, IR	250.98	—	277/251	278.5/248
B_1	R	62.36	56	58	—
	R	157.13	253	161	—
	R	240.64	—	253	—
B_2	R, IR	58.06	—	58/–	63/62.5
	R, IR	159.20	—	161/155	165/–
	R, IR	246.13	249	275/252	275.5/249.5

Ref. [a] [268]; Ref. [b] [269];

Using Eq. (6.17), the Raman spectra for the $AgGaSe_2$ crystal were calculated. Figure 6.9 shows the Raman spectra constructed for the wavelength of light of the fundamental beam incident on the investigated crystal $\lambda = 514.5$ nm and for temperature $T = 300$ K. The constructed spectrum is given in the frequency range $\omega = 0$ –400 cm^{-1}. The Raman spectrum consist of a number of peaks corresponding to the vibrations allowed in the Raman spectrum. The Fig. 6.9 shows for comparison the experimental spectra presented in the literature [269] (curve 2). The most intense, as predicted by the group-theoretical analysis, is the band of vibrations at a frequency $\omega = 180.53$ cm^{-1}. This band corresponds to the totally symmetric vibrations of symmetry A_1. As for the $AgGaS_2$ crystal, in the $AgGaSe_2$ crystal, the A_1 band has the highest intensity, while all other bands have a significantly lower. In general, the calculated spectrum coincides well with the experimentally obtained results of the Raman

spectra study reported in [268,269]. For calculation of the Raman spectra the band that corresponds to the irreducible representation A_1 has also a small shift to the higher frequencies ($\Delta\omega \approx$ 2 cm^{-1}). Also, we can see that the experimental curve of the novel spectrum contains a peak at the frequency $\omega = 276$ cm^{-1}, which is not active in the theoretical spectra (see Fig. 5.9.).
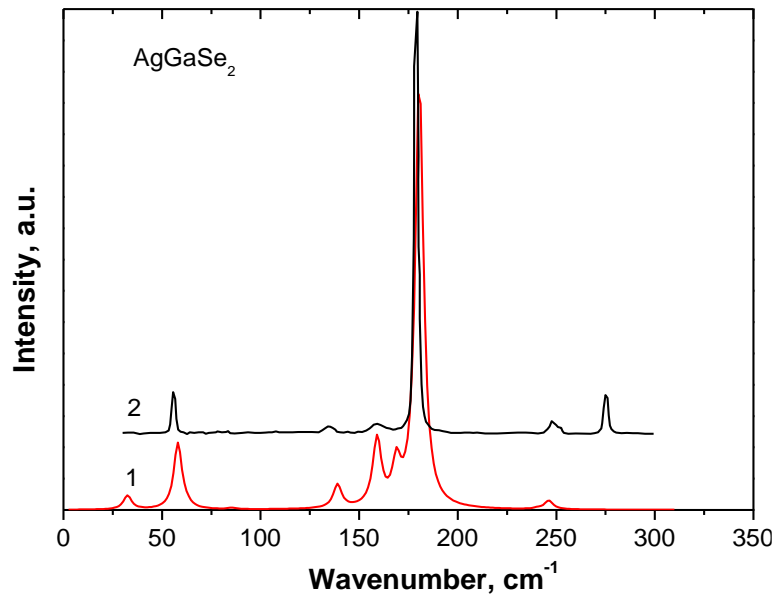
Figure 6.9. Calculated using LDA functional, and experimental [269] Raman spectra of AgGaSe$_2$ crystal.
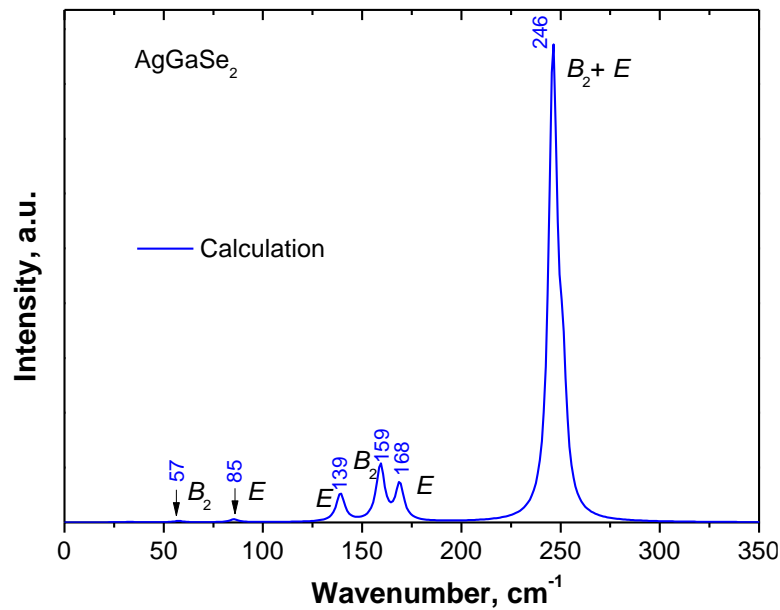
Figure 6.10. The calculated IR spectra of the AgGaSe$_2$ crystal obtained using the LDA functional.

From the Eq. 6.18 the infrared spectra was calculated whin the DFPT method. On the Fig. 6.10 the theoretically calculated infrared spectra of the AgGaSe₂ crystal calculated in the frequency range $\omega = 0 - 400$ cm^{-1} are given. You can see 6 peaks on the spectrum. One peak has the highest intensity. Three peaks have a lower intensity and two peaks have a lower intensity. For the IR spectra of the test compound, the highest frequency of the vibrational mode is $\omega = 246.49$ cm^{-1}. This peak corresponds to the sum of two vibrations of E and B_2 symmetry. It should be noted that these two high-frequency peaks in the AgGaS₂ crystal are well separated in the infrared spectra. The series of three peaks of lower intensity is located at lower frequencies: 168.49, 159.49, 139.49 cm^{-1}, belonging to E, B_2, and E symmetry, respectivaly. Two peaks (B_2 and E symmetry) of low intensity is located at $\omega = 85.19$ and 57.49 cm^{-1}.

6.3.2. Born effective charge tensor and dielectric constants for AgGaSe₂

For the AgGaSe₂ crystal, the components of the Born efficient charge tensor Z^* are also calculated. According to the symmetrical crystal structure for the AgGaSe₂ crystal, the tensor Z^* has a same symmetry as AgGaS₂ and other crystals of group I-III-VI₂. The calculated tensors of the effective Born charge for the displacement of Ag, Ga, and Se ions are collected in Table 6.10. The table also shows the eigenvalues of the symmetric part $Z^*(\lambda)$ and the dynamic charges Q_d (in units of charge e) of the AgGaSe₂ crystal.

From the table it can be seen that for Z^*-tensor has non-zero off-diagonal elements for all constituent atoms in the cell. We can see that the Ag effective charge is higher than 1 in the x and y directions while for the zz component tensor $Z^* = 0.82$ is smaller. For AgGaSe₂ crystal the Born effective charge is 0.12 e higher than for silver thiogallate crystal. The calculated Born effective charge tensors (Eq. 6.1) of the Ga atoms are found to be almost diagonal and isotropic. The largest component $Z^*_{zz} = 2.66$ is also smaller than the nominal value 3. In the case of galium we find $\frac{1}{3}\sum_\alpha Z^*_{\alpha\alpha,Ag} = +2.65$.

Selenium atoms, like sulfur for the AgGaS₂ crystal, are located at position 8d, so the Born effective charge tensor was calculated for Se1 and Se3 atoms. For selenium, we obtained the following components of the tensor: $Z^*_{Se,xx} = Z^*_{Se,yy} = -1.75$ or -2.24 and $Z^*_{Se,zz} =$

–1.74. The normal charges of the constituent atoms of AgGaSe$_2$ crystals are as follows: Ag +1; Ga +3; Se –2 (in charges e). The observed deviation of the nominal charges for the types of atoms forming the AgGaSe$_2$ compound indicates a covalent interaction between the constituent atom. This finding is consistent with the observation made in the case of AgGaSe$_2$ crystal. As a check of the electroneutrality of the system we verified that the total Born effective charge tensor of the unit cell is (almost) vanishing. We find the largest component to be $\max_{k,\alpha\beta} \sum_k Z^*_{k,\alpha\beta} = 0$.

Table 6.10. The Born effective charges Z^*, the eigenvalues of the symmetric part $Z^*(\lambda)$, and the dynamic charges Q_d (in units of e) of the AgGaSe$_2$ crystal.

| Atom	Z^*	$Z^*(\lambda)$	Q_d
Ag	$Z^*_{Ag} = \begin{pmatrix} 1.35 & 0.11 & 0.00 \\ -0.11 & 1.35 & 0.00 \\ 0.00 & 0.00 & 0.82 \end{pmatrix}$	$\begin{pmatrix} 1.35 \\ 1.35 \\ 0.82 \end{pmatrix}$	1.17
Ga	$Z^*_{Ga} = \begin{pmatrix} 2.64 & 0.31 & 0.00 \\ -0.31 & 2.64 & 0.00 \\ 0.00 & 0.00 & 2.66 \end{pmatrix}$	$\begin{pmatrix} 2.64 \\ 2.64 \\ 2.66 \end{pmatrix}$	2.65
Se1	$Z^*_{Se1} = \begin{pmatrix} -1.75 & 0.00 & 0.00 \\ 0.00 & -2.24 & 0.55 \\ 0.00 & 0.83 & -1.74 \end{pmatrix}$	$\begin{pmatrix} -1.28 \\ -2.71 \\ -1.75 \end{pmatrix}$	–1.91
Se3	$Z^*_{Se3} = \begin{pmatrix} -2.24 & 0.00 & -0.55 \\ 0.00 & -1.75 & 0.00 \\ -0.83 & 0.00 & -1.74 \end{pmatrix}$	$\begin{pmatrix} -1.28 \\ -2.71 \\ -1.75 \end{pmatrix}$	–1.91

Using equations (6.32) and (6.33), we calculated the high-frequency electron ε_∞ and static dielectric constant ε_0 for the AgGaSe$_2$ crystal within DFPT. The calculated coefficients of the tensors ε_0 and are given in Table 6.10. As can be seen from the table, both static and optical dielectric steels in the $xx = yy$ direction are greater than the corresponding values for the zz direction. For the optical dielectric constant, this behavior correlates with the AgGaS$_2$ crystal. Both static and electronic dielectric constants, like Born charges, have a slight anisotropy (1.23 for ε_∞ and 1.19 for ε_0). There is a slight increase in the anisotropy of the dielectric constants when replacing the S $\rightarrow$ Se anion. The ratios of $\varepsilon_0 / \varepsilon_\infty$ is equal to the to about 1.3. This corresponds to the very low LO – TO splittings. The experimental value of

the dielectric constant for the AgGaSe$_2$ crystal is equal to 10.5 for x direction and 12.0 for z direction [175].

Table 6.11. Static ε_0 and ε_∞ electron dielectric constants calculated for the AgGaSe$_2$ crystal using the LDA functional.

$\varepsilon_{\alpha\beta}^{\infty}$		$\varepsilon_{\alpha\beta}$	
$\varepsilon_{xx}^{\infty} = \varepsilon_{yy}^{\infty}$	9.11	$\varepsilon_{xx} = \varepsilon_{yy}$	11.62
$\varepsilon_{zz}^{\infty}$	7.38	ε_{zz}	9.79
$\varepsilon_{xx}^{\infty} / \varepsilon_{zz}^{\infty}$	1.23	$\varepsilon_{xx} / \varepsilon_{zz}$	1.19

6.4. Vibrational properties of the AgGaTe$_2$ crystal

6.4.1. Phonon dispersion of AgGaTe$_2$ crystal

In order to investigate the phonon spectrum of AgGaTe$_2$ crystal we used the linear response method in the DFPT approach together with the LDA functional using the similar parameters as for the AgGaS$_2$ and AgGaSe$_2$ crystals [165]. Before the calculations, the geometry optimization of the crystal model was performed. The phonon band structure $\omega(q)$ constructed along several lines connecting the high symmetry points $Z - \Gamma - X - P - N - \Gamma$ is presented in Fig. 6.11 (a). The figure shows that the longitudinal acoustic (LA) and transverse acoustic (TA) branches are linear in the vicinity of the Γ-point. There are no negative (imaginary) vibrational frequencies for the AgGaTe$_2$ crystal, which indicates the stability of lattice to the long-wavelength transverse thermal vibrations. As one can see, from the phonon band structure, the two TA branches in $\Gamma - X$ directions characterized by the higher symmetry (the branches are very close to each other) than the corresponding branches in AgGaS$_2$ and AgGaSe$_2$ crystals. In the $\Gamma - Z$ direction TA vibrational branches of two modes are degenerated.

a)   b)
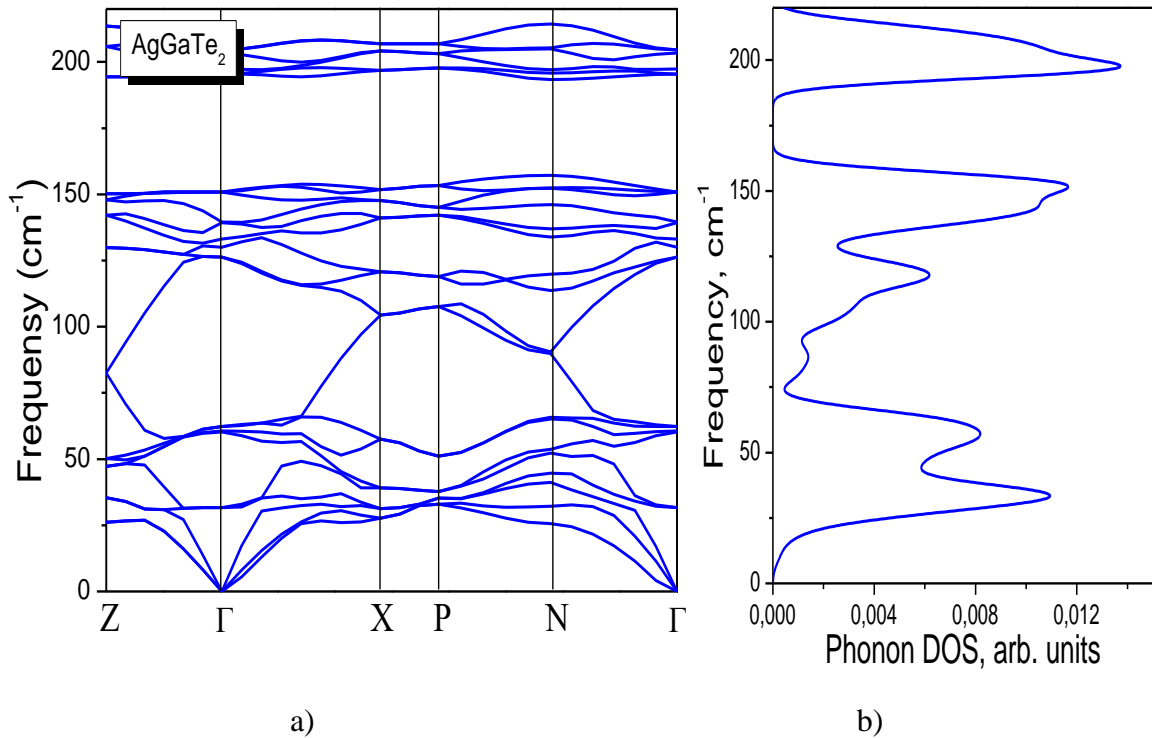
Figure 6.11. Calculated phonon dispersion $\omega(\mathbf{q})$ and phonon density of states for AgGaTe$_2$ crystal.

Additionally, the phonon density of states $N(\omega)$ was obtained by the BZ integration of the phonon dispersion relations (Fig. 6.11 (b)). As the feature of the phonon spectrum of AgGaTe$_2$ the presence of the forbidden frequency band, previously reported for the CuGaTe$_2$ crystal [270], should be noted. However, the band gap of the AgGaS$_2$ is much wider than in CuGaTe$_2$. Previously, the studies similar to ours were conducted by Yang et. al. [184] using the VASP program under DFT-GGA method. The calculated phonon band structure and the total density of states are in good agreement with the reported in [184]. Unfortunately, the data on the experimental study of inelastic neutron scattering required for comparison with the theoretical results obtained in this work is not available up to now.

Phonon partial density of states $N(\omega)$ of AgGaTe$_2$ crystal is is plotted and the information of lattice vibrational contribution of each atom to phonon dispersion is shown in Fig. 6.12. The figure shows that the vibrational spectrum of the crystal can be divided into three separate parts formed by different groups of atoms. The first part, which contains high-frequency optical modes, is formed mainly by contributions of the Ga atoms vibrations. Here the smaller contribution of Te atoms vibration is presented. The second part contains wide frequency region starting from the near-gap frequency (170 cm^{-1}) to the low frequency vibrations at 70 cm^{-1}. These phonons are formed by the mixed contributions of Ag, Te and

Ga atoms. In this region the main contribution is related with the Te atoms vibrations while the Ag modes give the lower intensity in the phonon DOS. It should be noted, that gallium atoms make a minor contribution to the vibration spectrum at values of the wave number of about 60 cm^{-1}. The low frequency spectral range in the $N(\omega)$ consist of the Te atoms vibration with large contribution of Ag ions vibrations. In addition, there are some low-frequency optical phonon modes, which are mixed with acoustic phonon modes. Such a mixture of optical and acoustic phonon modes contributes to a decrease in thermal conductivity, which, as a result, leads to an increase of the thermoelectric figure of merit *ZT*. Comparing the phonon densities of state for the crystals AgGaX$_2$ (X = S, Se, and Te) one can see that the maximal frequencies in the vibrational spectra obeys the following sequence $\omega_S^{max} > \omega_{Se}^{max} > \omega_{Te}^{max}$ for X = S, Se, and Te respectively.
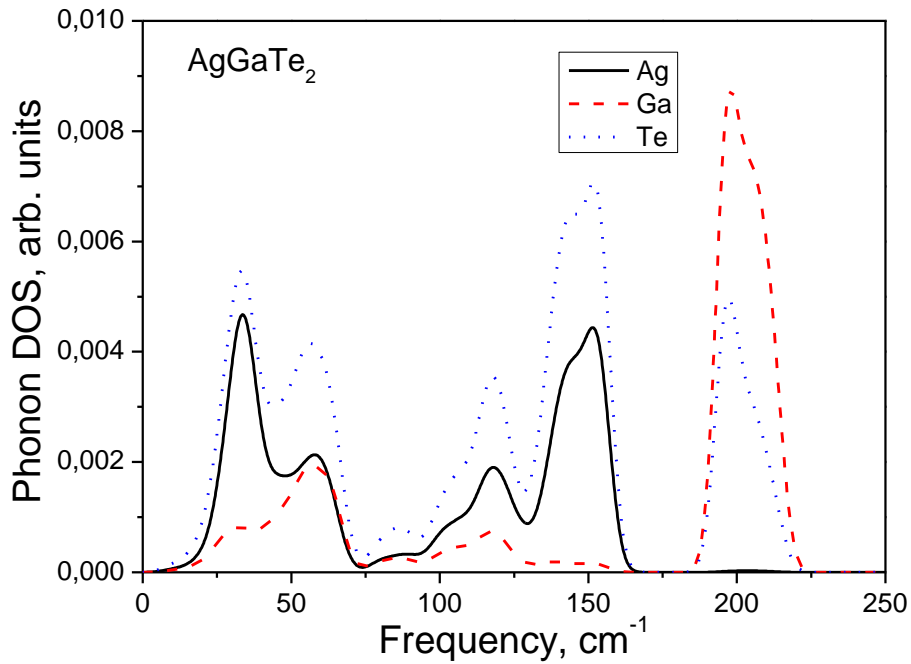
Figure 6.12. Calculated projected phonon density of states for AgGaTe$_2$ crystal.

Figure 6.13. Vibrations in the AgGaTe$_2$ crystal a) symmetry A_1; b) symmetry A_2; c) symmetry E; d) symmetry B_1; e) symmetry B_2. Ag atoms are blue, Ga atoms are brown and Te atoms are yellow balls.

6.4.2. Infrared and Raman spectra of AgGaTe₂ crystals

The theoretically calculated in this work Raman and infrared spectra of the AgGaTe₂ crystal are presented in Fig. 6.14 and 6.15. The experimental Raman scattering spectrum for the excitation radiation wavelength of 532 nm reported in [271,272] and IR spectrum [271] are presented in both figures for comparison.

The calculated Raman spectrum contains three distinctive non-symmetric peaks. The most intensive is at 135 cm^{-1} and correspond to the A_1 mode. This is the mode for which two pairs of anions vibrate in the following way: one in the direction of the *a*-axis and another one in the direction of *b*-axis. The calculated frequency of this mode is shifted for 5 cm^{-1} towards the higher frequencies in comparison with experimental value. The calculated peak at 209 cm^{-1} correspond to the B_1 mode, and the low-frequency vibration at 62 cm^{-1} is also of B_1 symmetry. For the AgGaTe₂ crystal, the most intense peak was observed at 135 cm^{-1} and also corresponded to the A_1 mode. For this crystal, the shift of the peak A_1 relative to the experimental spectrum was $\Delta\omega \approx 6$ cm^{-1} toward higher frequencies, which shows good agreement with the experimental spectrum of the novel obtained in [30].
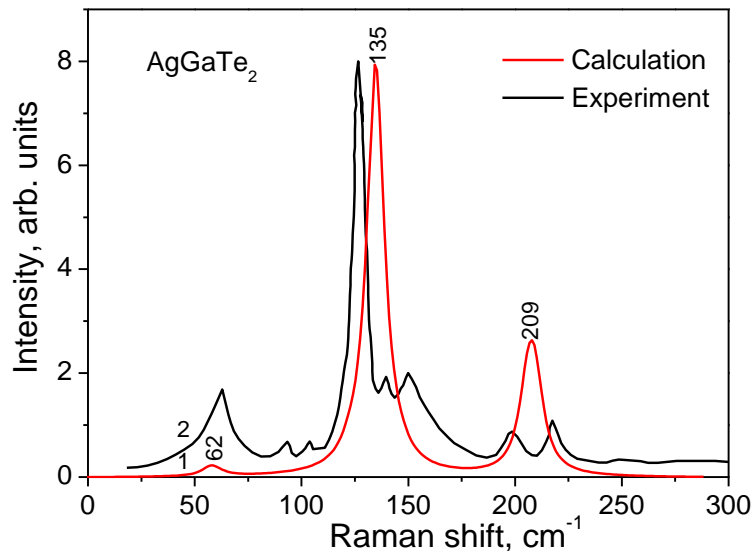
Figure 6.14. Calculated and experimental [30] Raman spectra of AgGaTe₂ crystal.

Figure 5.15 shows a diagram of the position of the band in the Raman spectrum for AgGaX₂ crystals (X = S, Se, Te), which is characterized by symmetry A_1 whose intensity is the highest. For comparison, the diagram shows the position of this mode in the experimental spectra of the Raman from [30,261,269]. It can be clearly seen from the diagram that the replacement of the anion S → Se → Te leads to a shift of the A_1 mode towards lower

frequencies. It is known that the vibrational frequency is inversely proportional to mass. This change in frequency corresponds to the change in the mass of the corresponding ions (m_{Te} (127.6 g / mol)> m_{Se} (78.96 g / mol)> m_S (32.065 g / mol)). Also, it is important to note that the theoretically calculated frequency shows good agreement with the experimental frequency of the corresponding band. The largest deviation from the experiment is 6 cm^{-1} for AgGaTe₂, while for AgGaS₂ the offset is 5 cm^{-1}. This shift is not observed for the AgGaSe₂ crystal.
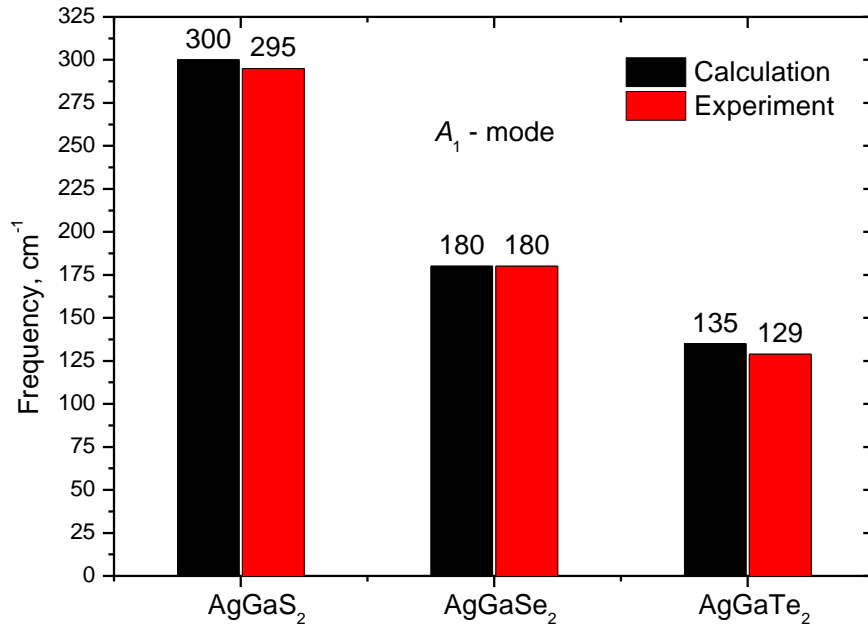
Figure 6.15. Position of the intensive A_1 mode in Raman spectra of AgGaX₂ (X = S, Se, and Te) crystals with chalcopyrite structure calculated using LDA functional.
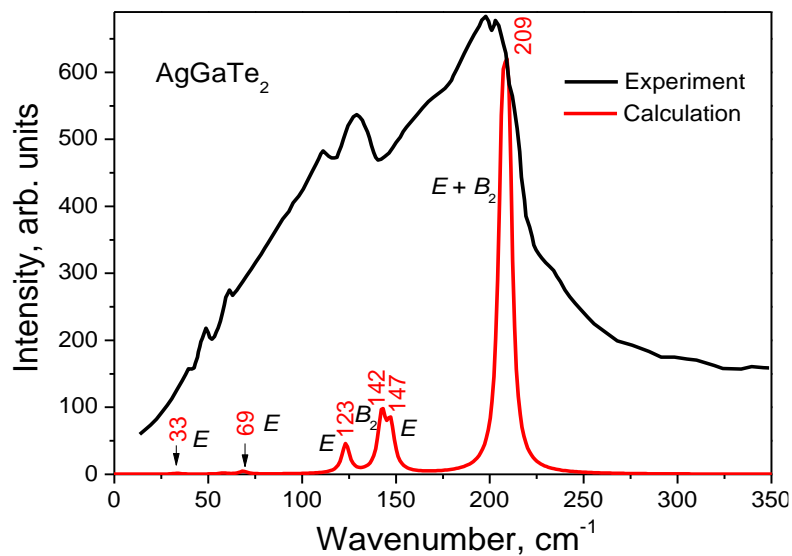
Figure 6.16. Calculated and experimental infrared spectra of AgGaTe₂ crystal.

The most intensive IR peak at 209 cm^{-1} is a superposition of two vibrational modes at 206 and 207 cm^{-1}, which are of the E and B_2 symmetry, respectively. Both the experimental and calculated phonon frequencies are summarized in Table 5.12. The overall good agreement between calculated and experimental spectra is observed. It should be noted that in order to fully identify the vibrational spectrum of the crystal, low-temperature measurements, which are not currently known in the literature, should be performed.

Table 6.12. A comparison of calculated phonon frequencies (in cm^{-1}) at the Γ point with experimental Raman spectra data for AgGaTe$_2$ crystal at room temperature.

Assignment	Activity	LDA	R[a]	IR[a]
A_1	R	135	129	—
A_2	Silent	129	—	—
		146	—	—
E	R, IR	33	—	43
		69	64	62
		123	—	115
		147	—	—
		206	201	201
		210	—	205
B_1	R	62	93	62
		136	152	—
		209	220	—
B_2	R, IR	59	—	51
		142	142	132
		207	201	201

[a]Ref. [22]

6.4.3. Born effective charge tensor and dielectric constants for AgGaTe₂

For the AgGaTe₂ crystal, the Born effective charges revealed using Eq. (6.31) are summarized in Table 6.13. The averaged Born effective charges of three main polarized orientations (*xx*, *yy*, and *zz*) is 1.47 for the Ag atoms in the AgGaTe₂ crystals. For silver atoms, the anisotropy coefficient of Born effective charges $Z_{xx = yy} / Z_{zz} = 1.01$, which indicates their isotropy.

Non-diagonal components of the tensor (*yx* and *xy*) have small charge values and are ± 0.19. For gallium atoms, the anisotropy of Born effective charges is $Z_{xx = yy} / Z_{zz} = 0.94$. The largest value of the coefficient of Born effective charge tensor of this atom is 2.63 and corresponds to the component of the tensor Z_{zz}. For gallium ions the off-diagonal elements *yx* and *xy* are slightly higher than for Ag and its value is equal ± 0.36. The dynamic charge for this atom is $Q_d = 2.53$. In the case of tellurium atoms, we find $\frac{1}{3}\sum_\alpha Z^*_{\alpha\alpha,Te} = -1.99$ and is close to the nominal value of charge (–2) for this ion. The nondiagonal nonzero components for Te ion is *zy, yz* and *zx, xz*. The components *zy* and *zx* are equal to ±0.76, while the *yz* an *xz* components has a value of charge equal to ±0.73.

It can be observed that the Ag and Ga Born effective charges Z^* of AgGaTe₂ crystal deviates larger from its nominal charge (1, 3) than that for Te, which demonstrates a stronger transferred ability of charges between Ag and Ga.

It is important to note that for this crystal the condition of electroneutrality is also fulfilled, which is expressed in the equality of zero sum of all components of the effective Born charges for the AgGaTe₂ crystal.

Figure 6.17 shows the dynamic charges Q_d for crystals of the AgGaX₂ system (where X = S, Se, and Te). The figure shows that the dynamic charges for Ag atoms increase with the replacement of the anion S → Se → Te. During the transition from a lighter X atom to a heavier chalcogen atom, the Q_d charge of the silver atom changes from 1.05 (for the AgGaS₂ crystal) to 1.47 (for the AgGaTe₂ crystal). For gallium atoms, the dynamic charge decreases monotonically from 2.71 to 2.53 during the transition from the structure with X, which varies from S to Se to Te. For chalcogen atoms, as well as for gallium atoms, a decrease in the dynamic charge is observed during the transition of a structure with a larger mass of chalcogen atom. As one can see, the largest changes in dynamic charge is observed for Ag atoms, while for two other species (Ga and X) this change is smaller.

Table 6.13. The calculated Born effective charges Z^*, the eigenvalues of the symmetric part $Z^*(\lambda)$ and the dynamic charges Q_d (in units of charge e) of the AgGaSe$_2$ crystal.

Atom	Z^*	$Z^*(\lambda)$	Q_d
Ag	$Z^*_{Ag} = \begin{pmatrix} 1.47 & 0.19 & 0.00 \\ -0.19 & 1.47 & 0.00 \\ 0.00 & 0.00 & 1.46 \end{pmatrix}$	$\begin{pmatrix} 1.47 \\ 1.47 \\ 1.46 \end{pmatrix}$	1.47
Ga	$Z^*_{Ga} = \begin{pmatrix} 2.48 & 0.36 & 0.00 \\ -0.36 & 2.48 & 0.00 \\ 0.00 & 0.00 & 2.63 \end{pmatrix}$	$\begin{pmatrix} 2.48 \\ 2.48 \\ 2.63 \end{pmatrix}$	2.53
Te1	$Z^*_{Te1} = \begin{pmatrix} -1.70 & 0.00 & 0.00 \\ 0.00 & -2.25 & 0.73 \\ 0.00 & 0.76 & -2.04 \end{pmatrix}$	$\begin{pmatrix} -1.39 \\ -2.90 \\ -1.70 \end{pmatrix}$	-1.99
Te3	$Z^*_{Te3} = \begin{pmatrix} -2.24 & 0.00 & -0.73 \\ 0.00 & -1.70 & 0.00 \\ -0.76 & 0.00 & -2.04 \end{pmatrix}$	$\begin{pmatrix} -1.39 \\ -2.89 \\ -1.70 \end{pmatrix}$	-1.99
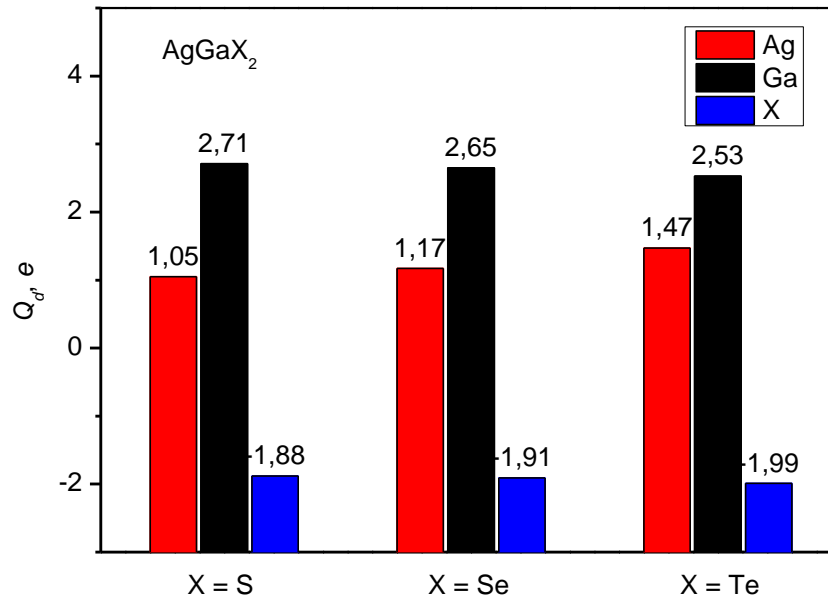
Figure 6.17. Dependence of dynamic charges of atoms on the type of anion in the AgGaX$_2$ system (X = S, Se, and Te).

In Table 6.14 we collected the high-frequency and static dielectric constant tensor elements for AgGaTe$_2$ crystal. For a tetragonal symmetry there are two components for the studied crystal. One can see that the static dielectric constants posseces the lower anisotropy than the AgGaS$_2$ and AgGaSe$_2$ crystals. The anisotropy of the high-frequency dielectric

constants $\varepsilon_{xx}^{\infty}/\varepsilon_{zz}^{\infty} = 0.48$ while for the static dielectric function the $\varepsilon_{xx}/\varepsilon_{zz}$ relation is higher and has a value 0.8. The ratios of $\varepsilon_0/\varepsilon^{\infty}$ for the $xx = yy$ and zz are 1.13 and 1.11 respectively. This corresponds to the wery low LO – TO splittings.

Table 6.14. Static ε_0 and electron ε_{∞} dielectric constants were calculated for the AgGaTe₂ crystal using the LDA functional.

$\varepsilon_{\alpha\beta}^{\infty}$		$\varepsilon_{\alpha\beta}$	
$\varepsilon_{xx}^{\infty} = \varepsilon_{yy}^{\infty}$	17.35	$\varepsilon_{xx} = \varepsilon_{yy}$	19.62
$\varepsilon_{zz}^{\infty}$	22.13	ε_{zz}	24.57
$\varepsilon_{xx}^{\infty}/\varepsilon_{zz}^{\infty}$	0.48	$\varepsilon_{xx}/\varepsilon_{zz}$	0.80

Figure 6.18 shows a diagram of dielectric constants for AgGaX₂ crystals where the X = S, Se, and Te. The figure shows that the replacement of the anion of the chalcogenide S by atoms of greater mass in the structure of AgGaX₂ leads to an increase in the value of the dielectric function. The figure also shows the increase in the anisotropy of both high-frequency and static dielectric constants with increasing mother anion. This increase in anisotropy is well consistent with the lag of anisotropy of elastic constants and optical functions of the studied materials (see Chapret 4). It should also be mentioned that the dielectric function is inversely proportional to the value of the band gap E_g.
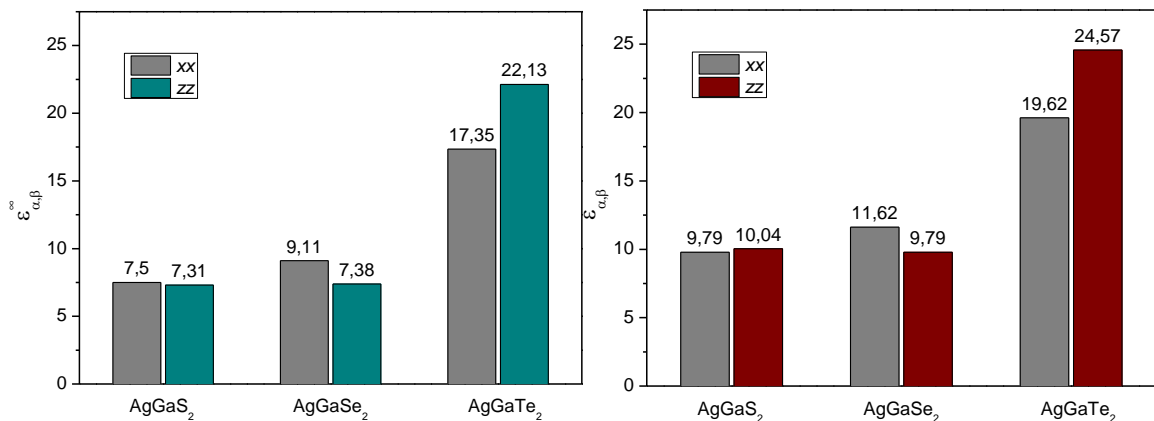
Figure 6.18. Dependence of static ε_0 a) and electronic ε_{∞} b) dielectric constant for AgGaX₂ (X = S, Se, Te) crystals.

6.5. Conclusions

1. In this section, theoretical study of the crystal lattice dynamics for AgGaX$_2$ crystals where X = S, Se, and Te is performed. For the studied class of crystals, a symmetric classification of vibrational spectra of interest from a fundamental point of view was performed. The crystals of I-III-VI$_2$ group have a D_{2d}^{12} spatial group of symmetry, which is isomorphic to the D_{2d} point group with the use of which a symmetric analysis was performed for chalcopyrites.

2. A symmetric classification of vibrational modes for I-III-VI$_2$ crystals is performed. Theoretical-group analysis gives 24 vibrational modes in a crystal lattice with a chalcopyrite structure. The complete irreducible representation of the vibrational modes for the studied group of crystals is as follows $\Gamma_v = 1A_1 + 2A_2 + 3B_1 + 4B_2 + 7E$. Acoustic vibrations correspond to three branches in the spectrum with the representation $\Gamma_a = 1B_2 + 1E$, while for optical branches the irreducible representation is as follows: $\Gamma_{opt} = 1A_1 + 2A_2 + 3B_1 + 3B_2 + 6E$. Obtained are general selection rules for quantum transitions in the tetragonal crystals, estimated for the Γ-point of BZ. Using the selection rules for IR and Raman spectra, it is shown that in the IR spectra the vibrations with the representation $\Gamma_\mu = 4B_2 + 7E$ will be active, while for the Raman spectra the irreducible representation has the form $\Gamma_\alpha = 1A_1 + 3B_1 + 4B_2 + 7E$.

3. The vibrational properties of the AgGaX$_2$ crystals were calculated using the linear response method within the density functional perturbation theory approach. Calculations of phonon band structures $\omega(q)$ and phonon density of states $N(\omega)$ were performed. The absence of imaginary (negative) vibration frequencies showed that the structure of these crystals is stable. For the AgGaX$_2$ crystals (X = S, Se, and Te) one can see that the maximal frequencies in the vibrational spectra obey the following sequence $\omega_{AgGaS_2}^{max} > \omega_{AgGaSe_2}^{max} > \omega_{AgGaTe_2}^{max}$, which indicates the compression of the vibrational spectrum towards lower frequencies when replacing S → Se → Te. From the calculations of the phonon spectrum it follows that there is a significant anisotropy for low-frequency acoustic branches of vibrations, and the presence of low-frequency optical branches that interact with acoustic ones is observed.

4. It is found that the vibrational spectrum can be divided into three regions: high-frequency, medium and low-frequency. The high-frequency region for the AgGaS$_2$ crystal is formed by the vibrations of sulfur atoms. The medium frequency region is formed by gallium atoms vibrations, while the low-frequency region corresponds to silver atoms. The transition from

S to heavier chalcogen atoms shifts the high-frequency region toward lower frequencies with an overlap with the middle region. For AgGaTe$_2$ crystal a high-frequency optical modes near 200 cm^{-1} are formed by the Ga and Te ions vibrations, while a wide frequency region from 150 to 0 cm^{-1} is mainly represented by Ag and Te vibrations. Calculated and identified frequencies of vibrational modes in the center of the Brillouin zone (Γ-point) showed good agreement with the available experimental data on IR and Raman spectra and theoretical data of other authors given in the literature.

5. The Raman intensities and the IR spectrum of AgGaX$_2$ compounds have been calculated. It was found that for AgGaX$_2$ crystals the most intense in the Raman spectrum is the peak corresponding to the fully symmetric vibration of symmetry A_1 The peak is located at ω = 300.27 cm^{-1} for AgGaS$_2$, ω = 180.53 cm^{-1} for AgGaSe$_2$, and ω = 135 cm^{-1} for AgGaTe$_2$. The shift of the intensive A_1 mode towards the higher frequencies relatively to the experimental peak position is of magnitude $\Delta\omega \approx 2.7$ cm^{-1}. The calculated theoretical Raman spectra showed good agreement with the experimental spectrum reported in the literature. An IR spectrum for this crystal was also obtained. The displacement vectors of the atoms corresponding to the active in these spectra normal vibrations are constructed.

6. The components of Born effective charge tensors for individual components of AgGaS$_2$ and AgGaSe$_2$ crystals atoms are calculated. It is shown that the effective Born charges Z^* for silver and chalcogen atoms increase with the replacement of the S → Se → Te anions, while for the gallium atoms the effective charges increase. The Born effective charges obey the summation rule $\sum_k \sum_{\alpha\alpha}^* = 0$. The calculated high-frequency ε_∞ and dielectric function ε_0 at static limit (ω → 0) in AgGaX$_2$ crystals indicate their insignificant anisotropy. There is a tendency to increase in the dielectric constants with increasing anion mass, and there is an inverse proportionality to the band gap.

7. Good agreement between all calculated and corresponding experimental data was achieved, which serves as a firm proof of applicability of the used calculation method to the studies of anisotropic crystalline materials.

7. STUDY OF STRUCTURE AND PROPERTIES OF CuGa(S$_{1-x}$Se$_x$)$_2$ SOLID SOLUTION

7.1. Details of calculations and crystal structure analysis

The calculations of the CuGa(S$_{1-x}$Se$_x$)$_2$ solid solution presented in this chapter are performed in the frame of the density functional theory (DFT) developed by Kohn and Hohenberg [18] and implemented in the CASTEP code [218]. To calculate the band structure and physical properties of CuGa(S$_{1-x}$Se$_x$)$_2$ solid solutions the following calculating settings were used. The exchange and correlation effects were taken into account as the generalized gradient approximation with Perdew-Burke-Ernzerhof [47,137] and the local density approximation with Ceperley-Alder and Perdew-Zunger parametrization [47]. The pseudopotential method in the basis of the Blokh-type plane waves was used. The maximum kinetic energy of the electrons was limited by the cut-off energy of plane waves equal to 440 eV. The ultrasoft Vanderbilt pseudopotentials were used to describe the ionic core of the constituent ions of the crystals. The electronic contributions of the atoms from the deep electronic levels near the nucleus were described by pseudopotential, while external valence electrons were described explicitly by their wave functions. The electronic configurations of valence electrons were as follows: $3d^{10}4s^1$ — Cu; $3d^{10}4s^24p^1$ — Ga; $3s^23p^4$ — S; $4s^24p^4$ — Se. The integration was performed on a 5×5×3 **k**-grid chosen by the Monkhrost-Pack method [154].

The effect of the anion substitution in CuGa(S$_{1-x}$Se$_x$)$_2$ was studied by a partial substitution of sulfur ions with selenium ions with x = 0; 0.25; 0.5; 0.75; and 1.0, thus forming solid solutions, constructed using the supercell method. When modeling the crystal unit cell, its optimization was performed for each solid solution composition. Crystal models were optimized at fixed symmetry using the BFGS algorithm [155] by varying the lattice parameters and the coordinates of atoms.

Before calculations of the electronic and optical properties of the crystals the total energy convergence test was performed. The convergence parameters were taken as follows: self-consistent field tolerance — 10^{-6} eV/atom; energy — $5×10^{-6}$ eV/atom; maximal force

— 1×10^{-2} eV/Å; maximal stress — 2×10^{-2} GPa; maximal displacement — 5×10^{-4} Å; energy convergence tolerance — 5×10^{-5} eV/atom.
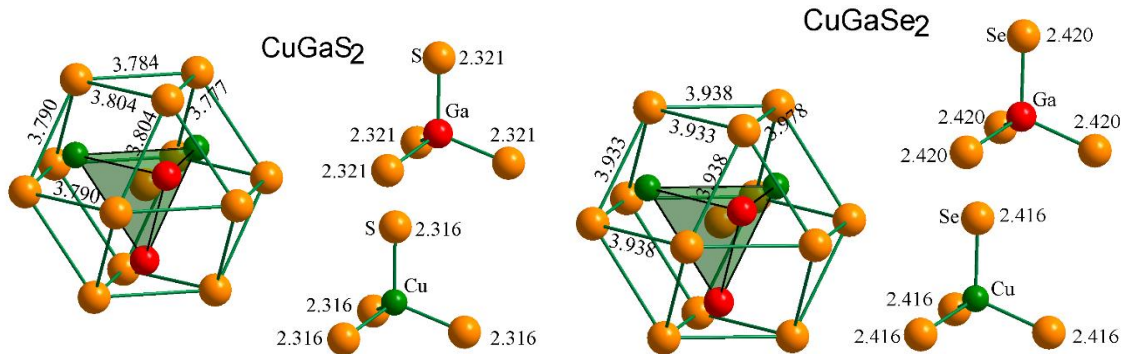
Figure 7.1. The second and the nearest coordination environment of metal atoms in the structure with interionic distances (in Å) for CuGaS$_2$ and CuGaSe$_2$ compounds.

CuGaS$_2$ and CuGaSe$_2$, as other crystals of I-III-VI$_2$ group crystallize in CP structure with tetragonal symmetry of unit cell (space group No. 122). The second coordination environment of chalcogen atoms in the structure of CuGaS$_2$ ($a = 5.3700$ Å, $c = 10.6433$ Å, $V = 306.92$ Å^3, V/at $= 19.18$ Å^3) [273] and CuGaSe$_2$ ($a = 5.6191$ Å, $c = 11.0260$ Å, $V = 348.14$ Å^3, V/at $= 21.76$ Å^3) [274] crystals with a CuFeS$_2$-type structure, tI16, 122, can be represented as the cuboctahedron, the cation atoms in which occupy centers of the tetrahedral cavities. The interatomic distances of the cation-anion are presented in Fig. 7.1.

For three samples, the CuGaSe$_{0.5}$S$_{1.5}$ (prototype – CuFeS$_2$, $a = 5.412$ Å, $c = 10.599$ Å, $V = 310.44$ Å^3, V/atom $= 19.40$ Å^3), CuGaSeS ($a = 5.478$ Å, $c = 10.718$ Å, $V = 321.63$ Å, V/atom $= 20.10$ Å^3) and CuGaSe$_{1.5}$S$_{0.5}$ ($a = 5.551$ Å, $c = 10.882$ Å, $V = 335.31$ Å, V/atom $= 20.96$ Å^3) [275], in which are in the range of existence of the continuous series of solid solutions CuGa(Se$_{1-x}$S$_x$)$_2$, the average atomic volume slightly decreases depending on the selenium content (Fig. 7.2), which may indicate some interaction of the sulfur and selenium sublattices causing an increase in the covalent anion-anion component.

In this work we use method of modeling the solid solution consisting in changing the chemical composition, by partially substitution in specific nodes of the crystallographic lattice sulphur for selenium. Such modeling allows one to predict the structural characteristics with the change in the percentage of composition. We have performed the theoretical study of the CuGa(S$_{1-x}$Se$_x$)$_2$ compounds in the concentration range $x = 0$–1. This allows to evaluate the properties of intermediate compounds in the entire range of possible

x values. The simulation of the solid solution was performed using the supercell method [176,276] by substituting S with Se in the following way: *x* =0 (no Se atoms in a unit cell with four formula units), 0.25 (two Se and six S atoms), 0.5 (four Se and two S atoms), 0.75 (six Se and two S atoms), 1 (eight Se atoms).
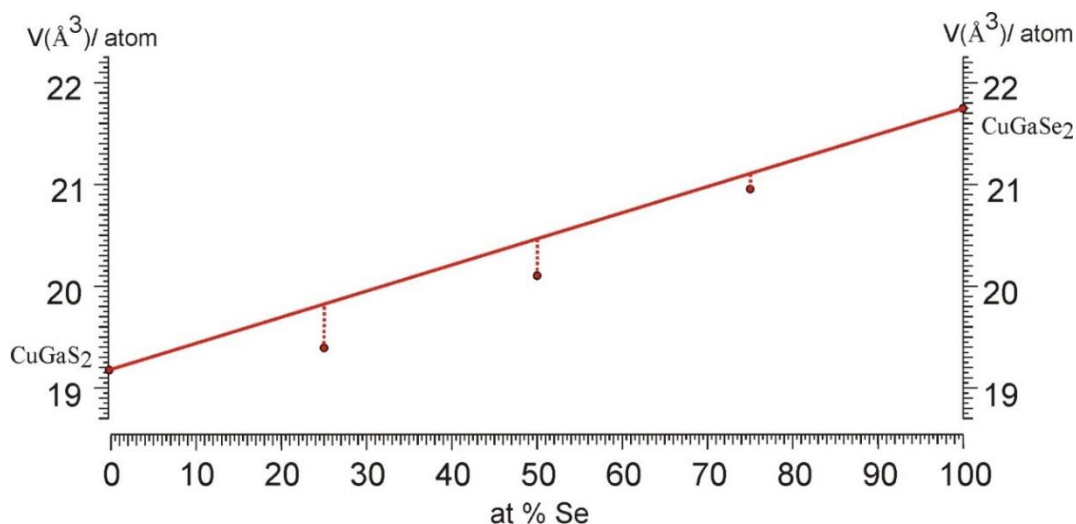
Figure 7.2. Average experimental atomic volume vs selenium content in CuGa(S$_{1-x}$Se$_x$)$_2$ compounds.

Before calculating the physical properties of the solid solutions, the crystal lattice was optimized in each case in order to obtain the equilibrium structure in the ground state corresponding to the minimum of its energy by varying the crystal lattice parameters and atomic positions with a fixed crystal symmetry. The unit cell parameters calculated in this work, as well as available experimental and theoretical parameters of the CuGa(S$_{1-x}$Se$_x$)$_2$ solid solutions are collected in Table 7.1. The structural parameters of pure CuGaS$_2$ and CuGaSe$_2$ crystals, are reported in Refs. [208,273] and [156,274,275], respectively.

Since both CuGaS$_2$ and CuGaSe$_2$ crystals have the same crystal structure, and the gradual anion substitution (S^{2-} with Se^{2-}) does not require the charge compensation, there is no reason to expect the change of the crystal structure for the solid solutions. Similar assumptions on the structural stability of the solid solutions that are isostructural to the end members of the studied series were made in Refs. [277–279].

As can be seen from Table 7.1, the optimized lattice parameters do not differ significantly from the experimental ones. The deviation from the experimental values for both *a* and *c* parameters does not exceed 1%. It is worth noting that the lattice parameters obtained with the LDA functional are reduced compared to the experimental values. This is

caused by the overbinding problem of this functional. On the contrary, for the GGA functional a slight overestimation of the *a* and *c* parameters is observed. Such features are typical for the LDA- and GGA-based calculations and has been observed previously for other inorganic crystals [172,196]. The parameters calculated in this work are also consistent with other theoretical calculations of structural properties of these crystals.

Table 7.1. Experimental and calculated structural data (in Å) for the CuGa(S$_{1-x}$Se$_x$)$_2$ solid solutions for $x = 0, 0.25, 0.5, 0.75$ and 1.

x	Experiment		Calculated (this work)				Calculated elsewhere	
			GGA		LDA			
	a	c	a	c	a	c	a	c
0	5.263[a] 5.37[b]	10.3786[a] 10.64[b]	5.37206	10.6376	5.22581	10.3653	5.3819[f] 5.3441[g] 5.33[h]	10.66[f] 10.4538[g] 10.47[h]
0.25	5.412[c]	10.599[c]	5.44455	10.7580	5.30847	10.4910	–	–
0.5	5.478[c]	10.718[c]	5.51526	10.8870	5.38374	10.6322	–	–
0.75	5.551[c]	10.882[c]	5.58152	11.0244	5.45080	10.7586	–	–
1	5.607[d] 5.619[e]	10.990[d] 11.026[e]	5.64268	11.1422	5.51445	10.8957	5.650[i]	11.102[i]

[a]Ref. [178], [b]Ref. [273], [c]Ref. [275], [d]Ref. [156], [e]Ref. [274], [f]Ref. [167], [g]Ref. [280], [h]Ref. [281], [i]Ref. [282]

Fig. 7.3 presents dependence of the lattice parameters of the CuGaS$_2$ – CuGaSe$_2$ system from the composition of the solid solution. The figure shows that both the lattice parameters *a* and *c* increase with increasing content of Se ions in CuGa(S$_{1-x}$Se$_x$)$_2$. The obtained results are perfectly fitted by a linear function. Such increase in the lattice parameters is well known as the Vegard rule [283]. It also correlates well with the increase of average ionic radius of the system while substituting S^{2-} (1.84 Å) with Se^{2-} (1.98 Å) [284].

The linear fitting functions for the lattice parameters are also given in the figure. These equations make it possible to obtain the values of the *a* and *c* cell parameters for any concentration of Se in the solid solution with $x = 0$–1. It should be noted that with increasing Se concentration the *c* parameter increases faster than the *a*-parameter. A similar behavior of the lattice parameters during the S $\rightarrow$ Se substitution was previously reported for

CuAl(S$_{1-x}$Se$_x$)$_2$ in Ref. [285]. The Al $\rightarrow$ Ga replacement, if consider the CuAl(S$_{1-x}$Se$_x$)$_2$ and CuGa(S$_{1-x}$Se$_x$)$_2$ solutions, leads to an increase in the rate of *c*-parameter change, whereas the parameter *a* varies almost equally in both systems.
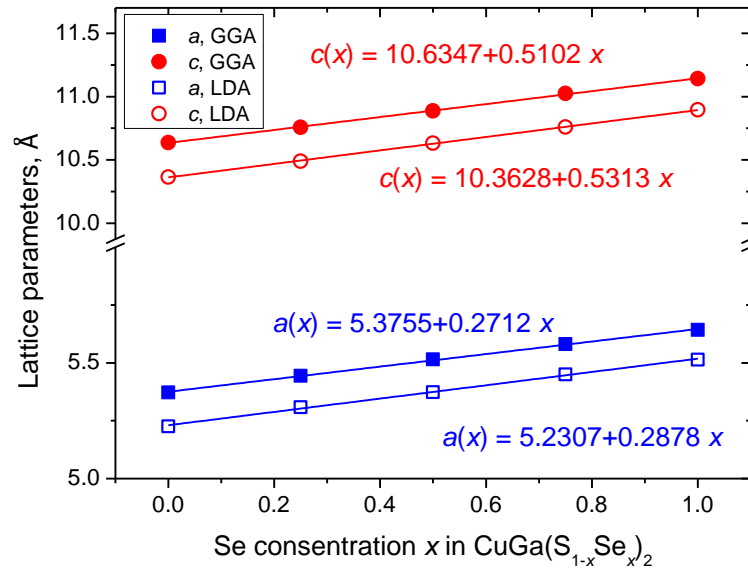
Figure 7.3. Calculated lattice parameters *a* and *c* (solid and open symbols for the GGA and LDA calculations, respectively) and their linear fits as functions of the Se content *x* in CuGa(S$_{1-x}$Se$_x$)$_2$.
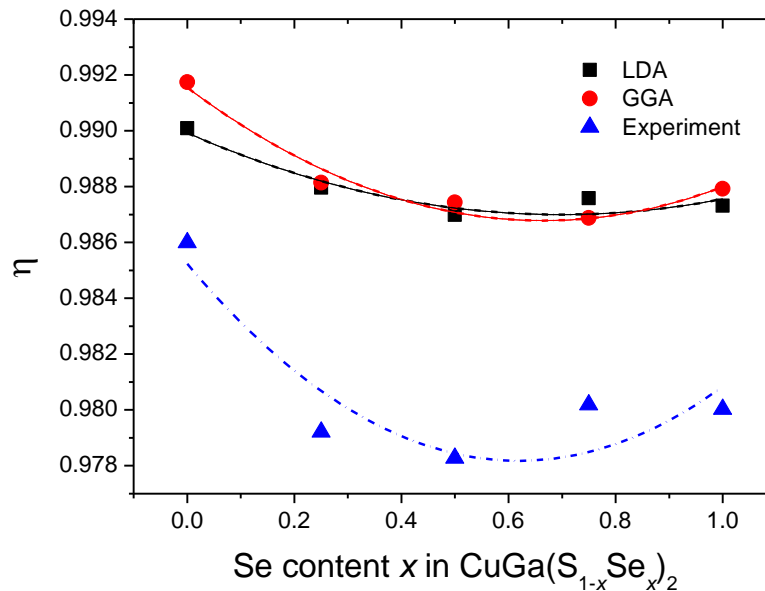
Figure 7.4. Experimental and theoretical (LDA and GGA functionals) tetrahedral deformation parameter η as the function of the Se concentration *x* in CuGa(S$_{1-x}$Se$_x$)$_2$.

Fig. 7.4 shows the calculated concentration dependences of the crystal lattice deformation degree $\eta(x)$ for different compositions of CuGa(S$_{1-x}$Se$_x$)$_2$ solid solution. The figure shows that $\eta(x)$ has a minimum, located at a concentration $x = 0.68$ for LDA and $x = 0.69$ for the GGA functionals. These results indicate that for a selenium content of approximately $x = 0.68$, the crystalline structure of the solid solution is of the greatest deformation. The obtained values agree well with the value of $x = 0.63$ we calculated from the experimental data on the crystal structure. Thus, the most prominent anisotropic properties of CuGa(S$_{1-x}$Se$_x$)$_2$ solid solution are assumed to appear at the content of Se ~ 63 %. The detailed structural information for the optimized solid solutions is given in the Appendix 1.

7.2. Electronic structure and optical spectra of CuGa(S$_{1-x}$Se$_x$)$_2$

7.2.1. Electronic structure of CuGa(S$_{1-x}$Se$_x$)$_2$

We have calculated the band energy diagram $E(\mathbf{k})$ for the optimized structures of pure CuGaS$_2$ and CuGaSe$_2$ crystals corresponding to the extreme concentrations of the solid solution. The obtained bandgap E_g for the CuGaS$_2$ crystals is 1.02 / 0.75 eV for the LDA / GGA methods (Table 7.2), whereas the experimental value is $E_g = 2.45$ eV [286]. In the case of CuGaSe$_2$ crystals, the calculated E_g value is 0.32 / 0.15 eV for the LDA / GGA methods, respectively, while the experimental value is 1.68 eV [287].

Table 7.2. Calculated and experimental band gap values and corresponding scissor operator values for CuGaS$_2$ and CuGaSe$_2$ crystals.

Crystal	E_g, eV (Exp.)	E_g, eV (Calc.)	Δ_g ,eV
CuGaS$_2$	2.45 [a]	1.02 (LDA)	1.43
		0.75 (GGA)	1.70
CuGaSe$_2$	1.68 [b]	0.32 (LDA)	1.36
		0.15 (GGA)	1.53

[a] Ref. [286] [b] Ref. [287]

As can be seen, the calculated band gap values are underestimated. This underestimation is a typical drawback of the DFT methods, so the scissor operator Δ_g is usually used to correct the band gap values (see chapter 4). The corresponding corrections Δ_g applied for our calculations using the LDA and GGA functionals are given in Table 7.2 and were accounted in the construction of $E(k)$ presented in Fig. 7.5. As is easy to notice, both crystals have a direct band gap. The top of the valence band and the bottom of the conduction band are located at the center of the Brillouin zone (at $\mathbf{k} = 0$) denoted as the $\Gamma(0, 0, 0)$ point.

a)   b)
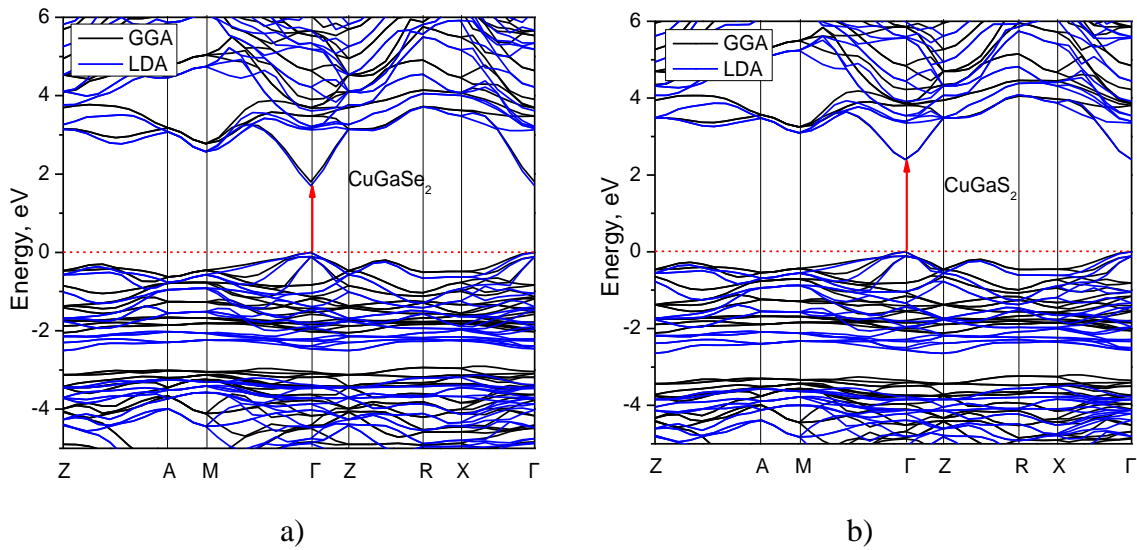
Figure 7.5. Calculated band structures of CuGaSe$_2$ (a) and CuGaS$_2$ (b) crystals. The coordinates of special points of the Brillouin zone (in units of the reciprocal lattice vectors) are as follows: Z(0, 0, ½); A(½, ½, ½); M(½, ½, 0); Γ(0, 0, 0); R(0, ½, ½); X(0, ½, 0).

Fig. 7.6 shows the dependence $E_g(x)$ of the band gap on the composition of the CuGa(S$_{1-x}$Se$_x$)$_2$ solid solution. This figure is given without considering the scissor operator Δ_g correction. Those data show the underestimation of the bandgap value comparing with the experimental data reported in Ref. [288]. As seen from the figure, a monotonous linear decrease in the E_g value with increasing Se concentration is observed. Equations describing band gap value variation calculated using LDA and GGA methods are shown in the figure. It can be seen, that the rate of E_g change with the change in concentration is higher for the LDA method than for the GGA. The rates of the band gap value changes for the studied system and for CuAl(S$_{1-x}$Se$_x$)$_2$ [285] are summarized in Table 7.3.

Table 7.3. The derivative of the band gap vs the concentration of Se ions in CuGa(S$_{1-x}$Se$_x$)$_2$ (this work) and CuAl(S$_{1-x}$Se$_x$)$_2$ solid solutions.

Crystal	dE_g/dx, eV		
	LDA	GGA	Exp.
CuGa(S$_{1-x}$Se$_x$)$_2$	–0.715	–0.603	–0.808[b]
CuAl(S$_{1-x}$Se$_x$)$_2$[a]	–0.884	–0.826	

[a] Ref. [285], [b]Ref. [288]
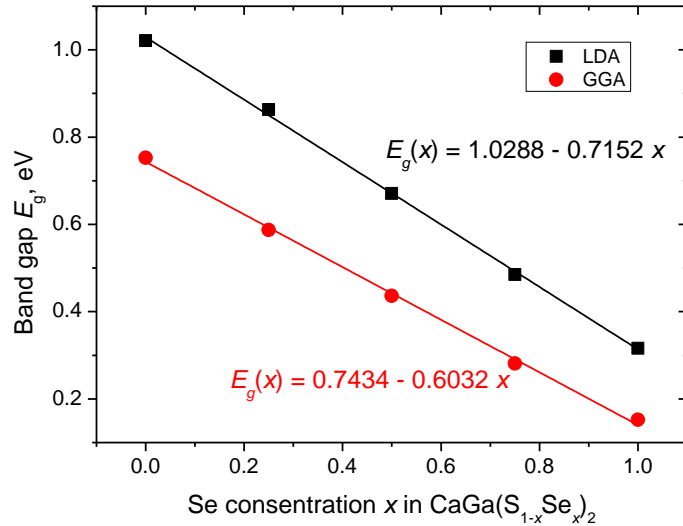
Figure 7.6. Calculated band gaps of the CuGa(S$_{1-x}$Se$_x$)$_2$ compounds and their linear fits.
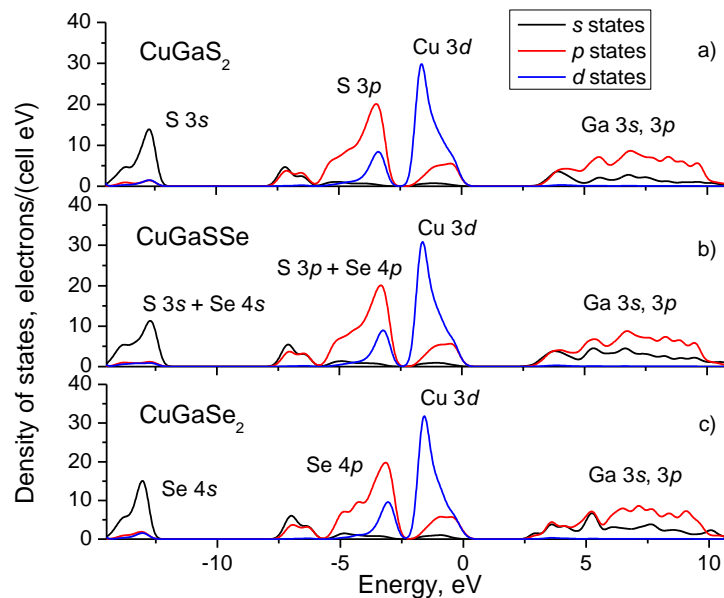
Figure 7.7. Partial density of states of CuGa(S$_{1-x}$Se$_x$)$_2$ chalcopyrite solid solution for a) x = 0; b) x = 0.5; c) x = 1 calculated using the GGA-PBE functional.

Note that for CuGa(S$_{1-x}$Se$_x$)$_2$ the $E_g(x)$ values calculated using two functionals become closer to each other with increase of the Se concentration, whereas for CuAl(S$_{1-x}$Se$_x$)$_2$ such approximation is observed in the direction of selenium concentration decrease [285]. The difference between these two systems is also that in the case of CuGa(S$_{1-x}$Se$_x$)$_2$ there is no quadratic dependence reported for CuAl(S$_{1-x}$Se$_x$)$_2$ by calculations using the GGA functional. In this regard the studied system reveals a similar linear behavior as reported for CuIn(S$_{1-x}$Se$_x$)$_2$ [289].

The detailed characteristics of the energy structure can be obtained from the analysis of the density of electronic states, which are obtained by integration of the band structure. Fig. 7.7 shows the partial densities of electronic states corresponding to different orbital momenta (*s, p, d*) of the CuGa(S$_{1-x}$Se$_x$)$_2$ system with $x = 0$, 0.5, and 1. The Fermi energy, which is matched with the top of valence band, is taken here as 0 eV. As can be seen, the top of valence band of the studied solid solutions is formed by the Cu 3*d*-states, which dominate in the upper region of valence band from 0 to –3 eV. For a pure CuGaS$_2$ crystal ($x = 0$), the lower levels of the valence band are formed by the S 3*p*-states. For the substituted solid solutions with concentration $0 < x < 1$, this band is formed by a mixture of the 3*p* S and 4*p* Se states. At the concentration of $x = 1$ (pure CuGaSe$_2$ crystal), the band with peak at –2 eV is formed by the 4*p*-states of Se. The band at –13 eV is formed by the states of sulfur and selenium: 3*s* S $x = 0$; 3*s* S and 4*s* Se at $0 < x < 1$ and 4*s* Se at $x = 1$. The bottom of the conduction band is formed by the 3*s*-and 3*p*-states of gallium ions.

7.2.2. Optical properties of CuAl(S$_{1-x}$Se$_x$)$_2$ solid solution

The optical properties of solids are described by the dielectric function. The calculations of the optical functions were performed in accordance with the methodology described in chapter 4.

The dispersion of real ε_1 and imaginary ε_2 parts of dielectric functions calculated for different compositions of CuGa(S$_{1-x}$Se$_x$)$_2$ are depicted in Fig. 7.8 (only the GGA results are shown for the sake of brevity). It should be noted, that the scissor operator Δ_g was taken into account for correcting the calculated results. The tetragonal crystals have two principal directions that correspond to the direction along polar Z axis and direction perpendicular to Z. The $\mathbf{E} \parallel Z$ and $\mathbf{E} \perp Z$ notations correspond to the wave polarizations along the (001) and (100) or (010) crystallographic directions, respectively. The dielectric function shows

insignificant optical anisotropy for the CuGa(S$_{1-x}$Se$_x$)$_2$ solutions. Decreasing of E_g due to the increase of Se concentration leads to the expected increase in Re(ε). Such behavior is described by the Penn model expressed as $\varepsilon(0) \approx 1 + \left(\dfrac{E_g}{\hbar \omega_p} \right)^2$, where ω_p is the plasma frequency.
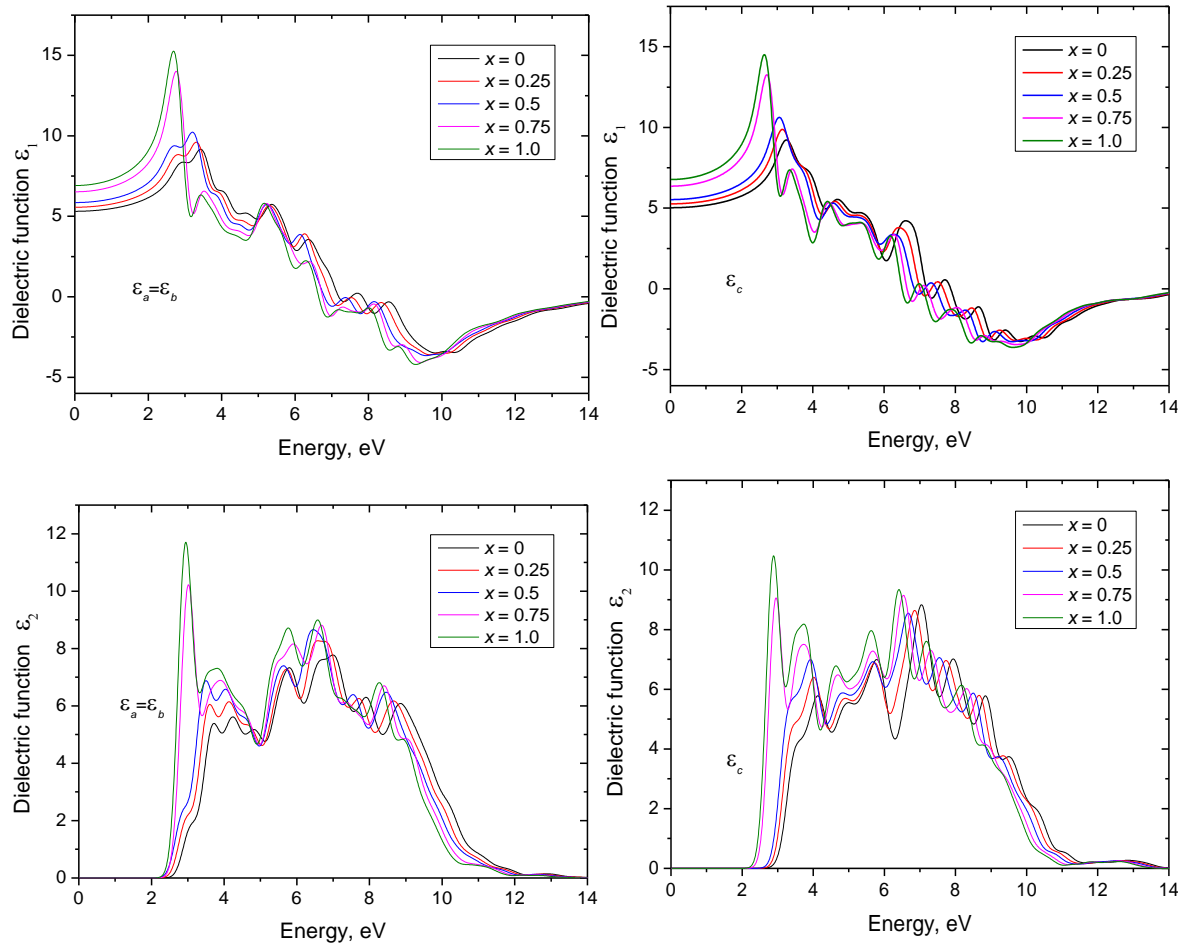
Figure 7.8. Dielectric functions of CuGa(S$_{1-x}$Se$_x$)$_2$ solid solution calculated using GGA functional. a) – Re(ε) for (1,0,0) polarization; b) - Re(ε) for (0,0,1) polarization; c) - Im(ε) for (1,0,0) polarization; d) - Im(ε) for (0,0,1) polarization.

Figure 7.9 shows the concentration dependence of the refractive indices of CuGa(S$_{1-x}$Se$_x$)$_2$ calculated for λ = 500 nm. The refractive indices increase monotonically with increasing percentage of Se content in solid solution for both the *a* and *c* principal directions and can be quite well described by the linear equations. The equations describing

the dependences $n_i(x)$ where $i = a$ and c are also shown in Fig. 7.8. The optical anisotropy of the solution decreases as the content of Se increases as seen from the tendency for the refractive indices n_a and n_c to approach in the Se high-concentration region. A similar behavior is reported for the CuAl(S$_{1-x}$Se$_x$)$_2$ crystal [285]. Based on these two systems one can conclude that the replacement of the S ions with heavier Se ions leads to the increase of the refractive indices of chalcopyrite materials and decrease of their optical birefringence. Here we note that the above calculations are carried out for the ideal crystals without taking into account impurities and defects (mainly V_{Cu}), which can make a significant contribution to the optical spectra. It should also be noted that only direct transitions are taken into account when calculating ε.
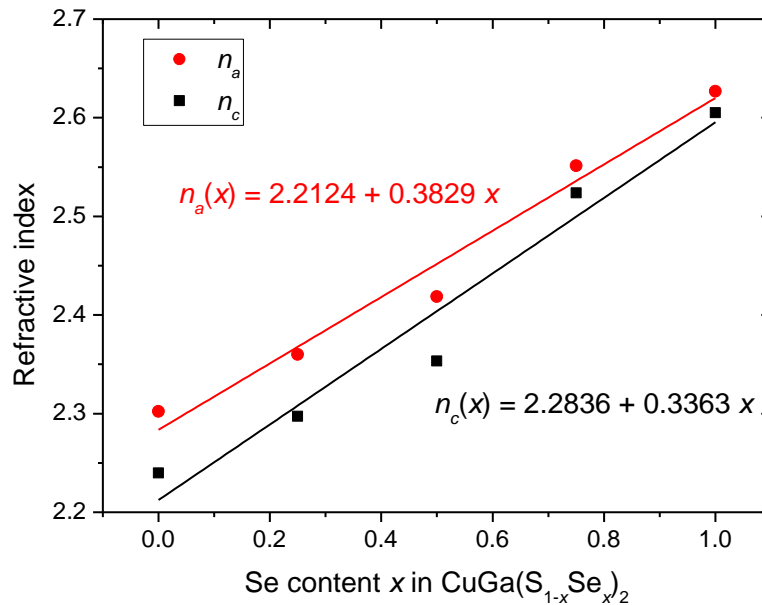
Figure 7.9. Refractive index of CuGa(S$_{1-x}$Se$_x$)$_2$ solid solution calculated using GGA functional (for 500 nm wavelength).

7.3. Elastic and thermodynamic properties

After optimization of the crystal structures for all considered solid solutions their elastic constants were calculated. As seen from Table 7.4, all these conditions are fulfilled, which allows to make a conclusion about mechanical stability of the considered compounds. The calculated bulk moduli for CuGaS$_2$ and CuGaSe$_2$ agree well with available in the literature values (we give in Table 7.4 the range of those data reported in different works).

Table 7.4. Calculated elastic constants (all in GPa, GGA/LDA results) for the CuGa(S$_{1-x}$Se$_x$)$_2$ solid solutions.

x	C_{11}	C_{33}	C_{44}	C_{66}	C_{12}	C_{13}	B	B (other data) [a]
0.00	104.79/ 131.64	102.90/ 133.80	51.29/ 58.40	51.49/ 58.17	58.70/ 79.21	60.10/ 80.41	74.47/ 97.45	74.6 – 96.0
0.25	98.70/ 122.32	97.72/ 118.13	42.38/ 54.38	43.68/ 53.22	54.48/ 71.30	57.11/ 73.34	70.00/ 88.60	
0.50	95.16/ 115.92	89.51/ 112.54	43.09/ 52.36	35.13/ 49.35	51.94/ 66.51	52.67/ 69.02	65.96/ 83.93	
0.75	92.09/ 112.75	89.74/ 107.65	39.98/ 49.91	42.30/ 47.29	48.44/ 64.53	50.29/ 66.43	63.44/ 81.01	
1.00	85.37/ 105.60	84.63/ 103.46	38.66/ 47.69	39.78/ 46.40	46.95/ 61.91	47.87/ 62.43	60.08/ 76.46	62.1 – 76.6

[a] Refs. [290,291]

Fig. 7.10 shows variation of the calculated bulk moduli vs anion composition. The trend is linear, as might be anticipated from the Vegard's law. The linear fits equations given in the figure allow for estimation of the bulk modulus for the CuGa(S$_{1-x}$Se$_x$)$_2$ solid solutions for any value of x.
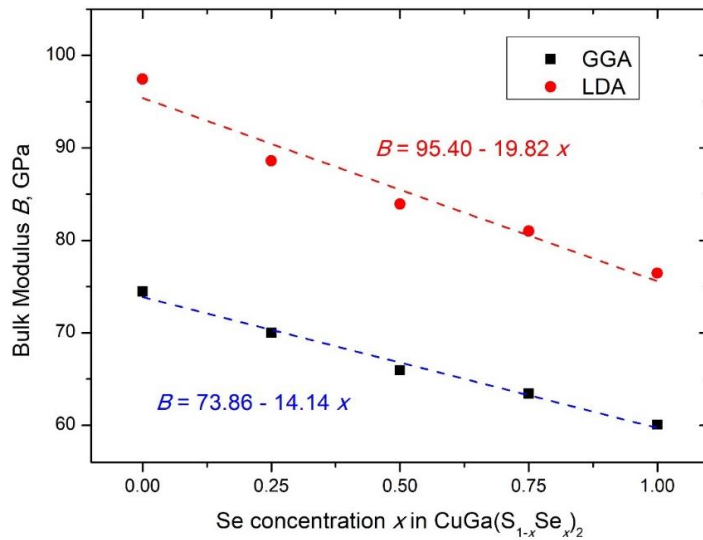
Figure 7.10. Calculated bulk moduli and their linear fits as functions of the Se content x in CuGa(S$_{1-x}$Se$_x$)$_2$.

A further use of the elastic constants can be made to estimate the Debye temperature for all studied materials. At first, we calculated based on the Reuss [228] and Voigt [229]

approximations the bulk B_R (B_V) and shear G_R (G_V) moduli in terms of the elastic constants C_{ij} and elastic compliance constants S_{ij}. After these quantities are calculated, the Debye temperature Θ_D can be found using Eq. 5.40.

Table 7.5 contains the calculated densities, sound velocities and Debye temperatures for all considered solid solutions. Agreement with available in the literature data is good. Fig. 7.11 exhibits a linear trend in changes of the Debye temperature with the anion composition x, along with the linear fit equations given in the figure. It is seen that the Debye temperature is decreased when introducing a heavier Se cation, since the phonon frequencies will become smaller in this case.

Table 7.5. Calculated densities ρ (kg/m^3), sound velocities v_l, v_t, v_m (m/s), Debye temperatures θ_D (in K) for the CuGa(S$_{1-x}$Se$_x$)$_2$ solid solutions.

x	ρ		v_l		v_t		v_m		Θ_D		
	GGA	LDA	GGA	LDA	GGA	LDA	GGA	LDA	GGA	LDA	Exp.
0.00	4269	4630	5377	5764	2932	3022	3271	3380	364.6	387.1	286.5[a], 330[b]
0.25	4598	4960	4962	5328	2646	2806	2956	3137	325.3	354.1	
0.50	4898	5283	4671	5027	2502	2659	2794	2972	303.7	331.3	
0.75	5177	5562	4504	4811	2451	2541	2734	2841	293.6	312.4	
1.00	5450	5836	4259	4576	2310	2425	2578	2711	273.8	294.6	239.7[a], 259.0[b]

[a] Ref. [72]; [b] Ref. [77]
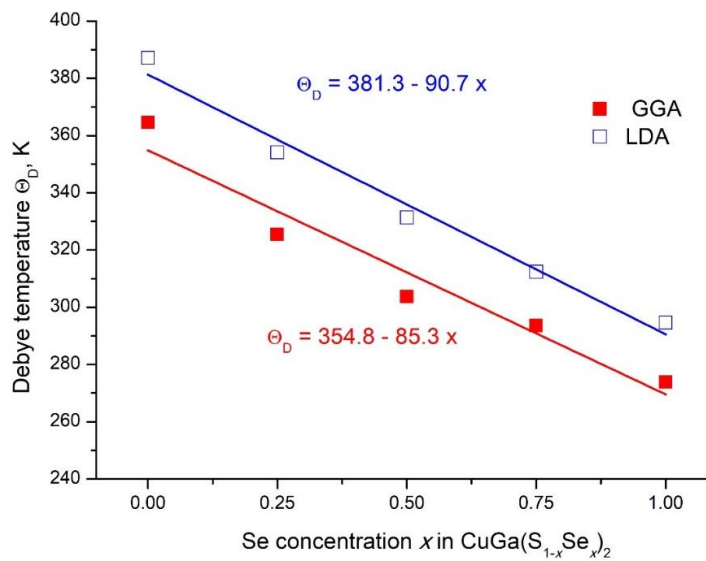
Figure 7.11. Calculated Debye temperatures and their linear fits as functions of the Se content x in CuGa(S$_{1-x}$Se$_x$)$_2$.

7.4. Conclusions

1. We have modelled and systematically investigated the atomic, electronic, and optical properties of $CuGa(S_{1-x}Se_x)_2$, $0 \leq x \leq 1$ chalcopyrite solid solutions by means of the first-principles (DFT) calculations within the supercell method. The performed calculations allowed us to analyze influence of isomorphic anion substitution on the electronic structure and optical properties of these compounds.

2. The obtained optimized structural parameters are in good agreement with the experimental values. The linear increase in the lattice parameters with increasing content of Se ions satisfying the Vegard's law is established. The obtained concentration (composition) dependence of deformation parameter $\eta(x)$ reveals the largest deviation from unity at $x = 0.68$-0.69 of Se concentration as obtained from calculations and at $x = 0.63$ as derived from experimental data. Thus, the most prominent anisotropic properties of $CuGa(S_{1-x}Se_x)_2$ solid solution is predicted to appear at the content of Se ~ 60-70%.

3. The band structure of the system reveals the direct band gap and large dispersion of energy levels. The conduction band bottom as well as the valence band top are located at Γ-point of the Brillouin zone. It is shown that the replacement S $\rightarrow$ Se results in the linear change of the band gap with concentration change. The calculation of the partial density of states allowed us to establish the considerable contribution of electronic states from constituent atoms into the formation of energy bands. The direct fundamental absorption edge is formed mainly by the transitions from the Cu $3d$-states of the valence band top to the Ga $3p$-states, which form the bottom of the conduction band. The calculated from the band structure dielectric functions spectra (ε_1 and ε_2) show insignificant anisotropy. It is found that the S $\rightarrow$ Se substitution leads to the linear increase in the refractive indices n_a and n_c and decrease of birefringence in the Se-rich concentration range.

4. The complete sets of elastic constants were calculated for all studied solid solutions. In addition to that, the Debye temperature was also estimated. It was shown that the bulk modulus and Debye temperature vary linearly with the anion composition. The results obtained provide important information on the possibility of controlling the physical properties by changing the composition in $CuGaS_2$-$CuGaSe_2$ system. The functional dependences revealed for $CuGa(S_{1-x}Se_x)_2$ solid solution offer an opportunity to prepare materials with desired properties (lattice parameters, refractive index, birefringence) and allow important for band gap engineering linear tuning of the fundamental band gap from a pure $CuGaS_2$ (2.45 eV) to a pure $CuGaSe_2$ (1.68 eV).

8. CONCLUSIONS

1. The crystal structure of materials of I-III-VI$_2$ group with the structure of chalcopyrite is considered and it is shown that the crystals have a tetragonal structure under normal conditions. Second coordination environment of chalcogen atoms in the structure of I-III-VI$_2$ crystals can be represented as a cuboctahedron. The cation atoms occupy the centers of the tetrahedral cavities. The analysis of the optimized crystal structure was performed and the relative deviation of the unit cell volume d_r and the relative mean squared deviation D_r were calculated, which showed good agreement with an experiment. An anomalous overestimation of the lattice c-parameter for crystals containing silver atoms was revealed when using the LDA functional for geometric optimization. A strong negative correlation between the tetragonal deformation parameter η of the crystal lattice and the anion shift parameter u was obtained.

2. Regularities of formation of electronic structure of crystals of I-III-VI$_2$ group are established. It is shown that all crystals of the studied group are direct-band gap semiconductors with extremums of energy branches corresponding to the bottom of the conduction band and the top of the valence band in the center of the Brillouin band (point Γ). It was found that the largest band gap is for I-AlS$_2$ crystals, where I = Cu, Ag. A typical underestimation of E_g for LDA and GGA functionals is shown. It was found that, in general, the band gap increases with increasing electronegativity of III and VI group ions. It is shown that the band gap is inversely proportional to the value of the total molar mass of the constituent atoms of the crystal $E_g \sim 1/\mu$ and has optimal values for use in photovoltaics as an absorbing layer for sunlight. The values of the crystal field energy of the investigated crystals were obtained and the decrease of Δ_{CF} with the approaching of the tetragonal deformation parameter η of the crystals to 1 was determined.

3. At energies greater than the band gap, the electronic levels form a wide band consisting of wide overlapping bands in which the intensity is much lower than at the valence band levels due to the significant dispersion of the electronic levels. It was found that the valence band of the studied crystals consists of two subgroups of levels in the range from 0 to –7 eV and about –14 eV. For crystals with I = Cu, the top of the valence band is formed by the level of 3d states of copper atoms split by the crystal field to two peaks with symmetry t_2 and e. A small contribution of the p-states of the S, Se, Te atoms is also present here. For

crystals with I = Ag, the structure of the levels of the top of the valence band does not change, but the splitting of the *d*-levels of silver is not observed.

4. An incorrect description of localized *d*-electrons for Ga and In atoms has been revealed, which consists in shifting the corresponding band towards higher energies. The example of $CuGaS_2$, $AgInSe_2$, $CuInSe_2$, $AgGaS_2$ crystals shows such a shift of localized *d*-states by 3.27 eV, 2.72 eV, 2.96 eV, 3.09 eV towards higher energies relative to the experimental levels recorded by XPS spectra. It is proposed to use the DFT + U approach to eliminate the shortcomings of the standard method using GGA functional. The efficiency of using the proposed approach to bring the theoretical data in line with the experimental position of the *d*-electrons of Ga and In atoms bands is shown.

5. From the band diagrams, the optical functions of the studied crystals were calculated, including the dielectric functions ε_1, ε_2, the reflection spectra *R*, the refractive index *n*, the extinction coefficient *k* and the absorption coefficient α. Significant anisotropy of the dielectric function is shown. Substitution of S → Se → Te reduces the anisotropy for a majority of crystals except $CuInX_2$.

It is shown that the first peak in the spectrum of the dielectric function corresponds to the optical transitions forming the edge of the fundamental absorption and corresponds to the transitions between states with symmetry $\Gamma_4 \rightarrow \Gamma_1$ and $\Gamma_4 \rightarrow \Gamma_1$ for $\mathbf{E} \perp z$ and $\mathbf{E} \parallel z$, respectively. It was found that the replacement of the anion S → Se → Te and the cation Al → Ga → In leads to an increase in static dielectric function in the I-III-VI$_2$ system. Studied crystals have high absorption coefficients up to 3.5×10^5 cm^{-1}, which makes them promising materials for use in solar energetics in photovoltaic cells as a material for the absorbing layer. It is shown that crystals containing copper have better absorption than crystals with silver. Using the DES model, the linear electro-optic, electrogyration coefficients and second-order nonlinear susceptibility of the $AgGaS_2$ crystal have been calculated.

6. A group-theoretical analysis of the phonon spectrum of $AgGaX_2$ crystals where X = S, Se, and Te with the D_{2d} symmetry was performed. The symmetry of the vibrational modes of the crystal lattice in the center of the Brillouin zone and the structure of the infrared and Raman spectra have been elucidated. Selection rules for optical dipole transitions are established. Phonon spectra for $AgGaX_2$ crystals were calculated for the first time. The transformation of phonon spectra, effective Born charges and dielectric constants of $AgGaX_2$ crystals at anionic substitution X = S → Se → Te is shown and analyzed.

7. A systematic study of the structural, electronic, optical and elastic properties of the system of solid solutions $CuGa(S_{1-x}Se_x)_2$ in the framework of the density functional theory using the supercell method has been performed. It is shown that the replacement $S \rightarrow Se$ results in the linear change in band gap value, allowing the band gap tuning by composition change. The linear increase in static refraction indices n_a and n_c and decrease of birefringence with increasing the Se concentration is established. The possibility of controlled changes in physical parameters in the system by changing the composition of the substitutional solid solution is shown.

PROSPECTS OF FUTURE STUDY

Given the great interest in materials belonging to group I-III-VI$_2$ and other related groups with the structure of chalcopyrite, it seems promising to continue research of such materials in the following areas. Investigation of the influence of external fields on the structure of materials and physicochemical properties. In particular, the influence of hydrostatic, uniaxial and biaxial pressures, the application of electric fields of different configurations. Investigation of the influence of defects of different types and nonstoichiometry on optoelectronic properties. Study of the influence of the incorporation of impurities of elements of rare earth and transition groups on the formation of electronic levels in the forbidden zone for use in IMB silar cells and luminescence. Study of surface formation for thin-film solar cells. Simulations of nanoparticles and its properties. Modelling of solar cells of different configurations and particularly of IMB solar cells. Optimization layers width, their composition, carrier concentration, defects etc. for reaching the higher efficiency of solar cells.

REFERENCES

[1] J.L. Shay, J.H. Wernick, Ternary chalcopyrite semiconductors: growth, electronic properties, and applications, Pergamon Press, Oxford; New York, 1975.

[2] H.G. Grimm, A. Sommerfeld, Über den. Zusammenhang des Abschlusses der Elektronengruppen im atom mit den chemischen valenzzahlen, *Z. Physik*. 36 (1926) 36–59.

[3] S. Hamad, S. Cristol, C.R.A. Catlow, Surface structures and crystal morphology of ZnS: computational study, *J. Phys. Chem*. B. 106 (2002) 11002–11008.

[4] L. Garbato, F. Ledda, A. Rucci, Structural distortions and polymorphic behaviour in ABC_2 and AB_2C_4 tetrahedral compounds, *Progress in Crystal Growth and Characterization*. 15 (1987) 1–41.

[5] I.D. Oleksiuk, O.V. Parasyuk, I.A. Ivashchenko, Chemistry of solid state, *Vezha-Druk*, Lutsk, 2016.

[6] S.X. Xia, C.H. Yang, G. Li, G.Li. Zhu, B.Q. Yao, Z.T. Lei, Growth of high quality non-linear optical crystal zinc germanium phosphide for mid-infrared optical parametric oscillator, *Laser Phys*. 21 (2011) 1366–1370.

[7] S. Xia, M. Wang, C. Yang, Z. Lei, G. Zhu, B. Yao, Vertical Bridgman growth and characterization of large $ZnGeP_2$ single crystals, *Journal of Crystal Growth*. 314 (2011) 306–309.

[8] G. Zhang, X. Tao, S. Wang, Q. Shi, H. Ruan, L. Chen, Growth improvement and quality evaluation of $ZnGeP_2$ single crystals using vertical Bridgman method, *Journal of Crystal Growth*, 352 (2012) 67-71.

[9] G.A. Verozubova, A.I. Gribenyukov, V.V. Korotkova, M.P. Ruzaikin, $ZnGeP_2$ synthesis and growth from melt, *Materials Science and Engineering: B*. 48 (1997) 191–197.

[10] K.T. Zawilski, P.G. Schunemann, S.D. Setzler, T.M. Pollak, Large aperture single crystal $ZnGeP_2$ for high-energy applications, *Journal of Crystal Growth*. 310 (2008) 1891–1896.

[11] D. Yang, Z. Yuan, B. Kang, P. Fang, Investigation of intermediate impurities on high quality $AgGaS_2$ single crystal grown by vertical gradient freezing method, *Journal of Crystal Growth*. 539 (2020) 125642.

[12] B.-J. Zhao, S.-F. Zhu, F.-L. Yu, H.-Y. Li, D.-Y. Gao, Z.-H. Li, Polycrystalline Synthesis and single crystal growth of $AgGaS_2$, *Crystal Research and Technology* 33(6) (1998) 943-948.

[13] C.-H. Ho, C.-C. Pan, Optical behavior and structural property of $CuAlS_2$ and $AgAlS_2$ wide-bandgap chalcopyrites, *Appl. Opt.*, 53 (2014) E7–E13.

[14] J. Thijssen, Computational physics, 2nd ed., *Cambridge University Press*, Cambridge, 2007.

[15] P.M. Yakibchuk, V.T. Shvets, Model methods in physics of metals, *Lviv University*, Lviv, 2012.

[16] S.C. Chen, J.Y. Wu, C.Y. Lin, M.F. Lin, Theory of magnetoelectric properties of 2D systems, *IOP Publishing*, 2017.

[17] R.M. Martin, ed., Pseudopotentials in electronic structure: basic theory and practical methods, in: *Cambridge University Press*, Cambridge, 2004: pp. 204–232.

[18] P. Hohenberg, W. Kohn, Inhomogeneous electron gas, *Phys. Rev*. 136 (1964) B864–B871.

[19] W. Kohn, L.J. Sham, Self-consistent equations including exchange and correlation effects, *Phys. Rev.* 140 (1965) A1133–A1138.

[20] G.F. Roach, Green's functions, 2nd ed., *Cambridge University Press*, 1982.

[21] D.G. Duffy, Green's functions with applications, *CRC Press*, 2018.

[22] J.L. Martins, N. Troullier, S.-H. Wei, Pseudopotential plane-wave calculations for ZnS, *Phys. Rev. B*. 43 (1991) 2213–2217.

[23] S. Richard, F. Aniel, G. Fishman, Energy-band structure of Ge, Si, and GaAs: A thirty-band *k·p* method, *Phys. Rev. B*. 70 (2004) 235204.

[24] P. Cervantes, Q. Williams, M. Côté, O. Zakharov, M.L. Cohen, Band structure of CdS and CdSe at high pressure, *Phys. Rev. B*. 54 (1996) 17585–17590.

[25] M. Piasecki, M.G. Brik, I.E. Barchiy, K. Ozga, I.V. Kityk, A.M. El-Naggar, A.A. Albassam, T.A. Malakhovskaya, G. Lakshminarayana, Band structure, electronic and optical features of Tl_4SnX_3 (X = S, Te) ternary compounds for optoelectronic applications, *Journal of Alloys and Compounds*. 710 (2017) 600–607.

[26] T. Babuka, K. Glukhov, Y. Vysochanskii, M. Makowska-Janusik, Structural, electronic, vibration and elastic properties of the layered $AgInP_2S_6$ semiconducting crystal – DFT approach, *RSC Adv*. 8 (2018) 6965–6977.

[27] W. Meng, X. Wang, Z. Xiao, J. Wang, D.B. Mitzi, Y. Yan, Parity-Forbidden Transitions and their impact on the optical absorption properties of lead-free metal halide perovskites and double perovskites, *J. Phys. Chem. Lett*. 8 (2017) 2999–3007.

[28] A.S. Poplavnoi, Yu.I. Polygalov, A.M. Ratner, Energy band structure of the compounds $AgGaS_2$, $AgGaSe_2$, and $AgGaTe_2$, *Soviet Physics Journal*. 17 (1974) 1495–1499.

[29] J.E. Jaffe, A. Zunger, Electronic structure of the ternary chalcopyrite semiconductors $CuAlS_2$, $CuGaS_2$, $CuInS_2$, $CuAlSe_2$, $CuGaSe_2$, and $CuInSe_2$, *Phys. Rev. B*. 28 (1983) 5822–5847.

[30] S. Sharma, A.S. Verma, V.K. Jindal, Ab initio studies of structural, electronic, optical, elastic and thermal properties of silver gallium dichalcogenides ($AgGaX_2$: X = S, Se, Te), *Materials Research Bulletin*. 53 (2014) 218–233.

[31] H. Hai-Jun, Z. Shi-Fu, Z. Bei-Jun, Y. You, X. Lin-Hua, First-principles calculations of the elastic, electronic and optical properties of $AgGaS_2$, *Phys. Scr*. 82 (2010) 055601.

[32] M.G. Brik, Electronic, optical and elastic properties of $CuXS_2$ (X = Al, Ga, In) and $AgGaS_2$ semiconductors from first-principles calculations, *Physica Status Solidi C*. 8 (2011) 2582–2584.

[33] M.G. Brik, First-principles study of the electronic and optical properties of $CuXS_2$ (X = Al, Ga, In) and $AgGaS_2$ ternary compounds, *J. Phys. Condens. Matter*. 21 (2009) 485502.

[34] S. Levchenko, N.N. Syrbu, V.E. Tezlevan, E. Arushanov, J.M. Merino, M. León, Exciton spectra and energy band structure of $CuGaSe_2$ single crystals, *J. Phys. D: Appl. Phys*. 41 (2008) 055403.

[35] J.L. Shay, Experimental studies of energy band structure of chalcopyrite crystals, *J. Phys. Colloques* 36 (1975) 109-113.

[36] A. Sajid, G. Murtaza, R. Khenata, A. Manzar, S.B. Omran, Electronic structure and optical properties of chalcopyrite $CuYZ_2$ (Y = Al, Ga, In; Z = S, Se): an ab initio study, *Journal of Optoelectronics and Advanced Materials* 16(1-2) (2014) 76-81.

[37] A.S. Poplavnoi, I.Y. Polygaliv, Energy-band structure of the compounds $CuGaS_2$, $CuGaSe_2$, and $CuGaTe_2$, *Izvest. Akad Nauk SSSR Neorg. Materialy*. (1971) 1711–1714.

[38] J. Polygalov, A. Poplavnoi, A. Ratner, Anion shift influence on band structure of crystals with chalcopyrite lattice, *J. Phys. Colloques* 36 (1975) 129–135.

[39] M.L. Cohen, T.K. Bergstresser, Band structures and pseudopotential form factors for fourteen semiconductors of the diamond and zinc-blende structures, *Phys. Rev.* 141 (1966) 789–796.

[40] P. Bendt, A. Zunger, New approach for solving the density-functional self-consistent-field problem, *Phys. Rev. B.* 26 (1982) 3114–3137.

[41] S. Mishra, B. Ganguli, Effect of *p–d* hybridization and structural distortion on the electronic properties of $AgAlM_2$ (M = S, Se, Te) chalcopyrite semiconductors, *Solid State Communications.* 151 (2011) 523–528.

[42] W.N. Honeyman, K.H. Wilkinson, Growth and properties of single crystals of group I-III-VI$_2$ ternary semiconductors, *J. Phys. D: Appl. Phys.* 4 (1971) 1182–1185.

[43] B. Tell, J.L. Shay, H.M. Kasper, Some properties of $AgAlTe_2$, $AgGaTe_2$, and $AgInTe_2$, *Phys. Rev. B.* 9 (1974) 5203–5208.

[44] J.E. Jaffe, A. Zunger, Theory of the band-gap anomaly in ABC_2 chalcopyrite semiconductors, *Phys. Rev. B.* 29 (1984) 1882–1906.

[45] D. Huang, Z. Ju, H. Ning, C. Li, C. Yao, J. Guo, First-principles study on $CuAlTe_2$ and $AgAlTe_2$ for water splitting, *Materials Chemistry and Physics.* 148 (2014) 882–886.

[46] G. Kresse, J. Hafner, Ab initio molecular dynamics for liquid metals, *Phys. Rev. B.* 47 (1993) 558–561.

[47] J.P. Perdew, K. Burke, M. Ernzerhof, Generalized gradient approximation made simple, *Phys. Rev. Lett.* 77 (1996) 3865–3868.

[48] O. Khaselev, J. Turner, A monolithic photovoltaic-photoelectrochemical device for hydrogen production via water splitting, *Science.* 280 (1998) 425–427.

[49] Y. Gai, J. Li, S.-S. Li, J.-B. Xia, S.-H. Wei, Design of narrow-gap TiO_2: a passivated codoping approach for enhanced photoelectrochemical activity, *Phys. Rev. Lett.* 102 (2009) 036402.

[50] W.-J. Yin, H. Tang, S.-H. Wei, M.M. Al-Jassim, J. Turner, Y. Yan, Band structure engineering of semiconductors for enhanced photoelectrochemical water splitting: The case of TiO_2, *Phys. Rev. B.* 82 (2010) 045106.

[51] S. Chen, X.G. Gong, A. Walsh, S.-H. Wei, Electronic structure and stability of quaternary chalcogenide semiconductors derived from cation cross-substitution of II-VI and I-III-VI$_2$ compounds, *Phys. Rev. B.* 79 (2009) 165211.

[52] P. Blaha, K. Schwarz, G.K.H. Madsen, D. Kvasnicka, J. Luitz, R. Laskowsk, F. Tran, L. Marks, L. Marks, WIEN2k: an augmented plane wave plus local orbitals program for calculating crystal properties, *Techn. Universitat*, (2019) 287.

[53] A.H. Reshak, S. Auluck, Electronic properties of chalcopyrite $CuAlX_2$ (X = S, Se, Te) compounds, *Solid State Communications.* 145 (2008) 571–576.

[54] S.N. Rashkeev, W.R.L. Lambrecht, Second-harmonic generation of I-III-VI$_2$ chalcopyrite semiconductors: Effects of chemical substitutions, *Phys. Rev. B.* 63 (2001) 165212.

[55] J.L. Shay, B. Tell, H.M. Kasper, L.M. Schiavone, *p-d* hybridization of the valence bands of I-III-VI$_2$ compounds, *Phys. Rev. B.* 5 (1972) 5003–5005.

[56] K. Yoodee, J.C. Woolley, V. Sa-yakanit, Effects of *p-d* hybridization on the valence band of I-III-VI$_2$ chalcopyrite semiconductors, *Phys. Rev. B.* 30 (1984) 5904–5915.

[57] B.V. Korzun, A.A. Fadzeyeva, A.V. Mudryi, S. Schorr, Optical absorption and photoluminescence of $CuAlTe_2$, *Physica Status Solidi c.* 3 (2006) 2626–2629.

[58] R.R. Reddy, Y. Nazeer Ahammed, A study on the Moss relation, *Infrared Physics & Technology.* 36 (1995) 825–830.

[59] T. Yamasaki, N. Suzuki, K. Motizuki, Electronic structure of intercalated transition-metal dichalcogenides: M_xTiS_2 (M = Fe,Cr), *J. Phys. C: Solid State Phys.* 20 (1987) 395–404.

[60] J.C. Rife, R.N. Dexter, P.M. Bridenbaugh, B.W. Veal, Optical properties of the chalcopyrite semiconductors $ZnGeP_2$, $ZnGeAs_2$, $CuGaS_2$, $CuAlS_2$, $CuInSe_2$, and $AgInSe_2$, *Phys. Rev. B.* 16 (1977) 4491-4500.

[61] T.V. Kuznetsova, V.I. Grebennikov, H. Zhao, C. Derks, C. Taubitz, M. Neumann, C. Persson, M.V. Kuznetsov, I.V. Bodnar, R.W. Martin, M.V. Yakushev, A photoelectron spectroscopy study of the electronic structure evolution in $CuInSe_2$-related compounds at changing copper content, *Appl. Phys. Lett.* 101 (2012) 111607.

[62] S. Kono, M. Okusawa, X-ray photoelectron study of the valence bands in I–III–VI_2 compounds, *J. Phys. Soc. Jpn.* 37 (1974) 1301–1304.

[63] M.J. Luciano, C.J. Vesely, X-ray photoelectron emission measurements of the valence band density of states and core levels of $CuAlS_2$, *Appl. Phys. Lett.* 23 (1973) 453-454.

[64] M.Y. Rudysh, M.G. Brik, O.Y. Khyzhun, A.O. Fedorchuk, I.V. Kityk, P.A. Shchepanskyi, V.Y. Stadnyk, G. Lakshminarayana, R.S. Brezvin, Z. Bak, M. Piasecki, Ionicity and birefringence of α-$LiNH_4SO_4$ crystals: ab initio DFT study, X-ray spectroscopy measurements, *RSC Adv.* 7 (2017) 6889–6901.

[65] M.Ya. Rudysh, M.G. Brik, V.Yo. Stadnyk, R.S. Brezvin, P.A. Shchepanskyi, A. Fedorchuk, O.Y. Khyzhun, I.V. Kityk, M. Piasecki, Ab initio calculations of the electronic structure and specific optical features of β-$LiNH_4SO_4$ single crystals, *Physica B: Condensed Matter.* 528 (2018) 37–46.

[66] M. Chrunik, A. Majchrowski, K. Ozga, M.Ya. Rudysh, I.V. Kityk, A.O. Fedorchuk, V.Yo. Stadnyk, M. Piasecki, Significant photoinduced increment of reflectivity coefficient in $LiNa_5Mo_9O_{30}$, *Current Applied Physics.* 17 (2017) 1100–1107.

[67] O.Y. Khyzhun, V.L. Bekenev, V.V. Atuchin, E.N. Galashov, V.N. Shlegel, Electronic properties of $ZnWO_4$ based on ab initio FP-LAPW band-structure calculations and X-ray spectroscopy data, *Materials Chemistry and Physics.* 140 (2013) 588–595.

[68] W. Braun, A. Goldmann, M. Cardona, Partial density of valence states of amorphous and crystalline $AgInTe_2$ and $CuInS_2$, *Phys. Rev. B.* 10 (1974) 5069–5074.

[69] F. Herman, S. Skillman, Atomic structure calculations, *Prentice-Hall*, Englewood Cliffs, N.J., 1963.

[70] S.J. Czyzak, W.M. Baker, R.C. Crane, J.B. Howe, Refractive indices of single synthetic zinc sulfide and cadmium sulfide crystals, *J. Opt. Soc. Amer.* 53 (1963) 240–243.

[71] T.M. Bieniewski, S.J. Czyzak, Refractive indexes of single hexagonal ZnS and CdS crystals, *J. Opt. Soc. Am.,* 53 (1963) 496–497.

[72] D.W. Langer, Temperature and pressure dependence of the index of refraction of CdS, *Journal of Applied Physics.* 37 (1966) 3530–3532.

[73] L.E. Solovyiov, V.S. Rudakov, Phenomenon of pseudointersection of dispersion curves, *Vestnik LGU.* (1968) 23–26.

[74] R.B. Parsons, W. Wardzinski, A.D. Yoffe, Temperatures optocal properties of single crystal of cadmium selenide, *Proc. Roy. Soc. A.* 262 (1961) 120–131.

[75] W.L. Bond, Measurement of the refractive indices of several crystals, *Journal of Applied Physics.* 36 (1965) 1674–1677.

[76] Y.S. Park, J.R. Scheider, Index of refraction of ZnO, *J. App. Phys.* 39 (1968) 3049–3052.

[77] V. Chandrasekharan, H. Damany, Anomalous dispersion of birefringence of sapphire and magnesium fluoride in the vacuum ultraviolet, *Appl. Opt.,* 8 (1969) 671–675.

[78] M. Balkanski, R.D. Waldron, Internal photoeffect and extion diffusion in cadmium and zinc sulfides, *Phys Rev*. 112 (1958) 123.

[79] J.P. Laurenty, K.G. Rustagi, M. Rouzeyere, Optical filters using coupled light waves in mixed crystals, *J. Appl. Phys. Lett*. 28 (1976) 212–213.

[80] J.P. Laurenty, K.G. Rustagi, M. Rouzeyere, Graded-composition semiconductors as tunable narrow-band optical filters, *J. Appl. Phys. Lett*. 48 (1977) 203–204.

[81] S.V. Marisova, On the nature of birefringence and some details of the structure of energy zones of crystals CdS and CdS_x-$CdSe_{1-x}$, *Ukrainian Journal of Physics* 9 (1964) 1084–1088.

[82] G.A. Ambrazyavichus, G.A. Babonas, A.Yu. Shylejka, Birefringence of pseudo-direct gap semiconductors $A^{II}B_{IV}C_2^V$, *Lytov. Phys. Zb*. 17 (1977) 205–211.

[83] M.V. Hobden, Optical activity in a non-enantiomorphous crystal: $AgGaS_2$, *Acta Crystallographica Section A*. 24 (1968) 676–680.

[84] M.V. Hobden, Optical activity in a non-enantiomorphous crystal silver gallium sulphide, *Nature*. 216 (1967) 678–678.

[85] C. Schwartz, D.S. Chemla, B. Ayrault, R.C. Smith, Direct measurement of the birefringence of $AgGaS_2$, *Optics Communications*. 5 (1972) 244–247.

[86] L.M. Suslikov, Z.P. Galdmashi, I.F. Kopinets, Birefringence of $CdGa_2S_4$ crystals, *Opt. and Spectr*. 49 (1980) 97–99.

[87] L.M. Suslikov, Z.P. Galdmashi, D.H. Kovach, Refractive index dispersionand birefringence of cadmium thiogallate, *Opt. and Spectr*. 53 (1982) 480–488.

[88] L.M. Suslikov, V.Yu. Slyvka, M.P. Lisica, Solid-state optical filters based on girotropic crystals, *Interpres LTD*, Kyiv, 1998.

[89] G.C. Bhar, Refractive index dispersion of chalcopyrite crystals., *J. Phys. D*. 13 (1980) 455–460.

[90] S.C. Abrahams, J.L. Bernstein, Crystal structure of luminescent $ZnSiP_2$, *J. Chem. Phys*. 52 (1970) 5607–5613.

[91] S.C. Abrahams, J.L. Bernstein, Crystal structure of piezoelectric nonlinear-optic $AgGaS_2$, *J. Chem. Phys*. 59 (1973) 1625–1629.

[92] V.I. Paniutin, B.E. Poniedielnikov, A.E. Rozenson, V.I. Chizykov, Band structure of semiconductors with cadmium thiogallate lattice, *Izv. Vuzov. Fizika*. (1979) 57–64.

[93] S.I. Radaucan, N.N. Syrbu, I. i. Nebola, Structure of energy zonesand two-photon absorption in $CdGa_2S_4$ and $CdGa_2Se_4$ crystals, *PTP*. 11 (1977) 69–74.

[94] D.A. Guseynova, T.G. Kerimova, R.Kh. Nani, Oprical spectra and band structure of $CdGa_2S_4$ and $CdGa_2Se_4$ crystals, *PTP*. 11 (1977) 1135–1142.

[95] A.G. Areshkin, V.F. Zhytar, Direct exitons in cadmium thiogallate, *PTP*. 13 (1979) 337–340.

[96] G.B. Abdullaev, D.A. Guseinova, T.G. Kerimova, R.K. Nani, Reflection spectra of $CdGa_2S_4$ and $CdGa_2Se_4$ in polarized light, *Physica Status Solidi (b)*. 54 (1972) K115–K117.

[97] S.H. Wemple, M. DiDomenico, Optical dispersion and the structure of solids, *Phys. Rev. Lett*. 23 (1969) 1156–1160.

[98] R.W. Shaw, Optical dispersion and ionicity, *Phys. Rev. Lett*. 25 (1970) 818–823.

[99] V.F. Zinyar, V.A. Raylan, Optical reflection and absorption in cadmium thiogallate, *Semiconducting Materials and its Application*. (1976) 206–209.

[100] P.A. Franken, A.E. Hill, C.W. Peters, G. Weinreich, Generation of optical harmonics, *Phys. Rev. Lett*. 7 (1961) 118–119.

[101] L.I. Isaenko, A.P. Yelisseyev, Recent studies of nonlinear chalcogenide crystals for the mid-IR, *Semiconductor Science Technology*. 31 (2016) 123001.

[102] M. Vainio, L. Halonen, Mid-infrared optical parametric oscillators and frequency combs for molecular spectroscopy, *Phys. Chem. Chem. Phys*. 18 (2016) 4266–4294.

[103] E. Garmire, Nonlinear optics in daily life, *Opt. Express*, 21 (2013) 30532–30544.

[104] D.A. Kleinman, Nonlinear dielectric polarization in optical media, *Phys. Rev*. 126 (1962) 1977–1979.

[105] K. Wu, S. Pan, A review on structure-performance relationship toward the optimal design of infrared nonlinear optical materials with balanced performances, *Coordination Chemistry Reviews*. 377 (2018) 191–208.

[106] M.J. Weber, Handbook of optical materials, *Routledge & CRC Press*. 2002.

[107] G. Boyd, H. Kasper, J. McFee, Linear and nonlinear optical properties of $AgGaS_2$, $CuGaS_2$, and $CuInS_2$, and theory of the wedge technique for the measurement of nonlinear coefficients, *IEEE Journal of Quantum Electronics*. 7 (1971) 563–573.

[108] H. Zhou, L. Xiong, L. Chen, L. Wu, Dislocations that decrease size mismatch within the lattice leading to ultrawide band gap, large second-order susceptibility, and high nonlinear optical performance of $AgGaS_2$, *Angew. Chem*. 131 (2019) 10084–10088.

[109] Y.X. Fan, R.C. Eckardt, R.L. Byer, R.K. Route, R.S. Feigelson, $AgGaS_2$ infrared parametric oscillator, *Appl. Phys. Lett*. 45 (1984) 313–315.

[110] J.-J. Zondy, D. Touahri, O. Acef, Absolute value of the d_{36} nonlinear coefficient of $AgGaS_2$: prospect for a low-threshold doubly resonant oscillator-based 3:1 frequency divider, *J. Opt. Soc. Am. B*, 14 (1997) 2481–2497.

[111] Y. Kim, I. Seo, S.W. Martin, J. Baek, P. Shiv Halasyamani, N. Arumugam, H. Steinfink, Characterization of new infrared nonlinear optical material with high laser damage threshold, $Li_2Ga_2GeS_6$, *Chem. Mater*. 20 (2008) 6048–6052.

[112] A.H.A. Harasaki, K.K.K. Kato, New data on the nonlinear optical constant, phase-matching, and optical damage of $AgGaS_2$, *Jpn. J. Appl. Phys*. 36 (1997) 700.

[113] K. Wu, C. Chen, Absorption-edge calculations of inorganic nonlinear optical crystals, *Appl. Phys*. A. 54 (1992) 209–220.

[114] L. Bai, Z.S. Lin, Z.Z. Wang, C.T. Chen, Mechanism of linear and nonlinear optical effects of chalcopyrites $LiGaX_2$ (X = S, Se, and Te) crystals, *Journal of Applied Physics*. 103 (2008) 083111.

[115] L. Kang, M. Zhou, J. Yao, Z. Lin, Y. Wu, C. Chen, Metal thiophosphates with good mid-infrared nonlinear optical performances: A first-principles prediction and analysis, *J. Am. Chem. Soc*. 137 (2015) 13049–13059.

[116] L. Isaenko, I. Vasilyeva, A. Merkulov, A. Yelisseyev, S. Lobanov, Growth of new nonlinear crystals $LiMX_2$ (M = Al, In, Ga; X = S, Se, Te) for the mid-IR optics, *Journal of Crystal Growth*. 1–2 (2005) 217–223.

[117] J. Chen, C. Lin, S. Yang, X. Jiang, S. Shi, Y. Sun, B. Li, S. Fang, N. Ye, Cd_4SiQ_6 (Q = S, Se): Ternary infrared nonlinear optical materials with mixed functional building motifs, *Crystal Growth & Design*. 20 (2020) 2489–2496.

[118] C. Battaglia, A. Cuevas, S.D. Wolf, High-efficiency crystalline silicon solar cells: status and perspectives, *Energy Environ. Sci*. 9 (2016) 1552–1576.

[119] Y. Hamakawa Thin-film solar cells - next generation photovoltaics and its applications, *Springer* (2004) 244.

[120] L. Wang, J. You, J. Shi, B. Peng, and P. K. Chu, Improving solar-cell efficiency, *SPIE* 2010.

[121] A. Barnett, D. Kirkpatrick, C. Honsberg, D. Moore, M. Wanlass, K. Emery, R. Schwartz, D. Carlson, S. Bowden, D. Aiken, A. Gray, S. Kurtz, L. Kazmerski, M. Steiner, J. Gray, T. Davenport, R. Buelow, L. Takacs, N. Shatz, J. Bortz, O. Jani, K. Goossen, F. Kiamilev, A. Doolittle, I. Ferguson, B. Unger, G. Schmidt, E.

Christensen, D. Salzman, Very high efficiency solar cell modules, *Progress in Photovoltaics: Research and Applications*. 17 (2009) 75–83.

[122] S. Merdes, D. Abou-Ras, R. Mainz, R. Klenk, M.Ch. Lux-Steiner, A. Meeder, H.W. Schock, J. Klaer, CdS/Cu(In,Ga)S$_2$ based solar cells with efficiencies reaching 12.9% prepared by a rapid thermal process: CdS/Cu(In,Ga)S$_2$ based solar cells with efficiencies reaching 12.9%, *Prog. Photovolt: Res. Appl*. 21 (2013) 88–93.

[123] A. Khadir, Simulation of effects of defects and layers thickness on the performance of CIGS solar cells, *Acta Phys. Pol. A*. 137 (2020) 1128–1134.

[124] K. Patel, J. Ray, Influence of carrier concentration on the performance of CIAS solar cell, *AIP Conference Proceedings*. 1961 (2018) 030029.

[125] N. Benseddik, B. Belkacemi, F. Boukabrine, K. Ameur, H. Mazari, A. Boumesjed, N. Benyahya, Z. Benamara, Numerical study of AgInTe$_2$ solar cells using SCAPS, *Advances in Materials and Processing Technologies*. 0 (2020) 1–9.

[126] A. Sylla, S. Touré, J.-P. Vilcot, Numerical modeling and simulation of CIGS-based solar cells with ZnS buffer layer, *OJMSi*. 05 (2017) 218–231.

[127] W. Li, W. Li, Y. Feng, C. Yang, Numerical analysis of the back interface for high efficiency wide band gap chalcopyrite solar cells, *Solar Energy*. 180 (2019) 207–215.

[128] Silvaco, Device simulation software. *Atlas User's Manual*. (2004) 740.

[129] J. Nishinaga, T. Koida, S. Ishizuka, Y. Kamikawa, H. Takahashi, M. Iioka, H. Higuchi, Y. Ueno, H. Shibata, S. Niki, Effects of long-term heat-light soaking on Cu(In,Ga)Se$_2$ solar cells with KF postdeposition treatment, *Appl. Phys. Express*. 10 (2017) 092301.

[130] S.S. Batsanov, E.D. Ruchkin, A.I. Poroshina, Refractive indices of solids, *Springer*, Singapore, (2016) 108.

[131] M. Burgelman, P. Nollet, S. Degrave, Modelling polycrystalline semiconductor solar cells, *Thin Solid Films*. 361–362 (2000) 527–532.

[132] A. Kowsar, M.B. Hosen, M.K. Ali, M. Asaduzzaman, A.N. Bahar, Performance optimization of ZnS/CIGS solar cell with over 25% efficiency enabled by using a CuIn$_3$Se$_5$ OVC layer, *International Journal of Renewable Energy Research,* 10 (2020) 2000–2005.

[133] S. Weinberg, Lectures on quantum mechanics, 2nd edition, *Cambridge University Press*, Cambridge, United Kingdom ; New York, (2015) 480.

[134] J.G. Lee Computational materials science: an introduction, *CRC Press* (2012) 269.

[135] D.J. Griffiths, Introduction to quantum mechanics, *Prentice Hall*, Englewood Cliffs, N.J, (1995) 394.

[136] D.M. Ceperley, B.J. Alder, Ground state of the electron gas by a stochastic method, *Phys. Rev. Lett*. 45 (1980) 566–569.

[137] J.P. Perdew, J.A. Chevary, S.H. Vosko, K.A. Jackson, M.R. Pederson, D.J. Singh, C. Fiolhais, Atoms, molecules, solids, and surfaces: Applications of the generalized gradient approximation for exchange and correlation, *Phys. Rev. B*. 46 (1992) 6671–6687.

[138] C. Lee, W. Yang, R.G. Parr, Development of the Colle-Salvetti correlation-energy formula into a functional of the electron density, *Phys. Rev. B*. 37 (1988) 785–789.

[139] K. Kim, K.D. Jordan, Comparison of density functional and MP2 calculations on the water monomer and dimer, *J. Phys. Chem*. 98 (1994) 10089–10094.

[140] P.J. Stephens, F.J. Devlin, C.F. Chabalowski, M.J. Frisch, Ab Initio calculation of vibrational absorption and circular dichroism spectra using density functional force fields, *J. Phys. Chem*. 98 (1994) 11623–11627.

[141] A.D. Becke, Density-functional exchange-energy approximation with correct asymptotic behavior, *Phys. Rev. A*. 38 (1988) 3098–3100.

[142] S.H. Vosko, L. Wilk, M. Nusair, Accurate spin-dependent electron liquid correlation energies for local spin density calculations: a critical analysis, *Canadian Journal of Physics*. 58 (1980) 1200–1211.

[143] P. Schwerdtfeger, The pseudopotential approximation in electronic structure theory, *Chem. Phys. Chem*. 12 (2011) 3143–3155.

[144] L. Kleinman, D.M. Bylander, Efficacious form for model pseudopotentials, *Phys. Rev. Lett*. 48 (1982) 1425–1428.

[145] D.R. Hamann, M. Schlüter, C. Chiang, Norm-conserving pseudopotentials, *Phys. Rev. Lett*. 43 (1979) 1494–1497.

[146] N. Troullier, J.L. Martins, Efficient pseudopotentials for plane-wave calculations, *Phys. Rev. B*. 43 (1991) 1993–2006.

[147] D. Vanderbilt, Soft self-consistent pseudopotentials in a generalized eigenvalue formalism, *Phys. Rev. B*. 41 (1990) 7892–7895.

[148] C. Kittel, Introduction to solid state physics, 8th ed., *Wiley*, 2005 680.

[149] Materials Studio 2019. CASTEP Guide, (2019) 229.

[150] M.D. Segall, P.J.D. Lindan, M.J. Probert, C.J. Pickard, P.J. Hasnip, S.J. Clark, M.C. Payne, First-principles simulation: ideas, illustrations and the CASTEP code, *J. Phys.: Condens. Matter*. 14 (2002) 2717–2744.

[151] J.P. Perdew, A. Zunger, Self-interaction correction to density-functional approximations for many-electron systems, *Phys. Rev. B*. 23 (1981) 5048–5079.

[152] M.Ya. Rudysh, P.A. Shchepanskyi, A.O. Fedorchuk, M.G. Brik, C.-G. Ma, G.L. Myronchuk, M. Piasecki, First-principles analysis of physical properties anisotropy for the Ag_2SiS_3 chalcogenide semiconductor, *Journal of Alloys and Compounds*. 826 (2020) 154232.

[153] B. Andriyevsky, M. Jaskólski, V.Y. Stadnyk, M.O. Romanyuk, Z.O. Kashuba, M.M. Romanyuk, Electronic band structure and influence of uniaxial stresses on the properties of K_2SO_4 crystal: ab initio study, *Computational Materials Science*. 79 (2013) 442–447.

[154] H.J. Monkhorst, J.D. Pack, Special points for Brillouin-zone integrations, *Phys. Rev. B*. 13 (1976) 5188–5192.

[155] B.G. Pfrommer, M. Côté, S.G. Louie, M.L. Cohen, Relaxation of crystals with the quasi-newton method, *Journal of Computational Physics*. 131 (1997) 233–240.

[156] H. Hahn, G. Frank, W. Klingler, A.-D. Meyer, G. Störger, Untersuchungen über ternäre chalkogenide. V. über einige ternäre chalkogenide mit chalkopyritstruktur, *Zeitschrift für anorganische und allgemeine Chemie*. 271 (1953) 153–170.

[157] I.V. Bodnar, N.S. Orlova, X-ray study of the thermal expansion in $CuAlS_2$, $CuGaS_2$, and $CuInS_2$ compounds over the temperature range from 90 to 650 K, *Physica Status Solidi A*, *Applied Research*. 78 (1983) K59–K63.

[158] A.A. Vaipolin, Y.V. Rud, I.V. Rozhdestvenskaya, Interatomic interaction aspect of phase transition in $AgInS_2$ crystals, *Crystal Research and Technology*. 23 (1988) 337–341.

[159] R. Lesueur, C. Djega-Mariadassou, P. Benoit, P. Charpin, Crystal structure of chalcopyrite $AgInSe_2$, *Japanese Journal of Applied Physics*. 19 (1980) 85–88.

[160] S. Kasiviswanathan, D.K. Rao, B.S.V. Gopalam, Preparation and characterization of the pseudobinary system $Cu_{1-x}Ag_xInTe_2$, *J. Mater. Sci. Lett*. 5 (1986) 912–914.

[161] Brandt G., Rauber A., Schneider J. ESR and X-ray analysis of the ternary semiconductors $CuAlS_2$, $CuInS_2$, and $AgGaS_2$ Locality: Synthetic sample note: chalcopyrite structure, *Solid State Communications*. 12 (1973) 481-483.

[162] A. Kraft, G. Kühn, Krist. W. Möller, Untersuchung von $CuGaSe_2$ und $CuGaTe_2$ unter hohem Druck, *ZAAC*, 504 (1983) 155-162.

[163] A.J. Wooten, D.J. Werder, D.J. Williams, J.L. Casson, J.A. Hollingsworth, Solution−liquid−solid growth of ternary Cu−In−Se semiconductor nanowires from multiple- and single-source precursors, *J. Am. Chem. Soc*. 131 (2009) 16177–16188.

[164] H. Welker, Über neue halbleitende Verbindungen, *Zeitschrift Naturforschung*. (1953) 744–749.

[165] M.Ya. Rudysh, M. Piasecki, G.L. Myronchuk, P.A. Shchepanskyi, V.Yo. Stadnyk, O.R. Onufriv, M.G. Brik, $AgGaTe_2$ – The thermoelectric and solar cell material: Structure, electronic, optical, elastic and vibrational features, *Infrared Physics & Technology*. 111 (2020) 103476.

[166] M.Ya. Rudysh, P.A. Shchepanskyi, A.O. Fedorchuk, M.G. Brik, V.Yo. Stadnyk, G.L. Myronchuk, E.A. Kotomin, M. Piasecki, Impact of anionic system modification on the desired properties for $CuGa(S_{1−x}Se_x)_2$ solid solutions, *Computational Materials Science*. 196 (2021) 110553.

[167] I. Aguilera, J. Vidal, P. Wahnón, L. Reining, S. Botti, First-principles study of the band structure and optical absorption of $CuGaS_2$, *Phys. Rev. B*. 84 (2011) 085145.

[168] M.I. Alonso, K. Wakita, J. Pascual, M. Garriga, N. Yamamoto, Optical functions and electronic structure of $CuInSe_2$, $CuGaSe_2$, $CuInS_2$, and $CuGaS_2$, *Phys. Rev. B*. 63 (2001) 075203.

[169] K. Koitabashi, S. Ozaki, S. Adachi, Optical properties of single-crystalline chalcopyrite semiconductor $AgInSe_2$, *Journal of Applied Physics*. 107 (2010) 053516.

[170] R. Smith, Device applications of the ternary semiconducting compounds, *J. Phys. Colloques* 36 (1975) C3-89-C3-99.

[171] R. Muruganantham, W.-R. Liu, C.-H. Lin, M. Rudysh, M. Piasecki, Design of meso/macro porous 2D Mn-vanadate as potential novel anode materials for sodium-ion storage, *Journal of Energy Storage*. 26 (2019) 100915.

[172] A. Majchrowski, M. Chrunik, M. Rudysh, M. Piasecki, K. Ozga, G. Lakshminarayana, I.V. Kityk, Bi_3TeBO_9: electronic structure, optical properties and photoinduced phenomena, *J. Mater. Sci*. 53 (2018) 1217–1226.

[173] P. Shchepanskyi, O. Kushnir, V. Stadnyk, A. Fedorchuk, M. Rudysh, R. Brezvin, P. Demchenko, A. Krymus, Structure and optical anisotropy of $K_{1.75}(NH_4)_{0.25}SO_4$ solid solution, *Ukr. J. Phys. Opt*. 18 (2017) 187.

[174] P.A. Shchepanskyi, V.Yo. Stadnyk, M.Ya. Rudysh, R.S. Brezvin, B.V. Andrievskii, Energy band structure and optical properties of $LiNaSO_4$ crystals, *Opt. Spectrosc*. 125 (2018) 353–357.

[175] O. Madelung, Semiconductors: data handbook, *Springer* (2004) 289–328.

[176] A.I. Kashuba, M. Piasecki, O.V. Bovgyra, V.Yo. Stadnyk, P. Demchenko, A. Fedorchuk, A.V. Franiv, B. Andriyevsky, Specific features of content dependences for energy gap in $In_xTl_{1-x}I$ solid state crystalline alloys, *Acta Phys. Pol. A*. 133 (2018) 68–75.

[177] R.Yu. Petrus, H.A. Ilchuk, A.I. Kashuba, I.V. Semkiv, E.O. Zmiiovska, Optical-energy properties of CdS thin films obtained by the method of high-frequency magnetron sputtering, *Opt. Spectrosc*. 126 (2019) 220–225.

[178] S. Laksari, A. Chahed, N. Abbouni, O. Benhelal, B. Abbar, First-principles calculations of the structural, electronic and optical properties of $CuGaS_2$ and $AgGaS_2$, *Computational Materials Science*. 38 (2006) 223–230.

[179] D.H. Fabini, M. Koerner, and R. Seshadri, Candidate inorganic photovoltaic materials from electronic structure-based optical absorption and charge transport proxies, *Chem. Mater*. 31 (2019), 1561–1574.

[180] S. Chaki, K. Mahato, M. Deshpande, Structural, electrical, and thermal properties study of CVT grown $CuAlS_2$ single crystals, *Chinese Journal of Physics* 52 (2014) 1588–1601.

[181] P. Gorai, E.S. Toberer, V. Stevanović, Thermoelectricity in transition metal compounds: the role of spin disorder, *Phys. Chem. Chem. Phys.* 18 (2016) 31777–31786.

[182] T. Omata, K. Nose, S. Otsuka-Yao-Matsuo, Size dependent optical band gap of ternary I-III-VI_2 semiconductor nanocrystals, *Journal of Applied Physics*. 105 (2009) 073106.

[183] Z.-L. Wang, W.-H. Xie, Y.-H. Zhao, Tunable band structure and effective mass of disordered chalcopyrite, *Front. Phys.* 12 (2017) 127103.

[184] J. Yang, Q. Fan, X. Cheng, Prediction for electronic, vibrational and thermoelectric properties of chalcopyrite $AgX(X = In, Ga)Te_2$: PBE + U approach, *R. Soc. Open Sci.* 4 (2017) 170750.

[185] V.K. Gudelli, V. Kanchana, G. Vaitheeswaran, $CuAlTe_2$: A promising bulk thermoelectric material, *Journal of Alloys and Compounds*. 648 (2015) 958–965.

[186] M.V. Yakushev, C. Faugeras, A.V. Mudryi, R.W. Martin, A Magneto-reflectivity study of $CuInTe_2$ single crystals, *Phys. Status Solidi B*. 257 (2020) 1900464.

[187] D.H. Fabini, M. Koerner, R. Seshadri, Candidate inorganic photovoltaic materials from electronic structure-based optical absorption and charge transport proxies, *Chemistry of Materials*. 31 (2019) 1561–1574.

[188] S.M. Wasim, J.G. Albornóz, Electrical and optical properties of *n*- and *p*-type $CuInTe_2$, *Physica Status Solidi (a)*. 110 (1988) 575–583.

[189] A.N. Fioretti, M.Morales-Masis, Bridging the *p*-type transparent conductive materials gap: synthesis approaches for disperse valence band materials, J. Photon. Energy, 10 (2020) 04202.

[190] A.H. MacDonald, S.H. Vosko, P.T. Coleridge, Extensions of the tetrahedron method for evaluating spectral properties of solids, *J. Phys. C: Solid State Phys.* 12 (1979) 2991–3002.

[191] R.S. Mulliken, Electronic population analysis on LCAO–MO molecular wave functions. *J. Chem. Phys.* 23 (1955) 1833–1840.

[192] M.D. Segall, C.J. Pickard, R. Shah, M.C. Payne, Population analysis in plane wave electronic structure calculations, *Molecular Physics*. 89 (1996) 571–577.

[193] D. Sanchez-Portal, E. Artacho, J.M. Soler, Projection of plane-wave calculations into atomic orbitals, *Solid State Communications*. 95 (1995) 685–690.

[194] E.R. Davidson, S. Chakravorty, A test of the Hirshfeld definition of atomic charges and moments, *Theoret. Chim. Acta*. 83 (1992) 319–330.

[195] J. He, E. Wu, H. Wang, R. Liu, Y. Tian, Ionicities of boron-boron bonds in B_{12} Icosahedra, *Phys. Rev. Lett.* 94 (2005) 015504.

[196] G.L. Myronchuk, G. Lakshminarayana, I.V. Kityk, A.S. Krymus, O.V. Parasyuk, M.Ya. Rudysh, P.A. Shchepanskyi, M. Piasecki, Optical absorption, piezoelectric effect and second harmonic generation studies of single crystal $AgGaGe_3Se_{7.6}Te_{0.4}$ solid solution, *Appl. Phys. A*. 123 (2017) 175.

[197] A.J. Read, R.J. Needs, Calculation of optical matrix elements with nonlocal pseudopotentials, *Phys. Rev. B*. 44 (1991) 13071–13073.

[198] G.A. Il'chuk, R.Yu. Petrus', A.I. Kashuba, I.V. Semkiv, E.O. Zmiiovs'ka, Peculiarities of the optical and energy properties of thin CdSe films, *Opt. Spectrosc.* 128 (2020) 49–56.

[199] S. Arai, S. Ozaki, S. Adachi, Optical properties and electronic band structure of $AgGaTe_2$ chalcopyrite semiconductor, *Appl. Opt.*, 49 (2010) 829–837.

[200] N.N. Syrbu, A.V. Dorogaan, A. Masniak, V.V. Ursaki, Exciton spectra and energy band structure of CuAlSe$_2$ crystals, *Moldavian Journal of the Physical Sciences*. 2 (2011) 143–154.

[201] V. Devarajan, A.M. Glazer, Theory and computation of optical rotatory power in inorganic crystals, *Acta Cryst A*. 42 (1986) 560–569.

[202] Crystal optics of D-mannitol, $C_6H_{14}O_6$: crystal growth, structure, basic physical properties, birefringence, optical activity, Faraday effect, electro-optic effects and model calculations, *Zeitschrift für Kristallographie - Crystalline Materials* 212 (1997) 283-296.

[203] W. Kaminsky, Experimental and phenomenological aspects of circular birefringence and related properties in transparent crystals, *Rep. Prog. Phys.* 63 (2000) 1575–1640.

[204] K. Claborn, B. Kahr, W. Kaminsky, Calculations of optical properties of the tetraphenyl-X family of isomorphous crystals (X = C, Si, Ge, Sn, Pb), *Cryst. Eng. Comm*. 4 (2002) 252–256.

[205] W. Kaminsky, D. Responte, D. Daranciang, J.B. Gallegos, B.-C. Ngoc Tran, T.-A. Pham, Structure, Morphology and Optical Properties of Chiral N-(4-X-phenyl)-N-[1(S)-1-phenylethyl]thiourea, X= Cl, Br, and NO$_2$, *Molecules*. 15 (2010) 554–569.

[206] S.C. Abrahams, J.L. Bernstein, Piezoelectric nonlinear optic CuGaS$_2$ and CuInS$_2$ crystal structure: Sublattice distortion in $A^IB^{III}C_2^{VI}$ and $A^{II}B^{IV}C_2^V$ type chalcopyrites Locality: Synthetic sample, *Journal of Chemical Physics*, 59 (1973) 5415-5420.

[207] J. Etxebarria, C.L. Folcia, J. Ortega, Origin of the optical activity of silver thiogallate, *J. Appl. Cryst*. 33 (2000) 126–129.

[208] S. Laksari, A. Chahed, N. Abbouni, O. Benhelal, B. Abbar, First-principles calculations of the structural, electronic and optical properties of CuGaS$_2$ and AgGaS$_2$, *Computational Materials Science*. 38 (2006) 223–230.

[209] A. Yariv, P. Yeh, Optical waves in crystals: propagation and control of laser radiation, *Wiley* (2002) 604.

[210] O. G. Vlokh, A. V. Zarik, I. M. Nekrasova, On the electro-gyration in AgGaS$_2$ and CdGa$_2$S$_4$ crystals, *Ukr. Fiz. Zhurn*., 28(9), (1983) 1334.

[211] J.R. Tessman, A.H. Kahn, W. Shockley, Electronic polarizabilities of ions in crystals, *Phys. Rev*. 92 (1953) 890–895.

[212] F. Oba, M. Choi, A. Togo, I. Tanaka, Point defects in ZnO: an approach from first principles, *Science and Technology of Advanced Materials*. 12 (2011) 034302.

[213] W. Körner, C. Elsässer, First-principles density functional study of dopant elements at grain boundaries in ZnO, *Phys. Rev. B*. 81 (2010) 085324.

[214] B. Himmetoglu, A. Floris, S. de Gironcoli, M. Cococcioni, Hubbard-corrected DFT energy functionals: The LDA+U description of correlated systems, *International Journal of Quantum Chemistry*. 114 (2014) 14–49.

[215] V.I. Anisimov, J. Zaanen, O.K. Andersen, Band theory and Mott insulators: Hubbard U instead of Stoner I, *Phys. Rev. B*. 44 (1991) 943–954.

[216] V.I. Anisimov, I.V. Solovyev, M.A. Korotin, M.T. Czyżyk, G.A. Sawatzky, Density-functional theory and NiO photoemission spectra, *Phys. Rev. B*. 48 (1993) 16929–16934.

[217] V.I. Anisimov, F. Aryasetiawan, A.I. Lichtenstein, First-principles calculations of the electronic structure and spectra of strongly correlated systems: the LDA+U method, *J. Phys.: Condens. Matter*. 9 (1997) 767–808.

[218] S.J. Clark, M.D. Segall, C.J. Pickard, P.J. Hasnip, M.I.J. Probert, K. Refson, M.C. Payne, First principles methods using CASTEP, *Crystalline Materials*. 220 (2005) 567–570.

[219] X. Ma, Y. Wu, Y. Lv, Y. Zhu, Correlation effects on lattice relaxation and electronic structure of ZnO within the GGA+U formalism, *J. Phys. Chem.* C. 117 (2013) 26029–26039.

[220] X.-Y. Deng, G.-H. Liu, X.-P. Jing, G.-S. Tian, On-site correlation of *p*-electron in d^{10} semiconductor zinc oxide, *International Journal of Quantum Chemistry*. 114 (2014) 468–472.

[221] K. Harun, N.A. Salleh, B. Deghfel, M.K. Yaakob, A.A. Mohamad, DFT + U calculations for electronic, structural, and optical properties of ZnO wurtzite structure: A review, *Results in Physics*. 16 (2020) 102829.

[222] B. Zoellner, E. Gordon, P.A. Maggard, A small bandgap semiconductor, *p*-type MnV_2O_6, active for photocatalytic hydrogen and oxygen production, *Dalton Trans*. 46 (2017) 10657–10664.

[223] Q.-J. Liu, Z.-T. Liu, L.-P. Feng, Elasticity, electronic structure, chemical bonding and optical properties of monoclinic ZrO_2 from first-principles, *Physica B: Condensed Matter*. 406 (2011) 345–350.

[224] L. Fast, J.M. Wills, B. Johansson, O. Eriksson, Elastic constants of hexagonal transition metals: Theory, *Phys. Rev. B*. 51 (1995) 17431–17438.

[225] J.F. Nye, Physical properties of crystals: Their representation by tensors and matrices, *Oxford University Press*, Oxford, New York, 1985.

[226] I. Waller, Dynamical theory of crystal lattices by M. Born and K. Huang, *Acta Cryst*. 9 (1956) 837–838.

[227] Y. Zhou, H. Xiang, F.-Z. Dai, Z. Feng, Cr_5Si_3B and Hf_5Si_3B: New MAB phases with anisotropic electrical, mechanical properties and damage tolerance, *Journal of Materials Science & Technology*. 34 (2018) 1441–1448.

[228] A. Reuss, Berechnung der Fließgrenze von mischkristallen auf grund der plastizitätsbedingung für einkristalle, *Z. angew. Math. Mech*. 9 (1929) 49–58.

[229] W. Voigt, Lehrbuch der Kristallphysik, *Taubner*, Leipzig, 1928.

[230] R. Hill, The elastic behaviour of a crystalline aggregate, *Proc. Phys. Soc. A*. 65 (1952) 349–354.

[231] F. Birch, Finite elastic strain of cubic crystals, *Phys. Rev*. 71 (1947) 809–824.

[232] F.D. Murnaghan, The compressibility of media under extreme pressures, *PNAS*. 30 (1944) 244–247.

[233] S. Appalakondaiah, G. Vaitheeswaran, S. Lebègue, N.E. Christensen, A. Svane, Effect of van der Waals interactions on the structural and elastic properties of black phosphorus, *Phys. Rev. B*. 86 (2012) 035105.

[234] S.F. Pugh, XCII. Relations between the elastic moduli and the plastic properties of polycrystalline pure metals, *The London, Edinburgh, and Dublin Philosophical Magazine and Journal of Science*. 45 (1954) 823–843.

[235] N. Guechi, A. Bouhemadou, R. Khenata, S. Bin-Omran, M. Chegaar, Y. Al-Douri, A. Bourzami, Structural, elastic, electronic and optical properties of the newly synthesized monoclinic Zintl phase $BaIn_2P_2$, *Solid State Sciences*. 29 (2014) 12–23.

[236] L. Sun, Y. Gao, Y. Li, K. Yoshida, T. Yano, D. Yi, Structural, bonding, anisotropic mechanical and thermal properties of Al_4SiC_4 and $Al_4Si_2C_5$ by first-principles investigations, *Journal of Asian Ceramic Societies*. 4 (2016) 289–298.

[237] S.I. Ranganathan, M. Ostoja-Starzewski, Universal elastic anisotropy index, *Phys. Rev. Lett*. 101 (2008) 055504.

[238] C.-G. Ma, D.-X. Liu, T.-P. Hu, Y. Wang, Y. Tian, M.G. Brik, Ab initio calculations of the structural, electronic and elastic properties of the MZN_2 (M = Be, Mg; Z = C, Si) chalcopyrite semiconductors, *Science of Advanced Materials*. 8 (2016) 466–475.

[239] H. Mohapatra, C.J. Eckhardt, Elastic Constants and Related Mechanical Properties of the monoclinic polymorph of the carbamazepine molecular crystal, *J. Phys. Chem. B*. 112 (2008) 2293–2298.

[240] G. Lan, B. Ouyang, J. Song, The role of low-lying optical phonons in lattice thermal conductance of rare-earth pyrochlores: A first-principle study, *Acta Materialia*. 91 (2015) 304–317.

[241] V. Kumar, A.K. Shrivastava, R. Banerji, D. Dhirhe, Debye temperature and melting point of ternary chalcopyrite semiconductors, *Solid State Communications*. 25–26 (2009) 1008–1011.

[242] C. Rincón, M.L. Valeri-Gil, Microhardness, Debye temperature and bond ionicity of ternary chalcopyrite compounds, *Materials Letters*. 28 (1996) 297–300.

[243] M.J. Weber, Handbook of optical materials, *CRC Press*, 2003.

[244] A.K. Kushwaha, C.-G. Ma, M.G. Brik, S.B. Omran, R. Khenata, Zone-center phonons and elastic properties of ternary chalcopyrite $ABSe_2$ (A = Cu and Ag; B = al, Ga and In), *Materials Chemistry and Physics*. 227 (2019) 324–331.

[245] G.N. Zhyzhyn, B.N. Mavrin, V.F. Shabanov, Optical vibrational spectra of crystals, *Nauka*, 1984.

[246] Ya.O. Dovhyi, A.V. Franiv, S.V. Ternavska, Izostructural phase transition in $In_xTl_{1-x}J$ system, *Ukr. J. Phys. Opt*. 2 (2001) 141–14.

[247] M. Cardona, G. Gruntherodt, Light Scattering in Solids III. Recent Results, *Springer-Verlag*, Berlin-Heidelberg-New-York, 1982.

[248] O.V. Kovalev, Irreducible and indced representations and co-representations of Fedorov groups, *Nauka*, Moscow, 1986.

[249] A. Pule, J.-P. Matye, Vibrational spectra and symmetry of crystals, *Mir*, Moscow, 1973.

[250] K. Nakimoto, IR spectra and Raman spectra of inorganic and coordinationals compounds, *Mir*, Moscow, 1991.

[251] A. Anderson, Application of Raman spectra, *Mir*, Moscow, 1977.

[252] M.Ya. Rudysh, A.I. Kashuba, P.A. Shchepanskyi, R.Yu. Petrus, V.Yo. Stadnyk, M. Piasecki, Calculation of the vibrational spectra of $AgGaS_2$ crystal with chalcopyrite structure, *J. Phys. Stud*. 25 (2021) 3704.

[253] S.P.S. Porto, J.A. Giordmaine, T.C. Damen, Depolarization of Raman scattering in calcite, *Phys. Rev*. 147 (1966) 608–611.

[254] S. Baroni, S. de Gironcoli, A. Dal Corso, P. Giannozzi, Phonons and related crystal properties from density-functional perturbation theory, *Rev. Mod. Phys*. 73 (2001) 515–562.

[255] H. Hellmann, Einführung in die Quantenchemie, *F. Deuticke,* Leipzig, 1937.

[256] R.P. Feynman, Forces in molecules, *Phys. Rev*. 56 (1939) 340–343.

[257] X. Gonze, D.C. Allan, M.P. Teter, Dielectric tensor, effective charges, and phonons in α-quartz by variational density-functional perturbation theory, *Phys. Rev. Lett*. 68 (1992) 3603–3606.

[258] X. Gonze, First-principles responses of solids to atomic displacements and homogeneous electric fields: Implementation of a conjugate-gradient algorithm, *Phys. Rev. B*. 55 (1997) 10337–10354.

[259] J. Łażewski, K. Parlinski, Lattice dynamics and elasticity of silver thiogallate ($AgGaS_2$) from ab initio calculations, *J. Chem. Phys*. 114 (2001) 6734–6738.

[260] D.J. Lockwood, H. Montgomery, Raman spectrum of $AgGaS_2$, *J. Phys. C: Solid State Phys*. 8 (1975) 3241–3250.

[261] H. Matsushita, S.E.S. Endo, T.I.T. Irie, Raman-Scattering Properties of I-III-VI2 Group Chalcopyrite Semiconductors, *Jpn. J. Appl. Phys*. 31 (1992) 18. https://doi.org/10.1143/JJAP.31.18.

[262] G.D. Holah, J.S. Webb, H. Montgomery, Lattice dynamics of AgGaS₂, *J. Phys. C: Solid State Phys*. 7 (1974) 3875–3890.

[263] D. Porezag, Infrared intensities and Raman-scattering activities within density-functional theory, *Phys. Rev. B*. 54 (1996) 7830–7836.

[264] M.Ya. Rudysh, A.I. Kashuba, V.Yo. Stadnyk, R.S. Brezvin, P.A. Shchepanskyi, V.M. Gaba, Z.O. Kohut, Raman scattering spectra of β-LiNH₄SO₄ crystals, *J. Appl. Spectrosc*. 85 (2019) 1022–1028.

[265] Y. Yu, Y.-J. Dong, Y.-H. Shen, G.-D. Zhao, X.-L. Zheng, J.-N. Sheng, Lattice dynamics properties of chalcopyrite ZnSnP₂ : Density-functional calculations by using a linear response theory, *Chinese Phys. B*. 26 (2017) 046302.

[266] X. Zhao, D. Vanderbilt, Phonons and lattice dielectric properties of zirconia, *Phys. Rev. B*. 65 (2002) 075105.

[267] P. Paufler, Landolt-Börnstein, New Series, K. H. Hellwege (ed.), Group III: Crystal and Solid State Physics, Vol. 12: Magnetic and Other Properties of Oxides and Related Compounds, Part c: Hexagonal Ferrites. Special Lanthanide and Actinide Compounds. Springer-Verlag Berlin, Heidelberg, New York*Crystal Research and Technology*. 18 (1983) 1546–1546.

[268] Y. Cui, U.N. Roy, P. Bhattacharya, A. Parker, A. Burger, J.T. Goldstein, Raman spectroscopy study of AgGaSe₂, AgGa₀.₉In₀.₁Se₂, and AgGa₀.₈In₀.₂Se₂ crystals, *Solid State Communications*. 150 (2010) 1686–1689.

[269] J. Camassel, L. Artus, J. Pascual, Lattice dynamics of AgGaSe₂. I. Experiment, *Phys. Rev. B. Condens. Matter*. 41 (1990) 5717–5726.

[270] Y. Yu, X.G. Kong, Y.H. Shen, J. Deng, Thermodynamic properties of CuAlS₂ with chalcopyrite structure from first-principles calculations, *Chalcogenide Letters*, 16 (2019) 5113-522.

[271] C. Julien, I. Ivanov, A. Khelfa, F. Alapini, M. Guittard, Characterization of the ternary compounds AgGaTe₂ and AgGa₅Te₈, *Journal of Materials Science*. 31 (1996) 3315–3319.

[272] T. Raadik, J. Krustok, M.V. Yakushev, Photoreflectance study of AgGaTe₂ single crystals, *Physica B: Condensed Matter,* 406 (2011) 418-420.

[273] S. Chen, X.G. Gong, S.-H. Wei, Band-structure anomalies of the chalcopyrite semiconductors CuGaX₂ versus AgGaX₂ (X =S and Se) and their alloys, *Phys. Rev. B*. 75 (2007) 205209.

[274] M. Souilah, A. Lafond, C. Guillot-Deudon, S. Harel, M. Evain, Structural investigation of the Cu₂Se–In₂Se₃–Ga₂Se₃ phase diagram, X-ray photoemission and optical properties of the Cu₁₋z(In₀.₅Ga₀.₅)₁₊z/₃Se₂ compounds, *Journal of Solid State Chemistry*. 183 (2010) 2274–2280.

[275] M. Robbins, V.G. Lambrecht, Preparation and some properties of materials in systems of the type M^I M^III S₂-M^I M^III Se₂ where M^I = Cu, Ag and M^III = Al, Ga, In, *Materials Research Bulletin*. 8 (1973) 703–709.

[276] J.-C. Chang, C.-T. Chen, M. Rudysh, M.G. Brik, M. Piasecki, W.-R. Liu, La₆Ba₄Si₆O₂₄F₂:Sm³⁺ novel red-emitting phosphors: Synthesis, photoluminescence and theoretical calculations, *Journal of Luminescence*. 206 (2019) 417–425.

[277] E.O. Gomes, L. Gracia, A.G. Santiago, R.L. Tranquilin, F.V. Motta, R.C. Amoresi, E. Longo, M.R.D. Bomio, J. Andres, Structure, electronic properties, morphology evolution, and photocatalytic activity in PbMoO₄ and Pb₁₋₂ₓCaₓSrₓMoO₄ (*x* = 0.1, 0.2, 0.3, 0.4 and 0.5) solid solutions, *Phys. Chem. Chem. Phys*. 22 (2020) 25876–25891.

[278] J.M. Guerra, C. Mahr, M. Giar, M. Czerner, C. Heiliger, Ab initio calculations of conduction band effective mass parameters of thermoelectric $Mg_2X_{1-x}Y_x$ (X, Y = Si, Ge, Sn) alloys, *Sci Rep*. 10 (2020) 16333.

[279] K. Hirata, H. Yamada, M. Uehara, S.A. Anggraini, M. Akiyama, First-principles study of piezoelectric properties and bonding analysis in (Mg, X, Al)N solid solutions (X = Nb, Ti, Zr, Hf), *ACS Omega*. 4 (2019) 15081–15086.

[280] P. Chen, M. Qin, H. Chen, C. Yang, Y. Wang, F. Huang, Cr incorporation in $CuGaS_2$ chalcopyrite: A new intermediate-band photovoltaic material with wide-spectrum solar absorption, *Physica Status Solidi (a)*. 210 (2013) 1098–1102.

[281] R. Ahuja, S. Auluck, O. Eriksson, J.M. Wills, B. Johansson, Calculated optical properties of a solar energy material: $CuGaS_2$, *Solar Energy Materials and Solar Cells*. 53 (1998) 357–366.

[282] J. Pohl, K. Albe, Intrinsic point defects in $CuInSe_2$ and $CuGaSe_2$ as seen via screened-exchange hybrid density functional theory, *Phys. Rev. B*. 87 (2013) 245203.

[283] A.R. Denton, N.W. Ashcroft, Vegard's law, *Phys. Rev. A*. 43 (1991) 3161–3164.

[284] R.D. Shannon, Revised effective ionic radii and systematic studies of interatomic distances in halides and chalcogenides, *Acta Cryst A*. 32 (1976) 751–767.

[285] M.G. Brik, M. Piasecki, I.V. Kityk, Structural, electronic, and optical features of $CuAl(S_{1-x}Se_x)_2$ solar cell materials, *Inorg. Chem.* 53 (2014) 2645–2651.

[286] S.F. Chichibu, T. Ohmori, N. Shibata, T. Koyama, T. Onuma, Fabrication of *p*-$CuGaS_2$/*n*-ZnO:Al heterojunction light-emitting diode grown by metalorganic vapor phase epitaxy and helicon-wave-excited-plasma sputtering methods, *Journal of Physics and Chemistry of Solids*. 66 (2005) 1868–1871.

[287] N. Romeo, G. Sberveglieri, L. Tarricone, C. Paorici, Preparation and characteristics of $CuGaSe_2$/CdS solar cells, *Appl. Phys. Lett.* 30 (1977) 108–110.

[288] L.K. Samanta, D.K. Ghosh, G.C. Bhar, Linear, nonlinear optical, and related properties of some mixed Cu-B^{III}-C_2^{VI} chalcopyrites, *Phys. Rev. B*. 35 (1987) 4519–4521.

[289] J.J. Frick, S.K. Kushwaha, R.J. Cava, A.B. Bocarsly, Characterization of primary carrier transport properties of the light-harvesting chalcopyrite semiconductors $CuIn(S_{1-x}Se_x)_2$, *J. Phys. Chem. C*. 121 (2017) 17046–17052.

[290] R.R. Reddy, Y.N. Ahammed, K.R. Gopal, D.V. Raghuram, Bulk modulus and Debye temperature of ternary chalcopyrite semiconductors, *IJPAP* 37. (1999) 25-28.

[291] V. Kumar, G.M. Prasad, D. Chandra, Bulk modulus of ternary chalcopyrite semiconductors, *Physica Status Solidi (b)*. 186 (1994) K45–K48.

LIST OF FIGURES, DIAGRAMS AND TABLES

List of figures

c) $CuAlTe_2$; d) $CuGaS_2$; e) $CuGaSe_2$; f) $CuGaTe_2$; g) $CuInS_2$; h) $CuInSe_2$; i) $CuInTe_2$, j) $AgAlS_2$; k) $AgAlSe_2$; l) $AgAlTe_2$; m) $AgGaS_2$; n) $AgGaSe_2$; o) $AgGaTe_2$; p) $AgInS_2$; q) $AgInSe_2$; r) $AgInTe_2$.

Figure 4.14. Dispersion of the real $\varepsilon_1(\omega)$ and imaginary $\varepsilon_2(\omega)$ part of dielectric function of I-III-VI_2 crystals calculated using GGA functionals.

Figure 4.15. The real (a) and imaginary (b) parts of the dielectric functions of the $AgGaTe_2$ semiconductor obtained using GGA (PBE) calculations (narrow line). The bold line present results of ellipsometry measurements [199].

Figure 4.16. The reflectance R, absorption coefficient α, refractive index n and extinction coefficient k of I-III-VI_2 crystals calculated using the GGA functional.

Figure 4.17. Contour plot of the calculated optical rotation (solid lines), mean refractive index (dashdotted lines) and linear birefringence (dotted lines) for $AgGaS_2$ crystals ($\alpha'_{Ga} = 0.010$ Å^3).

Figure 4.18. Calculated densities of state for $AgGaS_2$, $AgInSe_2$, $CuGaS_2$, та $CuInSe_2$ crystals together with the experimental XPS spectra taken from literature [29,60].

Figure 4.19. (a) Calculated electronic band structure using GGA+U method, (b) Partial density of states and (c) Total density of states (DOS) calculated using GGA+U approach and comparison of experimental XPS spectrum of MnV_2O_6 crystal.

Figure 4.20. Calculated density of state for $AgGaS_2$, $AgInSe_2$, $CuGaS_2$, та $CuInSe_2$ crystals with using different values of Hubbard parameter U, together with the experimental XPS spectra taken from literature [29,60].

Figure 5.1. Determination of stress components σ_{ij} and strains ε_{ij} on the faces of a unit cube: (a) Stress notation; (b) Strain notation.

Figure 5.2. The linear compressibility k_a, k_c, and k of I-III-VI_2 group crystals calculated with using the LDA and GGA functionals.

Figure 5.3. Comparison between experimental and DFT calculated bulk modulus of I-III-VI_2 chalcopyrites for LDA and GGA functionals.

Figure 5.4. Regression plot of (a) Bulk modulus B (GPa) versus molar mass M for I-III-VI_2 compounds for a) LDA and b) GGA calculation.

Figure 5.5. The volume dependence of bulk modulus B for LDA and GGA calculated (a) and experimental (b) results.

Figure 5.6. The density dependence of bulk modulus B for LDA and GGA calculated (a) and experimental (b) results.

Figure 5.7. Bulk modulus as function of band gap value for LDA and GGA functionals.

List of tables

Table 6.14. Static ε_0 and electron ε_∞ dielectric constants were calculated for the AgGaTe$_2$ crystal using the LDA functional.

Table 7.1. Experimental and calculated structural data (in Å) for the CuGa(S$_{1-x}$Se$_x$)$_2$ solid solutions for $x = 0$, 0.25, 0.5, 0.75 and 1.

Table 7.2. Calculated and experimental band gap values and corresponding scissor operator values for CuGaS$_2$ and CuGaSe$_2$ crystals.

Table 7.3. The derivative of the band gap vs the concentration of Se ions in CuGa(S$_{1-x}$Se$_x$)$_2$ (this work) and CuAl(S$_{1-x}$Se$_x$)$_2$ solid solutions.

Table 7.4. Calculated elastic constants (all in GPa, GGA/LDA results) for the CuGa(S$_{1-x}$Se$_x$)$_2$ solid solutions.

Table 7.5. Calculated densities ρ (kg/m^3), sound velocities v_l, v_t, v_m (m/s), Debye temperatures θ_D (in K) for the CuGa(S$_{1-x}$Se$_x$)$_2$ solid solutions.

ACADEMIC ACHIEVEMENTS

Papers with Impact Factor

1. V.Yo. Stadnyk, R.S. Breznin, **M.Ya. Rudysh**, P.A. Shchepanskii, V.M. Gaba, Z.A. Kohut, On isotropic state $LiNH_4SO_4$, *Optics and Spectroscopy*, (2014) 117(5), 756-758.

2. **M.Ya. Rudysh**, V.Yo. Stadnyk, R.S. Breznin, P.A. Shchepanskii Energy band structure of $LiNH_4SO_4$ crystals, *Physics of the Solid State*, 2015. 57(1), 53-58.

3. V.Yo. Stadnyk, R.S. Brezvin, **M.Ya. Rudish**, P.A. Shchepanskii, and V.Yu. Kurlyak, Piezo-optic properties of $LiNH_4SO_4$ crystals, *Crystallography Reports*, 2015. 60(3), 388-392.

4. **M.Ya. Rudysh**, M.G. Brik, O.Y. Khyzhun, A.O. Fedorchuk, I.V. Kityk, P.A. Shchepanskyi, V.Yo. Stadnyk, G. Lakshminarayana, R.S. Brezvin, Z. Bak, and M. Piasecki, Ionicity and birefringence of α-$LiNH_4SO_4$ crystals: ab-initio DFT study, X-ray spectroscopy measurements, *RSC Adv*. 2017. 7, 6889–6901.

5. G.L. Myronchuk, G. Lakshminarayana, I.V. Kityk, A.S. Krymus, O.V. Parasyuk, **M.Ya. Rudysh**, P.A. Shchepanskyi, M. Piasecki Optical absorption, piezoelectric effect and second harmonic generation studies of single crystal $AgGaGe_3Se_{7.6}Te_{0.4}$ solid solution, *Applied Physics A*. 2017. 123(3), 123-175.

6. M. Chrunik, A. Majchrowski, K. Ozga, **M.Ya. Rudysh**, I.V. Kityk, A.O. Fedorchuk, V.Yo. Stadnyk, M. Piasecki, Significant photoinduced increment of reflectivity coefficient in $LiNa_5Mo_9O_{30}$, *Current Applied Physics*, 2017. 17, 1100-1107.

7. P.A. Shchepanskyi, O.S. Kushnir, V.Yo. Stadnyk, A.O. Fedorchuk, **M.Ya. Rudysh**, R.S. Brezvin, P.Yu. Demchenko and A.S. Krymus, Structure and optical anisotropy of $K_{1.75}(NH_4)_{0.25}SO_4$ solid solution, *Ukr. J. Phys. Opt*. 2017. 18(4), 187-196.

8. P.A. Shchepanskyi, V.M. Gaba, V.Yo. Stadnyk, **M.Ya. Rudysh**, M. Piasecki, R.S. Brezvin, The influence of partial isomorphic substitution on electronic and optical parameters of $ABSO_4$ group crystals, *Acta Physica Polonica*. 2018. 133(4), 819-823.

9. A. Majchrowski, M. Chrunik, **M. Rudysh**, M. Piasecki, K. Ozga, G. Lakshminarayana, and I.V. Kityk, Bi_3TeBO_9: electronic structure, optical properties and photoinduced phenomena, *J. Mater. Sci*. 2018. 53(2), 1217–1226.

10. **M.Ya. Rudysh**, M.G. Brik, V.Yo. Stadnyk, R.S. Brezvin, P.A. Shchepanskyi, A. Fedorchuk, O.Y. Khyzhun, I.V. Kityk, M. Piasecki, Ab initio calculations of the

electronic structure and specific optical features of β-LiNH$_4$SO$_4$ single crystals, *Physica B: Physics of Condensed Matter*. 2018. 528, 37–46.

11. V.I. Stadnyk, **M.Ya. Rudish**, P.A. Shchepansky, I.M. Matviishyn, O.M. Gorina, The effect of uniaxial pressures on the infrared spectra of LiNH$_4$SO$_4$ crystals, *Optics and Spectroscopy*. 2018. 124(2), 216–220.

12. P.A. Shchepanskyi, V.Yo. Stadnyk, **M.Ya. Rudysh**, R.S. Brezvin and B.V. Andrievskii, Energy band structure and optical properties of LiNaSO$_4$ crystals, *Optics and Spectroscopy*. 2018. 125(3). 353–357.

13. J.-C. Chang, C.-T. Chen, **M. Rudysh**, M.G. Brik M. Piasecki, W.-R. Liu, La$_6$Ba$_4$Si$_6$O$_{24}$F$_2$: Sm^{3+} novel red-emitting phosphors: synthesis, photoluminescence and theoretical calculations, *Journal of Luminescence*. 2019. 206, 417–425.

14. **M.Ya. Rudysh**, A.I. Kashuba, V.Yo. Stadnyk, R.S. Brezvin, P.A. Shchepanskyi, V.M. Gaba, Z.A. Kogut, Raman spectra of β-LiNH$_4$SO$_4$ crystals, *Journal of Applied Spectroscopy*. —2018. — Vol. 85, — No. 6, — P. 896-903.

15. J. Podlesný, O. Pytela, M. Klikar, V. Jelínková, I.V. Kityk, K. Ozga, J. Jedryka, **M. Rudysh** and F. Bureš, Small isomeric push–pull chromophores based on thienothiophenes with tunable optical (non) linearities, *Org. Biomol. Chem.*, 2019, 17, 3623–3634.

16. V.Y. Stadnyk, R.B. Matviiv, P.A. Shchepanskii, **M.Ya. Rudysh**, and Z.A. Kogut. Photoelastic properties of potassium sulfate crystals, *Physics of the Solid State*. 2019. 61(11). 2130–2133.

17. V.Yo. Stadnyk, P.A. Shchepanskyi, R.S. Brezvin, **M.Ya. Rudysh**, Z.A. Kohut, O.R. Onufriv, Ya.P. Kost, On isotropic points in potassium ammonium sulphate crystals, *Crystallogr. Rep.* 2019. 64(5), 787–792.

18. V.Yo. Stadnyk, P.A. Shchepanskyi, R.S. Brezvin, **M.Ya. Rudysh**, and R.B. Matviiv Pressure-induced changes in parameters of the indicatrix of lithium sodium sulfate crystals, *Optics and Spectroscopy*, 2019, 127(6), 1023–1027.

19. **M.Ya. Rudysh**, V.Yo. Stadnyk, P.A. Shchepanskyi, R.S. Brezvin, J. Jedryka, I.V. Kityk Specific features of refractive, piezo-optic and nonlinear optical dispersions of β-LiNH$_4$SO$_4$ single crystals, *Physica B: Condensed Matter*. 2020, 508, 411919.

20. **M.Ya. Rudysh**, P.A. Shchepanskyi, A.O. Fedorchuk, M.G. Brik, C.-G. Ma, G.L. Myronchuk, M. Piasecki, First-principles analysis of physical properties anisotropy for the Ag$_2$SiS$_3$ chalcogenide semiconductor, *Journal of Alloys and Compounds*, 2020, 826, 154232.

21. V.Yo. Stadnyk, R.B. Matviiv, **M.Ya. Rudysh**, R.S. Brezvin, P.A. Shchepanskyi, and B.V. Andrievskii, Refractive parameters and band energy structure of K_2SO_4 crystals doped with copper, *Journal of Applied Spectroscopy*, 2020. 87(1), 143–149.

22. R. Muruganantham, W.-R. Liu, C.-H. Lin, **M. Rudysh**, M. Piasecki, Design of meso/macro porous 2D Mn-vanadate as potential novel anode materials for sodium-ion storage, *Journal of Energy Storage*. 2019. 26, 100915 (9).

23. **M.Ya. Rudysh**, M. Piasecki, G.L. Myronchuk, P.A. Shchepanskyi, V.Yo. Stadnyk, O.R. Onufriv, M.G. Brik, $AgGaTe_2$ - the thermoelectric and solar cell material: structure, electronic, optical, elastic and vibrational features, *Infrared Physics and Technology*, 2020, 111, 103476.

24. R.B. Matviiv, **M.Ya. Rudysh**, V.Yo. Stadnyk, A.O. Fedorchuk, P.A. Shchepanskyi, R.S. Brezvin, O.Y. Khyzhun, Structure, refractive and electronic properties of K_2SO_4:Cu^{2+} (3%) crystals, *Current Applied Physics*. 2021. 21, 80-88.

25. J.-A. Chen, M. Piasecki, C.-C. Yang, **M. Rudysh**, and W.-R. Liu, Synthesis, luminescent properties and ab initio study of yellow-emitting $Sr_8MgGa(PO_4)_7$:Eu^{2+} phosphors for white light-emitting diodes, *Journal of Luminesce*. 2021. 235, 117982.

26. R. Matviiv, V. Stadnyk, R. Brezvin, P. Shchepanskyi, **M. Rudysh**, O. Kostetskyi, Thermal and refractive properties of doped K_2SO_4 crystals in the region of the phase transition, *Journal of Physical Studies*. 2021. 25(2), 2703 (6).

27. **M.Ya. Rudysh**, P.A. Shchepanskyi, A.O. Fedorchuk, M.G. Brik, V.Yo. Stadnyk, G.L. Myronchuk, E.A. Kotomin, M. Piasecki, Impact of anionic system modification on the desired properties for $CuGa(S_{1-x}Se_x)_2$ solid solutions, *Computational Materials Science*. 2021. 196. 110553.

Other Scopus/Web of Science publications

1. V.Yo. Stadnyk, O.Z. Kashuba, R.S. Brezvin, I.M. Matviishyn, **M.Y. Rudysh**, Birefringence properties of uniaxially compressed K_2SO_4 crystals, *Ukr. J. Phys*. 2013. 58(9), 853-856.

2. **M. Rudysh**, V. Stadnyk, P. Shchepanskyi, R. Brezvin, O. Kushnir, G. Myronchuk, I. Matviishyn, Temperature and pressure changes of the refractive properties of $LiNH_4SO_4$ crystal in β-modification, *IEEE 12th International Conference on Electronics and Information Technologies (ELIT)*, 2019. 316-320.

3. R. Matviiv, V. Stadnyk, R. Brezvin, P. Shchepanskyi, **M. Rudysh**, O. Kostetskyi Thermal and refractive properties of doped K_2SO_4 crystals in the region of the phase transition, *Journal of Physical Studies*. 2021. 25(2) 2703 (6).

4. V. Stadnyk, P. Shchepanskyi, **M. Rudysh**, R. Matviiv and R. Brezvin, Phase transition in impurity crystals of potassium sulfate: refractive parameters, *IEEE 12th International Conference on Electronics and Information Technologies (ELIT)*, 2021, 305-309.

5. **M. Rudysh**, B. Horon, P. Shchepanskyi, V. Stadnyk and R. Brezvin, First principles calculation of band structure and physical properties of ferroelectric $(NH_4)_2BeF_4$ crystal, *IEEE 12th International Conference on Electronics and Information Technologies (ELIT)*, 2021, 310-314.

6. **M.Ya. Rudysh**, A.I. Kashuba, P.A. Shchepanskyi, R.Yu. Petrus, V.Yo. Stadnyk, M. Piasecki, Calculation of the vibrational spectra of $AgGaS_2$ crystal with chalcopyrite structure, *Journal of Physical Study*, 2021, 25(3). 3704 (11).

Other publications

1. V. Stadnyk, Z. Kohut, I. Matviishyn, **M. Rudysh**, P. Shchepanskyi, "*Search for new crystals with isotropic point*", *Visnyk of the Lviv University. Series Physics*. 2013, 48, 148-158.

2. V. Stadnyk, **M. Rudysh**, R. Brezvin, P. Shchepanskyi, Electronic structure and optical properties of lithium-ammonium sulphate crystal of α-modification, *Visnyk of the Lviv University. Series Physics*. 2016. 52. 74-84.

3. P. Shchepanskyi, V. Stadnyk, R. Brezvin, **M. Rudysh**, Refractive parameters of $K_{1.75}[NH_4]_{0.25}SO_4$ crystals, *Visnyk of the Lviv University. Series Physics*. 2016. 52, 108-115.

4. V. Stadnyk, P. Shchepanskyi, **M. Rudysh**, R. Brezvin, I. Matviishyn, L. Karpliuk, Z. Kohut, The band structure and refractive parameters of potassium ammonium sulphate solid solution crystal, *Electronics and information technologies*. 2017. 8, 143-152.

5. V. Stadnyk, P. Shchepanskyi, **M. Rudysh**, the influence of temperature and uniaxial stresses on the refractive parameters of $LiNaSO_4$ crystals, *Visnyk of the Lviv University. Series Physics*. 2017. 53, 42-50.

6. R. Matviiv, **M. Rudysh**, V. Stadnyk, R. Brezvin, I. Matviishyn, L. Karpluk, Structure and refractive parameters of doped K_2SO_4 crystals, *Visnyk of the Lviv University. Series Physics*. 2018. 55, 50-61.

7. P. Shchepanskyi, **M. Rudysh,** R. Matviiv, V. Stadnyk, R. Brezvin, O. Kushnir, L. Karpluk, Correlation analysis between structural and refractive parameters of $ABSO_4$ group crystals, *Visnyk of the Lviv University. Series Physics*. 2019. 56. 112-121.

8. **M.Ya. Rudysh**, P.A. Shchepanskyi, V.Yo. Stadnyk, R.S. Brezvin, Temperature study of structural transformation in β-$LiNH_4SO_4$ crystals, *Visnyk of the Lviv University. Series Physics*. 2020. 57. 46-56.

Presentations on the international conferences

Oral presentations:

8. M. Savchak, V. Stadnyk, R. Brezvin, V. Kurlyak, **M. Rudysh**, "*$LiNH_4SO_4$ – new crystal with isotropic point*", International conference of students and young scientists in theoretical and experimental physics "HEUREKA-2012", Lviv, Ukraine, April 23-25, 2012.

9. **M.Ya. Rudysh**, R.S. Brezvin, V.Y. Stadnyk, "*Piezo-optic properties of $LiNH_4SO_4$ crystals*", International conference of students and young scientists in theoretical and experimental physics "HEUREKA-2013", Lviv, Ukraine, May 15-18, 2013.

10. V.Yo. Stadnyk, O.V. Bovgyra, R.S. Brezvin, V.Yu. Kurlyak, I.M. Matviishyn, **M.Ya. Rudysh**, P.A. Shchepanskyi, "*The influence of uniaxial stresses on the physical properties of the crystals*", XI Internationa scientific conference "Physical properties in solids", Kharkiv, Ukraine, December 3-6, 2013.

11. **M.Ya. Rudysh**, P.A. Shchepanckyi, V.Y. Stadnyk, R.S. Brezvin, "*Band structure of $LiNH_4SO_4$ crystals*", XII conference of students, PhD students and young scientist "Shevchenkivska vesna", Kyiv, Ukraine, March 25-28, 2014.

12. P.A. Shchepanskyi, **M.Ya. Rudysh**, V.Y. Stadnyk, "*About new crystals with isotropic point*", International conference of students and young scientists in theoretical and experimental physics "HEUREKA-2014", Lviv, Ukraine, May 15-17, 2014.

13. **M.Ya. Rudysh**, P.A. Shchepanskyi, V.Yo. Stadnyk, R.S. Brezvin, "*Band energy structure of $LiNH_4SO_4$ single crystal*", International conference of students and young scientists in theoretical and experimental physics "HEUREKA-2014", Lviv, Ukraine, May 15-17, 2014.

14. **M.Ya. Rudysh**, P.A. Shchepanskyi, V.M. Gaba, V.Yu. Kurlyak, Z.O. Kohut, I.M. Matviishyn, V.Yo. Stadnyk, "*Band-energy structure calculation of crystals with isotropic point*", 6-th Ukrainian-Polish scientific and practical conference "Electronics and Information Technologies", Lviv-Chynadiyevo, Ukraine, August 28-31, 2014.

15. P.A. Shcheanskyi, V.Yu. Kurlyak, R.S. Brezvin, V.Yo. Stadnyk, **M.Ya. Rudysh**, "*Spectral-baric dependence of birefringence of α-LiNH$_4$SO$_4$ crystals with isotropic point*", International conference of young scientists and PhD students, Institute of electron physics NAS of Ukraine "IEP-2015", Uzhorod, Ukraine, May 18-22, 2015.

16. **M.Ya. Rudysh**, V.Yu. Kurlyak, V.Yo. Stadnyk, R.S. Brezvin, P.A. Shchepanskyi "*Calculation of electronic structure and optical properties of LiNH$_4$SO$_4$ crystals*", International conference of young scientists and PhD students, Institute of electron physics NAS of Ukraine "IEP-2015", Uzhorod, Ukraine, May 18-22, 2015.

17. **M.Ya. Rudysh**, "*Calculation of electronic structure and optical properties of LiNH$_4$SO$_4$ crystals from the first principles*", XIII International Scientific - practical conference of students and young scientists "Shevchenkivska Vesna 2015: Radiophysics. Electronics.Computer systems", Kyiv, Ukraine, April 1-3, 2015.

18. **M.Ya. Rudysh**, P.A. Shchepanskyi, V.Yo. Stadnyk, R.S. Brezvin, Z.O. Kohut, "*Optical-electronic properties of lithium-ammoium sulfate crystals*", International conference of students and young scientists in theoretical and experimental physics "HEUREKA-2015", Lviv, Ukraine, May 13-15 2015.

19. P. Shchepanskyi, **M. Rudysh**, V. Stadnyk, R. Brezvin, Z. Kohut, "*Temperature–spectral–baric study of the isotropic state of α-LAS crystals*", International conference of students and young scientists in theoretical and experimental physics "HEUREKA-2015", Lviv, Ukraine, May 13-15, 2015.

20. **M.Ya. Rudysh**, P.A. Shchepanskyi, V.Yu. Kurlyak, V.Yo. Stadnyk, R.S. Brezvin "*Pressure change of birefringence in ABSO$_4$ – type crystals*", XV-th international young scientists' conference on applied physics Taras Shevchenko National University of Kyiv Faculty of Radio Physics, Electronics and Computer Systems, Kyiv, Ukraine, June 10-13, 2015.

21. P.A. Shchepanskyi, **M.Ya. Rudysh**, V.Yo. Stadnyk, R.S. Brezvin, "*Study of partial isomorphic substitution on refractive parameters of K$_2$SO$_4$ single crystals*", International internet conference for young researchers and students «Topical Issues of Fundamental and Applied Studies», Lutsk, Ukraine, May 19-20, 2016.

22. **M.Ya. Rudysh**, P.A. Shchepanskyi, V.Yo. Stadnyk, R.S. Brezvin "*Study of temperature-spectral-baric characteristics of LINH$_4$SO$_4$ crystal of α-modification*", International internet conference for young researchers and students «Topical Issues of Fundamental and Applied Studies», Lutsk, Ukraine, May 19-20, 2016.

23. P.A. Shchepanskyi, **M.Ya. Rudysh**, V.Yo. Stadnyk, R.S. Brezvin, "*Refractive index dispersion and optical birefringence study of K$_{1.75}$[NH$_4$]$_{0.25}$SO$_4$ single crystal*", Relaxed, nonlinear and acoustic optical processes and materials "RNAOPM'2016", Lutsk-Lake "Svityaz", Ukraine, June 1-4, 2016.

24. **M.Ya. Rudysh**, P.A. Shchepanskyi, V.Yo. Stadnyk, R.S. Brezvin, "*Ab-initio study of electron band structure and optical properties of lithium-ammonium sulfate*", Relaxed, nonlinear and acoustic optical processes and materials "RNAOPM'2016", Lutsk-Lake "Svityaz", Ukraine, June 1-4 2016.

25. **M.Ya. Rudysh**, O.Y. Khyzhun, P.A. Shchepanskyi, V.Yo. Stadnyk, R.S. Brezvin, "*First principle calculations and X-ray spectroscopy study of α-LiNH$_4$SO$_4$ crystals*", XII International Scientific Conference "Electronics and Applied Physics", Kyiv, Ukraine, October 19-22, 2016.

26. P.A. Shchepanskyi, **M.Ya. Rudysh**, V.Yo. Stadnyk, R.S. Brezvin, "*Birefringence study of isotropic point in K$_{1,75}$[NH$_4$]$_{0,25}$SO$_4$ single crystal*", XII International Scientific Conference "Electronics and Applied Physics", Kyiv, Ukraine, October 19-22, 2016.

27. **M. Rudysh**, V. Stadnyk, R. Brezvin, P. Shchepanskyi, "*Birefringence properties of crystals β-lithium-ammonium sulfate*", International conference of students and young scientists in theoretical and experimental physics "HEUREKA-2017", Lviv, Ukraine, May 16-18, 2017.

28. P. Shchepanskyi, **M. Rudysh**, V. Stadnyk, R. Brezvin, O. Pankevych, "*Temperature study of birefringence in K$_{1,75}$[NH$_4$]$_{0,25}$SO$_4$ single crystal*", International conference of students and young scientists in theoretical and experimental physics "HEUREKA-2017", Lviv, Ukraine, May 16-18, 2017.

29. P. Shchepanskyi, **M. Rudysh**, V. Stadnyk, R. Brezvin, "*Band-energy structure of K$_{1.75}$[NH$_4$]$_{0.25}$SO$_4$ crystal*", International conference of students and young scientists in theoretical and experimental physics "HEUREKA-2017", Lviv, Ukraine, May 16-18, 2017.

30. **M. Rudysh**, V. Stadnyk, P. Shchepanskyi, R. Brezvin, I. Kityk, M. Piasecki, "*Optical study of β-LINH$_4$SO$_4$ crystals*", Second international workshop „Actual problems of fundamental science", Lutsk-Lake Svityaz', Ukraine, June 01-05, 2017.

31. P. Shchepanskyi, **M. Rudysh**, V. Stadnyk, R. Brezvin, I. Kityk, M. Piasecki, "*Electronic and optical properties simulation of $K_{1.75}(NH_4)_{0.25}SO_4$ crystals*", Second international workshop „Actual problems of fundamental science", Lutsk-Lake Svityaz', Ukraine, June 01-05, 2017.

32. M. Rudysh, M. Chrunik, A. Majchrowski, I. Kityk, M. Piasecki "*Giant increase of photoinduced reflectivity in $LiNa_5Mo_9O_{30}$*", International conference on oxide materials for electronic engineering – fabrication, properties and applications „OMEE 2017", Lviv, Ukraine, May 29 – June 2, 2017.

33. P.A. Shchepanskyi, V.Yo. Stadnyk, R.S. Brezvin, I. Kityk, **M.Ya. Rudysh**, M. Piasecki, "*$K_{1.75}[NH_4]_{0.25}SO_4$ – new crystal with isotropic point*", International conference on oxide materials for electronic engineering – fabrication, properties and applications „OMEE-2017", Lviv, Ukraine, May 29 – June 2, 2017.

34. **M. Rudysh**, M. Brik, M. Piasecki, P. Shchepanskyi and V. Stadnyk, "*Electronic structure and physical properties study of Ag_2XS_3 (X = Si, Ge, Sn) ternary semiconductors*", Joint conferences on advanced materials "Functional and Nanonstructured Materials (FNMA'2017) and Physics of Disordered Systems (PDS'2017)", Lviv-Yaremche, Ukrtaine, September 25-29, 2017.

35. P.A. Shchepanskyi, V.Yo. Stadnyk, **M.Ya. Rudysh**, R.S. Brezvin, "*Refractive parameters of $K_{1.75}[NH_4]_{0.25}SO_4$ crystals: ab initio calculations, experimental measurements*", Joint conferences on advanced materials "Functional and Nanonstructured Materials (FNMA'2017) and Physics of Disordered Systems (PDS'2017)", Lviv-Yaremche, Ukraine, September 25-29, 2017.

36. P.A. Shchepanskyi, V.Yo. Stadnyk, **M.Ya. Rudysh,** R.S. Brezvin and M. Piasecki, "*Electronic and refractive properties of $LiNaSO_4$ crystals*", Joint conferences on advanced materials "Functional and Nanonstructured Materials (FNMA'2017) and Physics of Disordered Systems (PDS'2017)", Lviv-Yaremche, Ukraine, September 25-29, 2017.

37. **M. Rudysh**, O. Kuryzko, P. Shchepanskyi, R. Brezvin, V. Stadnyk, "*Structure and refractive parameters of lithium-ammonium sulfate crystals*", International conference of students and young scientists in theoretical and experimental physics "HEUREKA-2018", Lviv, Ukraine, May 15-17, 2018.

38. **M. Rudysh**, P. Shchepanskyi, R. Brezvin, V. Stadnyk, "*Infrared reflection spectra of lithium-ammonium sulfate crystals*", International conference of students and young

scientists in theoretical and experimental physics "HEUREKA-2018", Lviv, Ukraine, May 15-17, 2018.

39. P. Shchepanskyi, V. Stadnyk, **M. Rudysh**, R. Brezvin, I. Ivanyshyn, "*Optical properties of LiNaSO$_4$ single crystal*", International conference of students and young scientists in theoretical and experimental physics "HEUREKA-2018", Lviv, Ukraine, May 15-17, 2018.

40. P. Shchepanskyi, V. Stadnyk, R. Brezvin, **M. Rudysh**, "*Influence of the cation substitution on the refractive properties of ABSO$_4$-group crystals*", International conference of students and young scientists in theoretical and experimental physics "HEUREKA-2018", Lviv, Ukraine, May 15-17, 2018.

41. **M. Rudysh**, M. Piasecki, M.G. Brik, "*La$_6$Ba$_4$Si$_6$O$_{24}$F$_2$:Sm^{3+} novel material for W-LED application*", International conference of students and young scientists in theoretical and experimental physics "HEUREKA-2018", Lviv, Ukraine, May 15-17, 2018.

42. P.A. Shchepanskyi, **M.Ya. Rudysh**, V.Yo. Stadnyk, R.S. Brezvin, O.S. Kushnir, A.O. Fedorchuk, M. Piasecki, "*Band-energy structure and optical anisotropy of LiNaSO$_4$ crystals*", IX International scientific conference «Relaxed, nonlinear and acoustic optical processes and materials» (RNAOPM'2018), Lutsk–Lake "Svityaz", Ukraine, June 1–5, 2018.

43. **M.Ya. Rudysh**, A.O. Fedorchuk, O.Y. Khyzhun, V.Y. Stadnyk, R.S. Brezvin, P.A. Shchepanskyi, "*Structure and properties of LiNH$_4$SO$_4$ crystals*", IX International scientific conference «Relaxed, nonlinear and acoustic optical processes and materials» (RNAOPM'2018), Lutsk–Lake "Svityaz", Ukraine, June 1–5, 2018.

44. P.A. Shchepanskyi, V.Yo. Stadnyk, **M.Ya. Rudysh**, A.O. Fedorchuk, O.S. Kushnir, R.S. Brezvin, "*The influence of cation substitution on refractive properties of ABSO$_4$-group crystals*", International workshop for young scientists "Functional materials for technical and biomedical applications", Kharkiv, Ukraine, September 5-8, 2018.

45. P.A. Shchepanskyi, V.Yo. Stadnyk, **M.Ya. Rudysh**, R.S. Brezvin, M. Piasecki, "*Optical and electronic properties of sodium ammonium sulphate dehydrate crystal*", International workshop for young scientists "Functional materials for technical and biomedical applications", Kharkiv, Ukraine, September 5-8, 2018.

46. P.A. Shchepanskyi, V.Yo. Sradnyk, O.S. Kushnir, A.O. Fedorchuk, **M.Ya. Rudysh**, R.S. Brezvin, "*Optical anisotropy of ABSO$_4$-family sulphates*", V Ukrainian-Polish-Lithuanian meeting on physics of ferroelectrics, Uzhhorod, Ukraine, September 18-20, 2018.

47. **M.Ya. Rudysh**, M.G. Brik, O.R. Onufriv, M. Piasecki, V.Yo. Sradnyk, P.A. Shchepanskyi, "*Ab initio study of crystal structure and physical properties of chalcopyrite CuGa(S$_2$)$_x$(Se)$_{1-x}$ solid solution*", V Ukrainian-Polish-Lithuanian meeting on physics of ferroelectrics, Uzhhorod, Ukraine, September 18-20, 2018.

48. **M.Ya. Rudysh**, M.G. Brik, M. Piasecki, G.L. Myronchuk, "*Optical spectra and band structure of Cu-based chalcopyrite for solar cell application: theoretical study*", International conference of students and young scientists in theoretical and experimental physics "HEUREKA-2019", Lviv, Ukraine, Maj 14-16, 2019.

49. P. Shchepanskyi, O. Kushnir, V. Stadnyk, **M. Rudysh**, "*Relationships between density and refractive index of ABSO$_4$-group crystals*", International conference of students and young scientists in theoretical and experimental physics "HEUREKA-2019", Lviv, Ukraine, Maj 14-16, 2019.

50. P. Shchepanskyi, V. Stadnyk, **M. Rudysh**, R. Brezvin, "*Refractive properties of sodium ammonium sulfate dehydrsate single crystal*", International conference of students and young scientists in theoretical and experimental physics "HEUREKA-2019", Lviv, Ukraine, Maj 14-16, 2019.

51. B. Goron, **M. Rudysh**, P. Shchepanskyi, R. Brezvin, V. Stadnyk, "*Study of pressure influence on structure and properties of potassiun sulfate crystals*", International conference of students and young scientists in theoretical and experimental physics "HEUREKA-2019", Lviv, Ukraine, Maj 14-16, 2019.

52. **M.Ya. Rudysh**, G.L. Myronchuk, "*Anisotropy and elastic properties of ternary chalcogenide Ag$_2$XS$_3$ (where X = Si, Ge and Sn)*", International conference of students and young scientists in theoretical and experimental physics "HEUREKA-2019", Lviv, Ukraine, Maj 14-16, 2019.

53. R. Matviiv, **M. Rudysh**, P. Shchepanskyi, P. Vankevych, V. Standyk, "*Influence of dopping on refractive parameters of K$_2$SO$_4$ crystals*", International conference of students and young scientists in theoretical and experimental physics "HEUREKA-2019", Lviv, Ukraine, Maj 14-16, 2019.

54. P.A. Shchepanskyi, O.S. Kushnir, V.Yo. Stadnyk, A.O. Fedorchuk, R.S. Brezvin, **M.Ya. Rudysh**, M. Piasecki, "*Relation between structure and refractive properties of ABSO$_4$-group crystals*", Third international conference "Actual Problems of Fundamental Science", Lutsk-Lake Svityaz', Ukraine, June 01-05, 2019.

55. **M.Ya. Rudysh**, M.G. Brik, M. Piasecki, V.Yo. Stadnyk, A.S. Krymus, P.A. Shchepanskyi, "*Electronic structure, optical and elastic properties of CuInX$_2$ (X =*

S, Se, and Te) crystals", Third international conference "Actual Problems of Fundamental Science", Lutsk-Lake Svityaz', Ukraine, June 01-05, 2019.

56. M. Piasecki, J.-C. Chang, C.-T. Chen, **M. Rudysh**, M.G. Brik, N. Veeraiah, W.-R. Liu, "*Synthesis, structure and photoluminescence of the novel red-emitting phosphor for the w-leds applications*", 12th international conference on excited states of transitions elements (ESTE 2019), Kudowa-Zdrój, Poland, September 08-13, 2019.

57. **M.Ya. Rudysh**, M. Piasecki, M.G. Brik, "*Theoretical study of electronic structure and physical properties of AgGaTe$_2$ chalcopyrite crystal*", International workshop for young scientists "Functional materials for technical and biomedical applications", Koropovo, Ukraine, September 9-12, 2019.

58. **M. Rudysh**, V. Stadnyk, P. Shchepanskyi, R. Brezvin, O. Kushnir, G. Myronchuk, I. Matviishyn, "*Temperature and pressure changes of the refractive properties of LiNH$_4$SO$_4$ crystal in β-modification*", 2019 XIth International scientific and practical conference on electronics and information technologies (ELIT), Lviv, Ukraine, September 16-18, 2019.

59. R. Muruganantham, W.-R. Liu, C.-H. Lin, **M. Rudysh**, B. Andrievskyy and M. Piasecki, "*Design of meso/macro porous 2D Mn-vanadate as potential novel anode materials for sodium-ion storage*", VIII International seminar „Properties of ferroelectric and superionic systems", Uzhhorod, Ukraine, October, 29-30, 2019.

60. **M.Ya. Rudysh**, M.G. Brik, M. Piasecki, A.O. Fedorchuk, G.L. Myronchuk, "*Ab initio study of crystal structure and physical properties of CuGa(S$_x$Se$_{1-x}$)$_2$ solid solutions*", XXII international seminar on physics and chemistry of solids "ISPCS 2020", Lviv, Ukraine, June 17-19, 2020.

61. **M.Ya. Rudysh**, R.B. Matviiv, V.Yo. Stadnyk, A.O. Fedorchuk, P.A. Shchepanskyi, R.S. Brezvin, O.Y. Khyzhun, "*Electronic structure of K$_2$SO$_4$: Cu^{2+} (3%) crystals*", XXII International seminar on physics and chemistry of solids "ISPCS 2020", Lviv, Ukraine, June 17-19, 2020.

62. V. Y. Stadnyk, R. B. Matviiv, P. A. Shchepanskyi, **M. Ya. Rudysh**, "*Refractive and spectral-baric properties of K$_2$SO$_4$ crystals doped with copper*", XXII International seminar on physics and chemistry of solids "ISPCS 2020", Lviv, Ukraine, June 17-19, 2020.

63. **M.Ya. Rudysh**, G.L. Myronchuk, A.O. Fedorchuk, M.G. Brik, M. Piasecki, "*Changing the physical properties of CuGa(S$_{1-x}$Se$_x$)$_2$ by changing the composition*", 10th

international conference "Relaxed, nonlinear and acoustic optical processes and materials" (RNAOPM 2020), Lutsk-Like Svityaz', Ukraine, June 25-29, 2020.

64. **M.Ya. Rudysh**, M. Piasecki, M.G. Brik, V.Yo. Stadnyk, G.L. Myronchuk, "*Theoretical investigation of electronic structure and physical properties of ABC$_2$ group crystals: DFT study*", International workshop for young scientists "Functional materials for technical and biomedical applications", Koropovo, Ukraine, September 7-10, 2020.

65. B. Goron, **M. Rudysh**, P. Shchepanskyi, R. Brezvin, V. Stadnyk, "*Structure and electronic levels of ammonium fluoroberyllate crystals*", International conference of students and young scientists in theoretical and experimental physics «HEUREKA-2020», Lviv, Ukraine, October 6-7, 2020.

66. **M. Rudysh**, "*Application of DFT+U method for study of the ABC$_2$ group crystals*", International conference of students and young scientists in theoretical and experimental physics «HEUREKA-2020», Lviv, Ukraine, October 6-7, 2020.

67. B. Horon, **M.Ya. Rudysh**, V.Y. Stadnyk, P.A. Shchepanskyi, R.S. Brezvin, "*Structure and electronic porperties of (NH$_4$)$_2$BeF$_4$ dielectric crystal*", IX International seminar "Properties of ferroelectric and superionic systems", Uzhhorod, Ukraine, October 27, 2020.

68. R. Matviiv, V. Stadnyk, P. Shchepanskyi, **M. Rudysh**, R. Brezvin, A. Fedorchuk, O. Khyzhun, "*Structure and refractive properties of K$_2$SO$_4$:Cu^{2+} (3%) crystals*", IX international seminar "Properties of ferroelectric and superionic systems", Uzhhorod, Ukraine, October 27, 2020.

69. **M. Rudysh**, "*Electronic structure, optical and elastic properties of AgGaS$_2$ crystals: theoretical study*", Young scientists conference on semiconductor physics «Lashkaryov's readings», Kyiv, Ukraine, April 5-7, 2021.

70. **M. Rudysh**, "*Modelling of vibrational properties of AgGaS$_2$ crystals*", III International internet conference for young researchers and students «Topical Issues of Fundamental and Applied Studies», Lutsk, Ukraine, April 12-13, 2021.

71. **M.Ya. Rudysh**, M. Piasecki, M.G. Brik, "*Investigation of electronic and elastic properties of AgGaTe$_2$ chalcopyrite crystals: DFT study*", III international internet conference for young researchers and students «Topical Issues of Fundamental and Applied Studies», Lutsk, Ukraine, April 12-13, 2021.

72. R. Matviiv, **M. Rudysh**, P. Shchepanskyi, R. Kildiyarov, V. Stadnyk, "*Influence of impurity on thermal and refractive parameters of K$_2$SO$_4$ crystals in phase transition*

region", International conference of students and young scientists in theoretical and experimental physics «HEUREKA-2021», Lviv, Ukraine, May 18-20, 2021.

73. **M.Ya. Rudysh**, A.O. Fedorchuk, V.Yo. Stadnyk, P.A. Shchepanskyi, R.S. Brezvin, B.I. Horon, A.I. Lupanov, "*Structure and properties calculation of $(NH_4)_2BeF_4$ crystals*", International conference of students and young scientists in theoretical and experimental physics «HEUREKA-2021», Lviv, Ukraine, May 18-20, 2021.

74. **M. Rudysh**, "*Elastic properties and anisotropy of I-III-VI$_2$ chalcopyrite crystals*", International conference of students and young scientists in theoretical and experimental physics «HEUREKA-2021», Lviv, Ukraine, May 18-20, 2021.

75. O. Kosteckyi, R. Brezvin, **M. Rudysh**, P. Shchepanskyi, V. Stadnyk, "*Structure and refractive parameters of β-LINH$_4$SO$_4$ crystals with manganese impurity*", International conference of students and young scientists in theoretical and experimental physics «HEUREKA-2021», Lviv, Ukraine, May 18-20, 2021.

76. P.A. Shchepanskyi, **M.Ya. Rudysh**, V.Yo. Stadnyk, R.S. Brezvin, "*Electronic structure of NaNH$_4$SO$_4$×2H$_2$O crystal*", International conference of students and young scientists in theoretical and experimental physics «HEUREKA-2021», Lviv, Ukraine, May 18-20, 2021.

77. **M.Ya. Rudysh**, G.L. Myronchuk, M.G. Brik, M. Piasecki "*Computational study of vibrational properties of AgGaX$_2$ (S =S, Se, and Te) crystals*", International conference of students and young scientists in theoretical and experimental physics «HEUREKA-2021», Lviv, Ukraine, May 18-20, 2021.

78. V. Stadnyk, P. Shchepanskyi, **M. Rudysh**, R. Matviiv and R. Brezvin, "*Phase transition in impurity crystals of potassium sulfate: refractive parameters*", XIIth international conference on «Electronics and Information Technologies (ELIT)», Lviv, Ukraine, May 19-21, 2021.

79. **M. Rudysh**, B. Horon, P. Shchepanskyi, V. Stadnyk and R. Brezvin, "*First principles calculation of band structure and physical properties of ferroelectric $(NH_4)_2BeF_4$ crystal*", XIIth international conference on «Electronics and Information Technologies (ELIT)», Lviv, Ukraine, May 19- 21, 2021.

Posters

1. V. Stadnyk, V. Kurlyak, M. Romanyuk, R. Brezvin, **M. Rudysh,** "*The influence of admixture on the optical properties of the crystals*", VI international conference

"Physics of Disordered Systems", dedicated to the 80th anniversary of Professor Yaroslav Dutchak, Lviv, Ukraine, October 14-16, 2013.

2. **M. Rudysh**, V. Kurlyak, V. Stadnyk, R. Brezvin P. Shchepanskyi, "*DFT study of electronic and optical properties of lithium ammonium sulphate*", XXth International seminar on physics and chemistry of solids, Lviv, Ukraine, September 12-15, 2015.

3. P. Shchepanskyi, V. Stadnyk, R. Brezvin, **M. Rudysh,** "*KNH_4SO_4-new crystal with isotropic point*", XXth International seminar on physics and chemistry of solids, Lviv, Ukraine, September 12-15, 2015.

4. P.A. Shchepanskyi, **M.Ya. Rudysh**, V.Yo. Stadnyk, R.S. Brezvin, M. Piasecki, "*Birefringence study of $K_{1,75}[NH_4]_{0,25}SO_4$ single crystal under the influence of uniaxial stresses*", 6th seminar "Properties of ferroelectric and superionic systems", Uzhhorod, Ukraine, November 17-18, 2016.

5. **M.Ya. Rudysh**, M.G. Brik, M. Piasecki, O.Y. Khyzun, P.A. Shchepanskyi, V.Yo. Stadnyk, R.S. Brezvin, "*Electronic band structure of α-$LiNH_4SO_4$ crystals: ab-initio DFT study and X-ray spectroscopty mesurements*", 6th seminar "Properties of ferroelectric and superionic systems", Uzhhorod, Ukraine, November 17-18, 2016.

6. P.A. Shchepanskyi, V.M. Gaba, V.Yo. Stadnyk, **M.Ya. Rudysh,** "*The influence of partial isomorphic substitution on band structure and optical parameters of $ABSO_4$ group crystals*", International conference on oxide materials for electronic engineering – fabrication, properties and applications „OMEE-2017", Lviv, Ukraine, May 29 – June 2, 2017.

7. **M.Ya. Rudysh**, A.O. Fedorchuk, M. G. Brik, M. Piasecki, I.V. Kityk, P.A. Shchepanskyi "*Structure and properties of Ag_2XS_3 (X = Si, Ge) ternary chalcogenide*", IX International scientific conference «Relaxed, nonlinear and acoustic optical processes and materials» (RNAOPM'2018), Lutsk–Lake "Svityaz", Ukraine, June 1–5, 2018.

8. P.A. Shchepanskyi, V.Yo. Stadnyk, O.S. Kushnir, A.O. Fedorchuk, R.S. Brezvin, **M.Ya. Rudysh**, M. Piasecki, "*Structure and refractive properties of $ABSO_4$-group crystals*", IX International scientific conference «Relaxed, nonlinear and acoustic optical processes and materials» (RNAOPM'2018), Lutsk–Lake "Svityaz", Ukraine, June 1–5, 2018.

9. P.A. Shchepanskyi, V.Yo. Sradnyk, **M.Ya. Rudysh**, R.S. Brezvin, M. Piasecki, "*Electronic structure of lithium sodium sulphate single crystal*", V Ukrainian-Polish-

Lithuanian meeting on physics of ferroelectrics, Uzhhorod, Ukraine, September 18-20, 2018.

10. **M.Ya. Rudysh**, M.G. Brik, M. Piasecki, "*Electronic structure, elastic and optical properties simulation of CuGa(S, Se)$_2$ chalcopyrite solid solution: DFT study*", Young scientists conference on semiconductor physics «Lashkaryov's readings», Kyiv, Ukraine, April 2-5, 2019.

Patents

1. Patent on utiluty model 128162 of Ukraine, IPC: G01N 21/39 (2006.01). Device for study of the single crystal optical quality / Stadnyk V. Yo., Gaba V. M., Sugak D. Yu., Brezvin R. S., **Rudysh M. Ya.**, Shchepanskyi P. A.; applicant and owner: Ivan Franko national University of Lviv, Lviv Polytechnik National University. – № u201801973; application 26.02.2018; published 10.09.2018, bul. № 17.

2. Patent on utiluty model 139890 of Ukraine, IPC: G01L 1/24 (2006.01). Device for measuring of the uniaxial stress / Stadnyk V. Yo., **Rudysh M. Ya.**, Shchepanskyi P.A., Matviiv R. B., Gaba V. M., Kogut Z. O., Brezvin R. S.; applicant and owner: Ivan Franko national University of Lviv, Lviv Polytechnik National University. – № u201907532; application 05.07.2019; published 27.01.2020, bul. № 2/2020.

3. Patent on utiluty model 140611 of Ukraine, IPC: G01K 11/00, G01K 11/32 (2006.01). Device for optical measuremet of temprature / Stadnyk V. Yo., Gaba V. M., **Rudysh M. Ya.**, Shchepanskyi P.A., Matviiv R. B., Brezvin R.S., Petrovych I. V.; applicant and owner: Ivan Franko national University of Lviv, Lviv Polytechnik National University. – № u201907533; application 05.07.2019; published 10.03.2020, bul. № 5/2020.

Scientific project

1. Grant number 2018/29/N/ST3/02901 „Theoretical investigation of physical properties of chalcopyrite semiconductors for solar cell applications" financed by the National Science Centre (Poland) realised from 31.01.2019 – 30.01.2022.

2. Polish-French project "POLONIUM" titled "Tailoring the optical properties of ferroelectric films at nanoscale" 2019.

Appendix 1

Atomic coordinates of CuGa(S$_{1-x}$Se$_x$)$_2$ solid solutions of different composition

X = 0

	GGA			LDA		
a, Å	5.37206			5.22581		
c, Å	10.6376			10.3653		
c/a	1.9801			1.9834		
V, Å^3	306.99			283.07		
Atom	*x*	*y*	*z*	*x*	*y*	*z*
Cu	0	0	0	0	0	0
Ga	0.5	0.5	0	0.5	0.5	0
S	0.248169	0.25	0.125	0.244399	0.25	0.125

X = 0.25

	GGA			LDA		
a, Å	5.444551			5.30847		
c, Å	10.758033			10.4910		
c/a	1.97592			1.97627		
V, Å^3	319.19			296.0302		
Atom	*x*	*y*	*z*	*x*	*y*	*z*
Cu1	-0.00084	0.00025	0.00001	-0.00336	-0.00261	-0.00004
Cu2	0.48000	0.50038	0.49987	0.49938	0.52688	0.50023
Cu3	0.48983	0.01092	0.75696	0.51374	-0.01545	0.76140
Cu4	0.00963	0.51110	0.24315	0.01077	0.51243	0.23856
Ga1	0.50159	0.49924	-0.00001	0.49659	0.49647	0.00000
Ga2	0.01349	-0.00011	0.50001	-0.00033	-0.01131	0.49996
Ga3	0.00569	0.49281	0.75537	-0.00529	0.50123	0.75487
Ga4	0.49452	-0.00690	0.24447	0.49116	-0.00473	0.24514
S1	0.24795	0.25014	0.12198	0.24196	0.24713	0.12120
S2	0.75080	0.74892	0.12182	0.74876	0.74986	0.12155
S3	0.25628	0.25001	0.62779	0.24731	0.75289	0.87844
S4	0.25116	0.74924	0.87814	0.25006	0.75382	0.87876
S5	0.74999	0.24640	0.87803	0.75305	0.25703	0.87884
S6	0.25077	0.74630	0.37200	0.25307	0.74999	0.37113
Se1	0.75058	0.25217	0.37284	0.73473	0.24687	0.37164
Se2	0.74856	0.74914	0.62758	0.75021	0.73879	0.62851

X = 0.5

	GGA			LDA		
a, Å	5.515261			5.38374		
c, Å	10.887034			10.6322		
c/a	1.97398			1.97487		
V, Å^3	331.162690			308.1689		
Atom	*x*	*y*	*z*	*x*	*y*	*z*
Cu1	-0.025970	0.00007	0.000007	-0.02462	-0.00283	0.000001
Cu2	0.48110	0.49995	0.50003	0.47493	0.49717	0.500004
Cu3	0.49747	0.01939	0.75111	0.50301	0.02484	0.74992
Cu4	0.00298	0.51949	0.24908	0.00264	0.52483	0.25009
Ga1	0.51886	0.49806	0.000058	0.51449	0.49588	0.00003
Ga2	0.01326	-0.00173	0.49992	0.01479	-0.00411	0.50003
Ga3	0.0047	0.48652	0.75068	0.0039	0.48535	0.74996
Ga4	0.49912	-0.01359	0.24912	0.50433	-0.01461	0.25011
S1	0.75398	0.74829	0.12578	0.75592	0.74704	0.12475
S2	0.25452	0.24854	0.62476	0.25587	0.24707	0.62483
S3	0.75124	0.24652	0.87392	0.75294	0.24406	0.87483
S4	0.2516	0.74582	0.37495	0.25295	0.74415	0.37475
Se1	0.24798	0.24905	0.12147	0.24155	0.24714	0.12533
Se2	0.25014	0.75181	0.87880	0.25290	0.75844	0.87501
Se3	0.75084	0.25223	0.37373	0.75287	0.25850	0.37535
Se4	0.74816	0.74957	0.62659	0.74151	0.74708	0.62501

X = 0.75

	GGA			LDA		
a, Å	5.58152			5.45080		
c, Å	11.0244			10.7586		
c/a	1.97516			1.97376		
V, Å^3	343.556			319.823		
Atom	*x*	*y*	*z*	*x*	*y*	*z*
Cu1	-0.00037	0.00004	0.00002	-0.02741	-0.00054	-0.00033
Cu2	0.48025	0.49976	0.49970	0.50170	0.49602	0.50003
Cu3	0.48915	0.01135	0.74361	0.51850	0.01416	0.76229
Cu4	0.01177	0.51160	0.25674	-0.01292	0.51096	0.23781
Ga1	0.50248	0.49921	-0.00002	0.50864	0.50023	0.00009
Ga2	0.00946	-0.00145	0.50018	0.00437	-0.00447	0.50003
Ga3	0.00809	0.49188	0.74535	-0.00132	0.49513	0.75426
Ga4	0.49510	-0.00849	0.25445	0.50581	-0.00912	0.24564
S1	0.75272	0.74861	0.12181	0.75229	0.75058	0.12088
S2	0.75090	0.24916	0.87803	0.75447	0.25293	0.87929
Se1	0.24763	0.24965	0.12623	0.24193	0.24561	0.12160
Se2	0.25260	0.24943	0.12610	0.26234	0.24520	0.12094
Se3	0.25030	0.75149	0.87411	0.24956	0.76300	0.87829
Se4	0.75028	0.25157	0.37580	0.75454	0.25680	0.37145
Se5	0.25056	0.74647	0.37339	0.24925	0.73284	0.37086
Se6	0.74913	0.74938	0.62442	0.73826	0.75066	0.62866

X = 1

	GGA			LDA		
a, Å	5.64268			5.51445		
c, Å	11.1422			10.8957		
c/a	1.9746			1.9758		
V, Å^3	354.76			331.328		
Atom	*x*	*y*	*z*	*x*	*y*	*z*
Cu	0	0	0	0	0	0
Ga	0.5	0.5	0	0.5	0.5	0
Se	0.251831	0.25	0.125	0.251831	0.25	0.125

X = 1